SEISMIC RETROFITTING OF RECTANGULAR REINFORCED CONCRETE COLUMNS WITH PARTIAL INTERACTION PLATING

By

Yu-Fei Wu

B.Sc. (Civil Engng., Zhejiang Uni., P.R. China)

M.Sc. (Civil Engng., Zhejiang Uni., P.R. China)

M.Eng. (Civil Engng., National Univ. Singapore)

A thesis presented for the degree of

Doctor of Philosophy

THE UNIVERSITY OF ADELAIDE

Department of Civil & Environmental Engineering

June 2002

STATEMENT OF ORIGINALITY

This work contains no material which has been accepted for the award of any other degree or diploma in any university or tertiary institution and, to the best of my knowledge and belief, contains no material previously published or written by another person, except where due reference has been made in the text.

I give consent to this copy of my thesis, when deposited in the University Library, being available for loan and photocopying.

Signature: _____

Date: 3/7/02

PUBLICATIONS

The following publications were written based on the work presented in this thesis.

Book chapter

RETROFITTING REINFORCED CONCRETE STRUCTURES BY STEEL OR FRP PLATING (Editor: D.J. Oehlers), Chapter 17 (authored by Y.F. Wu): Composite plated columns, John Wiley & Sons. To be published.

Refereed journal papers

Wu, Y.F., Oehlers, D.J., and Griffith, M.C. (2002). "Partial interaction analysis of composite beam/column members". *Mechanics of Structures and Machines,* scheduled for publication in Vol.30, N.3.

Wu, Y.F., Griffith, M.C. and Oehlers, D.J. (2002). "Improving the strength and ductility of rectangular RC columns through composite partial-interaction: tests". Submitted for publication to *Journal of Structural Engineering.*, ASCE.

Oehlers, D.J., Wu, Y.F. and Griffith, M.C. (2002) "Rectangular RC columns retrofitted for ductility by partial-interaction plating". Submitted for publication.

Wu, Y.F., Oehlers, D.J., and Griffith, M.C. (2002) "Numerical simulations of composite plated reinforced concrete columns". Submitted for publication to *Computers & Structures*.

Wu, Y.F., Oehlers, D.J., and Griffith, M.C. (2002) "Ductility of RC columns". In preparation.

Conference paper

Wu, Y.F., Oehlers, D.J. and Griffith, M.C. (2001). "Composite plated columns". *International Conference on FRP Composites in Civil Engineering, CICE 2001*, Dec. 12-14th, Hong Kong.

Departmental reports

Wu, Y.F., Griffith, M.C. and Oehlers, D.J. (2001). *Behavior of plated RC columns.* Research Report No.R173, Dept. of Civil & Environmental Engineering, The University of Adelaide.

Wu, Y.F., Oehlers, D.J. and Griffith, M.C. (2001) "Numerical simulation of composite plated columns", Research Report No. R172, Dept. of Civil & Environmental Engineering, The University of Adelaide.

ACKNOWLEDGEMENTS

The author wishes to express his heartfelt appreciation and gratitude to Associate Professors M.C. Griffith and D.J. Oehlers for being his supervisors for the research that is described herein. Their genuine interest in both the research project and my future career, their motivation, encouragement and intellectual supervision are sincerely appreciated. Their full support has made the past three years most productive and rewarding as well as an enjoyable stay. The new retrofit concept studied in this work was initially proposed by Associate Professor Oehlers which is specifically acknowledged.

The author would also like to thank the laboratory staff, Mr. Bruce Lucas, Mr. Gregory Atkins, Mr. David Hale, Mr Jeffrey Hiorns and Mr Steven Huskinson, in the Department of Civil & Environmental Engineering at The University of Adelaide for all their assistance with the experimental work. The laboratory technicians played an important role in the design and manufacture of the test rigs and test specimens. Special acknowledgement and thanks are due to Mr. David Hale for his full support and co-operation, excellent workmanship and intellectual input into the experimental work.

The author is also thankful to Dr. Stephen Carr and Mr Paul Carter for providing computing assistance, the departmental administrative staff, Ms. Diane Keable, Mrs. Bernice Golledge and Ms Josie Peluso, for their help throughout the course of his study.

This research work was made possible only under the sponsorship of a University of Adelaide Scholarship (UAS). The experimental work was funded by a Small Australian Research Council grant as well as the departmental financial support. All these supports are gratefully acknowledged.

The author appreciates the assistance and friendship of his fellow research scholars, academics, staff and all his friends who have made his stay during the entire period of the research a most rewarding and enjoyable one.

Special thanks are extended to his wife, daughter and son. This work is made possible only under their understanding, patience and support.

Finally, the author dedicates this thesis to his parents as a mark of respect and love.

ABSTRACT

Both steel jacketing and fibre reinforced polymer (FRP) wrapping have been shown to effectively enhance the seismic resistance of circular reinforced concrete (RC) columns by confining the concrete. However, jacketing and wrapping are much less effective in enhancing the flexural performance of rectangular shaped columns due to the ineffectiveness of the rectangular jacket in providing confinement. Although numerous efforts have been made in the literature to solve this problem, a satisfactory solution is yet to be achieved. As a new effort in tackling this problem, an alternative procedure that uses a completely different concept has been proposed and investigated in this work. This new retrofit scheme makes use of composite action by bolting plates to the column surfaces for improving the flexural strength and/or ductility of rectangular RC columns. This new composite partial-interaction plating approach does not rely on confinement to improve the strength/ductility but instead relies on the composite action between the plate and the RC column.

Numerical, mathematical and experimental works are conducted in this study to investigate the behaviour of the plated RC columns, from which the proposed retrofit scheme is found to be effective in

- increasing both the strength and ductility of RC columns; or
- increasing the ductility without significant increase in strength.

Furthermore, a simple and practical methodology is developed for engineers to design such a plating system based on the required inter-story drift ratio. Numerous theoretical breakthroughs, discoveries or improvement are made from this work.

TABLE OF CONTENTS

LIST OF FIGURES

LIST OF TABLES

NOTATION

A_b = area of stirrups of one leg

A_c = cross-sectional area of concrete

A_{ci} = cross-sectional area of sub-section 'i' of concrete

A_g = gross cross-sectional area of concrete column

A_p = cross-sectional area of plate

A_{pi} = cross-sectional area of sub-section 'i' of top/bottom plate

A_{psi} = cross-sectional area of sub-section 'i' of side plate

A_{rc} = transformed cross-sectional area of concrete of RC cross-section

A_s = cross-sectional area of longitudinal reinforcement

A_{sc} = cross-sectional area of longitudinal reinforcement at compression side

A_{si} = cross-sectional area of layer 'i' longitudinal reinforcement

A_{st} = cross-sectional area of longitudinal reinforcement at tensile side

a = thickness of concrete cover to centre of longitudinal reinforcement bar

a_0 = $\frac{L_s}{K_b}$, unit longitudinal flexibility of shear connector/bolt

a_1 = $\frac{\overline{EI}}{\overline{EA} \cdot \sum EI}$, passive slip strain coefficient

a_2 = $\frac{(h_1 + h_2)}{\sum EI}$, active slip strain coefficient

a_3 = $\frac{1}{(EA)_1}$, axial flexibility of element 1

a_4 = $\frac{(h_1 + h_2) \cdot \overline{EA}}{\overline{EI}}$, unit slip curvature

a_5 = $\frac{a_1}{a_0}$, slip resistance ability coefficient

B = breadth of column section

b = E_h / E_s, strain hardening ratio of steel

b_c = height or depth of concrete core of column section enclosed by stirrups measured from centre of stirrups

C = constant of integration

D = depth or diameter of cross-section

d = distance from centroid of stress block to compression face

d_b = diameter of longitudinal reinforcement

d_c = width of concrete core of column section enclosed by stirrups measured from centre of stirrups

d_i = distance from centre of layer 'i' to centroid of concrete section

E = modulus of elasticity

E_c = modulus of elasticity of concrete

E_c' = $\frac{f_{co}}{\varepsilon_{cu} - \varepsilon_{co}}$, slope of softening part of stress-strain curve

E_h = strain hardening stiffness of steel

E_p = modulus of elasticity of plate

E_{ph} = strain hardening stiffness of plate

E_r = modulus of elasticity of reloading branch of concrete

E_{re} = return point modulus of elasticity on monotonic stress-strain curve of concrete

E_s = modulus of elasticity of steel

E_{sec} = secant modulus of confined concrete at peak stress

E_t = tensile modulus of elasticity of concrete

E_u = initial concrete modulus of elasticity at onset of unloading

$\overline{EA}$ = defined as $\frac{1}{\overline{EA}} = \frac{1}{(E \cdot A)_1} + \frac{1}{(E \cdot A)_2}$

$(EA)_1$ = axial rigidity of element 1

$(EA)_2$ = axial rigidity of element 2

$\overline{EI}$ = $\sum EI + \overline{EA} \cdot (h_1 + h_2)^2$

$(EI)_1$ = flexural rigidity of element 1

$(EI)_2$ = flexural rigidity of element 2

$\sum EI$ = $(E \cdot I)_1 + (E \cdot I)_2$

e_c = eccentricity of compressive resultant

e_t = eccentricity of tensile resultant

F = lateral force applied at top of cantilever column

F' = lateral force at top of column considering P-Δ effect by simplified method

F_b = bolt shear force

F_{by} = yield strength of bolt in shear

F_f = longitudinal shear force on shear connectors in shear span of length x from top of column due to lateral force F only

F_n = longitudinal shear force on shear connectors in shear span of length x from top of column due to axial force N only

F_{shr} = $F_f + F_n + F_{sp}$, total longitudinal shear force on shear connectors in shear span of length x from top of column

F_{sp} = longitudinal shear force on shear connectors in shear span of length x from top of column due to non-zero boundary slip s_p only

f_c = longitudinal concrete stress

f_{co} = compressive strength (peak stress) of unconfined concrete

f_{cc} = compressive strength of confined concrete

f_{ct} = tensile strength of concrete

f_{hy} = yield strength of stirrups

f_l = lateral confining pressure of column

$f_l^{'}$ = effective confining pressure

f_{new} = new concrete stress on reloading branch at strain of ε_{un}

f_{py} = yield strength of plate

f_{re} = concrete stress at common return point from reloading branch to envelope curve in Mander's model

f_{ro} = stress at onset of reloading branch in Mander's model

f_{sy} = yield strength of steel reinforcing bar

f_t = tensile strength of concrete under monotonic loading in Mander's model

f_{un} = concrete stress at start of unloading branch in Mander's model

f_y = yield strength of steel

H = height or depth of column section

h_1 = distance from centroid of element 1 to interface

h_2 = distance from centroid of element 2 to interface

I = second moment of area

I_c = second moment of area of concrete cross-section

I_p = second moment of area of plate

I_{rc} = second moment of area of RC cross-section

K_b = elastic shear stiffness of bolt

K_{bh} = shear strain-hardening stiffness of bolt

k_e = confinement effectiveness coefficient

L = length of cantilever column

L_e = length of elastic part of member, $L_e = L - L_p$

L_i = length from top of column to section i (i = 0~n)

L_p = plastic hinge length of column

L_s = longitudinal spacing of bolts

M = moment of section

M_0 = moment at section where lateral load is applied

M_1 = moment due to element 1

M_2 = moment due to element 2

M_{bar} = moment due to reinforcement bar in composite cross-section

M_{co} = moment of cross-section when compressive strain at extreme fiber equals to ε_{co}

M_{conc} = moment due to concrete in composite cross-section

M_{cu} = moment of cross-section when compressive strain at extreme fiber equals to ε_{cu}

M_i = moment at section i (i = 1~n)

M_{plt} = moment due to plate in composite cross-section

N = axial load of column or total axial force in a cross-section

N_1 = axial force on element 1

N_2 = axial force on element 2

N_{bar} = axial force due to reinforcement bar only in an RC section

N_c = $f_{co} \cdot B \cdot D$, axial crush load of concrete section

N_{conc} = axial force on concrete

N_{cr} = compressive resultant in cross-section

N_{plt} = axial force on plate

N_{sc} = axial force in compressive reinforcement bar

N_{st} = axial force in tensile reinforcement bar

NLc = number of layer of discretised concrete section

NLp = number of layer of discretised top/bottom plate

NR = number of row of discretised concrete section

n = number of bolts

p = intensity of distributed load

Q = shear force in cross-section

Q_1 = shear force on element 1

Q_2 = shear force on element 2

q = longitudinal shear force per unit length or shear flow

R_o = experimentally determined material constant for Menegotto-Pinto model

R_s = slip radius

r = radius of curvature; or $r = \dfrac{E_c}{E_c - E_{\text{sec}}}$

s = longitudinal slip of bolt; or coordinate along length; or longitudinal centre to centre spacing of stirrups

s' = clear longitudinal spacing between stirrups

s_b = lateral deformation of bolt/shear connector

s_f = slip term due to lateral force F

s_n = slip term due to axial force N

s_p = slip at support of elastic member or top of plastic hinge

s_{pl} = slip component due to change of length of plate

s_r = plastic or residual deformation of bolt/shear connector

s_{rc} = slip component due to change of length of RC column

s_{ro} = slip component due to rotation of cross-section

s_{sp} = slip term due to non-zero boundary slip s_p

t = depth of element 1 or thickness of plate

v = lateral deflection of column

v_{full}^{F} = lateral deflection induced by lateral force F with full interaction

v_{full}^{N} = lateral deflection induced by axial load N with full interaction

w_g = longitudinal gap width between side of plate hole and side of bolt

w_i = ith clear transverse spacing between adjacent longitudinal bars

x = depth of neutral axis in a cross-section; or distance along beam; or $x = \frac{\varepsilon_c}{\varepsilon_{cc}}$; or some intermediate variable

y = y coordinate; functions

y_1 = y coordinate of focal point 1

y_2 = y coordinate of focal point 2

α = $L \cdot \sqrt{a_5}$

α_1 = experimentally determined material constant for Menegotto-Pinto model

α_2 = experimentally determined material constant for Menegotto-Pinto model

β = area coefficient of concrete stress block

Δ = lateral displacement of cantilever column

Δ_0 = top displacement of cantilever column without P-Δ effect

Δ_1 = longitudinal displacement of element 1 or RC column at centroid of cross-section

Δ_{1c} = axial shortening of element 1 at centroid

Δ_2 = longitudinal displacement of element 2 or plate at centroid of cross-section

Δ_{2c} = axial shortening of element 2 at centroid

Δ_e = lateral displacement at top of column due to elastic deformation above plastic hinge

Δ_i = lateral displacement of column at section i (i=0~n)

Δ_p = lateral displacement at top of column due to plastic hinge rotation only

Δ_y = lateral displacement at first yield of tensile reinforcement

Δ_u = ultimate lateral displacement when lateral force equals to 80% of lateral force at yield point

$\Delta\kappa$ = increment of curvature

ΔL_i = length of segment i (i=1~n)

δ = d/x, centroidal relative height

ε = strain

ε_o = (when used in Menegotto-Pinto model) strain at point where two asymptotes of branch under consideration meet

ε_1 = strain of element 1 at interface

ε_{1c} = strain at centroid of cross-section of element 1 or RC column

ε_2 = strain of element 2 at interface

ε_{2c} = strain at centroid of cross-section of element 2 or plate

ε_a = common strain at intersection of initial tangent and plastic unloading slopes

ε_c = longitudinal strain of concrete

ε_{co} = strain at maximum stress f_{co} of unconfined concrete

ε_{cc} = strain at maximum stress f_{cc} of confined concrete

ε_{cs} = strain of concrete on the plate/concrete interface

ε_{cu} = ultimate compressive strain of concrete

ε_{i} = strain at layer number i of section

ε_{pl} = plastic strain of concrete in Mander's model

ε_{ps} = strain of plate on the plate/concrete interface

ε_{py} = yield strain of steel plate

ε_{r} = (when used in Menegotto-Pinto model) strain at point where last strain reversal with stress of equal sign took place

ε_{re} = concrete strain at common return point from reloading branch to envelope curve in Mander's model

ε_{ro} = strain at onset of reloading branch in Mander's model

ε_{s} = steel strain

ε_{sc} = strain of reinforcement bar at compression side

ε_{slp} = slip strain

$\varepsilon_{s\max}$ = ultimate fracture strain of steel

ε_{sp} = strain at which cover concrete is considered to have completely spalled and ceases to carry any stress

ε_{st} = strain of reinforcement bar at tension side

ε_{sy} = yield strain of steel reinforcing bar

ε_{t} = tensile rupture strain of concrete = f_t / E_c; strain at tension face

ε_{un} = concrete strain at start of unloading branch in Mander's model

ε_y = yield strain of steel

κ = curvature of section

κ_{co} = curvature of section when extreme compressive fiber reaches yield strain ε_{co}

κ_{cu} = ultimate curvature or curvature of section when extreme compressive fiber of concrete reaches ultimate strain ε_{cu}

κ_i = curvature of section i (i=1~n)

κ_{scy} = curvature of section when compressive steel first yields

κ_{sty} = curvature of section when tensile steel first yields

μ = Poison's ratio; ductility factor

θ = rotation of a cross-section; inter-storey drift ratio

θ_p = rotation of plastic hinge

ρ_{cc} = ratio of area of longitudinal reinforcement to core of section

ρ_s = volumetric ratio of transverse reinforcement

σ = stress

σ_o = (when used in Menegotto-Pinto model) stress at point where two asymptotes of branch under consideration meet

σ_1 = axial or longitudinal stress

σ_2 = lateral or transverse stress

σ_c = stress of concrete

σ_{ci} = stress of concrete sub-section 'i'

σ_p = stress of plate

σ_{pi} = stress of top/bottom plate sub-section 'i'

σ_{psi} = stress of side plate sub-section 'i'

σ_r = stress in transverse radial direction;

(when used in Menegotto-Pinto model) stress at point where last strain reversal with stress of equal sign took place

σ_s = stress of longitudinal reinforcement bar

σ_{si} = stress of reinforcement layer 'i'

ξ = $\frac{x}{L}$, normalized coordinate x; variable of integration; plastic strain of last excursion when used in Menegotto-Pinto model

Symbols:

Δ = point when concrete on the tension face first cracks

$\times$ = point where f_{co} at ε_{co} attained at compression face of concrete

$+$ = onset of yielding of tension reinforcing bars

$\divideontimes$ = onset of yielding of compression reinforcing bars

$\Diamond$ = crushing of concrete at ε_{cu} at compression face

$-$ = crushing of concrete at ε_{cu} adjacent to compression reinforcing bars

$\blacksquare$ = onset of yielding of one bolt

$\bullet$ = yielding of all bolts

$\blacktriangle$ = yielding of plate in the whole bottom cross-section

$\blacklozenge$ = tensile yielding of compression reinforcing bars

CHAPTER 1 INTRODUCTION

1.1 BACKGROUND

Many existing reinforced concrete structures that were designed and constructed prior to the adoption of modern earthquake resistance design codes are vulnerable to the attack of an earthquake above the moderate scale. It has been repeatedly highlighted overseas as well as in Australia in recent earthquake experience that a large percentage of the buildings and elevated freeway/bridge structures that collapsed were designed and constructed before the application of modern earthquake codes (Melchers1990; Moehle and Mahin 1991; Blong 1993; Pham and Griffith 1995; Bracci et al. 1995a & b; Lynn et al. 1996; Seible et al. 1997; Park 2001). Therefore, "*The improvement of the seismic performance of vulnerable buildings is an urgent issue. Undoubtedly, seismic retrofitting before an event is one of the most essential strategies to mitigate disaster.*" (CEB report 1997)

Particularly vulnerable are reinforced concrete columns resulting from the then typically used nominal and inadequately detailed transverse reinforcement (Park 2001). Bridge columns in the U.S. that were designed before the 1971 San Fernando earthquake typically involved the use of No.4 (12.7mm diameter) transverse peripheral hoops placed at 12 in. (305mm) centers for both circular and rectangular columns, regardless of the column section dimension (Chai et al. 1991). These hoops were often closed by lap

splices in the cover concrete instead of being lap-welded or anchored by bending back into the core concrete. As a result, the ultimate curvature that can be developed within the potential plastic hinge region is limited by the strain at which the cover concrete begins to spall, which is typically around 5% strain. The hoop steel unravels when the longitudinal strain is higher than 5%, resulting in the loss of the small confinement and shear strength. Although the diameter and spacing of the hoops varies somewhat for different structures in different countries, insufficient transverse reinforcement and inadequate detailing are typical of pre-1971 building and other structures all over the world. Structures with such columns cannot satisfy the high ductility demand and will fail prematurely during a significant seismic event.

An experimental study at the University of California at Berkeley by Lynn et al. (1996) on eight full-scale RC columns with typical pre-1971 detailing, which was based on a survey of buildings built from 1919-1970, confirmed these observations. Research outside the US also indicated that most of the existing ground floor columns were expected to fail under a strong earthquake due to inadequate flexural ductility and brittle shear failure (Dritsos 1997). Therefore, retrofitting columns, a critical element of structures, is especially important in the rehabilitation of existing structures.

Three potential failure modes exist in existing RC columns with inadequate transverse reinforcement under seismic load (Seible et al. 1997). The first failure mode is the shear failure as shown in Fig.1.1, where inclined cracking, cover concrete spalling, rupture or opening of transverse reinforcement, bucking of longitudinal reinforcement, and disintegration of the concrete core develop sequentially in an earthquake. The second failure mode is the flexural plastic hinge failure due to large displacements incurred

where, subsequent to flexural cracking, cover concrete crushing and spalling, buckling of the longitudinal reinforcement, or compressive failure of the core concrete, initiates plastic hinge deterioration. Fig.1.2 shows a typical failure case of the flexural failure mode.

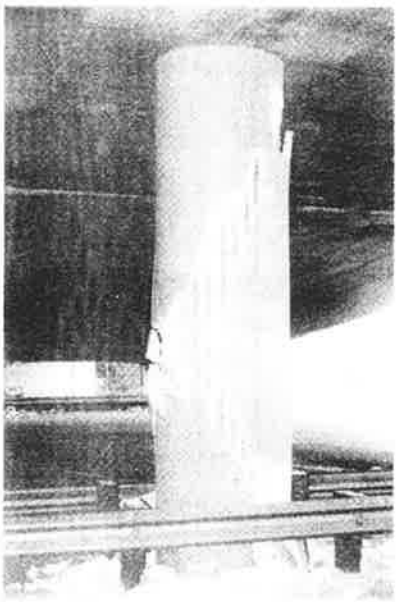

Fig. 1.1 Typical shear failure of columns in an earthquake (Seible et al. 1997)

Fig. 1.2 Typical flexural plastic hinge failure of columns (Green, 1987)

Thirdly, many existing columns have lap splices of the longitudinal reinforcement at the bottom where both the maximum flexural moment and potential plastic hinge occur. The lap length of the longitudinal bars in pre-1971 structures was typically designed as a compressive lap of usually 20 times the longitudinal bar diameter, which was insufficient for development of the tensile yield strength under load reversal due to seismic load. Lap splice debonding occurs once vertical cracks develop in the cover concrete and progresses with increased transverse dilation of the column and cover concrete spalling, associated with rapid degradation of strength and deformation capacity. Even lap-splices in a plastic hinge region that satisfy modern design code requirements invariably break down under cyclic inelastic action in a severe seismic event (Priestley & Seible, 1995).

One successful and widely implemented technique for retrofitting RC columns involves the use of steel or FRP (Fiber Reinforced Polymer) jackets, which wraps a layer of steel or FRP plate on the external face of the column to provide additional external hoop action in the transverse direction. This technique is effective in enhancing the shear strength of existing substandard columns by providing additional shear reinforcement with the jacket. The deformation capacity of plastic hinges can also be increased dramatically through external confinement to the core concrete by an external jacket. The confinement to a column's external face can prevent cover concrete spalling and buckling of longitudinal reinforcement, and most importantly, enhance the concrete strength and deformation capacity, as shown in Fig.1.3, hence improve the ductility performance. The ultimate compressive strain of unconfined concrete, at about 0.005, is insufficient to enable displacement ductility factors greater than 2.5 to 3.5 to develop (Priestley and

Seible, 1995), and typical ultimate compressive strain in the extreme fiber as high as 0.01 to 0.02 is needed to ensure satisfactory seismic response which can be achieved by jacketing. For the third failure mode, confinement in the form of jacketing can again be used to increase the bond of the longitudinal reinforcement by providing an external clamping pressure on the longitudinal bars to prevent them from slipping.

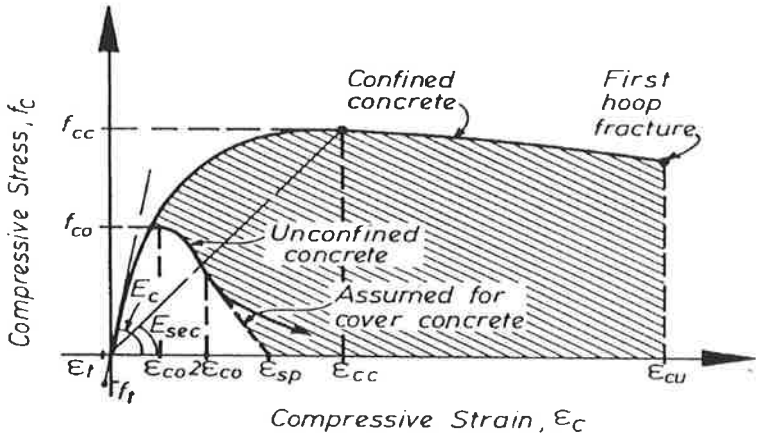

Fig. 1.3 Stress-strain relation for confined and unconfined concrete (Mander et al. 1988a)

Theoretical and experimental studies have already proved that external jacketing is highly effective in preventing existing columns from failure for all the above three failure modes in the case of circular columns. Therefore, this kind of retrofitting work has already been widely used in engineering (Chai et al. 1991&1994; Priestley et al. 1994b&c).

In the substructure retrofit program implemented by the California Department of Transportation (Caltrans) in the late 1980's, bridge columns with pre-1971 details for 1100 state-owned bridges and 1500 city- or county- owned bridges, to which a prime concern was the lack of adequate confinement, were scheduled for retrofit for the

estimated cost between US$420 million and $550 million (Chai et al. 1994). Steel jacketing was used extensively for the retrofitting of these columns. The effectiveness of steel jacketing was evident in the field in the 1994 Northridge Earthquake. An estimated sixty retrofitted bridges, many of which had been steel jacketed, were located in the region of intense ground shaking with peak ground acceleration exceeding 0.25g. None of the steel-jacketed columns were reported to have sustained any significant damage. In contrast, two adjacent un-retrofitted bridge structures collapsed due to column failures during the earthquake (Chai, 1996).

Successful application of column jacketing in the retrofit work of an existing building was also reported in Los Angeles (Elhassan and Hart, 1995). The building was a seven-story hotel with 2-story basement located in the City of Los Angeles. During the Magnitude 7.5 Landers Earthquake of 28 June 1992, centered 175 km away from the building, many of the ground floor columns suffered significant diagonal cracks. In the rehabilitation work, the ground floor story columns were retrofitted with fiberglass/epoxy composite jackets. This seismic retrofit scheme was completed a few weeks before the occurrence of the Northridge Earthquake of 1994, and the building suffered no damage during the earthquake.

However, jacketing with steel or FRP plate is not always as effective for square/rectangular columns as it is for circular columns. While it is still very effective in enhancing the shear capacity (Priestley et al. 1994b&c), the square/rectangular jackets provide less confinement to the concrete core inside compared to that for circular columns and so are less effective for the second and third failure modes. The reason is simple: the lateral dilation of concrete under compression must increase the perimeter

length of a circular jacket/wrap, as the circular shape encloses the maximum cross-sectional area for a given perimeter length. The change of perimeter length mobilizes the hoop resistance of the jacket/wrap to provide an effective confinement to the enclosed concrete. In contrast, it is theoretically possible for the perimeter length of a rectangular shaped jacket/wrap not to increase in spite of lateral dilation of the concrete, as a small change in the shape of the cross-section from the original rectangular shape towards a circular shape will provide sufficient room for the dilation to occur without hoop action being mobilized. In practice, even if the perimeter length of the rectangular section does increase due to the dilation effects, the confinement stresses are concentrated at the corners of the cross-section rather than being uniformly distributed around the cross-section, as shown in Fig.1.4, because of the straight-sided cross-section. Therefore, "*A rectangular thin steel jacket would not be so effective, due to the sides bowing out when dilation of the concrete occurs during a major earthquake, resulting in confinement applied mainly in the column corners.*" (Park 2001).

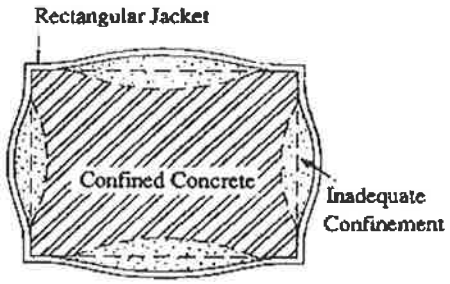

Fig. 1.4 Confinement from rectangular jacket (Priestley et al. 1994b)

The poor performance of rectangular jackets in confining the concrete core has already been experimentally verified (Chai et al. 1990; Mirmiran et al. 1998; Pessiki et al. 2001). However, there were also test results showing that effective confinement could

still be achievable with rectangular jacketing (Wang and Restrepo 2001; Parvin and Wang 2001; Chaallal and Shahawy 2000). Nevertheless, the general understanding is that jacketing for rectangular columns is more effective with smaller columns and thicker jackets and less effective for larger columns. The corner radius in a cross-section plays an important role in confining the concrete core (Mirmiran et al. 1998). It was also concluded that significantly more research work is necessary to investigate the effect of cross-section shape and size (Rochette and Labossière 2000; Pessiki et al. 2001).

Efforts to improve the confinement effectiveness of rectangular jackets have been reported in the literature. One technique was to enhance the out-of-plan flexural stiffness of the jacket by using additional stiffeners in the cross-section. However, test results showed that the improvement was not satisfactory (Chai et al. 1990). Corrugated steel jackets were also investigated to improve the out of plan flexural strength of the jacket by undulating the steel plate (Tomii 1993). The test results by Ghobarah et al. (1996; 1997) on beam/column joints strengthened with corrugated steel jackets exhibited increased shear strength of joints, whereas improved confinement to the concrete was also expected. Nevertheless, regardless of negative or positive conclusions on these techniques, it seems that no further research effort in this direction was made and no application of these techniques in practice has been found in the literature.

Another technique used for rectangular column jacketing employs an elliptical shaped jacket. Research works has shown that this technique is highly effective, and is therefore recommended for retrofitting of RC columns with rectangular shaped section (Priestley et al. 1994b; 1995). Nevertheless, changing square or rectangular shaped column sections to circular or elliptical sections by circular or elliptical jacketing is not

always desirable or practical in engineering. The major problem with this technique is that it changes the size and shape of the original columns significantly. A square/rectangular shape may still be the most suitable with respect to having the minimum disturbance to the original design both architecturally and structurally. A good example was the Bixby Creek Bridge in California, where due to its historic nature, the overall structure and member geometry had to be maintained for aesthetic purposes, thereby disallowing the use of circular or elliptical steel shell jacketing (Karbhari 2000).

Tens of thousands of existing large columns were urgently retrofitted by square/rectangular steel jacket after the 1995 Kobe earthquakes in Japan (Uehan and Meguro, 2000), regardless of the lack of (or immaturity of) design guidelines. Therefore, further research on retrofitting of square/rectangular RC columns is still necessary in order to reduce/prevent loss of human life and properties from future earthquake damage.

1.2 OBJECTIVE AND SCOPE OF WORK

As a new effort to tackle the problem of retrofitting square/rectangular RC columns and to avoid the difficult task of providing confinement to rectangular RC columns, a new composite partial-interaction plating system is introduced and studied in this work. A detailed description of this new retrofitting system and the research framework is given in Chapter3.

In general, mathematical, numerical and experimental tools are used to study the behavior of the new retrofitting system in this work. As no existing software is available for this specific complicated structural system, a numerical model and the corresponding computer program has been developed in this study to calculate the response of the

proposed system, which are reported in Chapter 4 and 5. The mathematical study in Chapter 6 &7 provides a better understanding of the fundamental mechanism of this structural system. Experimental works have also been conducted to verify the results and conclusions drawn from the theoretical studies that are reported in Chapter 9-11. Furthermore, a methodology for the design of the composite plating system is developed for engineering application that is presented in Chapter 8.

CHAPTER 2 LITERATURE REVIEW

A general review of the literature for the seismic retrofit of RC columns by jacketing is undertaken in this chapter to provide an overview of the structural retrofit history and technologies. More detailed reviews and discussions on related subjects are given elsewhere in respective chapters in this thesis.

The 1971 San Fernando earthquake caused the complete collapse of five, and serious damage to another 37, modern and apparently well-designed concrete freeway bridges (Priestley & Park, 1987). The lesson of this earthquake raised serious concerns over the seismic design philosophy embodied in the then existing design codes. An upsurge in research interest into the seismic behavior of concrete bridge structures has since sprung up in U.S., New Zealand, Japan and other countries.

Subsequently, a major funded research program started in the University of Canterbury, New Zealand headed by Professor R. Park, under the sponsorship of the New Zealand National Roads Board. As a pioneer work, fundamental problems such as the compression characteristics of confined concrete, flexural strength, shear strength and ductility of concrete columns were investigated (Priestley & Park, 1987). Particular emphasis and significant achievement was made on quantifying the influence and effectiveness of lateral confining steel (stirrups) in the plastic hinge region of RC columns in increasing ductility (Mander et al. 1988a & 1988b; Watson and Park 1994; Watson et al. 1994). In the mean time, research work on retrofitting of RC structures

were also conducted (Rodriguez and Park 1994; Hakuto et al. 1995; Liu and Park 2001; Wang and Restrepo 2001).

In the U.S., research emphasis was primarily directed towards the development of sophisticated time-history analysis techniques for bridges. The California Department of Transportation (Caltrans) embarked on an extensive bridge seismic assessment and retrofit program, which was based on ongoing experimental and analytical research being conducted at several institutes. A major research program was started in 1987 at the University of California at San Diego to study the various problems related to seismic response and retrofitting of bridge columns, headed by Professor M.J.N. Priestley. Substantial experimental and theoretical research on column jacketing with steel plates and other advanced composite materials has shown that circular or elliptical shaped steel jacketing was highly effective in enhancing the shear and flexural performance of existing substandard RC columns.

In the University of Texas at Austin, extensive research work has been conducted on retrofitting of existing non-ductile reinforced concrete moment-resisting frames featuring "strong beam-weak column" and non-ductile detailing, headed by Professor J.O. Jirsa. Research focused on the retrofit of frame joints (Alcocer and Jirsa 1993, Alcocer 1993) and inadequate lap splice of reinforcement in RC columns (Valluvan et al. 1993; Aboutaha et al. 1996).

In Japan comprehensive experimental and theoretical studies has been reported since the 1970's on concrete filled tubular (CFT) columns which were closely related to steel-jacketed RC columns. Significant progress was made in understanding the effect and effectiveness of confinement to the core concrete by the external steel tubes (jackets),

especially for square tubes, by the research group in Kyushu University headed by Professor Tomii and Professor Sakino.

In Australia, little work has been reported in the literature on the subject of retrofitting of existing RC columns. However, active research and significant progress have been made in a related subject – design of new concrete filled tubular columns (Bridge 1976; Bradford and Gilbert 1990&1992; Rangan 1991; Bradford 1991; Bridge and Webb 1992; Rangan and Joyce 1992; Bradford and Nguyen 1994; Bridge et al. 1997; Kilpatrick and Rangan 1997&1999; Bradford et al. 1999; O'Shea and Bridge 1999&2000; Uy 2000&2001).

2.1 EXISTING RETROFITTING METHODS

In engineering practice, there are several traditional ways to retrofit/repair an existing RC column. These traditional methods usually involve the application of an additional layer of concrete, steel plate or other material onto the external face of an existing RC column (Frangou et al. 1995; Ramirez 1996; Dritsos 1997). The retrofitting methods can be categorized, based on the additional material used, as follows:

1. Concrete jacketing

This retrofit/repair method applies an additional layer of concrete together with additional longitudinal and transverse reinforcement onto the surface of the existing columns, as shown in Fig.2.1. Concrete jacketing was widely used in Mexico City after the 1985 earthquake. It was the most popular jacketing method all over the world for strengthening of existing RC building columns. However, this retrofit method was found to be very

labor intensive (Park 2000). In addition, it significantly increases the size as well as stiffness of the existing columns.

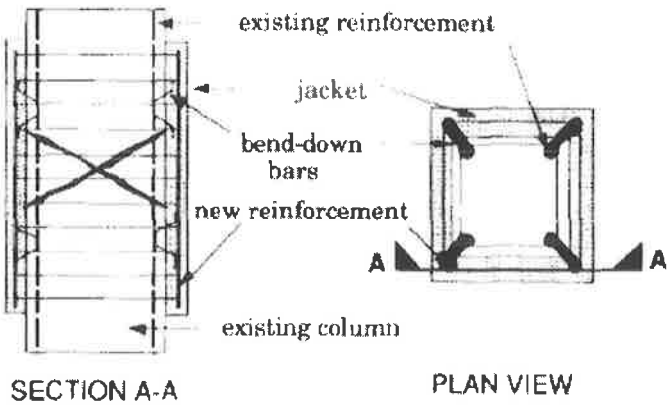

Fig. 2.1 Concrete jacketing (Frangou et al. 1995)

2. Steel jacketing

Steel jacketing is currently the most common retrofit technique (Tamai et al. 2000). There are many kinds of steel jacketing. It usually involves the use of steel plates, steel strips or steel bars in the transverse direction, which can be broken down further into two main approaches: steel encasement or steel caging.

For steel encasement, the RC column is encased or wrapped by a layer of steel plate around the external face of the column. In construction, two half-circle shells (for circular columns) or two L-shaped plates (for square/rectangular columns) are placed around the column and then site welded to provide a continuous jacket. The small gap between the steel plate and column face is normally pressure grouted with non-shrink grout subsequently to ensure a firm contact. Another popular method of steel jacketing involves the use of steel angles placed at the corners of the column. Steel plates are then

welded to the angles to form a jacket. Gluing steel plates to the face of the column using epoxy resin and site welding joints is also a common practice.

Steel caging consists of longitudinal angle sections at each corner of the column and transverse steel strips or bars. Transverse steel strips are welded onto the angle to create collars around the concrete column, as shown in Fig.2.2. The tie strips can be laterally stressed to ensure a tight fit by special wrenches prior to welding or pre-heated to about 200-400 degree before welding and left to shrink in cooling after welding. The spaces between the cage and column can be filled with cement or epoxy mortar. A cover of concrete or shotcrete reinforced with light welded fabric is usually also applied for corrosion or fire protection. Alternatively, the longitudinal steel angle may be omitted and thin steel strips or wires can be wrapped in a continuous spiral or in discontinuous rings around the column. A new technique, which involves pre-tensioning of steel strips around the column using standard strapping machines found in the packing industry and subsequently securing them in place by metal clips, has recently been developed for wrapping steel strips to columns (Dritsos 1997).

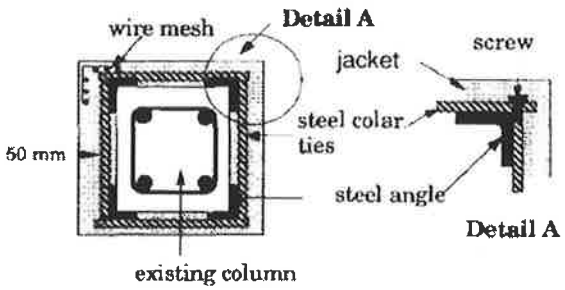

Fig. 2.2 Steel caging (Frangou et al. 1995)

The main advantages of steel jacketing are minimal increase in cross-sectional dimensions, minimal skilled labor required for application and speed of installation. The

cost of structural intervention and interruption of use is also brought to a minimum (Dritsos 1997).

3. Composite jacket

Advanced composite materials such as fiberglass and carbon fiber jacket/wrapping have been investigated to replace steel jackets in recent years (Fardis and Khalili 1981; Katsumata et al. 1988; Saadatmanesh et al. 1994&1996; Karbhari and Eckel 1994; Priestley and Seible 1995; Nanni and Bradford 1995; Seible et al. 1997; Xiao and Ma 1995&1997; Mirmiran and Shahawy 1997; Hanna and Jones 1997; Xiao et al. 1999; Saafi et al. 1999; Teng et al. 2000; Liu et al. 2000; Pantelides et al. 2000; Machida et al. 2000; Green 2000; Bonacci 2000; Banthia 2000; Karbhari 2000&2001; Fam and Rizkalla 2000; Thériault and Neale 2000; Yao et al. 2001; Lau and Zhou 2001; Pessiki et al. 2001; Parvin and Wang 2001). As compared to concrete and steel jacketing, composite jacketing has advantages in speed and ease of installation, reduced maintenance, high strength and better fatigue performance, as well as light weight and superior durability.

The retrofit of existing structures using fiber reinforced polymer (FRP) has been adopted for more than a decade in Japan (Arockiasamy 2000) with its first application to column wrapping in the mid 1980s. There have been many reports on retrofitting of RC columns using FRP jacketing since then. An increased interest in the research on composite jacketing has been found in the literature in recent years. It was found that jacketing with advanced composite materials can be economically competitive to the widely accepted procedure of steel jacketing, particularly where access was difficult, since in many cases, hand lay up procedures were used (Priestley and Seible 1995; Hwang and Wehnes 1997). Successful applications in engineering were also reported in

the retrofit of bridge piers (Gergely et al. 1998) and building columns (Elhassan and Hart 1995; Hwang and Wehnes 1997).

Although FRP is expected to become the material of choice for retrofitting/repairing in the future (Demers and Neale 1999), widespread application is yet to come mainly due to the high cost of the material (Dritsos 1997) and unfamiliarity of engineers with composites and the current lack of design guidelines (Karbhari and Gao 1997).

More detailed review on the above retrofitting methods is presented in the following sections.

2.2 CONCRETE JACKETING

Experimental work on strengthening (before damage) and repair (after damage) of RC columns and frames by concrete jacketing were conducted in the Middle East Technical University, Turkey as early as in 1986 (Ersoy et al. 1993). Square RC columns with concrete jacketing were tested under uniaxial load, axial load combined with monotonic bending, and axial load combined with reversed cyclic bending. It was found that for axially loaded columns the repair and strengthening of RC columns were effective when the jacketing was introduced after unloading. Columns strengthened under load also behaved well. However, repair under load was not very successful. For transverse load tests, the repair and strengthening jackets behaved well both under monotonic and reversed lateral cyclic loadings.

An experimental study on concrete jacketed rectangular RC columns conducted in the University of Canterbury (Rodriguez and Park 1994) showed that existing columns

with major deficiencies of inadequate transverse reinforcement could be retrofitted (before damage) or repaired (after damage) with this technique, which converted the original low ductility and fast degradation performance under cyclic load to a ductile manner with higher strength and much reduced strength degradation. This technique was found to be successful but labor-intensive. It also required an interruption in use of the structure while work was carried out and the column size was increased significantly.

Concrete jacketing of rectangular RC columns for a two story waffle-flat-plate structure at one-third scale was tested by Rodriguez and Santiago (1998). Test results showed the high flexibility and low measured displacement ductility capacity of the structural system.

2.3 JACKETING OF CIRCULAR COLUMNS WITH STEEL OR COMPOSITE JACKETS

The first phase of a Caltrans funded project, conducted at the University of California at San Diego, investigated the enhancement of the inadequate and undependable flexural strength and ductility capacity of tall flexure dominated bridge columns by encasing the plastic hinge region of the columns with steel jackets. Chai et al. (1991) conducted flexural tests on six 40% scale model (diameter D = 610mm, 3.657m high) bridge columns. The test results indicated that retrofit of pre-1971 columns with cylindrical 4.76 mm thick ASTM A36 (f_y=248MPa) hot-rolled steel jackets enabled the column to develop a dependable ductility factor of $\mu \geq 7$, or a corresponding drift ratio exceeding 5%. Displacement ductility in the range of 4-6 might be anticipated under extreme seismic response (Priestley et al. 1995). The response of the retrofitted column thus

indicated very satisfactory performance. The jacket was only provided in the potential plastic hinge region at the bottom of the column with a length of 1219mm ($2\times D$). An axial load of 1779KN, corresponding to 17% of the design column crush load or $0.17A_g \cdot f_{co}$, was applied to the test column. Bond failures that might otherwise develop in 'as-built' circular columns detailed with inadequately lapped longitudinal reinforcement were also prevented by steel jacketing. As compared to the complete loss of cover concrete in the lap-splice region and bond failure of longitudinal reinforcement of the un-retrofitted reference column, failure of the test column was eventually by low-cycle fatigue of the longitudinal reinforcement, a phenomenon associated with fracture at a strain lower than that obtained under monotonic load when subjected to large inelastic displacement cycles.

Figure 2.3 shows the typical hysteretic response of the retrofitted and un-retrofitted reference columns. It can be seen that both ductility and the energy dissipation capacity were significantly increased in the retrofitted columns. Design guidelines on the jacketing details to satisfy the strength and ductility requirements were also developed from their theoretical and experimental studies (Chai et al 1991).

Taylor and Stone (1994) theoretically studied the required thickness of circular steel jackets based on time history inelastic analysis of bridge columns and a cumulative damage index concept. Their study showed that even a very thin steel jacket (2mm jacket for columns with diameters of 610mm, 920mm, 1220mm, 1520mm) is sufficient to maintain the column within acceptable damage limits for important structures.

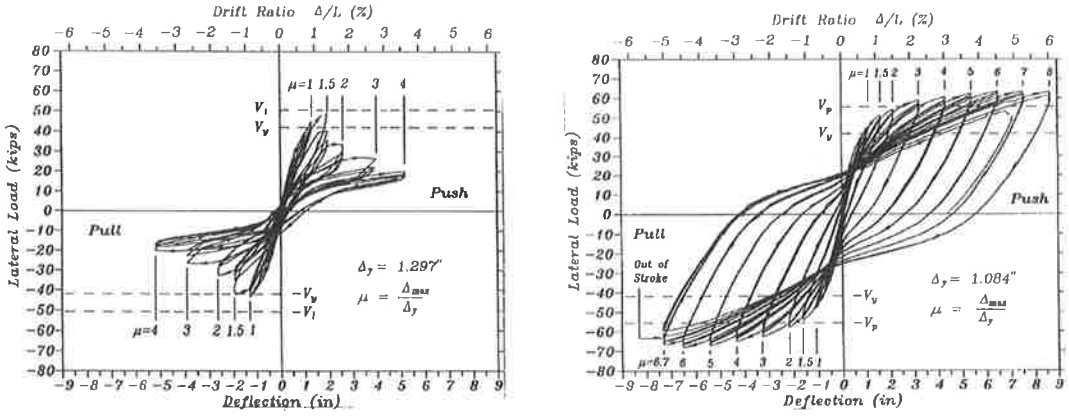

(a) Reference column (b) Jacketed column

Fig. 2.3 Comparison of hysteretic response of circular RC columns (Chai et al. 1991)

After the study of flexure dominated bridge columns, squat and shear dominated bridge columns were investigated at UC San Diego (Priestley et al. 1994b&1994c). Theoretically, the jacket was conservatively idealized as a series of independent closely spaced peripheral hoops. The experimental work showed that properly designed steel jackets on squat columns subjected to double bending could convert brittle shear failures to ductile flexural modes of inelastic deformation with remarkable ductility capacity.

Jacketing of existing RC circular columns was even found to be effective in improving the survivability of buildings from attacks by explosives (Crawford et al. 1997). Abundant research work has also been reported in the literature on FRP jacketing of circular columns (Toutanji 1999; Demers and Neale 1999; Thériault and Neale 2000). Its effectiveness in increasing the strength and ductility of circular RC columns is indisputable.

2.4 JACKETING OF SQUARE/RECTANGULAR COLUMNS WITH STEEL OR COMPOSITE JACKETS

Rectangular shaped jackets are as effective as circular shaped jackets in enhancing the shear capacity of RC columns (Priestley et al. 1994b&c; Aboutaha et al. 1999). Although rectangular jackets provide full effectiveness for shear retrofit, only limited enhancement of flexural ductility is provided by rectangular jackets due to its ineffectiveness in providing confinement, a conclusion that has been well established in the literature.

Tomii et al. (1987 as referred by Priestley et al. 1994b) investigated the flexural behavior of steel-jacketed short columns in building structures. To avoid the buckling of the jacket observed by Sakino and Ishibashi (1985), the jacket was deliberately debonded from the existing column ensuring that the jacket acted only as hoop reinforcement rather than also participating in flexure. Satisfactory results were obtained for circular columns. However it was found that a degradation of the response was inevitable for rectangular columns confined by rectangular jackets, even when very thick jackets were used. This was considered to be due to the inadequate confinement of the concrete and compression reinforcement in the flexural plastic hinge region rather than due to inadequate shear strength.

Three kinds of jacket have been tested for rectangular columns by Chai et al. (1990). The test columns were a cantilever type fixed at the bottom and free at top with a cross section of 19.25" by 28.75" (489mm by 730mm). The reinforcement detail was typical of the mid 1960s construction and lap spliced at the bottom. One jacket was an elliptical steel jacket made of 3/16 inch (4.8mm) thick steel plates. In this case, the space

between the rectangular column and elliptical jacket was filled with normal weight concrete. The second was 3/16 inch (4.8mm) thick rectangular steel jacket with orthogonal stiffeners. The third was a grouted steel collar made from channel section. All steel jackets were 48 inches (1219mm) in height and terminated slightly short of the adjoining footings. Specimens were tested under reversed quasi-static cyclic load at the top and a compressive axial load equivalent to $0.1A_g \cdot f_c$. The elliptical retrofitted column behaved well up to a 3.75% drift ratio. The steel channel retrofitted column showed an acceptable response up to 2.75% drift ratio. However the stiffened rectangular steel jacket showed rather poor response compared to the other two jackets. This poor response was attributed to the inability of the jacket to provide adequate confinement due to the poor out of plane flexural stiffness of the jacket.

Mirmiran et al. (1998 and 2000) systematically studied the square shape effect of composite jackets experimentally and theoretically. Twelve square section specimens of 152.5mm×152.5mm×305mm(tall) were tested under uniaxial compressive load together with 30 ϕ152.5mm×305mm(tall) cylindrical specimens. Square section jackets were shown to be generally less effective in confining concrete than circular ones. It was found that the confinement effect by a square section can be quantified by a shape factor of *2r/D*, where *r* is the corner radius of the square jacket and *D* is the depth of the concrete cross-section. Therefore, for a square jacket with a sharp corner (*r=0*), the confinement effect is zero or the jacket does not provide any confinement to the concrete inside. When the shape factor drops below 0.3 (in this case, the curved corner surface area is less than 34% of the flat surface area), a sharp decrease of hoop stress occurs. The same

observation was also made by others (Frangou et al. 1995; Rochette and Labossière 1996&2000).

Thériault and Neale (2000) concluded that the confinement effectiveness by FRP wrap is far less for rectangular columns than it is for circular columns. The gain in strength provided by FRP rectangular jackets is therefore very small compared to that attainable by circular jackets.

Pessiki et al. (2001) conducted full scale concentrated load tests on FRP jacketed columns including four 457mm square by 1830mm tall RC columns. The corners of the columns were rounded to a radius of 38mm. The test results showed that the confinement effect from the FRP jacket was significantly lower for the square columns compared to the circular columns.

However, some successful retrofitting of RC columns with rectangular FRP jacket has been reported in the literature (Xiao and Ma 1995; Katsumata et al. 1988).

The experimental work by Seible et al. (1997) found that for columns with side dimensions of depth/width=0.75m/0.5m, rectangular composite jackets with twice the theoretical thickness derived with their design guidelines for an equivalent circular column diameter performed well up to the design target ductility levels. However, it was also suggested that extrapolations beyond the tested side aspect ratios and side dimensions need to be supported by additional tests or analysis. The suggestion that additional confinement to square/rectangular columns can possibly be achieved by using more wrapping layers to compensate for the shape deficiency has also been made by Rochette and Labossière (2000).

It was observed by Demers and Neale (1999) that FRP wrapped square specimens showed increases in ductility comparable with those obtained for circular specimens. However, the maximum strength levels of these square specimens showed very little improvement over those of the un-wrapped specimens. However, significant enhancement on both strength and deformation capacity by square/rectangular FRP jacketing was reported by Parvin and Wang (2001); Wang and Restrepo (2001) and Chaallal and Shahawy (2000).

Due to the large scatter in experimental results and very limited data available in the literature (Thériault and Neale 2000), it was concluded that significantly more research is necessary to investigate the effect of cross-sectional shape and size (Rochette and Labossière 2000; Pessiki et al. 2001). It was also suggested that at the present time a conservative approach be used in considering the effectiveness of confinement provided by the rectangular jacket (Thériault and Neale 2000).

Different techniques have been reported in the literature to improve the confinement effect of rectangular columns from steel jacketing. Extensive tests in UC San Diego established that elliptical jackets could provide excellent enhancement of flexural performance of inadequately confined columns, since continuous confinement was provided by hoop membrane action in the jacket in the same way as in circular jackets. It was therefore recommended that oval shaped jackets or bolsters be used for the retrofitting of rectangular columns (Priestley et al. 1994b; Priestley and Seible 1995).

However, it is easy to imagine that the oval shaped jacket will lose it effectiveness when the one side of the rectangular cross-section is much longer than the other side. Experimental work by Tan and Yip (1999) showed that the effectiveness of confinement

by elliptical hoops diminishes as the side aspect ratio, that is the ratio of the major axis to the minor axis of the cross-section, increases and becomes insignificant when the aspect ratio is greater than 2.6.

Marsh (1992) investigated the use of pretensioned external steel hoops for strengthening columns with inadequate lap splices in the longitudinal reinforcement. He concluded that the steel hoop in the splice region dramatically improved the lateral resistance of concrete columns with inadequate flexural strength and ductility.

Steel jacket retrofitting of building columns was extensively used in Greece after the 1986 Kalamata Earthquake. Most of the jacketing used steel caging. Experimental studies of steel caging was conducted in the University of Patras, Greece on ten 150mm×150mm×750mm tall columns under monotonic axial load (Dritsos, 1997). Test results showed that the method was successful, provided that pretensioning of the transverse ties in the external cage is applied. When the method was used with low level or no pretensioning of the transversal bars, its effectiveness was questionable, regardless of the number of the transverse bars used.

Similar tests on steel caging were conducted in the Czech Republic (Cirtek 2001). The test program consisted of 39 specimens of dimension 300mm×300mm×1500mm tall with concrete strength f_c=12~17MPa. The cage were heated to 150~200°C prior to welding in order to provide active confinement (pre-stressing). The eccentrically axial loaded test results showed a possible maximum increase of 55% in load carrying capacity. This method of strengthening was reported to be successfully used on more than 5000 existing columns.

Valluvan et al. (1993) used external reinforcement ties to confine the lap splice region of longitudinal bars. Concrete cover was not removed in the work and the additional ties were grouted to the columns. Test results for the 12"×12" (305mm×305mm) columns showed a significantly improved confinement and splice strength. It was concluded that the external reinforcement must be grouted to the column to ensure effective confinement.

Anchor bolts were used to enhance the confinement from rectangular steel jacket by Aboutaha et al. (1996). Focus was placed on RC columns with inadequate lap splice in the longitudinal reinforcement. Steel plates augmented by adhesive anchor bolts were used to increase the passive pressure between splice bars to increase the frictional bond. Anchor bolts were used when the column size was large and the steel jacket itself failed to provide sufficient confinement to the column. Eleven columns, including four unretrofitted reference columns, were tested with the test variables of concrete strength, width of column, number and location of anchor bolts, spacing between anchor bolts, and height of steel jackets. Results showed that up to 36 inch (914mm) wide (longer side of the rectangular section) columns were successfully retrofitted with ¼ inch (6.4mm) thick steel jackets combined with a small number of adhesive anchor bolts. Satisfactory ductile response under cyclic load to drift ratios in excess of 4% and large energy dissipation capacity were obtained, compared to the very limited energy dissipation and virtually no ductility of the reference un-retrofitted column. No axial load was applied to the column in any of the tests because that was considered to be a more critical case for lap splice problem.

Recently, design guidelines on retrofitting of RC columns by rectangular steel jackets were proposed by Japanese researchers based on their extensive research work (Sakino and Sun 2000). The jacket thickness can be calculated with simple formulae based on the flexural/shear strength and ductility requirements. However, good seismic response will be predicted if these design guidelines are applied to the column tested by Chai et al. (1990) which was observed to behave poorly in the experiment.

2.5 CONCRETE FILLED STEEL TUBULAR SECTION

Concrete filled steel tubes (CFT) are usually used in new construction. Although the construction process of CFT is different from that for steel jacketing of RC columns, there are similarities between their structural behavior in terms of interaction between the steel plate (tube) and the concrete inside. Therefore, results obtained from CFT studies are often referred by research work on steel jacketing.

However, it has been suggested that little interaction exists between the concrete and the steel tube when both the concrete and the steel tube are loaded longitudinally (Saafi et al. 1999). The reason was given in two parts. First, prior to minimum volume, concrete has a smaller Poisson's ratio than steel, and separates from the latter when both materials are under the same axial strain. Second, shrinkage of new concrete causes a gap at the interface between the two materials, even prior to any loading. As a result, such columns fail by longitudinal yielding of the steel if yield stress is less than 400 MPa, or by concrete crushing if yield stress is higher than 530 MPa. Therefore, the effect of composite action is limited to prevention of local steel buckling and, to some extent, an increase in concrete ductility. For this reason, the steel tube was cut short of the support

in many studies of CFT columns in order to avoid activating the longitudinal strength of the steel tube (Tomii et al. 1987; Aboutaha and Machado 1999). In this case, the CFT columns are similar to steel jacketed RC columns from a confinement point of view.

The use of CFT columns dates back to the early 1900s when a number of bridges and buildings were built using CFT columns in some countries such as England, Belgium and Switzerland. Research on CFT columns were reported since early 1950's (Russell 1953; Kloppel and Goder 1957a&1957b; Furlong 1967&1968; Gardner and Jacobson 1967; Knowels and Park 1969&1970). In the early study by Furlong (1967), twenty-two circular and seventeen square columns were tested under various levels of constant axial load as moments were increased. Another eight circular and five square columns were loaded only axially. The interaction of the steel tube and the concrete was studied by measuring longitudinal and transverse strain at four faces of the specimens. In the test, the confinement of the concrete core by the steel tube was noticed when a sudden increase in the ratio of transverse to longitudinal strain was observed.

In Japan extensive studies have been carried out on CFT columns. These investigations have been focused on the effects of cross-sectional shape, aspect ratio (diameter to tube thickness), concrete strength and column length (Tomii et al. 1973; Tomii and Yoshimaro 1977; Tomii and Sakino 1979; Okamato and Maeno 1988; Orito et al. 1989; Sugano and Nagashima 1992; Nakanishi et al. 1999).

Tomii and Yoshimaro (1977) conducted 286 column tests on CFT columns under concentric axial load. Six sizes of circular, square, and octagonal steel tubes with different wall thickness were used in the tests. For short columns, it was found that the load deformation behavior of CFT columns was remarkably affected by the thickness of

steel tube, the cross sectional shape and concrete strength. The load-deformation relation for circular and octagonal columns showed strain hardening or an elastic-perfectly plastic behavior with considerable increase in ultimate strength due to confinement, while for all square columns the load-deformation curves were of a degrading type without an increase in axial load capacity.

Sakino and Ishibashi (1985) investigated the seismic performance of CFT columns and found that plastic buckling of the steel tube in the hinge regions tended to occur when the columns were subjected to large cyclic lateral displacement.

Sugano and Nagashima (1992) conducted cyclic lateral load tests on 250mm×250mm square and 300mm diameter circular CFT columns. Thirty-eight specimens were tested with the variables of axial force, aspect ratio (diameter to thickness of tube), strength of constituent materials. Circular columns demonstrated rich hysteresis response with large ductility and stable loops. Local buckling of the steel tube occurred when the aspect ratio was greater than 39. The maximum load was determined by the local buckling in this case. Local buckling was formed in the square columns with an aspect ratio greater than 33. Square columns with smaller aspect ratios indicated richer hysteresis response. The circular columns behaved in ductile manner despite the level of axial force and aspect ratio. It was observed that ductile behavior can be expected only from those square columns with small aspect ratio and low level of axial load. A similar conclusion was also drawn by Marino et al. (1992).

Sakino et al. (1996) reported that the degree of confinement by the square steel tubes decreased as the aspect ratio B/t (sectional breadth/thickness of tube) and/or the

concrete strength increased. It was also found that the effects of steel tubes on the flexural behavior of tubed columns became more significant as the applied axial load was higher. Stress-strain model for the concrete confined by a steel tube was also studied and proposed (Tomii, 1991).

Seismic performance of circular CFT columns was also studied by Boyd et al. (1995). Tests conducted on five 8" (203mm) diameter circular columns with aspect ratios (*D/t*) of 73 and 107 gave poor hysteresis responses similar to those for ordinary RC columns with poor confinement. A constant axial load equal to $0.17A_g f_{co}$ was applied in the tests. It was concluded that the seismic performance of CFT columns with a large aspect ratio was questionable. This conclusion contradicted with others such as Chai et al (1991) where aspect ratios more than 128 were found to be effective for a similar axial load level of $0.177A_g f_{co}$.

Aboutaha and Machado (1999) tested six full scale 305mm(*B*)×508mm(*D*) columns to investigate the flexural performance of steel-tubed high-strength RC columns. To maximize the lateral strength of steel for confinement, the steel tube was cut 25mm short of column-beam joint, so no direct axial load could be applied to the steel tube. Three levels of constant axial load corresponding to 0.0, $0.12A_g \cdot f_{co}$, and $0.16A_g \cdot f_{co}$ were used when the cantilever column was tested under cyclic push and pull at the top. In contrast to many other researches, significant improvement on ductility was reported for the steel-tubed columns compared to the normal RC column without steel tube. Outward bulging of steel tube due to crushing and dilation of concrete was observed in the potential plastic hinge region, but it was reported to have no detrimental effect on the

performance of the column. The performance of these CFT columns appears similar to those steel caged columns with pretension in the hoop reported by Dritsos (1997). However, it was not mentioned in the report that any measure such as expansive concrete was used to apply pretension in the steel tube. Similar test results were reported by the same author in another paper (Aboutaha 2000) with axial load levels of $0.25A_g \cdot f_{co}$ and $0.36A_g \cdot f_{co}$.

CHAPTER 3 STUDY OF A NEW RETROFIT SCHEME OF COMPOSITE PLATING

In the study of column retrofitting, most attention in the literature was focused on providing confinement to the core concrete. However, due to the congenital property of the rectangular shape, it is difficult for a rectangular jacket to achieve a confinement which is as effective as that from a circular jacket. Therefore, the possibility of using different retrofitting measures that are not dependent on confinement is explored in this work. As shear retrofitting is not a problem with rectangular shaped RC columns, the research focus is placed on columns with defective flexural performances that is plastic hinge failure modes. The major problem with the plastic hinge failure mode is concrete crushing under large flexural strain. Therefore, the enhancement of the compressive resistance will be a prime target of a retrofitting design. Because of this reason, and also as an initial attempt towards this direction, a new composite partial-interaction plating scheme, as introduced in Section 3.1, is investigated in this work.

3.1 INTRODUCTION OF A NEW SCHEME

The new retrofit system is illustrated in Fig.3.1. With this new scheme, steel or FRP plates are bolted to the opposite faces of a rectangular column as in Fig.3.1(a) and (d). It is therefore suitable for rectangular columns because of their flat surfaces. The L-shaped corner of the plate, as shown in Fig.3.1(c), is designed to provide compressive continuity

and tensile discontinuity of the plate across the joint as illustrated in Fig.3.1(b). When the lateral force F is to the left as shown, the restraint at the bottom of the left hand plate acts as fixed as in Fig.3.1(b). In contrast, the right hand plate can rise as shown in Fig.3.1(c) with a comparatively small tensile restraint as indicated by the spring in Fig.3.1(b). Reversal of the force F, such as occurs under seismic loading, simply reverses the restraint conditions.

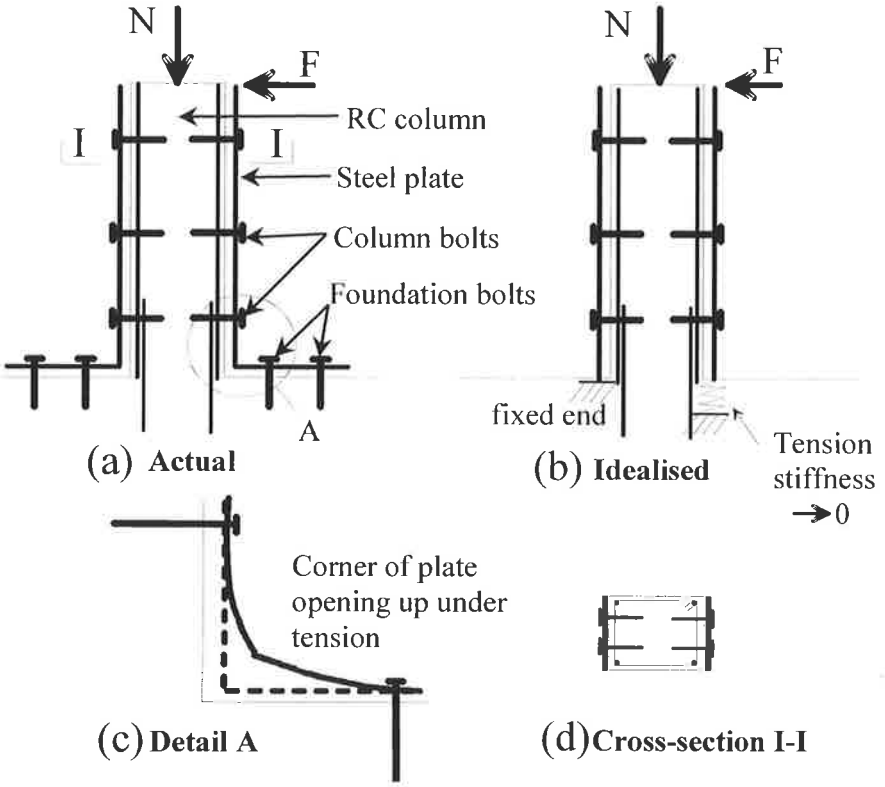

Fig. 3.1 Composite plating system of RC columns

This novel retrofitting system has the following characteristics and/or advantages:

1. It increases the capacity of the compressive resistance of the column. The bearing of the steel plate at the corner can transmit additional compressive force from the column to the joint, thereby increase the compressive resistance of the column which

is a major defect for RC columns with the potential plastic hinge failure mode. The increase in the compressive resistance in the column delays the onset of concrete crushing hence increases the lateral deformation capacity.

2. It provides a minimal increase in the tension capacity of the column. The tensile resistance of the tension plate is limited as a result of the "flexible" tension connection of the plate to the joint. The increase in tension capacity of a cross-section is not desirable from a ductility point of view. The reason is that it will offset the additional compressive resistance of a cross-section gained from the compression plate. In addition, the moment capacity of the column will be significantly increased if significant tensile resistance is provided in the tension plate. An increase in moment resistance in a column is not always desirable as it may transmit additional load to the foundation structures (Priestley et al. 1994b). Of course, if the objective of retrofitting is to increase the strength (moment resistance) of the column, it can also be achieved by moving the foundation bolts closer to the face of the column.

3. It provides a flexible partial interaction between the plate and the RC column through the bolt connections. The stiffness of the additional compressive resistant system, that helps to stop or delay concrete crushing, depends on the stiffness of the steel plate as well as the stiffness of the bolts. It will be shown later in this work that proper handling of this system stiffness can be used to achieve different design purposes.

While confinement jacketing makes use of the transverse (circumferential) strength of plates, composite steel plating makes use of the steel plate strength in the other direction – longitudinal direction of the column. The longitudinal plate strength was purposely avoided or minimized by many researchers previously from a concern that it

might increase the flexural resistance of the retrofitted column that would in turn apply additional load to the foundations (Priestley et al. 1994b). However, from this study it has been observed (see Chapter 5 and 12) that by proper design of the composite plating system, it is possible to manage the longitudinal strength of steel plates in order to serve the following two purposes:

1. Increase both the strength and ductility of an RC column; or
2. Increase only the ductility without affecting the strength of a column.

3.2 COMPOSITE PLATING MECHANISM

The mechanism by which the above plating system improves the deformation capacity/ductility of the column is illustrated by considering the equilibrium of forces and compatibility of strains at a cross-section of the column, as shown in Fig.3.2.

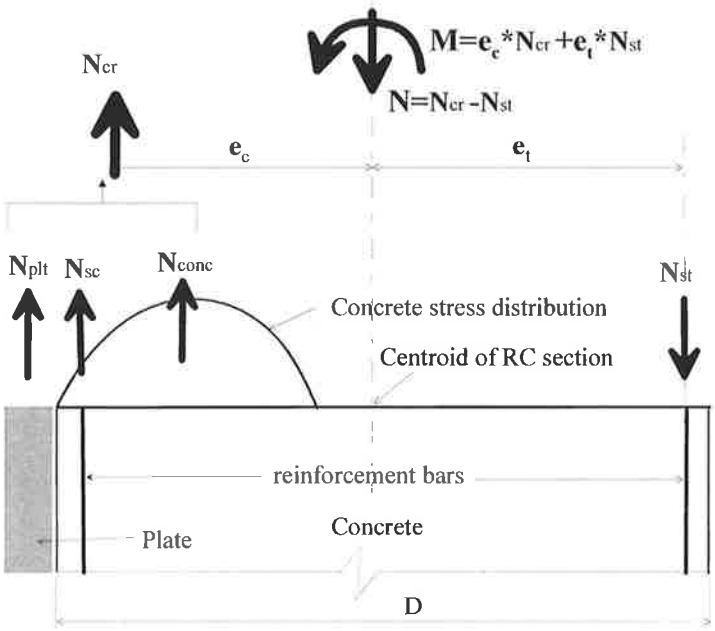

Fig. 3.2 Forces on cross-section

The tension plate is ignored in this analysis for the reason mentioned in Section 3.1. Bending in the plate is also ignored in Fig.3.2 due to its negligible contribution to the total flexural moment of the column cross-section ($(EI)_{\text{plate}} << (EI)_{RC\ \text{column}}$). From Fig.3.2, the following relation for axial loads is obtained

$$N = N_{plt} + N_{conc} + N_{sc} - N_{st} \tag{3.1}$$

in which N_{conc} is the axial force applied to the concrete only; N_{plt} is the axial force on the plate; N_{sc} and N_{st} are the axial forces from the compression and tension reinforcement bars respectively; and N is the total axial force or applied external axial load of the cross-section. For a special case in which both the compression and tension reinforcement bars yield before column failure and in which the column is symmetrically reinforced, the following relation applies

$$N_{sc} = N_{st} \tag{3.2}$$

Therefore, Eq.3.1 becomes

$$N = N_{plt} + N_{conc} \tag{3.3}$$

The strain distributions at failure are shown in Fig.3.3(b) for the unplated and in Fig.3.3(c) for the plated column. It is assumed that the column fails when the strain at the extreme fiber of the compression zone reaches an ultimate value ε_{cu} (the strain at complete crushing or zero strength is chosen, see further discussion in Chapter 7). From Eq.3.3 and for the case of an RC column without a plate, the total axial load is resisted by the concrete alone as in Fig.3.3(b). Whereas, and in contrast for the columns with a plate, part of the axial load is transmitted to the plate as in Fig.3.3(c). Therefore, the axial force on the concrete is reduced.

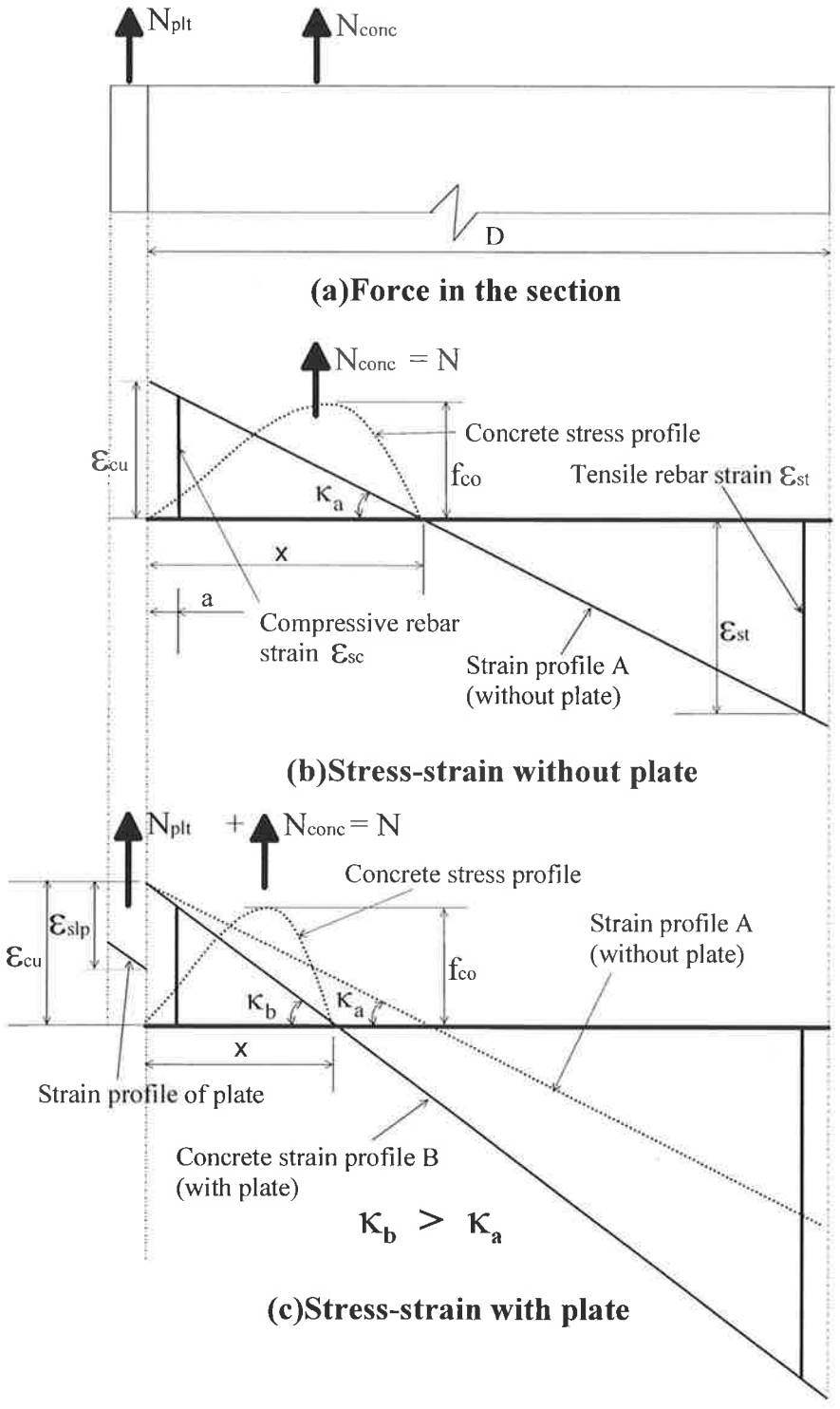

Fig. 3.3 Strain profile and stress block in the cross-section

Comparing Figs.3.3(b) and 3.3(c), it can be seen that when the axial force in the concrete or the area of the concrete stress block reduces, the compression zone depth x reduces, as the height of the concrete stress block f_{co} is the same for both cases. For a certain ultimate strain ε_{cu} at the compressive face, reduction of the compressive zone depth x means an increase in the ultimate curvature of the cross section, from κ_a to κ_b ($\because \kappa = \varepsilon_{cu}/x$) as shown. Therefore, the curvature capacity of the cross-section is increased due to the existence of a plate.

From the above analysis, it can be seen that the reason for steel plating to increase the deformation capacity of an RC column is because the plate attracts part of the axial load and, hence, reduces the axial load on the RC column.

Although the above analysis is based on the assumptions associated with Eq.3.2 and the criteria that the column fails when the ultimate compressive strain is achieved in the compressive face, the conclusion that plating the compression face increases the deformation capacity of RC columns is general. This is because the steel plate in the compression face generally reduces the axial load in the RC column, and reducing the axial load on an RC column will increase the deformation capacity of the column. The observation that the deformation capacity/ductility decreases rapidly when axial load increases is well documented in the literature from both experimental and numerical studies (Berwanger 1975; Sheikh and Khoury 1993; Watson and Park 1994; Watson et al. 1994; Bayrak and Sheikh 1997).

The above analysis provides a fundamental mechanism for the plating system to enhance the deformation capacity of the plastic hinge in an RC column. Detailed

numerical, mathematical and experimental studies will be conducted in the following chapters to further investigate this system. However, limitations and assumptions apply in these studies as described in the next section.

3.3 LIMITATIONS AND ASSUMPTIONS OF THE STUDY

As the initial step toward retrofitting RC columns by composite plating, the work reported in this thesis began from first principles. Considering the given time frame, it is therefore necessary to apply the following limitations and restrictions to both the theoretical and experimental work:

1. The study focuses on the plastic hinge failure mode. The shear failure mode has effectively been resolved previously by jacketing, and the lap splice failure of longitudinal bars is also beyond the scope of this work.

2. The study is limited to the flexural behavior of the cantilever column shown in Fig.3.1 where the deformation occurs inside the loading plane. Therefore, only single-axis (one-way) bending about the principal axis is considered. This means that the conclusions drawn from this work are immediately applicable only to uni-directional columns and frames that are restricted to move predominately in one direction. This often occurs in bridge columns or in buildings that are stiffened in the other direction by strong shear walls. The cantilever model can represent either a cantilever bridge column or a typical portion of a column in sway frames from the point of contra-flexure near the column mid-height to the point of maximum bending moment. From this point of view, the cantilever model can represent a typical part of a general column in a frame.

3. Steel plates are only placed on the compression and tension faces. Side plated columns where the lateral load F is parallel to the plane of the steel plates and columns that are plated on all four faces are beyond the scope of this study.

4. All the results from this study are based on the following loading sequence. Firstly, the plates are installed to the unloaded column. Secondly, the axial load is applied to the centroid of the RC cross-section at the top and held constant thereafter. Finally, the lateral load that varies subsequently in magnitude and direction throughout the loading process is applied to the same point on top of the column as the axial load. In practice, the axial load (even some lateral load) is applied to the column before the installation of a retrofitting system. However, numerical simulations predicted that the difference in response between a column that is retrofitted before axial loading and a column that is axially loaded before retrofitting is minimal. Therefore, no other loading sequences are considered in this study.

5. The width of the plates is the same as that of the RC column, for convenience of study.

Further assumptions applicable only to the theoretical studies are:

1) The RC column is prismatic, having the same rectangular concrete cross section, longitudinal reinforcement layout and material properties along its entire length. The lateral confinement to the concrete due to variation of stirrup spacing along its length is allowed.

2) Bernoulli's principle that plain sections remain plain applies to the RC section and the plate sections, separately. That is, the relative movement, or slip, between the plates and the RC column is permitted.
3) Perfect bond is assumed to exist between the longitudinal reinforcement and concrete.
4) Shear strain is neglected in the calculation of displacements.
5) No transverse separation occurs between the RC column and the plate on the contact interface. Therefore, the curvatures for the RC column and the plates are the same at each cross-section. This assumption is based on the observation that little, if any, separation occurs when bolts are placed sufficiently close. While in reality some separation occurs between two adjacent bolts, the overall average deformed shapes of the plates and the RC column are almost identical.

Detailed studies on this new retrofit scheme are described in the following chapters, which include numerical, mathematical and experimental works as mentioned in Section 1.2.

CHAPTER 4 NUMERICAL MODELS

The numerical models developed to simulate the response of the composite plated RC columns shown in Fig.3.1 are presented in this chapter. This numerical model and the corresponding computer program named "PLTCOL" are specifically developed to analyze this type of composite structure as no existing software can be used for the purpose of this study. The computer program is required to have the following functions:

- It is able to simulate the response of a plated cantilever column, loaded as shown in Fig.4.1, for both ascending and descending (softening) response branches, as well as under quasi-static cyclic loading.
- Material and geometric (Eqs. 4.41 and 4.42) non-linearities are allowed in the program.
- P-Δ effect is catered for.
- It is able to model the formation of a plastic hinge in the column at the large deformation stage.
- It is able to model the lateral confinement to concrete produced by stirrups.
- It is able to model the partial interaction, or slip, at the interface between the plates and the RC column.

Based on these requirements, a segmental layered method is used for the numerical modeling. This method basically discretises the cantilever column into a series

of independent cross-sections along its length, as shown in Fig.4.1. Each cross-section is further divided into many sub-sections as shown in Figs.4.2 and 4.3. The instantaneous moment-curvature relation of each cross-section is established at each loading step by integration of all the forces in the sub-sections that retain their individual loading history throughout the process to allow for full non-linear modeling. The curvature of all sections along the column length is integrated to obtain the deflection of the column. Details of this procedure are presented separately in the following sections.

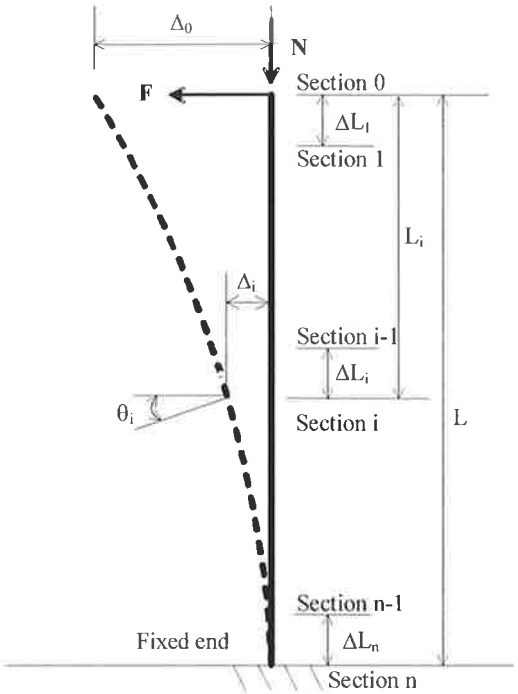

Fig. 4.1 Numerical model of the cantilever column

The cross-sectional analysis to get the moment-curvature relation of a cross-section is firstly presented in Section 4.1. It is followed by the derivation in Section 4.2 of the mathematical formulas for integrating the curvatures to get the deflection. Simple numerical tests are performed in Sections 4.3 to establish the minimum refinement of

meshes for an allowable error margin due to discretisations. The procedures to calculate the response of an RC cantilever column with full interaction plating, where the slip at the interface is considered zero, is presented in Section 4.4. Finally, in Section 4.5 the methodology and procedure to calculate the response of the partial interaction (where slip≠0) plated columns is introduced.

The assumptions and limitations as detailed in Section 3.3 apply in the development of the numerical model.

4.1 CROSS-SECTIONAL ANALYSIS

4.1.1 Discretisation of Cross-Sections

The typical cross-sectional layout considered in this study is shown in Fig.4.2, where all plate thicknesses are assumed to be the same.

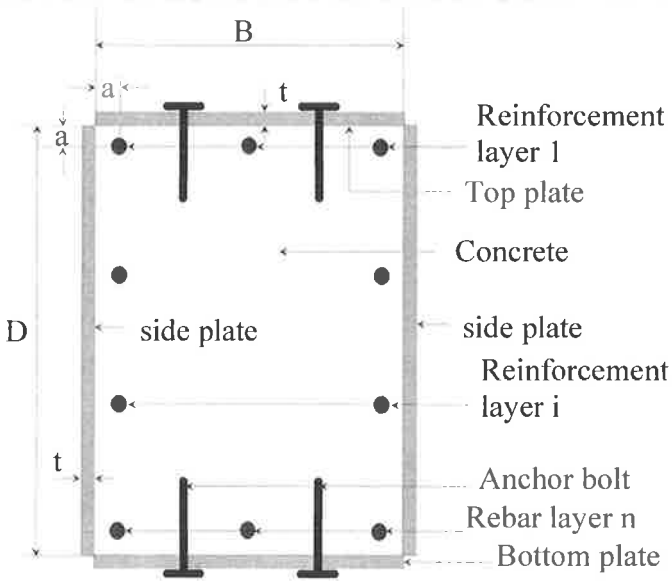

Fig. 4.2 Typical cross section

The reinforcement bars are modeled by "n" layers of steel with the positions of the first and last layer allocated at '*a*' distance away from the face of concrete, as shown in Fig.4.2. The internal layers of the reinforcement are assumed to be equally spaced in between the first and last layers. Each reinforcement layer can have a different area of steel. Plates can be placed on any of the 4 column faces. The top and bottom plates can be bolted (allowing slip) or glued (preventing slip) to the concrete faces. The side plates can only be glued to the concrete face at the current model.

To model non-linear stress distributions, the cross section is discretised into horizontal layers and vertical slices, as shown in Fig.4.3(a). The strain distribution of the cross-section is modeled with the discretised distribution shown in Fig.4.3(b).

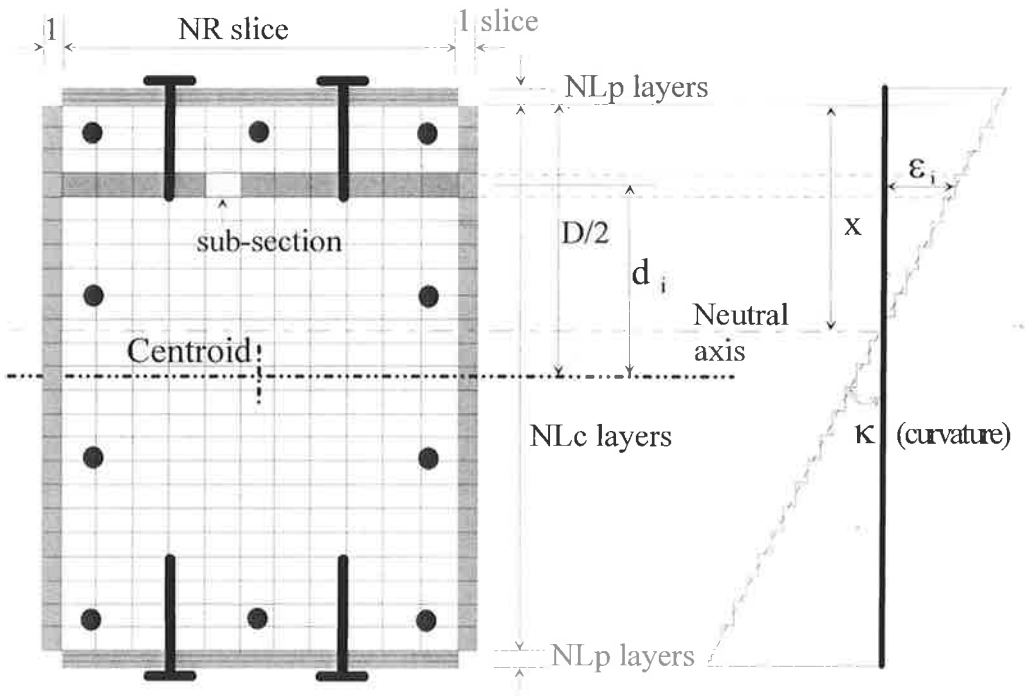

(a) Discretised section (b) Discretised strain distribution

Fig. 4.3 Discretisation of the cross-section

The strain at each layer is calculated at the center of that layer and assumed to be a constant for the entire layer. The concrete section is equally divided into *NLc* numbers of layers as shown in Fig.4.3(a). In order to account for the bending moment in the plate, the top and bottom plates are also equally divided into *NLp* numbers of layers with smaller thickness than that for the concrete layers. To allow for variations of concrete properties at the same layer due to variations in lateral confinement (confinement level is different at different points inside the cross-section), the concrete cross-section is further divided into *NR* vertical slices. The vertical slicing is not applicable to the steel plate.

The strain at layer number '*i*' is given by

$$\varepsilon_i = (x + d_i - \frac{D}{2}) \cdot \kappa \tag{4.1}$$

in which κ is the curvature of the cross-section; x is the neutral axis depth from the top of the concrete section; d_i is the distance from the center of the layer to the centroid of the concrete section, as shown in Fig.4.3. The stresses for the concrete, reinforcement and plate are calculated corresponding to the respective strains and using their respective non-linear stress-strain models as described in Sections 4.1.2 and 4.1.3.

The axial force of the section, which is assumed to remain constant, is given by the summation of forces in all the discretised areas (sub-sections) of the concrete, reinforcing bars and plates

$$\begin{aligned} N &= N_{conc} + N_{bar} + N_{plt} \\ &= \sum_{i=1}^{NLc} (\sum_{j=1}^{NR} A_{cij} \cdot \sigma_{cij}) + \sum_{i=1}^{n} A_{si} \cdot \sigma_{si} + \sum_{i=1}^{(NLp)_{top}+(NLp)_{bot}} A_{pi} \cdot \sigma_{pi} + \sum_{i=1}^{NLc} A_{psi} \cdot \sigma_{psi} \end{aligned} \tag{4.2a}$$

where $A_{cij} = \frac{B}{NR} \cdot \frac{H}{NLc}$ is the area of one discretised sub-section of concrete and σ_{cij} is the concrete stress at the corresponding sub-section; A_{si} and σ_{si} are the area and stress of layer 'i' reinforcement, respectively. The 3rd term in Eq.4.2a is for the top and bottom plates where A_{pi} is the sub-area given by $A_{pi} = B \cdot t / NLp$ and σ_{pi} is the stress of the corresponding sub-section. The subscripts 'top' and 'bot.' denote the top and bottom plate, respectively. The fourth term is for the side plates, where A_{psi} is the sub-area given by $A_{psi} = 2t \cdot D / NLc$ ($A_{psi} = t \cdot D / NLc$ if one side plated only), and σ_{psi} is the stress at the corresponding sub-area.

The moment at the cross-section is given by taking moment of the forces in each sub-section with respect to the centroid of the cross-section

$$M = M_{conc} + M_{bar} + M_{plt}$$

$$= \sum_{i=1}^{NLc} \left(\sum_{j=1}^{NR} A_{cij} \cdot \sigma_{cij} \right) \cdot d_i + \sum_{i=1}^{n} A_{si} \cdot \sigma_{si} \cdot d_i + \sum_{i=1}^{(NLp)_{top}+(NLp)_{bot}} A_{pi} \cdot \sigma_{pi} \cdot d_i + \sum_{i=1}^{NLc} A_{psi} \cdot \sigma_{psi} \cdot d_i \qquad (4.2b)$$

4.1.2 Stress-Strain Model for Concrete

Two stress-strain models are used for the concrete in this work. The first model is a simple triangular model that is mainly used to correlate the numerical results to the analytical results where the simplified stress-strain model is adopted. Another more complicated model is used for the numerical simulation in order to model the response of an actual column more accurately.

The stress-strain behavior of normal-strength concrete tied columns has been extensively studied in the literature (Sinha et al. 1964; Karsan and Jirsa 1969; Popovics 1970&1973; Kent and Park 1971; Park et al. 1972; Desayi et al. 1979; Muguruma et al. 1980; Sheikh and Uzumeri 1980&1982; Ahmad and Shah 1982; Maher and Darwin 1982; Park et al. 1982; Shah et al. 1983; Yankelevsky and Reinhardt 1987; Mander et al. 1988a&b; Fujii et al. 1988; Razvi and Saatcioglu 1989; Saatcioglu. and Razvi 1992; Madas and Elnashai 1992; Pekau et al. 1992; El-Dash and Ahmad 1994&1995; Almusallam and Alsayed 1995; Attard and Setunge 1996; Martinez-Rueda and Elnashi 1997; Hoshikuma et al. 1997; Bahn and Hsu 1998; Spoelstra and Monti 1999; Sakai and Kawashima 2000). The non-linear stress-strain model proposed by Mander et al. (1988a) accounts for lateral confinement effects due to the transverse reinforcement. This model has been extensively tested against experimental data and appears to be the most widely accepted and used in the literature for the steel confined concrete (confinement is provided from steel elements such as stirrups). The advantage of this model is that its simple and explicit form minimizes the computational effort. As the confinement considered in this work is only from the lateral reinforcement or stirrups, Mander's model is considered adequate and hence adopted.

4.1.2.1 Triangular model

The simple triangular model is an idealized stress-strain relationship as shown in Fig.4.4, in which a linear relation is used for both ascending and softening branches of the stress-strain curve. The tensile strength is ignored. The vertical axis f_c and horizontal axis ε_c specify the stress and strain of concrete, respectively. The strength of the concrete is

denoted by f_{co} with the corresponding strain at the maximum strength given by ε_{co}. The ultimate strain of the concrete is given by ε_{cu} at which the concrete is completely crushed with zero strength. The elastic modulus of concrete is given by E_c used for the slope of the loading/unloading branches, and E'_c gives the slope of the post-peak softening branch as shown in Fig.4.4.

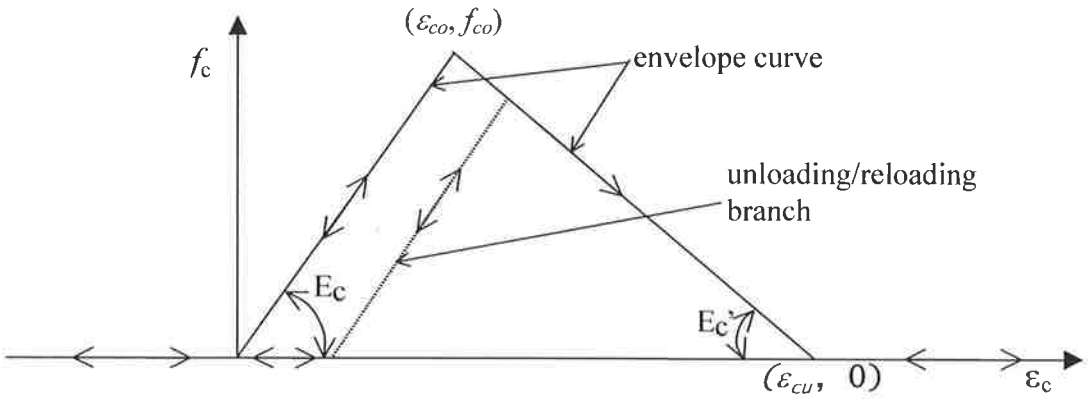

Fig. 4.4 Idealized stress-strain model of the concrete

4.1.2.2 Mander's model

Mander's model is illustrated in Fig.4.5 and is described in detail from Section 4.1.2.2.1 to Section 4.1.2.2.5. Minor modifications have been made to the original model due to some subtle problems in using the original model. These modifications will be introduced, along with a detailed discussion of Mander's model, in the following sections.

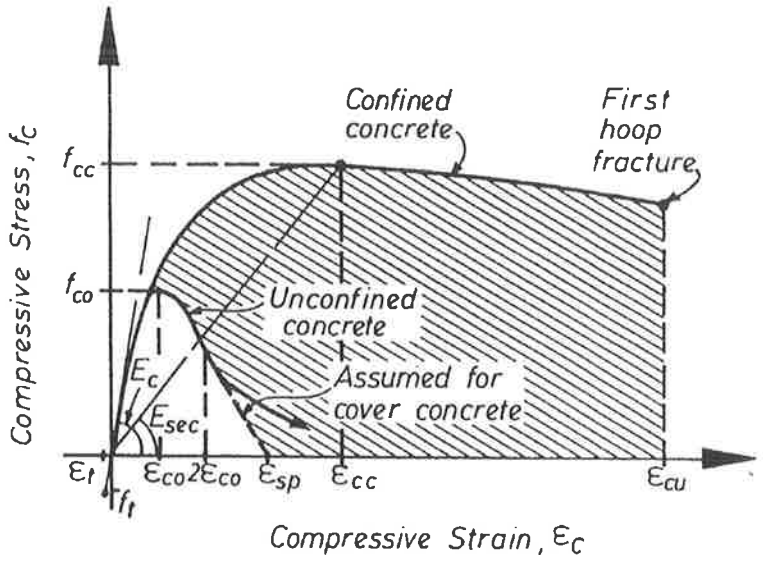

Fig. 4.5 Mander's model

4.1.2.2.1 Monotonic compression loading

The monotonic compression loading curve, as shown in Fig.4.5, is given by

$$f_c = \frac{f_{cc} \cdot x \cdot r}{r - 1 + x^r} \tag{4.3}$$

where

$$x = \frac{\varepsilon_c}{\varepsilon_{cc}} \tag{4.4}$$

$$\varepsilon_{cc} = \varepsilon_{co}\left[1 + 5\left(\frac{f_{cc}}{f_{co}} - 1\right)\right] \tag{4.5}$$

$$f_{cc} = f_{co}(-1.254 + 2.254\sqrt{1 + \frac{7.94 f_l^{'}}{f_{co}}} - 2\frac{f_l^{'}}{f_{co}}) \tag{4.6}$$

$$r = \frac{E_c}{E_c - E_{\sec}} \tag{4.7}$$

$$E_c = 5000\sqrt{f_{co}} \qquad MPa \tag{4.8}$$

and

$$E_{\text{sec}} = \frac{f_{cc}}{\varepsilon_{cc}} \tag{4.9}$$

In Equations 4.3 to 4.9, f_{co} and ε_{co} represent the unconfined concrete strength and corresponding strain, respectively, and f_{cc} and ε_{cc} denote the confined concrete strength and corresponding strain, respectively; $f_l^{'}$ is the effective lateral confining pressure due to the lateral reinforcement. Mander et al. (1988a) and Watson, Zahn and Park (1994) proposed a series of formulae to calculate the effective confining pressure for circular and rectangular cross sections for various arrangements of transverse reinforcement.

By specifying different f_{cc} values at different sub-sections of a cross-section, the general configuration of confining zones can be accounted for in the cross-sectional analysis. This will be illustrated in Section 4.4.3.

4.1.2.2.2 Unloading branches of compression loading

The compression branch unloading is modeled as shown in Fig.4.6, which is given by

$$f_c = f_{un} - \frac{f_{un} \cdot x \cdot r}{r - 1 + x^r} \tag{4.10}$$

where

$$r = \frac{E_u}{E_u - E_{\text{sec}}} \tag{4.11}$$

$$E_{\text{sec}} = \frac{f_{un}}{\varepsilon_{un} - \varepsilon_{pl}} \tag{4.12}$$

$$x = \frac{\varepsilon_c - \varepsilon_{un}}{\varepsilon_{pl} - \varepsilon_{un}} \tag{4.13}$$

$$E_u = b \cdot c \cdot E_c \tag{4.14}$$

$$b = \frac{f_{un}}{f_{co}} \geq 1 \tag{4.15}$$

$$c = \left(\frac{\varepsilon_{cc}}{\varepsilon_{un}} \right)^{0.5} \leq 1 \tag{4.16}$$

$$\varepsilon_{pl} = \varepsilon_{un} - \frac{(\varepsilon_{un} + \varepsilon_a) \cdot f_{un}}{(f_{un} + E_c \cdot \varepsilon_a)} \tag{4.17}$$

$$\varepsilon_a = a\sqrt{\varepsilon_{un} \cdot \varepsilon_{cc}} \tag{4.18}$$

and

$$a = \frac{\varepsilon_{cc}}{\varepsilon_{cc} + \varepsilon_{un}} \quad or \quad \frac{0.09\varepsilon_{un}}{\varepsilon_{cc}} \quad whichever \quad greater \tag{4.19}$$

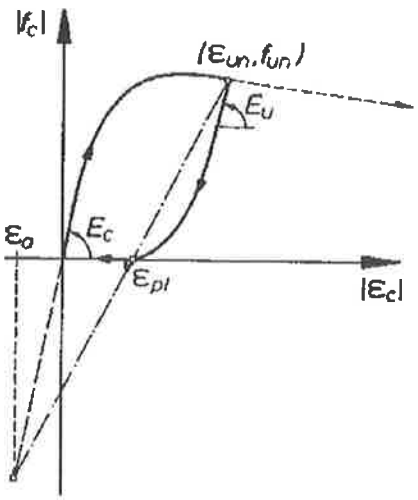

Fig. 4.6 Un-loading model

in which f_{un} and ε_{un} are the stress and strain at the onset of unloading branch, respectively.

4.1.2.2.3 Compression reloading branches

A linear stress-strain relation, shown in Fig.4.7, is adopted to model the reloading branch between the reloading strain ε_{ro} and ε_{un}, and is given by

$$f_c = f_{ro} + E_r(\varepsilon_c - \varepsilon_{ro}) \tag{4.20}$$

where

$$E_r = \frac{f_{ro} - f_{new}}{\varepsilon_{ro} - \varepsilon_{un}} \tag{4.21}$$

and

$$f_{new} = 0.92 f_{un} + 0.08 f_{ro} \tag{4.22}$$

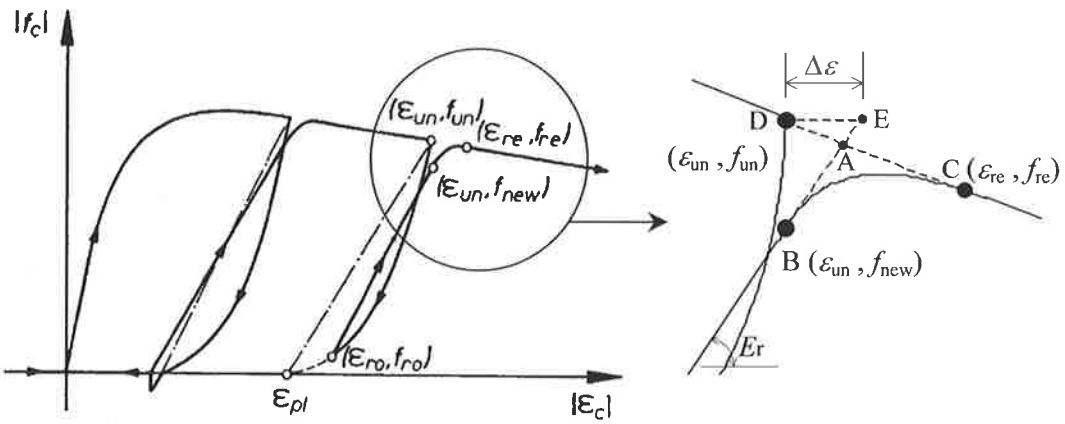

(a) (b)

Fig. 4.7 Re-loading model

The parabolic transition curve between the linear reloading branch and the monotonic stress-strain envelope curve, i.e. curve from point B to C in Fig.4.7(b), is given by

$$f_c = f_{re} + E_{re} \cdot x + A \cdot x^2 \tag{4.23}$$

where

$$x = \varepsilon_c - \varepsilon_{re} \tag{4.24}$$

$$\varepsilon_{re} = \varepsilon_{un} + \frac{f_{un} - f_{new}}{E_r(2 + \frac{f_{cc}}{f_{co}})} \tag{4.25}$$

and

$$A = \frac{E_r - E_{re}}{-4[(f_{new} - f_{re}) - E_r(\varepsilon_{un} - \varepsilon_{re})]} \tag{4.26}$$

in which E_{re} is the return point modulus of elasticity on the monotonic stress-strain curve.

The original model by Mander et al (1988a) gives unreasonable results at the transition curve with two apparent problems. Firstly, the common return point C calculated with Eq.4.25 is irrational for the following reason. If we extend the linear reloading path with the same slope E_r from point B to point E which is at the same level as the unloading point D, as shown in Fig.4.7(b), it can be seen that the strain at point E is given by

$$\varepsilon_E = \varepsilon_{un} + \Delta\varepsilon = \varepsilon_{un} + \frac{f_{un} - f_{new}}{E_r} \tag{4.27}$$

where $\Delta\varepsilon = \frac{f_{un} - f_{new}}{E_r}$. Substituting $\Delta\varepsilon$ into Eq.4.25 gives

$$\varepsilon_{re} = \varepsilon_{un} + \Delta\varepsilon' = \varepsilon_{un} + \frac{\Delta\varepsilon}{2 + \frac{f_{cc}}{f_{co}}}$$

$$\because f_{cc} > f_c$$

$$\therefore 2 + \frac{f_{cc}}{f_c} \geq 3$$

$$or \quad \Delta\varepsilon' \leq \frac{\Delta\varepsilon}{3}$$

From the above relation and Fig.4.7(b) it can be seen that Eq.4.25 gives a return strain ε_{re}, i.e. the x co-ordinate of the common return point C, within 1/3 of DE from point D. This return point is therefore usually on line DA to the left of point A (A is the intersection of DC and BE). The purpose of this parabolic transition curve is to account for the cyclic degradation. When the common return point is to the left of point A, the stress-strain curve is not degraded, instead it is 'upgraded'. This return point is therefore unreasonable. Furthermore it gives an unreasonable shape of the transition curve.

This same difficulty has been noted by other researchers in applying this model. Elnashai and Elghazouli (1993) found that the transition curve of Mander's model "*gives occasionally stresses that exceed the envelope curve, a straight line passing through* $(\varepsilon_{un}, f_{new})$*, and having a reduced slope was therefore used* (from point B to C in Fig.4.7(b))". Actually, based on the above analysis, the transition curve of the original Mander's model gives erroneous result more than "*occasionally*". However, using a straight line to connect point B to C is acceptable because the transition curve is only a very small part of the total curve and will only have minor effect to the overall behavior.

Actually a simple solution exists to provide a nice smooth transition curve by moving ε_{re} from left side of point A to the right side of point A with the following revision to Eq.4.25

$$\varepsilon_{re} = \varepsilon_{un} + \frac{f_{un} - f_{new}}{E_r}\left(1 + \frac{1}{2 + \frac{f_{cc}}{f_{co}}}\right) \tag{4.28}$$

This revised reloading branch produces a nice and smooth transition, as will be seen later from Fig.4.10.

The second problem with Mander's original model is that the value of E_{re} is not given and the coefficient A given by Eq.4.26 is incorrect. The transition curve must satisfy three conditions based on Mander's original model: (1) it must pass through point B; (2) it must pass through point C; and (3) it is tangent to the monotonic curve at point C. These three conditions can used to determine the three coefficients f_{re}, E_{re} and A in Eq.4.23, which gives

$$f_{re} = \frac{f_{cc} \cdot r \cdot \left(\frac{\varepsilon_{re}}{\varepsilon_{cc}}\right)}{r - 1 + \left(\frac{\varepsilon_{re}}{\varepsilon_{cc}}\right)^r} \tag{4.29}$$

$$E_{re} = r \cdot E_{\sec} \cdot \left[\frac{1}{r - 1 + \left(\frac{\varepsilon_{re}}{\varepsilon_{cc}}\right)^r} - \frac{r \cdot \left(\frac{\varepsilon_{re}}{\varepsilon_{cc}}\right)^r}{\left(r - 1 + \left(\frac{\varepsilon_{re}}{\varepsilon_{cc}}\right)^r\right)^2}\right] \tag{4.30}$$

and

$$A = \frac{f_{new} - f_{re} - E_{re}(\varepsilon_{un} - \varepsilon_{re})}{(\varepsilon_{un} - \varepsilon_{re})^2} \tag{4.31}$$

The coefficient A given by Eq.4.31 is clearly different from Mander's original Eq.4.26.

4.1.2.2.4 Tensile stress model

The tensile stress is modeled by Fig.4.8 in Mander's model. For monotonic loading

$$f_c = \begin{cases} E_c \cdot \varepsilon_c & when \quad f_c \le f_t \\ 0 & otherwise \end{cases} \tag{4.32}$$

where f_t is the tensile strength of concrete under monotonic loading. To account for the deterioration of the tensile strength due to pre-loading in compression, the following relations are used in Mander's model

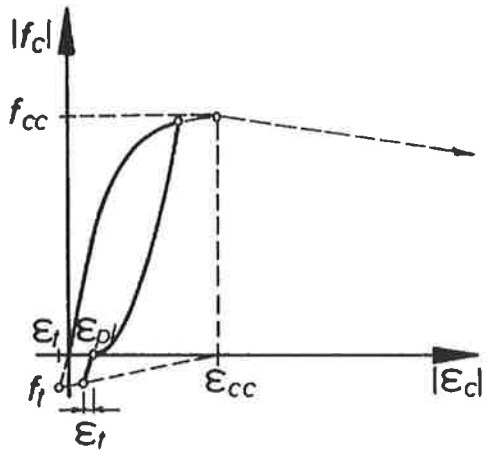

Fig. 4.8 Mander's tensile stress model

$$f_c = E_t \cdot (\varepsilon_c - \varepsilon_{pl}) \tag{433}$$

$$E_t = \frac{f_{tc}}{\varepsilon_t} \tag{4.34}$$

$$\varepsilon_t = \frac{f_t}{E_c} \tag{4.35}$$

$$f_{tc} = \begin{cases} f_t \cdot \left(1 - \dfrac{\varepsilon_{pl}}{\varepsilon_{cc}}\right) & when \quad \varepsilon_{pl} \le \varepsilon_{cc} \\ 0 & when \quad \varepsilon_{pl} > \varepsilon_{cc} \end{cases} \tag{4.36}$$

When the tensile strength is exceeded, cracks open and the tensile strength for all subsequent loading is assumed to be zero.

This tension model sometimes causes problems in numerical calculations, e.g. when searching for the neutral axis of a cross section. The sudden drop of the tensile stress when the tensile strength is reached can cause non-convergence of the searching algorithm due to this non-continuity. To improve the convergence behavior, modifications to the above model are made with reference to the tension model by Rots et al. (CEB report 1996). Rots' model is shown in Fig.4.9(a). The modified model used in this work is given in Fig.4.9(b).

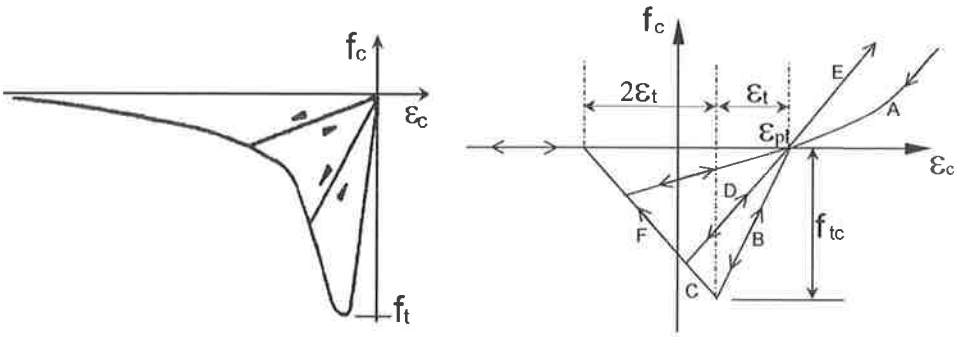

(a) Tension model by Rots et al. (b) Modified tensile stress model

Fig. 4.9 Modification to Mander's tension model

In the modified model, the values of ε_t, ε_{pl} and f_{tc} in the modified model are the same as that in Mander's model. Each time the peak of the tensile curve is passed, the remaining tensile strength drops, e.g. if the previous tension loading goes along the path A-B-C-D-E, the next tensile loading will go along D-F path.

4.1.2.2.5 Example of the modified Mander's model

A typical stress-strain curve from Mander's model with the modifications to the transition curve and the tension model is shown in Fig.4.10. The following parameters were used to produce this curve: $f_{co} = 44MPa$, $\varepsilon_{co} = 0.002$, $f_{cc} = 48MPa$, $f_t = 8.0MPa$.

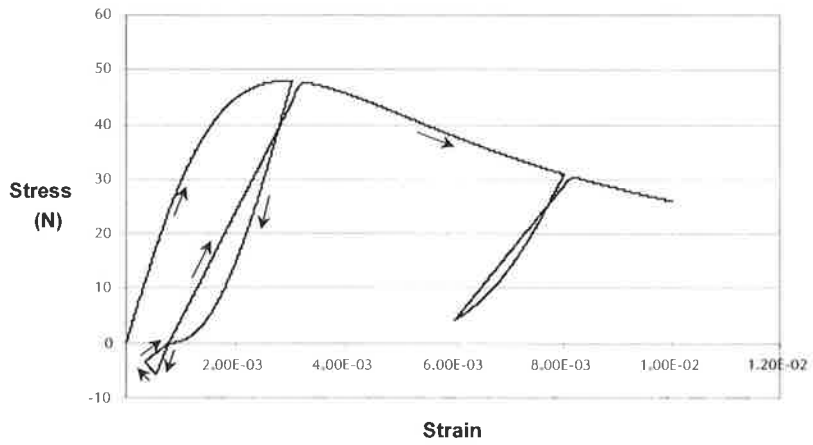

Fig. 4.10 Typical stress-strain curve of the modified Mander's model

4.1.3 Stress-Strain Model for Steel

For a similar reason to that for concrete, one simple and one sophisticated non-linear model is used as the constitutive relation for steel elements which include reinforcing bars and steel plates.

4.1.3.1 Idealized bi-linear model

The idealized bi-linear model is shown in Fig.4.11. This model is mainly used for the steel plates. It is also used for reinforcing bars when verifications between numerical and mathematical results are made, where the simple stress-strain relation is used for both numerical and mathematical analyses.

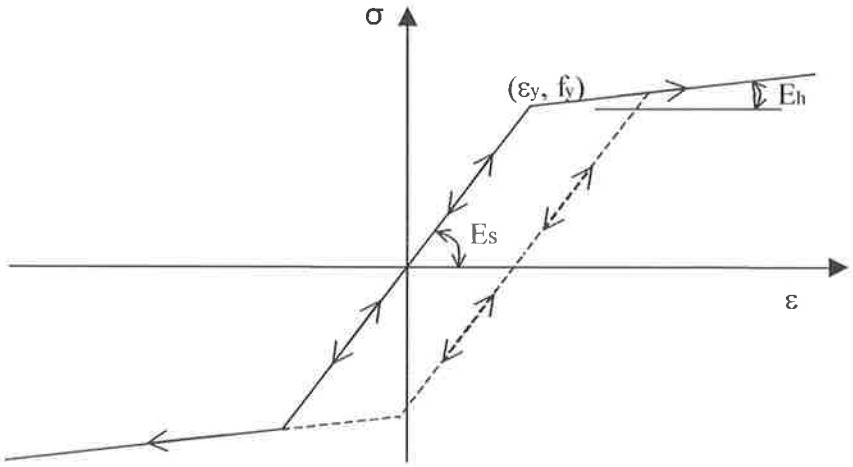

Fig. 4.11 Idealized bi-linear model of steel

4.1.3.2 Menegotto-Pinto model

The Menegotto-Pinto model, with modifications by Filippou et al. (Gomes and Appleton 1997; CEB report 1996), is shown in Fig.4.12 and is given by Eq.4.37.

$$\sigma^* = b \cdot \varepsilon^* + \frac{(1-b)\cdot \varepsilon^*}{\left(1+\varepsilon^{*R}\right)^{\frac{1}{R}}} \tag{4.37}$$

where

$$\sigma^* = \frac{\sigma - \sigma_r}{\sigma_0 - \sigma_r} \tag{4.38}$$

$$\varepsilon^* = \frac{\varepsilon - \varepsilon_r}{\varepsilon_0 - \varepsilon_r} \tag{4.39}$$

and

$$R = R_o - \frac{\alpha_1 \cdot \xi}{\alpha_2 + \xi} \tag{4.40}$$

in which σ and ε are stress and strain of the steel respectively; σ_o and ε_o are the stress and strain at the point where the two asymptotes of the branch under consideration meet (e.g. point A in Fig.4.12); σ_r and ε_r are stress and strain at the point where the last strain reversal with stress of equal sign took place (e.g. point B in Fig.4.12); b is the strain hardening ratio or the ratio between E_h and E_s; and R, given by Eq.4.40, is a constant taking into account the Baushinger effect. R depends on the absolute value of the plastic strain of last excursion ξ (e.g. ξ_1 and ξ_2 in Fig.4.12) as well as the material properties R_o, α_1 and α_2 which are experimentally determined parameters.

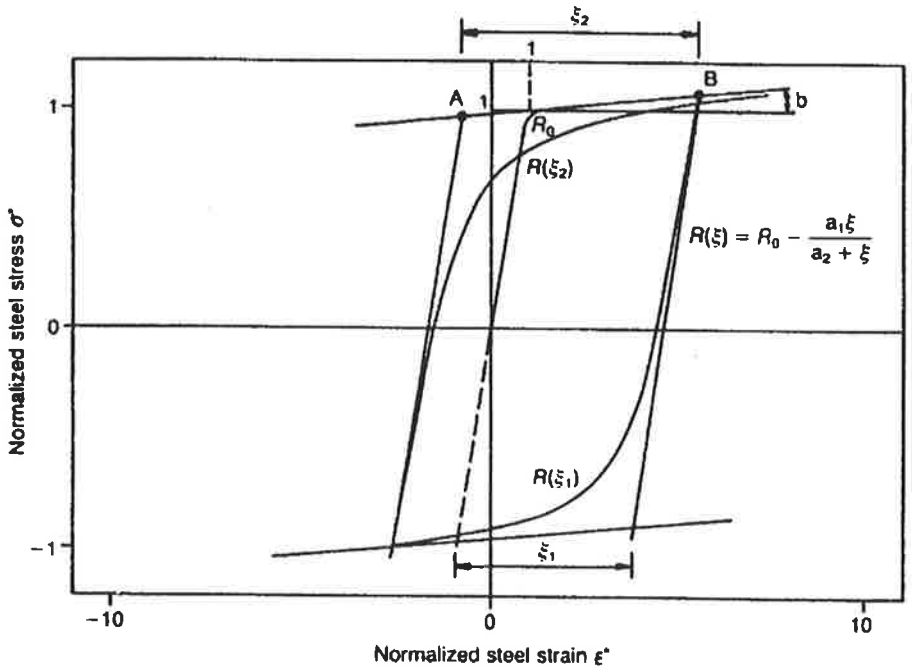

Fig. 4.12 Menegotto-Pinto model of steel

4.1.4 Load-Deformation Relation for Bolt Shear Connector

To quantify the interaction between the plates and the RC column, the load deformation relationship of the connecting agent, i.e. the anchor bolts or shear connectors, has to be defined. The relation between the lateral load F_b on a bolt and the lateral deformation of the bolt, or the slip s as shown in Fig.4.13(a), is actually very complicated. This relation is not only affected by the geometric and material properties of the bolt, but also related to the geometric and material properties of the concrete and the plate. Because of the complexities, the load-slip relation is usually determined from experiments. A typical experimental result by Teh et al. (1999) is shown in Fig.4.13(b).

Similar load-slip tests are conducted in this work (reported in Chapter 10). Based on the test results, a bi-linear model, similar in shape to that shown in Fig.4.11, is adopted in this work. The softening part from point C to D shown in Fig.4.13(b) is not likely to occur in a practical column, as the concrete will have crushed long before such a large slip occurs.

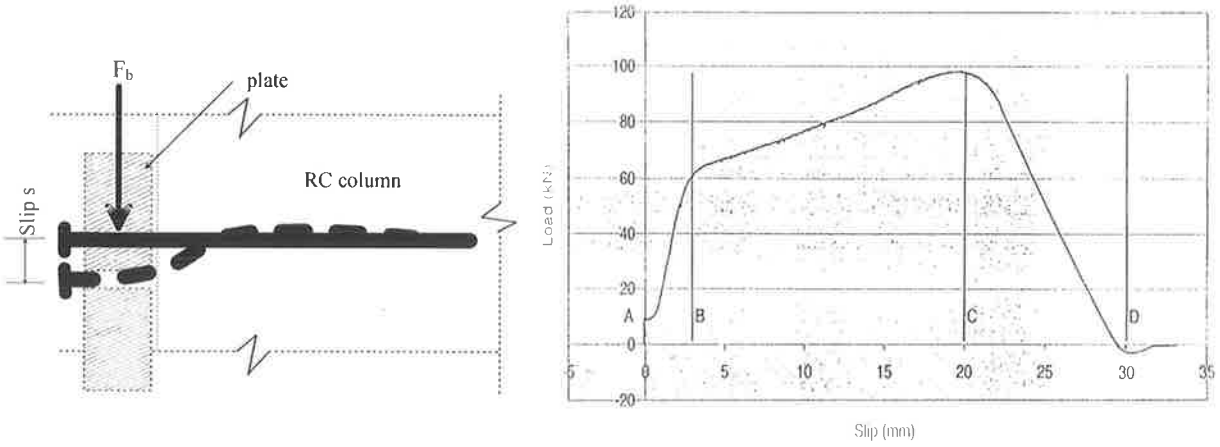

(a) Slip of bolt (b) Experimental load-slip relation

Fig. 4.13 Typical load-slip relation of an anchor bolt (Teh et al. 1999)

4.2 CALCULATION OF DISPLACEMENT

The displacement at the top of the cantilever column can be calculated from the integration of curvature along its length. In discrete form, the column is divided along its length into 'n' segments as shown in Fig.4.1. The curvatures at section '1' to section 'n' are then used to calculate the displacement of the cantilever. Different discrete forms of integration exist in the literature. From numerical tests, some were found to converge faster (to get certain precision with fewer number of element), others slower. In this section, equations relating sectional curvatures and deflection are derived which are found to converge relatively fast.

From fundamental principles (Timoshenko 1955), we know

$$\theta = \arctan(\frac{dv}{dx}) \tag{4.41}$$

and

$$\kappa = \frac{1}{r} = -\frac{d\theta}{ds} = -\frac{\frac{d^2v}{dx^2}}{\left[1+(\frac{dv}{dx})^2\right]^{3/2}} \tag{4.42}$$

in which v is the lateral deflection of the column; θ is the rotation of a cross-section; x is the vertical coordinate; κ is the curvature; r is the radius of curvature; and s is the coordinate along the length. Eqs.4.41 and 4.42 are general equations without approximation, taking into account large deflections.

4.2.1 Small Deflection

For small deflection, $ds \approx dx$, *and* $\theta \approx \tan\theta = dv/dx$. Eqs.4.41 and 4.42 can then be simplified to

$$\theta = \frac{dv}{dx} \tag{4.43}$$

$$\kappa = -\frac{d\theta}{dx} = -\frac{d^2v}{dx^2} \tag{4.44}$$

or

$$\theta = \theta_n + \int_0^x \kappa \cdot dx \tag{4.45}$$

$$v = v_n + \int_0^x \theta \cdot dx \tag{4.46}$$

where θ_n and v_n are the rotation and deflection at the boundary. For a cantilever without rotation and deflection at the bottom (fixed end), the top deflection is given by

$$\Delta_0 = \int_0^l \theta \cdot dx \tag{4.47}$$

$$\theta = \int_0^x \kappa \cdot dx \tag{4.48}$$

In discrete form

$$\theta_i = \sum_{j=n}^{i+1} \overline{\kappa}_j \cdot \Delta L_j \approx \sum_{j=n}^{i+1} 0.5 \cdot (\kappa_{j-1} + \kappa_j) \cdot \Delta L_j = \sum_{j=i+1}^{n} 0.5 \cdot (\kappa_{j-1} + \kappa_j) \cdot \Delta L_j \tag{4.49}$$

$$\Delta_0 = \sum_{i=n}^{1} \overline{\theta}_i \cdot \Delta L_i = \sum_{i=1}^{n} \overline{\theta}_i \cdot \Delta L_i \approx \sum_{i=1}^{n} 0.5 \cdot (\theta_{i-1} + \theta_i) \cdot \Delta L_i \tag{4.50}$$

Substituting Eq.4.49 into Eq.4.50 gives

$$\Delta_0 = \sum_{i=1}^{n} 0.5 \cdot \left[\sum_{j=i}^{n} 0.5 \cdot (\kappa_{j-1} + \kappa_j) \cdot \Delta L_j + \sum_{j=i+1}^{n} 0.5 \cdot (\kappa_{j-1} + \kappa_j) \cdot \Delta L_j \right] \cdot \Delta L_i$$

$$= 0.25 \cdot \sum_{i=1}^{n} \left[\sum_{j=i}^{n} (\kappa_{j-1} + \kappa_j) \cdot \Delta L_j \right] \cdot \Delta L_i + 0.25 \cdot \sum_{i=1}^{n} \left[\sum_{j=i+1}^{n} (\kappa_{j-1} + \kappa_j) \cdot \Delta L_j \right] \cdot \Delta L_i \tag{4.51}$$

Equation 4.51 has double summations that are not convenient to use. It can be simplified by the following transformation. For the first part of Eq.4.51

$$\Delta_a = 0.25 \cdot \sum_{i=1}^{n} \left[\sum_{j=i}^{n} (\kappa_{j-1} + \kappa_j) \cdot \Delta L_j \right] \cdot \Delta L_i$$

$$= 0.25 \cdot \left[(\kappa_0 + \kappa_1) \cdot \Delta L_1 + (\kappa_1 + \kappa_2) \cdot \Delta L_2 + \ldots + (\kappa_{i-1} + \kappa_i) \cdot \Delta L_i + \ldots + (\kappa_{n-1} + \kappa_n) \cdot \Delta L_n \right] \cdot \Delta L_1$$
$$+ 0.25 \cdot \left[(\kappa_1 + \kappa_2) \cdot \Delta L_2 + \ldots + (\kappa_{i-1} + \kappa_i) \cdot \Delta L_i + \ldots + (\kappa_{n-1} + \kappa_n) \cdot \Delta L_n \right] \cdot \Delta L_2$$
$$+ \ldots$$
$$+ 0.25 \cdot \left[(\kappa_{i-1} + \kappa_i) \cdot \Delta L_i + \ldots + (\kappa_{n-1} + \kappa_n) \cdot \Delta L_n \right] \cdot \Delta L_i$$
$$+ \ldots$$
$$+ 0.25 \cdot \left[(\kappa_{n-1} + \kappa_n) \cdot \Delta L_n \right] \cdot \Delta L_n$$

$$= 0.25 \cdot (\kappa_0 + \kappa_1) \cdot \Delta L_1 \cdot \Delta L_1 + 0.25 \cdot (\kappa_1 + \kappa_2) \cdot \Delta L_2 \cdot (\Delta L_1 + \Delta L_2) + \ldots + 0.25 \cdot (\kappa_{i-1} + \kappa_i) \cdot \Delta L_i \cdot (\Delta L_1 + \Delta L_2 + \ldots + \Delta L_i)$$
$$+ \ldots + 0.25 \cdot (\kappa_{n-1} + \kappa_n) \cdot \Delta L_n \cdot (\Delta L_1 + \Delta L_2 + \ldots + \Delta L_i + \ldots + \Delta L_n)$$
$$= 0.25 \cdot (\kappa_0 + \kappa_1) \cdot \Delta L_1 \cdot L_1 + 0.25 \cdot (\kappa_1 + \kappa_2) \cdot \Delta L_2 \cdot L_2 + \ldots + 0.25 \cdot (\kappa_{i-1} + \kappa_i) \cdot \Delta L_i \cdot L_i + \ldots + 0.25 \cdot (\kappa_{n-1} + \kappa_n) \cdot \Delta L_n \cdot L_n$$
$$= 0.25 \cdot \sum_{i=1}^{n} (\kappa_{i-1} + \kappa_i) \cdot \Delta L_i \cdot L_i$$

in which $L_i = \sum_{j=1}^{i} \Delta L_j$. Similarly the second part of Eq.4.51 can also be transformed to

$$\Delta_b = 0.25 \cdot \sum_{i=1}^{n} \left[\sum_{j=i+1}^{n} (\kappa_{j-1} + \kappa_j) \cdot \Delta L_j \right] \cdot \Delta L_i$$

$$= 0.25 \cdot \sum_{i=1}^{n-1} (\kappa_i + \kappa_{i+1}) \cdot \Delta L_{i+1} \cdot L_i$$

$$\therefore \Delta_0 = \Delta_a + \Delta_b$$
$$= 0.25 \cdot \sum_{i=1}^{n} (\kappa_{i-1} + \kappa_i) \cdot \Delta L_i \cdot L_i + 0.25 \cdot \sum_{i=1}^{n-1} (\kappa_i + \kappa_{i+1}) \cdot \Delta L_{i+1} \cdot L_i$$

$$=0.25\cdot\sum_{i=1}^{n}(\kappa_{i-1}+\kappa_i)\cdot\Delta L_i\cdot L_i+0.25\cdot\sum_{i=2}^{n}(\kappa_{i-1}+\kappa_i)\cdot\Delta L_i\cdot L_{i-1}$$

let $L_0=0$

$$\Delta_0=0.25\cdot\sum_{i=1}^{n}(\kappa_{i-1}+\kappa_i)\cdot\Delta L_i\cdot(L_i+L_{i-1})$$

$$=\sum_{i=1}^{n}\frac{\kappa_{i-1}+\kappa_i}{2}\cdot\Delta L_i\cdot\frac{L_i+L_{i-1}}{2} \tag{4.52}$$

As compared to Eq.4.51, Eq.4.52 is simpler and is the form used in this work. This relation can be illustrated by the geometrical relation as shown in Fig.4.14, where

$$\Delta_0=\sum_{i=1}^{n}\delta_i=\sum_{i=1}^{n}\delta\theta_i\cdot\overline{L_i}=\sum_{i=1}^{n}\frac{\kappa_{i-1}+\kappa_i}{2}\cdot\Delta L_i\cdot\frac{L_{i-1}+L_i}{2}$$

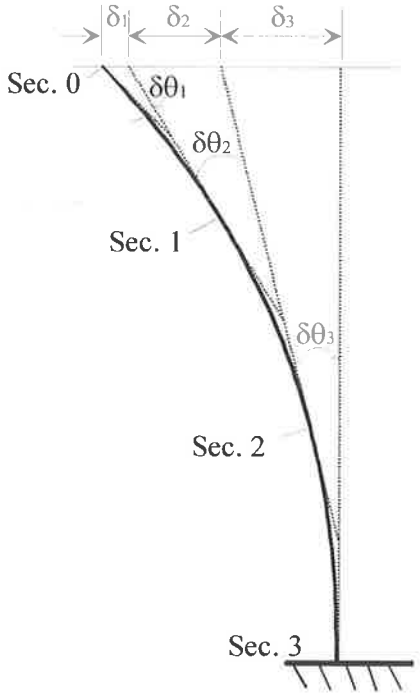

Fig. 4.14 Calculation of displacement at top

Equation 4.52 relates the deflection of the column directly to the curvature of sections instead of relating to rotation of cross-sections that is then related to curvature. It

simplifies the programming procedure and calculations. It is also found to converge relatively faster as compared to the expression given in Eq.4.53 which is sometime used by others.

$$\Delta_0 \approx \sum_{i=1}^{n} \theta_i \cdot \Delta L_i \tag{4.53}$$

4.2.2 Large Deflection

Large deflections refer to the largely deformed shapes where it is not accurate to use the simplifications of $ds \approx dx$, *and* $\theta \approx \tan\theta = dv/dx$. In this case, the exact expressions of Eq.4.41 and 4.42 must be used. Therefore

$$\theta = \int_0^x \kappa \cdot ds \tag{4.54a}$$

and

$$\sin\theta = \frac{dv}{ds} \tag{4.54b}$$

From Eq.4.54b

$$\Delta_0 = \int_{s=0}^{l} dv = \int_0^l \sin\theta \cdot ds$$

In discrete form, the following relations can be derived with reference to Fig.4.15 which represents a typical segment from section *i-1* (point A) to section *i* (point B).

$$\Delta_0 = \sum_{i=1}^{n} \Delta v_i = \sum_{i=1}^{n} AB_i \cdot \sin\bar{\theta}_i \approx \sum_{i=1}^{n} AB_i \cdot \sin\frac{\theta_{i-1}+\theta_i}{2} \tag{4.55a}$$

$$AB_i = 2\cdot(\bar{R}\cdot\sin\frac{\theta_{i-1}-\theta_i}{2}) = \frac{2}{\bar{\kappa}}\cdot\sin(\frac{\theta_{i-1}-\theta_i}{2}) \approx \frac{4}{\kappa_{i-1}+\kappa_i}\cdot\sin(\frac{\theta_{i-1}-\theta_i}{2}) \tag{4.55b}$$

Based on Eq.4.54a, the discrete form to calculate θ_i is still given by Eq.4.49. Therefore, deflections shall be calculated by Eqs.4.49 and 4.55a&b when large deformations are involved.

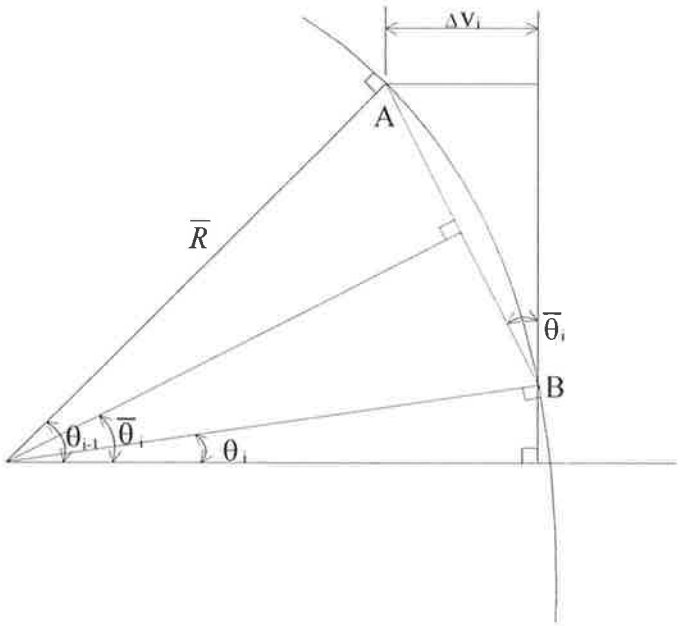

Fig. 4.15 Large deflection

4.2.3 Formation of Plastic Hinge

When the column member is in an elastic deformation stage, the deflection of the cantilever column can be calculated by the formulae given in the previous 2 sections. In this case, the calculated deflection result will not be sensitive to the choice of the segmental length ΔL_i (i=1~n) as long as enough segments, or a fine enough mesh, is used. However, this is not the case when a plastic hinge forms. Once the inelastic deformation stage is reached, only the bottom cross-section can pass the peak (point A of the moment-curvature curve shown in Fig.4.16) and proceed onto the descending part of the curve. All other cross-sections above the bottom section will go along their unloading

paths from some point to the left of A as shown in Fig.4.16 after the bottom section passes its peak. This is because the reduction of moment in the bottom cross-section reduces the moment of all the other sections above the base which are linearly related for the cantilever column. Therefore, further increases in deformation of the cantilever can only come from the deformation of the column at the bottom part, namely the plastic hinge region.

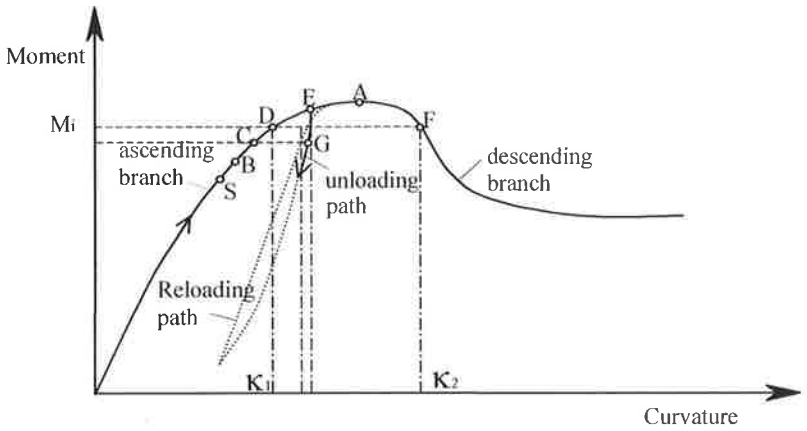

Fig. 4.16 Typical curvature-moment relation of an RC section

This plastic hinge region must have a certain length, because deformation of a cross-section with zero longitudinal length will not produce an overall deflection and hence no further deflection after the peak point can be predicted which is certainly not true in practice. This analysis is consistent with engineering experience that when large inelastic deformations occur, the inelastic deformation concentrates in small areas or plastic hinge zones in the vicinity of peak moment zones (Paulay and Priestley 1992).

The deformation of the plastic hinge is an extremely complicated subject. However, it can be simply modeled by applying the curvature of the bottom cross-section

to a certain length or the plastic hinge length L_p (Priestley and Park 1987) which might be calculated for a cantilever column by

$$L_p = 0.08 \cdot L + 6 \cdot d_b \tag{4.56a}$$

where L is the cantilever length shown in Fig.4.1 and d_b is the diameter of the longitudinal bars. Amendment to Eq.4.56a was made by Paulay and Priestley (1992) that took the form

$$L_p = 0.08 \cdot L + 0.022 \cdot f_{sy} \cdot d_b \tag{4.56b}$$

For convenience of discussion, Eq.4.52 is changed to

$$\Delta_0 = \sum_{i=1}^{n} \frac{\kappa_{i-1} + \kappa_i}{2} \cdot \Delta L_i \cdot \frac{L_{i-1} + L_i}{2} = \sum_{i=1}^{n} (\kappa_{i-1} \frac{\Delta L_i}{2} + \kappa_i \frac{\Delta L_i}{2}) \cdot \frac{L_{i-1} + L_i}{2}$$

where it can be seen that the curvature of the bottom cross-section is applied to half the length of the last segment $\frac{\Delta L_n}{2}$ by Eq.4.52. This half-length of the last segment where the bottom curvature κ_n is applied to is essentially the plastic hinge length L_p if Eq.4.52 is used. In this case, the choice of length for the last segment will directly affect the result of the deflection, which is certainly undesirable. This problem is solved by a simple modification to Eq.4.52 that applies the curvature of the bottom cross-section to a plastic hinge length that is calculated using either Eq.4.56a or 4.56b. The curvature of the adjacent section or section n-1 is then applied to an adjusted length of $\frac{\Delta L_{n-1}}{2} + \Delta L_n - L_p$ instead to the original length of $\frac{\Delta L_{n-1} + \Delta L_n}{2}$. For convenience, the bottom curvature is applied to the plastic hinge length regardless of whether the plastic hinge has formed or not in this work.

4.2.4 Base Rotation

It is assumed in the previous sections that the cantilever column is perfectly fixed at the bottom, or θ_n=0 in Eq.4.45. However, this is seldom the case. The cantilever column may have a base rotation θ_n which is not zero, and which is caused by pulling out of the tension bars and pushing in of the compression bars relative to the fixed base under flexural loading, as shown in Fig.4.17a. This base rotation may have a significant effect on the calculated displacement of the column. Of course, this base rotation depends on the anchorage method of the reinforcing bars.

In fact, the base rotation was considered in the calculation of the plastic hinge length in Eq.4.56a by Priestley and Park (1987). The additional rotation in the plastic hinge due to the base deformation was allowed for in the second term of Eq.4.56a by $6d_b$ which was attributed to "yield penetration" into the base. The first term of $0.08 \cdot L$ in Eq.4.56a was obviously due to the plastic deformation of the column itself. In their original model, all plastic rotation from both the column and base was considered to be accounted for by applying the plastic curvature at the bottom section to the plastic hinge length calculated with Eq.4.56a. This plastic rotation was then concentrated into the center of the plastic hinge that was above the fixed base. Based on this concept, the curvature distribution is modeled with Fig.4.17b in this numerical model.

However, it is found from the numerical simulations in Section 12.2.2 that the theoretical response curves based on the model (Fig.4.17b) do not agree well with the experimental curves. This discrepancy is found to be caused by the shifting up of the base

rotation, which actually takes place at the bottom of the column, to the center of the plastic hinge in Fig.4.17b.

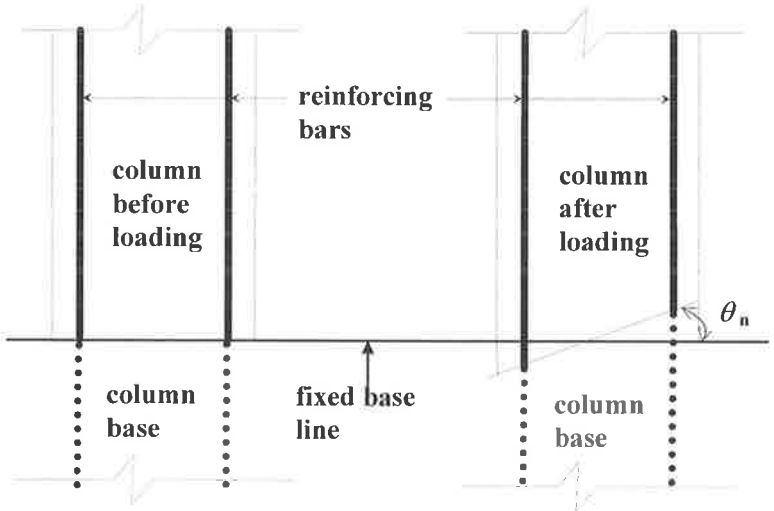

(a) Base rotation

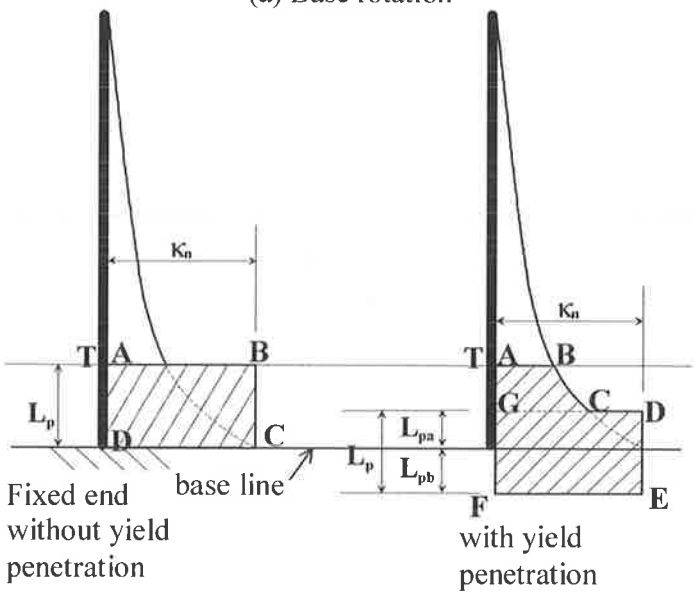

(b) Curvature distribution A (c) curvature distribution B

Fig. 4.17 Calculation of base rotation

If the same plastic hinge length L_p in Eq.4.56a and Fig.4.17b is now split into two parts of L_{pa}=0.08L which is above the base and $L_{pb}=6d_b$ which is below the base, as shown in Fig.4.17c, the calculated rotations at point T in Fig.4.17b and c, as given by

the shaded areas, will be different. Obviously, the model of Fig.4.17c gives an extra rotation at cross-section T that is equal to the area of ABCG. This means these two different models give different response curves with the same plastic hinge length. Obviously the model of Fig.4.17c gives a larger displacement.

When the fixed end rotation is significant, it is found in numerical simulations that model Fig.4.17b cannot reflect the actual distribution of deformation and will not give an accurate response curve even if the plastic hinge length is adjusted arbitrarily (changing plastic hinge length to check it's effect on the response curve). This will be seen by the numerical simulations in Section 12.2.2. In contrast, the fixed end rotation is adequately accounted for by the model of Fig.4.17c, where the plastic hinge is split into the two parts of L_{pa} and L_{pb} which are given by

$$L_{pa} = 0.08 \cdot L \tag{4.56c}$$

$$L_{pb} = 6 \cdot d_b \quad or \quad L_{pb} = 0.022 \cdot f_{sy} \cdot d_b \tag{4.56d}$$

where the fixed end rotation is now given by $\theta_n = \kappa_n \cdot L_{pb}$ which is the rotation at the base. The fixed end rotation or yield penetration into the support has also been experimentally observed in this work as shown by Fig.11.10.

4.3 NUMERICAL CONVERGENCE TESTS

The following numerical tests are conducted to check the convergence and accuracy of the proposed numerical models. The tests consist of a 100mm(depth)×50mm(breadth)×1000mm(length) steel cantilever column with E_s=200000 (N/mm^2), f_y=250 (N/mm^2), and no axial load applied.

1. Test No.1 – Identifying the number of layers required for discretisation of a cross-section.

   For the cantilever column with a bottom curvature of $\kappa=1.5\times10^{-5}$, the maximum strain in the column is given by $\varepsilon_{max}=\kappa\times50=7.5\times10^{-4}$ < $\varepsilon_y=250/200000=1.25\times10^{-3}$. Therefore the member is in a linear elastic state. In this case, the moment at the bottom is calculated to be $M=E\cdot I\cdot\kappa=1.25\times10^{7}(\text{Nmm})$, where $EI=8.3333\times10^{11}$.

The numerical results from the program "PLTCOL", using different numbers of layers to discretise the cross-section, are given in Table 4.1. From these results, it can be seen that 10-15 layers are usually adequate to give a result with an error less than 1%.

Table 4.1 Numerical results of the moment

No. of Layer	Numerical Moment (Nmm x 10^7)	Error (%) compared to analytical result
3	1.17187891	6.25
6	1.23047285	1.56
9	1.24132358	0.69
15	1.246879	0.25
30	1.24922291	0.06
75	1.249879	0.01
150	1.24997292	0.002

2. Test No.2 – Identifying the number of segments required

For the same case as test no.1, the theoretical results for the lateral load and the deflection are

$F = M/L = 12500$ (N), and

$$\Delta_0 = \frac{F \cdot L^3}{3EI} = 5 \text{ (mm)}$$

In the numerical calculations, 150 layers were used to discretise the cross-section in order to minimize the error due to cross-sectional discretisation. Longitudinally, the column is discretised with different numbers of segments and the numerical results of the top displacement calculated using both Eq.4.52 and Eq.4.53 are listed in Table 4.2.

Clearly, the results using Eq.4.52 has a much smaller error for the same number of segments compared to Eq.4.53.

Table 4.2 Numerical results of displacement

No of segment × segment length (mm)	Equation 4.53		Equation 4.50 or 4.52	
	Top displace-ment (mm)	Error (%)	Top displace-ment (mm)	Error (%)
2 × 500	2.8125	43.75	4.6875	6.25
4 × 250	3.9844	20.31	4.9219	1.56
8 × 125	4.5117	9.77	4.9805	0.39
16 × 62.5	4.7608	4.78	4.9951	0.098
40 × 25	4.9055	1.89	4.9992	0.016

It can be seen from these results that 4~8 number of segments are usually adequate to give a result with an error less than 1% using Eq.4.52.

3. Test No.3 – Large deflection calculations

The same test column is discretised into 150 layers in cross-section and longitudinally with 8 segments of 125mm long each. It can be seen from Table 4.3 that the deflection calculated by Eq.4.52 with small deflection assumption is good enough for most cases unless the inter-storey drift ratio is very large in which case the rigorous Eqs.4.49, 4.55a&b shall be used. For all practical purpose, $\Delta_0/L<10\%$ so that Eq.4.52 can be safely used.

Table 4.3 Large deflection

Curvature at bottom (1/mm)	Top Displacement (mm)		Storey Drift Δ_0/L (%)
	By equation for small deflection (Eq.4.52)	By equation for large deflection (Eq.4.49, 4.55)	
1.5E-5	4.9805	4.9805	0.498
6.0E-5	13.5760	13.5754	1.357
2.4E-4	25.1783	25.1750	2.517
9.6E-4	67.4447	67.3877	6.739
1.92E-3	123.6987	123.3530	12.335
3.84E-3	236.1996	233.8170	23.382

4.4 OVERALL NUMERICAL PROCEDURES

The methodology to calculate the force-displacement response of an RC cantilever column with steel plates glued to its sides is described in this section. When the plates are glued to the sides of the column, the strain distribution is assumed to be linear and continuous across the entire cross section including the plates. In this case, no slip occurs between the concrete and the plates. The numerical analysis is performed using a deformation control procedure. The curvature at the bottom of the cantilever column, where the bending moment is a maximum, is used as the control parameter. The advantage of using this curvature as the control variable is that it can follow both the ascending and descending parts of the moment versus curvature curve. It can also cater for cyclic loading by just reversing the increment of the control parameter and can allow for the formation of a plastic hinge at the bottom of the column.

4.4.1 Procedure

The cantilever column is discretised longitudinally as shown in Fig.4.1 and all cross-sections are discretised with an identical pattern as shown in Fig.4.3. However, the plate arrangement is allowed to vary from section to section in case different plate arrangements, such as termination of plate, at different sections are made. The following procedure is used in this work to calculate the response of the column.

1. Starting with an initial curvature of the bottom cross-section $\kappa_n = 0$; set curvature increment $\Delta\kappa_n$
2. For the new curvature of the bottom cross-section $\kappa_n(new) = \kappa_n(old) + \Delta\kappa_n$, assume a neutral axis position, then calculate the corresponding strain and stress distributions

in the section. The axial force of the cross-section is then calculated based on the stress distribution as described in Section 4.1.1. If the axial force of the cross-section is not equal to the constant axial load applied, the neutral axis position is adjusted until the difference between the calculated axial force and the constant axial load is less than the allowable tolerance. This iterative process is called the search for the neutral axis. Then the bending moment M_n of the cross-section is calculated based on the actual stress distribution.

3. The moment M_i for the rest of cross-sections along its length is calculated by

$$M_i = M_n \cdot L_i / L \quad (i = 1 \text{ to } n\text{-}1) \tag{4.57}$$

where L_i is the length from the top of the column to section *i* as shown in Fig.4.1.

4. For section *i* (*i*=*1*~*n-1*), assuming a curvature κ_i, conduct a cross-sectional analysis to locate the neutral axis position based on κ_i and the constant axial load. Then calculate the bending moment of the cross-section. If this trial moment is not equal to the moment M_i calculated in step 3, adjust the trial curvature κ_i until the difference between the trial moment and M_i is within the allowable tolerance. This process is called the search for curvature of the cross-section.

The curvature search may have multiple values of κ_i for the same M_i value, as shown in Fig.4.16. For a non-linear system, the stress of an element is not only determined by the strain but also depends on the loading history. With different loading histories, the stress-strain curve goes along different paths. Therefore, the loading history information must be recorded for all sub-section elements in all cross-sections separately. For a specific loading history, there is only one identical

loading/reloading (go forward) or unloading (go backward) branch. However, even in one identical branch, normally two different values of κ_i can be obtained for the same M_i value, e.g. κ_1 and κ_2 as shown in Fig.4.16. Fortunately, only the bottom cross section can pass the peak (point A) of the corresponding moment-curvature curve. All the other cross-sections will follow the unloading path when the bottom cross-section passes the peak point A going along the descending branch. In other words, only one value on the left hand side of the peak on the corresponding curve is the actual solution of κ_i for cross-section *i*.

To keep correct track of loading history, the step length or $\Delta\kappa_n$ must be sufficiently small. Otherwise incorrect results may be obtained. For example, if $\Delta\kappa_n$ is so big that the bottom cross-section moves from the current point B to next point F as shown in Fig.4.16, a nearby cross-section, say section n-1, should move from point S to G following the path of S-E-G. However, the program will give an erroneous result that is from point S to point C which has the same moment value as point G. This is because the current loading history for the element only has the information that occurs before point S for section *n-1*. When section *n* goes to point F which has the same moment as point D, the calculation of moment for section *n-1* in step 3, i.e. $M_{n-1} = M_n \cdot L_{n-1} / L$, gives the same moment as point C. Therefore the program will take point C as the new solution for section *n-1*. If the curvature increment of cross-section n or $\Delta\kappa_n$ is small enough, the computer will be able to trace the loading history closely and this kind of mistake will not happen.

5. After obtaining the curvatures for all the cross-sections along its length from step 4, calculate the displacement Δ_0 using formulae given in Section 4.2. The lateral force at the top is given by $F = M_n / L$. This gives one new point for the force-displacement response curve.
6. Record this step of the loading history. The information to be recorded includes the maximum excursion along the envelope curve, unloading and reloading points information for Mander's model; similar information for steel in Menegotto-Pinto's model, current and previous points information, etc. All the discretised sub-sections of concrete and plates, as well as all reinforcement layers for cross-section *1* to cross-section *n* must have their separate records. Therefore, when a fine discretisation mesh is used for the cross-section and along its length, the information to be recorded is substantial.
7. To calculate the next point of the force-displacement curve, go back to step 2 for another new κ_n. Repeat this process until the required force-displacement response curve has been generated. When cyclic response is required, simply reverse $\Delta\kappa_n$ when the required amplitude of displacement is reached.

4.4.2 P-Δ Effect

In the calculation of displacement by Eq.4.57, the P-Δ effect is ignored. For slender columns, the P-Δ effect can be substantial. To consider the P-Δ effect, Eq.4.57 must be revised as follows with reference to Fig.4.1.

$$M_i = F \cdot L_i + N \cdot (\Delta_0 - \Delta_i) \quad (i = 0 \sim n\text{-}1) \tag{4.58}$$

$$F = (M_n - N \cdot \Delta_0) / L \tag{4.59}$$

The above equations cannot be solved directly since the moment distribution which is required to calculated the displacement along the length is not known before the displacement is given.

4.4.2.1 Rigorous method

To solve Eqs.4.58 and 4.59, the following iterative process is adopted.

1. For a new curvature κ_n at the bottom section, calculate the column displacement $\Delta_i (i = 0 \sim n-1)$ with the same procedure as in Section 4.4.1 without considering P-Δ effect.
2. Revise bending moments for section *1* to *n-1* using Eqs.4.58 and 4.59 with the displacement distribution obtained from the previous step. Search section curvatures for section *1* to *n-1* based on the revised moment. Then calculate the revised column displacement $\Delta_i (i = 0 \sim n-1)$ based on the new set of curvatures.
3. Repeat step 2 with the revised set of Δ_i until the difference between the two consecutive iterations is within the allowable tolerance, or $\sum_{i=0}^{n-1} \left| (\Delta_i)_{current} - (\Delta_i)_{previous} \right| \le \delta$.

This iteration process calculates the accurate distribution of displacement and moment along the column and, therefore, is called the rigorous method. However, it is numerically intensive and very time consuming. To get each point in a force-displacement response curve, about four iterations are needed. That is to say four times the original computation time is required compared to the case where no P-Δ effect is considered. This increase in time can be quite substantial.

4.4.2.2 Simplified method

To reduce the computation time without significant loss of accuracy, a simplified method has been developed in this work for the P-Δ effect. From Eq.4.59, it can be seen that

$$F' = (M_n - N \cdot \Delta_0)/L = F - \Delta_0 \cdot \frac{N}{L} \tag{4.59a}$$

where F' is the lateral force required to achieve a moment M_n at the base of the cantilever column considering the P-Δ effect, and $F = M_n/L$ is the lateral force required to achieve the base moment M_n without considering P-Δ effect. Based on the above equation, the lateral force considering the P-Δ effect, F', can be obtained from the lateral force without considering the P-Δ effect, F, if the deflection Δ_0 at the top which considers the P-Δ effect is known.

Based on the above observation, a simplified method is proposed. Firstly, the response curve without considering the P-Δ effect is produced, as shown in Fig.4.18a by the curve marked with 'without P-Δ effect'. Each point in the response curve 'without P-Δ effect', e.g. point A, is then transformed to a new point, e.g. point B, in a new curve as marked with 'simplified method' in Fig.4.18a. The y coordinate transformation is given by the following formula

$$F' = F - \frac{N}{L} \cdot \Delta'_0 \tag{4.60}$$

where F' and F are the y coordinates of the new point B and the old point A, respectively; Δ'_0 is the x coordinate of point A, i.e. the calculated top displacement under the lateral force F without considering the P-Δ effect. The x coordinate of a point in the

new curve, e.g. Δ'_0 of point B, is the same as that of the old point A. The transformed new curve will be proved to be very close to the actual response curve with the P-Δ effect strictly considered, as illustrated in Fig.4.18a.

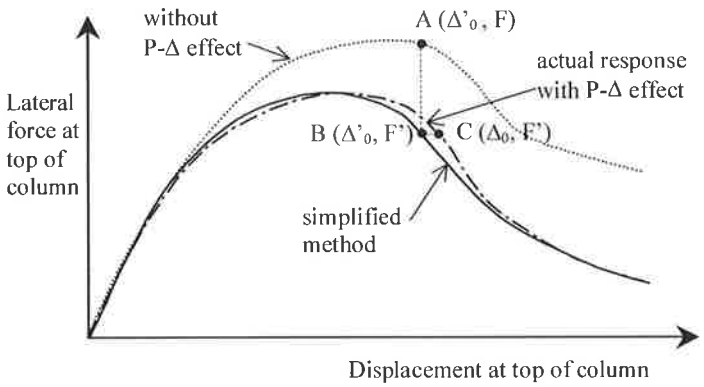

(a) Simplified method for P-Δ effect

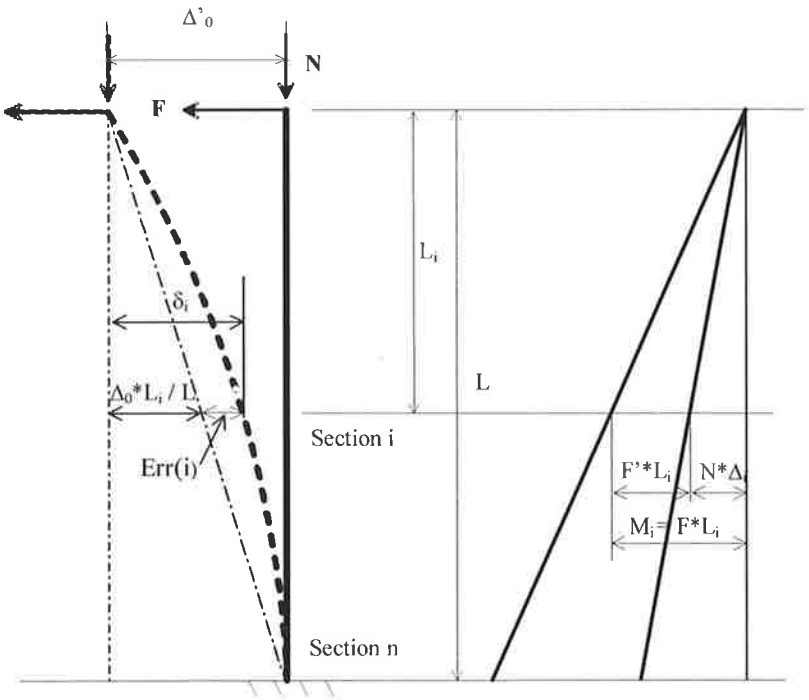

(b) Deflected shape (c) Moment distributions

Fig. 4.18 P-Δ effect

The above transformation can be visualized as dropping the original response curve by an additional slope of $\theta=N/L$, because Eq.4.60 can be rewritten as $F'= F - \frac{N}{L}\cdot\Delta'_0 = F - \theta\cdot\Delta'_0 = F - \Delta F$. This transformation is similar (but not exactly equivalent) to rotating the original force-displacement curve without considering the P-Δ effect clockwise by an additional slope of $\theta=N/L$ about the origin.

To estimate the error in the response curve produced from the simplified method, consider the moment distribution of $M_i = F\cdot L_i$ without the P-Δ effect, as shown in Fig.4.18c, and the corresponding deflected shape of the cantilever column, as shown by Fig.4.18b. Introducing the revised lateral force F' which satisfies Eq.4.60 and substituting into $M_i = F\cdot L_i$ gives

$$M_i = (F'+\frac{N}{L}\cdot\Delta'_0)\cdot L_i = F'\cdot L_i + (\frac{L_i}{L}\cdot\Delta'_0)\cdot N \qquad (4.61)$$

Eq.4.61 implies that the moment distribution of $M_i = F\cdot L_i$ can be considered as equivalent to a moment $F'\cdot L_i$ caused by a revised lateral force F' plus a moment of $N\cdot\frac{L_i}{L}\cdot\Delta'_0$ caused by the axial load with the eccentricity of $\Delta_i = \frac{L_i}{L}\cdot\Delta'_0$. If the eccentricity $\frac{L_i}{L}\cdot\Delta'_0$ is the same as that under the deflected shape of Fig.4.18b which corresponds to the moment distribution of $M_i = F'\cdot L_i + (\frac{L_i}{L}\cdot\Delta'_0)\cdot N$, then the revised lateral force F' together with the lateral deflection Δ'_0 is a precise point in the force-displacement response curve with the P-Δ effect strictly considered. In other words, the moment distribution of $M_i = F\cdot L_i$ without the P-Δ effect is caused by a reduced lateral

force F' with the exact P-Δ effect considered if the eccentricity of $\frac{L_i}{L} \cdot \Delta'_0$ is correct. However, the deflected shape under the moment distribution of $M_i = F \cdot L_i$ is not a straight line, hence the eccentricity given by $\Delta_i = \frac{L_i}{L} \cdot \Delta'_0$ is not accurate except at the top and bottom of the cantilever. Nevertheless, the error due to this linear assumption of eccentricity is generally not significant and can be estimated as follows.

The actual eccentricity under the deflected shape that is calculated from the moment distribution of $M_i = F' \cdot L_i + (\frac{L_i}{L} \cdot \Delta'_0) \cdot N$ is shown as δ_i at section i in Fig.4.18b, giving an actual moment of

$$M'_i = F' \cdot L_i + N \cdot \delta_i \tag{4.62}$$

Subtracting Eq.4.62 by Eq.4.61 gives the error in moment caused by Eq.4.61

$$M'_i - M_i = N \cdot (\delta_i - \frac{L_i}{L} \cdot \Delta'_0) = N \cdot Err(i) \tag{4.63}$$

in which $Err(i) = \delta_i - \frac{L_i}{L} \cdot \Delta'_0$ is the error due to the linear assumption of eccentricity as shown in Fig.4.18b. This error in moment is insignificant compared to Eq.4.62 for the following reasons.

- When the deflection of the column is small, P-Δ effect is small. The error in moment caused by deflection of column is therefore small. In other words, the error introduced by Eq.4.60 is negligible.
- When the deflection is large and the plastic hinge forms, the deflection of the column is mostly due to the plastic hinge rotation at the bottom, and the deflected shape above the hinge base of the column is relatively straight. In this case, Err(i) is

relatively small compared to the total eccentricity δ_i in Fig.4.18b. Therefore, the error introduced by Eq.4.60 is also small.

- For deflections in between the above two cases (between the small deflection and the large deflection), the relative error can be estimated by dividing Eq.4.62 by Eq.4.63, which gives

$$\frac{M'_i}{M'_i - M_i} = \frac{F' \cdot L_i + N \cdot \delta_i}{N \cdot Err(i)} = \frac{F'}{N} \cdot \frac{L_i}{Err(i)} + \frac{\delta_i}{Err(i)} \tag{4.64}$$

If it can be proved that Eq.4.64 gives a value much greater than 1, then the error in moment by Eq.4.63 due to the linear assumption of eccentricity is relatively small compared to the total moment of Eq.4.62. In the first part of Eq.4.64, i.e. $\frac{F'}{N} \cdot \frac{L_i}{Err(i)}$, $L_i >> Err(i)$. As the deflection is in between the small and large deflections, F' cannot be very small. Hence F'/N is usually not very small. Therefore, the term $\frac{F'}{N} \cdot \frac{L_i}{Err(i)}$ usually gives a very large value. From Fig.4.18b, it can be seen that the second part of Eq.4.64, i.e. $\frac{\delta_i}{Err(i)}$, is also a very large value near the bottom of the column where the moment contributes most to the deflection of the column. At the middle and top part of the column this second part of $\frac{\delta_i}{Err(i)}$ is relatively smaller than that in the bottom of the column, however, it is still greater than 1.0. In the mean time, the contribution of a moment in this middle and top part of the column to the deflection of the whole column is also smaller than that from the bottom part (as can be seen from Eq.4.52), which means that an error in moment at this region causes less

error in deflection than that caused by the same error in moment at the bottom of the column. As both the first and the second parts of Eq.4.64 are positive, the summation of these two parts gives an even bigger value. Therefore, generally $\frac{M'_i}{M'_i - M_i} >> 1$, or $M'_i - M_i << M'_i$.

The above discussion concludes that the linear assumption of eccentricity by Eq.4.61 will only cause a relative small error in moment as compared to the total moment of a cross-section. For all the cross-sections except the bottom section, the moment-curvature relation is in the ascending part of the curve to the left of the peak (point A) as shown in Fig.4.16. A small error in moment will only cause a small error in curvature value hence a small error to the deflection. Although, a small error in moment may cause a large error in curvature for the bottom cross-section in the descending part of the curve shown in Fig.4.16, the error introduced by Eq.4.60 for the bottom cross-section is zero. In other words, the error in curvature distribution hence the deflection caused by the simplified method or Eq.4.60 is generally small.

The error in eccentricity introduced by Eq.4.60 will cause an under-estimation of the deflection as can be seen from Eq.4.63 which is transformed to

$$M'_i = N \cdot Err(i) + M_i \geq M_i \qquad (\because Err(i) \geq 0)$$

Therefore, the moment at all cross-sections, except the top and the bottom, is underestimated slightly. That is to say the actual deflection should be slightly larger than Δ'_0, as shown by point C in Fig.4.18a. In other word, the actual deflection under the lateral force F' should be Δ_0 at point C instead of Δ'_0 at point B. This small increment

in displacement from the simplified response curve to the actual response curve where the P-Δ effect is strictly considered will be seen from the numerical example in Fig.4.19.

The conclusion that the error due to the simplified method is small has been verified by numerous numerical simulations. As an example, the force-displacement relation for a 200(B)×200(D) RC cantilever column with an axial load of 360kN is shown in Fig.4.19. In this numerical example, Mander's model and Menegotto-Pinto's model are used for the stress-strain relation of the concrete and the longitudinal reinforcement, respectively. Material properties of the column are summarized below:

Concrete - $\varepsilon_{co} = 0.002$, $\varepsilon_{cu} = 0.006$, $f_{co} = 40$ MPa, $f_{ct} = 4$ MPa; a = 35.7mm;

Longitudinal reinforcing bars - 4 Y16 with f_{sy} = 547 MPa, E_s = 200 GPa, $E_h = 600\,\text{MPa}$, $R_o = 20$, $a_1 = 19$, $a_2 = 0.3$;

Stirrups - $f_{hy} = 690\,\text{MPa}$.

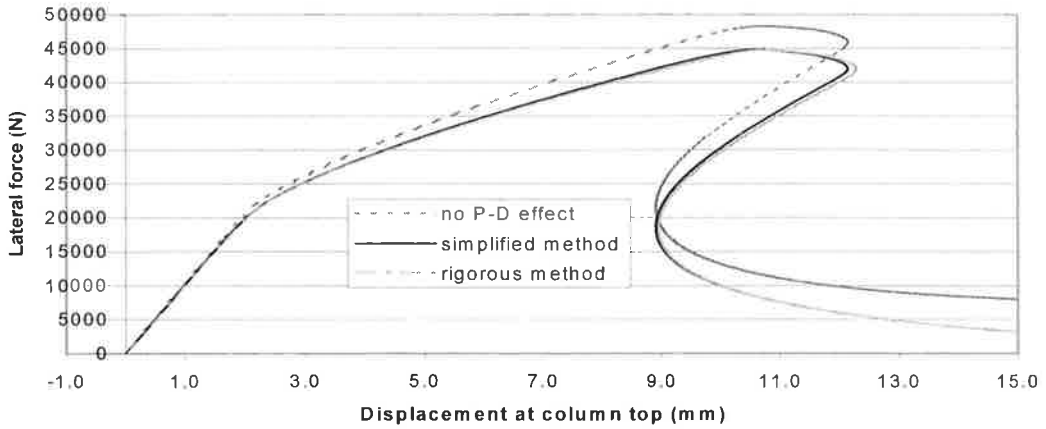

(a) Column without stirrups, L=1115, L_p=200

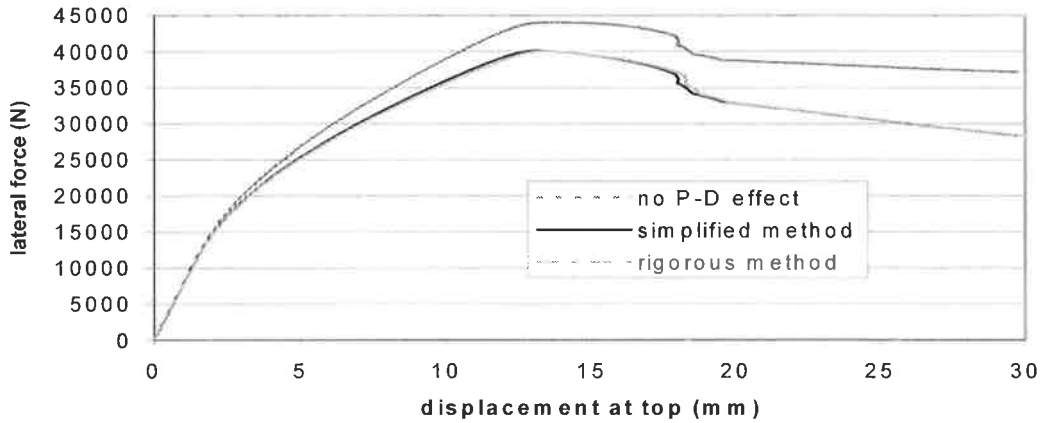

(b) Column with Y6-100 stirrups, L=1218, L_p=100

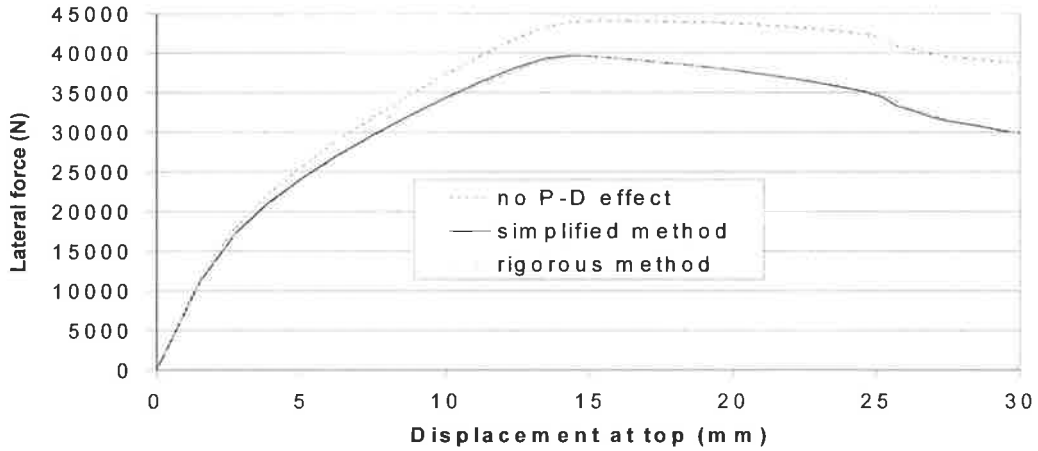

(c) Column with Y6-100 stirrups, L=1218, L_p=200

Fig. 4.19 Comparison of simplified P-Δ method with rigorous method

4.4.3 Numerical Examples

As an example to demonstrate the overall numerical model, an RC column tested by Watson and Park (1994) is analyzed in this section. The test column, as shown in Fig.4.20, has the following material properties:

Concrete: $f_{co} = 44MPa$, $\varepsilon_{co} = 0.002$ (assumed), $f_{ct} = 5MPa$ (assumed)

Longitudinal bars: $12Y16$, $f_{sy} = 446MPa$, $E_s = 200000MPa$ (assumed), $E_h = 600MPa$ (assumed); Constants for Menegotto-Pinto's model - $R_o = 20$, $\alpha_1 = 19$, $\alpha_2 = 0.3$ (assumed based on Gomes and Appleton 1997)

Stirrups: $\phi 8@78mm$, $f_{hy} = 360MPa$

Axial load ratio: $\dfrac{N}{f_{co} \cdot A_g} = 0.3$, or $N = 2112\text{KN}$

In the numerical modeling, the column cross-section is discretised into 25 layers and 25 slices as shown in Fig.4.21. Four layers of reinforcement are located exactly at their design positions in the cross-section with the areas of $804\,mm^2$ (4Y16), $402\,mm^2$ (2Y16), $402\,mm^2$ and $804\,mm^2$ for the 1st to fourth layer, respectively. The actual double cantilever columns with a stub are modeled with a 1.7m long cantilever column fixed at the bottom. It is longitudinally discretised into 5 segments with lengths of 400mm, 400mm, 400mm, 270mm and 230mm from top to bottom, respectively. The 230mm long bottom segment is used to model the plastic hinge length of 230mm as calculated in the next paragraph.

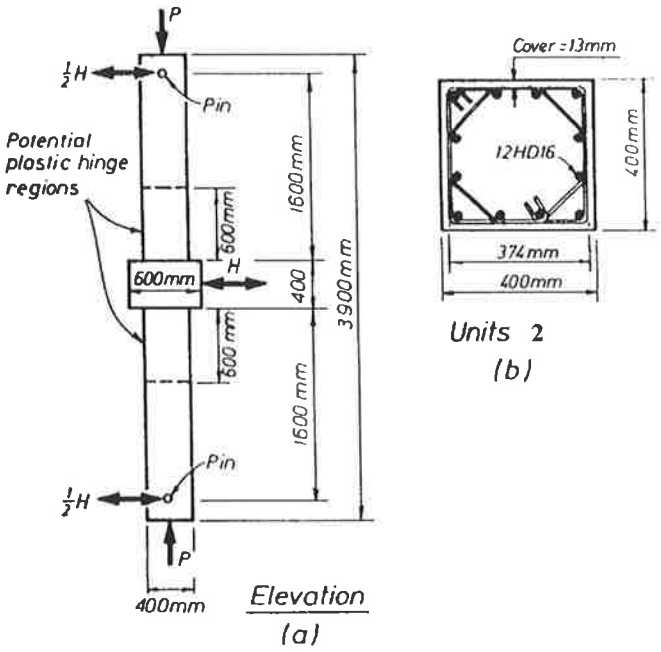

Fig. 4.20 Test column by Watson and Park (1994)

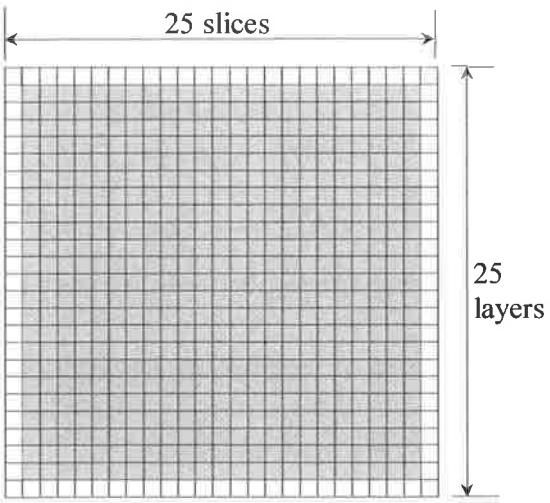

Fig. 4.21 Discretised cross-section and confinement zones

Mander's model and Menegotto-Pinto's model are used for the stress-strain relation of the concrete and the longitudinal reinforcement, respectively. The P-Δ effect is considered and the rigorous method (Section 4.4.2.1) is used in this example. The plastic hinge length is calculated with Eq.4.56a

$$L_p = 0.08 \cdot L + 6 \cdot d_b = 232 \text{ (mm) say } 230\text{mm}$$

where L is the length of the cantilever column and d_b is the diameter of the longitudinal bars. The calculation of lateral confinement is performed manually as follows. The lateral confinement pressure is given by (Watson, Zahn and Park 1994)

$$f_l = \frac{3.41 \cdot A_b \cdot f_{hy}}{s \cdot b_c} = \frac{3.41 \times 50.27 \times 360}{78 \times (400 - 13 \times 2 - 8)} = 2.16(MPa)$$

where A_b is the area of one leg of transverse reinforcement; s is the spacing of stirrups; and b_c is the height or depth of concrete core of column section enclosed by stirrups measured from center of stirrups. The effective confinement pressure and the confined concrete strength are given by (Mander et al. 1988a)

$$f_l' = k_e \cdot f_l = \frac{(1 - \sum_{i=1}^{n} \frac{(w_i')^2}{6b_c \cdot d_c}) \cdot (1 - \frac{s'}{2b_c}) \cdot (1 - \frac{s'}{2d_c})}{1 - \rho_{cc}} \cdot f_l = 0.713 \times 2.16 = 1.54(MPa)$$

$$f_{cc} = f_{co}(-1.254 + 2.254\sqrt{1 + \frac{7.94 f_l'}{f_{co}}} - 2\frac{f_l'}{f_{co}}) = 53.9 \approx 54(MPa)$$

where w_i' is the ith clear transverse spacing between adjacent longitudinal bars; $d_c = b_c$ in this case; ρ_{cc} is the ratio of area of longitudinal reinforcement to the core of section; and s' is the clear longitudinal spacing between stirrups.

The confinement effect of the concrete is allowed for by assigning the concrete strength as f_{cc} or 54MPa in the confined zone as shaded in Fig.4.21. The confined zone is assumed to be the area within the center-line of the perimeter stirrups in Mander's model. The unconfined concrete strength f_{co} or 44 MPa is used for the unconfined concrete in the non-shaded area in Fig.4.21.

The cycling of the response is controlled by driving the control parameter, i.e. the curvature of the bottom cross-section κ_n. The initial value of κ_n is set to zero. An increment $\Delta\kappa_n = 4\times10^{-6}$ is then applied to the previous curvature κ_n to calculate a new point in the force-displacement curve. The calculation of successive new points continues until the displacement at the top of the cantilever reaches the specific "target" value, when $\Delta\kappa_n$ changes sign so that the column is moved in the opposite direction. The "target" displacements are chosen to match the cyclic amplitudes of the experimental results.

The numerical results for the test column are given in Figs.4.22 and 4.23. Figure 4.22 shows the moment-curvature relation of the bottom cross-section. The displacement-force relation of the cantilever column is given in Fig.4.23. The calculation terminates and cannot finish all the cycles as the experiment did when the strain in the concrete reaches a value of more than 0.0614 at which time an error occurs in Mander's model. This error seems always to occur in Mander's model when the strain is extremely high. However, such high strains are not of practical significance, as can be seen from Fig.4.23 where the column has actually failed at the last point.

The test results by Watson and Park (1994) are given in Fig.4.24. For comparison, the force H or y coordinates in Fig.4.24 has to be divided by two, because two columns are loaded simultaneously in the test and the force applied at one cantilever column is $0.5H$ as shown in Fig.4.20. The comparison between Fig.4.23 and the test result shows that the test column is stronger and degrades slower than the numerical one. It suggests the possibility that the actual materials of the test column were stronger than the material properties given, and the actual confinement was greater than the calculated one.

As mentioned in Section 4.1.2.2.1, the computer program can also account for general configurations of confinement such as that shown in Fig.4.25, where the confined concrete strength is 57.4MPa in the shaded area and the unconfined strength is 44MPa in the non-shaded area. Basically, the computer program allows for independent confined or un-confined concrete strengths for every individual sub-section. The response corresponding to the confinement configuration shown by Fig.4.25 is given by Fig.4.26. As the response curve is much 'weaker' than Fig.4.23 and the test results, it suggests that the confinement is not properly modeled by Fig.4.25.

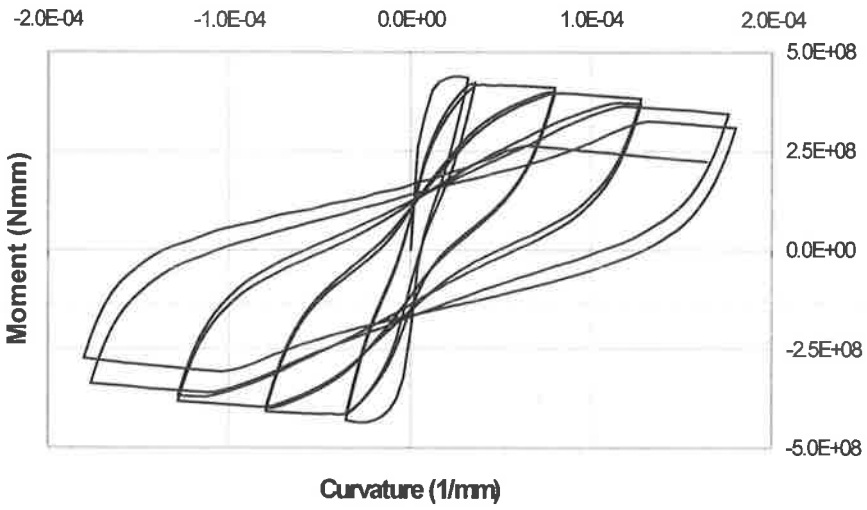

Fig. 4.22 Curvature-moment relation

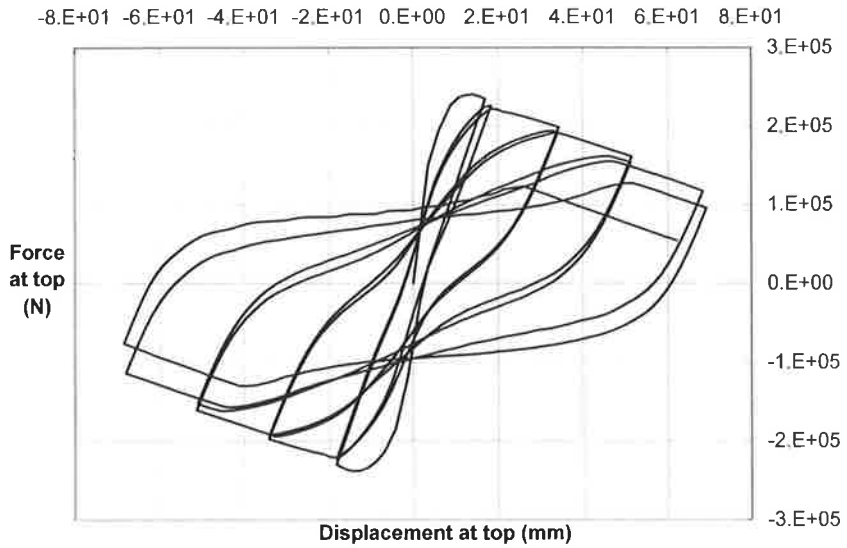

Fig. 4.23 Displacement-force relation

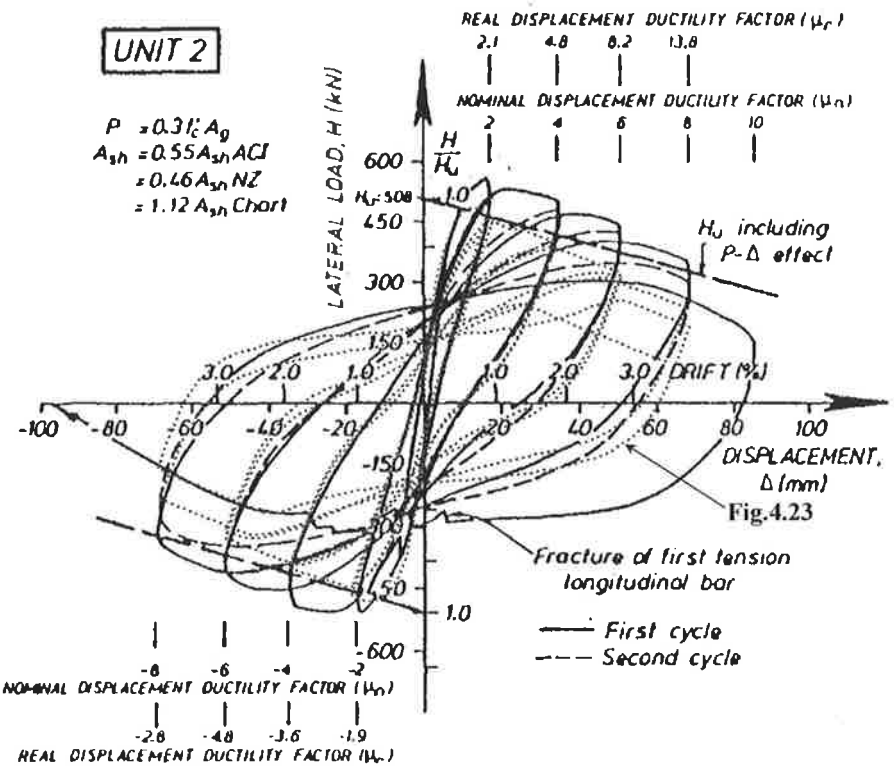

Fig. 4.24 Test result compared to Fig.4.23

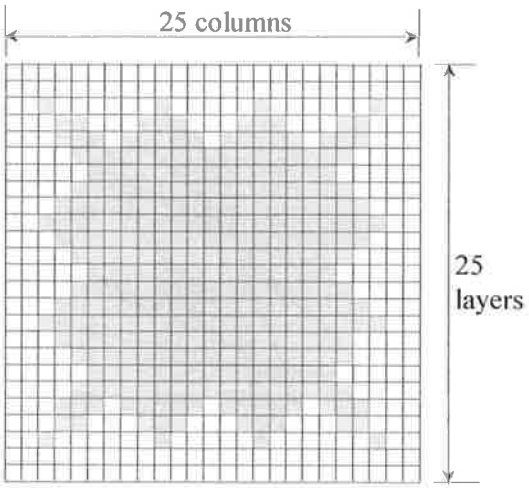

Fig. 4.25 Complex confinement zone configuration

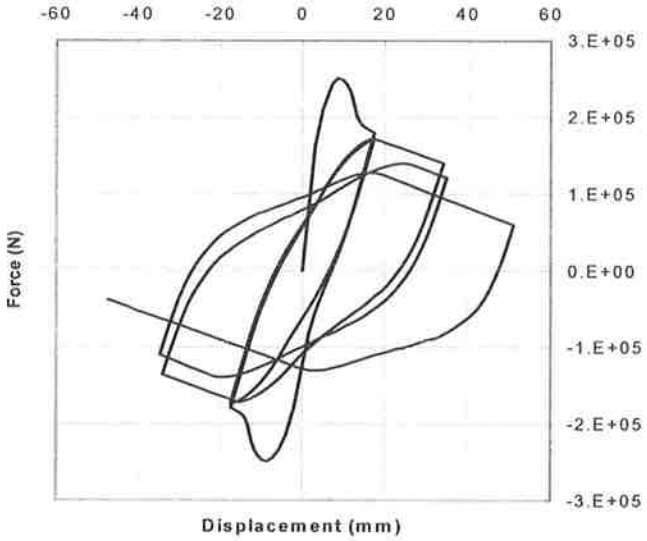

Fig. 4.26 Response of column with confinement configuration of Fig.4.25

4.5 COLUMNS WITH PLATES BOLTED TO TENSION AND COMPRESSION FACES

When plates are bolted, instead of glued, to the faces of a column, methods developed in the previous sections cannot be used, because of the relative movement or slip between

the plates and the RC column. For columns with bolted plates, the slip on the interface causes discontinuity in the strain profiles in a cross-section. In this case, the strain of the plate cannot be determined directly from the curvature and neutral axis position of an RC cross-section.

To simulate the response of the composite plated column shown in Fig.3.1, new mathematical models that consider slip or partial interaction between the RC column and the plates that are bolted on the tension and compression faces are developed in this section. Columns with plates bolted on the other two side faces are not covered in this study.

To calculate the slip on the two interfaces, the longitudinal segments are divided in such a way that one segment is taken between two adjacent longitudinal bolts, as shown in Fig.4.27. The first and last segments are taken from top and bottom of the column to the first and last bolt, respectively.

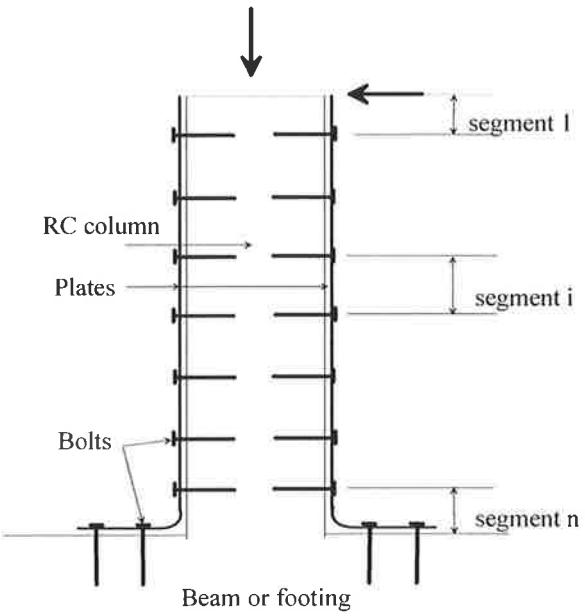

Fig. 4.27 Longitudinal discretization of plated column

4.5.1 Existence of Solution

The variables on a typical cross-section considering partial interaction are shown in Fig.4.28, where the superscripts '*L*' and '*R*' represent the left-hand-side (LHS) and the right-hand-side (RHS) respectively.

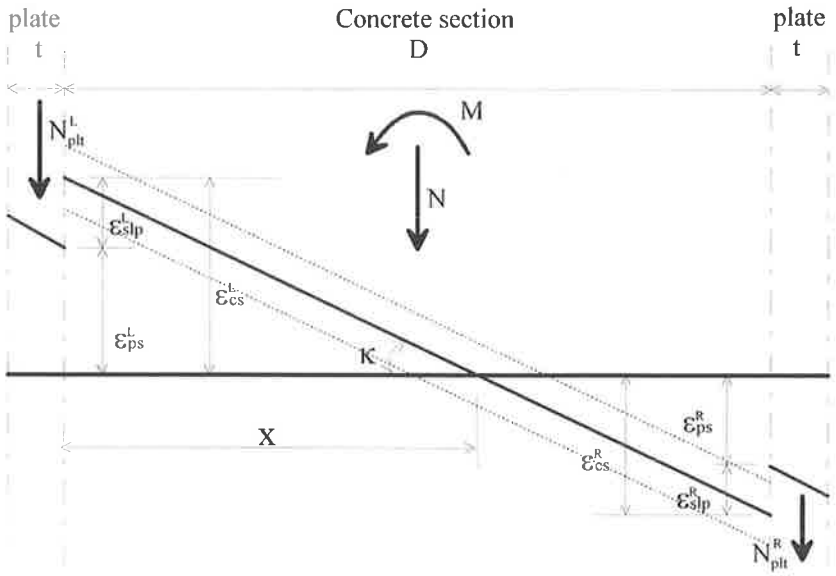

Fig. 4.28 Typical strain profile in a cross section with partial interaction

There are 10 unknowns at a cross-section. Six of them are related to the cross-sectional analysis for each cross-section *i* (*i*=*1*~*n*) as follows

- The curvature of the cross-section κ_i;
- The depth of concrete compressive zone x_i;
- The slip strains at the LHS $\varepsilon^L_{slp}(i)$ and RHS $\varepsilon^R_{slp}(i)$, respectively;
- The axial forces on the LHS and RHS plates: $N^L_{plt}(i)$ and $N^R_{plt}(i)$, respectively.

The other 4 unknowns are related to the movement of the bolts at each cross-section. It is assumed that the longitudinal slip at the interface between the plate and the RC column is

equal to the lateral movement of the bolt (when a gap exists between a bolt and the plate, it is not equal. See Section 4.5.4) as shown in Fig.4.29. The four unknowns are:

- The LHS & RHS slips, s_i^L and s_i^R, respectively; and
- The lateral (shear) forces on the LHS & RHS bolts, $F_b^L(i)$ and $F_b^R(i)$, respectively.

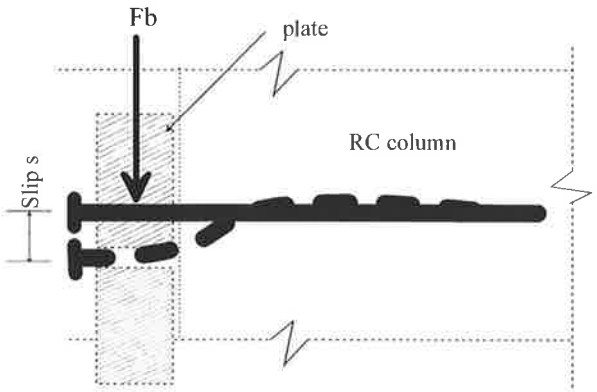

Fig. 4.29 Slip-shear force relation of a bolt

The 10 conditions that can be used to solve for the above unknowns are:

- The axial load at any cross-section is a constant, i.e. $N_i = C$.
- The bending moment M_i must satisfy the overall equilibrium condition given by Eq.4.57 or 4.58.
- The relations between the slip strains and slips are given by

$$s_i^L = s_{i+1}^L + \varepsilon_{slp}^L(i+1)\cdot\Delta L_{i+1} \tag{4.65}$$

$$s_i^R = s_{i+1}^R + \varepsilon_{slp}^R(i+1)\cdot\Delta L_{i+1} \tag{4.66}$$

- The relation between the shear force applied to the bolt and the amount of slip, as shown in Fig.4.29, is given by a shear force versus deformation model (based on test data as shown in Fig.4.13b) which can be expressed mathematically as

$$F_b^L(i) = f(s_i^L) \tag{4.67}$$

$$F_b^R(i) = f(s_i^R) \tag{4.68}$$

- The relation between the shear force of bolt and the axial force on the plate is given by

$$N_{plt}^L(i) = N_{plt}^L(i+1) + F_b^L(i) \tag{4.69}$$

$$N_{plt}^R(i) = N_{plt}^R(i+1) + F_b^R(i) \tag{4.70}$$

where F_b is defined positive when the bolt is bent downwards.

- The relation between the strain distribution of the plate and axial force in the plate can be expressed mathematically as

$$N_{plt}^L(i) = f(\varepsilon_{ps}^L(i), \kappa_i) \tag{4.71}$$

$$N_{plt}^R(i) = f(\varepsilon_{ps}^R(i), \kappa_i) \tag{4.72}$$

where $\varepsilon_{ps}^L(i)$, $\varepsilon_{ps}^R(i)$ are the strains on the interface for the LHS and RHS plates, as shown in Fig.4.28.

From the above analysis, it can be seen that there are 'n' cross-sections, hence $n \times 10$ unknowns in total for the whole cantilever column. There are also 10n independent equations available. Therefore, the system is theoretically solvable. However, to solve these equations directly is not practical when non-linearity is involved. Trial and error methods, i.e. iterative procedures, are used in this study to solve the problem.

4.5.2 Iterative Solution Procedure

If the slip strains or forces of the plate in a cross-section are known, the analysis of the cross-section will be no different than that given in Section 4.1. By assuming the forces

in both the tension and compression plates at the bottom cross-section (control cross-section), the forces in the plates at other cross-sections can be calculated one by one using equations 4.65-4.72, ending with the forces in the plates at the top of the column. The forces in the top of the plates should be zero for both the LHS and RHS plates. If this "boundary" condition is not satisfied, then the trial forces at the bottom cross-section were incorrect and another pair of forces is tried until a solution is found. Based on this idea, the following iterative procedure is developed to solve the problem.

1. Set the initial curvature $\kappa_n = \Delta\kappa_n$ for the bottom cross-section.
2. Guess the axial forces $N_{plt}^{L}(n) \& N_{plt}^{R}(n)$ in the LHS and RHS plates at the bottom cross-section.
3. Find the strain distributions and $\varepsilon_{ps}^{L}(n) \& \varepsilon_{ps}^{R}(n)$ in the LHS and RHS plate based on $N_{plt}^{L}(n), N_{plt}^{R}(n)$ and the curvature κ_n.
4. Calculate the slips $s_n^L \& s_n^R$ for both the LHS and RHS plates at the bottom of the cantilever. The slip-force relation at the bottom is modeled by a spring as shown in Fig.3.1(b). The slip or displacement of the spring can be calculated from the force on the spring, i.e. $N_{plt}^{L}(n), N_{plt}^{R}(n)$. Assuming the plate cannot penetrate through the concrete, the slip is set to zero when a downward slip going into the concrete is calculated.
5. For the given curvature κ_n and plate forces $N_{plt}^{L}(n), N_{plt}^{R}(n)$, adjust the strain profile in the RC section as shown by the dotted lines in Fig.4.28 or search for the neutral axis depth x to satisfy the condition of constant axial force N in the cross-section. Then calculate $\varepsilon_{cs}^{L}(n) \& \varepsilon_{cs}^{R}(n)$.

6. Calculate the moment M_n of the bottom cross-section based on the stress and force distribution obtained in step 5.
7. Calculate the moment M_i for cross-sections 1 to n-1 based on $M_i = M_n * L_i / L$, ignoring the P-Δ effect. Set the cross-section number $i=n$ for calculations in the following steps.
8. For both the LHS and RHS plates, calculate slip strain ε_{slp} of the cross-section i based on $\varepsilon_{slp}(i) = \varepsilon_{ps}(i) - \varepsilon_{cs}(i)$, as illustrated in Fig.4.28. Then calculate the slip at the adjacent upper cross-section by $s_{i-1} = s_i + \varepsilon_{slp}(i) \cdot \Delta L_i$.
9. Calculate the shear forces $F_b(i-1)$ on both the LHS and RHS bolts located at section i-1 based on Eqs.4.67 and 4.68, i.e. $F_b(i-1) = f(s_{i-1})$. A bi-linear slip versus force relation as discussed in Section 4.1.4 is used at the moment in the computer model.
10. The axial forces of the LHS and RHS plates in cross-section i-1 are calculated by $N_{plt}(i-1) = N_{plt}(i) + F_b(i-1)$.
11. Based on $N_{plt}^{L}(i-1) \& N_{plt}^{R}(i-1)$, the moment M_{i-1} and the total axial force N for cross-section i-1, search for the curvature κ_{i-1} and neutral axis x_{i-1}.
12. Calculate strain distribution and $\varepsilon_{ps}^{L}(i-1) \& \varepsilon_{ps}^{R}(i-1)$ in the plates for cross-section i-1 based on $N_{plt}^{L}(i-1) \& N_{plt}^{R}(i-1)$ and κ_{i-1}. Calculate $\varepsilon_{cs}^{L}(i-1) \& \varepsilon_{cs}^{R}(i-1)$ from the strain distribution obtained in step 11.
13. i = i-1. Repeat steps 8 to 13 until i = 1.

14. (a) If the axial forces of the plates $N_{plt}^{L}(1)\,\&\,N_{plt}^{R}(1)$ at cross-section 1 are not zero, the trial axial forces $N_{plt}^{L}(n)\,\&\,N_{plt}^{R}(n)$ are not correct. Adjust $N_{plt}^{L}(n)\,\&\,N_{plt}^{R}(n)$. Go back to step 3. The method used to adjust $N_{plt}^{L}(n)\,\&\,N_{plt}^{R}(n)$ is discussed in Section 4.5.3.

    (b)If $N_{plt}^{L}(1)\,\&\,N_{plt}^{R}(1)$ are both zero, the trial forces $N_{plt}^{L}(n)\,\&\,N_{plt}^{R}(n)$ are correct. Calculate the lateral displacement Δ of the column based on the curvatures along the column. The force at the top is given by $F = M_n / L$. This $F\&\Delta$ pair gives a point in the F-Δ chart.

15. Record the stress-strain history for all the elements of the concrete, plates, bolts and springs for the calculation of the next point of the F-Δ chart.

16. $\kappa_n = \kappa_n + \Delta\kappa_n$, go back to step 2 until the required F-Δ chart is produced.

While the P-Δ effect is not considered in the above calculations, both the rigorous and simplified methods as given in Sections 4.4.2.1 and 4.4.2.2 can be incorporated into the above process to include the P-Δ effect. However, the rigorous method adds another loop to the already very intensive numerical calculations. In view of the reasonable accuracy of the simplified method, it is adopted to calculate the P-Δ effect for a plated column with partial interaction. This means that the final results from the above process, i.e. the force-displacement relation at the top of the column, are simply transformed by Eq.4.60 to get the response curve with the P-Δ effect.

4.5.3 Iteration Method

An iterative method is used to find the values of $N_{plt}^{L}(n) \& N_{plt}^{R}(n)$ in the procedures discussed in Section 4.5.2. Mathematically speaking this process is a root finding process for the following equations.

$$\begin{cases} N_{plt}^{L}(1) = f_1(N_{plt}^{L}(n), N_{plt}^{R}(n)) = 0 \\ N_{plt}^{R}(1) = f_2(N_{plt}^{L}(n), N_{plt}^{R}(n)) = 0 \end{cases} \tag{4.73}$$

The target functions are $N_{plt}^{L}(1) = 0$, $N_{plt}^{R}(1) = 0$. The two variables are $N_{plt}^{L}(n) \& N_{plt}^{R}(n)$. In this work, the Newton's method for non-linear system of equations with 2 variables are used to find the roots (Kendall, 1978).

4.5.4 Gap between Bolt and Plate

Longitudinal gaps between the bolts and plates, as shown in Fig.4.30, are unavoidable for a practical column. This gap will affect the interaction between the plate and the bolt and, hence, the overall behavior of the plated column.

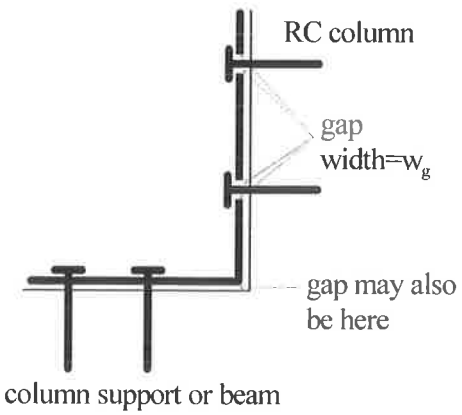

Fig. 4.30 Longitudinal gaps

When gaps exist, the slip s at a cross-section between the plate and the RC column is no longer equal to the lateral deformation of the bolt. The lateral deformation s_b of the bolt has to be modified by the following relation

$$\begin{cases} s_b = s_r & when \quad |s - s_r| \le w_g \\ s_b = s - w_g & when \quad s - s_r > w_g \\ s_b = s + w_g & when \quad s - s_r < -w_g \end{cases} \tag{4.74}$$

where s_r is the plastic or residual deformation of the bolt which depends on the loading history; and w_g is the gap width. This s_b is the true lateral deformation of the bolt. The bolt force can then be obtained with the same model as discussed in Section 4.1.4 using s_b as the horizontal axis.

In Eq.4.74 when $|s - s_r| \le w_g$, that is before the gap is closed, the bolt force is always zero as given by the above model. This means that the bolt force is a constant over a range of slip values. This kind of constant value will usually cause problems in various searching procedures of the program. In order to avoid this kind of difficulty, the following equation is used

$$F_b = K_b^0 \cdot (s - s_r) \quad when \quad |s - s_r| \le w_g \tag{4.75}$$

where K_b^0 is an arbitrary but very small value. By providing this very small variation of force in the bolt before the gap is closed up, numerical searching procedures are well behaved.

4.5.5 Numerical Examples

Numerical examples for a plated column are shown in Fig.4.31. The column studied is a 1218mm long cantilever column with a cross-section of 200×200. Longitudinal bars are 4Y16 with concrete cover 35.7mm from the center of the bar to the face of the column. Properties used in the numerical analysis are:

Concrete - f_{co} = 40 MPa, f_{ct} = 4.2 MPa, ε_{co} = 0.002, ε_{cu} = 0.006;

Steel plate – t=6mm, f_{py} = 250 MPa, E_p = 200 GPa, E_{ph} = 600MPa;

Main reinforcement bars – f_{sy} = 547 MPa , E_s = 200 GPa, E_h = 600MPa;

Stirrups - f_{hy} = 690 MPa;

Bolt - F_{by} = 35kN, K_b = 23 kN/mm, K_{bh}=0.7kN/mm; Bolt spacing: 100mm c/c except 1st bolt 200mm from bottom of the column with a total number of 2 × 8 on each side (2 bolts on one side of a cross-section).

The plastic hinge length is calculated by Eq.4.56a to be $L_p \approx 200mm$. Confinement due to the stirrups of R6 at 100mm is considered in the calculations. The confinement effect is calculated based on the method discussed in Section 4.4.3. The confined concrete strength is calculated to be f_{cc}=47MPa inside the confined core enclosed by the stirrups. The P-Δ effect is also included in the calculations to reflect the realistic response.

The first case indicated with "no plate" in Fig.4.31 is an RC column without plating. The second case is the plated column without gaps around the bolts. The third case is the plated column with a 1.5mm gap around the bolts. The last case is a full

interaction plated column where the steel plate is glued to the face of the RC column or the bolt stiffness is infinity. Detailed discussions on these response curves are given in Chapter 5.

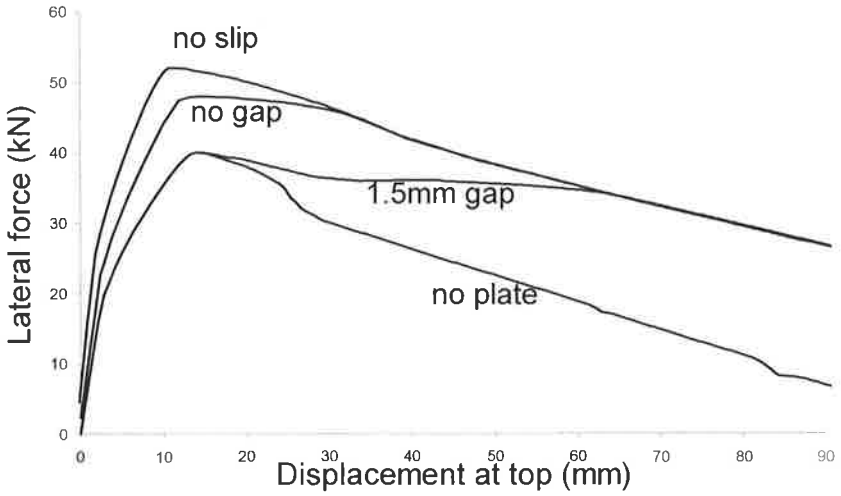

Fig. 4.31 Response of columns with different plating

4.6 SUMMARY

The numerical models to simulate the response of the plated RC columns are developed in this chapter. This numerical model can simulate the response of RC columns under monotonic load both on the ascending part and softening branches, as well as under quasi-static cyclic loading. Each part of the numerical modeling and computer programming has been carefully tested and verified and compared to theoretical results where available. Reasonable responses for RC columns have been obtained by the computer program "PLTCOL" as compared to test results which will be discussed further in Chapter 12. This numerical model will be used to analyze the response of plated RC columns in the next chapter in order to study the behavior of these columns.

CHAPTER 5 NUMERICAL STUDIES OF PLATED RC COLUMNS

In this chapter, the effect of composite partial-interaction plating is studied through numerical simulations of column responses. The responses of the plated columns are calculated using the computer program "PLTCOL" described earlier in Chapter 4.

5.1 EFFECT OF COMPOSITE PLATING

In order to gauge the effects of composite partial-interaction plating, the RC column with plating on the compression face only, as illustrated in Fig.5.1, is studied.

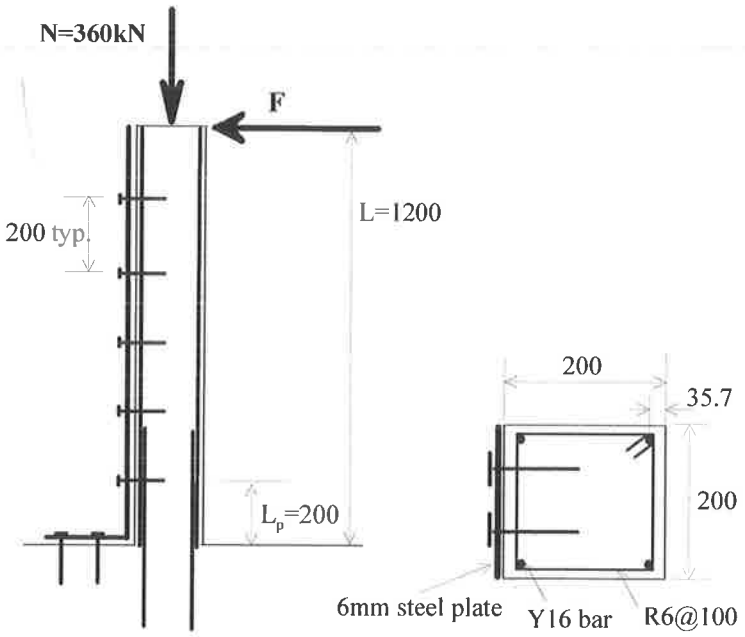

Fig. 5.1 Column details

Properties used in the numerical simulation are listed below:

Concrete: f_{co} = 40 MPa, f_{ct} = 6 MPa, ε_{co} = 0.002, ε_{cu} = 0.006;

Steel plate: f_{py} = 250 MPa, E_p = 200 GPa, E_{ph} = 600MPa;

Main reinforcement bars: f_{sy} = 547 MPa, E_s = 200 GPa, E_h = 600MPa, R_0=20.0, α_1=19.0, α_2=0.3;

Stirrups: f_{hy} = 690 MPa (cold pulled mild steel);

Bolts: F_{by} =35kN, K_b = 23 kN/mm, K_{bh}=0.7kN/mm.

The confinement to the concrete core due to the stirrups and the P-Δ effect are not considered in the present analyses (results from Figs.5.2 to Fig.5.5) in order to isolate the effect of the composite action. These effects, however, will be incorporated later in Section 5.2 in the further study.

The responses of columns with different plating details are given in Fig.5.2. The response curve marked 'original unplated column' is for the RC column without plating, which is used as a benchmark for direct comparison. The curve indicated 'plate bolted 1 side' is for the plated column shown in Fig.5.1. The case with plating on both the tension and compression sides is also studied, which gives almost identical results to the 'plate bolted 1 side' case when the tension spring stiffness shown in Fig.3.1(b) is small. This both sides plated case verified the assumption that Fig.5.1 is equivalent to that in Fig.3.1(a) when the plate can be easily opened up at the corner. The result for 'plates glued 2 sides' is for the case where both sides are bonded with full interaction plates (no slip between concrete and plate) and without the uplift facility illustrated in Fig.3.1(c), which is equivalent to adding extra fully anchored reinforcing bars. The case 'plate bolted

1 side plus wrapping' is for the 'plate bolted 1 side' column plus an assumed lateral confinement effect due to wrapping. This additional confinement is assumed to be able to increase the concrete strength from 40MPa to a confined concrete strength of f_{co} = 48 MPa which can be achieved theoretically with FRP wrapping (Mirmiran et al. 1998).

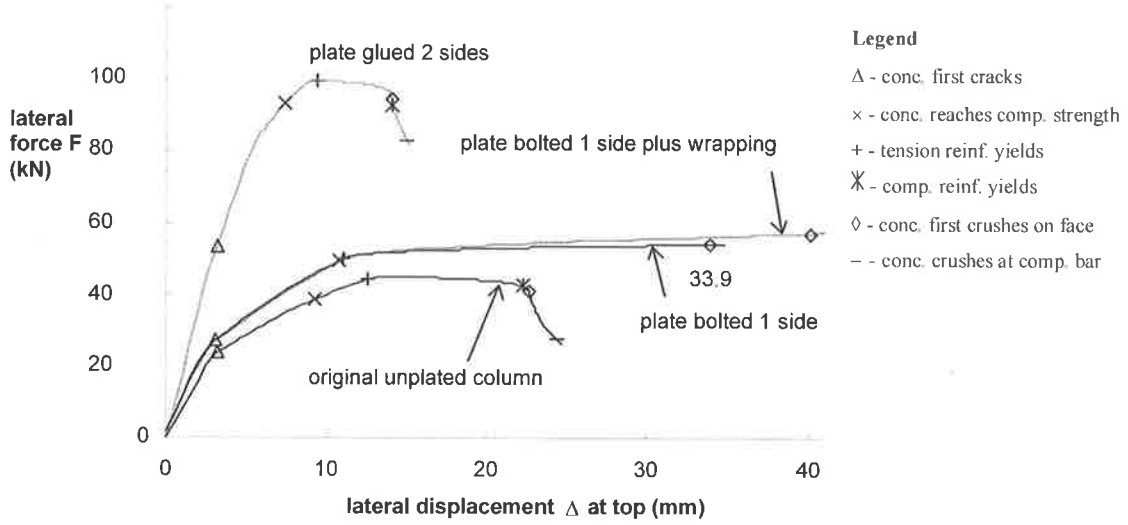

Fig. 5.2 Lateral responses of columns

Critical points are highlighted in Fig.5.2 by various marks that indicate different deformation stages as shown in the legend. More detailed definitions of these marks are given in the Notation. All these critical points or stages refer to the cross-section at the bottom of the column where the applied moment is a maximum.

It can be seen in Fig.5.2 that adding extra reinforcement, that is the case of 'plate glued 2 sides', can substantially increase the strength but at a considerable loss of ductility which may not be beneficial in seismic retrofitting. In contrast, the system represented by the 'plate bolted 1 side' case in Fig.5.2 substantially increases the ductility with a relatively small increase in strength as is often required in seismic retrofitting in order not to increase loads on the foundations. It is also worth noting that combining

wrapping with partial-interaction plating, as in the case of 'plate bolted 1 side plus wrapping', further increases the ductility.

Figure 5.3 shows the variation of axial force on the concrete alone at the bottom cross-section, which excludes the axial forces on the reinforcement bars and the plate. It can be seen that the axial force on the concrete is reduced for the 'plate bolted 1 side' case compared to the 'unplated column', resulting in the increased deformation capacity. For the case of the 'plate glued 2 sides', the plates reduce the axial force on the concrete when the lateral displacement is small. However, the axial force on the concrete increases rapidly with curvature because of the increased tensile force in the tension plate. This additional axial force causes the concrete to crush earlier, as indicated by the mark '◊' in Figs.5.2 and 5.3.

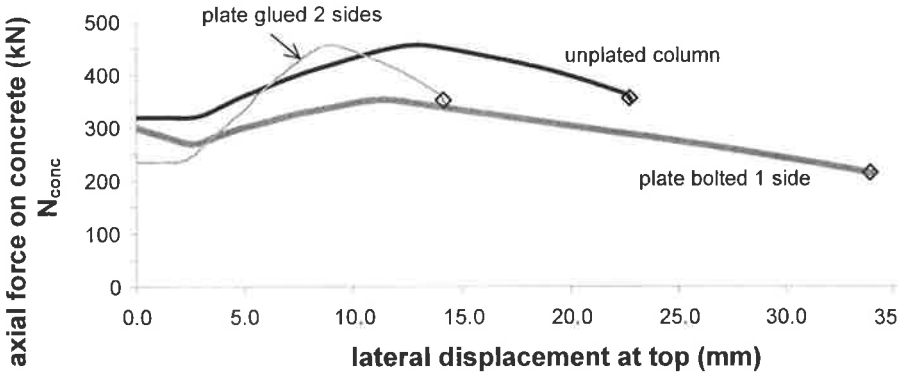

Fig. 5.3 Variation of axial force on concrete

To further demonstrate the effect of applied axial force on the deformation capacity, the column case with the plate bolted only to the compression face is studied in Fig.5.4 with different axial loads N, where $N_c = f_{co} A_g$ and A_g is the gross cross-sectional area of the RC section. The responses of the plated columns are shown with dark lines. For comparison, the responses of the original column without plating under

the same axial loads are also shown with light lines. It can be seen that partial-interaction plating increases the ductility in all cases. In addition, the detrimental effect of increasing axial load on the ductility/deformation capacity of the columns, which may be reflected by the point '◊' when the concrete crushes on the compression face, is also clearly shown in Fig.5.4.

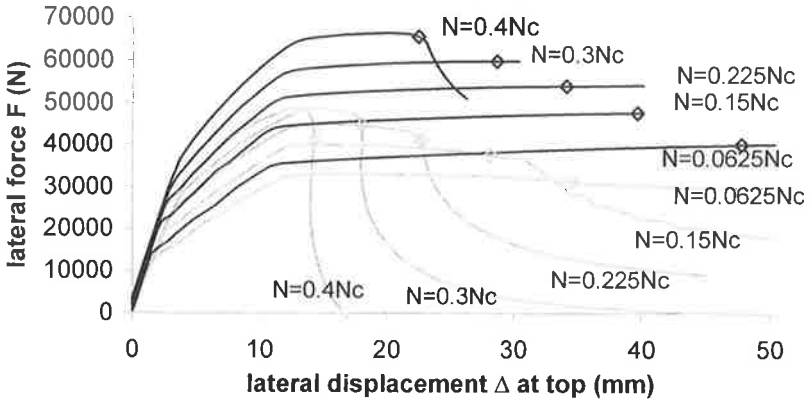

Fig. 5.4 Response of columns with different axial loads

Figure 5.5 gives the curvature distributions along the length of the column at the various critical points or stages for the case of 'plate bolted 1 side'. It can be seen that the curvature increase concentrates in the plastic hinge region from yielding of the tensile reinforcement, indicated by '+', to crushing of the concrete, indicated by '◊', whilst the curvature above the plastic hinge remains relatively unchanged (in fact it reduces a little bit). That is to say the plastic deformation of the column can be considered to occur mostly in the plastic hinge region, which is generally accepted in the literature. This concept will be used in the development of a displacement based design procedure in Chapter 8.

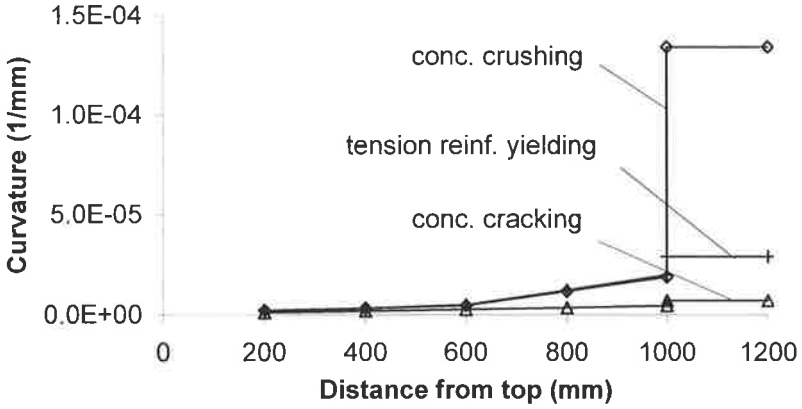

Fig. 5.5 Distribution of curvature

5.2 FACTORS AFFECTING RESPONSE

The advantages of partial interaction plating are clearly seen in the previous section. More numerical simulations for columns with different plating, such as different plate thickness, bolt stiffness, yield strength, gap etc., are presented in this section to further study the plating effects. The column details are almost identical to those of the previous section with only slight changes to match the experimentally tested columns: the column length is L=1218mm; the first bolt is 200mm away from the bottom of the column; the spacing of the other bolts are 100mm c/c with a total number of 16 bolts at 8 cross-sections (2 bolts at a cross-section, only plated on the compression face). This bolt configuration is identical for all the case studies in this section. However, the stiffness of bolts can be changed for different cases. Confinement due to the stirrups (R6@100) is considered. The confinement effect is calculated based on the method discussed in Chapter 4, which gives the confined concrete strength of f_{cc}=47MPa that applies to the concrete core enclosed by the centre line of stirrups. The P-Δ effect (by simplified method) is also included in these calculations.

Figure 5.6 shows the responses of plated columns with different plate thicknesses but with a constant bolt stiffness (K_b=23kN/mm). The top curve, indicated by '30mm plated column with infinite stiffness', is the result for a column plated with a 30mm thick plate having an elastic modulus and yield strength increased by 1000 times the actual values. With these values, the plate is essentially a rigid plate that represents an upper bound.

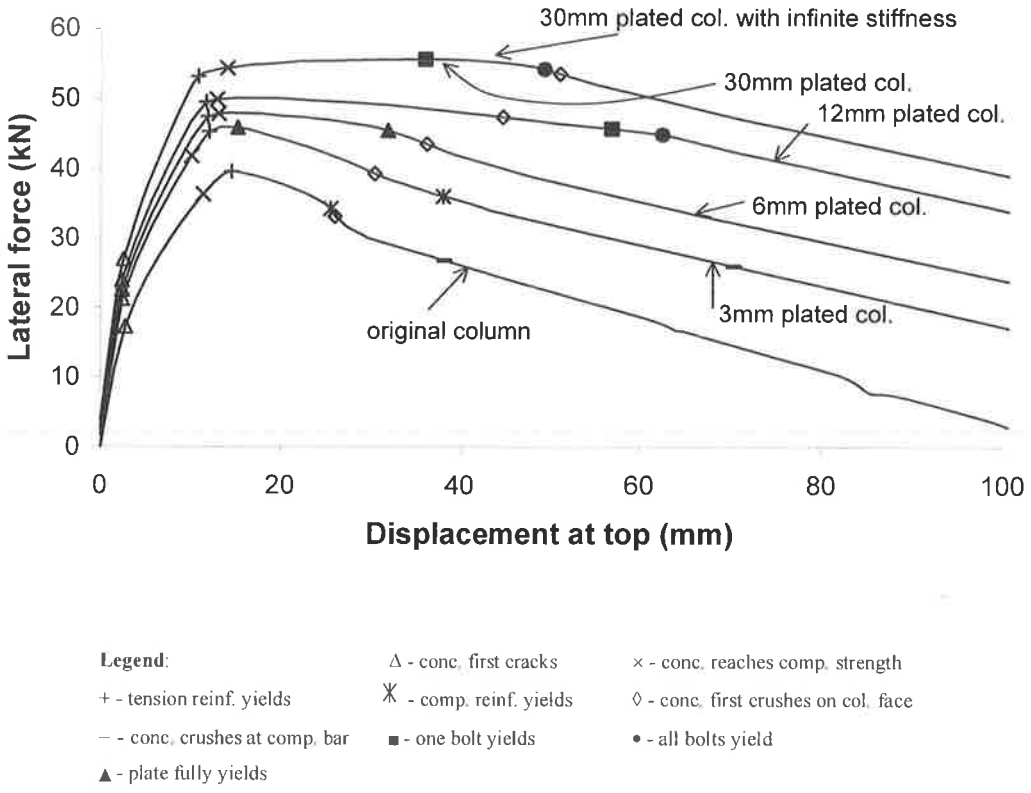

Fig. 5.6 Responses of columns with different plate thickness

Four more development stages are shown in Fig.5.6 by the four new marks that are defined in legend. The more detailed definitions of all the marks can be found in the Notation. Not every mark appears on every curve in Fig.5.6, because they do not occur in some cases. For example, the bolts in the 3mm and 6mm plated columns do not yield

because the plate yields first. Similarly, the plate does not fully yield for the cases of 12mm and thicker plated columns because yielding of all bolts occurs first. Fig.5.7 gives the results for 6mm plated columns with a range of bolt stiffnesses. For simplicity, only points '+', '▲' and '◆' are given in Fig.5.7. The plate does not yield for the case of K_b=0.75kN/mm in Fig.5.7, as the yielding of all bolts occurs first.

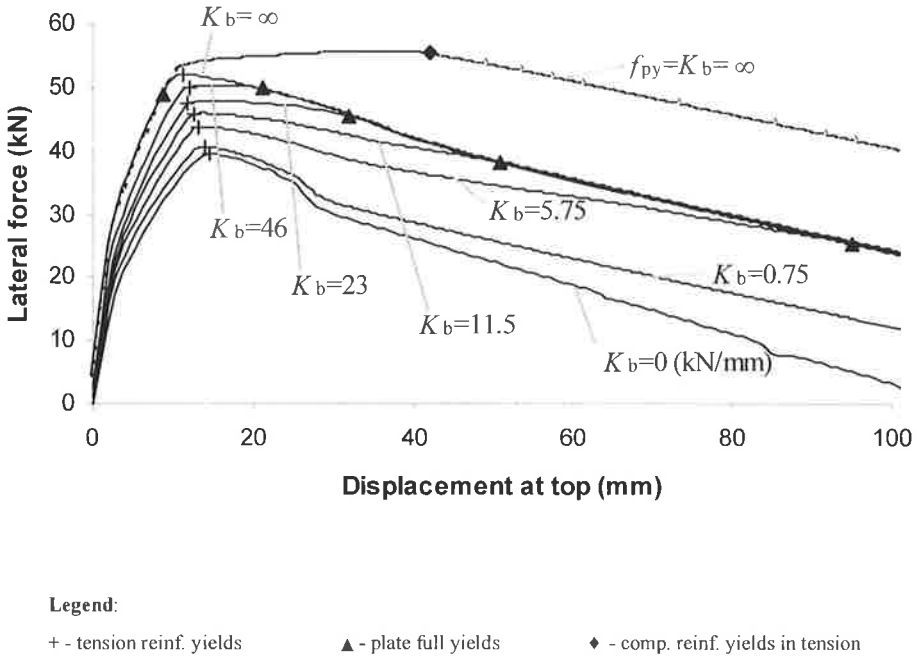

Fig. 5.7 Responses of columns with different bolt stiffness (t=6mm, f_{py}=250MPa)

The following observations can be made from Figs.5.6 and 5.7:

1. The lateral stiffness of a column is increased by an increase in plate thickness and/or bolt stiffness in the ascending branches before yielding of the tensile reinforcement. The yield strength of the column (at point '+' where the tension reinforcement first yields) also increases with increases in either plate thickness and/or bolt stiffness. The yield points are very close the peak lateral resistance of the columns.

2. There is a slight reduction in the lateral stiffness for all the cases when the concrete cracks in the tension zone, as indicated by the point 'Δ' in the curves.
3. The attainment of the compressive strength at the compressive face, which is indicated by the point '×', is delayed relative to the yielding of the tension reinforcement (point '+') as the plate thickness increases. For example, point '×' occurs before point '+' for curves with t=0 and 3mm, whilst it occurs after point '+' for cases with t=6mm and above. This indicates that the compressive resistance of the column increases when the plate thickness increases. Consistently, the increase in plate thickness also delays the onset of concrete crushing at the compression face as indicated by the point '◊' in Fig.5.6.
4. The plating reduces the steepness of the post-peak softening branch, with thicker plates giving less steep slopes, as shown in Fig.5.6. Similarly, an increase in bolt stiffness also reduces the slope of the softening branch up to the point '▲' where the whole plate section yields, as shown in Fig.5.7. However, Fig.5.7 also shows that the bolt stiffness has no effect on the softening slope once the yielding of the whole plate occurs. This is logical since the bolt stiffness cannot generate further increases in the compressive resistance from the plating system if the plate has fully yielded. Generally, in the post-yield range of response curve between point '+' and the yield point of the plating system (full yielding point of either plate '▲' or bolts '●'), the softening steepness (speed of deterioration) of a column reduces when the plate thickness and/or the bolt stiffness increases.
5. The plating system improves the integrity (capacity to keep stability) of the column. As seen from Fig.5.6, the yielding of the compression reinforcement, as marked with

'✳', and the crushing of concrete in the vicinity of compression bar, as indicated by the point '━', do not occur up to the end of the chart for the 6mm and thicker plated columns. This signifies a better integrity in the compression zone compared to the original (benchmark) un-plated column. The points of '━' and '✳' for the 3mm-plated column also occur much later than that for the benchmark column.

6. The plating system improves the displacement ductility of the column. The displacement ductility factor here is defined as

$$\mu = \Delta_u / \Delta_y \tag{5.1}$$

where Δ_y is the yield displacement (the point where the tensile reinforcement first yields), as indicated by the point '+', and Δ_u is the ultimate lateral displacement at the point where the lateral resistance force on the softening branch equals 80% of the lateral force at point '+'. The ductility factors for the curves in Figs.5.6 and 5.7 are calculated and shown in Table 5.1.

Table 5.1 Displacement ductility factors of plated columns

Fig.5.6	t (mm)	0	3	6	12	30	30	
(K_b=23k	f_{py} (MPa)	250	250	250	250	250	Rigid plate	
N/m)	μ	1.9	3.1	4.2	6.9	8.1	7.6	
Fig.5.7	K_b (kN/mm)	0.75	5.75	11.5	23.0	46.0	∞	∞
(t=6mm)	f_{py} (MPa)	250	250	250	250	250	250	250000
	μ	2.1	3.6	4.5	4.2	3.8	3.7	8.1

From Table 5.1 it can be seen that the plating generally improves the ductility. However, increasing plate thickness or bolt stiffness does not always increase the

ductility of the column. Generally, a response curve has a larger ductility factor when it has a smaller yield strength as well as a larger plateau, or more accurately, a less steep softening branch. Further discussions are given in Sections 5.2.1-5.2.3.

5.2.1 P-Δ Effect

The steepness of the softening branch is an important factor affecting ductility. The softening slope is largely decided by the P-Δ effect. Without the P-Δ effect, the response curve of a column has a less steep softening branch, as shown in Fig.5.8. As discussed in Section 4.4.2.2, the P-Δ effect causes a steepening of the softening slope by an additional slope that satisfies $\theta=N/L$, as shown in Fig.5.8, where N is the axial load and L is the cantilever length.

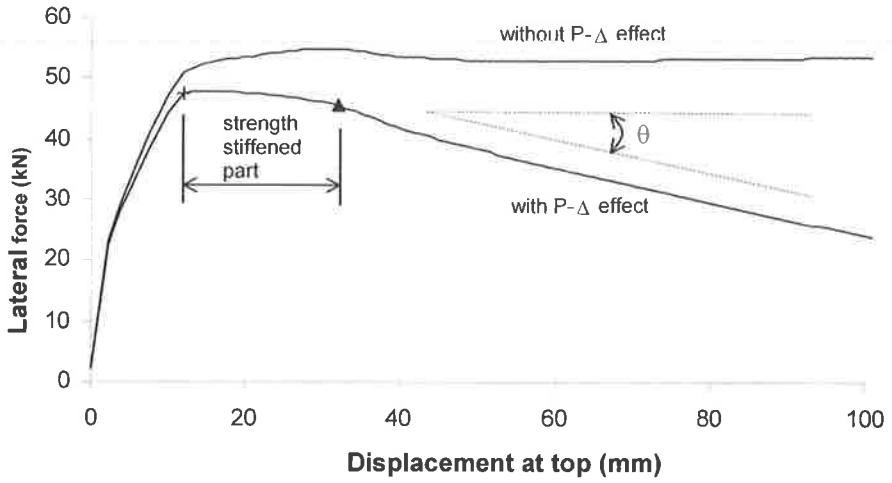

Fig. 5.8 P-Δ effect

Therefore, columns with a larger axial load N have a larger θ, and hence, a steeper softening slope. So do columns with a shorter length L. This latter relationship with

regard to the length of the column seems illogical according to the engineering common sense that the P-Δ effect is more prominent for a longer member. The shorter columns do have a smaller lateral displacement response than that for longer columns. However, the value of a response is different from the slope of the response curve. For any given additional lateral displacement beyond the peak of the curve, the shorter columns have a larger decrease in lateral strength than the longer columns, leading to a steeper softening slope as shown in Fig.5.9.

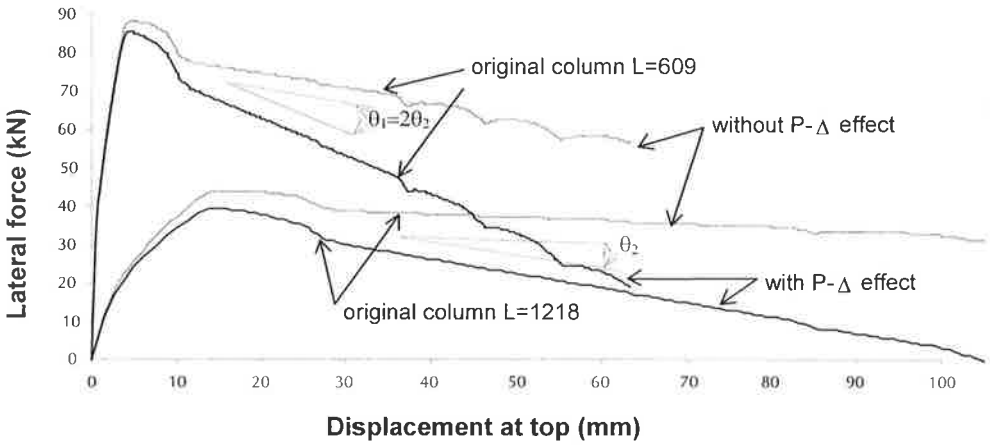

Fig. 5.9. Effect of column length to the softening slope

5.2.2 Strength Stiffening

As seen in Fig.5.8, the softening branch from the point '+' to the point '▲' is less steep than the curve after the point '▲'. This less steep part of the curve, which extends from yielding of the tension reinforcement (point '+') to yielding of the plating system, as defined by either full yielding of the plate (point '▲') or full yielding of the bolts (point

'•'), is named "strength stiffened region" in this work. It is this part of curve that produces the most important advantage of plating.

For convenience of discussion, Eq.4.59 is reproduced below

$$F = (M_n - N \cdot \Delta_0) / L \tag{5.2}$$

where F is the lateral force at the top of the column; M_n is the resistant moment from the bottom cross-section; Δ_0 is the lateral displacement at the top. In the ascending part of Fig.5.8 before the yielding point '+', the resistant moment M_n keeps increasing, leading to the monotonic increase of F. After yielding of the column, if the resistant moment M_n remains constant or reduces, F given by Eq.5.2 will decrease as and because the column displacement Δ_0 further increases. Therefore, to maintain F constant or reduce the rate of decrease after yielding (point '+'), the resistant moment M_n must continue to increase. If the increase in the resistant moment M_n is sufficient to counter balance the increase in the second term $N \cdot \Delta_0$ of Eq.5.2, a constant F can be maintained.

For an unplated RC column, the increase in moment resistance due to the strain hardening of the tension reinforcing bars is limited. Therefore, adequate increase in M_n is not possible unless the axial load is very small, in which case the required increase in M_n to balance $N \cdot \Delta_0$ is also small. However, it is possible to gain an adequate increase in M_n for a plated column even with a large axial load, as illustrated by Fig.5.10.

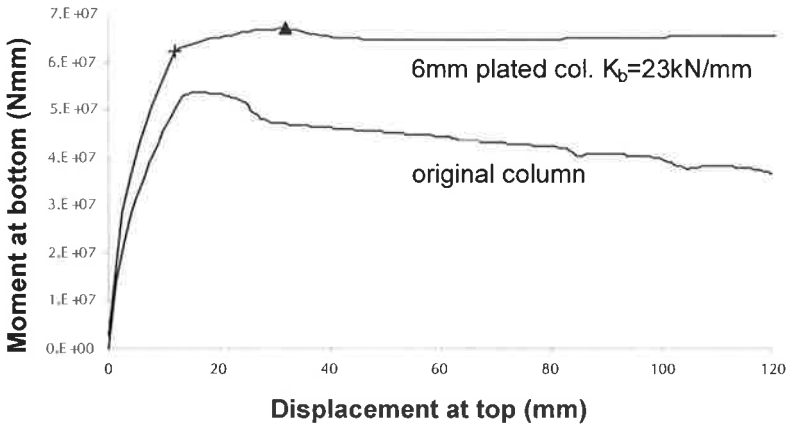

Fig. 5.10 Moment at the bottom section

Based on the force diagram shown in Fig.3.2, the resisting moment of the cross-section is given by

$$M = e_c \cdot N_{cr} + e_t \cdot N_{st} \tag{5.3}$$

where e_c and e_t are eccentricities of N_{cr} and N_{st}, respectively, with respect to the centriod of the cross-section and

$$N_{cr} = N_{conc} + N_{sc} + N_{plt} = N + N_{st} \tag{5.4}$$

When the tensile reinforcement yields, N_{st} can be considered as constant, hence based on Eq.5.4 N_{cr} is also a constant. Therefore, the only variable that changes in Eq.5.3 is e_c, which means that any increase in the resisting moment M can only come from the increase in e_c. This increase in the eccentricity e_c of the compressive resultant is due to the transfer of axial force from the RC column to the plate as shown in Fig.5.11.

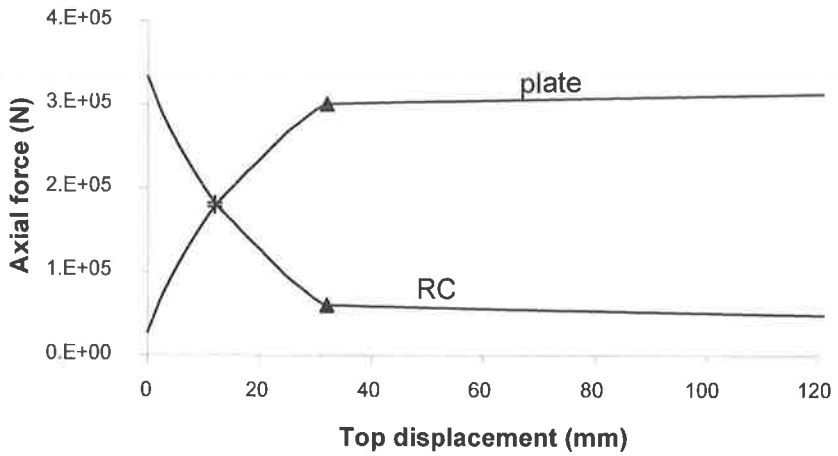

Fig. 5.11 Distribution of axial forces at bottom section (t=6mm, K_b=23kN/mm)

In reality, strain hardening of the tensile reinforcement increases N_{sl} slightly, which also has an effect in increasing the moment resistance. However, the contribution from strain hardening of the tension bars is small compared to the effect of the lever arm increase.

The softening slope of the strength stiffened region, as illustrated in Fig.5.8, is closely related to the stiffness of the plating system, i.e. the stiffness of the plate and bolt. Increasing the stiffness of the plating system reduces the softening steepness of the strength-stiffened part, which can be seen from Figs.5.6 and 5.7. This is because the increase in the resisting moment M_n of the cross-section due to the strength stiffening, i.e. the transfer of axial load from the RC column to the plate, is faster for stiffer plating systems. If M_n increases as fast as $N \cdot \Delta_0$ does, then $M_n - N \cdot \Delta_0$, and hence F, remains constant, leading to a zero softening slope. Therefore, in order to get a small softening

steepness, the plating system must be able to increase the moment resistance of the bottom cross-section at a similar speed as the P-Δ effect increases the additional moment.

Once full yielding of either the plate or all bolts occurs, defined by the points '▲' and '•' respectively in Figs.5.6 and 5.7, no further extension of the strength stiffened region can take place, because no more transfer of axial load happens. Therefore, increasing the strength of the plate or bolts, by using thicker plates, stronger bolts or larger numbers of bolts, can extend the strength stiffening part. For example, the plate yielding point '▲' occurs much later for a 6mm plated column compared to the 3mm plated column in Fig.5.6. Plate yielding does not occur at all for the 12mm or thicker plated columns in Fig.5.6, resulting in the yielding of all bolts at point '•'.

However, the strength stiffening part cannot be extended indefinitely by using a stronger plating system. The reason is given below. For a plating system that is sufficiently strong so that the plate and bolts will not fully yield under any large displacement, the strength stiffening starts, as before, with the yielding of the tensile reinforcement. However, the continuous increase in curvature at the bottom section will move the neutral axis very close towards the side of the plate if the plating system is sufficiently strong. When the compression zone is so small that the neutral axis moves to the region between the compression reinforcement and the plate, the longitudinal reinforcement at the compression side will actually be loaded in tension. In this case, N_{sc} becomes a negative value and N_{conc} becomes very small. This further increases the load N_{plt} on the plate. In this case, Eq.5.3 can be re-written as

$$M = e_{conc} \cdot N_{conc} + e_p \cdot N_{plt} + e_t \cdot (N_{st} + N_{sc}) \tag{5.5}$$

where e_{conc} and e_p are the eccentricities of N_{conc} and N_{plt}, respectively, with respect to the centroid of the cross-section. If the compression bar yields in tension and the strain hardening is ignored, the moment terms due to N_{sc} and N_{st} cancel each other, as the reinforcement is assumed to be symmetrical about the centroid, and Eq.5.5 becomes

$$M = e_{conc} \cdot N_{conc} + e_p \cdot N_{plt} \tag{5.6}$$

If the axial force in the concrete is ignored as the compression zone is small, substituting $N_{plt} = N + N_{st} - N_{sc} \approx N + (A_{st} + A_{sc}) \cdot f_{sy}$ and $e_p \approx (D+t)/2$ into Eq.5.6 gives

$$M \approx e_p \cdot N_{plt} \approx \frac{D+t}{2} \cdot \left[N + f_{sy} \cdot (A_{sc} + A_{st}) \right] \tag{5.7}$$

At this time, the maximum moment resistance of the cross-section has been achieved. No further increase in the resistant moment, or strength stiffening, can be made regardless of how strong the plating system is. This case gives the upper limit for strength stiffening. An example of this case is shown by the top curve in Fig.5.7, where the resistant moment of the bottom cross-section from the computer simulation is 82.7 kNm at the point '◆' where the compression bar just yields in tension. This moment value is very close to the result given by Eq.5.7 that gives 82.4 kNm.

When the neutral axis moves to the compression concrete cover area, the entire applied axial load *N* plus the tensile forces in all the reinforcement, which is sometimes much bigger than the axial load *N* itself, acts on a very small compression zone. This highly stressed narrow compression zone raises concern over the stability of this region. However, experimental work (see Section 11.2) showed that no excessive distress

occurred in the test columns in the compression zone and the integrity of the column remained satisfactory even after all longitudinal reinforcement yielded in tension.

5.2.3 Yield Strength

From Table 5.1, it can be seen that an increase in the plating stiffness, i.e. stiffness of the bolt and/or the plate, does not always increase the ductility of the column. For example, the displacement ductility reduces from 4.5 to 4.2 when the bolt stiffness K_b increases from 11.5kN/mm to 23kN/mm. The reason is that a stiffer plating system will have a stiffer ascending response branch and greater yield strength, i.e. a greater "y" co-ordinate value at point '+'. The greater yield strength of the column causes a reduction of the ductility factor as calculated at a point corresponding to 80% of the yield strength in the softening branch. A stiffer plating system may also result in an earlier yielding point of the plating system, i.e. a smaller "x" co-ordinate value at point '◆' or '●', as shown in Figs.5.6&5.7. From these points of view, a plating system, that mobilises the compressive resistance only after onset of yielding of the tensile reinforcement, produces a larger ductility factor.

To verify this, a plating system with gaps between the bolts and the plate, as shown in Fig.5.12, is analysed. The numerical results for the 6mm plated columns with gaps of varying sizes between the plate and the bolts (bottom gap is set to zero in these cases) are given in Fig.5.13. From a ductility point of view, the advantage of the plating system with gaps is obvious from these numerical results. The ductility factors for the cases with 1mm and 2mm gap are 4.7 and 5.0 respectively, as compared to 4.2 for the case without gap. It can be seen from Fig.5.13 that the initial responses of the plated

columns with gaps are "exactly" the same as that of the un-plated column before the gap closes up at the bifurcation point where the response of the plated column splits from the response curve of the un-plated column.

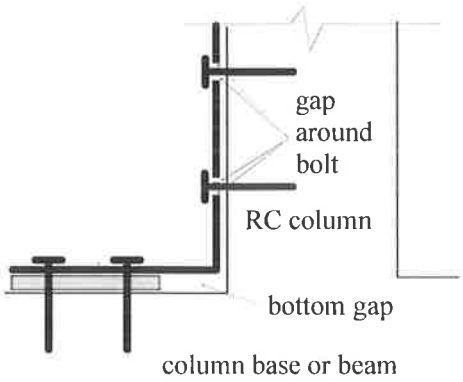

Fig. 5.12 Gap between bolt and plate

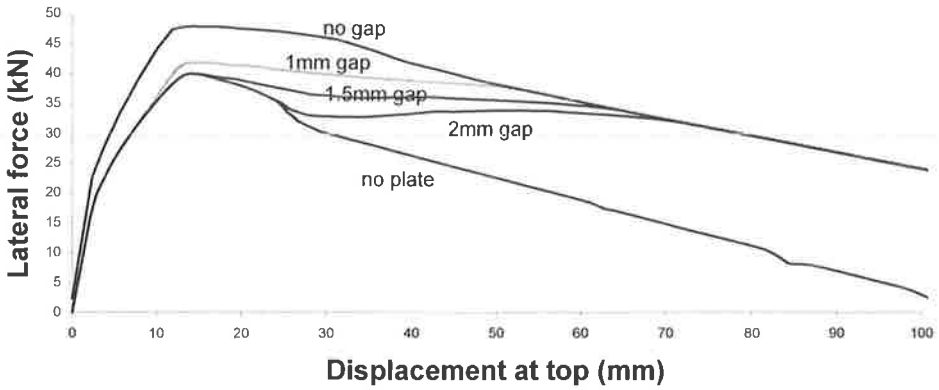

Fig. 5.13 Effect of gap for the 6mm plated column, K_b=23kN/mm

Theoretically, there are both an axial force and a flexural moment in a plate cross-section. The flexural stiffness of the plate will also contribute to the moment resistance of the whole plated cross-section even when the axial force in the plate is zero (before the gap closes up). However, the flexural stiffness of the plate is negligible compared to the

RC column. This explains why the plating system has virtually no effect on the RC column before the gap closes up.

Clearly, the bifurcation point can be designed to occur anywhere by properly designing the width of the gap. Ideally, a gap would close up when the column just yields, as shown by the case with the 1.5mm gap in Fig.5.13. The slope of the response curve after the bifurcation point can also be designed by properly choosing the rigidity of the plate and/or the stiffness of the bolts as discussed in the previous section, which is demonstrated by the cases with K_b=23 and 92kN/mm in Fig.5.14.

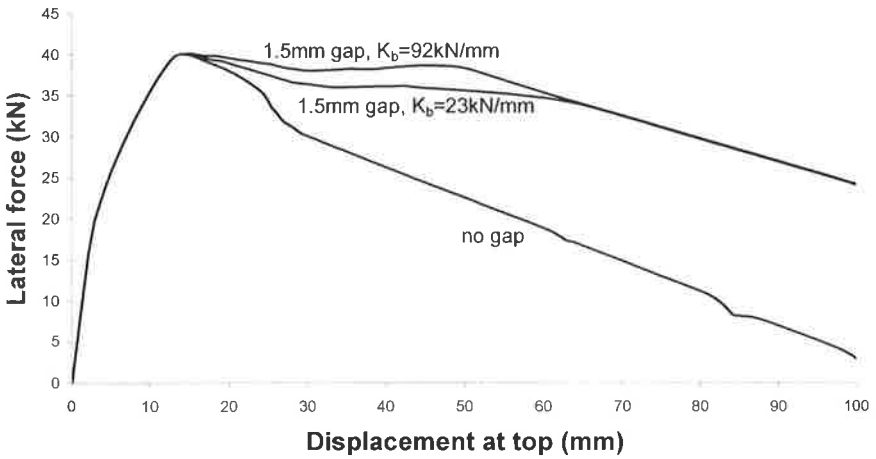

Fig. 5.14 Effect of stiffness of plating system

It has been shown in the previous section that "strength stiffening" terminates when the plating system yields, i.e. yielding of either the whole plate section or all the bolts. Increasing the yield strength of the plating system can increase the ductility of the system. As mentioned earlier in this section, increasing the stiffness of the plating system may not increase the ductility. However, it has also been shown in Section 5.2.2 and Fig.5.14 that a smaller softening steepness in the strength stiffened region can be

achieved by a stiffer plating system. Therefore, a proper balance of the strength and stiffness of the plating system is important. An idealised plating system shall be: (1) weak or not effective before the onset of column yielding point '+'; (2) adequately stiff after yielding point to provide a small softening steepness; and (3) sufficiently strong (tough) to delay the yielding of the plating system in order to achieve the maximum extent of the strength stiffened region.

A good example is demonstrated with the 6mm-plated column that combines a gap with infinite yield strength but normal stiffness for both the plate and bolts, as shown in Fig.5.15. The example further demonstrates that a higher yield strength for the plate and bolts can increase the ductility of plated columns. This result suggests that FRP materials may have advantages over steel for both plate and bolt. The strength stiffening in Fig.5.15 stops at tensile yielding of the compression bars shown by the point '◆'.

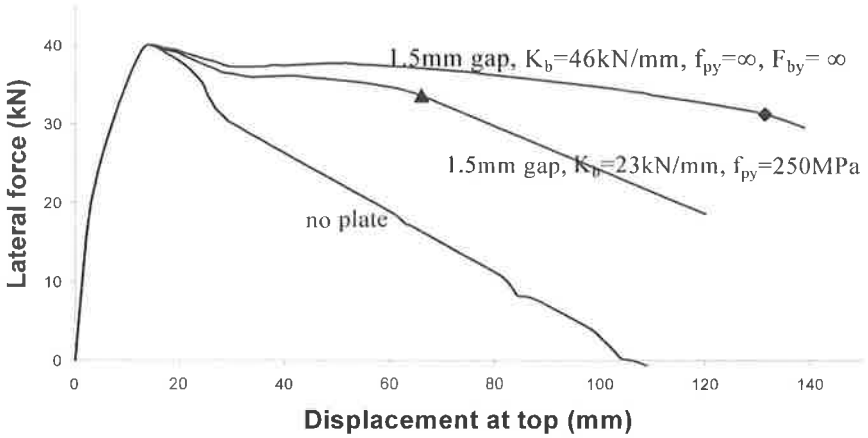

Fig. 5.15 Effect of strength of plating system

Theoretically, the strength stiffening can further be extended if the tensile resistance in the tension face can be further increased so that the resistant moment of the

bottom cross-section further increases. Tension plating on the tension face, as shown in Fig.5.16, with the tension gap closing just before point '◆' can be used to serve this purpose. However, this kind of system may not be practical in the sense that the compressive force may be too high in the compression plate. On the other hand, the tensile strain of the reinforcement bar may also be too high in the tension side at that stage, causing fracture of the reinforcement bar. The tensile strains at the end of the chart for the top curve in Fig.5.15 are 0.0816 and 0.00387 for the reinforcement bars at the tension and the compression side, respectively.

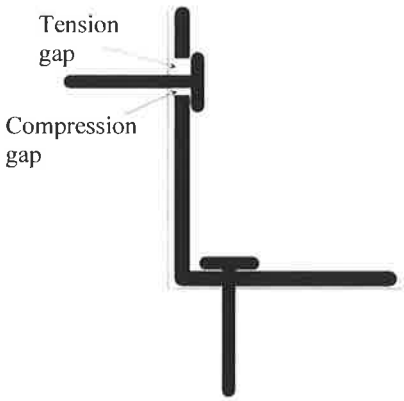

Fig. 5.16 Tension gap

5.3 SLIP DISTRIBUTIONS

Longitudinal slip between the RC column and the plate is very important in composite structures as it reflects the degree of composite interaction between elements that are connected by bolts/shear connectors, which in turn affects the overall stress distributions in the members. Furthermore, mechanical shear connectors have only a limited slip capacity. Excessive slip will cause the fracture of the bolts/connectors. Therefore, slip

and its distribution are very important considerations in the study of composite structures (Johnson and Molenstra 1991; Burnet and Oehlers 2001).

Figure 5.17 gives the slip distributions along the length for the 'plate bolted 1 side' column studied in Section 5.1 at the three different stages of: concrete cracking at the stress of f_{ct}, as shown by the mark 'Δ'; yielding of the tension reinforcement shown by '+'; and crushing of the concrete at the compressive face indicated by '◊'. The slip distributions at the first and second stages shown by 'Δ' and '+' are similar to the slip distribution given by the classic linear theory (Newmark et al. 1951 and 1952) of composite beams which gives a zero slip at the maximum moment position, a maximum slip at the zero moment position and a convex shaped distribution. The third distribution indicated by '◊' looks quite different from the classic distribution. The figure shows that the slip near the bottom part, which is around the plastic hinge region, increases faster than that of the other parts of the column. It is even possible for the slip of the first bolt to become larger than that of the remaining bolts. Fig.5.18 gives an example for the case where the spacing of bolts is half that for the case represented in Fig.5.17 and K_b is increased from 23kN/mm to 30.5 kN/mm.

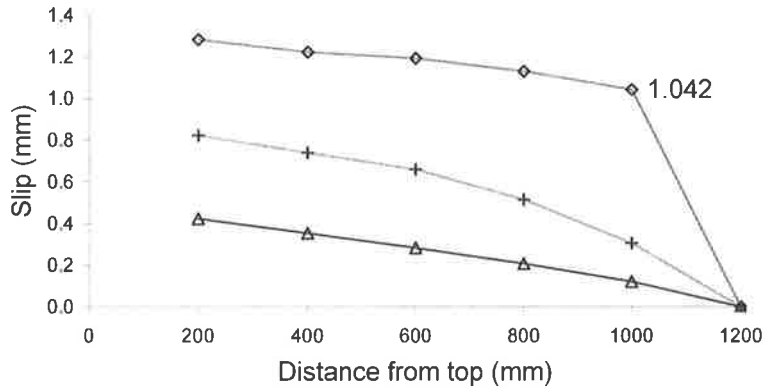

Fig. 5.17 Distributions of slip

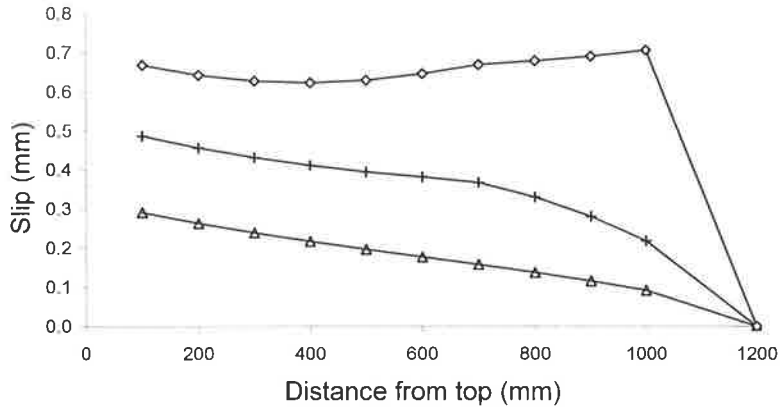

Fig. 5.18 Slip distributions when maximum slip occurs at the bottom

It will be shown in Section 8.2.1 that the slip of the first bolt at the top of the plastic hinge is only determined by the deformation of the plastic hinge (see Eq.8.5) which is largely determined by the total rotation of the hinge or the overall displacement of the column. The slips of the other bolts are largely affected by the stiffness and total number of bolts, i.e. the total longitudinal shear resistance of the bolts, which will be seen from the linear elastic study in Sections 6.3-6.4. Therefore, for columns with strong shear connections on the interface, i.e. stiff and/or large number of bolts, and when large deformations occur in the plastic hinge, it is possible that the largest slip occurs at the bottom where the maximum moment occurs rather than at the top of the column where the moment is zero. This conclusion has practical implications for the design of composite members. In the literature, the classical slip distribution developed from linear elastic theory, by which the maximum slip is considered to occur at the position where the bending moment is zero, is generally adopted to guide the design of shear connectors (Oehlers and Bradford 1995). From the above study, it can be seen that this conclusion

may not be applicable for a composite beam/column loaded to the plastic deformation stage. Further studies on the slip distribution will be conducted in Section 6.4.

From Figs.5.17 and 5.18 it can be seen that the slip distributions may be considered to be uniform along the length at the ultimate loading stage. This observation will be used to simplify the plating design procedure presented in Section 8.3.

CHAPTER 6 MATHEMATICAL STUDIES

The advantage of partial interaction plating for RC columns has been shown in the numerical studies in Chapter 5. In this chapter, further studies by mathematical analysis are performed. These analytical studies help to better understand the fundamental behaviour of plated columns. Some results from these analytical studies will also be directly used in Chapter 8 where the design of plated columns is discussed.

The mathematical studies of this section are based on linear elastic theory, which is applicable to serviceability limit state analysis. In order to extend the linear theory from serviceability analysis to ultimate limit state analysis, where large in-elastic deformation occurs, an elastic analysis plus plastic hinge model is introduced in Section 6.1. In Section 6.2, the linear elastic theory of composite members (including beams and columns) is developed which extends the classic linear elastic theory of composite beams. It is shown in Section 6.3 that the response of composite members is governed by just a few composite parameters regardless of the large number of variables involved, which is a new concept first introduced from this work. The slip distributions are also studied in further detail in Section 6.4.

6.1 LINEAR ELASTIC PLUS PLASTIC HINGE MODEL

Linear elastic theory is only applicable when the load and deflection is relatively small, or more correctly, within the linear elastic limit for both material and geometrical

conditions. Strictly speaking, it cannot be applied when any part of the structure yields. However, when plastic deformation occurs, most of the plastic deformation of the member is concentrated in a zone where maximum moment occurs, namely the plastic hinge zone as discussed in Section 4.2.3. Therefore, the region of the column above the plastic hinge zone, as shown in Fig.6.1, may still be considered to be essentially elastic where linear-elastic theory is applicable.

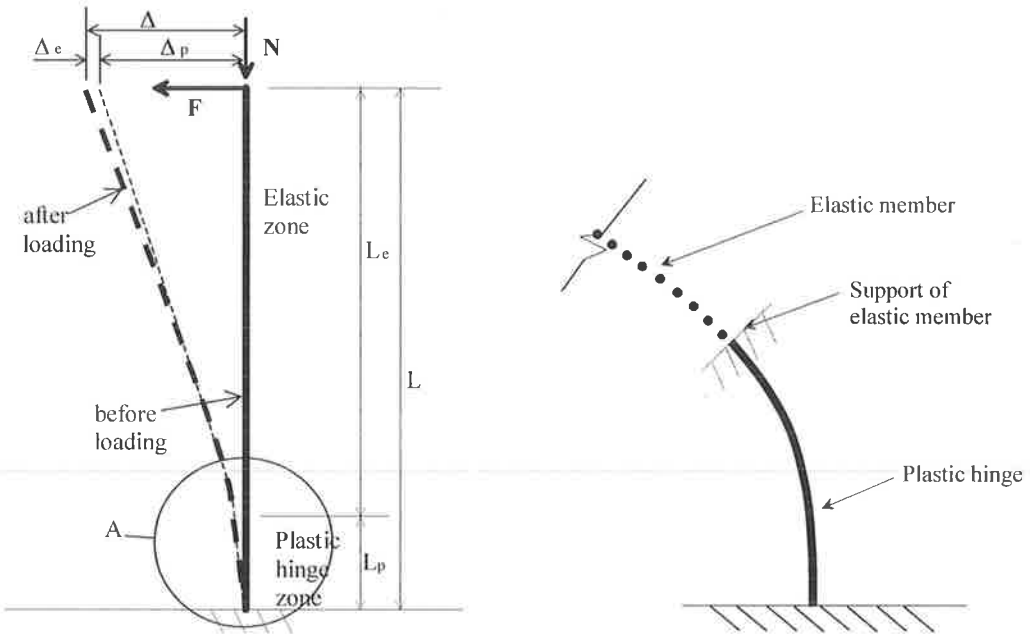

(a) Elastic and plastic zone (b) Detail A

Fig. 6.1 Plastic-elastic model

For the elastic member above the plastic hinge, the slip at the imaginary support or the interface of the elastic and the plastic part, as shown in Fig.6.1(b), will not be zero. Therefore a non-zero slip boundary condition, as discussed in Section 6.2.2, must be used in the linear theory. This boundary slip s_p can be calculated by the plastic hinge analysis introduced in Section 8.2. Therefore, by using the model shown in Fig.6.1, the difficult

problem of a partial interaction non-linear analysis is transformed into a relatively simple linear-elastic analysis of the member with a shorter length L_e and a given boundary slip s_p at the support of the elastic member, plus a plastic hinge analysis.

6.2 LINEAR ELASTIC ANALYSIS

Classic linear elastic partial-interaction theory for composite steel and concrete beams was first developed by Newmark et al (1951, 1952) and more recently extended to allow for non-linearity by Johnson and Molenstra (1991) and Burnet and Oehlers (2001). In this study, Newmark's classic linear-elastic theory for composite beams is extended to include axial load so that it can be applied to plated columns as well as prestressed RC composite beams. Furthermore, a non-zero slip boundary condition at the fixed end support is introduced to allow Newmark's linear elastic serviceability analysis to be extended to encompass beams and columns at the ultimate limit state where large deformations occur at the plastic hinge, using the model of Section 6.1.

6.2.1 Generic Mathematical Model

The basic geometric model under consideration is shown in Fig.6.2. The origin of the co-ordinate system is located at the geometric centroid of the cross-section of element 1 at the top of the member. The *x*-axis is in the longitudinal direction of the column. A typical portion from the top of the column to a cross-section that is *x* distance away from the origin is isolated as a free body as shown in Fig.6.2(a).

A constant axial load N is applied at the centroid of the cross-section of element 1. For generality, a constant moment M_0 at the origin and a distributed load *p(x)* along

the length are applied. In the free body diagram of Fig.6.2(a), the normal (y direction) stress on the interface is not shown as it has no effect in the following derivations.

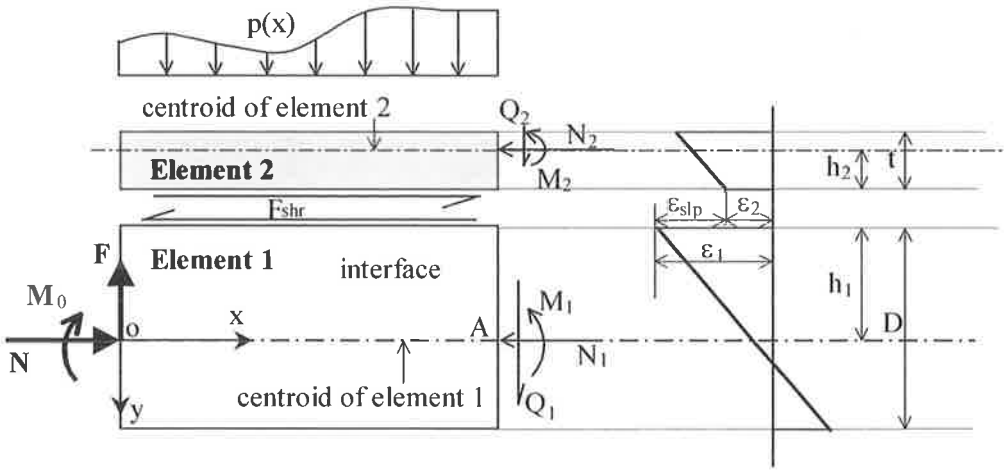

(a) Free body diagram (b) Strain profile in the section

Fig. 6.2 Analytical model

The theory developed in this section is based on the assumptions specified in Section 3.3 plus linear assumption. For convenience of reference, they are listed as follows:

(1) All the constitutive materials behave linearly;

(2) The cross-section is uniform along the length;

(3) Bernoulli's principle that plane sections remain plane applies to individual elements, as shown by the strain profile in Fig.6.2(b);

(4) The shear connectors between the two elements are continuous and uniformly distributed longitudinally; and

(5) No transverse separation occurs on the contact interface, therefore the curvature is the same for both elements at the same cross-section.

6.2.1.1 Equilibrium and compatibility

Force equilibrium for the individual elements in Fig.6.2 requires

$$N_2 - F_{shr} = 0 \tag{6.1}$$

$$N - F_{shr} - N_1 = 0 \tag{6.2}$$

Taking moments about point A gives

$$M_1 + M_2 + N_2 \cdot (h_2 + h_1) - M(x) = 0 \tag{6.3}$$

where *M(x)* is the applied moment in the cross-section given by $M(x) = M_0 + F \cdot x - \int_0^x p(\xi) \cdot (x - \xi) d\xi$. Hence from Eq.6.1 and Eq.6.3

$$M_1 + M_2 + F_{shr} \cdot (h_2 + h_1) - M(x) = 0 \tag{6.4}$$

The strain in the x-direction at the interface of element 1 in Fig.6.2(b) is given by

$$\varepsilon_1 = \frac{M_1 \cdot h_1}{(EI)_1} + \frac{N_1}{(EA)_1} \tag{6.5}$$

and that at the interface of element 2 is

$$\varepsilon_2 = -\frac{M_2 \cdot h_2}{(EI)_2} + \frac{N_2}{(EA)_2} \tag{6.6}$$

Assumption 5 requires that

$$\kappa = \frac{M_1}{(EI)_1} = \frac{M_2}{(EI)_2} \tag{6.7}$$

Applying Assumption 4, the longitudinal slip *s* is given by

$$s = \frac{F_b}{K_b} = \frac{q \cdot L_s}{K_b} \tag{6.8}$$

where F_b is the shear force applied to the shear connectors at a given cross-section that has a stiffness of K_b; L_s is the longitudinal spacing of the shear connectors; and q is the longitudinal shear force per unit length, or shear flow, which is given by

$$q = \frac{dF_{shr}}{dx} \tag{6.9}$$

Hence

$$s = \frac{L_s}{K_b} \cdot \frac{dF_{shr}}{dx} \tag{6.10}$$

The slip strain in Fig.6.2(b) is given by

$$\varepsilon_{slp} = \varepsilon_1 - \varepsilon_2 = -\frac{ds}{dx} \tag{6.11}$$

Differentiating Eq.6.10 gives

$$\frac{ds}{dx} = \frac{L_s}{K_b} \cdot \frac{d^2F_{shr}}{dx^2} \tag{6.12}$$

By referring to Eqs.6.1, 6.2, 6.4-6.7, the slip strain in Eq.6.11 can be transformed to

$$\varepsilon_{slp} = \varepsilon_1 - \varepsilon_2 = -\frac{\overline{EI}}{\overline{EA} \cdot \sum EI} \cdot F_{shr} + \frac{(h_1 + h_2) \cdot M(x)}{\sum EI} + \frac{N}{(EA)_1} \tag{6.13}$$

in which

$$\frac{1}{\overline{EA}} = \frac{1}{(EA)_1} + \frac{1}{(EA)_2} \tag{6.14}$$

$$\sum EI = (EI)_1 + (EI)_2 \tag{6.15}$$

and

$$\overline{EI} = \sum EI + \overline{EA} \cdot (h_1 + h_2)^2 \tag{6.16}$$

where $\overline{EI}$ is (can be proved to be) the flexural rigidity of the composite member with full interaction. However, $\overline{EA}$ is not the axial rigidity of the composite member.

6.2.1.2 Governing differential equation

From Eqs.6.11, 6.12 and 6.13, the following differential equation is obtained

$$\frac{L_s}{K_b}\cdot\frac{d^2F_{shr}}{dx^2}-\frac{\overline{EI}}{\overline{EA}\cdot\sum EI}\cdot F_{shr}+\frac{(h_1+h_2)\cdot M(x)}{\sum EI}+\frac{N}{(EA)_1}=0 \tag{6.17}$$

Letting

$$a_0=\frac{L_s}{K_b} \tag{6.18}$$

$$a_1=\frac{\overline{EI}}{\overline{EA}\cdot\sum EI} \tag{6.19}$$

$$a_2=\frac{(h_1+h_2)}{\sum EI} \tag{6.20}$$

and

$$a_3=\frac{1}{(EA)_1} \tag{6.21}$$

Eq.6.17 simplifies to

$$a_0\cdot\frac{d^2F_{shr}}{dx^2}-a_1\cdot F_{shr}+a_2\cdot M(x)+a_3\cdot N=0 \tag{6.22}$$

This differential equation can be solved for a given applied moment distribution of *M(x)*. The slip then can be obtained from Eq.6.10. To obtain the deflection of the member, the following relation is used

$$-\frac{d^2v}{dx^2}=\kappa=\frac{M_1}{(EI)_1} \tag{6.23}$$

Combining Eqs.6.4, 6.7 and 6.17 gives

$$\frac{M_1}{(EI)_1} = \frac{M(x)}{\overline{EI}} - \frac{(h_1+h_2)\cdot\overline{EA}}{\overline{EI}}\cdot\frac{I_s}{K_b}\cdot\frac{d^2F_{shr}}{dx^2} - \frac{(h_1+h_2)\cdot\overline{EA}\cdot N}{\overline{EI}\cdot(EA)_1} \tag{6.24}$$

Substituting Eq.6.24 into Eq.6.23 gives

$$\frac{d^2v}{dx^2} = a_4\cdot a_0\frac{d^2F_{shr}}{dx^2} - \frac{M(x)}{\overline{EI}} + a_4\cdot a_3\cdot N \tag{6.25}$$

where

$$a_4 = \frac{(h_1+h_2)\cdot\overline{EA}}{\overline{EI}} \tag{6.26}$$

6.2.2 Solution for the Case of A Cantilever Column

The solution for the cantilever column shown in Fig.6.3 is just a special case of Section 6.2.1.

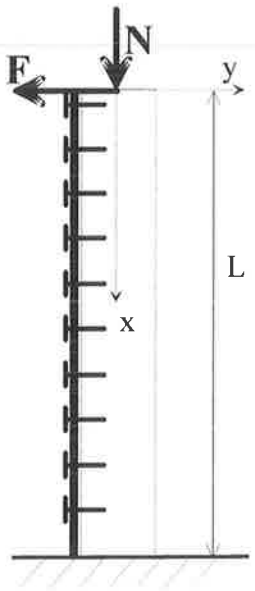

Fig. 6.3 Model of the cantilever column

In this case, $M(x) = F \cdot x$ and the general solution of Eq.6.22 is given by

$$F_{shr} = c_1 \cdot e^{\sqrt{\frac{a_1}{a_0}} \cdot x} + c_2 \cdot e^{-\sqrt{\frac{a_1}{a_0}} \cdot x} + \frac{a_2 \cdot F}{a_1} \cdot x + \frac{a_3 \cdot N}{a_1} \tag{6.27}$$

where the constants c_1 and c_2 can be determined from the following boundary conditions:

$$F_{shr}\Big|_{x=0} = 0 \tag{6.28}$$

$$s\Big|_{x=L} = \frac{L_s}{K_b} \cdot \frac{dF_{shr}}{dx}\Big|_{x=L} = s_p \tag{6.29}$$

For a fixed end support as shown in Fig.6.3, the boundary slip $s_p = 0$ at x=L. For generality, a non-zero value s_p is adopted. This non-zero boundary slip condition is useful as discussed in Section 6.1 where the linear theory is extended to a non-linear analysis. From Eqs.6.28 and 6.29, the constants are calculated to be

$$c_1 = \frac{s_p}{2 \cdot \sqrt{a_0 \cdot a_1} \cdot \cosh(\alpha)} - \frac{a_3 \cdot N \cdot e^{-\alpha} + a_2 \cdot F \cdot \sqrt{\frac{a_0}{a_1}}}{2a_1 \cdot \cosh(\alpha)} \tag{6.30}$$

$$c_2 = -c_1 - \frac{a_3 \cdot N}{a_1} \tag{6.31}$$

in which

$$\alpha = L \cdot \sqrt{\frac{a_1}{a_0}} = L \cdot \sqrt{a_5} = L \cdot \sqrt{\frac{K_b \cdot \overline{EI}}{L_s \cdot \overline{EA} \cdot \sum EI}} \tag{6.32}$$

where

$$a_5 = \frac{a_1}{a_0} \tag{6.33}$$

Substituting c_1 and c_2 into Eq.6.27 and re-arranging gives

$$F_{shr} = \frac{s_p \cdot \sinh(\alpha \cdot \xi)}{\sqrt{a_0 \cdot a_1} \cdot \cosh(\alpha)} + \frac{1}{a_1}\left[a_3 \cdot N \cdot (1 - e^{-\alpha \cdot \xi} - \frac{2\sinh(\alpha \cdot \xi)}{e^{2\alpha}+1}) + a_2 \cdot F \cdot \sqrt{\frac{a_0}{a_1}} \cdot (\alpha \cdot \xi - \frac{\sinh(\alpha \cdot \xi)}{\cosh(\alpha)}) \right]$$

$$= F_f + F_n + F_{sp} \tag{6.34}$$

where F_f, F_n and F_{sp} are the longitudinal shear forces induced by the lateral force F, the axial load N and the boundary slip s_p, respectively. They are given by

$$F_f = F \cdot L \cdot (h_1 + h_2) \cdot \frac{\overline{EA}}{\overline{EI}} \cdot \left[\xi - \frac{\sinh(\alpha \cdot \xi)}{\alpha \cdot \cosh(\alpha)} \right] \tag{6.35}$$

$$F_n = \frac{N}{(EA)_1} \cdot \frac{\overline{EA} \cdot \sum EI}{\overline{EI}} \cdot \left[1 - e^{-\alpha \cdot \xi} - \frac{2\sinh(\alpha \cdot \xi)}{e^{2\alpha}+1} \right] \tag{6.36}$$

$$F_{sp} = s_p \cdot L \cdot \frac{K_b}{L_s} \cdot \frac{\sinh(\alpha \cdot \xi)}{\alpha \cdot \cosh(\alpha)} \tag{6.37}$$

where ξ is the normalized coordinate x, or

$$\xi = \frac{x}{L} \qquad 0 \le \xi \le 1 \tag{6.38}$$

The slip is obtained from Eq.6.10

$$s = \frac{L_s}{K_b} \cdot \frac{dF_{shr}}{dx} = s_f + s_n + s_{sp} \tag{6.39}$$

where s_f, s_n and s_{sp} are the slip terms due to F, N and s_p, respectively, and are given by

$$s_f = F \cdot (h_1 + h_2) \cdot \frac{\overline{EA}}{\overline{EI}} \cdot \frac{L_s}{K_b} \left[1 - \frac{\cosh(\alpha \cdot \xi)}{\cosh(\alpha)} \right]$$

$$= F \cdot \frac{a_2}{a_5} \cdot \left[1 - \frac{\cosh(L \cdot \sqrt{a_5} \cdot \xi)}{\cosh(L \cdot \sqrt{a_5})} \right] \tag{6.40}$$

$$s_n = \frac{N}{(EA)_1} \cdot \sqrt{\frac{L_s}{K_b} \cdot \frac{\overline{EA}}{\overline{EI}} \cdot \sum EI} \cdot \left[e^{-\alpha\xi} - \frac{2\cosh(\alpha \cdot \xi)}{e^{2\alpha}+1} \right]$$

$$= \frac{N \cdot a_3}{\sqrt{a_5}} \cdot \left[e^{-(L\cdot\sqrt{a_5})\xi} - 2\cosh(L \cdot \sqrt{a_5} \cdot \xi) \Big/ (e^{2(L\cdot\sqrt{a_5})}+1) \right] \tag{6.41}$$

$$s_{sp} = \frac{s_p \cdot \cosh(\alpha \cdot \xi)}{\cosh(\alpha)} = \frac{s_p \cdot \cosh(L \cdot \sqrt{a_5} \cdot \xi)}{\cosh(L \cdot \sqrt{a_5})} \tag{6.42}$$

To solve for the deflection, Eq.6.25 is integrated twice to give

$$v = v_{full}^{F} + a_4 \cdot a_0 \cdot F_{shr} + \frac{a_4 \cdot a_3 \cdot N}{2} \cdot x^2 + c_3 \cdot x + c_4 \tag{6.43}$$

where

$$v_{full}^{F} = \int dx \int \left(-\frac{M}{\overline{EI}} \right) dx = \int dx \int \left(-\frac{F \cdot x}{\overline{EI}} \right) dx$$

$$= -\frac{F \cdot L^3}{6\overline{EI}} \cdot (\xi^3 - 3\xi + 2) \tag{6.44}$$

which is the deflection due to the lateral force F with full interaction, i.e. no slip between elements 1 and 2. The constants c_3 and c_4 are determined from the boundary conditions:

$$v\big|_{x=L} = 0 \tag{6.45}$$

$$\left.\frac{dv}{dx}\right|_{x=L} = 0 \tag{6.46}$$

which gives

$$c_3 = -a_4 \cdot a_3 \cdot L \cdot N - a_4 \cdot a_0 \cdot \frac{s_p \cdot K_b}{L_s} \tag{6.47}$$

$$c_4 = \frac{a_4 \cdot a_3 \cdot L^2 \cdot N}{2} - a_4 \cdot a_0 \cdot \left[2c_1 \sinh(\alpha) + \frac{a_3 \cdot N}{a_1} \cdot (1 - e^{-\alpha}) + \frac{a_2 \cdot F}{a_1} \cdot L - \frac{s_p \cdot L \cdot K_b}{L_s} \right] \tag{6.48}$$

Substituting c_3 and c_4 into Eq.6.43 and re-arrangement gives

$$v = v_{full}^{F} + v_{full}^{N} + F \cdot g_1(\xi) + N \cdot g_2(\xi) + s_p \cdot g_3(\xi) \tag{6.49}$$

where

$$v_{full}^{N} = \frac{(h_1 + h_2) \cdot \overline{EA} \cdot L^2}{2\overline{EI} \cdot (EA)_1} \cdot N \cdot (\xi - 1)^2$$

$$= \frac{1}{2} \cdot N \cdot a_4 \cdot a_3 \cdot L^2 \cdot (\xi - 1)^2 \tag{6.50}$$

which is the deflection caused by a constant moment due to the eccentricity of the axial load about the centroid of the combined composite cross-section of elements 1 and 2 with full interaction.

The three additional terms in Eq.6.49, $F \cdot g_1(\xi)$, $N \cdot g_2(\xi)$ and $s_p \cdot g_3(\xi)$, reflect the partial interaction effects for the lateral force, axial force and boundary slip, respectively, where

$$g_1(\xi) = (h_1 + h_2)^2 \cdot \left(\frac{\overline{EA}}{\overline{EI}}\right)^2 \cdot \frac{L_s}{K_b} \cdot L \cdot \left[\xi - \frac{\sinh(\alpha \cdot \xi)}{\alpha \cdot \cosh(\alpha)} - 1 + \frac{1}{\alpha} \cdot \tanh(\alpha)\right]$$

$$= a_4^2 \cdot a_0 \cdot L \cdot \left[\xi - \frac{\sinh(\alpha \cdot \xi)}{\alpha \cdot \cosh(\alpha)} - 1 + \frac{1}{\alpha} \cdot \tanh(\alpha)\right] \tag{6.51}$$

$$g_2(\xi) = (h_1 + h_2) \cdot \left(\frac{\overline{EA}}{\overline{EI}}\right)^2 \cdot \frac{\sum EI}{(EA)_1} \cdot \frac{L_s}{K_b} \cdot \left[-e^{-\alpha \cdot \xi} - \frac{2\sinh(\alpha \cdot \xi)}{e^{2\alpha} + 1} + \frac{1}{\cosh(\alpha)}\right]$$

$$= \frac{a_3 \cdot a_4}{a_5} \cdot \left[-e^{-\alpha \cdot \xi} - \frac{2\sinh(\alpha \cdot \xi)}{e^{2\alpha} + 1} + \frac{1}{\cosh(\alpha)}\right] \tag{6.52}$$

$$g_3(\xi) = (h_1 + h_2) \cdot \frac{\overline{EA}}{\overline{EI}} \cdot L \cdot \left[\frac{\sinh(\alpha \cdot \xi) - \sinh(\alpha)}{\alpha \cdot \cosh(\alpha)} + 1 - \xi\right]$$

$$= a_4 \cdot L \cdot \left[\frac{\sinh(\alpha \cdot \xi) - \sinh(\alpha)}{\alpha \cdot \cosh(\alpha)} + 1 - \xi \right] \tag{6.53}$$

The functions $g_1(\xi)$ and $g_2(\xi)$ approach zero when the stiffness of shear connectors approaches infinity, which leads to the result given by full interaction theory.

6.3 COMPOSITE PARAMETERS

For a composite member, there are many member properties that affect the response. Furthermore, the effect of each variable is not obvious. Some of the variables are inter-related, further complicating matters. For example, in Eq.6.40 the slip appears to be in direct proportion to $(h_1 + h_2)$, however, $\overline{EI}$ and $\overline{EA}$ are also related to $(h_1 + h_2)$. Furthermore, α also depends on h_1 and h_2. However, careful study of the variables reveals that the response of a composite member is determined by only a few composite parameters that are combinations of basic material and geometric properties as described in the following sections.

6.3.1 Fundamental Parameters Governing Longitudinal Slip

In order to establish which factors affect the slip distribution in a composite member with arbitrary loading and boundary conditions, Eq.6.13 is rewritten with reference to Eqs.6.19-6.21 as

$$\varepsilon_{slp} = -a_1 \cdot F_{shr} + a_2 \cdot M(x) + a_3 \cdot N \tag{6.54}$$

For a linear system, the superposition law applies. Therefore, the total slip strain of Eq.6.54 can be considered to be the algebraic sum of the following 3 components

$$(\varepsilon_{slp})_1 = -\frac{ds_1}{dx} = -a_1 \cdot F_{shr} \tag{6.55}$$

$$(\varepsilon_{slp})_2 = -\frac{ds_2}{dx} = a_2 \cdot M(x) \tag{6.56}$$

$$(\varepsilon_{slp})_3 = -\frac{ds_3}{dx} = a_3 \cdot N \tag{6.57}$$

where $(\varepsilon_{slp})_1$, $(\varepsilon_{slp})_2$ and $(\varepsilon_{slp})_3$ are the slip strain terms caused by (1) longitudinal shear force F_{shr}, (2) bending moment $M(x)$ and (3) axial load N, respectively. The corresponding slip terms are indicated by s_1, s_2 and s_3, respectively. Therefore

$$\varepsilon_{slp} = (\varepsilon_{slp})_1 + (\varepsilon_{slp})_2 + (\varepsilon_{slp})_3 \tag{6.58}$$

$$s = s_1 + s_2 + s_3 \tag{6.59}$$

Integrating Eq.6.56 and 6.57 gives

$$s_2 = -a_2 \cdot \int M(x) \cdot dx = a_2 \cdot F_2(x) \tag{6.60}$$

$$s_3 = -a_3 \cdot \int N \cdot dx = a_3 \cdot F_3(x) \tag{6.61}$$

where $F_2(x) = -\int M(x) \cdot dx$ and $F_3(x) = -\int N \cdot dx$. By referring to Eq.6.10, Eq.6.55 can be rewritten as

$$-\frac{ds_1}{dx} = -a_1 \cdot \frac{1}{a_0} \int s \cdot dx \tag{6.62}$$

Taking derivative of both sides and referring to Eqs.6.33, 6.59-6.61 gives

$$\frac{d^2 s_1}{dx^2} - a_5 \cdot s_1 - a_5 \cdot [a_2 \cdot F_2(x) + a_3 \cdot F_3(x)] = 0 \tag{6.63}$$

The factors affecting the slip can now be clearly seen from Eqs.6.59-6.61 and 6.63. Apart from the loading conditions which determine $F_2(x)$ and $F_3(x)$, there are only three composite parameters that affect the slip: a_2, a_3 and a_5. These three composite parameters are functions of geometric and material properties of the member.

Furthermore, these parameters have clear physical meanings as discussed below. To discuss the parameter a_5, the parameters a_0 and a_1 are also analyzed.

1. *The unit longitudinal flexibility of shear connectors* a_0

   As given by Eq.6.18, it can be seen that $1/a_0$ is the shear connector lateral stiffness over a unit longitudinal length. In other words, a_0 is the flexibility coefficient of shear connection. Therefore, a larger value of a_0 indicates a smaller resistance to slip from the shear connectors, tending to give a larger value of slip in the interface.

2. *The active slip strain coefficient* a_2

   Letting $F_{shr}=0$, $N=0$ and $M=1$ in Eq.6.54 gives $\varepsilon_{slp}=a_2$, where a_2 is given by Eq.6.20. This means that the coefficient a_2 is the slip strain caused by a unit external bending moment at the cross-section when no interaction exists at the interface (no shear connectors). A larger value of a_2 means that, for a given external bending moment, a larger slip strain will occur. In other words, a member with a larger a_2 value is prone to have larger slips under flexural loading. From Eq.6.20, it can be seen that a_2 is a cross-sectional property of the individual elements 1 and 2.

3. *The passive slip strain coefficient* a_1

   Let $M=N=0$ and $F_{shr}=1$ in Eq.6.54, then $\varepsilon_{slp}=-a_1$, in which a_1 is also a function of the cross-sectional properties as given by Eq.6.19. Therefore, the coefficient a_1 is the slip strain of the cross-section caused by a unit longitudinal shear force. For a cross-section with a larger a_1, a given longitudinal shear force will cause larger longitudinal slip strains and hence slip. As the longitudinal shear force always tries to

stop the slip caused by the external forces (hence the name ***passive*** *slip strain coefficient* as opposed to the ***active*** *slip strain coefficient* a_2), a larger a_1 indicates that the longitudinal shear is more effective in stopping the slip or resisting the slip strain caused by external forces. In other word, for composite members of the same length but with a larger cross-sectional property a_1, the same shear connection (same bolt and same number) will result in a smaller slip at the interface under the same loading conditions.

4. *The axial flexibility* a_3

Letting $F_{shr}=0$, $N=1$ and $M=0$, then Eq.6.54 gives $\varepsilon_{slp}=a_3$, where a_3 is given by Eq.6.21. That is to say, a_3 is the slip strain cause by a unit axial force applied at the centriod of element 1. When the axial flexibility a_3 of element 1 is greater, a given axial load will cause a larger axial shortening of element 1 which in turn causes a larger slip between elements 1 and 2.

5. *The slip resistance ability coefficient* a_5

As given by Eq.6.33, this coefficient is the combination of a_0 and a_1, i.e. $a_5=a_1/a_0$. It reflects the overall ability of the composite member in restraining the slip at the interface, which can be observed by considering the physical meanings of a_0 and a_1. As mentioned in 3, composite members with a larger *passive slip strain coefficient* a_1 and the same shear connection will have a smaller slip at the interface under the same loading conditions. When the shear connector stiffness $1/a_0$ is larger, there is a stronger shear connection in the interface, providing greater slip resistance, which further reduces the slip. Therefore, for composite members with larger a_5, the ability

of the member to restrain the slip is greater, and the slip caused by a given loading condition will be smaller.

The above relations can be verified by the slip results from the example of Section 6.2.2 where the slip terms are given by Eqs.6.40-6.42. In all three terms, which respectively are caused by the external moment or lateral force at the top (Eq.6.40), the axial load (Eq.6.41) and the boundary slip (Eq.6.42), the slip resistance ability coefficient a_5 plays a key role in resisting the amount of slip. In other word, all three slip terms given by Eq.6.40-6.42 reduce monotonically when a_5 increases, which will be discussed further in Sections 6.4.1-6.4.3.

6.3.2 Parameters Affecting Deformations

Similar to slip, the deflection of a composite member is also governed by just a few key parameters regardless of the many variables involved. With reference to Eqs.6.11 and 6.12, Eq.6.24 can be rewritten as:

$$\kappa = \frac{M(x)}{\overline{EI}} + \frac{(h_1 + h_2)\cdot \overline{EA}}{\overline{EI}} \cdot \varepsilon_{slp} - \frac{(h_1 + h_2)\cdot \overline{EA}}{\overline{EI}\cdot (EA)_1} \cdot N$$

$$= \frac{M(x)}{\overline{EI}} + a_4 \cdot \varepsilon_{slp} - a_4 \cdot a_3 \cdot N \qquad (6.64)$$

where a_4 is given by Eq.6.26. The first term in the above equation is the curvature caused by the external moment with full interaction (no slip). The second is the additional curvature of the cross-section caused by a given slip strain ε_{slp}. And the third term is the curvature caused by the axial load due to the eccentricity between the centriod of element 1 and the centriod of the composite section with full interaction.

From Eq.6.64, the factors affecting the curvature and hence deformation of the member are clearly seen. Apart from the external member forces N and $M(x)$ as well as the full interaction flexural rigidity $\overline{EI}$, the only other composite parameters that affect the deformations are a_2, a_3, a_5 and a_4, as the slip strain ε_{slp} is determined by a_2, a_3, a_5 and the loadings as discussed in Section 6.3.1. This observation is verified by the deflection results given by Eqs.6.49-6.53 and 6.44.

Similar to a_2, a_3, and a_5, there is also a clear physical meaning for coefficient a_4. To visualise this physical meaning, let $M(x)=0$ and $N=0$ in Eq.6.64 and consider Eq.6.54 to get

$$\kappa = a_4 \cdot \varepsilon_{slp} = -a_4 \cdot a_1 \cdot F_{shr} \tag{6.65}$$

For convenience, the corresponding free body diagram and strain profile in this case is shown in Fig.6.4.

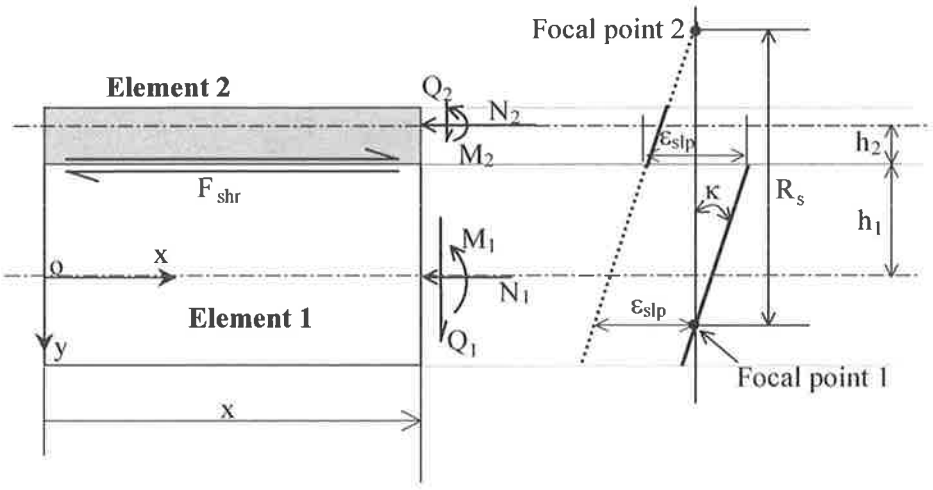

Fig. 6.4 Strain profile due to longitudinal shear force

The strain distribution of element 1 is given by $\varepsilon = \frac{N_1}{(EA)_1} - \kappa \cdot y$. Considering Eq.6.65 and $N_1 = -F_{shr}$ leads to

$$\varepsilon = -\frac{F_{shr}}{(EA)_1} + a_1 \cdot a_4 \cdot F_{shr} \cdot y = F_{shr} \cdot (a_1 \cdot a_4 \cdot y - a_3) \tag{6.66}$$

It is noted that at the point where $a_1 \cdot a_4 \cdot y - a_3 = 0$ in Eq.6.66, $\varepsilon \equiv 0$ for any value of F_{shr}. The y co-ordinate of this point is given by

$$y_1 = \frac{a_3}{a_1 \cdot a_4} \tag{6.67}$$

In other words, the additional strain caused by longitudinal shear (or slip) is always zero at this point no matter how the longitudinal shear force or slip changes. This means that all the strain profiles, for any combination or distribution of shear connections, pass through this point or are "focused at this point".

The strain profile 'focal point' is an important new concept in the study of composite structures that was first discovered and introduced by Seracino, Oehlers and Yeo (2001). It was found initially from their numerical simulations. They later verified this finding using linear elastic analysis to show that all strain profiles calculated from the elastic theory, with different shear connections, intersected at a common point. However, the physical reason as to why the focal point exists was still not clear from their study.

From the above discussion, it can now be seen clearly that the longitudinal shear force F_{shr} causes an additional axial force $N_1 = -F_{shr}$ and an additional moment $M_1 = -a_4 \cdot a_1 \cdot F_{shr} \cdot (EI)_1$ in the cross-section of element 1. This additional force and moment lead to the additional strain of $-F_{shr}/(EA)_1$ and $a_4 \cdot a_1 \cdot F_{shr} \cdot y$, respectively, in

the cross-section, which cancel each other at the focal point regardless of the value of F_{shr} that is affected by the shear connection details.

This investigation also reveals that the 'focal point' concept is, strictly speaking, the characteristic of linear systems. The linear strain distribution given by Eq.6.66 is not applicable to a general non-linear system which cannot have a single y value for $\varepsilon=0$ as was used to get Eq.6.67 in the above derivation.

For the same reason, element 2 also has a focal point. The y co-ordinate of focal point 2 can be easily calculated as

$$y_2 = -\frac{1}{a_1 \cdot a_4 \cdot (EA)_2} - h_1 - h_2 \tag{6.68}$$

The distance between these two focal points, R_s as shown in Fig.6.4, is given by

$$R_s = y_1 - y_2 = \frac{1}{a_1 \cdot a_4 \cdot (EA)_1} + \frac{1}{a_1 \cdot a_4 \cdot (EA)_2} + h_1 + h_2$$

$$= \frac{1}{a_4} \tag{6.69}$$

From Eq.6.65, it can be seen that a_4 is the curvature when the slip strain caused by the longitudinal shear $\varepsilon_{slp} = 1$. Because of this reason, a_4 is named as the *unit slip curvature*. Therefore, according to Eq.6.69, R_s is named the *slip radius* as oppose to the unit slip curvature a_4. It is noted that the slip radius (and unit slip curvature) is also function of cross-sectional properties.

From Fig.6.4, it can also be seen that the slip strain can be expressed as the slip radius times the curvature caused by the longitudinal shear force, or

$$\varepsilon_{slp} = R_s \cdot \kappa = \frac{\kappa}{a_4} \tag{6.70}$$

Comparing Eq.6.70 with Eq.6.65, it can be seen that they are the same which further supports the concept of 'focal points'. Interestingly, the first and third terms in Eq.6.64 can also be obtained with the concept of slip radius or unit slip curvature. For a composite member without interaction, the curvature due to an external moment is given by $\kappa = M(x)/\sum EI$. The slip strain at the interface is simply

$$\varepsilon_{slp} = \frac{M(x)}{\sum EI} \cdot (h_1 + h_2) \tag{6.71}$$

For a composite member with full interaction, this slip strain must be resisted by the longitudinal shear force so that $\varepsilon_{slp} = 0$, or the slip strain due to the longitudinal shear force is

$$\varepsilon_{slp} = -\frac{M(x)}{\sum EI} \cdot (h_1 + h_2) \tag{6.72}$$

From Eq.6.70, the additional curvature due to longitudinal shear is given by

$$a_4 \cdot \varepsilon_{slp} = -a_4 \cdot \frac{M(x)}{\sum EI} \cdot (h_1 + h_2) \tag{6.73}$$

The final curvature, assuming full interaction, is therefore the summation of the two parts, or

$$\kappa = \frac{M(x)}{\sum EI} - a_4 \cdot \frac{M(x)}{\sum EI} \cdot (h_1 + h_2) = \frac{M(x)}{\overline{EI}} \tag{6.74}$$

which is the same as the first term in Eq.6.64. The third term of Eq.6.64 can also be obtained with the same concept.

6.4 SLIP DISTRIBUTION OF THE CANTILEVER COLUMN

Due to the importance of the longitudinal slip, its distributions are further discussed in this section based on the results from linear elastic theory. Typical slip distributions for the cantilever column obtained from Section 6.2.2, as given by Eqs.6.40-6.42, are shown in Fig.6.5.

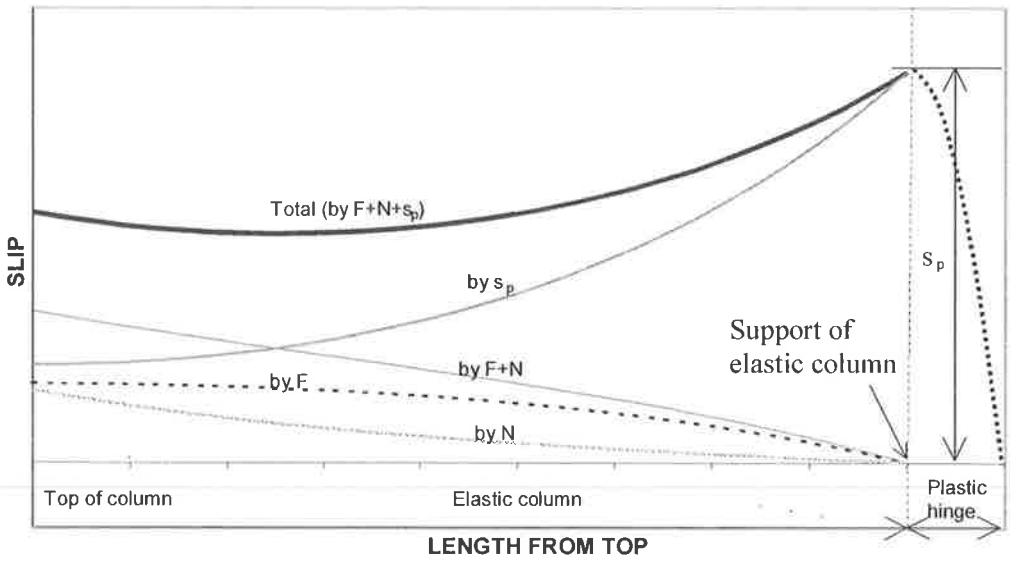

Fig. 6.5 Typical slip distributions

The slip term due to flexural deformation given by Eq.6.40 is shown by the curve marked with "by F" in Fig.6.5. The slip term caused by the axial load N given by Eq.6.41 is marked with "by N" in the figure. When the load and deflection is small, no plastic hinge forms and the total slip is given by the curve marked with "by F+N". The other term given by Eq.6.42 is induced by the boundary slip s_p at the elastic-zone/plastic-hinge interface when the plastic hinge forms at large deformations, as marked with "by s_p" in Fig.6.5. Summation of the above three terms depicts the total slip when large plastic deformation occurs, as shown by the thick line indicated with "Total" in Fig.6.5.

After the formation of the plastic hinge, the slip on top of the plastic hinge, s_p in Fig.6.5, continues to increase when the deflection of the column is further increased. The slip s_p depends on the deformation of the plastic hinge that will be shown in Section 8.2.1 (see Eq.8.5). However, the slip term due to N does not change. The slip term due to F is actually determined by the moment distribution along the column that will not increase significantly, instead it may decrease significantly after formation of the plastic hinge. Therefore, this F term may continue to increase slightly after yielding of the column, but this increase will be limited as compared to the fast increase in slip s_p caused by the fast increase in plastic deformation in the hinge. It is, therefore, possible that when the plastic hinge deformation of the column is sufficiently large, which is directly related to the slip s_p, the slip term 'by s_p' is more prominent than the other two terms. In this case, the position of maximum slip will occur at the top of the plastic hinge instead at the top of the column. An example that compares the analytical results to the numerical results, produced by the computer program "PLTCOL", is given in Fig.6.6.

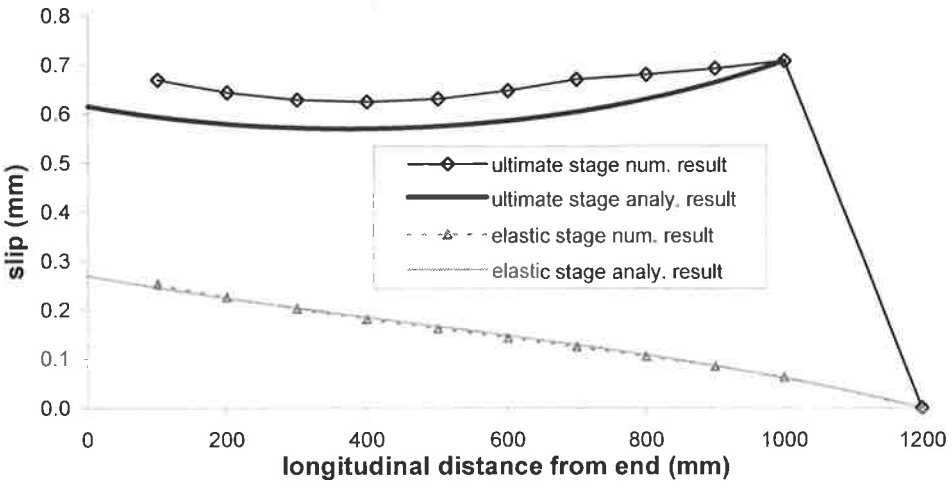

Fig. 6.6 Slip distributions compared with the numerical results

The numerical slip distribution just before the concrete cracks at the tension face, as indicated by 'Δ' in Fig.6.6, agrees very well with the analytical results. This means that the deformation of the column can be reasonably modeled as linear elastic before the concrete cracks on the tension face. At large deformations, however, the numerical results are generally greater than the analytical results, as shown by the curve marked with '◊' which indicates the stage just before the concrete crushes (compressive strength=0) on the compression face. This difference is mainly due to the assumption made in Section 6.1 that the column is still linear elastic above the plastic hinge at large deformations. The small non-linearity in the part of the column above the plastic hinge causes the numerical, or "actual", column to deform slightly more than predicted by elastic theory. The slight increase in column deformation corresponds to an extra amount of slip. This is the reason that the analytical slip distribution at the large deformation stage underestimates the amount of slip. However, the numerical results may slightly overestimate the true slip due to the neglect of tension stiffening. If tension stiffening were considered, the column would be slightly stiffer hence experiencing less deflection, which would lead to a smaller slip. That is to say there would be a closer agreement between the analytical and the numerical results if tension stiffening were considered in the numerical calculations. As the difference in Fig.6.6 is not substantial, this comparison verifies the legitimacy of the linear assumption outside the plastic hinge region.

6.4.1 Slip Due to Flexural Moment

From the slip term caused by the flexural moment as given by Eq.6.40, the slip s_f

- decreases monotonically when *the slip resistance ability coefficient* a_5 increases. This relation is shown in Fig.6.7(a) by the function $y = \frac{1}{a_5} \cdot \left[1 - \cosh(L \cdot \sqrt{a_5} \cdot \xi) / \cosh(L \cdot \sqrt{a_5})\right]$ which is part of the slip term. There are two asymptotes for the curve in Fig.6.7(a). Mathematically it can be proved that $\lim_{a5 \to 0} y = \frac{1}{2} \cdot L^2 \cdot (1 - \xi^2)$. In this case, Eq.6.40 gives $s_f = \frac{1}{2} F \cdot a_2 \cdot L^2 \cdot (1 - \xi^2)$. This is the case of zero interaction where no shear connection exists on the interface. In another extreme case of full interaction when a_5 approaches infinity, y approaches zero giving $s_f = 0$;

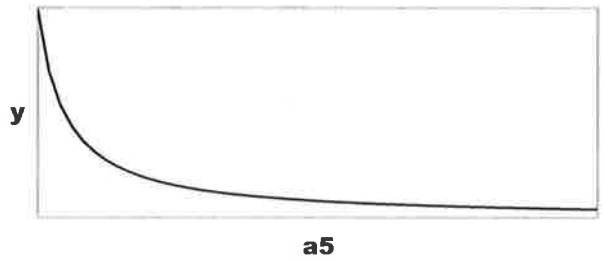

(a). Function $y = \frac{1}{a_5} \cdot \left[1 - \cosh(L \cdot \sqrt{a_5} \cdot \xi) / \cosh(L \cdot \sqrt{a_5})\right]$

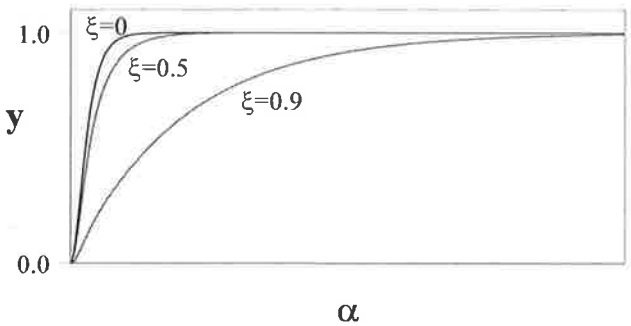

(b). Function $y = 1 - \frac{\cosh(\alpha \cdot \xi)}{\cosh(\alpha)}$

Fig. 6.7 Functions of Eq.6.40

- is directly proportional to the active slip strain coefficient a_2;
- is directly proportional to the lateral force F;
- increases monotonically with increase in L. This relation is shown in Fig.6.7(b) in which $\alpha = L \cdot \sqrt{a_5}$. When L increases, α increases hence s_f ($\dot{s}_f = F \cdot \frac{a_2}{a_5} \cdot y$ with y shown in Fig.6.7(b)) increases. However, it approaches an asymptote when L approaches infinity;
- is a maximum at the top of the column ($\xi = 0$), where the moment is zero. The maximum slip is given by

$$s_{\max} = F \cdot \frac{a_2}{a_5} \cdot \left[1 - \frac{1}{\cosh(L \cdot \sqrt{a_5})} \right] \tag{6.75}$$

and;

- decreases monotonically in a convex shape to zero at the support where the bending moment is a maximum.

6.4.2 Slip Due to Axial Load

From Eq.6.41 it can be seen that the slip caused by the axial load s_n

- decreases monotonically when the slip resistance ability coefficient a_5 increases, as shown in Fig.6.8(a) by the function $y = \frac{1}{\sqrt{a_5}} \cdot \left[e^{-(L\sqrt{a_5})\xi} - 2\cosh(L \cdot \sqrt{a_5} \cdot \xi) / (e^{2(L\sqrt{a_5})} + 1) \right]$ which is part of the slip term. Similar to s_f, there are also two asymptotes for this function: $\lim_{a5 \to 0} y = L \cdot (1 - \xi)$ which gives $s_n = N \cdot a_3 \cdot L \cdot (1 - \xi)$; and $\lim_{a5 \to \infty} y = 0$ gives $s_n = 0$.

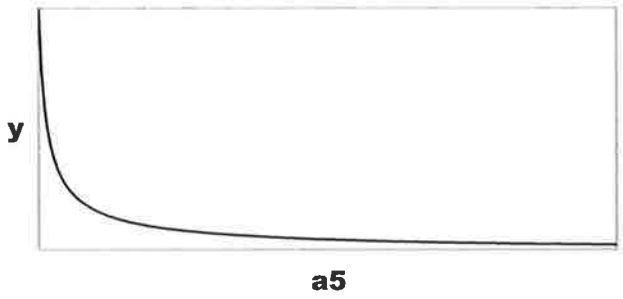

(a) $y=\frac{1}{\sqrt{a_5}}\cdot\left[e^{-(L\cdot\sqrt{a_5})\cdot\xi}-2\cosh(L\cdot\sqrt{a_5}\cdot\xi)\Big/(e^{2(L\cdot\sqrt{a_5})}+1)\right]$

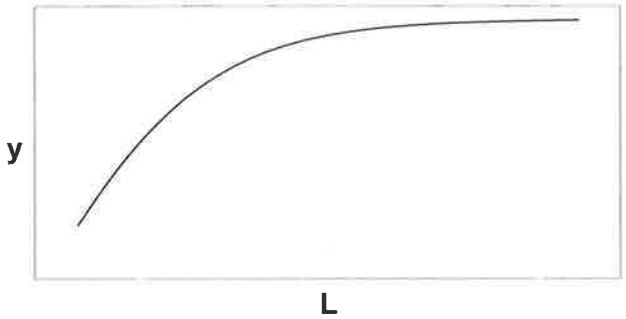

(b) $y=e^{-\sqrt{a_5}\cdot x}-2\cosh(\sqrt{a_5}\cdot x)\Big/(e^{2(L\cdot\sqrt{a_5})}+1)$

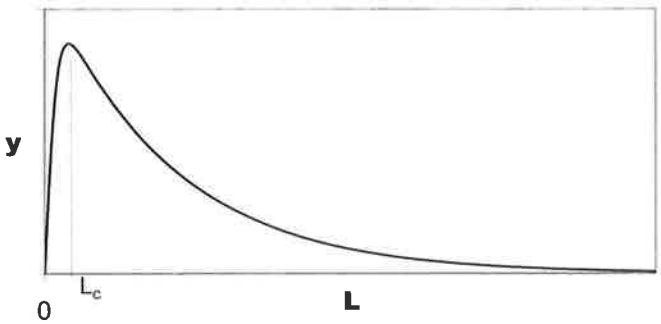

(c) $y=e^{-(L\cdot\sqrt{a_5})\cdot\xi}-2\cosh(L\cdot\sqrt{a_5}\cdot\xi)\Big/(e^{2(L\cdot\sqrt{a_5})}+1)$

Fig. 6.8 Functions of Eq.6.41

- is in direct proportion to the axial flexibility of element 1 a_3;
- is in direct proportion to axial force N;
- increases monotonically with increase in L at a point that keeps a fixed distance away from the top (L increases but $x = \xi \cdot L = \text{constant}$), as shown in Fig.6.8(b), with an asymptote when L approaches infinity, i.e. $\lim_{L\to\infty} s_n = \frac{N \cdot a_3}{\sqrt{a_5}} \cdot e^{-x\cdot\sqrt{a_5}}$ where x is the distance from the top of the column to the point considered. However, at a point that has a relative position fixed (i.e. ξ=constant but $\xi \neq 0$, for example the point at the middle of the column where ξ=0.5), the slip initially increases with increase in L, when L is less than a certain length L_c. After this point L_c, the slip will reduce when the length of the member is further increased, as shown in Fig.6.8(c);
- is a maximum at the top. The maximum slip is given by

$$s_{\max} = \frac{N \cdot a_3}{\sqrt{a_5}} \cdot \left[1 - 2/(e^{2(L\cdot\sqrt{a_5})} + 1)\right] \tag{6.76}$$

and;

- decreases monotonically to zero at the fixed end.

6.4.3 Slip Due to Boundary Slip

Equation 6.42 shows that the slip along the column induced by the boundary slip s_p

- decreases when the slip resistance ability coefficient a_5 increases. For the case of no interaction i.e. a_5=0, the slip is a constant value s_p along the length. For the case of

approaching full interaction when a_5 approaches infinity, the slip approaches zero except at the vicinity of the support where the slip is equal to s_p at the support;

- is in direct proportion to boundary slip s_p; and
- reduces monotonically with the increase in length L. Mathematically, it can be shown from Eq.6.42 that the slip at a point that has a certain distance away to the bottom of the column approaches an asymptote value when L approaches infinity; and
- monotonically increases from the top to the bottom of the column in a concave shape. The maximum slip value at the support when $\xi=1$ is s_p, and the minimum slip at the top is given by $s_{sp} = \frac{s_p}{\cosh(L \cdot \sqrt{a_5})}$.

CHAPTER 7 ULTIMATE CURVATURE OF RC SECTIONS

In Chapter 8, a methodology will be developed to design the plating system where the plated column is designed to an "adequate strength" when the ultimate displacement of the column is reached. Therefore, the ultimate displacement of an RC column must be firstly defined and studied. In order to study the ultimate displacement, the flexural behavior of RC cross-sections is analysed with some very simple models in this chapter. This analytical study also provides a clearer insight into the various factors that affect the deformation capacity of an RC column. To start with, an idealised plain concrete column section is first studied. Then, the effect of reinforcement is investigated.

7.1 MONOTONIC MOMENT CURVATURE RELATIONS OF PLAIN CONCRETE SECTIONS

The model to be studied first is a plain concrete column with a typical cross-section of breadth B and a depth D as shown in Fig.7.1. For simplicity, the stress-strain relationship of the concrete is idealised with the bi-linear model of Fig.4.4 in this section.

For convenience of study, the strain in every fibre of the cross-section is assumed to increase monotonically under the monotonic increase in the cross-sectional curvature. This assumption means that the stress in any fibre always goes along the envelope curve without going into the unloading/reloading branch shown in Fig.4.4. Strictly speaking, this assumption is not correct, as some areas in the cross-section do load and unload in

the course of the monotonic curvature increase in the section. However, most of this unload/reload takes place within the ascending branch of the envelope curve, or in the linear elastic range, where the unloading/reloading does not affect the loading history at all. Therefore, the monotonic assumption is still reasonable. Nevertheless, the conclusions drawn from this part of the analytical study are verified by the numerical study in Sections 7.1.4 and 7.3 where full non-linear loading/unloading history in every fibre is followed by the computer program.

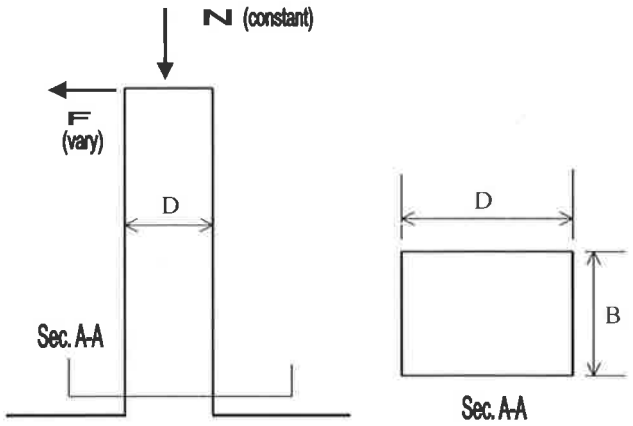

Fig. 7.1 Plain concrete column and section

The variation of the stress profiles of the typical cross-section with monotonic increase in the curvature of the section is shown in Fig.7.2. As the column is initially loaded with the axial load *N* only without lateral force or moment, the initial stress profile is an uniform stress distribution shown by stress distribution A. With the curvature increasing in the cross-section, the stress distribution changes from distribution A to distribution A', B, C, D and E successively, as shown in Fig.7.2. In all these cases, the

area of the stress blocks keeps unchanged due the condition of constant axial load. These different stages of stress distribution are studied in detail in the following sections.

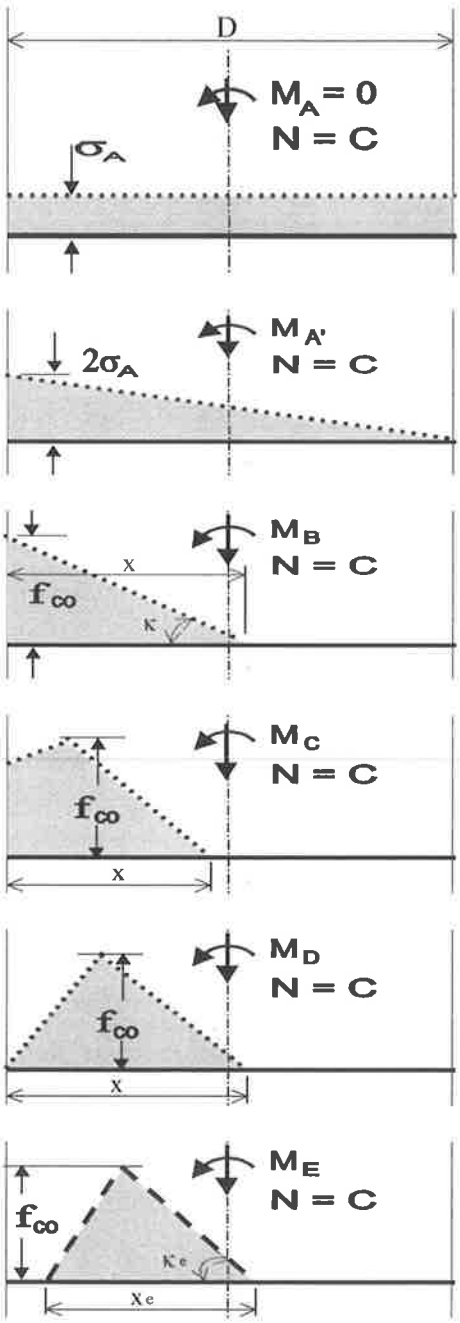

Fig. 7.2 Variation of stress blocks in section A-A

7.1.1 Elastic Stage

From distribution A to distribution B in Fig.7.2 is a linear elastic deformation stage. When the curvature increases monotonically, the stress on the left-hand side of the section is increased while the stress on the right-hand side is decreased. When the stress at the top extreme fibre on the left-hand side reaches the compressive strength f_{co}, as shown by the stress profile B, a non-linear or plastic deformation starts to occur when the curvature further increases. From distribution A to B, the centroid of stress block is moving from the center of the cross-section towards the left-hand side monotonically. Therefore the lever arm and hence the moment of the section is also increasing monotonically.

From stress distribution B, the following equation is obtained assuming the neutral axis depth x is less than the depth of the cross-section D which is an adequate assumption and will be discussed further in the end of Section 7.1.

$$\begin{aligned} N &= B \cdot f_{co} \cdot x/2 \\ &= B \cdot f_{co} \cdot \frac{\varepsilon_{co}}{\kappa_{co}}/2 \\ &= \frac{B \cdot f_{co} \cdot \varepsilon_{co}}{2\kappa_{co}} \end{aligned} \tag{7.1}$$

or

$$\kappa_{co} = \frac{f_{co} \cdot \varepsilon_{co} \cdot B}{2N} = \frac{\varepsilon_{co}}{2D \cdot (N/N_c)} \tag{7.2}$$

where B is the breadth of the section; ε_{co} and f_{co} are the strain and stress at the peak of the stress-strain curve as shown in Fig.4.4; N_c is the crush load given by

$N_c = f_{co} \cdot A_g = f_{co} \cdot B \cdot D$; and κ_{co} is the curvature of the section when the compressive strength f_{co} is just achieved at the extreme fiber.

7.1.2 Deteriorating Stage

This stage starts from distribution B and ends with distribution D in Fig.7.2. The stress at the face of the left-hand side starts to decrease with further increase in curvature, as shown by distribution C, until it reaches zero as shown by distribution D. The deterioration of the concrete in the extreme compression fiber starts with distribution B and completely crushes at distribution D. In this process, the centroid of the stress block moves further left then starts to move back towards right-hand side. In other words, the moment increases further then begins to drop.

From distribution D in Fig.7.2, the following relations are obtained

$$x = \varepsilon_{cu} / \kappa_{cu}$$

$$N = B \cdot f_{co} \cdot x / 2 = \frac{B \cdot \varepsilon_{cu} \cdot f_{co}}{2\kappa_{cu}} \tag{7.3}$$

or

$$\kappa_{cu} = \frac{f_{co} \cdot \varepsilon_{cu} \cdot B}{2N} = \frac{\varepsilon_{cu}}{2D \cdot (N/N_c)} \tag{7.4}$$

where ε_{cu} is the ultimate concrete strain at zero strength as shown in Fig.4.4; κ_{cu} denotes the curvature of the section at which the strain of the extreme compressive fibre just reaches ε_{cu}.

It is noted that distributions B and D must have the same neutral axis depth x in order to satisfy the constant N condition. In the meantime, the centroid of the stress block D is on the left to that of distribution B. In other words, there must be a drop in moment resistance from distribution B to distribution D. The magnitude of the drop in moment resistance depends on the depth of the compression zone x or axial load level.

The moment corresponding to a given curvature κ can be calculated at this stage. The following relation is derived using the stress distribution C as shown in Fig.7.2

$$\frac{M}{B}=f_{co}\cdot\left[\frac{\varepsilon_{co}^2\cdot\beta\cdot(1+\beta)}{6\kappa^2}+\frac{\varepsilon_{co}}{2\kappa}\cdot(\frac{D}{2}-x)\cdot\beta-\frac{1}{6}\cdot(1+\alpha-\frac{\alpha\cdot\kappa\cdot x}{\varepsilon_{co}})\cdot(\frac{\beta\cdot\varepsilon_{co}}{\kappa}-x)\cdot(\frac{3D}{2}+\frac{\beta\cdot\varepsilon_{co}}{\kappa}-x)\right] \tag{7.5}$$

in which M is the moment of the section under the curvature κ; and x is the compression zone depth given by

$$x=\frac{\varepsilon_{co}}{\kappa}+\frac{\varepsilon_{co}}{\alpha\cdot\kappa}\left[1-(1+\alpha-\frac{2\kappa\cdot\alpha\cdot N}{f_{co}\cdot\varepsilon_{co}\cdot B})^{1/2}\right] \tag{7.6}$$

and

$$\begin{cases}\alpha=\dfrac{E_c'}{E_c}\\ \beta=\dfrac{\varepsilon_{cu}}{\varepsilon_{co}}=1+\dfrac{1}{\alpha}\end{cases} \tag{7.7}$$

where E_c and E_c' are the elastic modulus of the ascending branch and slope of the softening branch of the concrete model, respectively, as shown in Fig.4.4.

7.1.3 Crushing of Section

Any further increase in curvature from distribution D in Fig.7.2 will move the zero stress point in the cross-section towards the right-hand side as shown by distribution E. However, the axial load level cannot be sustained in this case. The reason is given below.

The stress distribution E in Fig.7.2 gives

$$x_e = \varepsilon_{cu} / \kappa_e \tag{7.8}$$

$$\begin{aligned} N_e &= B \cdot f_{co} \cdot x_e / 2 \\ &= \frac{B \cdot \varepsilon_{cu} \cdot f_{co}}{2\kappa_e} \end{aligned} \tag{7.9}$$

Comparing Eq.7.3 with Eq.7.9

$$\because \kappa_e > \kappa_{cu}$$

$$\therefore N_e < N \tag{7.10}$$

in which κ_e is the curvature of the section under distribution E, and x_e is the distance from neutral axis to the point where the compressive strain equals to ε_{cu}, as shown in Fig.7.2; and N_e is the axial load under stress distribution E.

The physical reason behind Eq.7.10 is that the horizontal length of the triangle stress block reduces when the curvature further increases after distribution D. While the maximum stress maintains constant at f_{co}, the area of the stress block must reduce. If the axial load remains constant at this time, the whole concrete section will crush suddenly.

7.1.4 Case Study

To further illustrate the results of Section 7.1.1 to Section 7.1.3, an example of the curvature moment relation for a plain concrete section is shown in Fig.7.3. Details of the column section is give below:

Cross-section size 400mm×400 mm, f_{co}=44 N/mm^2, ε_{co}=0.002, ε_{cu}=0.006 and N=0.3 · f_{co} · B · D=2112KN.

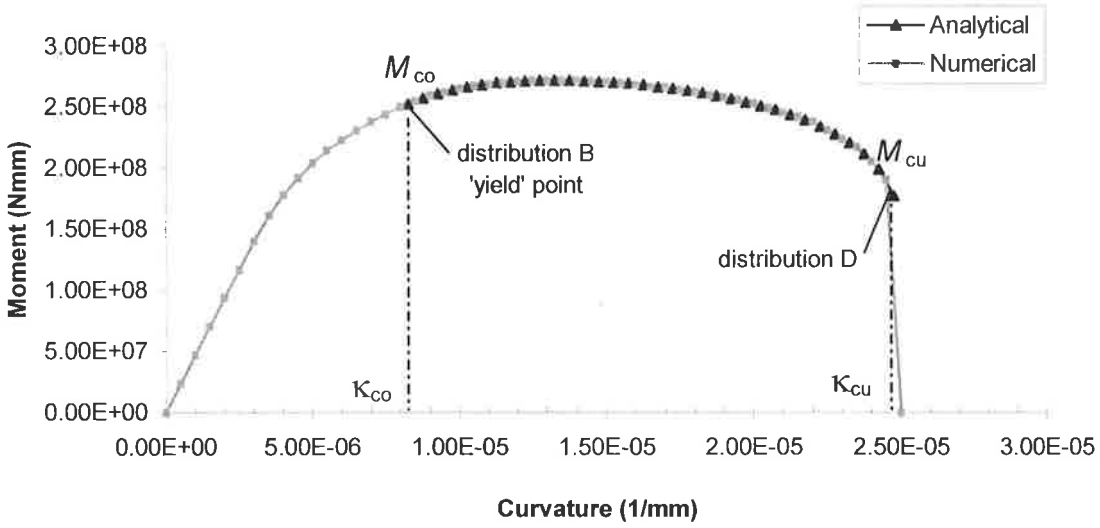

Fig. 7.3 Moment curvature relation of a plain concrete section

The analytical result in Fig.7.3 is given by Eq.7.5. The numerical result is obtained by the computer program PLTCOL that considers full loading/unloading history. The same stress-strain relation as shown by Fig.4.4 is used in the numerical calculation. The agreement of these two results verifies the monotonic strain assumption given in the beginning of Section 7.1.

7.1.5 Displacement Ductility of Plain Concrete Sections

From the above discussion it can be seen that the concrete section completely crushes when the compressive strain at the extreme fibre reaches ε_{cu}. Therefore, the ultimate deformation of a plain concrete column is reached when the curvature of a cross-section reaches a value that satisfies Eq.7.4. This curvature is defined as the ultimate curvature of a section in this work.

In the literature, the ultimate curvature is usually defined as the curvature at a point where the resistant moment of the section drops to a certain percentage of the maximum strength (Watson, Zahn and Park 1994). Different values for this drop, such as 10%, 20% or 30%, have been used. This definition of ultimate deformation is based on the strength concern and it is not the true ultimate deformation.

In fact, the strength drop at the true ultimate curvature given by Eq.7.4 can be calculated from Eq.7.5. Substituting Eq.7.4 or $\kappa_{cu} = f_{co} \cdot \varepsilon_{cu} \cdot B/2N$ into Eq.7.5 gives

$$M_{cu} = N \cdot (\frac{D}{2} - \frac{4\beta - 2}{3\beta} \cdot \frac{N}{f_{co} \cdot B}) \tag{7.11}$$

where M_{cu} is the moment of a cross-section when the ultimate strain ε_{cu} is reached at the extreme fibre. The 'yield' moment M_{co} of the cross-section is obtained by substituting Eq.7.2 or $\kappa_{co} = f_{co} \cdot \varepsilon_{co} \cdot B/2N$ into Eq.7.5, giving

$$M_{co} = N \cdot (\frac{D}{2} - \frac{2}{3} \cdot \frac{N}{f_{co} \cdot B}) \tag{7.12}$$

From Eq.7.11 and Eq.7.12, the following relation is obtained

$$\frac{M_{co}-M_{cu}}{M_{co}}=\frac{2(\beta-1)}{3\beta}\cdot\frac{(\frac{N}{N_c})}{\left[\frac{1}{2}-\frac{2}{3}\cdot(\frac{N}{N_c})\right]} \tag{7.13}$$

where N/N_c gives the axial load level. It can be seen from Eq.7.13 that the moment drop at the true ultimate deformation as relative to the yield point is only determined by the material property β and the axial load level. Typical curves given by Eq.7.13 are shown in Fig.7.4. However, the moment drop given by Eq.7.13 is relative to the yield point not the maximum strength point as can be seen in Fig.7.3. This modification simplifies the discussion.

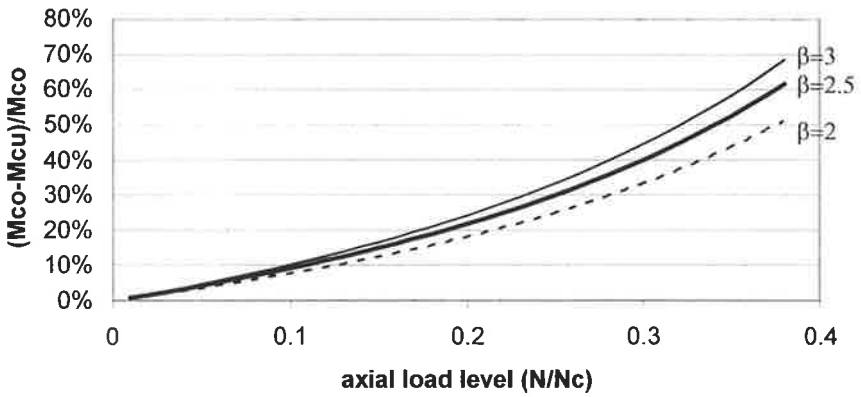

Fig. 7.4 Moment drop-axial load relation

In engineering, the maximum axial load level is usually limited by design codes. AS3600-2001: Concrete structures (Australian Standard) specifies the maximum axial load for short columns with insignificant bending moment to be

$$N=0.75\cdot\phi\cdot N_{uo}=0.382 f_{co}\cdot A_g \tag{7.14}$$

Therefore, Fig.7.4 covers the whole practical range of the axial load level.

As seen from Fig.7.4, the moment drop from the 'yield' point to the true ultimate displacement ranges from 10% to 20% of the 'yield' moment for axial load levels of 0.1 to 0.2. Therefore, the traditional ultimate displacement defined at a 10% of moment drop will be equivalent to the true ultimate displacement for a column with axial load level of 0.1(10% of the crush load). For other axial load levels, the traditional ultimate displacement cannot reflect the true deformation capacity of a column.

From Fig.7.3, it can be seen that the curve from the yield point to the ultimate point may be defined as a yield plateau. In this case, the maximum curvature ductility of the concrete section may be defined as

$$\Delta\kappa = \kappa_{cu} - \kappa_{co} = \frac{f_{co} \cdot B}{2N}(\varepsilon_{cu} - \varepsilon_{co}) = \frac{\varepsilon_{cu} - \varepsilon_{co}}{2(N/N_c) \cdot D} \tag{7.15}$$

In terms of the curvature ductility factor

$$\kappa_{cu} / \kappa_{co} = \varepsilon_{cu} / \varepsilon_{co} \tag{7.16}$$

Of course, this definition of curvature ductility is different from the traditional definition where a certain percentage drop of the peak moment value is used to locate the point of the ultimate curvature, regardless of the axial load level. In the current literature, it is well established that the behaviour of a concrete column is closely related to its axial load level. From this point of view, the traditional definition of ultimate curvature cannot reflect the true extent of physical deterioration in the column. The above definition given by Eq.7.15 adequately reflects the degree of damage to the concrete of the column based on the specific axial load level. The yield plateau starts at the very first point at which the

extreme compressive fibre just starts to yield and ends at the true ultimate curvature where any further curvature increase will cause the complete crushing of the whole concrete section. Therefore, distributions B and D in Fig.7.2 have very clear physical meanings: the qualitative turning points of the concrete material in the cross-section from complete elastic to yielding and from yielding to completely crushing, respectively.

Equation 7.15 tells us that the curvature ductility of a plain concrete section is

(a) in direct proportion to the material plastic deformation capacity $\varepsilon_{cu} - \varepsilon_{co}$;

(b) in reverse proportion to the axial load level N/N_c. This relation was observed by many researchers from experimental works (Berwanger 1975; Sheikh and Khoury 1993; Watson and Park 1994; Bayrak and Sheikh 1997); and

(c) in reverse proportion to the section depth. It is consistent with the common sense that a deeper column is stiffer and more brittle than a shallower column.

The ductility factor given by Eq.7.16 is only affected by strain properties $\varepsilon_{cu}, \varepsilon_{co}$ of the concrete material.

The above conclusions are based on the simplified stress-strain model of Fig.4.4. Another assumption made in this study is that the neutral axis is within the depth of the cross-section from distribution B to D. When the axial load level is very high ($N > 0.5 f_{co} A_g$), the neutral axis will fall outside the right hand side of the section at stress distribution B. However, it is outside the practical range of axial load level as mentioned above.

7.2 EFFECT OF LONGITUDINAL REINFORCEMENT

From Eqs.7.4 and 7.15, it can be seen that the deformation capacity of a plain concrete section is determined by three factors: the material property or stress-strain relationship of the concrete (ε_{co} and ε_{cu}), the geometry of the cross-section (D), and the axial load level (N/N_c). For RC columns, there exist two constitutive materials of concrete and reinforcing bars. In this section, the transverse reinforcement or stirrups are ignored and only the longitudinal bars are considered. If an RC column is treated as a concrete column and the longitudinal reinforcing bars as external members that apply additional load to the concrete, then the effect of the longitudinal reinforcing bars is clear. Since the presence of the longitudinal reinforcement will not change the material and geometric property of a concrete section, the only way it affects the deformation capacity of the concrete section is through changing the axial load level applied onto the concrete section.

The axial load produced from the longitudinal reinforcement varies with the change of cross-sectional curvature. However, the ultimate curvature of the section is only affected by the instantaneous axial load when the strain of the extreme compressive fibre just reaches ε_{cu}. Therefore, the effect of the longitudinal reinforcement on the ultimate curvature of a concrete section can be studied with the ultimate strain profiles as shown in Fig.7.5. For convenience of study, the reinforcement is assumed to be symmetrical in Fig.7.5.

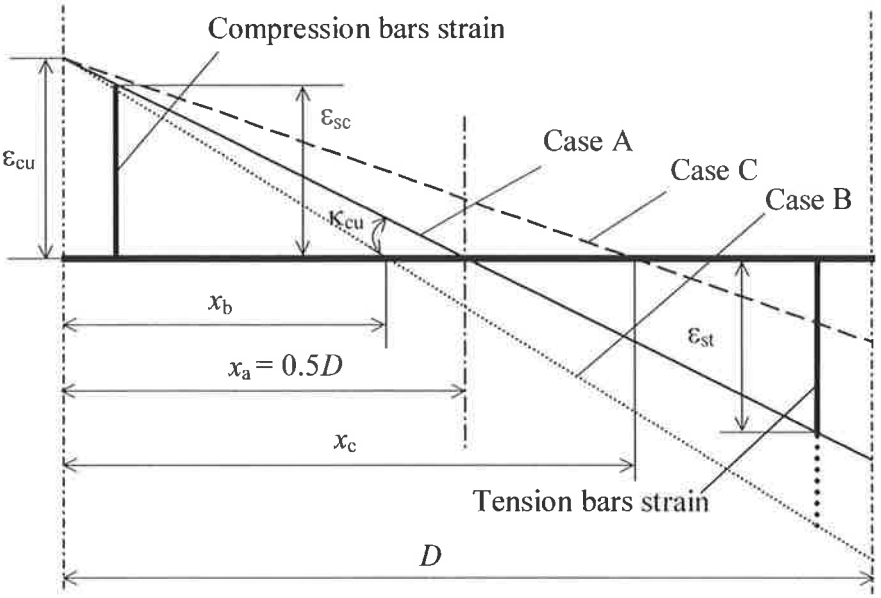

Fig. 7.5 Ultimate strain profiles in an RC section

7.2.1 At Critical Axial Load

Firstly let us look at the strain profile case A shown in Fig.7.5, where the depth of the compression zone is exactly half of the section depth. In this case, the strain of the compression bars ε_{sc} is exactly the same as that of the tension bars ε_{st}. If the same stress-strain relationship is assumed for both compression and tension, the net additional axial load produced by the longitudinal reinforcement is zero. In other words, the existence of the longitudinal reinforcement will not affect the axial load level, hence it will not affect the ultimate deformation of the RC section. In this case, the axial load satisfies

$$N = 0.25D \cdot B \cdot f_{co} \tag{7.17}$$

which indicates that the axial load level is 25% of crush load. Therefore, this is a critical axial load level at which no matter how much longitudinal reinforcement is used the deformation capacity of the section remains the same. This phenomenon will be seen in the full non-linear numerical simulations in Section 7.3.

Equation 7.17 is applicable only when the bi-linear triangular concrete model is used. When a different stress-strain model is used, this critical load level will be different due to the difference in the area of the stress-blocks under different models. When Mander's model is used, the critical axial load is given by (see Section 8.2.2)

$$N = \beta \cdot f_{co} \cdot (\frac{D}{2}) \cdot B = 0.5\beta \cdot N_c \qquad (7.18)$$

where β is a function of the concrete strength given in Fig.8.4.

7.2.2 For Axial Load Level Lower Than Critical Load

When the axial load level is lower than the critical load (approximately 25% of crush load as given by Eq.7.17), the compression zone depth will be smaller than half the section depth at the ultimate curvature κ_{cu}, as shown by the strain distribution B in Fig.7.5. In this case, the tensile strain in the tensile reinforcement will be greater than that in the compression reinforcement, and therefore there will be a compression force applied to the concrete in addition to the external axial load *N*. In other words, the presence of the longitudinal reinforcement will cause an increase in the axial load level to the concrete section. Based on Eqs.7.4 and 7.15, the deformation capacity of the concrete section will be reduced by the longitudinal reinforcement. The more longitudinal reinforcement, the greater the reduction of the deformation capacity of the concrete section. This

observation is consistent with the conclusion that the ductility of an RC beam (where the axial load is zero) reduces with the increase in the longitudinal reinforcement ratio (Warner et al. 1998). This phenomenon will also be seen in the full non-linear numerical simulations in Section 7.3.

Unlike the plain concrete section, which crushes suddenly if the curvature is further increased after the extreme compression fibre reaches ε_{cu}, the RC section will not crush immediately. Further increase in curvature will cause some concrete to crush on the top of the compression zone and the maximum axial load that can be carried by the concrete will be reduced for the reason given in Section 7.1.3. In this process, the neutral axis moves toward the right hand (tensile) side so that the compression force in the reinforcement is increasing and tension force is reducing. As a result, the additional axial load due to the steel bars is reducing hence the total axial load applied to the concrete is reducing. Therefore, the axial load balance of the section can still be sustained regardless of the continuous crushing of concrete and diminishing size of the concrete stress block. The change in axial load on the concrete and variation of the stress block will be illustrated by the numerical studies in Section 7.3.

7.2.3 For Axial Load Level Higher Than Critical Load

The compression zone depth will be more than half D at the ultimate curvature when the axial load level is higher than the critical load. Therefore, the compression force in the reinforcement will be larger than that in the tension reinforcement, as shown by the case C in Fig.7.5. The resultant force in the longitudinal reinforcement will be such that it reduces the axial load level applied to the concrete section. Based on the conclusion in

Section 7.1 (see Eqs.7.4 and 7.15), the ultimate curvature of the concrete section will be increased due to the presence of the longitudinal reinforcement. However, the increase in the ultimate curvature due to the longitudinal bars is limited due to the high axial load level and this will be seen in the numerical study in Section 7.3.

7.2.4 Ultimate Curvature of RC Columns with Few Stirrups

It has been shown in Section 7.1 that the true ultimate curvature of a plain concrete column is achieved at the onset of the ultimate concrete strain ε_{cu} at the compression face of the column. This criterion may still be applicable to RC columns with little confinement such as old columns with inadequately designed and detailed stirrups. The reason is that (for old RC columns) *the ultimate curvature that can be developed within the potential plastic hinge region is limited by the strain at which the cover concrete begins to spall, which is typically around 5% strain. The hoop steel unravels when the longitudinal strain is higher than 5%, resulting in the loss of small confinement and shear strength* (Chai et al. 1991). As a result, buckling of longitudinal reinforcement or shear failure may occur at any time. Although the RC columns may not crush immediately after the attainment of the ultimate concrete strain ε_{cu} (spall strain) on the compression face, the concrete resistance in the cross-section starts to drop significantly after this point which will be seen in the numerical example of next section.

As the target of this study is on RC columns with potential concrete failure problems in the plastic hinge zone which were usually designed and constructed with inadequate stirrups, the ultimate curvature of RC columns is therefore defined in this

work as the curvature at which the extreme compressive fibre of concrete reaches the ultimate strain ε_{cu}.

This definition is not applicable to columns with adequately designed and detailed stirrups. For columns well confined by stirrups, the spalling of the concrete cover does not impair the column significantly, as the well confined core concrete is strong and ductile enough to further take additional load and displacement. In this case, the final failure may be caused by fracturing of the stirrups, or longitudinal reinforcing bars, or crushing of the core concrete. Therefore, the attainment of ε_{cu} or spalling of cover concrete cannot be used as a criterion to determine the ultimate curvature of these RC columns.

7.3 NUMERICAL CASE STUDIES

Numerical case studies are conducted in this section to visualise and further understand the conclusions of Sections 7.1 and 7.2. Analytical studies in the previous sections of this chapter were based on simplified models and assumptions. To enable general conclusions to be made, the numerical simulations in this section will be based on full non-linear models, such as Mander's model for concrete and Menegoto-Pinto model for steel bars as described in Chapter 4.

The RC column cross-section studied is 400mm×400mm with 12 numbers of reinforcing bars (4 bars each face), which is the same as the case of Fig.4.20 studied by Watson and Park (1994). No stirrups and confinement is considered in this study in order to investigate the net effect due to the longitudinal bars only. The following material properties are used:

Concrete - f_{co}=44 N/mm^2, ε_{co}=0.002, ε_{cu}=0.006, f_{ct}=5 N/mm^2;

Longitudinal bars - f_{sy} = 446 MPa, E_s = 200000 N/mm^2, E_h = 600 N/mm^2,

R_0=20.0, α_1=19.0, α_2=0.3.

To vary the reinforcement ratio, different bar diameters are used: 16mm, 20mm, 25mm and 32mm corresponding to reinforcement ratios of 1.5%, 2.36%, 3.68% and 6.03%, respectively. Concrete cover thickness (to the centre of reinforcing bar) is calculated to be 29mm from Fig.4.20 for the case of Y16 bars (=13+8+8). To provide a uniform benchmark for comparison, this cover thickness is adopted for all the other reinforcement arrangements regardless of bar diameter; as changing cover thickness effectively changes the lever arm of the longitudinal bars which is not desirable for comparison. A plain concrete section without any reinforcement is also included in this study.

Several axial loads are used in the study. They are 352KN, 704KN, 1408KN, 2112KN, 2816KN, and 3520KN corresponding to 5%, 10%, 20%, 30%, 40%, and 50% of column crush load N_c, respectively. The concrete cross-section is discretised into 25 number of layers. As no confinement is considered in this study, vertical division of cross-section into different slices is not necessary.

The results for the case of N=5% of crush load are given in Figs.7.6-7.8. Fig.7.6 shows the moment curvature relations for sections with various reinforcement ratios. Fig.7.7 shows one case of Fig.7.6 with 3.68% steel and in which the moment contributions from the concrete and the steel bars are split out. The splitting of the axial force in the cross-section for the same case is given in Fig.7.8. The definitions of the symbols "×", "◊", "+" and "✶" are given in the Notation. The corresponding curvatures

for the above four stages are named κ_{co}, κ_{cu}, κ_{sly} and κ_{scy}, respectively. The locations of points "×", "◊", "+" and "✳" on the curves may not be exact as the numerical outputs are not continuous. They are plotted at the nearest numerical points. Fluctuations or wobbling are seen in these figures at large deformation. It was later found to be caused by the discretisation of the cross-section. When a higher layer number or finer layers are used, the fluctuations diminish.

From Fig.7.6, it can be seen the difference on the horizontal coordinate between point + (onset of yielding of tension bars) and point ◊ (onset of complete crushing of concrete on the compression face) gives a good indication of the ductility of the cross-section. Although considerable strength and a large plateau remains after points ◊ as seen from the chart, this remaining strength is only theoretical and not reliable. The reason is that the concrete deteriorates (strength drops) significantly after point ◊ as seen from Figs.7.7 and 7.8. To further illustrate the extent of damage to the concrete, a concrete stress block (at $\kappa = 7.5\times10^{-5}$ 1/mm) after point ◊ is shown in Fig.7.9, where it can be seen that a significant area in the compression zone has completely crushed. After crushing of the cover concrete, the longitudinal bars will lose support and hence may buckle at any time. Therefore, the remaining strength in Fig.7.6 after point ◊, which comes mainly from the reinforcement bars as can be seen in Fig.7.7, is not reliable and hence is only a theoretical strength. Figure 7.8 confirms the theoretical conclusion given in Section 7.2.2 that the presence of longitudinal bars increases the axial load on the concrete section in this case.

The numerical results for other axial load levels are shown in Fig.7.10 to Fig.7.14. From the appearance of these figures, it also looks reasonable to define points ◊ as the ultimate displacement of the RC columns. The key point curvatures κ_{co} (onset of peak concrete strain ε_{co} at compression face), κ_{cu} (onset of ultimate concrete strain ε_{cu} at compression face), κ_{sty} (yielding of tension bars) and κ_{scy} (yielding of compression bars) versus axial load for different reinforcement ratios are depicted from Fig.7.15 to Fig.7.18. More cases with higher axial load levels are calculated and included in Figs.7.15 to 7.18 for comparison, although these axial load levels are not practical.

From Figs.7.15, 7.16 and 7.18, it can be seen clearly that κ_{co}, κ_{cu}, and κ_{scy} reduce when the axial load increases. For the same axial load level and when the axial load level is lower than 30%, Fig. 7.15 shows that κ_{cu} reduces when steel content increases. It is the other way round for axial load levels higher than 30% in Fig.7.15. Similar observations can also be made for κ_{co} and κ_{scy} in Figs.7.16 and 7.18. It was concluded theoretically in Section 7.2 that the ultimate curvature κ_{cu} reduces when the steel content increases for axial loads less than the critical axial load and vice versa for axial loads higher than the critical load. This critical axial load is given by Eq.7.18 to be $N = 0.5\beta \cdot N_c = 0.5 \times 0.59 N_c = 0.295 N_c$, or 29.5% of crush load, where β=0.59 from Fig.8.4 when the concrete strength is 44MPa. These theoretical conclusions are confirmed by the numerical results of Fig.7.15 where it can be seen that the reinforcement content does not affect the ultimate curvature at the axial load level of about 30% of the crush load. In other words, the numerical calculated critical axial load is about 30%.

Actually, the discussions on the effects of the longitudinal reinforcement in Sections 7.2.1-7.2.3 are still applicable if ε_{cu} and κ_{cu} in Fig.7.5 are changed to ε_{co} and κ_{co}, which explains the same trends in Fig.7.16 as seen in Fig.7.15. For κ_{sty} as shown in Fig.7.17, it increases when axial load increases and the steel content apparently has no effect on its values. When axial load level is more than 40%, the tensile reinforcement will not yield at all.

Another observation that can be made from the moment-curvature charts is that the yield plateau can be well reflected between point + (first yield of tension bars) and point ◊ (spalling of concrete cover) for axial load levels lower than 30% of crush load, as seen in Figs. 7.6, 7.10 and 7.11. However, for higher axial load levels as shown in Figs.7.12, 7.13 and 7.14, it is apparently more reasonable to define the yield plateau from point × (onset of maximum concrete strength on the column face) to point ◊. In fact, point + or yielding of tension bars does not occur for any of the columns represented in Fig.7.14 where N=50% N_c. No matter which definition is used for the yield plateau, it is clear from these moment-curvature charts that the yield plateau decreases when the reinforcement ratio increases for axial loads lower than the critical load, as shown by Figs.7.6, 7.10 and 7.11. For axial loads higher than the critical load as shown by Figs.7.12, 7.13 and 7.14, the yield plateau increases when the reinforcement ratio increases. This observation further verifies the theoretical conclusions in Section 7.2.

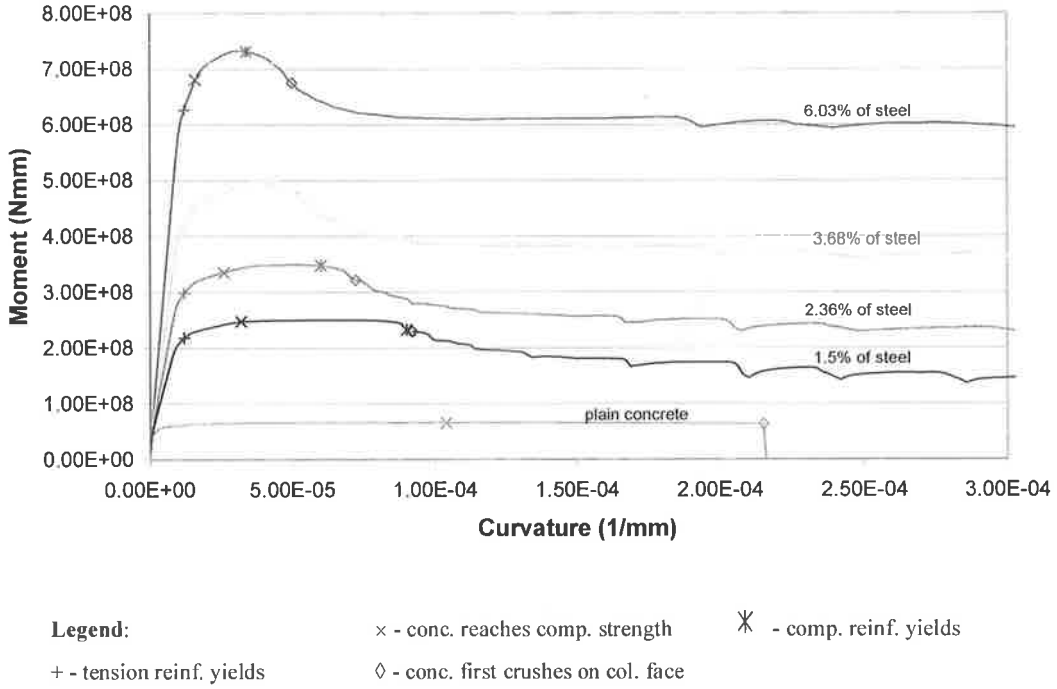

Fig. 7.6 Moment-curvature chart of RC sections with N=5%N_c

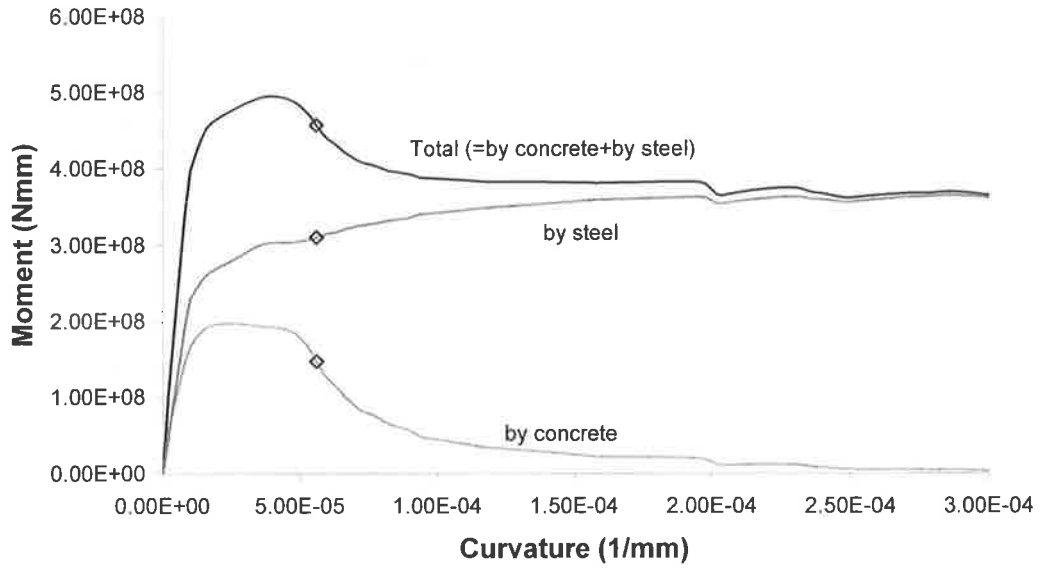

Fig. 7.7 Moment-curvature chart for section with 3.68% steel and N=5%N_c

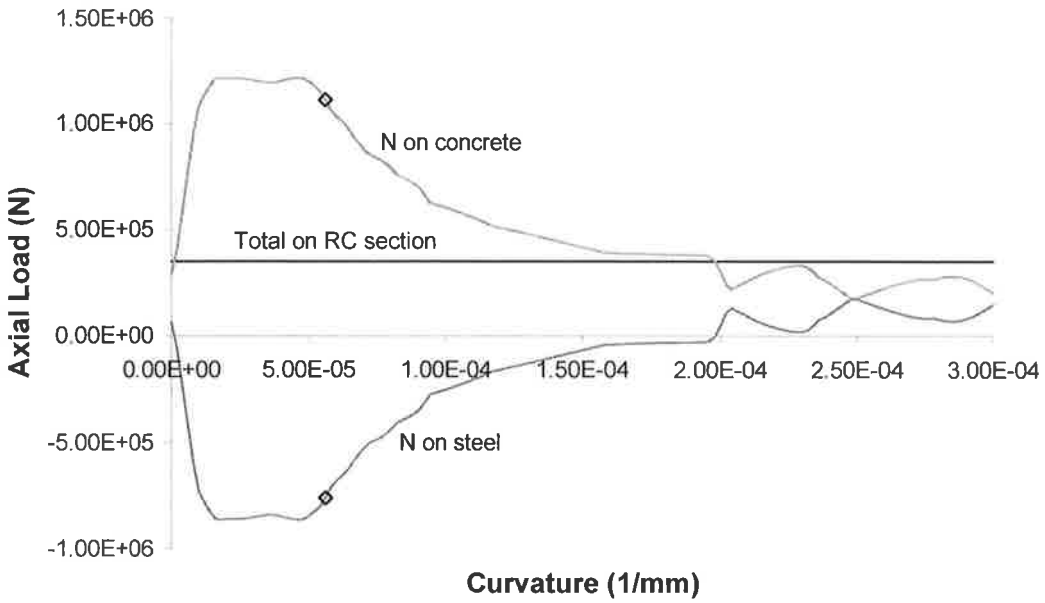

Fig. 7.8 Axial force-curvature chart for section with 3.68% steel and N=5%N_c

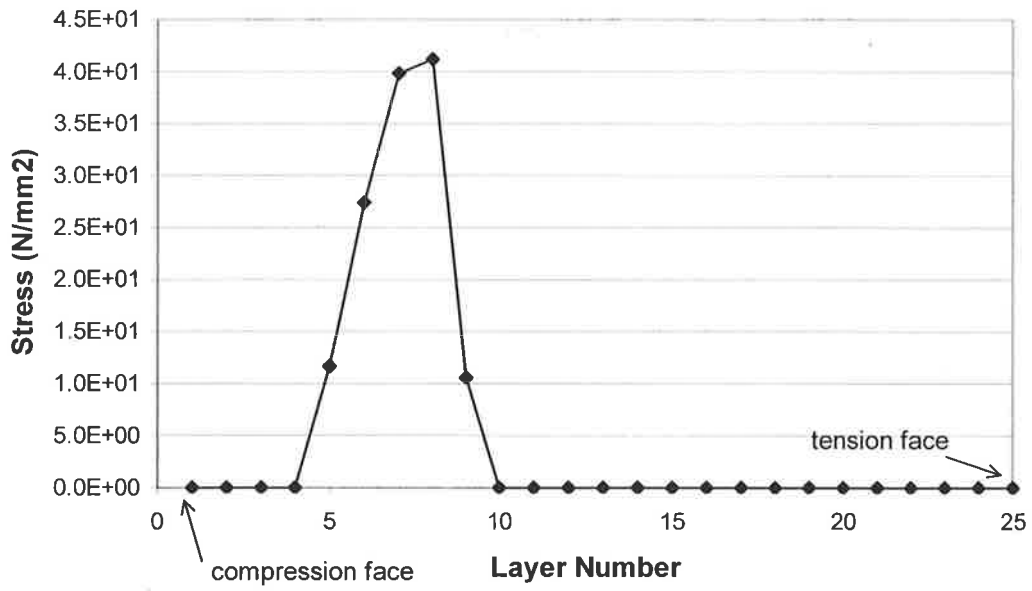

Fig. 7.9 Concrete stress block at a curvature of 7.5×10^{-5} (1/mm) for section with 3.68% steel and N=5%N_c

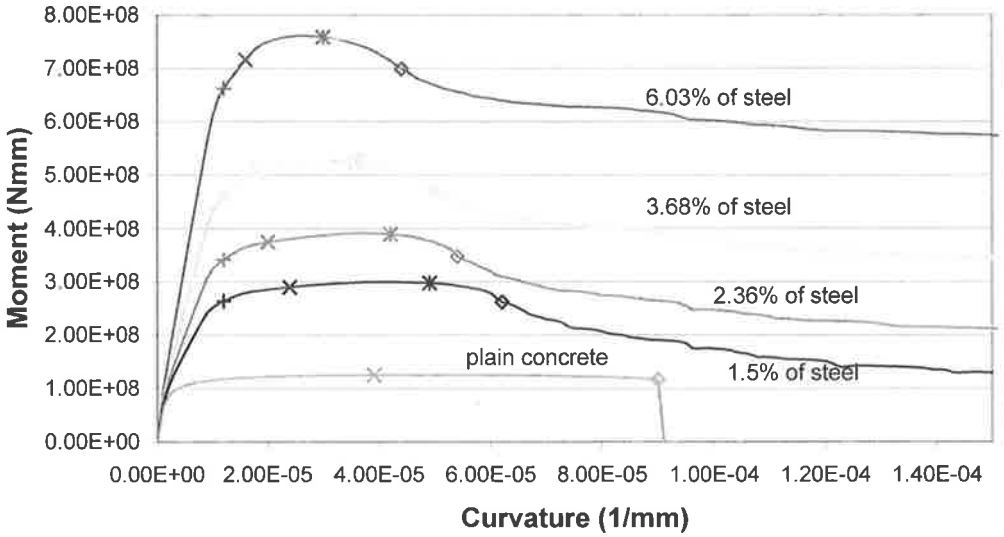

Fig. 7.10 Moment-curvature chart of RC sections with N=10%N_c

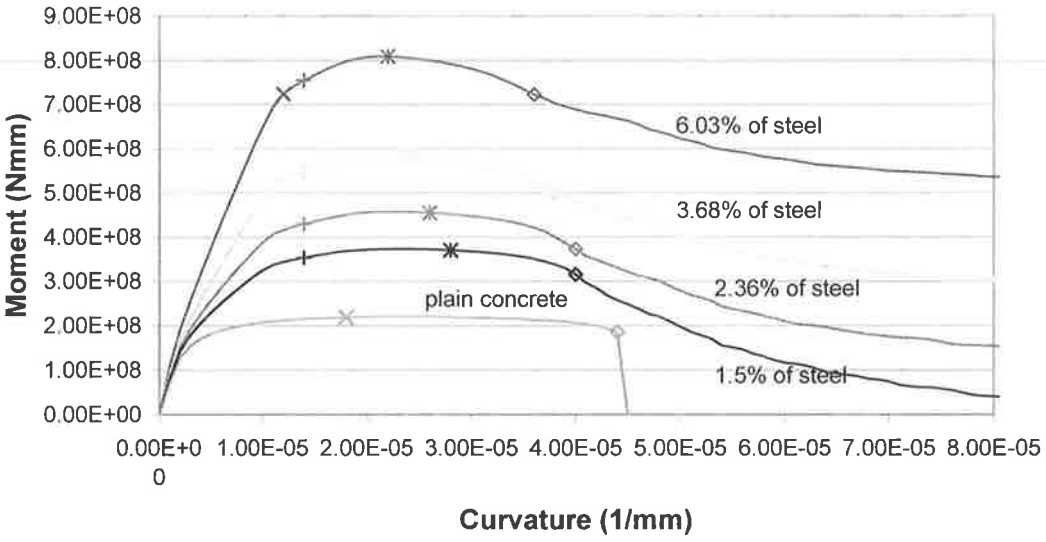

Fig. 7.11 Moment-curvature chart of RC sections with N=20%N_c

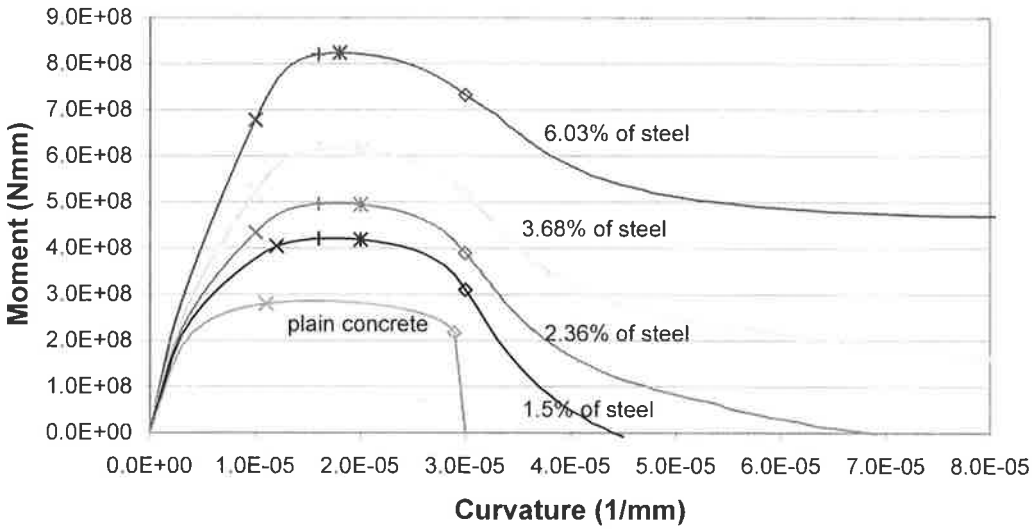

Fig. 7.12 Moment-curvature chart of RC sections with N=30%N_c

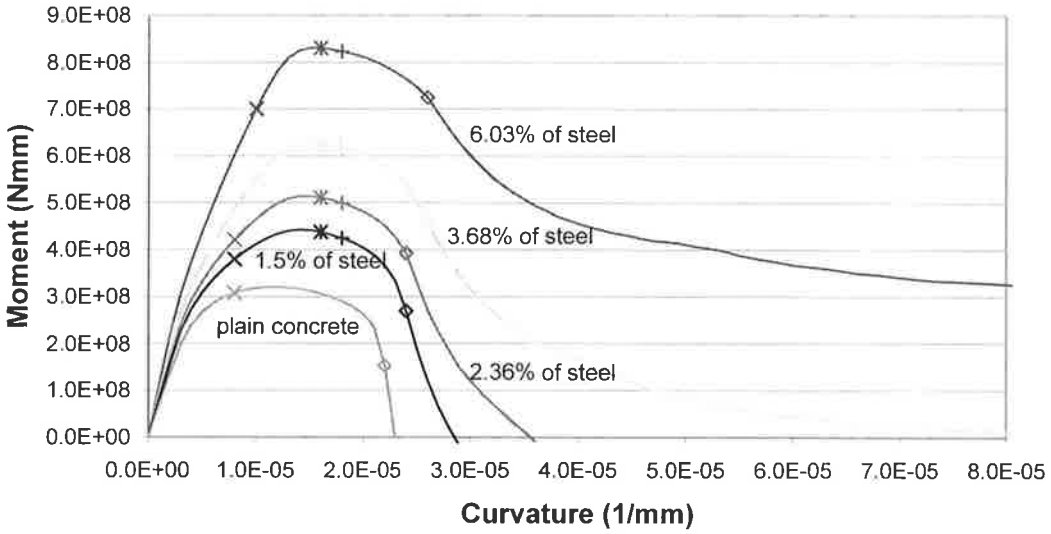

Fig. 7.13 Moment-curvature chart of RC sections with N=40%N_c

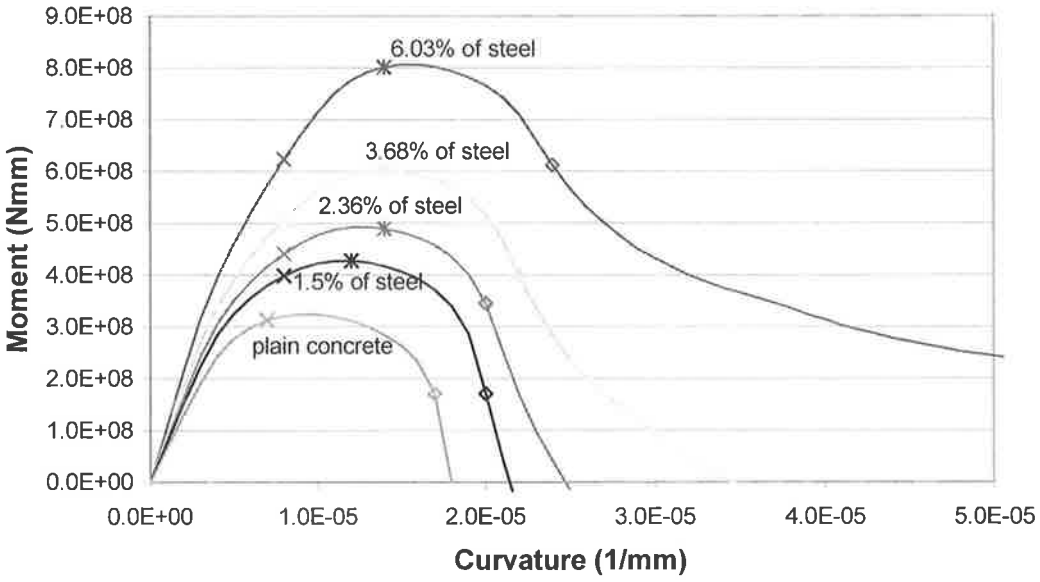

Fig. 7.14 Moment-curvature chart of RC sections with N=50%N_c

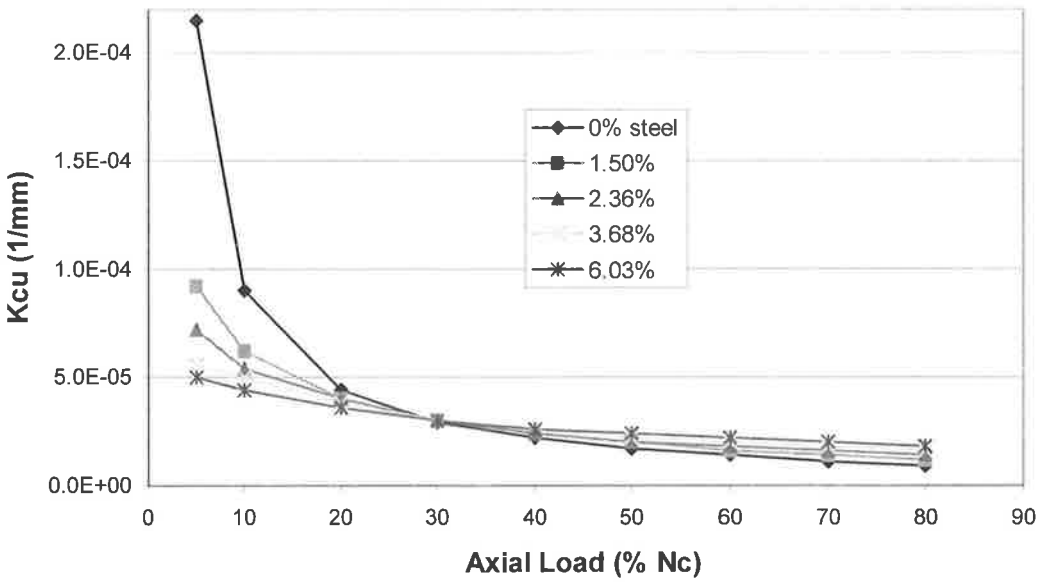

Fig. 7.15 Axial load-κ_{cu} relations

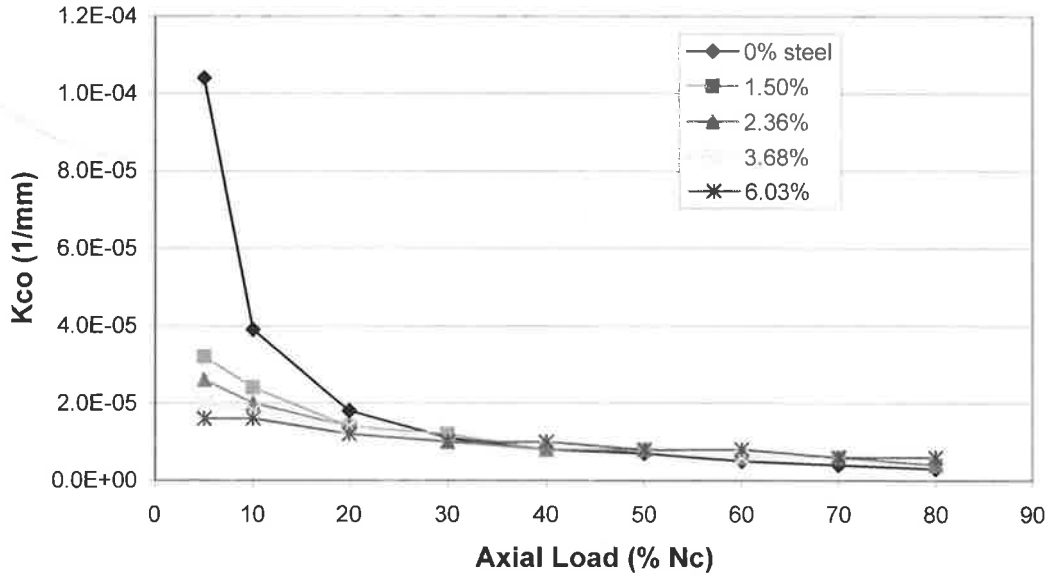

Fig. 7.16 Axial load-κ_{co} relations

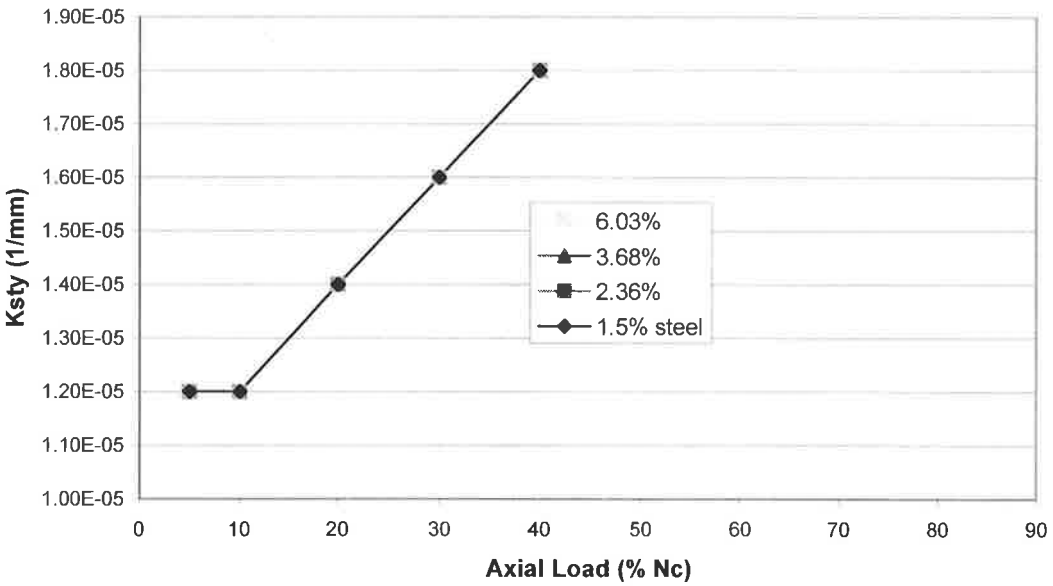

Fig. 7.17 Axial load-κ_{sty} relations

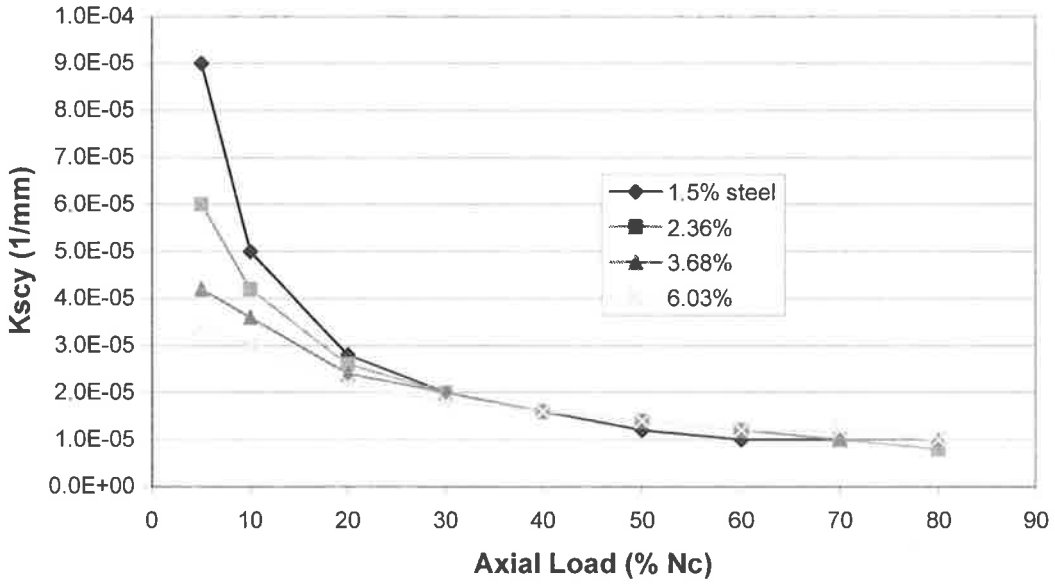

Fig. 7.18 Axial load-κ_{scy} relations

CHAPTER 8 DESIGN OF PLATING SYSTEMS

A design methodology or procedure for the retrofitting system is developed in this chapter. For a column, the ability to sustain a certain level of lateral resistance after yielding until the required maximum lateral drift is important. Therefore, this concept is adopted as a guideline to the retrofit design in this study. The design procedure developed in this section is based on a specified target maximum lateral displacement, or drift, at which the retrofitting system is required to work in its 'strength stiffened' region of the response curve as discussed in Section 5.2.2. In this way, the lateral resistance capacity and the integrity of the column can be assured at the target displacement. To achieve this, the target displacement is designed to occur simultaneously with the onset of the ultimate curvature, as defined in Chapter 7, of the cross-section in the plastic hinge zone of the column. With this condition, the ultimate curvature of the RC column will not be exceeded for drifts less than or equal to the target displacement, this ensures no excessive deterioration of the concrete. This design procedure is fundamentally consistent with, and can be easily adapted for use with, the modern displacement-based seismic design philosophy (Calvi and Kingsley, 1995; Moehle, 1996; Priestley, 1997 and 1998).

To develop the design procedure, several fundamental relations are needed which are firstly derived in Sections 8.1 and 8.2. The design procedures are then presented in Section 8.3, followed by a design example in Section 8.4 to illustrate the procedure.

8.1 GENERIC DEFORMATION - SLIP RELATION

The design procedure in Section 8.3 requires the slip on top of the plastic hinge. To calculate this slip, a general relation between slip and deformation of a column is derived in this section. With reference to Fig.8.1, the strains in the plate and the RC column at the interface can be expressed as

$$\varepsilon_1 = \kappa \cdot h_1 + \varepsilon_{1c} \tag{8.1}$$

$$\varepsilon_2 = \varepsilon_{2c} - \kappa \cdot h_2 \tag{8.2}$$

where ε_{1c} and ε_{2c} are the strains at the cross-sectional centroids of element 1 (RC column) and element 2 (plate), respectively.

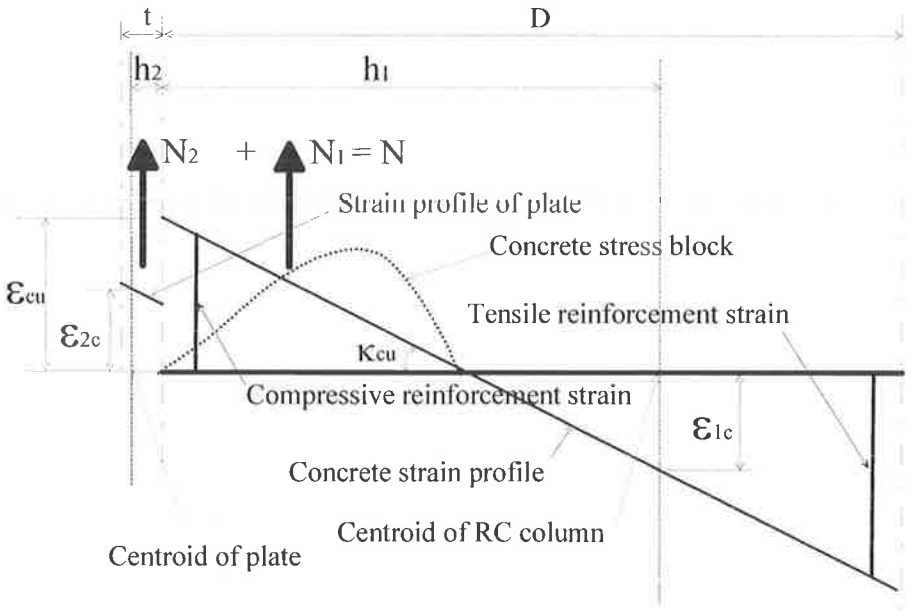

Fig. 8.1 Strains and forces in the cross-section

Substituting Eqs.8.1 and 8.2 into Eq.6.11 and integrating with respect to x gives

$$s = -(h_1 + h_2) \cdot \int \kappa \cdot dx + \int \varepsilon_{2c} \cdot dx - \int \varepsilon_{1c} \cdot dx + C \tag{8.3}$$

$$\because d\theta = -\kappa \cdot dx$$
$$d\Delta_2 = -\varepsilon_{2c} \cdot dx$$
$$d\Delta_1 = -\varepsilon_{1c} \cdot dx$$

where s is the slip; θ is the rotation of the cross-section; and Δ_2 and Δ_1 are the longitudinal displacements at the cross-sectional centroids of element 1 and 2, respectively.

Therefore, Eq.8.3 is re-written as

$$s(x) = (h_1 + h_2) \cdot \theta(x) + \Delta_1(x) - \Delta_2(x) + C$$
$$\because s\big|_{x=L} = 0;\ \ \theta\big|_{x=L} = 0;\ \ \Delta_2\big|_{x=L} = 0;\ \ \Delta_1\big|_{x=L} = 0$$
$$\therefore C = 0$$

which gives

$$s = (h_1 + h_2) \cdot \theta + \Delta_1 - \Delta_2 \qquad (8.4)$$

The above relation shows that the slip at any cross-section is given by the rotation of that cross-section times the distance between centroids of element 1 and 2, plus the difference of axial shortening between element 1 and 2. This relation is general, because it is derived from the geometric relations with the only assumption being that plane sections remain plane for element 1 and 2 separately. Therefore, it is applicable for general non-linear analyses.

8.2 ULTIMATE PLASTIC HINGE ANALYSIS

The formulae related to the plastic hinge calculations that will be used in Section 8.3 are derived in this section. It must be noted that the derivations in this section are only applicable for monotonic loading because the stress of both the concrete and steel cannot be determined by strain only under cyclic loading, as it is also dependent on the loading

history. Therefore, all the analytical results that are related to stresses or forces are only applicable to monotonic loading conditions.

8.2.1 Slip in Plastic Hinge Region

The slip at the top of the plastic hinge can be calculated using Eq.8.4

$$s_p = (h_1 + h_2) \cdot \theta_p + \Delta_{1c} - \Delta_{2c} \tag{8.5}$$

where θ_p is the rotation of the cross-section on top of the plastic hinge, i.e. the total plastic hinge rotation; and Δ_{1c} and Δ_{2c} are the respective axial shortening of the plastic hinge at the centroids of element 1 and element 2. The three terms in Eq.8.5 are discussed separately in the following paragraphs.

As discussed in Sections 4.2.3 and 6.1 (also see Fig.5.5), the plastic deformation concentrates in the plastic hinge zone. Furthermore, the total elastic deformation is relatively small compared to the plastic deformation in the ultimate deformation stage, as illustrated in Fig.6.1(a). Therefore, the total lateral displacement can be approximated by the plastic deformation, or $\Delta \approx \Delta_p$ as shown in Fig.6.1(a). When the ultimate displacement is achieved in the column, the displacement at the top of the column due to the plastic hinge is given by

$$\Delta_p = \theta_p \cdot (L - 0.5 \cdot L_p) = \kappa_{cu} \cdot L_p \cdot (L - 0.5 \cdot L_p) \tag{8.6}$$

where the ultimate curvature κ_{cu} is assumed to be constant within the plastic hinge. The plastic hinge length of the cantilever column L_p can be estimated by Eq.4.56. Eq.8.6 was given by Priestley and Park (1987) assuming that the plastic rotation θ_p is concentrated at the centre of the plastic hinge. In fact, this relation can be derived mathematically

without this assumption by double integration of the curvature along the length, or more easily, by the geometrical relation shown in Fig.8.2.

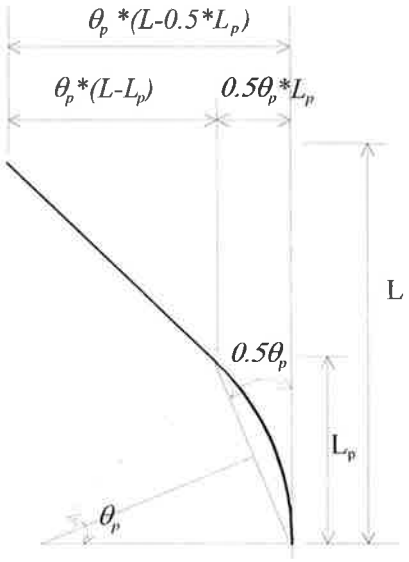

Fig. 8.2 Top displacement due to hinge rotation

From Eq.8.6, the ultimate curvature is given by

$$\kappa_{cu} = \frac{\Delta_p}{(L - 0.5 \cdot L_p) \cdot L_p} \approx \frac{\Delta}{(L - 0.5 \cdot L_p) \cdot L_p} \tag{8.7}$$

Therefore, θ_p in the first term of Eq.8.5 can be calculated by

$$\theta_p = \kappa_{cu} \cdot L_p \approx \frac{\Delta}{(L - 0.5 \cdot L_p)} \tag{8.8}$$

The second and third terms in Eq.8.5 are given by

$$\Delta_{1c} = \varepsilon_{1c} \cdot L_p \tag{8.9}$$

$$\Delta_{2c} = \varepsilon_{2c} \cdot L_p \tag{8.10}$$

where ε_{1c} is given by (see Fig.8.1)

$$\varepsilon_{1c} = \varepsilon_{cu} - \kappa_{cu} \cdot h_1 \tag{8.11}$$

in which ε_{cu} is the ultimate concrete strain on the compression face at which the RC member is considered failed. The strain of concrete when it is completely crushed (spalling strain) is considered as ε_{cu} in this work. This assumption sets the scene in which the ultimate limit state occurs: when the column achieves the required maximum drift, the concrete strain on the compression face reaches the ultimate strain ε_{cu}. The legitimacy of identifying the ultimate displacement by this concept was fully discussed in Chapter 7.

To calculate ε_{2c}, first the axial load N_2 on the plate section is calculated, which is derived in Section 8.2.2. With the axial force N_2 known and the curvature of the plate given by Eq.8.7, ε_{2c} can then be calculated. One of the ways to calculate ε_{2c} is shown in Section 8.2.3.

8.2.2 Cross-Sectional Forces

When the concrete strain at the ultimate stage is ε_{cu} on the compression face with zero strength, the stress block is shown in Fig.8.3. If this stress profile is assumed to be triangular as shown by the shaded area, the axial force on the concrete is given by

$$N_{conc} = \frac{1}{2} \cdot f_{co} \cdot \frac{\varepsilon_{cu}}{\kappa_{cu}} \cdot B \tag{8.12}$$

where B is the width of the column and the remainder of the function of the right hand side $f_{co}\varepsilon_{cu}/2\kappa_{cu}$ is the area of the triangular stress block. When the stress block is not triangular, it can generally be written as

$$N_{conc} = \beta \cdot f_{co} \cdot \frac{\varepsilon_{cu}}{\kappa_{cu}} \cdot B = \beta \cdot \frac{N_c}{\kappa_{cu}} \cdot \frac{\varepsilon_{cu}}{D} \tag{8.13}$$

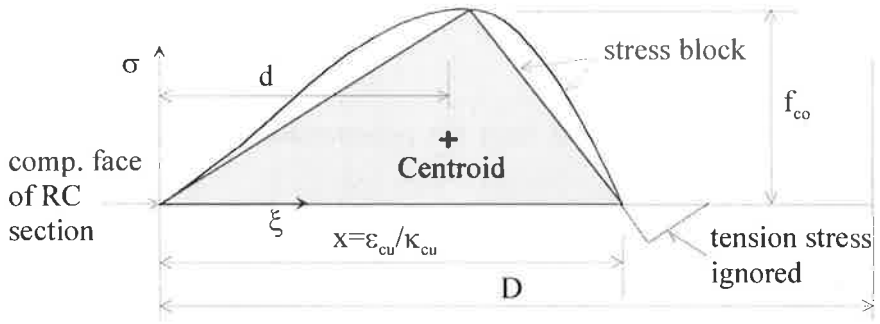

Fig. 8.3 Concrete stress block

The above equation is similar to Eq.8.12 with the constant coefficient ½ replaced by a general coefficient β. For a given stress-strain model, the shape of the stress block is defined from which β can be calculated by

$$\beta = \frac{\int_0^x \sigma \cdot d\xi}{f_{co} \cdot x} \tag{8.14}$$

where $\int_0^x \sigma \cdot d\xi$ is the stress block area in which ξ is the distance of a point in the cross-section from the compression face, σ is the concrete stress at the corresponding point, and x is the depth of compression zone shown in Fig.8.3. If Mander's stress-strain model (see Section 4.1.2.2) for concrete is adopted, the value β is found to be only a function of the concrete strength. Thus, β can then be calculated through numerical integration of the stress block. The results from the numerical integration of Eq.8.14 are given in Fig.8.4 for concrete strength between 20MPa to 50 MPa.

The centroid of the stress block, which is needed to calculate the moment of the cross-section, is also a function of the concrete strength with Mander's model. Its position, as shown in Fig.8.3, can be related to a parameter δ by

$$\delta = \frac{d}{x} \tag{8.15}$$

where d is the position of centroid from the compression face shown in Fig.8.3 that is given by

$$d = \frac{\int_0^x \sigma \cdot \xi \cdot d\xi}{\int_0^x \sigma \cdot d\xi} \tag{8.16}$$

The numerical integration of Eq.8.16 gives the value of δ as shown in Fig.8.5.

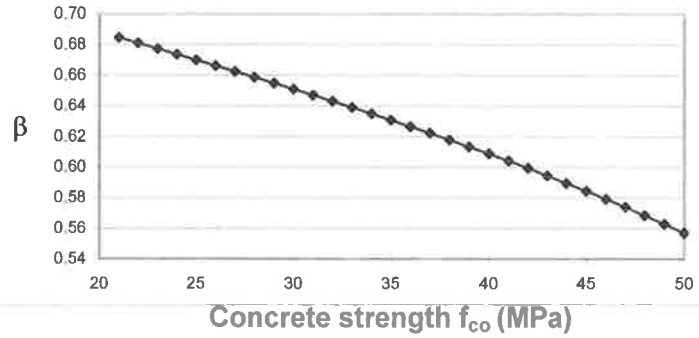

Fig. 8.4 Area coefficient β

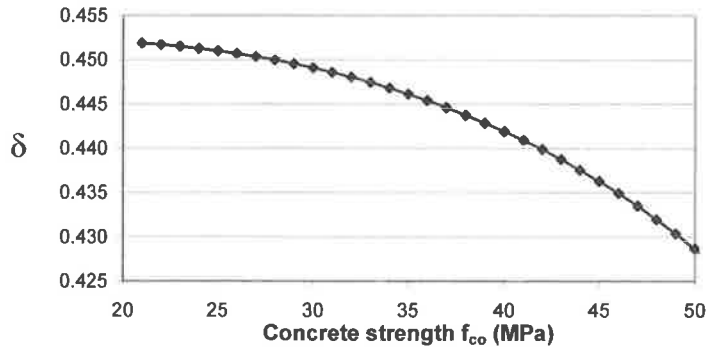

Fig. 8.5 Centroid coefficient δ

For longitudinal reinforcing bars, the strains at the compression and tension sides are respectively

$$\varepsilon_{sc} = \varepsilon_{cu} - \kappa_{cu} \cdot a \tag{8.17}$$

$$\varepsilon_{st} = \varepsilon_{cu} - \kappa_{cu} \cdot (D - a) \tag{8.18}$$

where a is the 'concrete cover' distance from the face of the column to the centre of the reinforcing bars. Forces on the tension and compression reinforcement are respectively

$$N_{st} = \begin{cases} \varepsilon_{st} \cdot E_s \cdot A_{st} & (when \quad |\varepsilon_{st}| \le \varepsilon_{sy}) \\ f_{sy} \cdot A_{st} & (when \quad \varepsilon_{st} \ge \varepsilon_{sy}) \\ -f_{sy} \cdot A_{st} & (when \quad \varepsilon_{st} \le -\varepsilon_{sy}) \end{cases} \tag{8.19}$$

$$N_{sc} = \begin{cases} \varepsilon_{sc} \cdot E_s \cdot A_{sc} & (when \quad |\varepsilon_{sc}| \le \varepsilon_{sy}) \\ f_{sy} \cdot A_{sc} & (when \quad \varepsilon_{sc} \ge \varepsilon_{sy}) \\ -f_{sy} \cdot A_{sc} & (when \quad \varepsilon_{sc} \le -\varepsilon_{sy}) \end{cases} \tag{8.20}$$

where ε_{sy} is the yield strain of the reinforcing bars.

As the total force on the RC cross-section is

$$N_1 = N_{conc} + N_{sc} + N_{st} \tag{8.21}$$

Then the axial force on the plate can be calculated from

$$N_2 = N - N_1 \tag{8.22}$$

8.2.3 Calculation of Plate Strain

With the axial load on the steel plate given by Eq.8.22 and the curvature of the plate at the column base given by Eq.8.7, the strain at the cross-sectional centroid of the plate ε_{2c}, which is required in Eq.8.10, can be easily calculated. For convenience, the explicit form of ε_{2c} is derived in this section, assuming an elastic-plastic stress-strain model for

the plate material. Based on different yielding conditions on the faces, it is derived for the following 3 cases.

(1) Full elastic condition

When a compression axial load ($N_2 \geq 0$) is applied and when the compression face is linear elastic, the tension face must also be linear elastic. Therefore, the strain at the sectional centroid of the plate is simply given by

$$\varepsilon_{2c} = \frac{N_2}{B \cdot t \cdot E_p} \tag{8.23}$$

where E_p is the elastic modulus of the plate.

(2) Compression face yielded and tension face elastic

Figure 8.6 shows the stress and strain profiles of the plate under the elastic-plastic stress-strain relation.

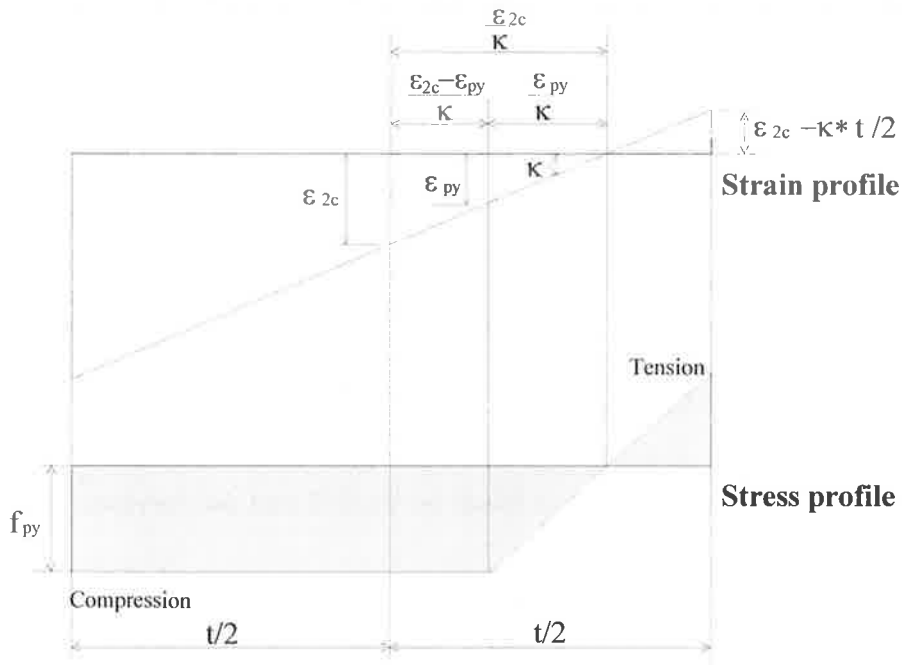

Fig. 8.6 Strain at centroid of plate

The axial force in the plate can be calculated as

$$N_2 = B \cdot \left[(\frac{t}{2} + \frac{\varepsilon_{2c} - \varepsilon_{py}}{\kappa}) \cdot f_{py} + \frac{1}{2} \cdot \frac{\varepsilon_{py}}{\kappa} \cdot f_{py} + \frac{1}{2} \cdot (\varepsilon_{2c} - \frac{t}{2} \cdot \kappa) \cdot E_p \cdot (\frac{t}{2} - \frac{\varepsilon_{2c}}{\kappa}) \right] \quad (8.24)$$

Substituting $f_{py} = \varepsilon_{py} \cdot E_p$ into Eq.8.24 and re-arranging gives

$$\varepsilon_{2c}^2 - (2\varepsilon_{py} + \kappa \cdot t) \cdot \varepsilon_{2c} + \frac{\kappa^2 \cdot t^2}{4} - (\kappa \cdot t - \varepsilon_{py}) \cdot \varepsilon_{py} + \frac{2\kappa \cdot N_2}{B \cdot E_p} = 0 \quad (8.25)$$

Equation 8.25 has two solutions

$$\varepsilon_{2c} = \frac{2\varepsilon_{py} + \kappa \cdot t - \sqrt{(2\varepsilon_{py} + \kappa \cdot t)^2 - 4 \cdot \left[\frac{\kappa^2 \cdot t^2}{4} - (\kappa \cdot t - \varepsilon_{py}) \cdot \varepsilon_{py} + \frac{2\kappa \cdot N_2}{B \cdot E_p} \right]}}{2}$$

$$= \varepsilon_{py} + \frac{1}{2} \cdot \kappa \cdot t - \Delta\varepsilon \quad (8.26)$$

and

$$\varepsilon_{2c} = \frac{2\varepsilon_{py} + \kappa \cdot t + \sqrt{(2\varepsilon_{py} + \kappa \cdot t)^2 - 4 \cdot \left[\frac{\kappa^2 \cdot t^2}{4} - (\kappa \cdot t - \varepsilon_{py}) \cdot \varepsilon_{py} + \frac{2\kappa \cdot N_2}{B \cdot E_p} \right]}}{2}$$

$$= \varepsilon_{py} + \frac{1}{2} \cdot \kappa \cdot t + \Delta\varepsilon \quad (8.27)$$

where $\Delta\varepsilon$ is a positive term given by

$$\Delta\varepsilon = \frac{\sqrt{(2\varepsilon_{py} + \kappa \cdot t)^2 - 4 \cdot \left[\frac{\kappa^2 \cdot t^2}{4} - (\kappa \cdot t - \varepsilon_{py}) \cdot \varepsilon_{py} + \frac{2\kappa \cdot N_2}{B \cdot E_p} \right]}}{2} \quad (8.28)$$

One of the two solutions above is false and can be found through the following calculation. The strain at the tensile face is given by

$$\varepsilon_t = \varepsilon_{2c} - \frac{1}{2} \cdot \kappa \cdot t \quad (8.29)$$

Substituting Eq.8.27 into Eq.8.29 gives

$$\varepsilon_t = \varepsilon_{py} + \Delta\varepsilon \geq \varepsilon_{py} \tag{8.30}$$

Equation 8.30 means that with the solution of Eq.8.27 the whole cross-section yields for any given axial load and curvature. Obviously it is not the correct solution and should be discarded. Therefore, only Eq.8.26 is the correct solution.

The solution given by Eq.8.26 includes two special cases:

(a) The first one is when the tension face just yields in compression or the whole cross-section just yields in compression. The conditions for this to occur can be derived as follows.

When $\Delta\varepsilon = 0$, from Eq.8.30, the strain at the tensile face is $\varepsilon_t = \varepsilon_{py}$ or just yields. Based on Eq.8.28, $\Delta\varepsilon = 0$ necessitates

$$(2\varepsilon_{py} + \kappa \cdot t)^2 - 4 \cdot \left[\frac{\kappa^2 \cdot t^2}{4} - (\kappa \cdot t - \varepsilon_{py}) \cdot \varepsilon_{py} + \frac{2\kappa \cdot N_2}{B \cdot E_p} \right] = 0 \tag{8.31}$$

Therefore, Eq.8.31 gives the condition (relation between κ and N_2) at which the whole cross-section just yields in compression.

When the left-hand side of Eq.8.31 gives a negative solution, i.e.

$$(2\varepsilon_{py} + \kappa \cdot t)^2 - 4 \cdot \left[\frac{\kappa^2 \cdot t^2}{4} - (\kappa \cdot t - \varepsilon_{py}) \cdot \varepsilon_{py} + \frac{2\kappa \cdot N_2}{B \cdot E_p} \right] < 0 \tag{8.32}$$

Equation 8.28 and hence Eq.8.25 has no solution. Physically, this case occurs when the balance of axial forces in the cross-section cannot be achieved even after the whole cross-section yields. In this case, the plate thickness is too small to sustain the axial force and must be increased.

(b) The second special case occurs when the tension face just yields in tension. The condition for this to occur is

$$\varepsilon_{2c} = \frac{1}{2} \cdot \kappa \cdot t - \varepsilon_{py} \tag{8.33}$$

because substituting Eq.8.33 into Eq.8.29 gives $\varepsilon_t = -\varepsilon_{py}$. This means the tension face just yields in tension.

If Eq.8.33 becomes $\varepsilon_{2c} < \frac{1}{2} \cdot \kappa \cdot t - \varepsilon_{py}$, Eq.8.29 gives $\varepsilon_t < -\varepsilon_{py}$. In other words, the tension face has already yielded in tension. In this case, the stress distribution shown by Fig.8.6, which is used to drive Eq.8.26, is incorrect and therefore a third case must be considered as discussed below.

(3) Compression face yielded and tension face yielded in tension

In this case, the stress distribution is changed to that shown in Fig.8.7.

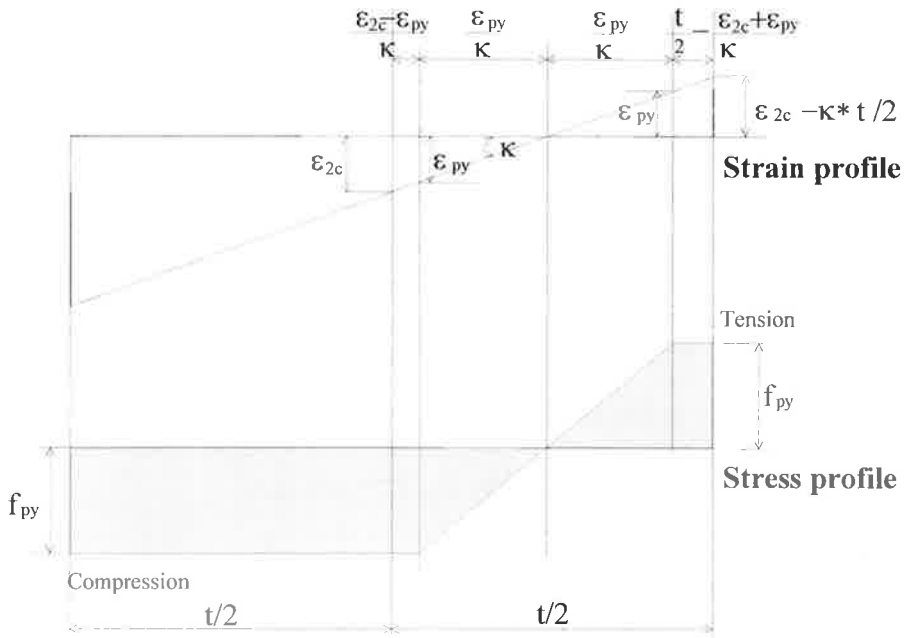

Fig. 8.7 Profiles when tension side yielded in tension

The axial force on the cross-section is given by

$$N_2 = B \cdot \left[\left(\frac{t}{2} + \frac{\varepsilon_{2c} - \varepsilon_{py}}{\kappa} \right) \cdot f_{py} - \left(\frac{t}{2} - \frac{\varepsilon_{2c} + \varepsilon_{py}}{\kappa} \right) \cdot f_{py} \right] \tag{8.34}$$

which gives the solution

$$\varepsilon_{2c} = \frac{N_2 \cdot \kappa}{2B \cdot f_{py}} \tag{8.35}$$

8.3 DISPLACEMENT BASED PLATING DESIGN PROCEDURE

With all the necessary formulae derived in Sections 8.1 and 8.2, the design of the plating system is straightforward. It is outlined by the following 7 steps.

1. Calculate the ultimate curvature at the plastic hinge based on the target maximum displacement Δ, or drift ratio $\theta = \Delta/L$.

   The design displacement or inter-storey drift Δ is given. Assume that the plastic deformation is concentrated in the plastic hinge and the elastic deformation is relatively small compared to the plastic deformation, hence Eq.8.7 is used to calculate the ultimate curvature κ_{cu} in the plastic hinge zone of the column.

2. For the cross-section at the plastic hinge location, calculate the following when the ultimate curvature is reached:

   i) The axial force on the concrete using Eq.8.13 and Fig.8.4;

   ii) The axial forces in the reinforcement using Eqs.8.17-8.20; and

   iii) The axial force in the plate N_2 by Eqs.8.21 and 8.22

3. Estimate steel plate thickness t.

The estimation can be based on the full yield thickness $t_{\min} = N_2/(f_{py} \cdot B)$ taking into account an allowance (e.g. a factor of 1.2) for non-uniform stress distribution in the cross-section of the plate; e.g.

$$t = 1.2 \cdot \frac{N_2}{B \cdot f_{py}} \tag{8.36}$$

This is only a first approximation and can be adjusted following the calculations in step 4.

4. Assuming the first bolt is immediately above the plastic hinge, calculate the slip s_p of this bolt by Eq.8.5. The three terms in Eq.8.5 are calculated using Eq.8.8, Eqs.8.9 and 8.11, and Eq.8.10, respectively, in which the plastic hinge length is calculated by Eq.4.5.6. Formulae derived in Section 8.2.3 are needed to calculate the strain term ε_{2c} in Eq.8.10. The calculation of ε_{2c} will indicate whether the plate thickness assumed in step 3 is adequate or not. Adjust t if it is not adequate, and repeat this step, otherwise go to step 5.
5. Calculate the force on the first bolt.

   Based on the slip s_p calculated in step 4 and the load-slip relation as shown by the typical curve of Fig.4.13, the force at the first bolt can be calculated.

   When s_p is less than the elastic limit (from point A to B in Fig.4.13(b)), a simple linear relation between slip and shear load on the bolt can be assumed, i.e. $F_b = s_p \cdot K_b$. The bolt is usually working in the elastic range, because the limit in the ultimate compressive concrete strain ε_{cu} does not allow large slips to occur. If the bolt is working outside its elastic range of deformation, another type of bolt should be

used since yielding of (all) bolts will result in a plated column working outside its "strength stiffening" range of response curve resulting in excessive degradation.

6. Estimate the required number of bolts.

   As a first approximation, assume the slip is uniformly distributed along its length. This assumption is usually a good approximation at the ultimate limit stage, as was seen from Figs.5.17, 5.18 and 6.6. Therefore, the shear forces can be assumed to be the same in all the bolts. Based on Eq.6.1, the number of bolts required is then given by

$$n = \frac{N_2}{F_b} \tag{8.37}$$

   This estimation can be sufficient for design purpose. If higher precision is required or the distribution of slip cannot be reasonably considered uniform at the ultimate limit stage, the result from this step can be further modified by step 7.

7. Adjust bolts number.

   First, calculate the bolt spacing based on the previously estimated number of bolts. Second, calculate the moment of the bottom cross-section based on the forces calculated in step 2, which determines the lateral force applied on top of the column. Eq.8.15 and Fig.8.5 are needed to calculate the moment due to the concrete. The slip distribution is then calculated from linear elastic theory using Eqs.6.39-6.42 based on the lateral force, axial load, bolt spacing and slip s_p calculated previously. The slip at each bolt position can then be calculated to get the shear force on each bolt. The summation of all the bolt forces gives the axial force in the steel plate at the plastic hinge. If this plate force is close enough to the value of N_2 that was calculated in step

2, the bolt design is adequate. Otherwise, adjust the number of bolts and spacing and repeat step 7 until the required precision is achieved.

8.4 EXAMPLE

The column in Fig.5.1 is to be designed for an axial load of 360 kN and a maximum drift ratio of $\theta = \Delta/L = 2.5\%$ or Δ=30mm. The geometric and material properties are the same as those given in Section 5.1.

From Eq.4.56(a), $L_p = 0.08L + 6d_b = 192$ (mm), say 200mm.

Eq.8.7 gives $\kappa_{cu} \approx \dfrac{\Delta}{(L - 0.5 \cdot L_p) \cdot L_p} = 1.36\text{x}10^{-4}$ (mm^{-1}).

From Fig.8.4, β=0.61, and by Eq.8.13

$$N_{conc} = \beta \cdot f_{co} \cdot \frac{\varepsilon_{cu}}{\kappa_{cu}} \cdot B = 215 \text{ (kN)}.$$

By Eqs.8.17 and 8.18, $\varepsilon_{sc} = \varepsilon_{cu} - \kappa_{cu} \cdot a = 0.00115 < \varepsilon_{sy}$,

$\varepsilon_{st} = \varepsilon_{cu} - \kappa_{cu} \cdot (D - a) = -0.016 < -\varepsilon_{sy}$, yielded in tension,

$\therefore N_{sc} = A_{sc} \cdot E_s \cdot \varepsilon_{sc}$ =92.5 (kN), $N_{st} = A_{st} \cdot f_{sy}$ = -219.9 (kN).

From Eqs.8.21 and 8.22, $N_2 = N - N_{conc} - N_{sc} - N_{st} = 272$ (kN).

The minimum steel plate thickness is $N_2/(B \cdot f_{py})$ = 5.4 (mm), so a plate thickness of 6 mm is chosen.

The first bolt is placed 200 mm (L_p=200mm) above the bottom of the column. To calculate the slip of the first bolt, the following are calculated:

By Eq.8.8, $\theta_p = \kappa_{cu} \cdot L_p$=0.0272;

From Eqs.8.9 and 8.11, $\Delta_{1c} = (\varepsilon_{cu} - \kappa_{cu} \cdot h_1) \cdot L_p$ = -1.52 (mm);

Using Eq.8.26 to calculate ε_{2c},

$$\varepsilon_{2c} = \frac{2\varepsilon_{py} + \kappa_{cu} \cdot t - \sqrt{(2\varepsilon_{py} + \kappa_{cu} \cdot t)^2 - 4 \cdot \left[\frac{\kappa_{cu}^2 \cdot t^2}{4} - (\kappa_{cu} \cdot t - \varepsilon_{py}) \cdot \varepsilon_{py} + \frac{2\kappa_{cu} \cdot N_2}{B \cdot E_p} \right]}}{2}$$

= 0.00124, checking with Eq.8.31 and Eq.8.33 indicates that the tension side of the plate is neither yielded in tension nor yielded in compression. This confirms that the condition to use Eq.8.26 is satisfied. It also suggests that the selected plate thickness is adequate.

By Eq.8.10, $\Delta_{2c} = \varepsilon_{2c} \cdot L_p$ = 0.25 (mm);

From Eq.8.5, $s_p = (h_1 + h_2) \cdot \theta_p + \Delta_{1c} - \Delta_{2c}$ = 1.03 (mm).

Assuming the same slip in the remaining bolts, the force at each bolt is

$F_b = s_p \cdot K_b$ = 23.7 (kN), and therefore the number of bolts required from Eq.8.37 is

$n = \frac{N_2}{F_b}$ = 12, or 6 rows of two.

The above design results can be compared to the column in Fig.5.1 analysed by the non-linear numerical computer program. The numerical results in Fig.5.2 gives the lateral displacement Δ = 33.9 mm when the strain at the extreme compressive fibre of the concrete is equal to the ultimate strain of 0.006. This displacement of 33.9mm includes the elastic deformation above the plastic hinge which is calculated to be 4.4 mm. Therefore the lateral displacement due to the plastic hinge rotation only is 29.5 mm which is very close to the specified design displacement of 30 mm. The slip at the first

bolt is calculated to be 1.034 mm in the above design that is also very close to the result of 1.042mm given by the non-linear computer program, which is shown in Fig.5.17.

In summary, a methodology for the design of the plating system is developed in this Chapter. With this design procedure, engineers can calculate the required thickness of the steel plate as well as number of bolts in order to achieve a given target displacement drift ratio.

CHAPTER 9 EXPERIMENTAL WORKS

Laboratory tests were conducted in this work for the following purposes:

1) To verify the effectiveness of the new retrofitting system in improving the ductility and strength of RC columns.
2) To evaluate the accuracy of the numerical simulations by the computer program "PLTCOL".
3) To demonstrate the practicality of the new retrofitting system.

Six half-scale columns of size 200mm(B)×200mm(D)×1218mm(L) were designed, manufactured and tested to serve the above purposes.

9.1 TEST PLAN

Many different methods are described in the literature for cantilever column tests. The method used depends on the purpose of the tests and laboratory capabilities. Two of the most commonly used test methods may be categorized as (1) the single cantilever test and (2) the double cantilever test. The single cantilever column test is schematically shown by the test setup of Fig.9.1 (Chai et al 1991; Priestley and Seible 1995; Xiao and Ma 1997; Bayrak and Sheikh 1998). In this scheme, one cantilever column, which is cast together with a footing that is then anchored to a strong floor, is tested under a variable lateral force and a constant axial load on top of the column. The double column test is illustrated in Fig.9.2 (Park et al 1982; Priestley and Park 1987; Rodriguez and Park 1994; Watson

and Park 1994), where two cantilever columns on both sides of a beam stub are tested simultaneously.

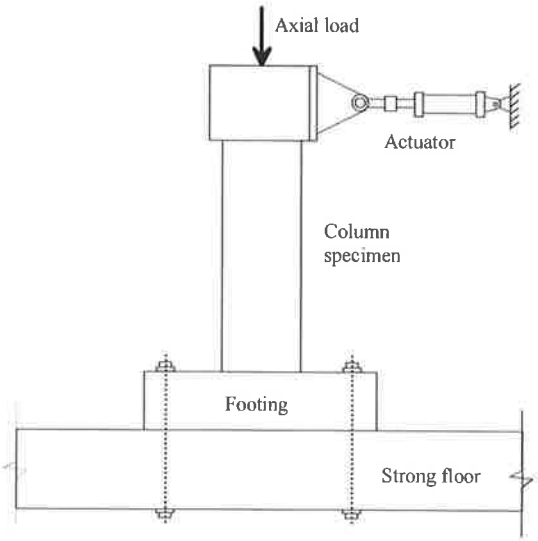

Fig. 9.1 Single column test

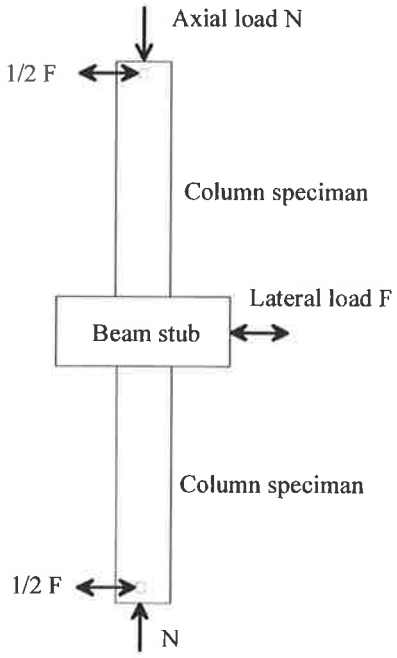

Fig. 9.2 Double columns test

Both of the above schemes were studied and designed in detail for consideration in this work. After comparing the two schemes, the double-column test method was

adopted for this project due to the laboratory conditions, convenience of testing and cost. However, details of the test setup and the method of testing used here are quite different from others. One major difference is that the specimens were tested horizontally instead of vertically, as shown in the schematic sketch of Fig.9.3. Lateral restraints, as shown in Fig.9.3(b), were also provided to prevent the undesirable out-of-plan movement of the specimen.

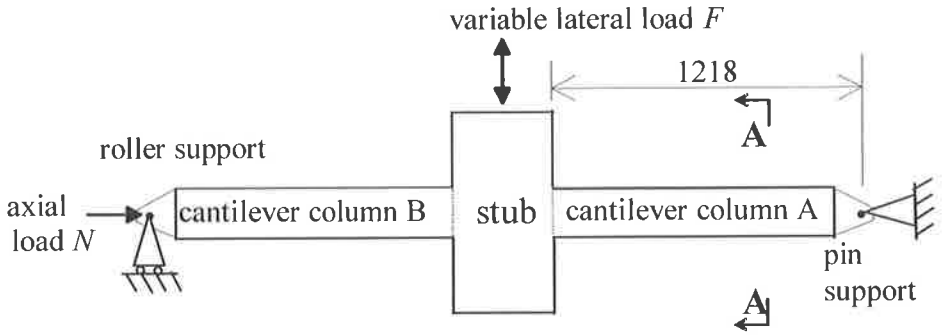

(a) Elevation

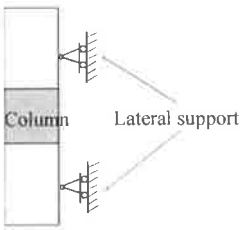

(b) Section A-A

Fig. 9.3 Schematic testing system

Another special feature of this testing system is that each specimen was used for two tests. In the first test, one half of the specimen was strengthened by steel members so that the deformations (and member failure) occurred only on one side of the specimen, as shown in Fig.9.4. On completion of testing on one end of the double-column specimen, the strengthening was moved to the tested side and the undamaged side (that was

protected by strengthening in the first test) was tested in the second test. In this way, the cost of the tests was significantly reduced. To further minimize the stress on the strengthened side, the vertical load was applied 100mm away from the center of the specimen as shown in Figure 9.4a.

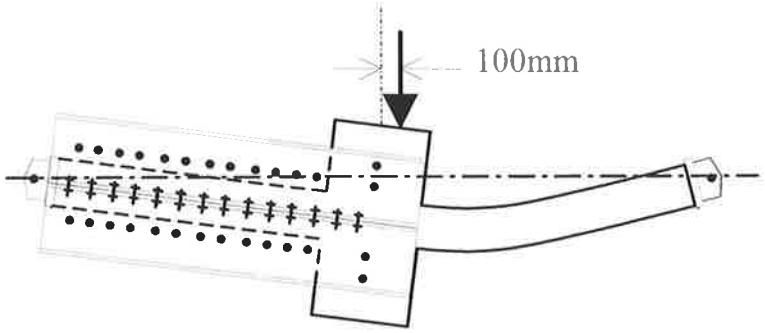

(a) Strengthening scheme

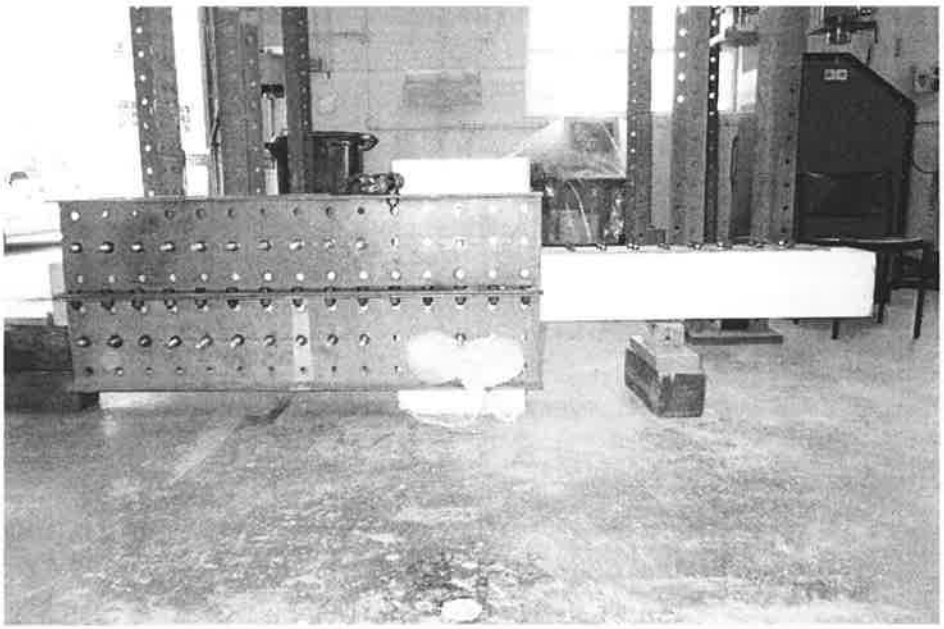

(b) A strengthened specimen

Fig. 9.4 Strengthening of specimen

The main test variables were chosen to be load type, stiffness of plating system and gap (as discussed in Section 9.2.3). Two load types were used in these tests: monotonic static loading and quasi-static cyclic loading with full load-displacement reversal. The stiffness of the plating system depends on the stiffness of steel plate as well as the bolt stiffness. The plate stiffness was varied by using different plate thicknesses as well as different grades of steel. The same type of bolt was used for all the tests. However, the overall shear connection stiffness was varied by employing full interaction plating, which consists of plates both glued and bolted to the column, and partial interaction plating which used only bolts to fix the plate to the column. One specimen was tested with a bottom gap under the base plate to study the gap effect, as discussed in Section 5.2.3.

Six tests were planned to achieve the stated aims for the tests. In the following sections of this thesis, each test is referenced using a code reflecting the characteristics of the test as indicated below.

1. 1AMR – Monotonic loaded test of the benchmark RC column without plating.
2. 2AMF12 – Monotonic loaded test of the full interaction plated column with 12mm thick mild steel plate.
3. 1BMP6 – Monotonic loaded test of the partial interaction plated column with 6mm thick mild steel plate.
4. 3ACR – Cyclic loaded test of the benchmark column without plating.
5. 4ACP6 – Cyclic loaded test of the partial interaction plated column with 6mm thick mild steel plates.

6. 2BCP6G – Cyclic loaded test of the partial interaction plated column with 6mm thick high tensile strength steel plates and gaps.

The first character of the code name identifies the specimen number, i.e. specimen 1, 2, 3 and 4, respectively. The second letter specifies the first (by letter 'A') or second (by letter 'B') test on a specific specimen, e.g. 2A is the first test on specimen 2 and 2B is the second test on specimen 2 but on the previously strengthened side of the first test. The third letter shows the loading type with 'M' for monotonic loading and 'C' for cyclic loading. The fourth letter gives the type of plating; the letter 'P' is used for partial interaction plating and 'F' for full interaction plating. The number following 'P' or 'F' specifies the thickness of the plate. The last letter 'G' is used when gaps are set on the specimen.

9.2 DESIGN AND CONSTRUCTION OF TEST SPECIMENS

9.2.1 RC Specimens

The design details of the RC specimens are shown in Fig.9.5. Four numbers of ϕ14mm PVC sleeves were cast into the side of the beam stub that was used to anchor the steel plates. The other four ϕ21mm PVC sleeves provided holes for the installation of the strengthening steel frame which can be seen from Fig.9.4. The reinforcement details of each bar are given below.

a) Y16 straight bars – 2.6m long main longitudinal reinforcement of the test column.

b) Y20 U shaped bars - the main reinforcement of the beam stub with dimensions shown in Fig.9.5(c).

c) ϕ6 stirrups - the transverse reinforcement of the RC column with dimensions shown in Fig.9.5(d).

d) ϕ10 stirrups - the transverse reinforcement of the beam stub with dimensions shown in Fig.9.5(e).

e) Top steel plates – the capping plate of the cantilever column welded to the ends of the Y16 bars. Dimension: 12mm (thick) × 200mm (Breadth) × 200 mm (Depth) as shown in Fig.9.5a.

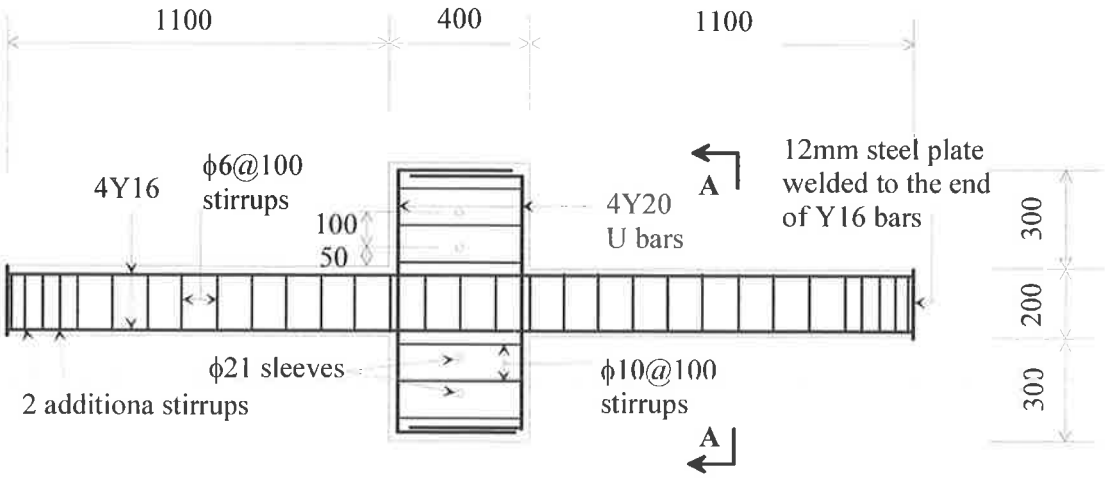

(a) Elevation

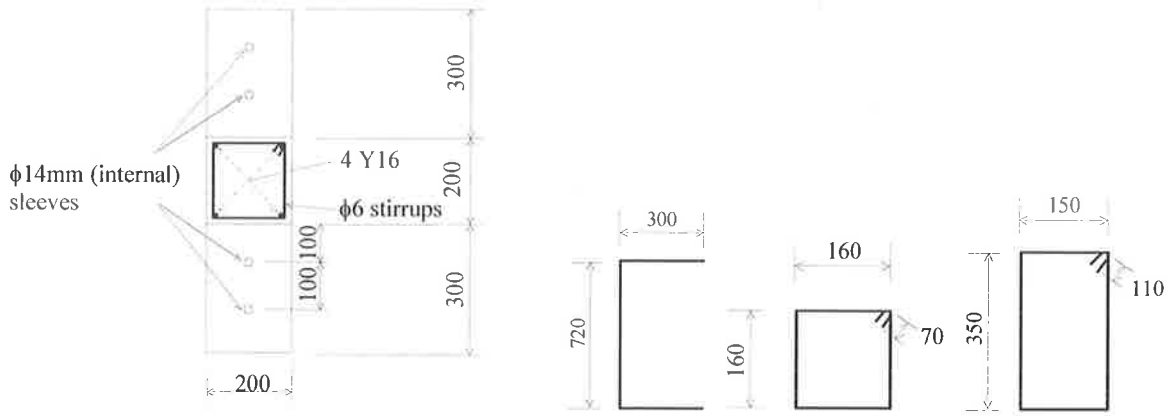

(b) Section A-A (c) (d) (e)

Fig. 9.5 Details of RC specimen

The design concrete cover from column surface to the outermost side of the stirrups was 20mm. The design effective cover from column surface to the center of the Y16 bars was therefore $a=20+6+16/2=34$mm. The measured average value of a from the completed reinforcement cages was about 35.7mm. This mean value will be used in the numerical simulations in Chapter 12. Figures 9.6 and 9.7 show the completed reinforcement cage and the formwork ready for casting.

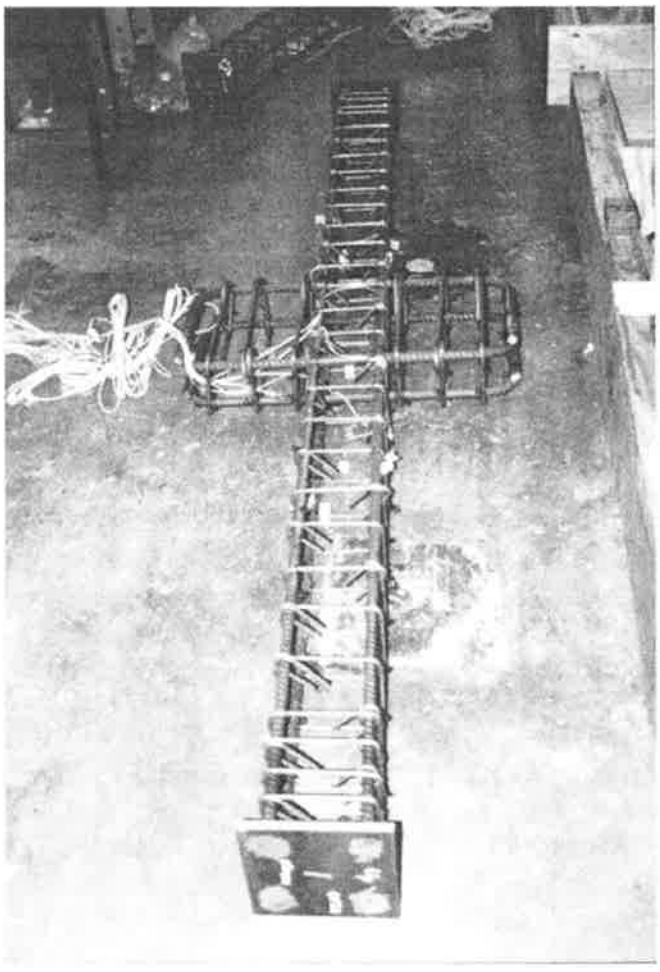

Fig. 9.6 Reinforcement cage

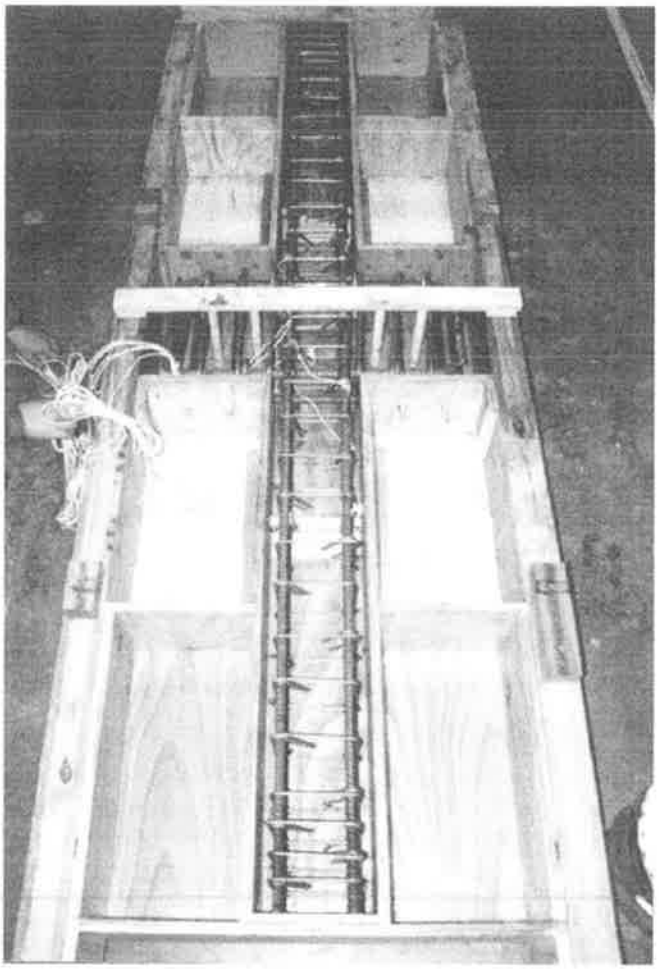

Fig. 9.7 Specimen ready for casting

9.2.2 Steel Plating

Based on the testing plan, four kinds of plating were manufactured.

(a) For the 12mm thick full-interaction plating on one side – the 12mm thick mild steel plate was glued as well as bolted to the compression face of the column. Details of this plating system are shown in Fig.9.8. All bolts were ϕ12mm threaded rod bolts with an embedment length of 70mm, which is described in further detail in Section 10.4. The holes in the steel plate for bolting were 12.2mm.

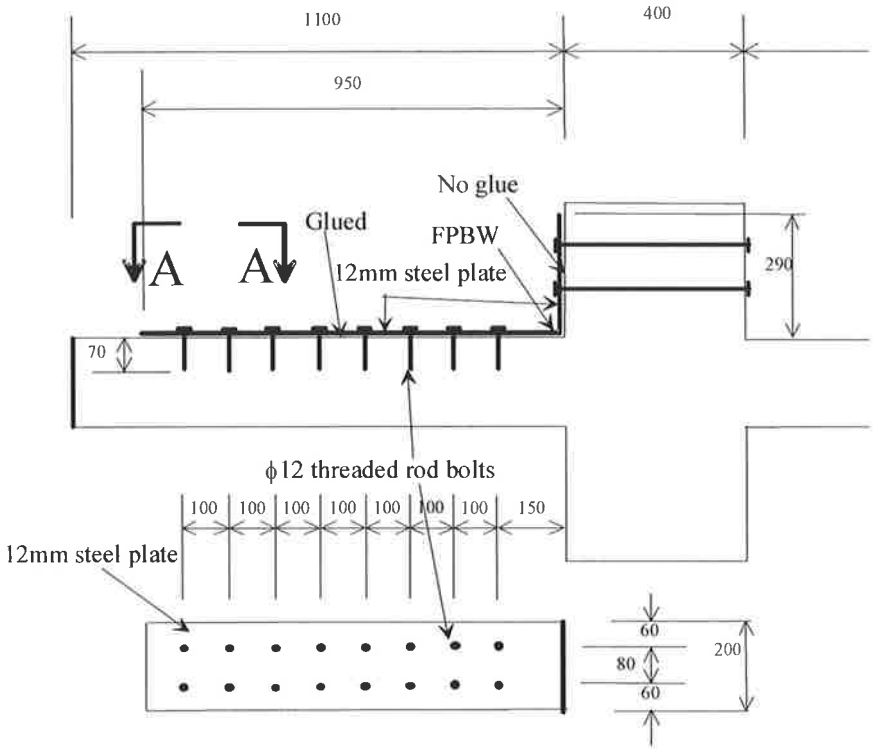

Note: FPBW – Full Penetration Butt Weld

Fig. 9.8 Plating details

(b) For the 6mm thick partial-interaction plating on one side – the 6mm mild steel plate was bolted to the compression face of the column. Bolting details are the same as that shown in Fig.9.8 except that no gluing was used.

(c) For the 6mm thick partial-interaction plating on two sides – the bolting details are the same as for case (b) above, except that both compression and tension faces were plated.

(d) For the 6mm thick high-strength plating – the bolting details are the same as for case (c) except that high yield strength steel plate (see Section 10.3) was used and gaps were set at the bottom of the plate (see Section 9.2.3).

When plating the concrete columns, the following procedures were used for partial-interaction plating. While this plating procedure was more complicated than what might be done on a real construction site due to the very small clearance between the bolt and the hole in the plate, the minimal gap between the bolt and the hole in the plate was designed to more accurately quantify the 'gap effect'.

1. Making of anchor bolts - the bolts were cut from ϕ12mm high tensile strength threaded steel rod with each bolt having a length of 110mm.
2. Making of steel plates – Longitudinal and base plates were cut separately into the dimensions shown in Fig.9.8. Holes were driven at all bolting positions by a ϕ12.2mm drill. Then the two perpendicular pieces of longitudinal and base plate steel were full penetration butt welded (FPBW) at the corner.
3. The plate was then fitted to the RC specimen and clamped in position, as shown in Fig.9.9. The RC specimen was then drilled to a depth of 80mm through holes in the plate using a ϕ12mm drill.
4. Remove clamps and plate. Re-drill the holes in the RC specimen with a ϕ14mm drill to enlarge the holes in the concrete, as shown in Fig.9.10. This was necessary to leave enough clearance between the bolts and concrete for the glue.
5. Clear concrete dust in the holes of the RC specimens with compressed air and inject Hilti HIT-HY 150 adhesive into the holes, as shown in Fig.9.11.
6. Re-fit the plate to the specimen with 20mm thick packers to leave a space for excess adhesive to be squeezed out from the holes, as shown in Fig.9.12.
7. Push bolts into RC specimens ensuring a 70mm deep embedment, as shown in Fig.9.13. Allow adhesive to fully cure.

8. Remove nuts, plate and packers. Remove hardened excess adhesive squeezed out from holes with a sharp chisel. This finished the bolt installation as shown in Fig.9.14.
9. Refit the plate and fix it with washers and nuts. All nuts were tightened with a 25Nm torque using a torque wrench. The finished specimen is shown in Fig.9.15.

For the full-interaction plating of case (a), i.e. gluing plus bolting 12mm thick plate, the procedures are similar to that of partial interaction plating with the addition of gluing. Before installation of the steel plate, the interface of the concrete was roughened with a needle gun. The interface of the steel plate was roughened by sand blasting. After applying glue, the plate was installed and clamped to the RC column until the glue had fully cured, as shown in Fig.9.16. The brand of glue used was Ciba Performance Polymers Araldite LC 340 with Hardener LC340.

Fig. 9.9 Drilling of holes in RC specimen through holes in steel plate

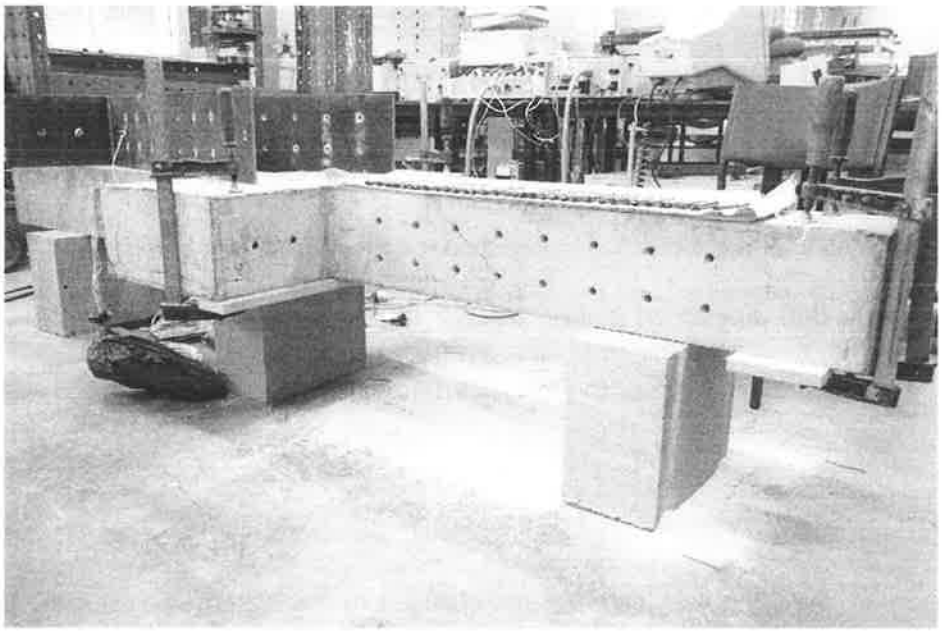

Fig. 9.10 Enlarged holes in concrete

Fig. 9.11 Injection of adhesive

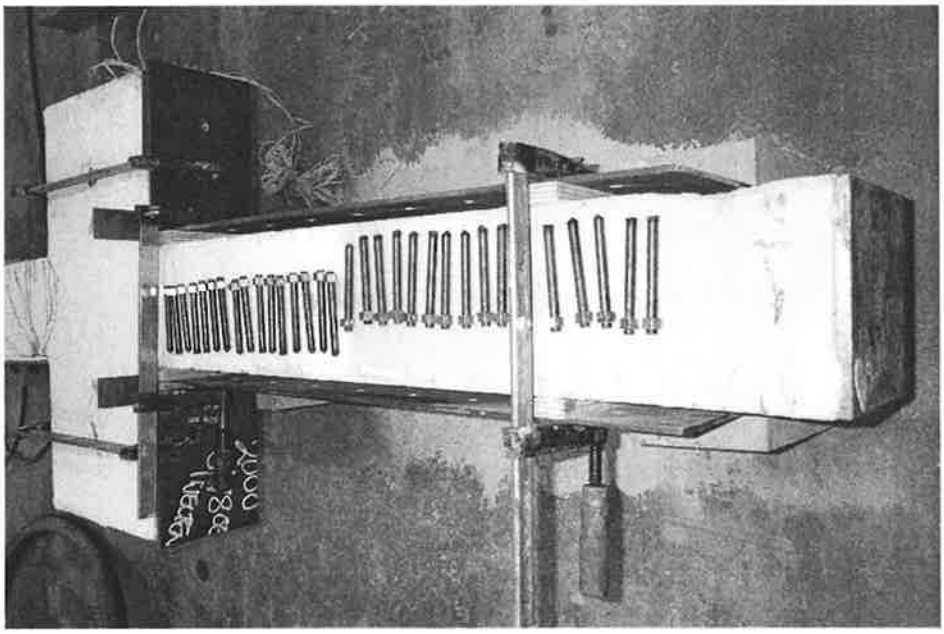

Fig. 9.12 Re-fit of plate with packers

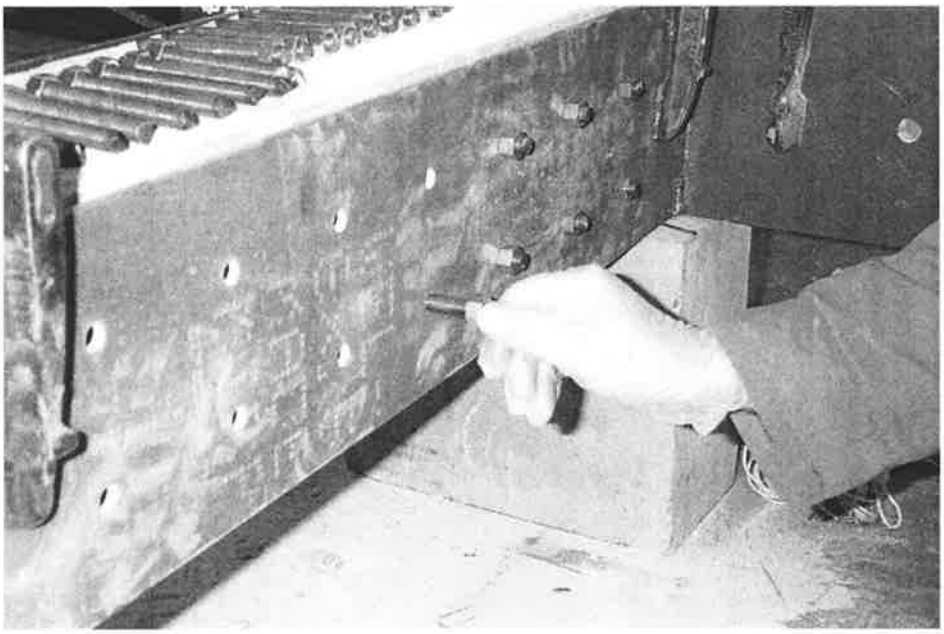

Fig. 9.13 Installation of bolts

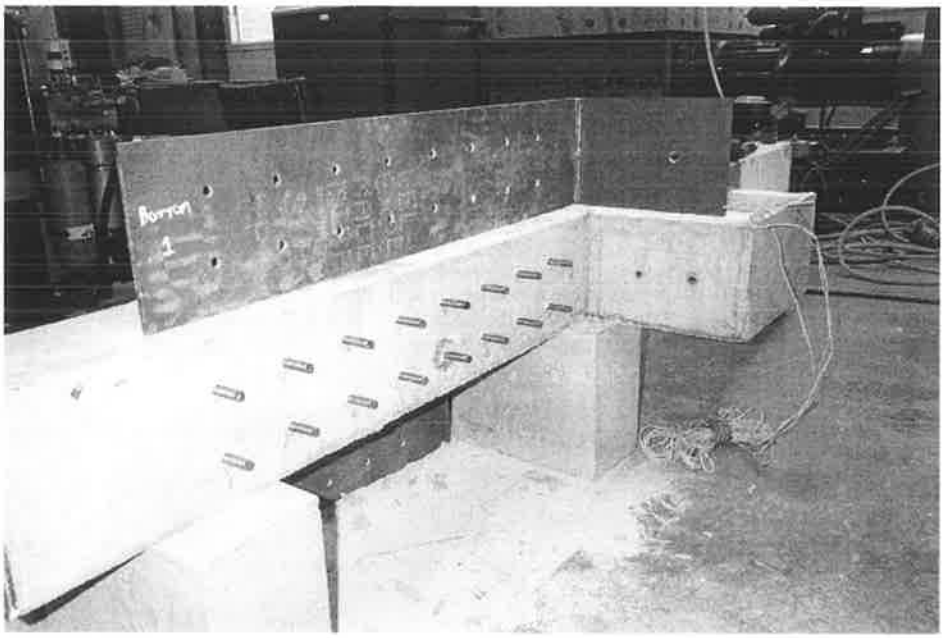

Fig. 9.14 Completion of bolts installation

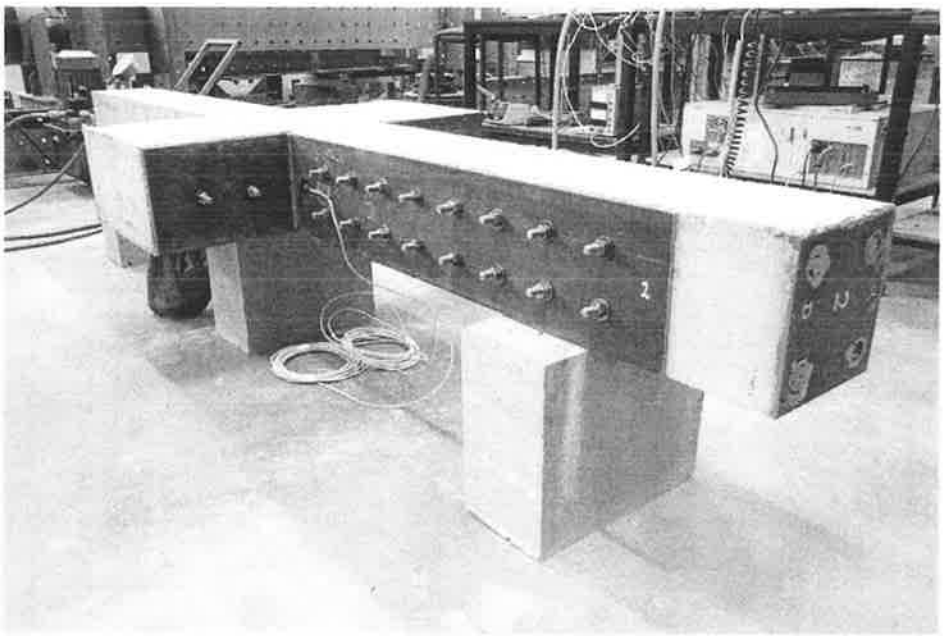

Fig. 9.15 The plated specimen

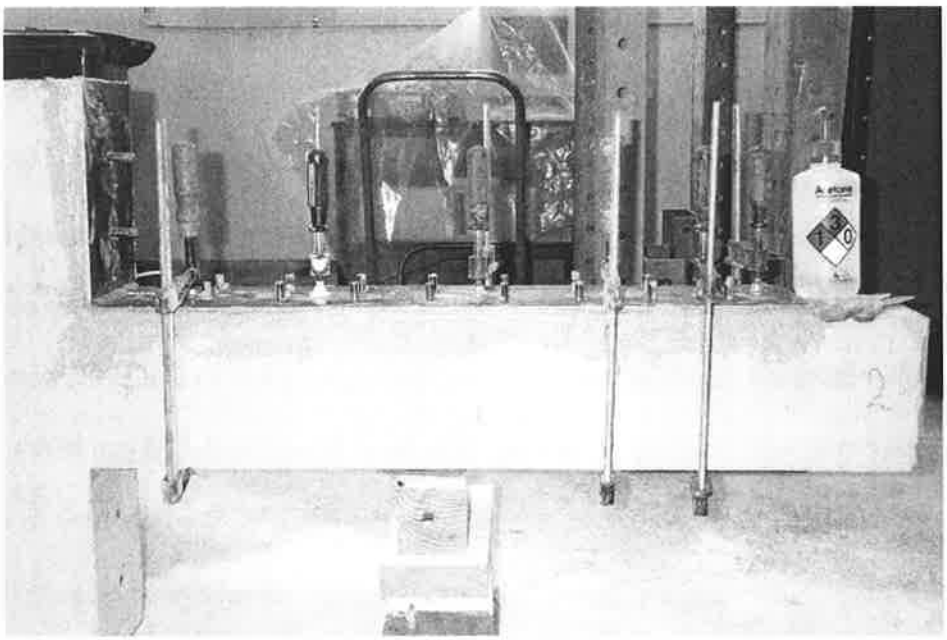

Fig. 9.16 Gluing of plate

9.2.3 Gaps

For case (d) (bolted plates with gaps), the construction procedures were the same as for partial-interaction plating. The bottom gap was set by installing a steel sheet between the face of the stub and the base steel plate, as shown in Fig.9.17. The thickness of the steel sheet was 1.2mm.

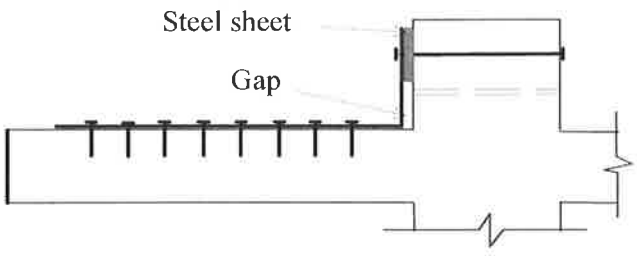

Fig. 9.17 Gap setting

However, it was difficult to achieve a uniformly wide gap. The reason is that the concrete face of the stub was not flat and smooth. In practice, it may even not be exactly parallel to the face of the bottom steel plate. Therefore, the actual gap width is difficult to quantify by the construction method used in these tests. Attention must be paid in future tests to this issue. One potentially better way to control the gap width more accurately, for example, involves installing the steel plate with dental paste between the bottom steel plate and the stub, and then lifting the steel plate up to leave the design gap width.

Furthermore, there are other gaps around the bolts, as the hole size in the steel plate is 0.2mm larger than the diameter of the bolts. However, this average 0.1mm gap around the bolts has a much smaller effect than the much larger gap at the bottom.

The uncertainty in the gap width caused a problem when comparing the test results to the numerical simulations results. However, it should not affect the qualitative observations.

9.3 DESIGN OF TEST RIG

A schematic of the test set up is shown in Fig.9.18. The supporting steel frame is shown behind the specimen. There is another identical steel frame in front of the specimen but is not shown for clarity. A steel member spanning transversely between these two frames supports the vertical load jack as shown. The completed test set up is shown in Fig.9.19. There is another horizontal steel member, which is not shown in Fig.9.18, in both the front and rear steel frames at the same level as the test specimen. These two steel members provided lateral restraint against out-of-plan movement of the test specimens, which can be seen in Fig 9.19 and in more detail in Fig.9.20.

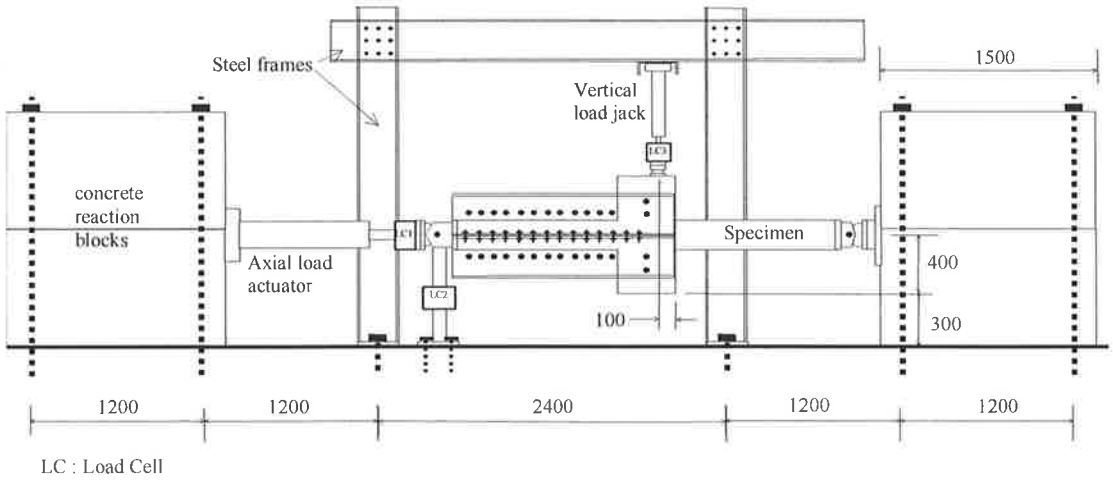

Fig. 9.18 Test set up

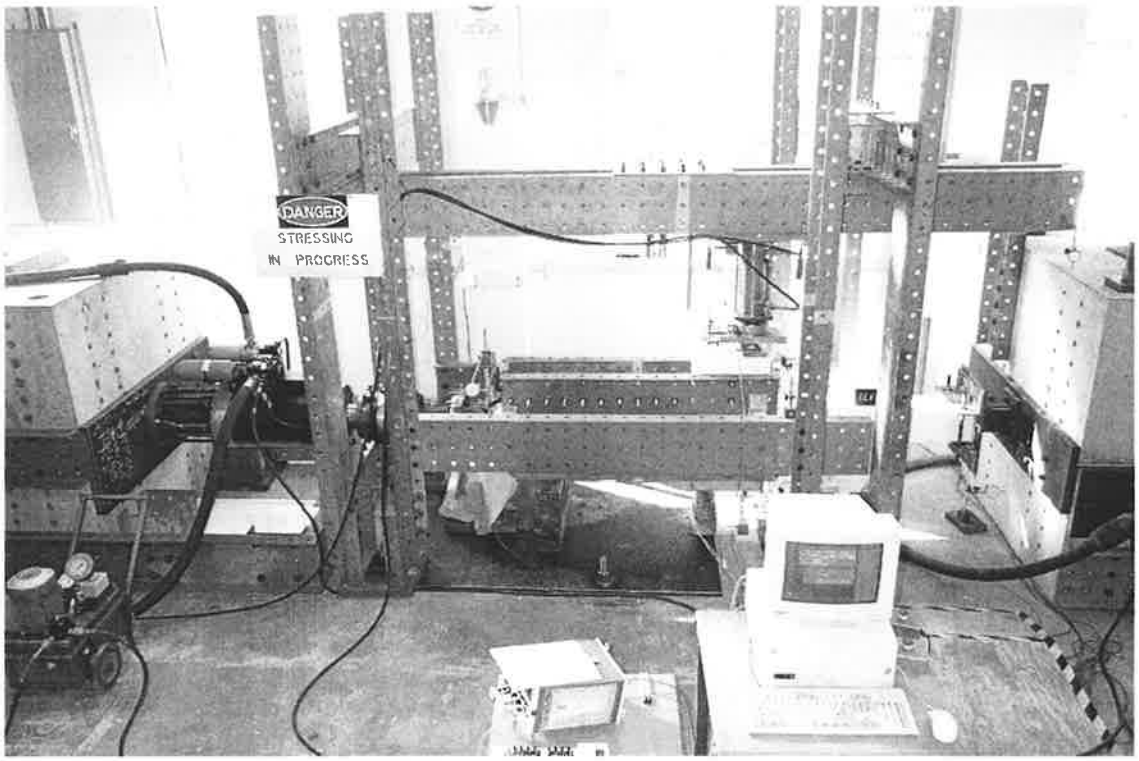

Fig. 9.19 Completed test rig

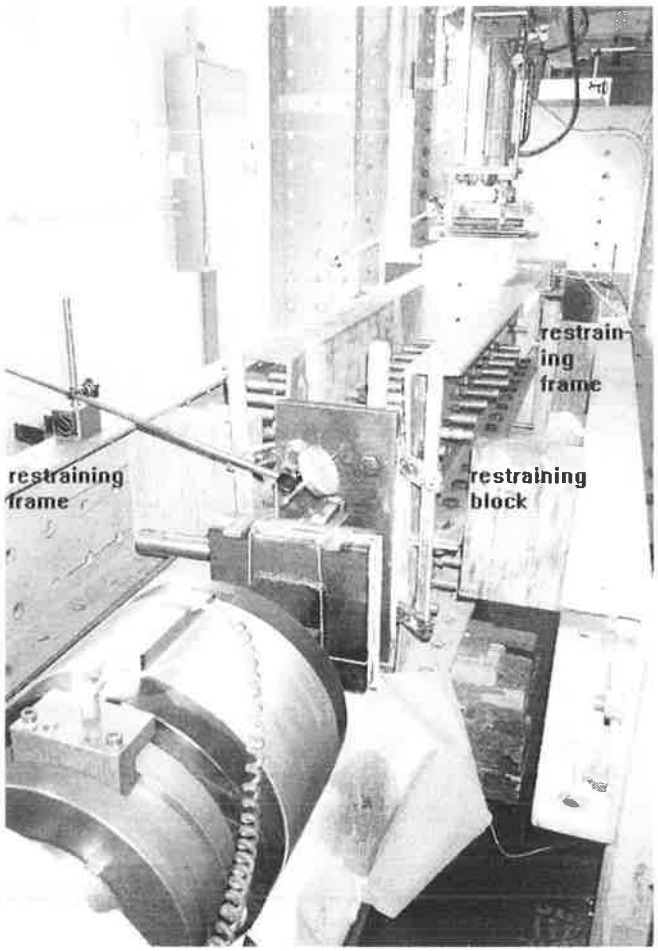

Fig. 9.20 Details of lateral movement restraining system

The hinge support on the right hand side of the specimen that kept the test specimen in position is shown in Fig.9.21 The hinge has two angle brackets that were used to clamp the end of the test specimen. These angle brackets were bolted to the end plate of the hinge that was mounted to the concrete reaction block as shown in Fig.9.21. Fig.9.22 shows the left-hand side roller support. The supporting bracket was similar to that of the right-hand side but narrower in order to avoid contact with the strengthening frames installed on both sides of test specimen, as shown by Figs.9.22 and 9.23. The

bracket was connected to a vertical load cell through a vertical fin. The load cell was then mounted to another hinge that was fixed to the ground as shown in Fig.9.22.

Fig. 9.21 Right hand side pin support

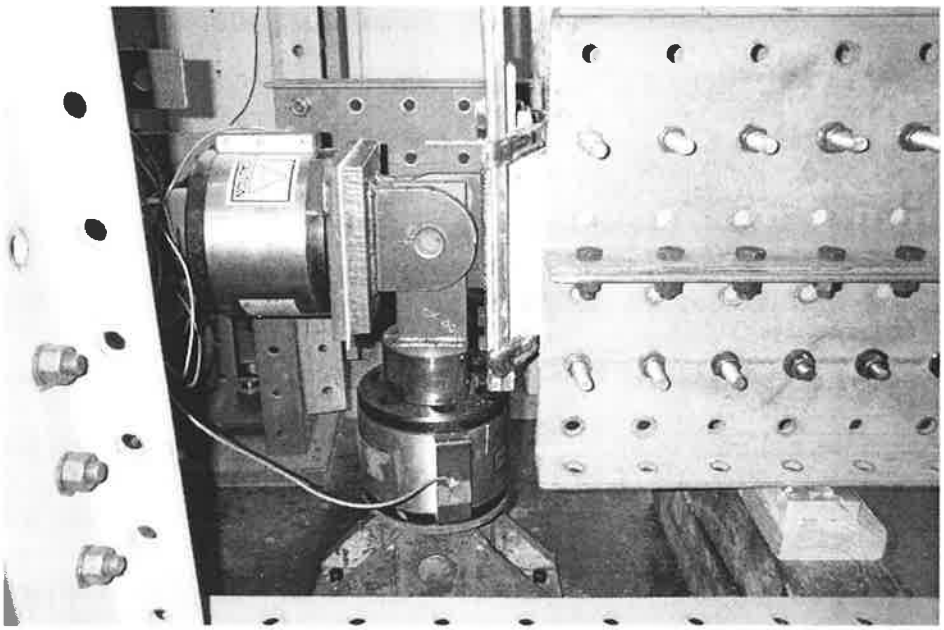

Fig. 9.22 Left hand side pin support

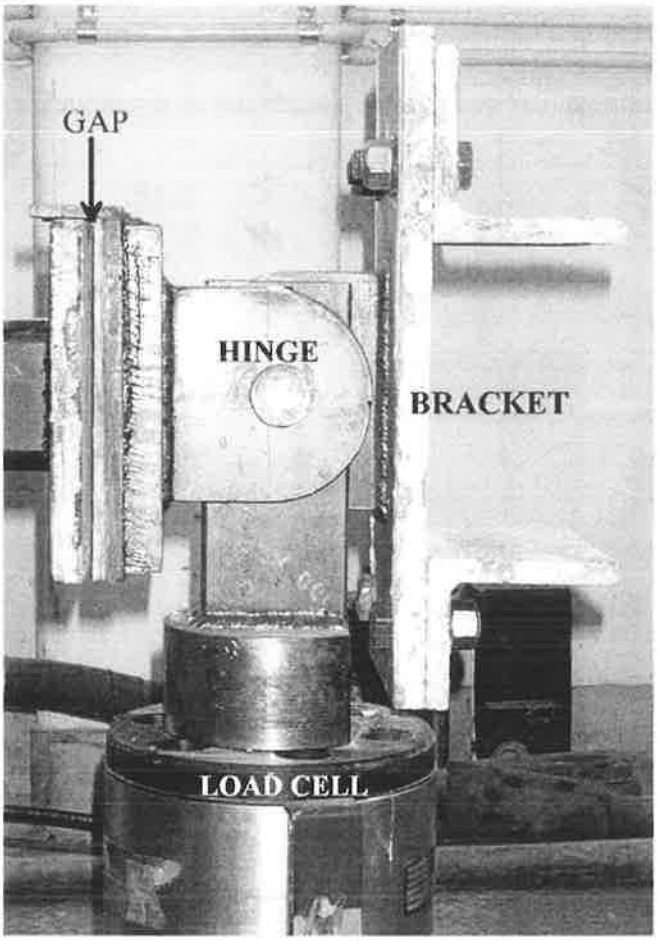

Fig. 9.23 Details of left hinge

However, the roller support was not mounted directly to the top of the axial load actuator. The actuator was not designed to take large transverse forces. To prevent possible transverse loading to the actuator, a gap was maintained between the end plate of the hinge and the end plate of the actuator as shown in Fig.9.23. The gap was filled with high strength low friction plastic membranes (TEFLON sheets) that were greased to further reduce the friction. Therefore, the hinge support and the end of the actuator could move relatively and freely in the transverse direction without affecting the application of the horizontal axial force to the column.

The vertical load was applied to a test specimen through the vertical load jack shown in Fig.9.18. The connection details are shown in Fig.9.24. The downward load was applied through the compression roller, as shown in Fig.9.24, which sat on top of the beam stub. The upward direction load was applied through two tension rods, one in front and the other behind the test specimen, that were anchored to the strengthening frames on both sides of RC specimen as shown in Fig.9.24.

This relatively simple test set up proved to work very well in the experiments.

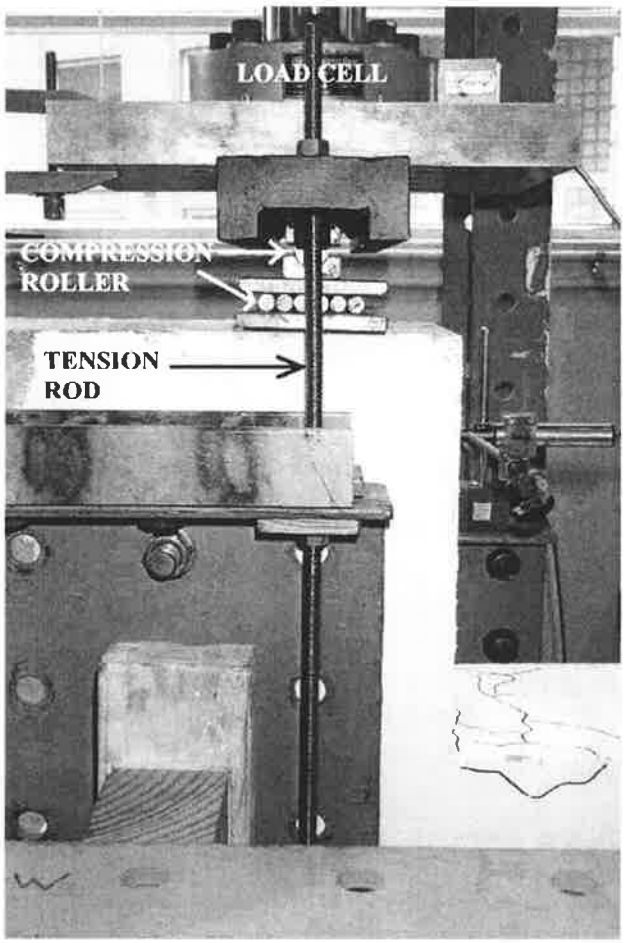

Fig. 9.24 Vertical load application system

9.4 INSTRUMENTATION

A combination of electronic and manual instrumentation was used to measure the vertical and horizontal loads, the displacements of the test specimens, strains at key locations in the column reinforcement bars and steel plates, the slip of bolts, as well as shear deformations in the plastic hinge zone of the column.

The loads were measured using three load cells as shown in Fig.9.18. Load cell 1 (LC1) measured the horizontal load from the axial load actuator. Load cell 2 (LC2) gave the vertical load on the left-hand hinge support, and load cell 3 (LC3) provided the vertical load from the vertical load jack.

The displacements were measured at the five points shown in Fig.9.25. Point A was used to measure the horizontal movement of the left-hand support. This horizontal movement was monitored during each test. As excessive movement of point A, which reflects the axial shortening of a specimen, signaled the loss of integrity of the test column and alerted the technicians to stop the test to avoid a drastic failure mode. It was also used to convert the LC2 reading, which did not remain in a vertical direction when point A moved, into vertical and horizontal components. A Linear Voltage Digital Transducer (LVDT) was used to record the horizontal displacement at point A.

The deflection at point E is a direct measurement of the lateral displacement at the top of a cantilever column (i.e. Δ_0 shown in Fig.4.1). The steel arm, as shown, was fixed to the stub of each test specimen that acted as the base of the cantilever column. Therefore, the stub and the steel arm together were considered as the reference ground of the cantilever column and any relative movement to the steel arm at point E was the lateral displacement of the cantilever column relative to the reference ground. A string

pot was used at point E, as the maximum travel distance of the available LVDTs was not sufficient for this large movement.

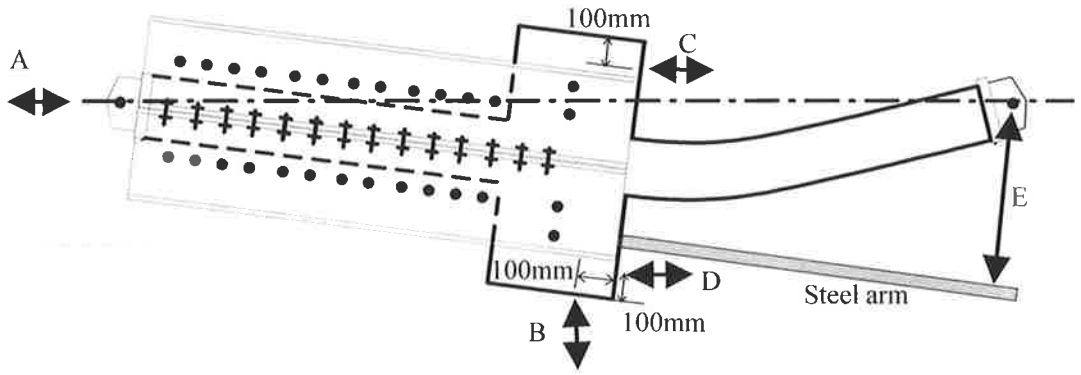

Fig. 9.25 Displacement measurement points

Points C and D together were used to calculate the rotation of the beam stub. The beam stub rotation was needed in order to convert the vertical and horizontal forces into the axial and lateral (shear) forces of the column. Details of these conversions are given in Section 9.6. LVDTs were used at these two points (C & D), as shown in Fig.9.26. Point B measured the movement of a point at the bottom of the stub with respect to the ground. A string pot was again used at point B. The displacements measured at points B, C and D, as shown in Fig.9.25, were used to calculate the displacement of a cantilever column, which is derived in Section 9.6. It was found from tests that the calculated displacement by displacement measurements at points B, C and D was very close to the directly measured displacement at point E. This test methodology provides redundancy in the acquisition of data and as there was no direct measurement at point E in the first few tests, it provided confirmation that the specimen deformations calculated using the measurements at points B, C and D were reliable.

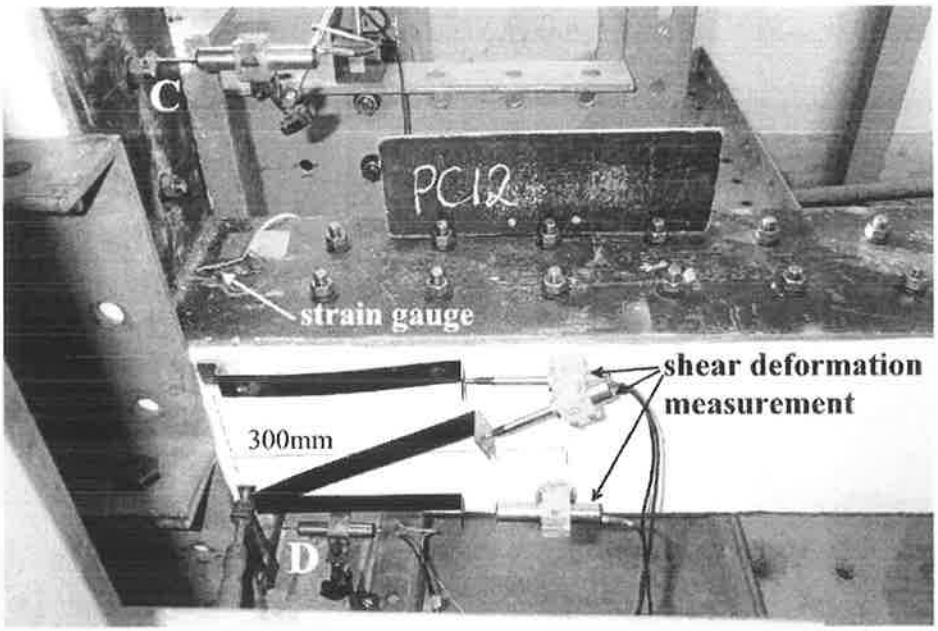

Fig. 9.26. LVDTs and Strain gauges

The strains in the reinforcing bars were measured at three key locations as shown in Fig.9.27(a). One strain gauge was installed on both upper and lower longitudinal bars, approximately 50mm away from the face of the beam stub. The third strain gauge was installed on the first stirrup that was located 100mm way from the face of the stub. The accuracy of the strains measured by this method is limited as only one strain gauge was provided on the face of the reinforcing bar. When the strain inside a reinforcing bar is not uniform, as occurs under bending of the bar, significant differences in strain reading may be expected between the strain gauge attached on the internal face of the bar and on the external face of the bar (difference between compression face and tension face of the bar). However, the strain measurement was not a prime target in this work and the strain data was collected only for reference purposes.

Two strain gauges were installed on each steel plate, one on the external face and the other on the internal face, as shown in Fig.9.26 and Fig.9.27(b). Their position was also about 50mm away from the face of the beam stub.

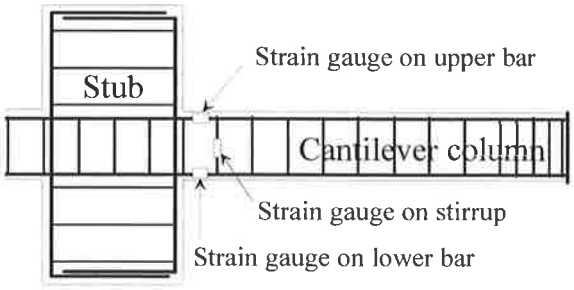

(a) Strain gauges on reinforcing bars

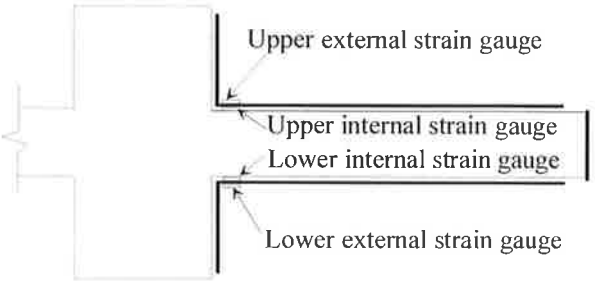

(b) Strain gauges on steel plates

Fig. 9.27 Installation of strain gauges

The shear deformation of the column was measured in two of the tests to find out the significance of this deformation. The measuring system, as shown in Fig.9.26, employed three LVDTs installed in the bottom 300mm segment (expected plastic hinge zone) of the cantilever column. This set up could only measure the shear deformation within the 300mm long segment. As the shear deformation is mainly due to shear cracks instead of elastic shear deformation, the shear deformation was considered to be insignificant in the rest of the column. Observations from the tests confirmed that no visible shear crack occurred outside the bottom 300mm segment. Detailed calculations of

the shear deformation from these measurements are given in Section 9.6. As the shear deformation was found to be insignificant, even in the highly stressed and deformed plastic hinge region, no other specimen was measured for shear deformation, thereby simplifying the instrumentation setup slightly in the subsequent tests.

The slip of the steel plate (relative movement between the plate and the column) was measured in one (specimen 1BMP6) of the tests at three points along the length of the cantilever column. One slip measurement point was at the top of the plate, one at the middle of the plate and the other at the bottom of the plate. Three LVDTs, were mounted on the face of the steel plate to measure the relative movements between these 3 points on the steel plate and the corresponding side face of the RC column as shown in Fig.9.28. These relative movements were considered to give a good indication of the amount of slip between the steel plate and the face of the RC column. However, strictly speaking slip is defined as the relative movement at the same point on the interface.

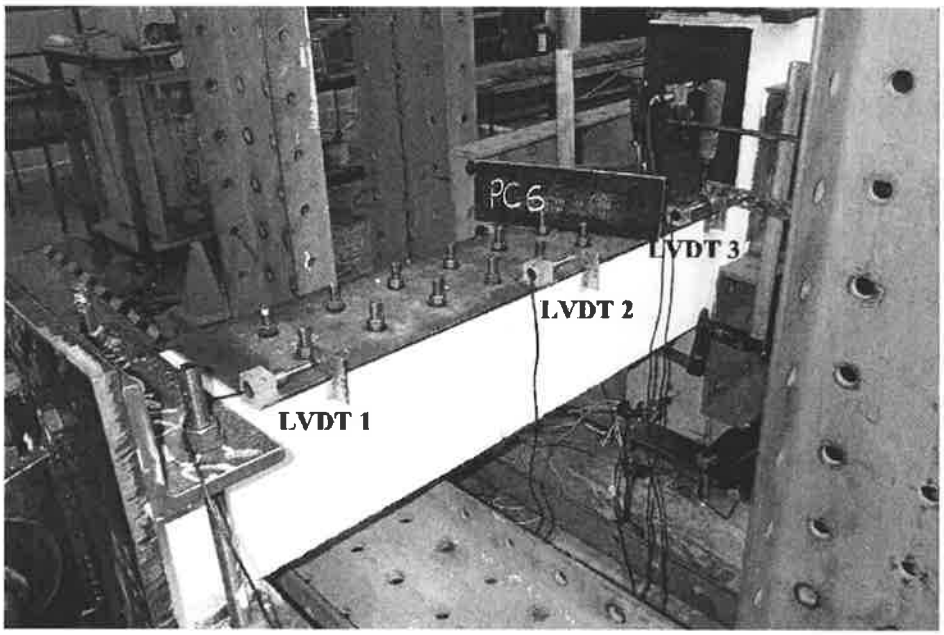

(a) Slip measurement points

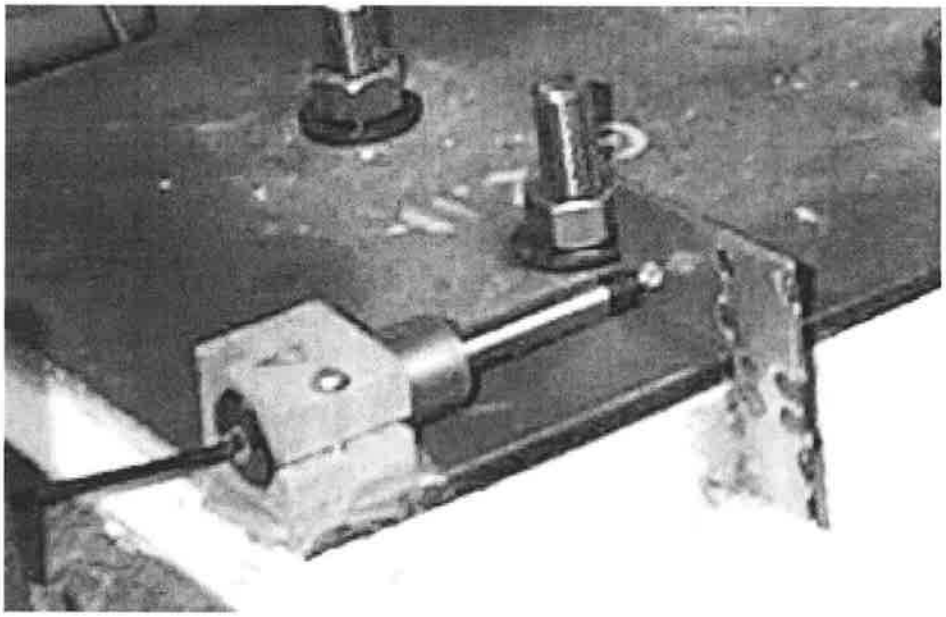

(b) Method of slip measurement

Fig. 9.28 Slip measurements

9.5 LOADING

The axial and lateral loads were applied to each test specimen using a 50 tonne Instron hydraulic actuator (Model No A10115E) and a 50 tonne hand operated double acting hydraulic ram, respectively. The center of the two hinges at the ends of a test specimen, as shown in Fig.9.3(a), were located at the centroid of the corresponding RC cross-section. This ensured that the axial load was applied at the centroid of the RC section at the top of the column.

Strictly speaking, the method of loading, i.e. loading path and rate, will affect test results for non-linear structures. However, the possible influence of the loading procedure was not significant in this work for the purpose of assessing the effect of plating, as long as the relevant specimens, that were used for comparison, were loaded in the same way. The following methods of loading were used in this work.

9.5.1 Monotonic Loading

A requirement for this project was that the axial load was to be maintained constant throughout each test. However, in order to obtain the softening branch of a lateral force (y-axis) versus displacement (x-axis) response curve for a column, tests must be conducted under x-axis (displacement) control mode, i.e. to change the x co-ordinate value and measure the corresponding y co-ordinate values. Therefore in these tests, the constant axial load was first applied to each specimen under load control mode, i.e. the horizontal movement of the axial load actuator shown in Fig.9.18 was automatically adjusted to maintain (within a tolerance of ±0.2kN) a constant axial load of 360kN. Next, the vertical loading jack shown in Fig.9.18 was pumped manually to impose a specific

upward/downward movement (i.e. lateral displacement) to the column. At each specific displacement, readings from all instruments were taken. This process produced one point in each response curve. The 2nd and 3rd steps were repeated until the whole response curve was obtained.

However, due to inexperience with such tests as well as safety concerns that the very large axial load (360kN or 22.5% of actual concrete squash load) could cause instability of the specimen and/or the test rig, the axial load actuator was actually operated under a displacement control mode in the initial monotonic loading tests. In a test where the displacement of the axial load actuator is fixed, drastic failure is not likely to occur, as the axial force will be released immediately should instability occur. Thus, for the initial monotonic test the loading procedure was, first, the axial load was applied and the corresponding axial displacement was fixed. Second, the specified lateral displacement was applied and then instrumentation readings were taken. With the change in lateral displacement, small changes in axial load occurred. Hence in the third step, the axial load was re-adjusted, through additional movement of the axial load actuator, to restore it to the desired axial load value. The readings were then recorded which gave the correct point in the response curve corresponding to the correct axial load. The process of applying lateral deflection and adjusting axial load continued until the whole response curve was obtained.

The process of displacement control on axial load, or adjustment of axial load, was considered to have a minor effect on the column response because small loading steps were used for the lateral deflection and so the adjustment of axial load was small (generally within ±10kN) in each step.

Furthermore, from the monotonic tests, it was found that the testing system was actually quite robust. With increased confidence in the safety and the test procedure, it was decided to use load control for the axial load in the remainder of the tests.

9.5.2 Loading Rate

It is well known that loading rate can influence experimental results. Abrams (1996) observed that damage was much more prominent at a slower loading rate because of increased crack propagation. It is also established in the literature that while fast-rate loaded specimens tend to have larger ultimate loads (strengths) than slow-rate loaded specimens, fast-rate loaded specimens tend to lose strength at lower ductility ratios.

In the monotonic tests of this work, several seconds (5~30 seconds) were allowed between each load step to wait for the specimen to set and cracks to develop. However, as the load steps were controlled manually, the time intervals were not constant, especially when the specimen was inspected and photos were taken. However, it is believed that a few seconds is sufficient for specimens to set.

For cyclic loading tests, which were conducted as quasi-static loading, the loading rate was similar but slightly faster (about 5 seconds between loading increment). A marginally faster loading rate was used to save time due to the large number of points to be tested. In fact, one of the cyclic tests lasted for 3 days. When a test could not be finished in one day, the test was stopped at a zero displacement position. The axial load actuator and vertical jack were then un-loaded to zero force, and the specimen was left overnight. The test resumed the next day by first applying the axial load and then applying the lateral displacement as before.

9.5.3 Cyclic Loading

The purpose of the quasi-static cyclic loading tests was to simulate the response of a structure under an earthquake type loading. Therefore, it was important to select a method of load cycling in order for the test results to be useful for inferring the likely seismic behavior for the specimens. Many different cycling loading procedures have been used. Comprehensive studies have been conducted at the University of Auckland (Liddell, D.P. et al. 2001; Liddell 2000) to study the influence of applied loading history on the performance and failure characteristics of reinforced concrete structures. Twelve loading histories, including conventional procedures employed in the United States, Japan and New Zealand, and artificially generated histories derived from recorded earthquake ground motions were considered. The following conclusions were made from their research:

- There is little agreement between research institutions throughout the world regarding the applied loading history.
- The New Zealand loading history replicates the earthquake demand of a reinforced concrete member more closely than loading histories from other research institutions.

Because of the above reasons, the New Zealand loading history, which is shown in Fig.9.29, was adopted in this project. The ductility factor in Fig.9.29 was defined as the ratio of the displacement to the yield displacement. There were different definitions in the literature for yield displacement. In this work, the yield displacement is defined as the point where the longitudinal tension bar first yields.

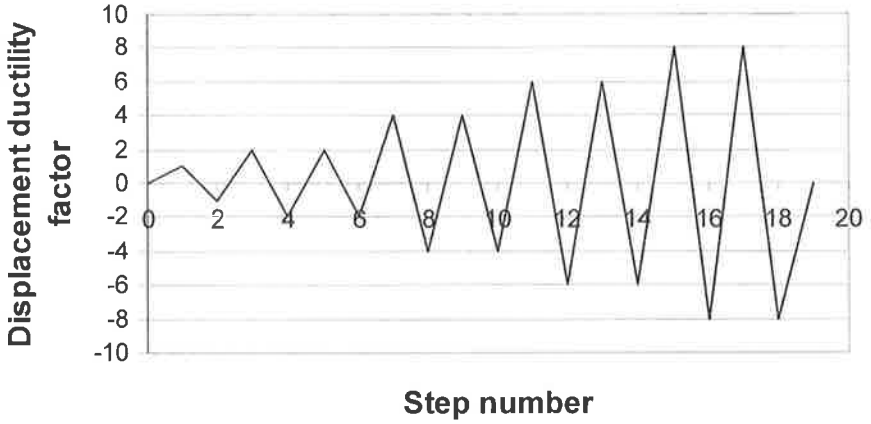

Fig. 9.29 New Zealand loading history

From the monotonic test of the un-plated column, it was found that the yield displacement was 26mm, which is exactly the peak point of the response curve as shown in Fig.11.1. The column axial instability (difficult to maintain axial load) occurred at a displacement of 120mm. Following Fig.9.29, the following displacement history should be applied: +26mm, -26mm, +52mm, -52mm, +52mm, -52mm, +104mm, -104mm, +104mm, -104mm. This will give only three displacement steps of 26mm, 52mm and 104mm, which raised the concern that not enough load steps would be tested. To give more load steps, the New Zealand loading history was modified in this work to give a loading history shown in Fig.9.30. This loading was used for all cyclic loading tests regardless of the difference in their yield displacement, which provided a good benchmark for comparison. However, not all specimens were able to withstand all the loading steps as indicated in Figure 9.30.

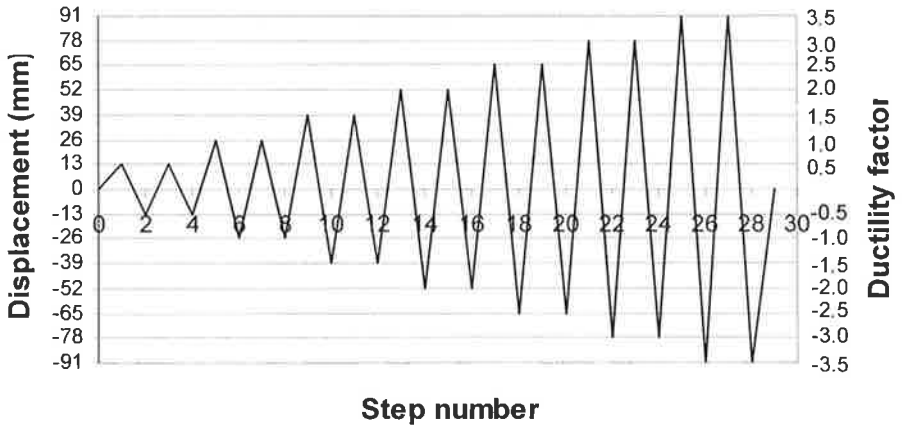

Fig. 9.30 Cyclic loading history adopted

9.5.4 Initial Load and Initial Reading

As the double-column test specimens were tested horizontally, the gravity load of the test specimen including the strengthening frames was expected to cause a small initial deflection in the column. For convenience of data acquisition, all instrumentation readings were set to zero after the specimen had been placed in position but before the application of any axial and lateral loads. In other words, the effect of initial gravitational loading was recorded as zero in the test. The self-weight can be corrected in the response curve as discussed in Chapter 12.

The first data point reported in the test results is the point when the axial load was increased to the specified load and before any movement of the vertical load jack. At this point, the response of the cantilever column, in terms of both lateral force and displacement on top of the column, may not be zero due to flexure, especially for the plated columns. This is because the axial load, which was applied to the centriod of the RC cross-section, produced an initial flexural moment to the composite member.

9.6 CONVERSION OF MEASUREMENTS

As noted earlier in Section 9.4, not all of the key column responses could be measured directly. The conversions of the measurements are derived in this section for data that had to be combined, or geometrically adjusted, to give the desired column responses.

9.6.1 Column Lateral Force

The column lateral force F is the force component at joint B that is parallel to the long side of the stub, as shown in Fig.9.31. It can be calculated from the readings given by load cell 1, 2 and 3, as indicated by F_1, F_2 and F_3 in Fig.9.31. The rotation angle θ of the beam stub is calculated from displacement measurements at points C and D as shown in Fig.9.25.

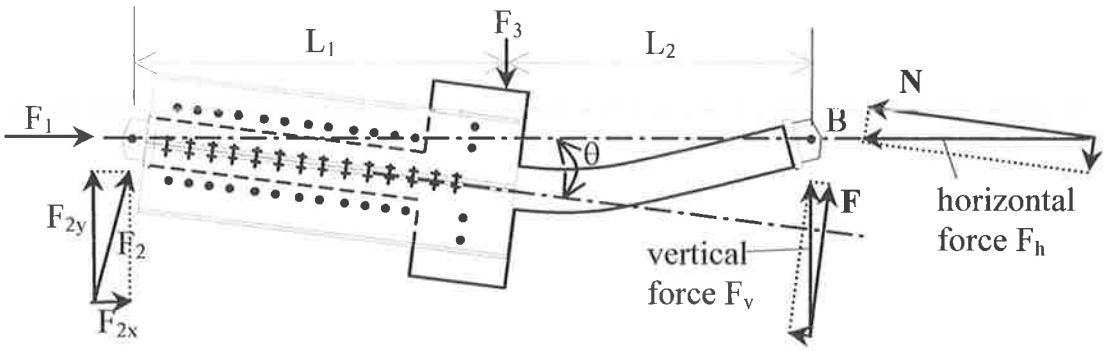

Fig. 9.31 Conversion of lateral force

From Fig.9.31, the following relations are obtained

$$F_v = F_3 \cdot L_1 / (L_1 + L_2) \tag{9.1}$$

$$F_h = F_1 + F_{2x} \approx F_1 \tag{9.2}$$

Therefore,

$$F = F_v \cdot \cos(\theta) - F_h \cdot \sin(\theta) \tag{9.3}$$

The axial load of the column is given by

$$N = F_h \cdot \cos(\theta) + F_v \cdot \sin(\theta) \tag{9.4}$$

9.6.2 Deflection of Column

The deflection of a cantilever column can be measured directly through the steel arm shown in Fig.9.25. However as noted earlier, this steel arm was not installed in the first few tests. Therefore, it had to be calculated from other measurements. As the top of the column is supported by a hinge, the deflection of the column, which is the relative displacement of the hinge to the base of the cantilever column, was determined by the movement of the central stub which was measured at points B, C and D shown in Fig.9.25. The central stub was assumed to be a rigid body in these calculations.

The measurement at point B was a string pot with one end fixed to a point B on the ground and the other to a point P at the bottom of the stub, as shown in Fig.9.32. The movement of point P, from P to P' as shown, was measured by the change in length of the string, from LB_0 to LB. The measurements at points C and D were given by two LVDTs that were mounted to the supporting frame which was considered to be fixed with respect to ground. These two LVDTs give the horizontal movements of the stub at these two fixed positions, as shown by ΔC and ΔD in the figure.

In the following derivation, the horizontal movement DX, vertical movement DY and rotation θ of point O, an intersection point of the stub with the center line of the RC column, were first derived in terms of LB, ΔC and ΔD. The lateral displacement of the column was then calculated with DX, DY and θ.

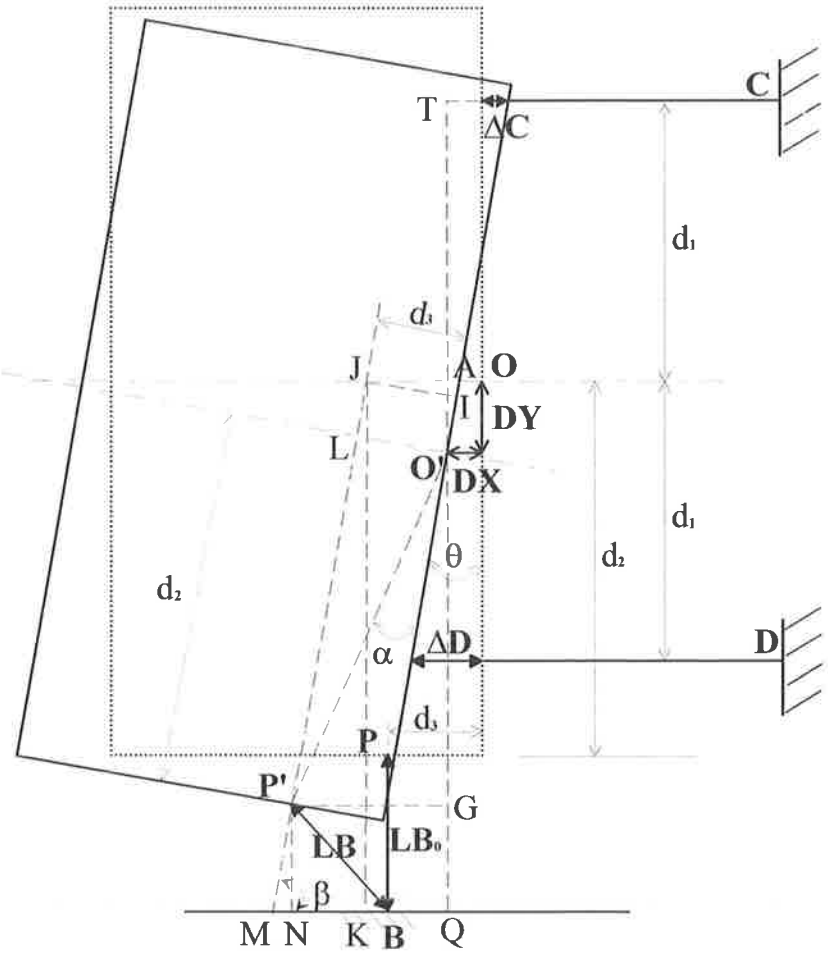

Fig. 9.32 Calculation of lateral displacement

From Fig.9.32, the following two relations are obtained

$$\Delta C = O'T \cdot \tan\theta - DX = (d_1 + DY) \cdot \tan\theta - DX \tag{9.5}$$

$$\Delta D = (d_1 - DY) \cdot \tan\theta + DX \tag{9.6}$$

Adding Eq.9.5 to Eq.9.6 gives

$$\Delta C + \Delta D = 2d_1 \cdot \tan\theta$$

or

$$\theta = \arctan\left[(\Delta C + \Delta D)/2d_1\right] \tag{9.7}$$

Subtracting Eq.9.6 from Eq.9.5 gives

$$\Delta C - \Delta D = 2DY \cdot \tan\theta - 2DX$$

or

$$DX = DY \cdot \tan\theta + (\Delta D - \Delta C)/2 \tag{9.8}$$

Similarly, another three relations can be obtained

$$JL = IO' = AO' - AI = DY/\cos\theta - d_3 \cdot \tan\theta \tag{9.9}$$

$$\begin{aligned} P'M &= JM - JL - LP' = JK/\cos\theta - JL - LP' \\ &= \frac{(d_2 + LB_0)}{\cos\theta} - (\frac{DY}{\cos\theta} - d_3 \cdot \tan\theta) - d_2 \end{aligned} \tag{9.10}$$

and

$$\begin{aligned} MB &= MN + NB = P'M \cdot \sin\theta + P'G - BQ \\ &= P'M \cdot \sin\theta + O'P' \cdot \sin(\alpha + \theta) - (d_3 - DX) \\ &= P'M \cdot \sin\theta + \sqrt{d_2^2 + d_3^2} \cdot \sin(\alpha + \theta) + DX - d_3 \end{aligned} \tag{9.11}$$

From the Law of Cosines

$$\begin{aligned} LB^2 &= P'M^2 + MB^2 - 2P'M \cdot MB \cdot \cos\beta \\ &= P'M^2 + MB^2 - 2P'M \cdot MB \cdot \sin\theta \end{aligned} \tag{9.12}$$

Substituting Eqs.9.10 and 9.11 into Eq.9.12 and re-arranging gives

$$LB^2 = \frac{DY^2}{\cos^2\theta} + 2 \cdot (b \cdot \tan\theta - a) \cdot DY + a^2 + b^2 \tag{9.13}$$

where

$$a = LB_0 + d_3 \cdot \sin\theta + d_2 \cdot (1 - \cos\theta) \tag{9.14}$$

and

$$b = \sqrt{d_2^2 + d_3^2} \cdot \sin(\alpha + \theta) - d_3 + \frac{\Delta D - \Delta C}{2} \tag{9.15}$$

Solving Eq.9.13 gives

$$DY = \cos\theta \cdot [a \cdot \cos\theta - b \cdot \sin\theta \pm \sqrt{LB^2 - (a \cdot \sin\theta + b \cdot \cos\theta)^2}] \quad (9.16)$$

One of the two solutions given by Eq.9.16 is false. It can be found by letting $\theta = \Delta D = \Delta C = 0$ in Eqs.9.14~9.16, which gives

$$DY = LB_0 \pm LB \quad (9.17)$$

Obviously, the correct answer is $DY = LB_0 - LB$. Therefore, the only reasonable solution of Eq.9.16 is

$$DY = \cos\theta \cdot [a \cdot \cos\theta - b \cdot \sin\theta - \sqrt{LB^2 - (a \cdot \sin\theta + b \cdot \cos\theta)^2}] \quad (9.18)$$

From Fig.9.33, the lateral displacement at top of the cantilever column can be calculated as

$$\Delta_0 = DY / \cos\theta + L \cdot \tan\theta \quad (9.19)$$

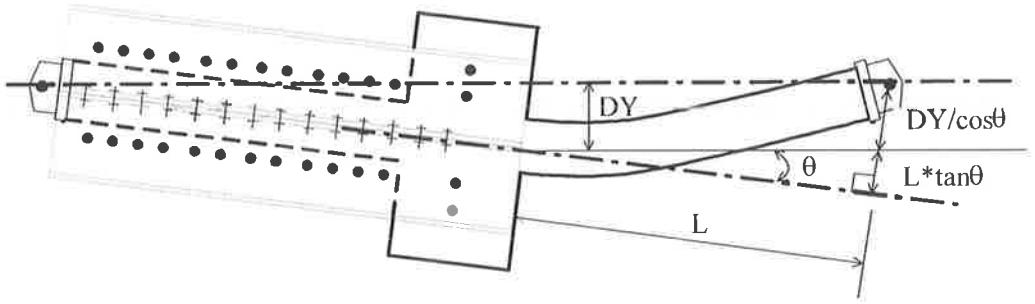

Fig. 9.33 Deflection of cantilever column

9.6.3 Shear Deformation

The shear deformation measurement system shown in Fig.9.26 is schematically reproduced in Fig.9.34. Lines AB, CD and BC in Fig.9.34 represent the positions of the top, bottom and diagonal LVDTs, respectively. Deformation within the rectangle ABCD

is measured by these three LVDTs. In this section, the shear deformation of the measured rectangle is derived in terms of the readings of the three LVDTs.

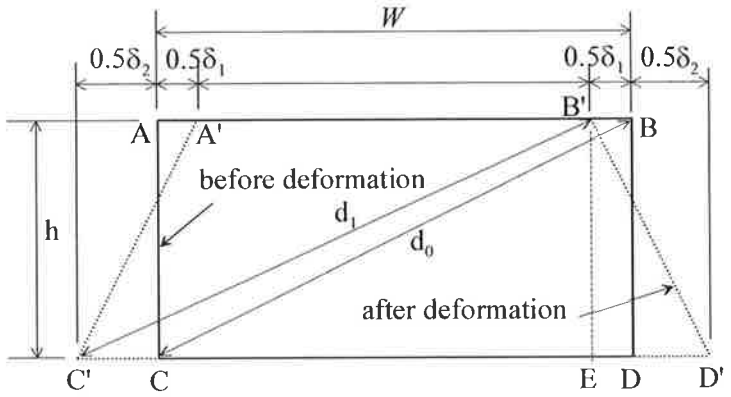

(a) Pure flexural deformation

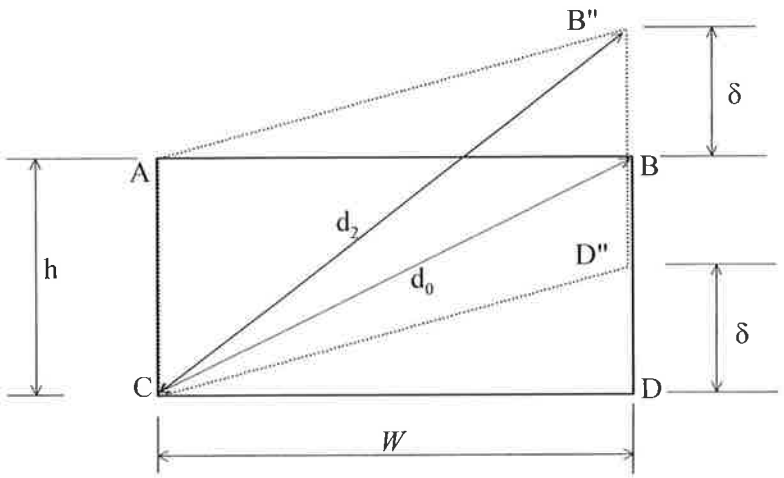

(b) Pure shear deformation

Fig. 9.34 Deformations of the measured rectangle

Under pure flexural deformation without shear, the deformation of the measured rectangle is shown by Fig.9.34(a), where the un-deformed shape is given by ABCD and the deformed shape is shown by A'B'C'D'. The flexural deformation changes the length of the top and bottom sides as well as the diagonal line, causing a change of readings in all three LVDTs. Under pure shear deformation, as shown by Fig.9.34(b), the un-

deformed rectangle ABCD is skewed to the deformed shape AB"CD". In this case, the side length of the deformed shape is still equal to its original length, i.e. AB"=AB and CD"=CD. In other words, the readings from the top and bottom LVDTs measure only the flexural deformation. However, readings of the diagonal LVDT include both flexural and shear deformation.

From Fig.9.34(a), the diagonal length after deformation is given by

$$d_1 = \sqrt{C'E^2 + h^2} = \sqrt{\left[W + \frac{1}{2}\cdot(\delta_2 - \delta_1)\right]^2 + h^2} \tag{9.20}$$

where δ_1 and δ_2 are readings from the top and bottom LVDT, respectively.

From Fig.9.34(b), the deformed diagonal length is

$$d_2 = \sqrt{(\delta + h)^2 + W^2} \tag{9.21}$$

where δ is the shear deformation.

Assuming small deformations, the superposition law applies. Therefore, the diagonal LVDT reading δ_3 is equal to the summation of diagonal length change due to flexure and shear, or

$$\delta_3 = (d_1 - d_0) + (d_2 - d_0) = d_1 + d_2 - 2d_0 \tag{9.22}$$

Substituting Eq.9.21 into Eq.9.22 and re-arranging gives the shear deformation

$$\delta = -h + \sqrt{(\delta_3 + 2d_0 - d_1)^2 - W^2} \tag{9.23}$$

CHAPTER 10 MATERIAL TESTS

Tests were conducted to obtain the actual (average, or mean, values as opposed to the characteristic, or design, values) material properties for the concrete, reinforcing bars, steel plates, anchor bolts and for the full interaction gluing used in the fabrication of the test specimens. These properties were needed for the analysis of the test results, especially in the numerical simulations of the test columns. The methodology and results are presented in this section for each of the material tests.

10.1 CONCRETE

All four double-column test specimens were cast on 7th July 2000 from a single batch of concrete supplied by CSR Readymix. The required design concrete strength was specified to be 25N/mm^2 with the expectation that the actual strength would be higher. Concrete samples of cylinders (ϕ100mm × 200mm high) were taken from the same batch of concrete. To estimate the actual compressive strength, tensile strength and Young's modulus of the concrete for each column specimen as accurately as possible, cylinders were tested around (but not exactly on) the test date of each column test.

Typically, two tests were conducted on each cylinder: (1) a Young's Modulus test and (2) a compressive strength test. The Young's Modulus tests were performed first, which involved application of a compression load to a cylinder in the elastic stress range to establish the stress vs. strain properties of the concrete. The maximum stress applied in the Young's Modulus test was approximately 40% of the compressive strength of the

concrete. The slope of a linear trend line that gave the best fit to the stress-strain curve was considered as the Young's Modulus. The results of the Young's Modulus tests are given in column 9 of Table 10.1 and plots of the tests are shown in Figs.A1 to A17 in Appendix A. After each Young's Modulus test, the cylinder was loaded in compression until failure in order to determine the compressive strength of the concrete. The results of these tests are given in column 8 of Table 10.1.

Table 10.1 Compression test results of concrete

Brand	Test date (d/m/y)	Age (days)	Diameter (mm)	Height (mm)	Weight (g)	Ultimate load (kN)	f_{co} (N/mm^2)	E_c (N/mm^2)
CYL01	2/8/00	23	100.5	200	3500.4	205.6	25.9	22671
CYL02	2/8/00	23	100.5	201	3522	201.2	25.4	22300
CYL03	2/8/00	23	100.5	201	3492.1	194.4	24.5	23491
CYL04	11/8/00	32	100.5	201.5	3519	260.4	32.8	24457
CLY05	11/8/00	32	100.5	201	3553	204.8	25.8	28790
CLY06	11/8/00	32	100.1	200	3546	220.6	28.0	27468
CYL07	10/11/00	123	101	201	3602.2	311.8	38.9	31764
CYL08	10/11/00	123	100.7	200	3547.7	306.6	38.5	30168
CYL09	10/11/00	123	100.6	200	3561	315.6	39.7	29640
CYL10	28/2/01	233	100.5	200	3552.2	318.5	40.2	27941
CYL11	28/2/01	233	100.3	200	3547.9	290.5	36.8	29407
CYL12	28/2/01	233	100.7	200	3511.6	280.4	35.2	26462
CYL14	18/5/01	312	100	200.5	3555.8	299	38.1	---
CYL15	18/5/01	312	101	201	3618.6	290.2	36.2	32263
CYL16	18/5/01	312	100.5	200.5	3590.8	284	35.8	32343
CYL18	3/7/01	358	100.5	199	3557.7	323	40.7	32029
CYL19	3/7/01	358	100.3	200	3645.8	357	45.2	34833
CYL20	3/7/01	358	100.4	200	3585.7	288.5	36.4	32912

To estimate the tensile strength of the concrete, Brazilian tests, or indirect tensile tests, were conducted. As the tensile strength was not a major concern in this work, only two such tests were performed. The test results are given in Table 10.2, in which the tensile strength was calculated by $f_t = \frac{2 \cdot (applied \quad load)}{\pi \cdot (diameter) \cdot (height)}$ and is listed in column 8.

Table 10.2 Tensile test results of concrete

Brand	Test date (d/m/y)	Age (days)	Diameter (mm)	Height (mm)	Weight (g)	Ultimate load (kN)	f_t (N/mm^2)
CYL13	28/2/01	233	100.3	201	3552	133	4.2
CYL17	18/5/01	312	100.5	201	3624.1	116.2	3.7

10.2 REINFORCING BARS

Three tensile tests were conducted to determine the tensile strength for both the Y16 and R6 reinforcing bars. The detailed results are given in Table 10.3.

Table 10.3 Tensile test results of reinforcing bars

Brand	Diameter (mm)	Yield force (kN)	Yield strength (MPa)	Peak force (kN)	Peak strength (MPa)
Y16a	16	110.6	550.1	127.5	634.1
Y16b	16	110.0	547.1	126.6	629.7
Y16c	16	110.4	549.1	126.8	630.7
R6a	6	19.53	690.7	--	--
R6b	6	19.5	689.7	--	--
R6c	6	19.54	691.1	--	--

Typical machine displacement vs. tensile force plots for the Y16 and R6 bars are shown in Figs.10.1 and 10.2, respectively. The "yield force" in Table 10.3 is the *y* (vertical) co-ordinate of the yield plateau in the displacement vs. tensile force chart. The maximum *y* co-ordinate of the chart is referred as "peak force" in Table 10.3.

The above tensile tests give the yield and maximum strength of the reinforcing bars, as listed in Table 10.3. However, it was not possible to determine the stress-strain relation, or the Young's modulus and strain hardening stiffness, from this data, as the displacement or horizontal co-ordinate of Figs.10.1 and 10.2 did not give the true

elongation of the bar due to slip of the bars in the end grips. To determine the stress-strain relation, another three specimens of the Y16 bars were tested with strain gauges installed on the surface of the bars. The results of these tests are given in Figs.10.3-10.5.

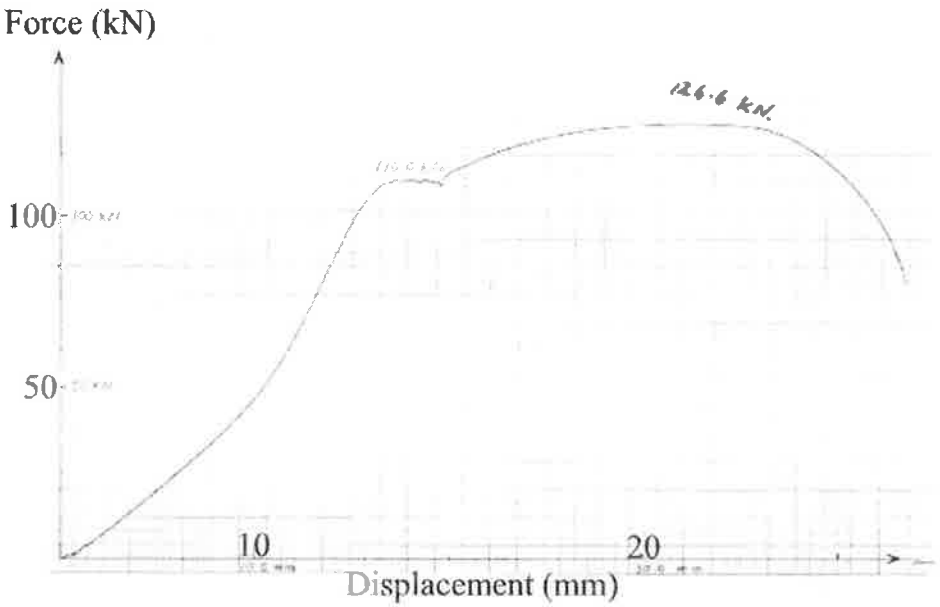

Fig. 10.1 Tensile test result of Y16 bar

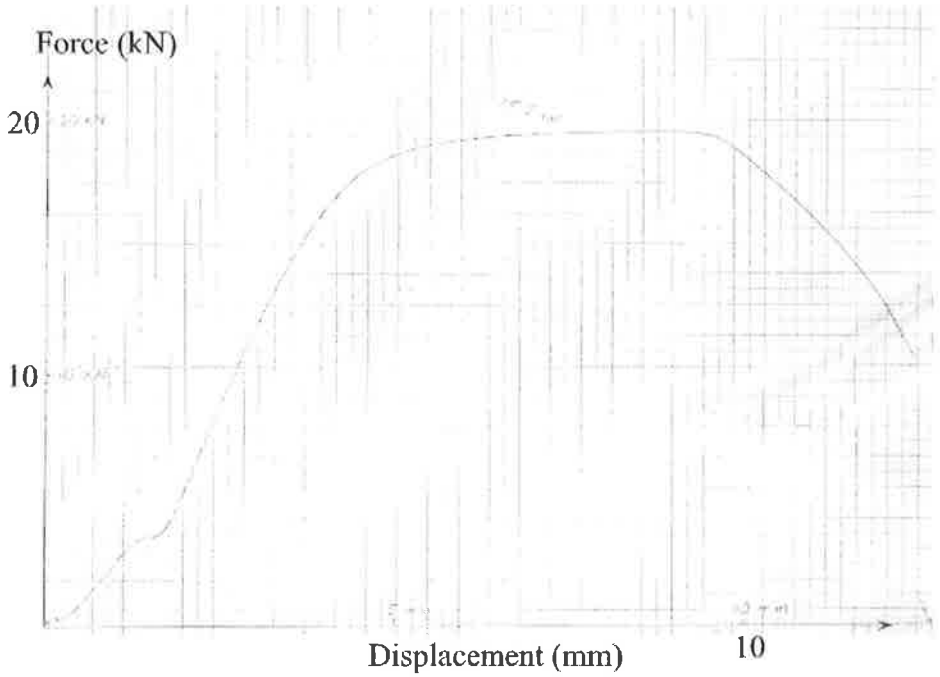

Fig. 10.2 Tensile test result of R6 bar

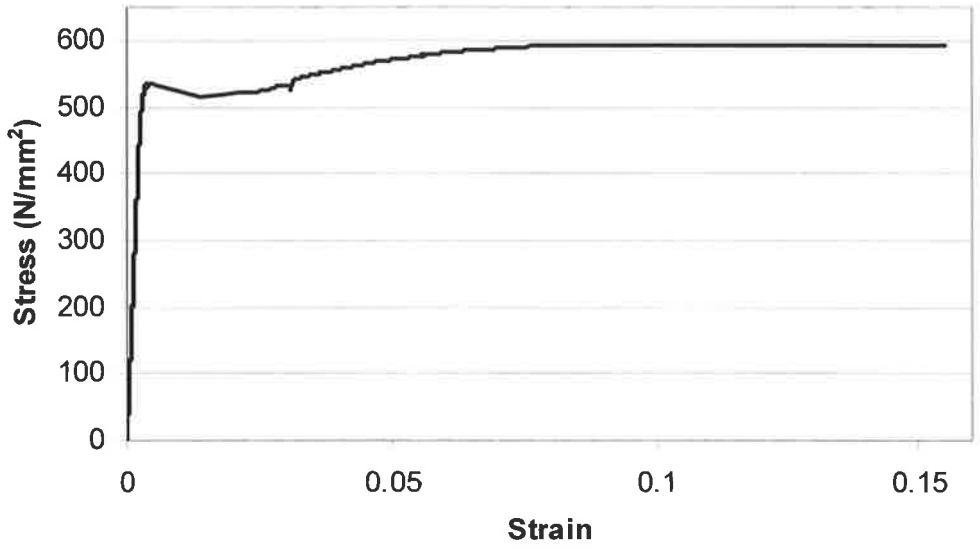

(a) Whole curve

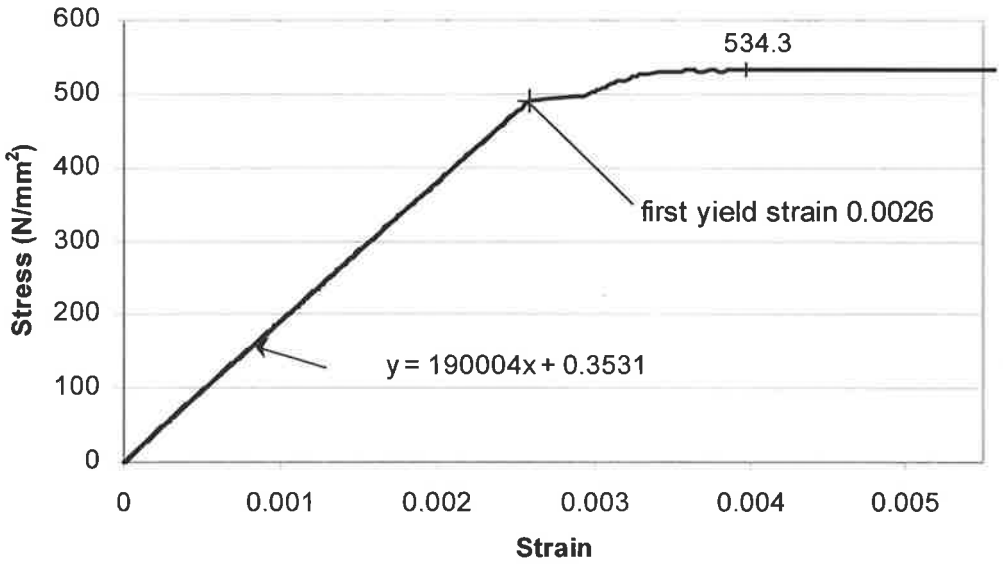

(b) Enlarged linear part with trend line equation

Fig. 10.3 Stress-Strain curves of Y16 bar sample Y16d

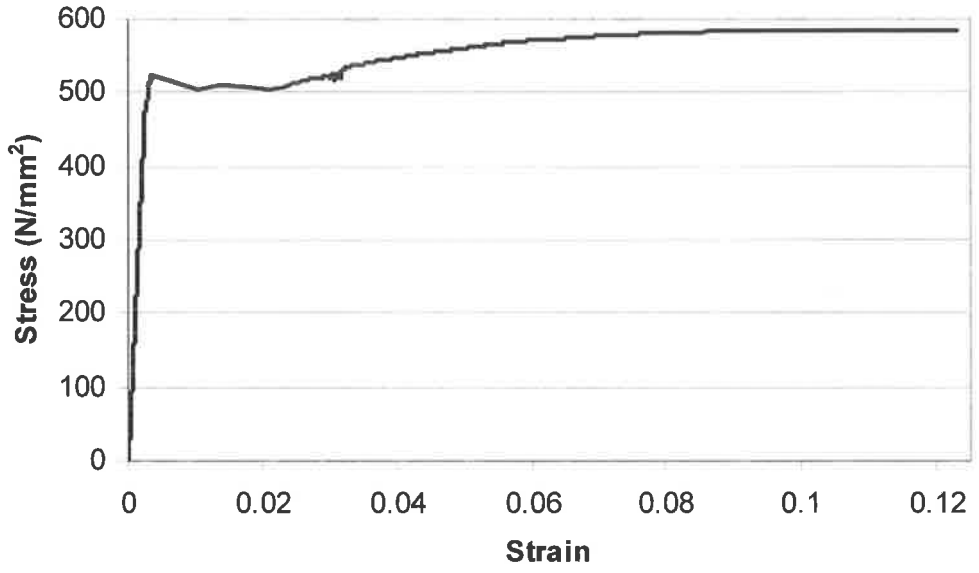

(a) Whole curve

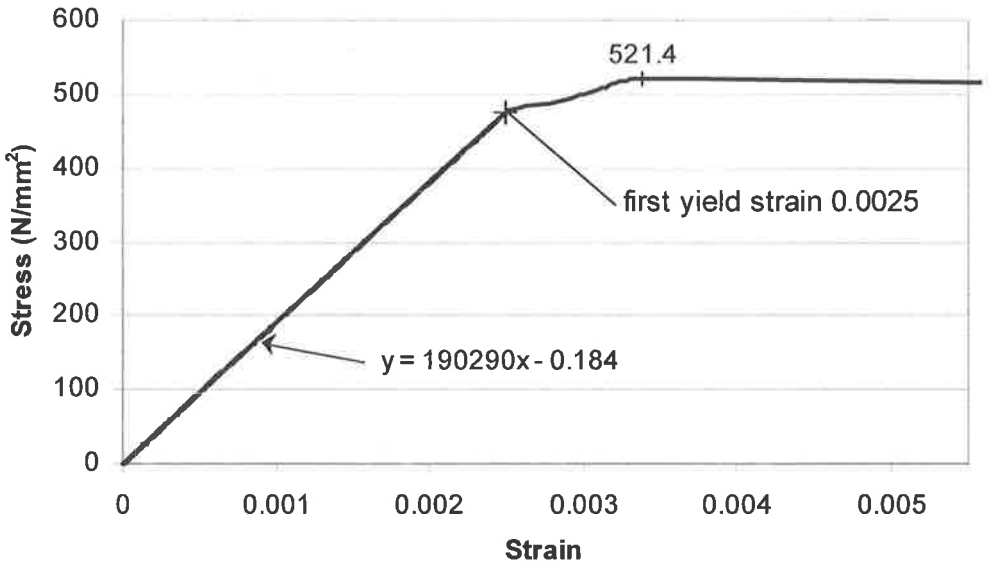

(b) Enlarged linear part with trend line equation

Fig. 10.4 Stress-Strain curve of Y16 bar sample Y16e

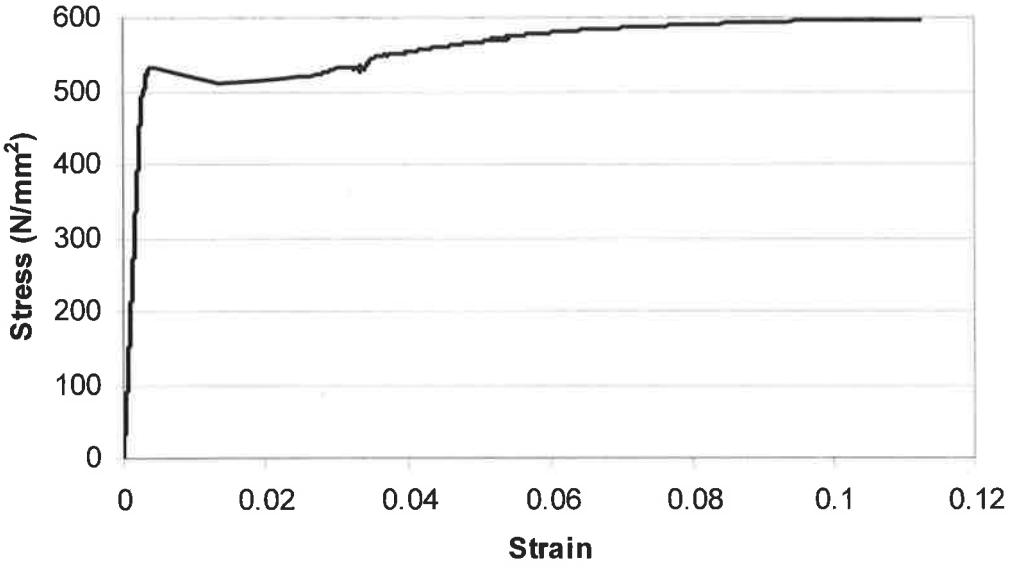

(a) Whole curve

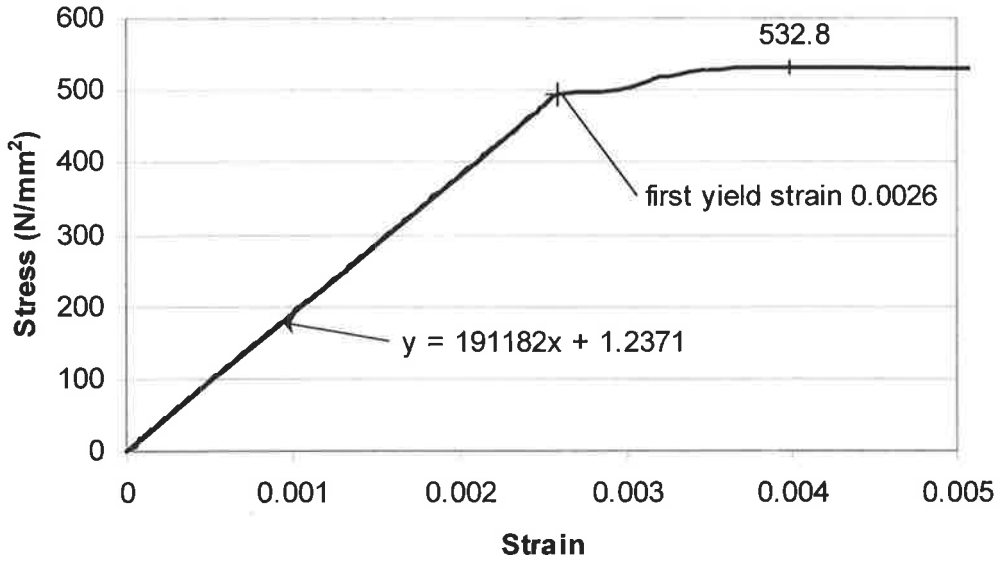

(b) Enlarged linear part with trend line equation

Fig. 10.5 Stress-strain curve of Y16 bar sample Y16f

From the stress-strain tests, the yield strength of the three Y16 specimens were found to be 534.3, 521.4 and 532.8 MPa, respectively, giving an average value of 529.5 MPa. The Young's Modulus is the gradient of the linear part, as shown by the coefficient of x in the linear equation of the trend lines. The average value of the Young's Modulus is *(190004+190290+191182)/3=190492* MPa.

It is noted that the yield strength values from the stress-strain tests are consistently lower than those given in Table 10.3 that have an average value of 548.8MPa. The reason is that the cross-sectional area of the reinforcing bar was slightly reduced by grinding the surface of the bar to make a smooth surface for strain gauge installation. The reduction in the cross-sectional area was difficult to measure. Therefore, the nominal cross-section area of 201.06 mm^2 without reduction was used to calculate the yield strength and Young's Modulus in Figs.10.3-10.5. The average reduced cross-sectional area can be estimated using the average yield strength from the stress-strain tests, 529.5MPa, and the average yield strength from the normal tensile tests, 548.8Mpa. If 548.8MPa is considered as the actual yield strength of the Y16 bar, then the reduced cross-sectional area in the stress-strain tests is given by $A_s=529.5*201.06/548.8=194\ mm^2$. With this more "accurate" cross-sectional area, the Young's Modulus from the stress-strain tests was also revised to $E_s=190492*201.06/194=197424$ MPa. Of course, this kind of "accurate" adjustment is insignificant and unnecessary in practice.

The strain hardening stiffness of the Y16 bar was estimated from the three stress-strain curves, as shown in Fig.10.6. The simplified strain hardening line was drawn between a point in the yield plateau and a point near the peak of the curve as shown in Figure 10.6, which gave a strain hardening stiffness of 798.4 MPa. For consistency, it

was also revised using the more "accurate" cross-sectional area to give E_h=798.4*201.06/194=827.5 MPa.

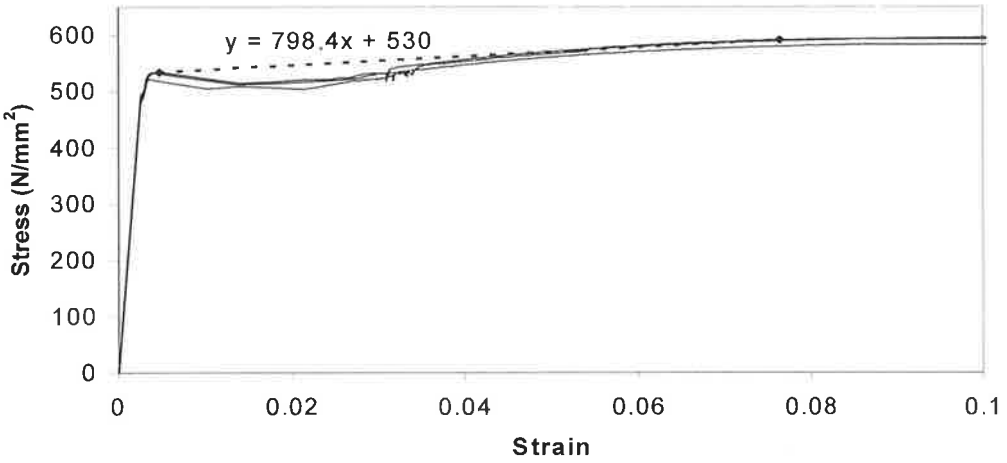

Fig. 10.6 Strength hardening stiffness of Y16 bar

In summary, the average yield strength from the Y16 bar tensile tests without a strain gauge was used as the yield strength of the Y16 bars. The Young's Modulus and strain hardening stiffness values were obtained from the average stress-strain test results, which were modified with the "accurate" cross-sectional area. For the R6 bar material, the average yield strength given in Table 10.3 was used. The final test results are summarized in Table 10.4.

Table 10.4 Summary of reinforcing bar properties

Brand	Diameter (mm)	Yield strength (MPa)	Young's Modulus (MPa)	Strain hardening stiffness (MPa)	First yield strain
Y16	16	548.8	197424	827.5	0.00255
R6	6	690.5	--	--	--

10.3 STEEL PLATES

Three types of steel plates were used for plating the columns in the experimental work. To obtain the steel plate properties, tensile tests, similar to those performed on the reinforcing bars, were conducted to obtain representative stress-strain relations. The results for the 12mm thick mild steel plate (MS12), 6mm thick mild steel plate (MS6) and 6mm thick high tensile steel plate (HT6) are given in Figs.10.7, 10.8 and 10.9, respectively. Three specimens were tested for each type of steel plate, corresponding to the three curves in each figure.

For the mild steel plates, i.e. MS12 and MS6, the yield strength was taken as the average y co-ordinate of the yield plateau from Figs.10.7 and 10.8, respectively. For the high strength plate HT6, the yield strength was taken at the first yielding point shown by "▲" in Fig10.9. The Young's modulus was taken as the gradient of the linear segment, as shown by the x coefficient for the linear trend lines. The average values of the three specimens were used for the steel plate properties and are summarized in Table 10.5. The strain hardening stiffness depends on the position of the last point on the stress-strain curve. As this value may not critical in this study, an arbitrary value of 600MPa was used.

Table 10.5 Summary of steel plate properties

Brand	Thickness (mm)	Yield strength (MPa)	Young's Modulus (MPa)	Strain hardening stiffness (MPa)
MS12	12	306.9	198679	600
MS6	6	307.3	200031	600
HT6	6	734.4	196798	600

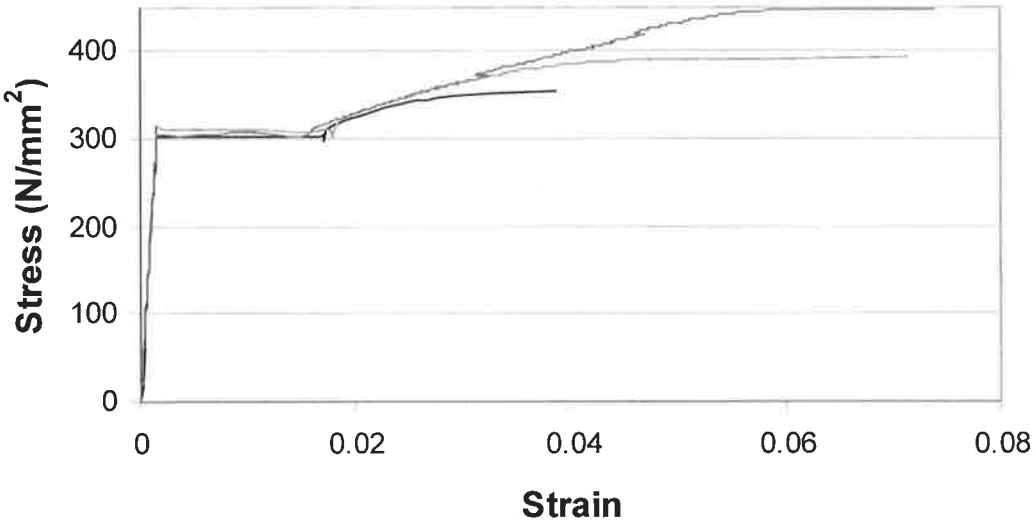

(a) Whole curve

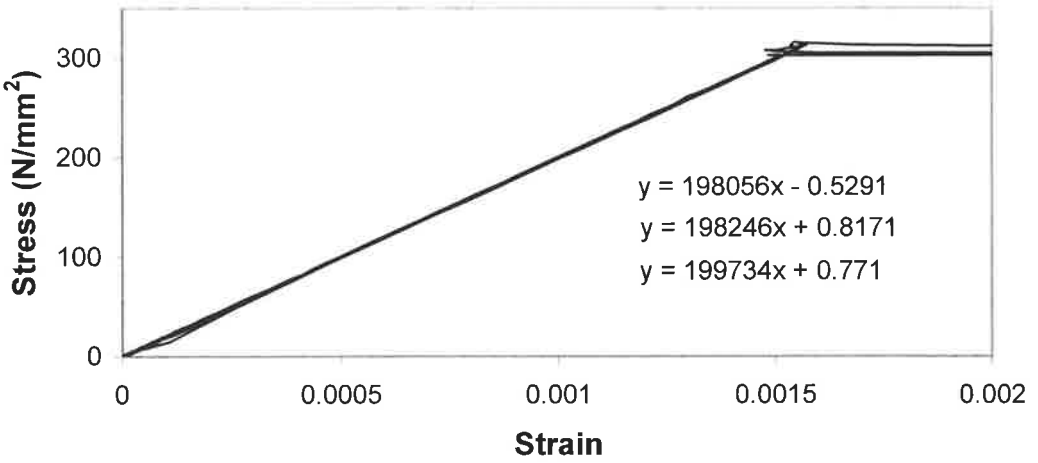

(b) Enlarged linear part with trend line equations

Fig. 10.7 Stress-strain test results of MS12 steel plate

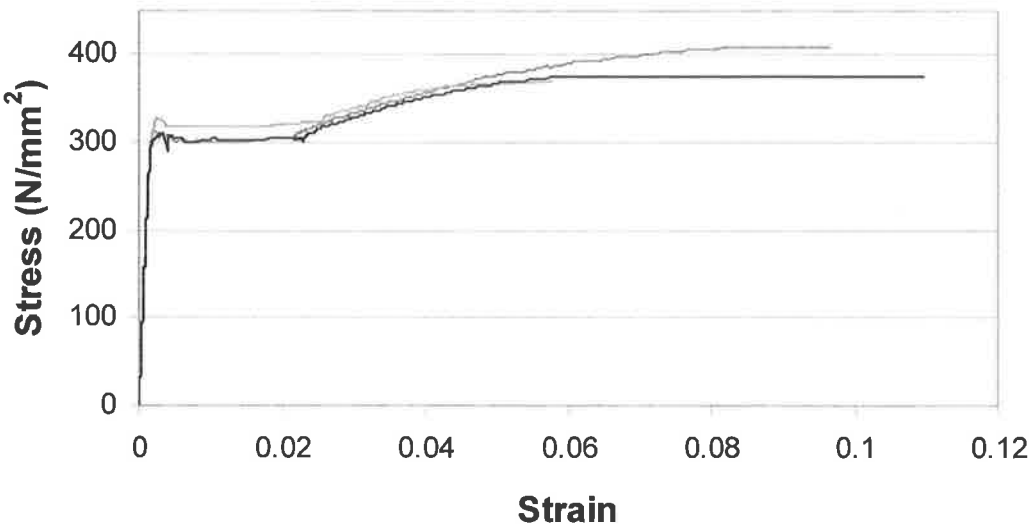

(a) Whole curve

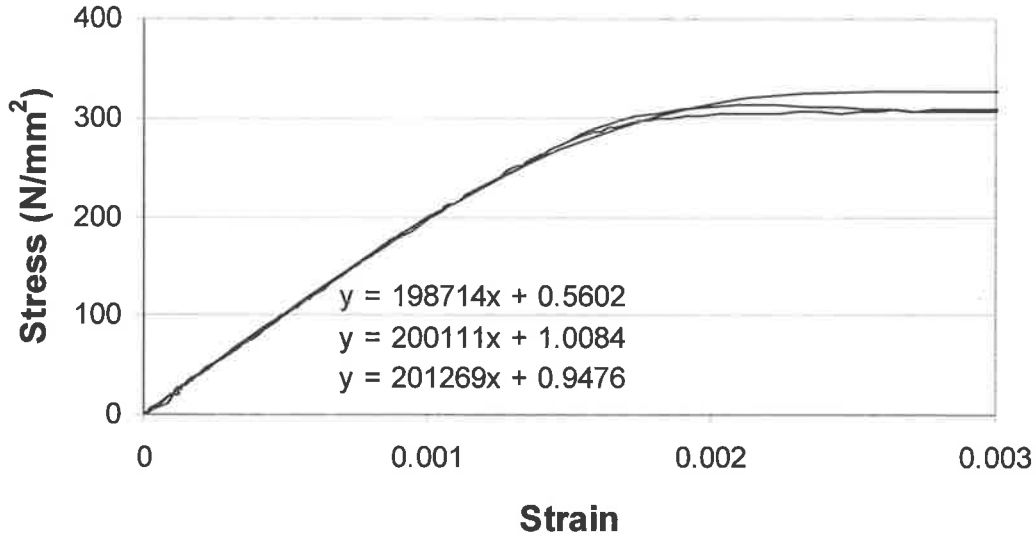

(b) Enlarged linear part with trend line equations

Fig. 10.8 Stress-strain test results of MS6 steel plate

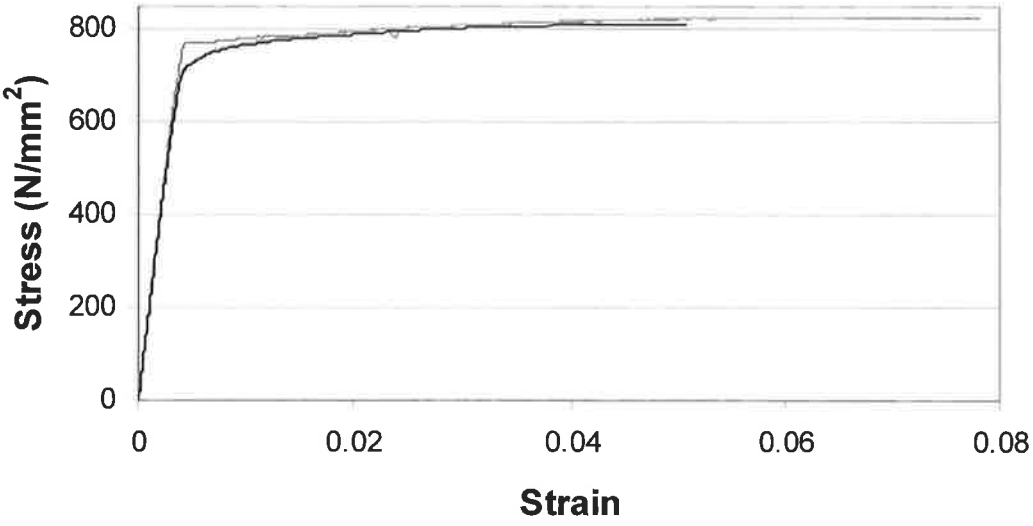

(a) Whole curve

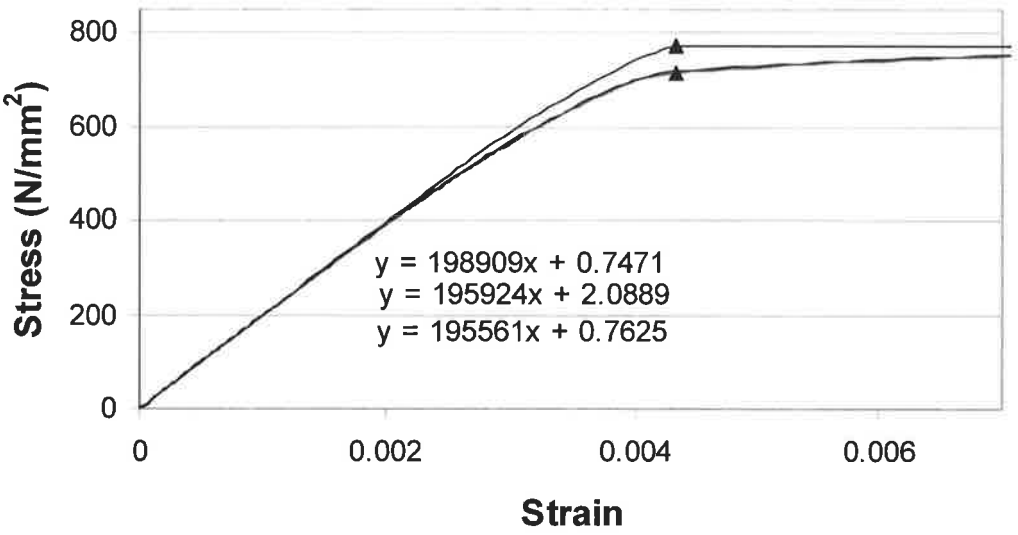

(b) Enlarged linear part with trend line equations

Fig. 10.9 Stress-strain test results of HT6 steel plate

10.4 ANCHOR BOLTS

The shear force vs. deflection (slip) relation is needed to define the properties of the shear connectors on the interface of the plated columns. The shear connector properties are not only affected by the properties of the bolt but also by the properties of the concrete and steel plate. Therefore, bolt shear tests, as illustrated by Fig.10.10, were conducted to determine the shear connection properties. The actual test set up is shown in Fig.10.11. The concrete blocks were cast from the same batch of concrete that was used to fabricate the column specimens. Hence, the material properties were considered to be the same.

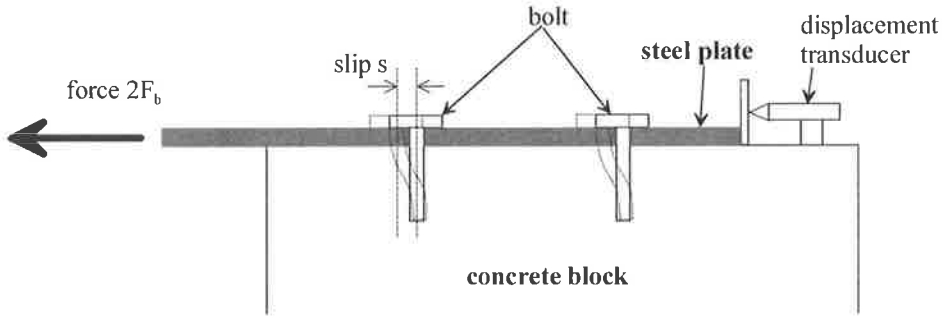

Fig. 10.10 Bolt shear test

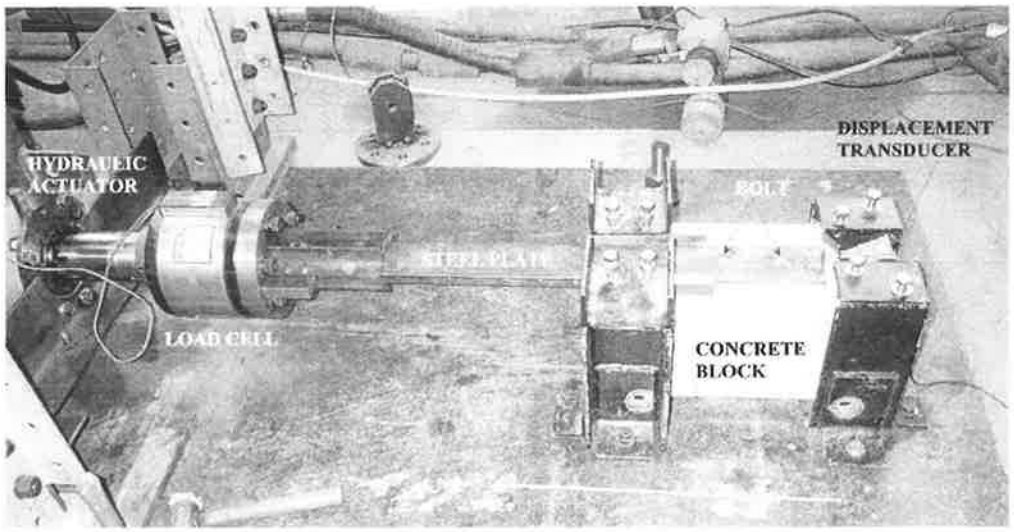

Fig. 10.11 Bolt shear test set up

To identify a suitable bolt for bolting plates to the test columns, three types of bolt were tested. These are shown in Fig.10.12. Two of the bolts are common Hilti bolts: the Hilti HSL ϕ12 bolt and the Hilti HIS ϕ12 bolt. The Hilti HSL ϕ12 bolt is a mechanical bolt that relies on mechanical interlocking from the end expansion to provide the anchor force. The Hilti HIS ϕ12 bolt is a chemical bolt. It relies on chemical bond to provide the anchor force. Hilti HIT HY 150 adhesive is used as the bonding agent for this bolt.

The third type of bolt considered was a threaded rod bolt. It was cut from ϕ12 threaded rod of high tensile steel. The internal diameter of the threaded rod was 9.853mm with an effective diameter of 10.863mm. Tensile tests similar to those conducted on the reinforcing bars without strain gauges were conducted to determine the yield strength of the threaded rod, which is given in Fig.10.13. This bolt was anchored by chemical bond using Hilti Hit HY 150 as the bonding agent.

Fig. 10.12 Types of bolts

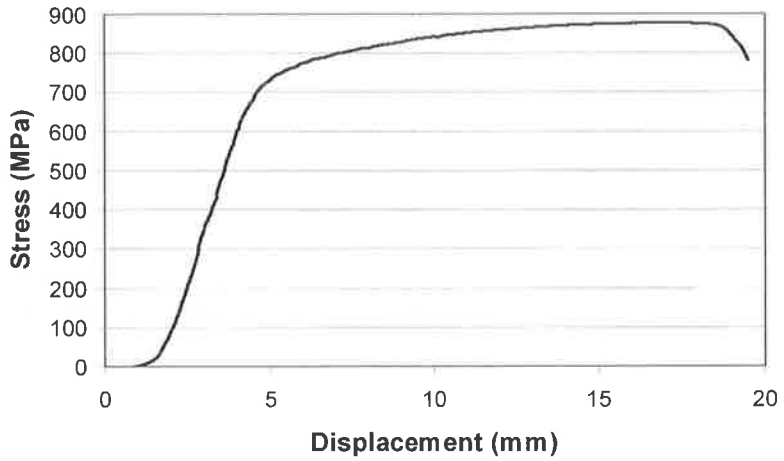

Fig. 10.13 Tensile test result of the threaded rod

The installation procedure for the two Hilti bolts followed the standard procedure as per specifications. The installation procedure for the threaded rod bolt was described in Section 9.2.2. All types of bolt were tightened with 25 Nm torque using a torque wrench. The embedment length of all the bolts was 70mm from the face of the concrete to the end of bolts.

In the testing as shown in Fig.10.11, a pull force was applied by the hydraulic actuator to the steel plate in a displacement control manner. The displacement was applied at a (slow) rate of about 1~3mm/per minute. The applied force and the movement of the steel plate (slip) were then recorded using a load cell and displacement transducer, respectively. This data was then used to produce the load vs. slip plots.

The Hilti HSL bolt was tested on the 2nd November 2000 when the concrete age was 116 days. The Hilti HIS bolt was tested on the 10th November 2000 at a concrete age of 124 days. The threaded rod bolt test was conducted on 7th November 2000 at a concrete age of 121 days. Figures 10.14, 10.15 and 10.16 show the bolt slip test results for the Hilti HSL bolt, Hilti HIS bolt and threaded rod bolt, respectively.

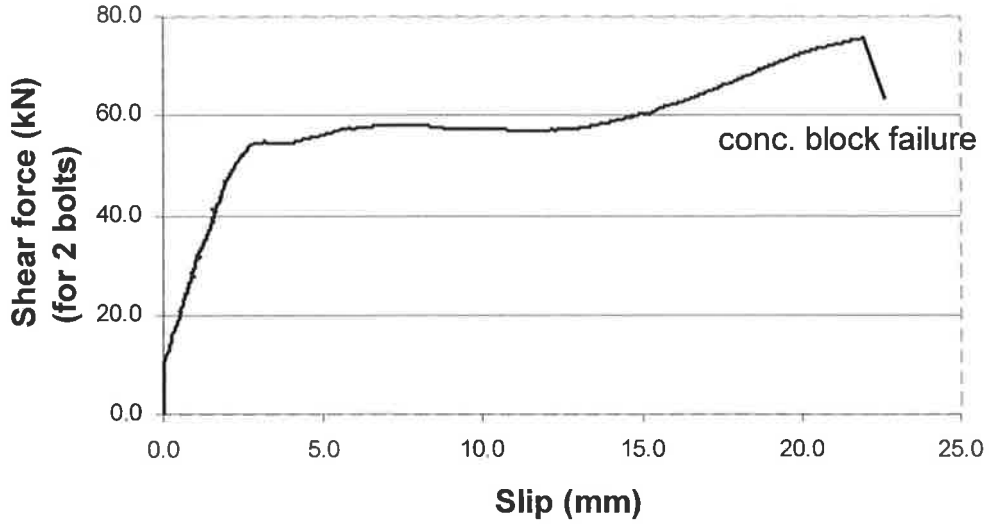

Fig. 10.14 Hilti HSL ϕ12 bolt test

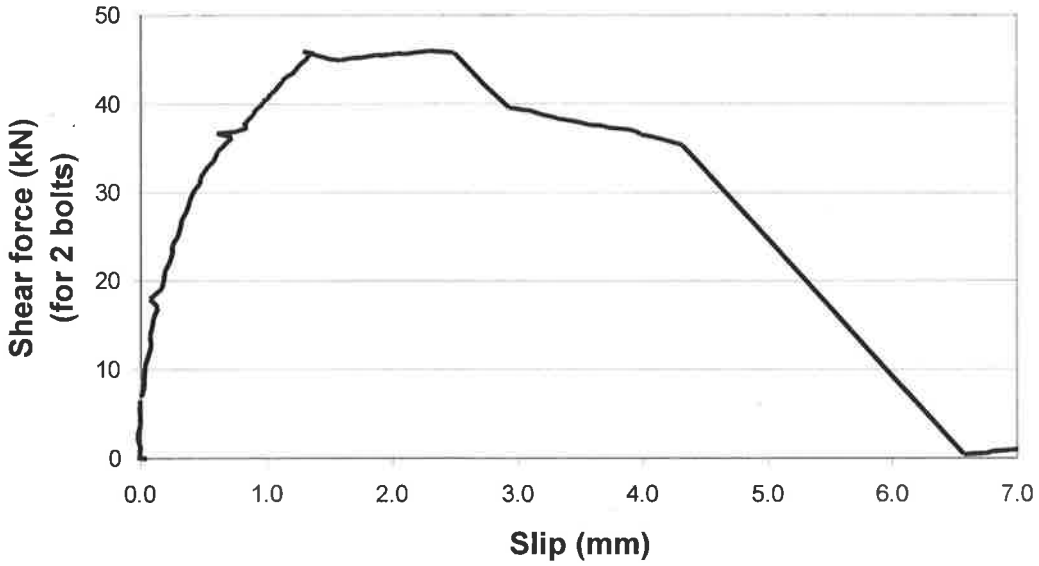

Fig. 10.15 Hilti HIS ϕ12 bolt test

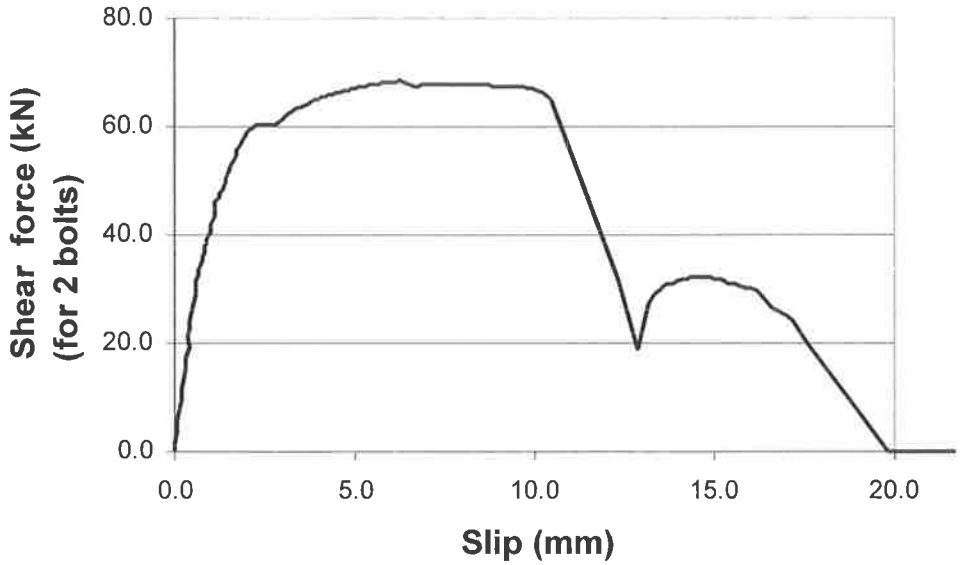

Fig. 10.16 Threaded rod bolt test

In all the three tests, the bolt on the far side of the loading arm was slightly pulled up in the final stage of loading, as shown in Fig.10.17 where the Hilti HSL bolt was pulled up about 5mm prior to failure. The Hilti HSL bolt test ended with the breaking of the concrete block, as shown in Fig.10.18 and Fig.10.19. Since most of the important curve for this bolt had already been obtained, this test was not repeated. However, additional measures were taken to prevent concrete block failures in the remainder of these tests. Two strong steel rods were added between the two corner anchor points that changed the point supports to uniformly distributed supports, as shown in Fig.10.20.

The Hilti HIS bolt test failed with the shearing off of the bolts below the plate in the concrete layer as shown in Fig.10.21. From Fig.10.15, it can be seen that the two bolts did not fail simultaneously as suggested by the two drops on the curve. It seems that the

first bolt (closer to the load cell) snapped first and the second bolt broke about a minute later. The failure mode of the threaded rod bolt was similar, as shown in Fig.10.22.

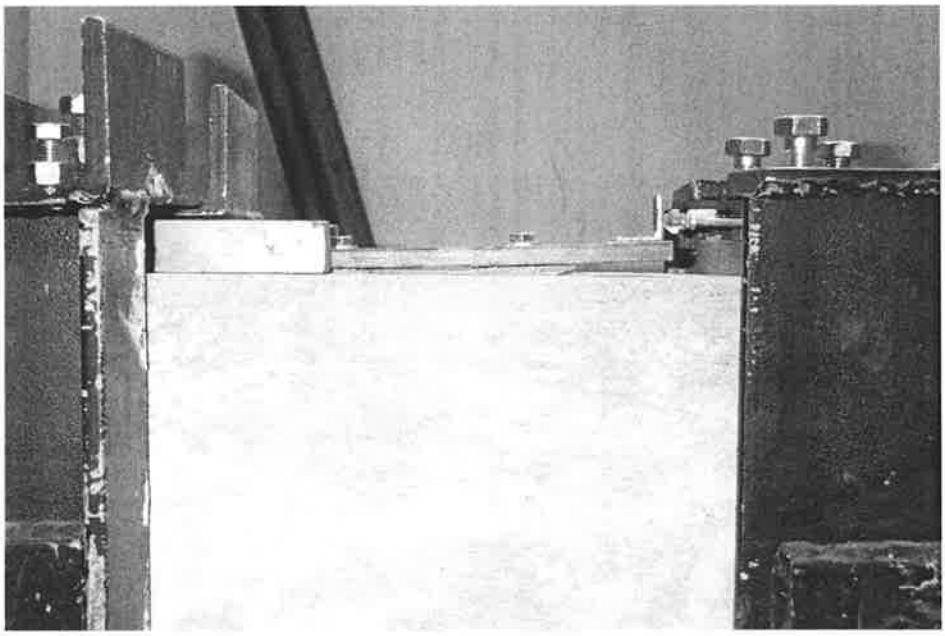

Fig. 10.17 Lifting up of second bolt

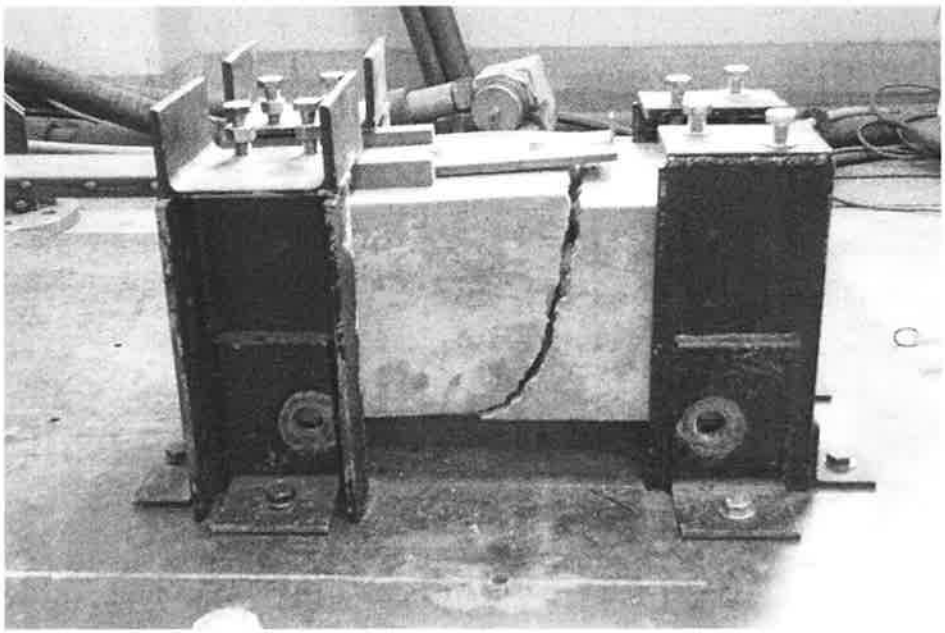

Fig. 10.18 Failure mode of Hilti HSL ϕ12 bolt test

Fig. 10.19 Hilti HSL bolt and concrete block after test

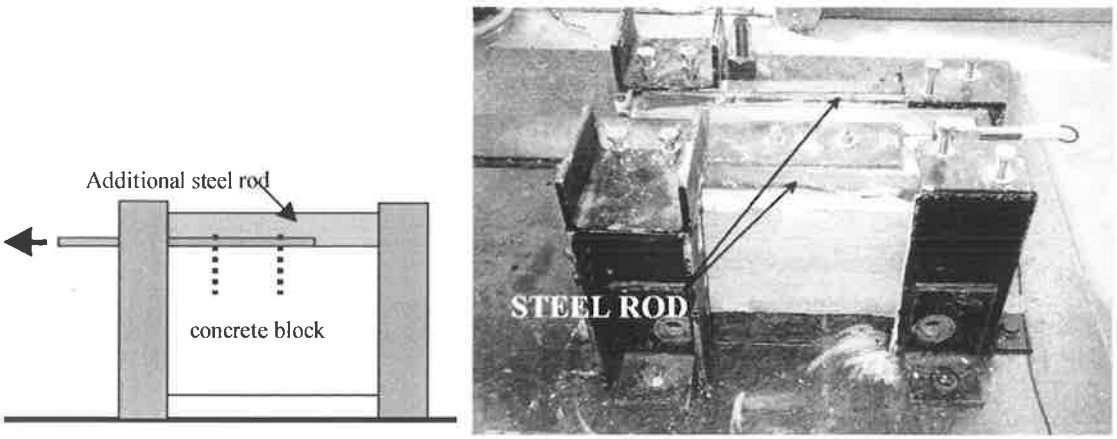

Fig. 10.20 Uniform distributed supports to prevent concrete block failure

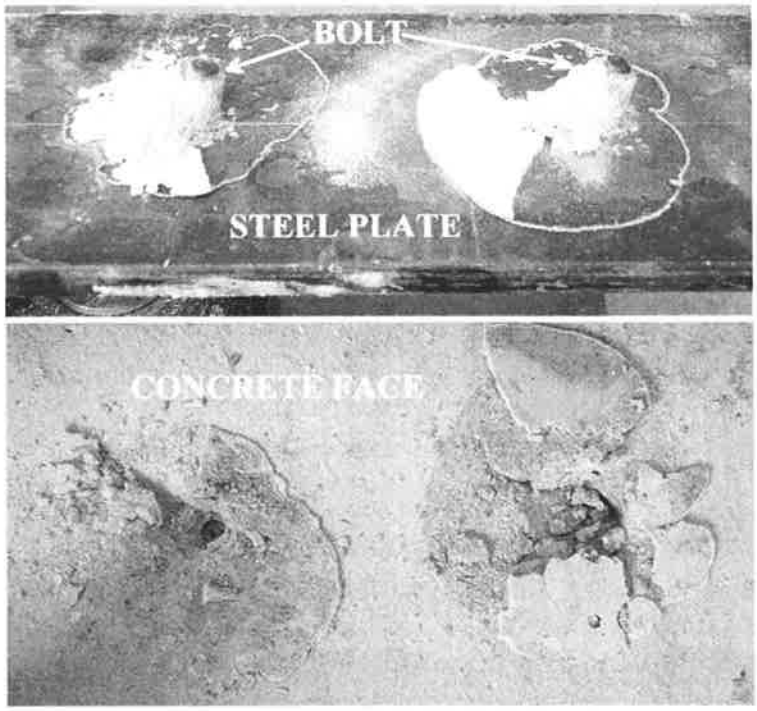

Fig. 10.21 Failure mode of Hilti HIS bolts

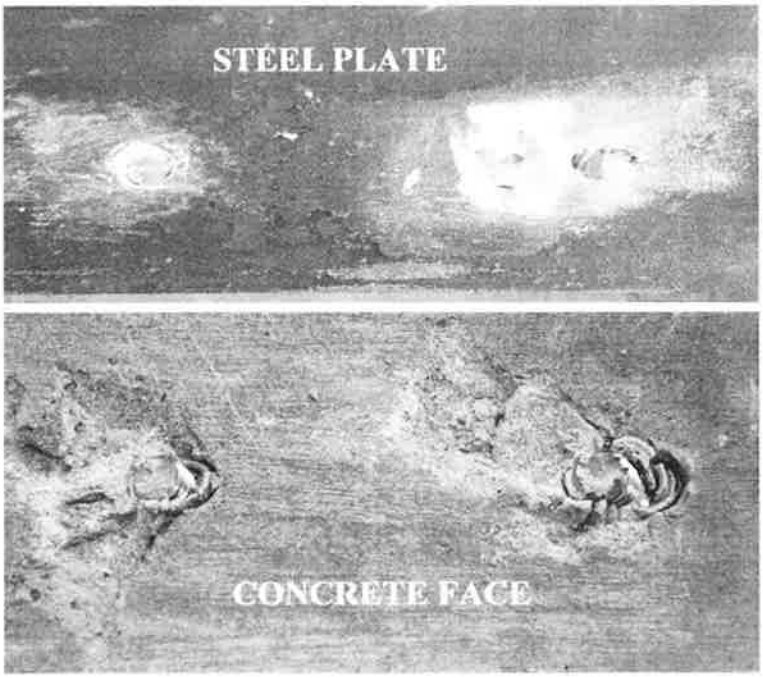

Fig. 10.22 Failure mode of threaded rod bolts

From the bolt test results of Figs.10.14-10.16, it can be seen that the threaded rod bolt is the strongest and stiffest. From a ductility point of view, the Hilti HSL ϕ12 bolt is the best. From the theoretical studies in this thesis, it has been shown that the stiffness and strength of bolts are more important to plated columns than the ductility which is not critical since columns fail (concrete crushes) before excessive slip takes place. Therefore, it was decided to use the threaded rod bolts for column plating. Furthermore, the threaded rod bolts are also much cheaper than Hilti bolts.

As discussed in Section 4.1.4, the load vs. slip relation is represented by a bi-linear model in the numerical simulations. The bi-linear "best fit" curve for the original test data of the threaded rod bolts is shown in Fig.10.23, from which the properties of the bolt shear connector were obtained and which are summarized in Table 10.6.

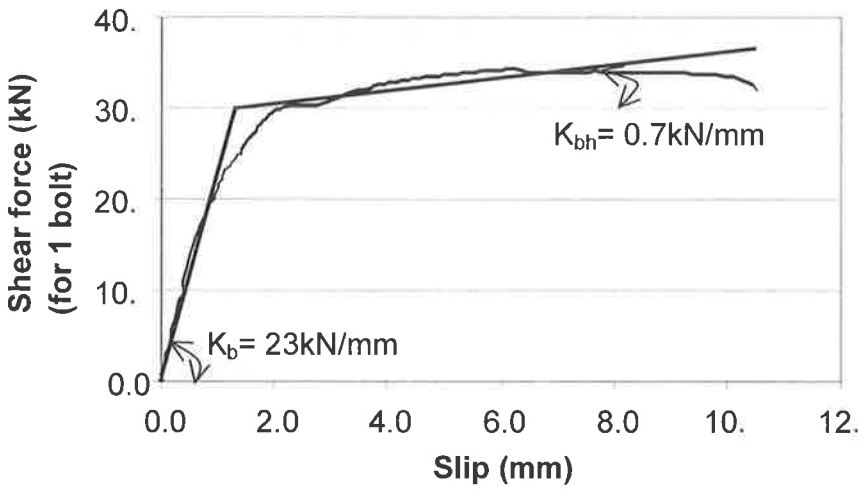

Fig. 10.23 Load-slip model of threaded rod bolt

Table 10.6 Summary of bolt properties

Brand	Diameter (mm)	Yield strength F_{by} (kN)	Elastic stiffness K_b(kN/mm)	Strain hardening stiffness K_{bh}(kN/mm)
Threaded rod bolt	12	30.0	23	0.7

10.5 GLUING AND BOLTING

As one test column was retrofitted by gluing and bolting a plate to the face of the column, this connection was also tested. The same setup as described in Section 10.4 for the bolt connector tests was used for this test. The actual test specimen is shown in Fig.10.24 where the cross-hatched area indicates the section of the plate (200mm × 100mm) that was glued. The brand of glue used was Ciba Performance Polymers Araldite LC 340 with Hardener LC340. Before gluing, the face of the steel plate was sand blasted to provide a better bond. The concrete face was roughened with a needle gun. Threaded rod bolts, applied as described in Section 10.4, were used for bolting. The glued area and the two bolts were equivalent to one row of bolting in the actual plated column at a same cross-section.

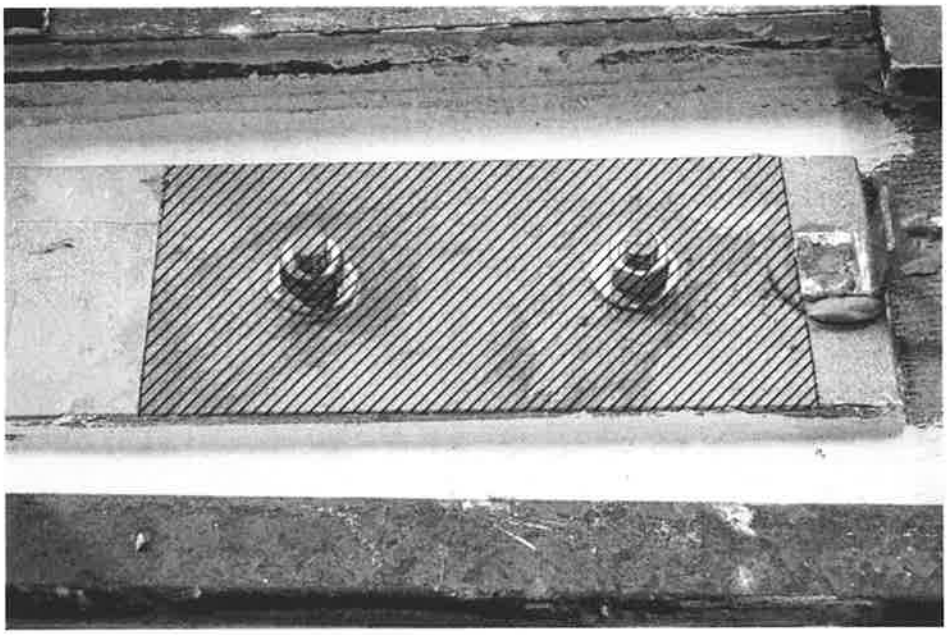

Fig. 10.24 Test specimen of gluing plus bolting

The test was conducted on 9th November 2000 at a concrete age of 123 days. To get the softening branch of the load vs. slip response curve, a displacement control procedure was adopted for loading. Because there is essentially no slip with a glued plate before the bond breaks down on the interface, the movement of the loading arm of the hydraulic actuator had to be very slow. A loading rate of 3mm/per hour (in contrast to 1-3mm/minute for the unglued bolting tests) was tried initially but this was eventually increased to 8mm/per hour.

The movement of the actuator actually did not produce any slip on the interface before the bond break down. Instead, it produced an elongation of the steel plate and the lateral deformation of the supporting frame that fixed the concrete block to the ground. Actually, it is the increase in deformation of the test set up that gives a continuous increase in the test load. As the external force from the hydraulic actuator must be balanced by the reaction force from the supporting frame, the more the supporting frame deforms, the more reaction load is applied. The test result is shown in Fig.10.25.

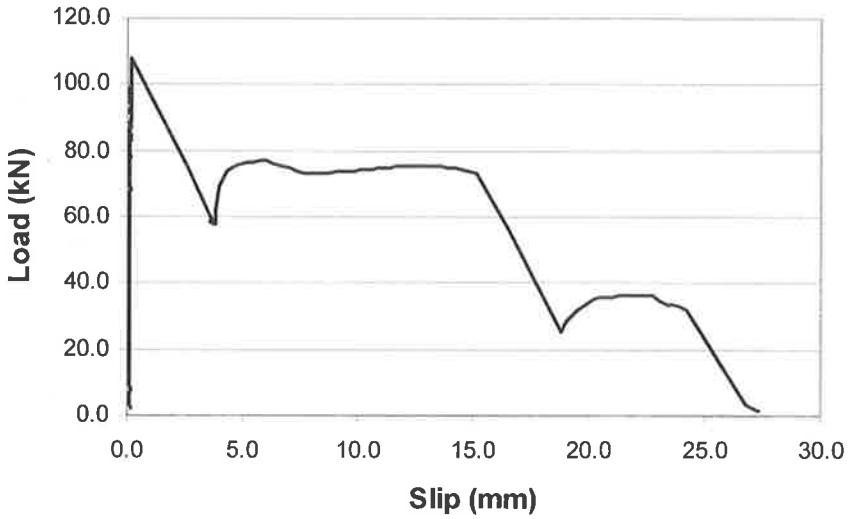

Fig. 10.25 Gluing plus bolting test

In the test, the bond broke down suddenly at a load of 108kN. Up to this point negligible slip had been measured at the interface. The test then continued at an increased loading rate of 3mm/per minute until the bolts failed in shear as observed previously. After the glue bond broke, the system behaved similarly to the threaded rod bolting system giving a similar result as can be seen by comparing Fig.10.25 with Fig.10.16.

The failed specimen is shown in Fig.10.26 and 10.27. The failure plane shows that the gluing on the front area near the loading side is partly debonded, as indicated in Fig.10.27. The rest of the plane failed due to concrete peeling off.

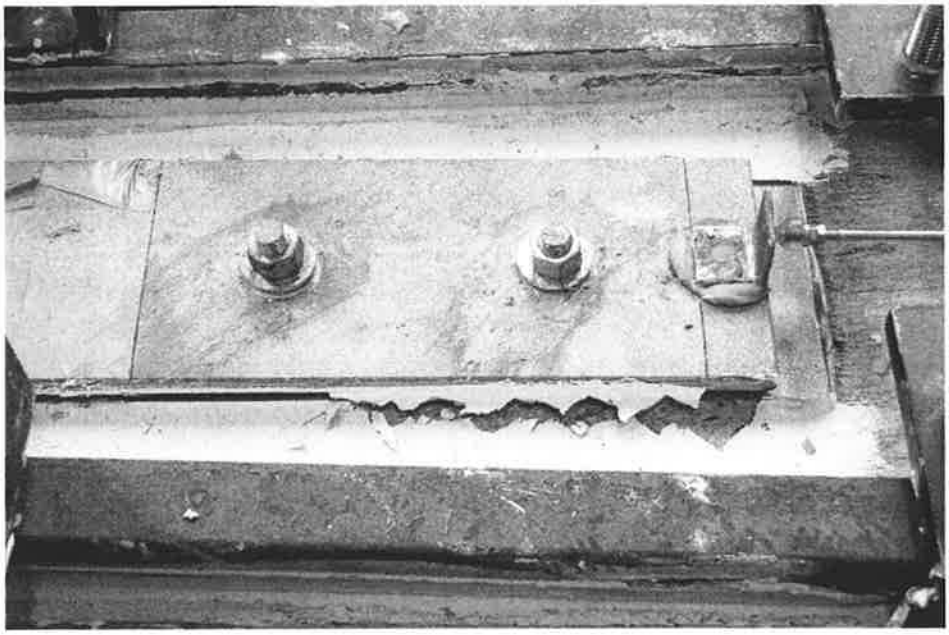

Fig. 10.26 Failed specimen of gluing plus bolting

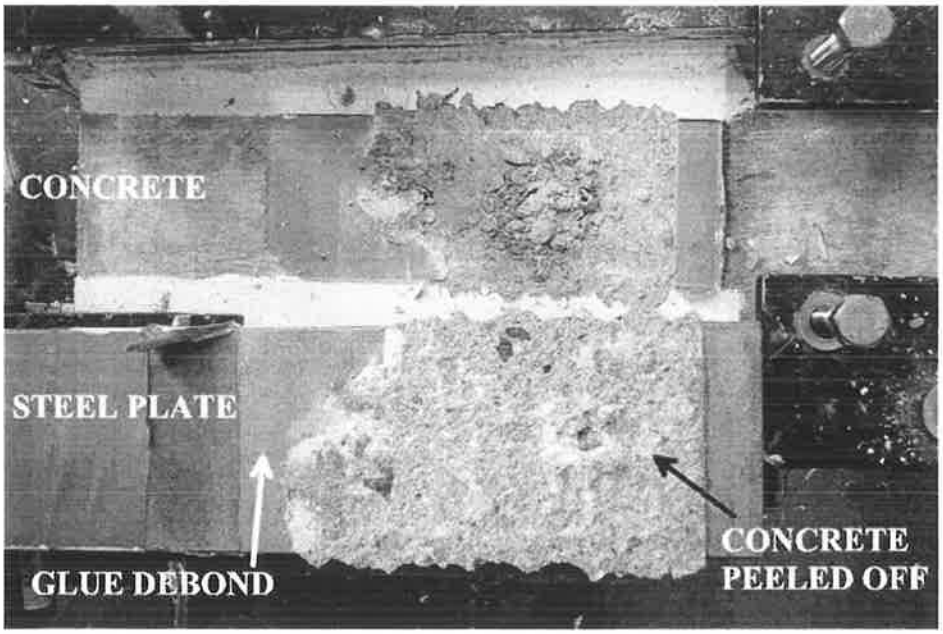

Fig. 10.27 Failure plane

The conclusion from this test was that the average bond stress by this type of gluing may be estimated by

$$\sigma_b = 108000/(200\times100) = 5.4 \text{ (MPa)}$$

This is a very rough but simple estimation. However, it is sufficient for estimating the minimum glue length (or area) for full interaction plating. At full yielding of the steel plate, the minimum glue length for the 12mm thick steel plate can be estimated by

$$l = 306.9\times12/5.4 = 682 \text{ (mm)}.$$

As the full glue length is 950mm as shown in Fig.9.8, this bond length is considered adequate. The column test result that will be presented in Section 11.2 confirmed this bond length, as no debonding was observed in the test.

CHAPTER 11 COLUMN TESTS

Six column tests, consisting of three monotonic static tests and three quasi-static cyclic tests, were conducted to investigate the effectiveness of the new retrofitting scheme as well as to verify the results of numerical simulations. The details of the testing procedures are given in Chapter 9. The test process, observations and test results are reported in this chapter. The discussion of the test results will be presented in Chapter 12. The notation used to identify each of the six test specimens in the following sections is defined in Section 9.1. The test data, such as displacements and strains, were collected at specific locations that are indicated in Section 9.4 where it is also noted that the strain reading shall be treated as a reference only and may not be accurate. A constant axial load of 360kN was applied to all the specimens.

11.1 TEST RESULTS OF SPECIMEN 1AMR

The first test consisted of a monotonically loaded test of the "benchmark" reinforced concrete column without any plating. It was tested on 22nd February 2001 at a concrete age of 228 days. The applied load versus deflection response of the column is given in Fig.11.1, where it can be seen that the maximum load (peak point) was 36kN that occurred at a lateral displacement of 25.7mm (2.1% drift). The measured strain values of the longitudinal reinforcing bars and stirrups are shown in Fig.11.2, where it can be seen that the yield point of the tension reinforcement coincided with the peak point of

Fig.11.1. The compression reinforcement yielded at the lateral displacement of about 38.5mm. The stirrups did not yield in Fig.11.2(a).

The progressive damage recorded during testing of the specimen is indicated by Fig.B.1 to Fig.B.6 in Appendix B. The number marked on the small black board and on the cracks of the specimen in the photos, e.g. 4mm in Fig.B.1, is the string pot reading at the bottom of the stub that was not the actual lateral deflection of the column at top. (As noted in Section 9.4, the actual column deformations were calculated using the data from three separate displacement measurements at point B, C and D.) The actual lateral deflections are given in the title of the corresponding figures.

During the test, fine tension cracks in the concrete were noticed at about 5mm of lateral displacement (0.4% drift). First signs of significant distress (early signs of crushing and spalling) of the concrete in the compression side occurred at about 20mm of lateral displacement (1.6% drift). The specimen failed due to concrete crushing at a displacement of approximately 120mm (10% of drift), when the axial load could no longer be maintained. The test stopped at this point.

Front and rear views of the failed specimen are shown in Figs.11.3 and 11.4, respectively. The final crack pattern and extent of concrete crushing are highlighted in Fig.11.3 where it can be seen that the tension crack opening was concentrated in the first crack about 100mm away from the face of the stub, and the extent of concrete crushing was about 140mm at the bottom of the column.

Table 11.1 Test results of specimen 1AMR

	Peak point	Failure point	Failure mode	Softening slope
Lateral force (kN)	35.9	1.0	Concrete crushing	0.36 KN/mm
Displacement (mm)	25.7	122.4		
Tensile bar strain	0.0027	0.0037		

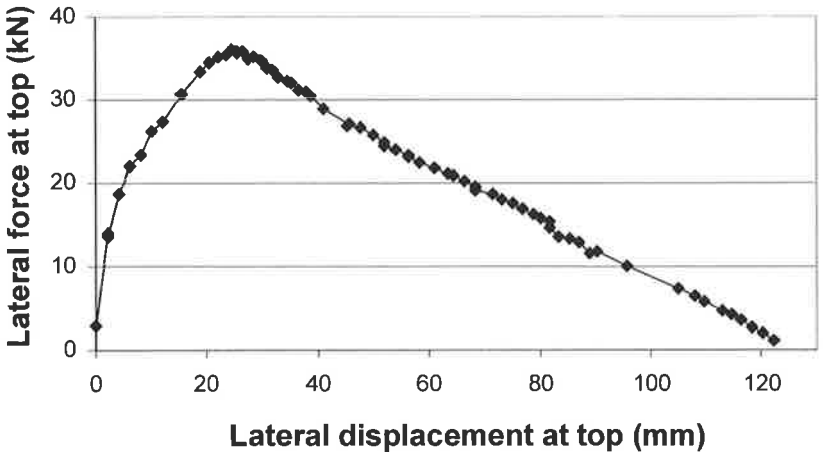

Fig. 11.1 Response of column specimen 1AMR

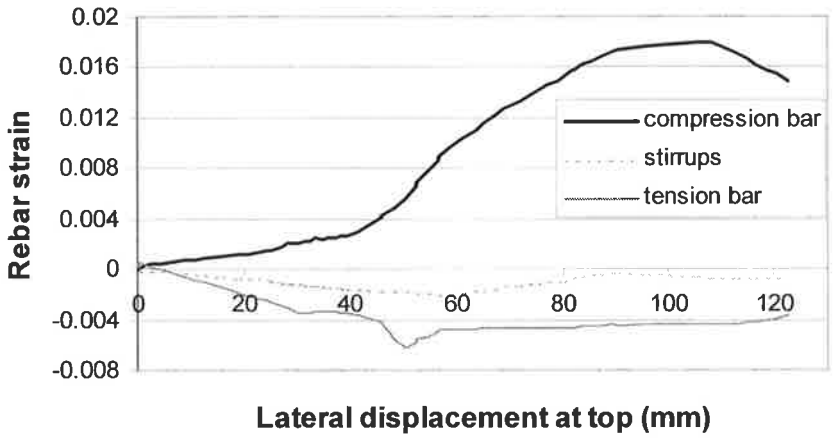

(a) Whole curve

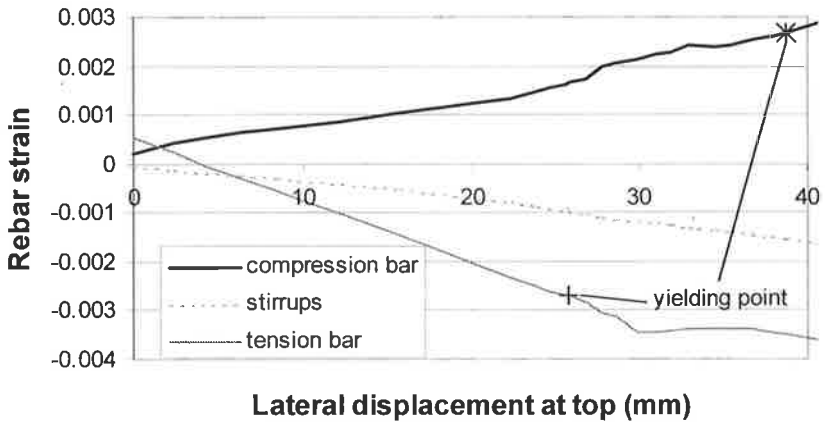

(b) Enlarged linear part

Fig. 11.2 Measured strains in reinforcing bars for specimen 1AMR

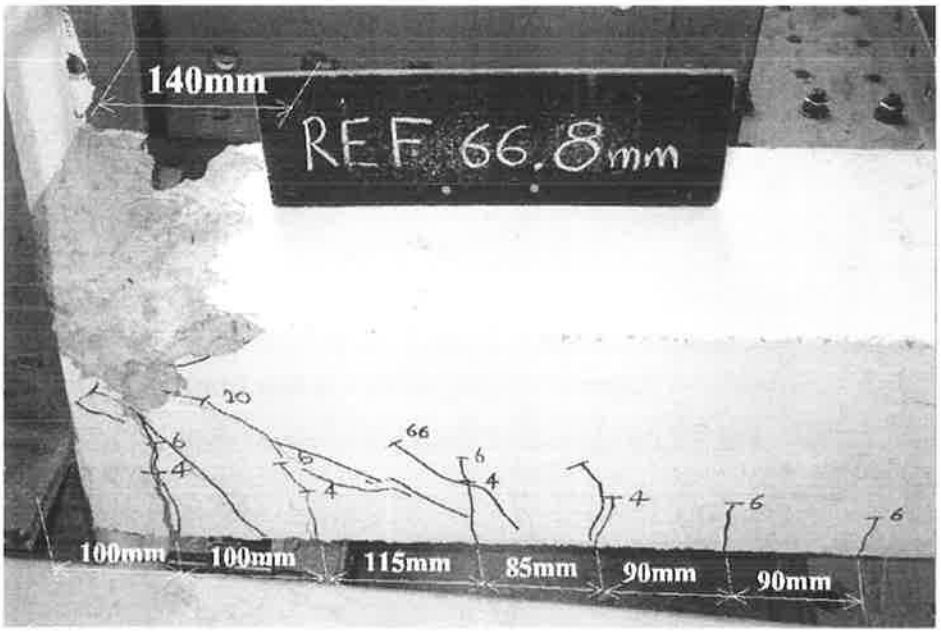

Fig. 11.3 Front view at displacement of 123mm for specimen 1AMR

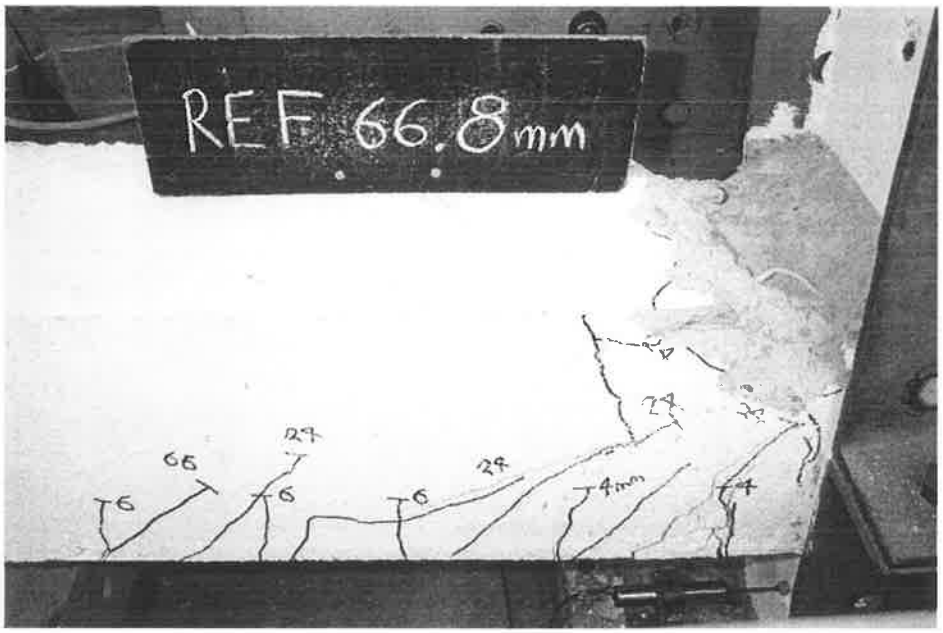

Fig. 11.4 Rear view at displacement of 123mm for specimen 1AMR

11.2 TEST RESULTS OF SPECIMEN 2AMF12

This was a monotonically loaded test of the column with a 12mm thick mild steel plate glued and bolted on the compression face (full-interaction plated column). It was tested on 13th March 2001 at a concrete age of 247 days. The load versus deflection response for the column is given in Fig.11.5 where the maximum load (peak point) reached 55.3kN at a lateral displacement of 20.7mm (1.7% drift). It is noted that the initial displacement of the column was a negative value. As mentioned in Section 9.5.4, the first data point was recorded after the application of the axial load and before any movement of the vertical load jack. Therefore, the negative displacement of the first data point was caused by the rotation of the stub due to flexure in the member. The flexural moment was caused by the eccentricity of the axial load that was applied at the centroid of the RC cross-section instead at the centroid of the overall composite cross-section.

The measured strain values of the longitudinal reinforcing bars and stirrups are shown in Fig.11.6, where the tension reinforcement yielded (ε_{sy}=0.0026) at about 30mm of lateral displacement which occurred after the peak point of Fig.11.5. The possible reasons for this delay in yielding will be discussed in Section 12.1.1. It can also be seen in Fig.11.6 that the compression reinforcement was loaded into tension at about 22mm of lateral displacement, which was predicted for columns with a strong plating system by the theoretical study in Section 5.2.2. The compression bars yielded in tension after the lateral displacement exceeded 100mm. The stirrups yielded at a displacement of about 76mm (ε_{sy}=0.0035).

Figure 11.7 shows the strains that were recorded in the steel plate on the external face and internal face (interface between concrete and plate) near the base of the column. The steel plate started yielding on the external face at a lateral displacement of about 65mm, after which the strain on the external face increased quickly. The internal face of the steel plate remained elastic before the strain gauge broke at about 56mm of lateral displacement. The shear deformation measured from the bottom 300mm long segment (plastic hinge region) is depicted in Fig.11.8. This shear deformation increased nearly in direct proportion to the lateral displacement and reached a maximum value of about 8.5mm at the end of the test that was equal to about 6.8% of the total lateral displacement of the column.

The progressive damage to the specimen is indicated by Figures B.7 to B.12 in Appendix B. As noted earlier, the numbers marked on the small black board and on the cracks of the specimen in the photos were the string pot readings at the bottom of the stub. The actual lateral deflections are given in the respective title of figures. The overall crack pattern (rear view) at the completion of testing is shown in Fig.11.9. A close-up view of the major cracks (front view) are shown in Fig.11.10.

During the test, fine tension cracks in the concrete were first noticed at about 2mm of lateral displacement. Early signs of shear cracking were observed at about 10mm displacement. Signs of plate debonding at the top of the column occurred at about 50mm displacement, as shown in Fig.B.10. However, no further debonding developed throughout the remainder of this test. Testing was stopped when the maximum travel distance that the setup allowed was reached at the displacement of 125mm. No excessive

sign of distress in terms of instability was observed at any stage during this test except for one major tension crack of more than 5mm width, as shown in Fig.B.12.

Extension of tension cracks into the stub, or column base, was evident, as shown in Fig.11.10. This observation indicates that yield penetration into the support and rotation of the bottom cross-section as relative to the stub occurred in the test. Minor fine cracks between the steel plate and concrete were found at the bottom of the column (see enlarged corner view in Fig.11.11) which indicated possible slip at that region, but no sign of concrete crushing were noticed.

Therefore, it was concluded that the ultimate displacement of this test specimen was not reached during the test. The specimen was still intact in the end of the test.

Table 11.2 Test results of specimen 2AMF12

	Peak point	Failure point	Failure mode	Softening slope
Lateral force (kN)	55.3	N.A.	N.A.	0.21 KN/mm
Displacement (mm)	20.7			
Tensile bar strain	0.0021			

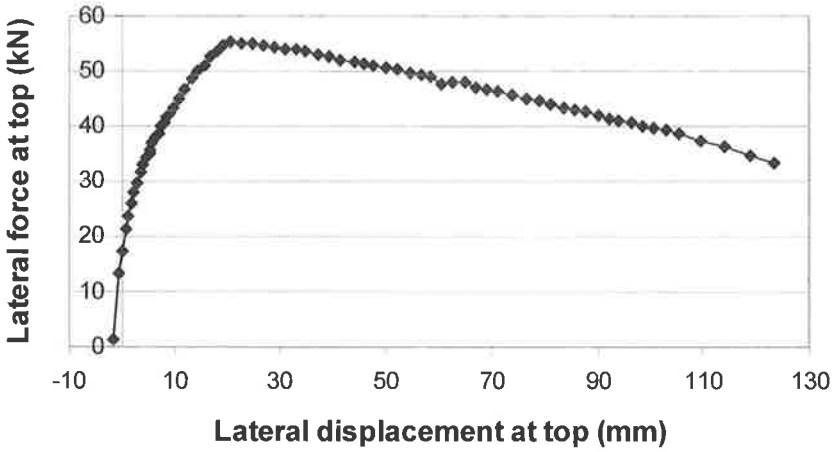

Fig. 11.5 Response of column specimen 2AMF12

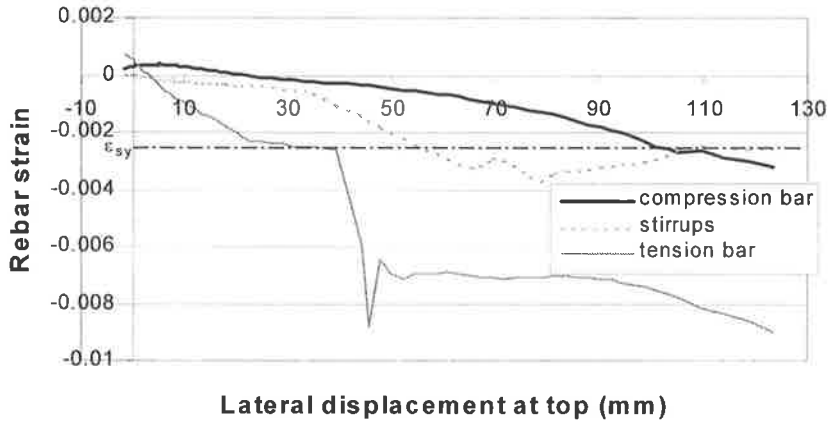

(a) Whole curve

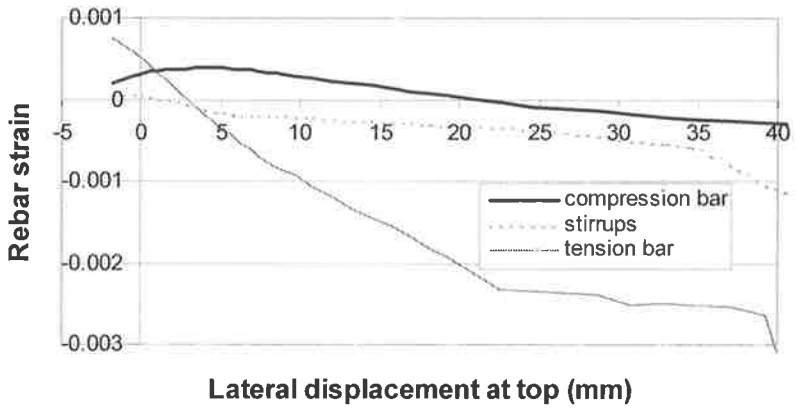

(b) Enlarged linear part

Fig. 11.6 Measured strains in reinforcing bars for specimen 2AMF12

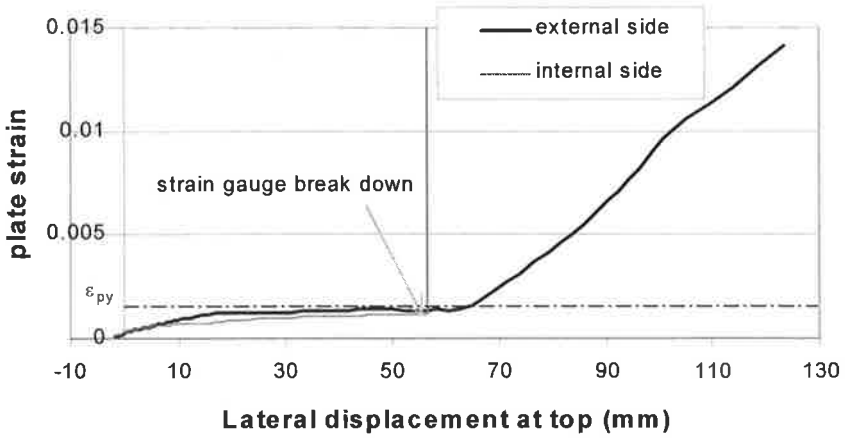

(a) Whole curve

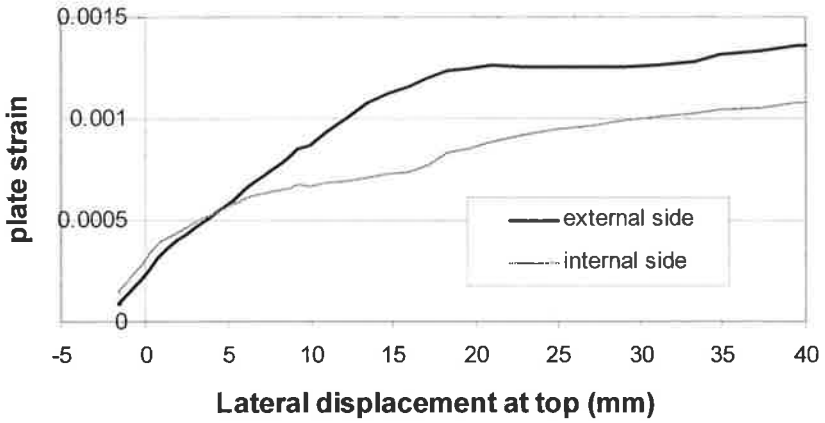

(b) Enlarged linear part

Fig. 11.7 Measured strains in steel plate for specimen 2AMF12

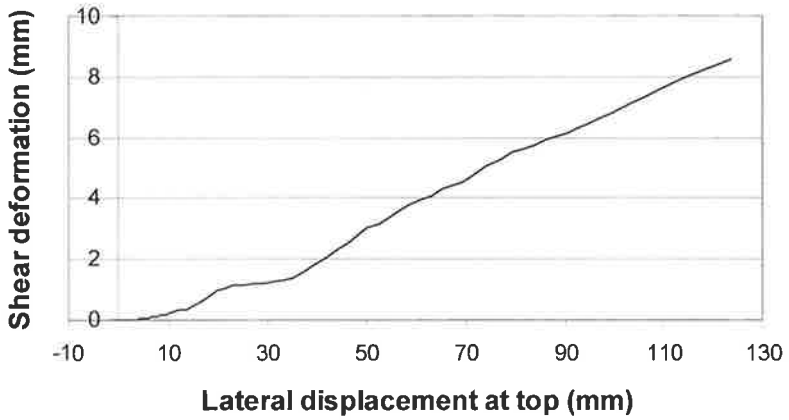

Fig. 11.8 Measured shear deformation for specimen 2AMF12

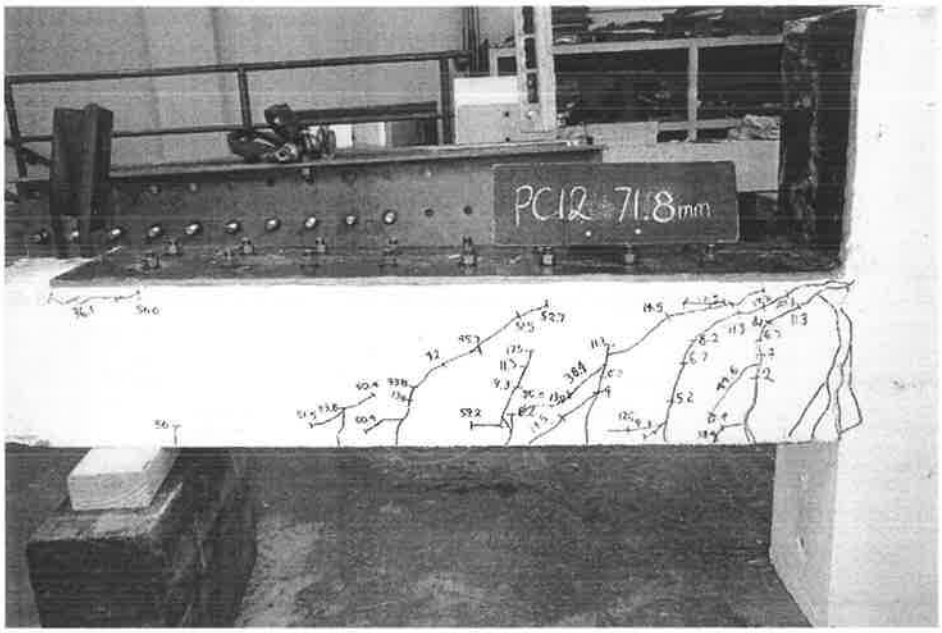

Fig. 11.9 Rear view after test for specimen 2AMF12

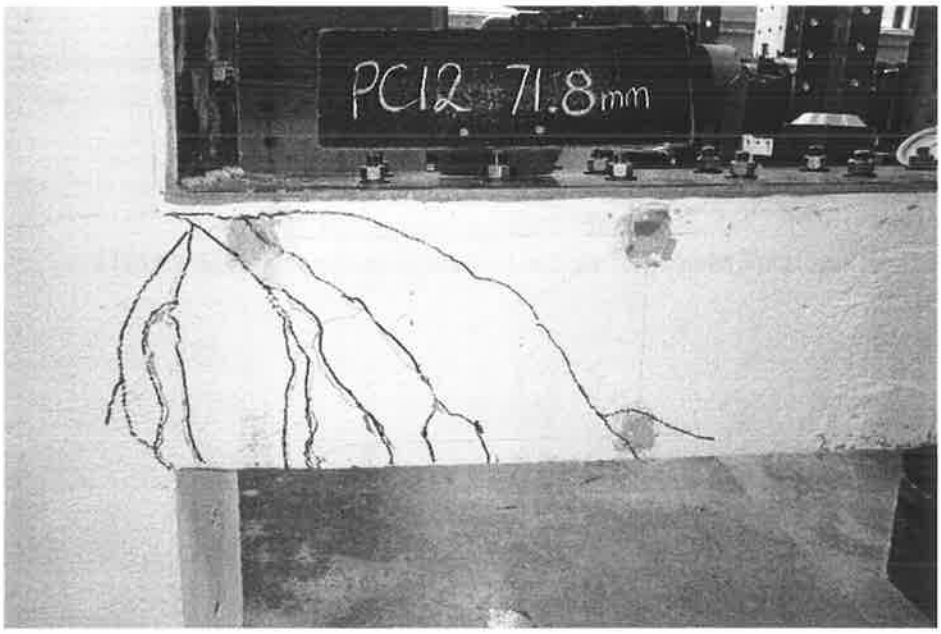

Fig. 11.10 Front view after test showing major cracks for specimen 2AMF12

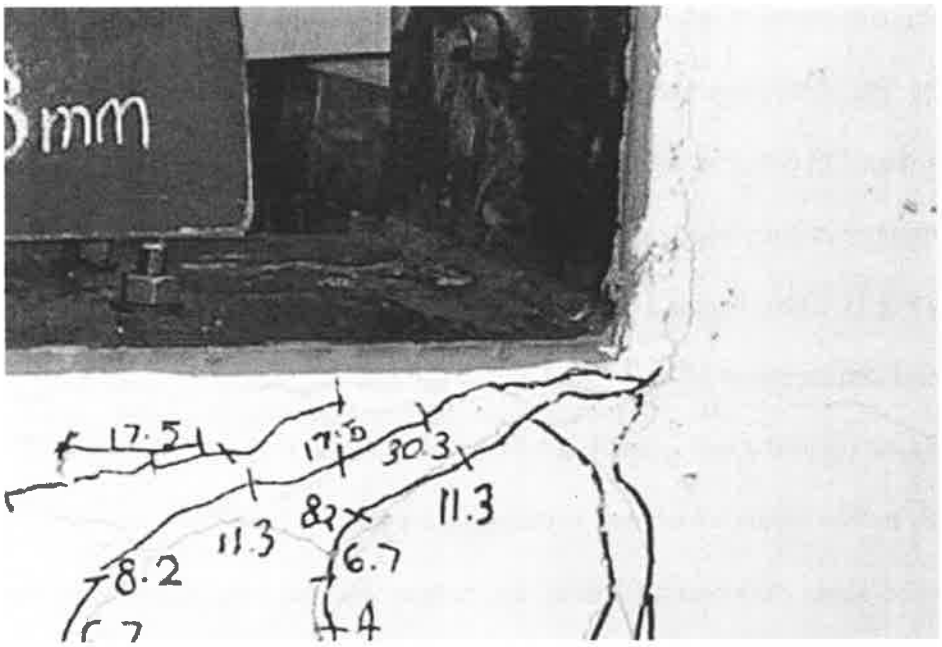

Fig. 11.11 Enlarged view of corner for specimen 2AMF12

11.3 TEST RESULTS OF SPECIMEN 1BMP6

This was a monotonically loaded test of the column with a 6mm thick mild steel plate bolted on the compression face (partial-interaction plated column). It was tested on 27th March 2001 at a concrete age of 261 days. The load versus deflection response of the column is given in Fig.11.12 where it can be seen that its peak strength was 39.3kN which occurred at a lateral displacement of about 26.3mm (2.2% drift).

The measured strain values of the longitudinal reinforcing bars and stirrups are shown in Fig.11.13. Figure 11.14 gives the strains recorded on both sides of the steel plate near the bottom of the column. From Fig.11.13, it can be seen that the tension reinforcement yielded at the same lateral displacement as the peak load was achieved in Fig.11.12 (39.3kN, 26.3mm). In contrast to the full interaction plated column 2AMF12

where the compression reinforcement changed from compression strain to tension strain when the lateral displacement increased, the strain of the compression reinforcement in this test stayed in compression and monotonically increased with the lateral displacement. The compression bar yielded at a lateral displacement of about 26mm. The stirrup did not yield in Fig.11.13(a). Figure 11.14 shows that the external face of the steel plate yielded at a lateral displacement of about 46mm, and the internal face of the steel plate remained linear elastic up to the end of the test which meant that full yielding of the steel plate did not occur before failure which was buckling of the plate.

The shear deformation within the bottom 300mm long segment is depicted in Fig.11.15 but it is incomplete due to failure of the instrumentation in the middle of the test. One of the fixing points for the instrumentation broke due to debonding of the glue caused by cracks in the concrete, as can be seen in Fig.11.19.

The slip between the steel plate and the RC column, which was also measured for this specimen, is given by Fig.11.16. The slip measurement positions are detailed in Section 9.4. This was the only test in which the slips were measured. The maximum measured slip was about 2mm as shown in Fig.11.16. This slip was just over the linear elastic limit and much less than the breaking slip of about 10mm, as can be seen from Fig.10.23. The slip distribution was such that it increased from the bottom of the column toward the top of the column. The slips at the measurement points monotonically increased with the lateral displacement except at the bottom point that showed a negative slip at the beginning of the test caused by the initial moment from the axial load eccentricity.

The progressive damage to the specimen is illustrated by Figures B.13 to B.19 in Appendix B. The numbers marked on the small black board and on the cracks of the specimen in the photos were reading of the response "E" (refer Fig.9.25) from the steel arm as described in Section 9.4. This reading was intended to give a direct recording of the actual top displacement of the cantilever column. However, the steel arm was mistakenly fixed to the strengthening frames instead of to the stub of the column in this test. It was found during the test that there was substantial relative movement between the stub and the strengthening frames. Therefore, this reading did not reflect the actual column deflection. In fact, significant discrepancy was found between this direct measurement and the true displacement calculated from readings B, C and D (refer to Fig.9.25 and Section 9.6.2), which is shown in Fig.11.17. This problem was subsequently resolved in the remaining tests by attaching the steel arm directly to the concrete of the stub instead to the strengthening frames. The difference between the directly measured displacement (response "E") in subsequent tests and the calculated displacement (using responses B, C and D) was found to be negligible. The actual lateral deflections (calculated) for this test, therefore, are given in the respective title of figures.

As shown in Fig.B.13, two G-clamps were used at the bottom of the column to prevent sudden buckling of the plate in the early stages of the test. The G-clamps were provided due to safety concerns. They were removed at the column displacement of 93mm, however, when it was felt that sudden instability would not occur even if the plate buckled. Another concern, and reason for the removal of the G-clamps, was that they might strengthen the plating system and possibly affect the test results. Luckily, these clamps were not effective at the time of removal, as the contact between the legs of the

clamps with the plate was still loose, and buckling of steel plate did not occur until a displacement of 106mm was reached. The G clamps were not used in the rest of tests. The test column failed due to buckling of the steel plate, as shown by Figs.11.18 and 11.19. The test was stopped immediately after the plate buckled and the column was unloaded.

Cracks in the concrete at the corner where the steel plate was bearing down were first noticed at a displacement of 6mm, as marked in Fig.B.13. This damage developed continuously through out the test. However, the concrete was able to provide sufficient support to the plate until the end of the test when the plate buckled and the maximum damage to concrete occurred, as shown in Fig.11.18. Sign of concrete crushing in the compression zone of the plastic hinge was noticed at a displacement of about 40mm. Significant concrete crushing in the plastic hinge region occurred after buckling of the steel plate, as shown in Figs.11.18 and 11.19. Cracking was concentrated in 3 major cracks as shown in Fig.11.19.

Table 11.3 Test results of specimen 1BMP6

	Peak point	Failure point	Failure mode	Softening slope
Lateral force (kN)	39.3	24.2	Steel plate buckling	0.19 KN/mm
Displacement (mm)	26.3	105.6		
Tensile bar strain	0.0025	0.0038		

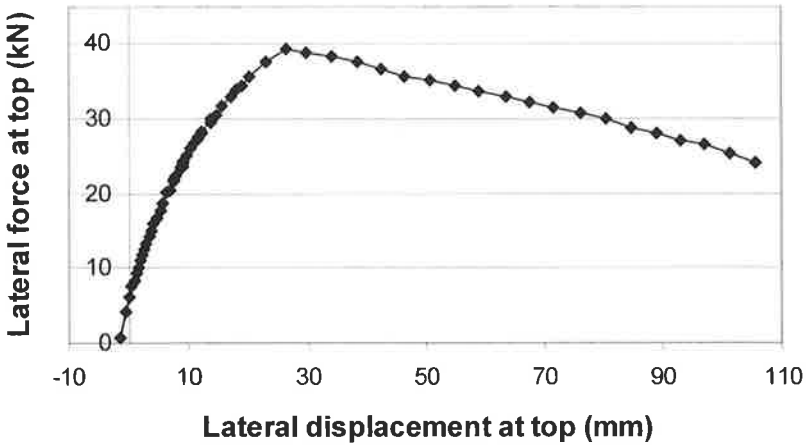

Fig. 11.12 Response of column specimen 1BMP6

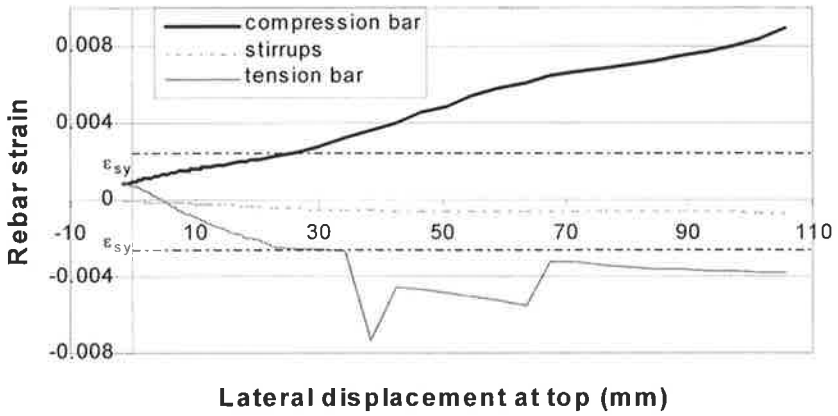

(a) Whole curve

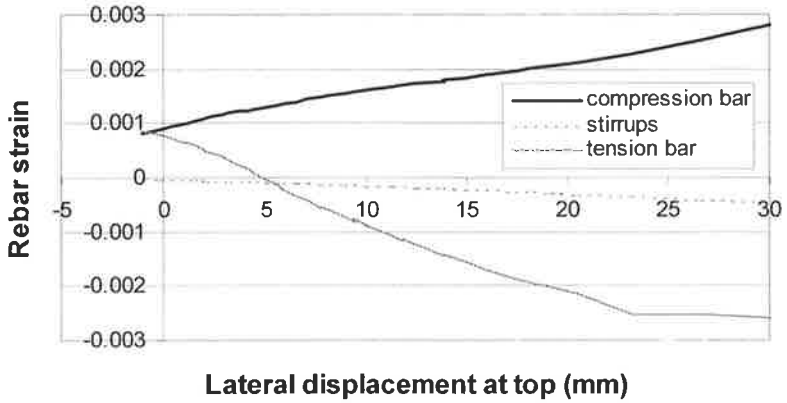

(b) Enlarged linear part

Fig. 11.13 Measured strains in reinforcing bars for specimen 1BMP6

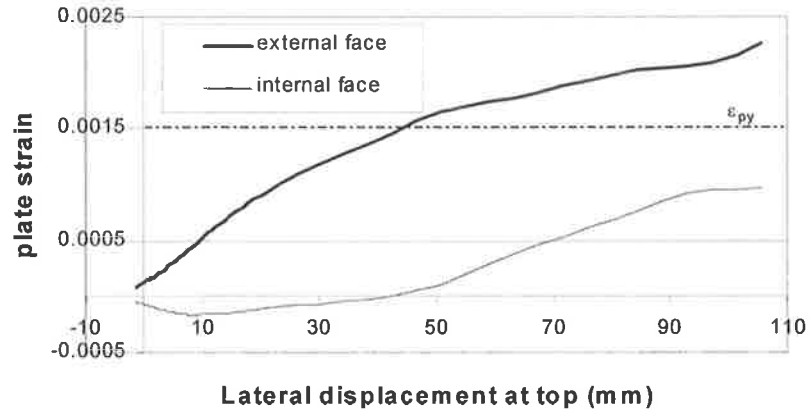

Fig. 11.14 Measured strains in steel plate for specimen 1BMP6

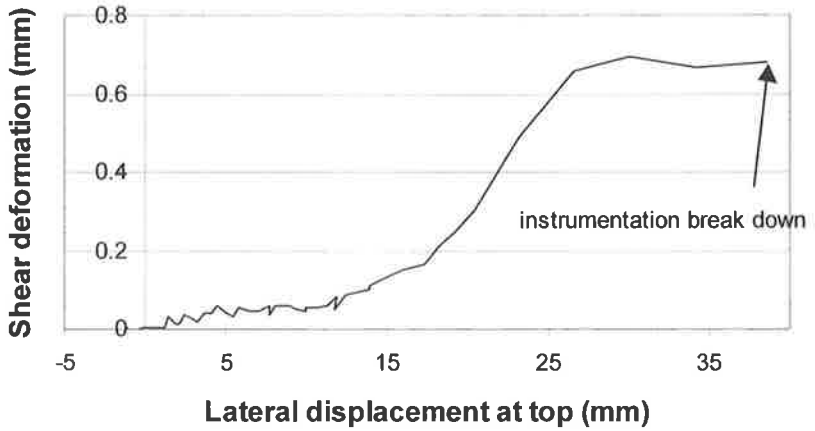

Fig. 11.15 Measured shear deformation for specimen 1BMP6

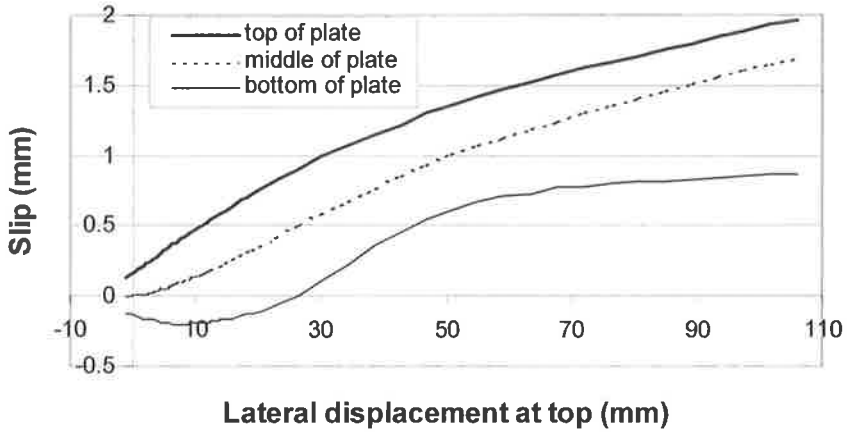

Fig. 11.16 Measured slips for specimen 1BMP6

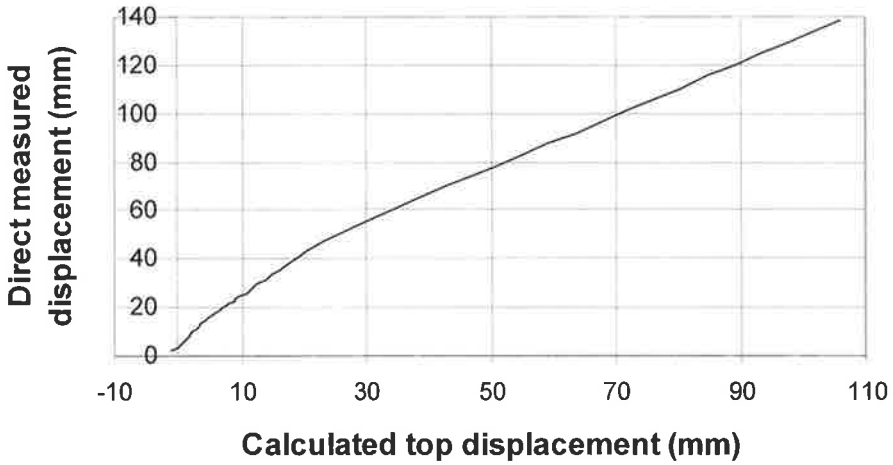

Fig. 11.17 Direct measured displacement for specimen 1BMP6

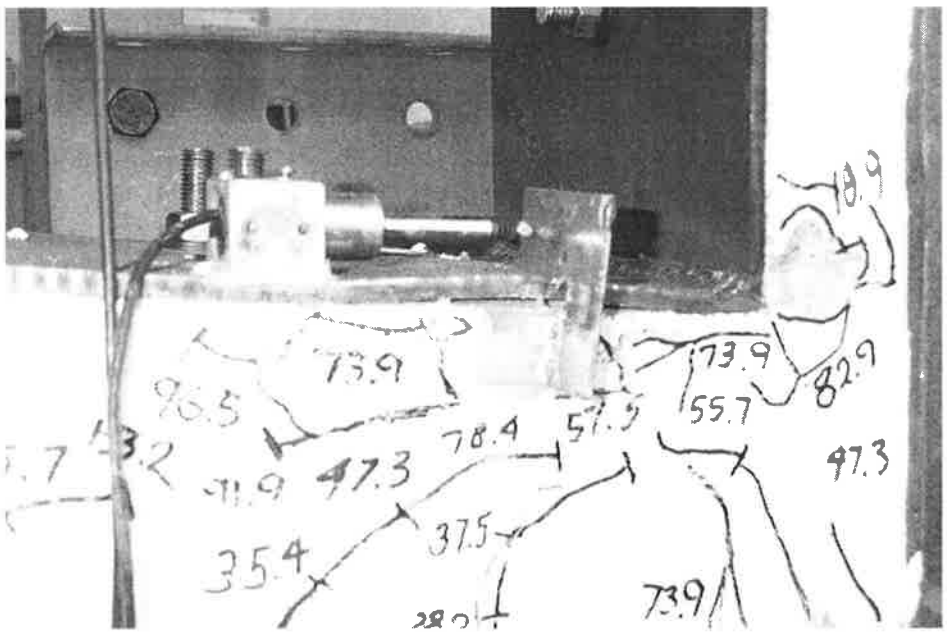

Fig. 11.18 Enlarged rear view at displacement of 106mm for specimen 1BMP6

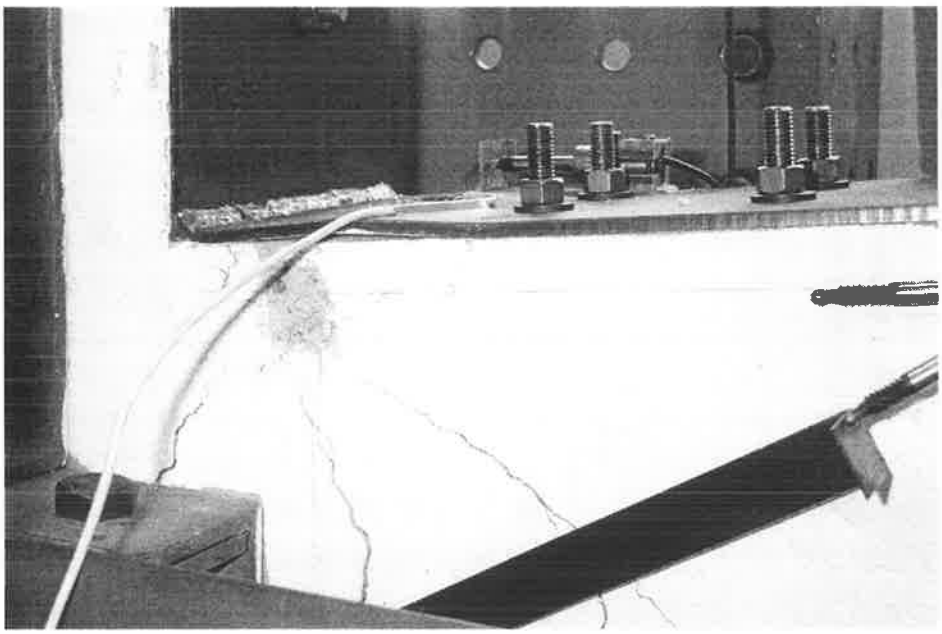

Fig. 11.19 Front view at displacement of 106mm for specimen 1BMP6

11.4 TEST RESULTS OF SPECIMEN 3ACR

This test involved applying quasi-static cyclic loading (as described in Section 9.5.3) to the benchmark column without plating. It was tested from the 16th to 17th of May 2001 at a concrete age of 311 days. The load versus deflection response for the column is given in Fig.11.20, where the lateral load varied from –38.7KN to +32.5KN (as compared to 35.9kN for the monotonic specimen 1AMR). A positive displacement shown in the figure indicates pushing down toward the ground from the initial position and a negative displacement shows a pulling up.

The measured strain values of the longitudinal reinforcing bars and stirrups are shown in Figs.11.21-11.23. The definition (location) of upper and lower bars is given in Fig.9.27. Figure 11.21 shows that the upper reinforcement bar reached a tensile strain of

0.0025 at the negative peak response point (-38.7kN, -26.4mm) of Fig.11.20. The strain at this point was close to the monotonic yield strain of 0.0025-0.0026. However, it needs to be noted that these strain values do not generally indicate yielding status or stress level, as yielding depends on the strain history under cyclic load conditions (as seen in Fig.4.12). A tensile strain of 0.00135 was recorded in the lower bars in Fig.11.22 at the positive peak point (32.5kN, 23.9mm) of Fig.11.20. The reason was not exactly clear for the tensile strain difference between the positive and negative peaks apart from the possible variation in the strain gauge positions as noted in Section 9.4. The stirrups apparently yielded (the monotonic yield strain was about 0.0035) in the last two cycles as can be seen from Fig.11.23.

The progressive damage to the specimen is depicted by Figures B.20 to B.23 in Appendix B and Figs.11.24-11.26. The numbers marked on the small black board in these photos were the actual lateral deflection of the column measured from the steel arm E (see Fig.9.25). However, the "+" and "-" signs in the pictures were opposite to the sign convention of Fig.11.20. The correct sign is given in the respective titles of the figures.

It was noticed that there are a few sudden, but small, drops in the response curve of Fig.11.20. These drops were attributed to the frictional force exerted on the side of the specimen from the lateral restraints shown in Fig.9.20, which were provided to prevent the specimen from swaying out-of-plane. The sway of the specimen can be seen in a photograph of the specimen in Fig.11.26 which was taken after failure. This frictional force from the lateral restraint blocks was reduced in the subsequent tests by greasing the contact faces.

During testing, concrete crushing was observed at about ±20mm of lateral displacement, as shown in Fig.B.20 in Appendix B. The specimen failed due to concrete crushing at a displacement of –56.3mm (compared to 120mm in the monotonic specimen 1AMR), when the axial load could no longer be maintained at which point the test was stopped. The extent of concrete crushing at failure was more than 200mm as shown in Figs.11.24 and 11.25. Obviously, the damage to concrete was more severe under cyclic loading compared to the monotonic test as shown Figs.11.3 and 11.4.

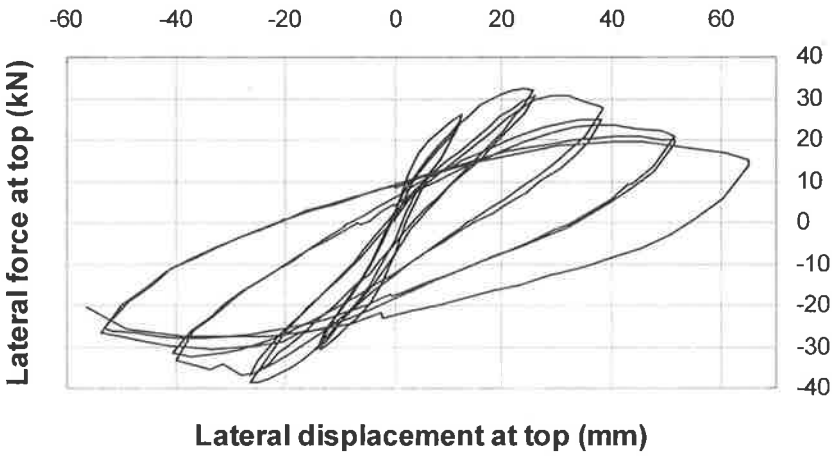

Fig. 11.20 Response of column specimen 3ACR

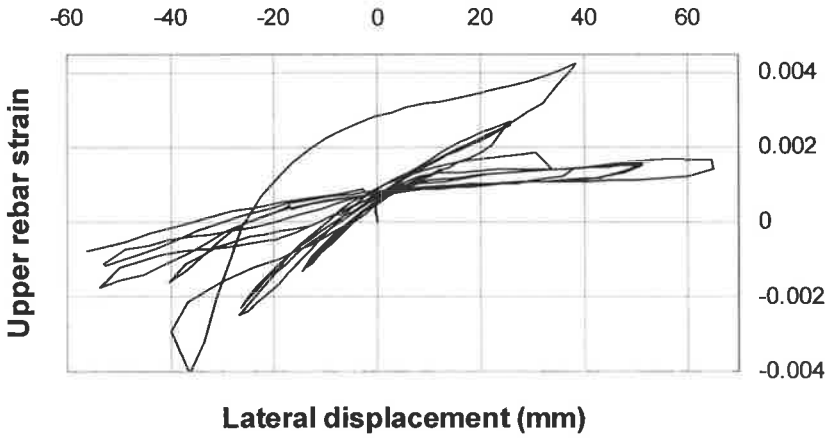

Fig. 11.21 Measured strains in upper reinforcing bar for specimen 3ACR

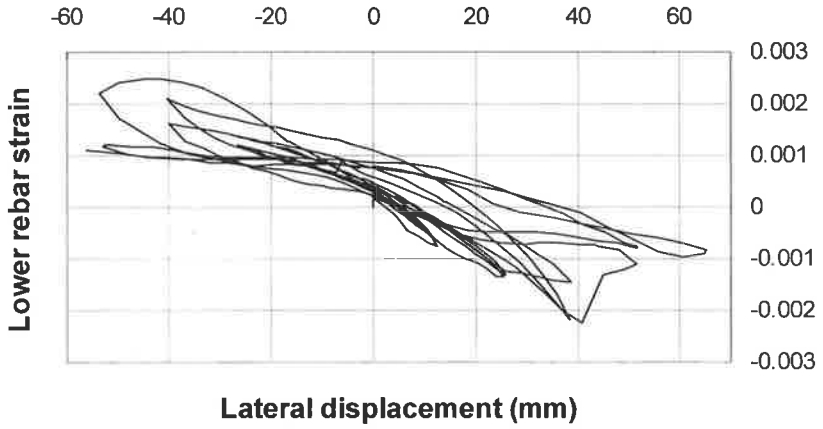

Fig. 11.22 Measured strains in lower reinforcing bar for specimen 3ACR

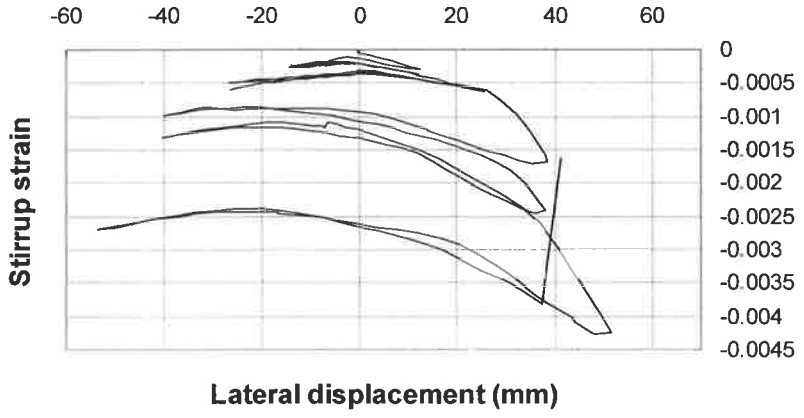

Fig. 11.23 Measured strains in stirrups for specimen 3ACR

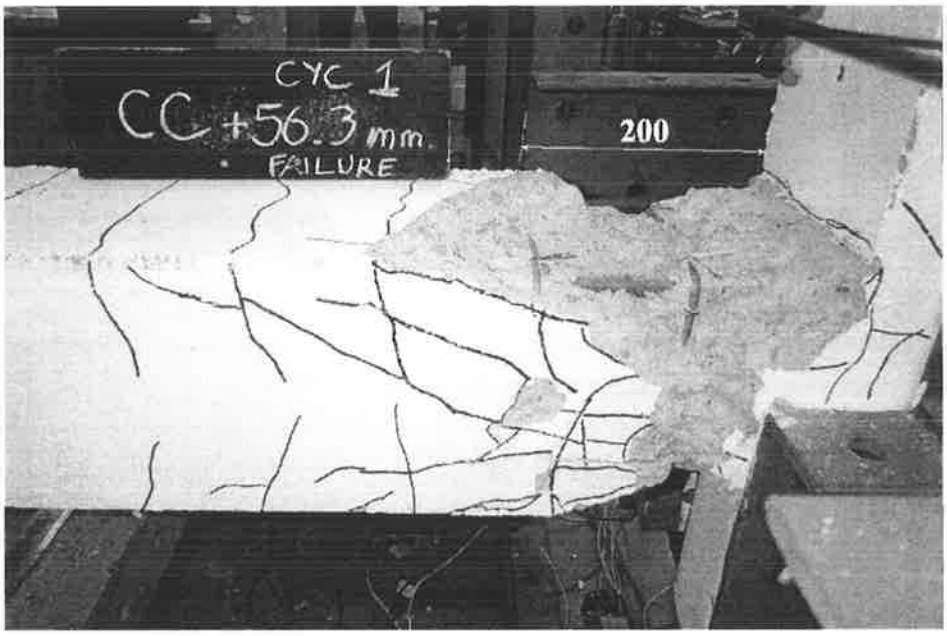

Fig. 11.24 Rear view at –56.3mm displacement of 1st cycle for specimen 3ACR

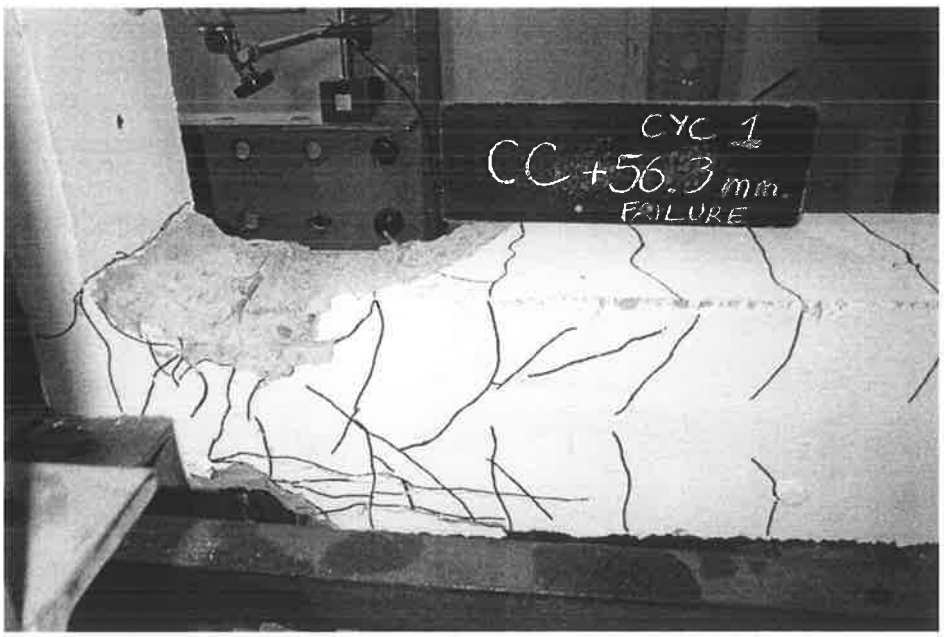

Fig. 11.25 Front view at –56.3mm displacement of 1st cycle for specimen 3ACR

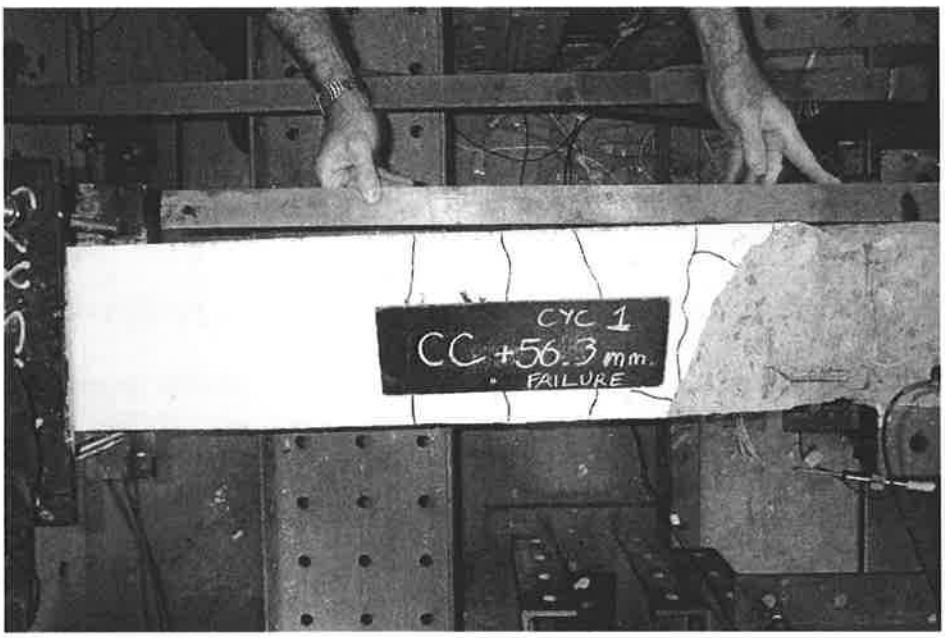

Fig. 11.26 Top view at failure for specimen 3ACR

11.5 TEST RESULTS OF SPECIMEN 4ACP6

This test involved applying quasi-static cyclic loading to a partial-interaction plated column with 6mm thick mild steel plates bolted on both the tension and compression faces. This column was tested from the 6th to 8th of June 2001 at a concrete age of 332 days. The load-deflection response of the column is given in Fig.11.27, where the lateral load varied from –45.9kN to 47.4kN.

The measured strains of the reinforcing bars and steel plates are shown in Figs.11.28-11.36. Figure 11.28 shows that the upper reinforcing bars reached a tensile strain of 0.0042 at the negative peak point (-45.9kN, -32.3mm) of Fig.11.27. At the positive peak point (47.4kN, 26.1mm) of Fig.11.27, the tensile strain of the lower reinforcing bars was 0.0023 as shown in Fig.11.29. Although the monotonic yield strain

0.0025-0.0026 of the reinforcing bar cannot be used to identify the yielding of the reinforcement directly in the cyclic test, the range of the strain variation in Fig.11.28 and Fig.11.29 clearly shows that both the upper and lower reinforcement experienced alternative tension and compression yielding. The stirrups were apparently yielded when the push amplitude exceeded about 60mm of displacement (ε_{sy}=0.00345), as shown in Fig.11.30. The range of strain variation in Figs 11.31 to 11.36 also apparently suggests that both faces of both plates experienced alternative tension and compression yielding (the monotonic yield strain was 0.0015). The steel plate was completely yielded at the end of the test as can be seen from Fig.11.31 and Fig.11.33.

The progressive damage to the specimen is depicted in Figures B.24 to B.48 in Appendix B. As noted above, the "+" and "-" signs of the displacement on the small black board were opposite to the sign convention of Fig.11.27. The correct sign is given in the respective titles of the figures.

In testing, the first sign of concrete crushing was noticed at about ±39mm of lateral displacement (see Figs.B.28 and B.29). The crushing of the concrete continued to develop with further increases in displacement. However, the steel plate seemed to provide adequate compressive resistance (strength) to replace the crushed concrete, as no excessive axial shortening of the specimen was noticed in the test. The integrity of the specimen was also evident from the response curve where no excessive degradation was shown up to the end of the test.

The maximum upward travel distance of the vertical jack was reached at a displacement of –82mm. Therefore, the last 2 cycles went from –82mm to +91mm instead of from the intended –91mm to +91mm, as shown in Figs.B.44 to B.47. Fig.11.37

illustrates damage to the concrete in the plastic hinge zone and the opening of the steel plate at the corner on the tension face in the final cycle.

The test was concluded at this point with monotonic downward pushing of the specimen until the maximum downward travel distance was reached. Fig.11.38 depicts the compression zone of the plastic hinge at the final displacement of about +150mm, from which it can be seen that significant damage to the concrete occurred and signs of buckling of the steel plate was evident. However, because the buckling was toward the concrete side, no instability of the steel plate was observed. Theoretically, the steel plate should always buckle toward the concrete side because the curvature of the plate makes it bends toward the concrete.

The test was then stopped at +150mm of displacement. The extent of the final damage to the specimen is depicted in Figs.11.39 and 11.40. These two photos were taken after the specimen was removed from the test rig and the loose concrete was brushed away. Buckling of reinforcing bars can also be clearly seen in these figures.

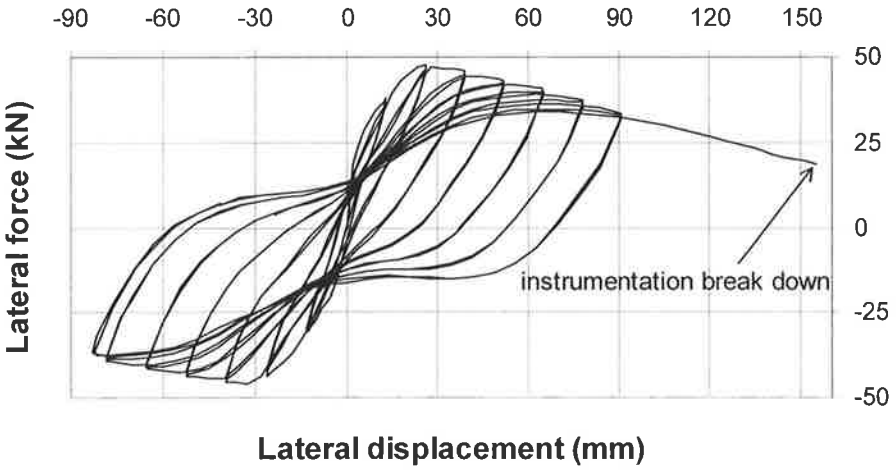

Fig. 11.27 Response of column specimen 4ACP6

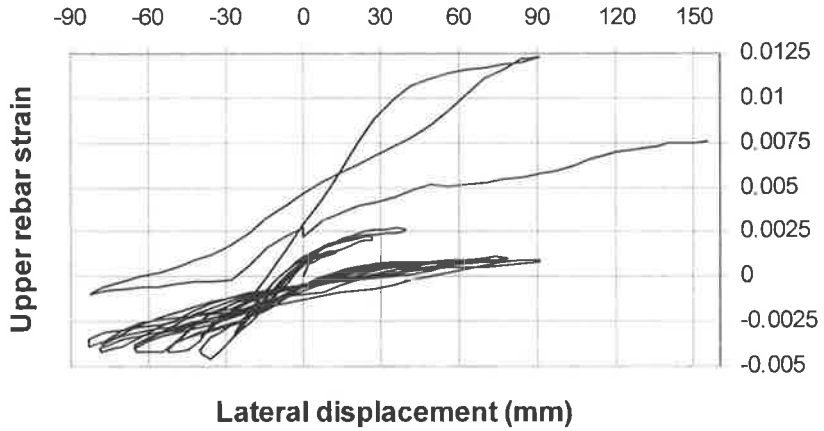

Fig. 11.28 Measured strains in upper reinforcing bar for specimen 4ACP6

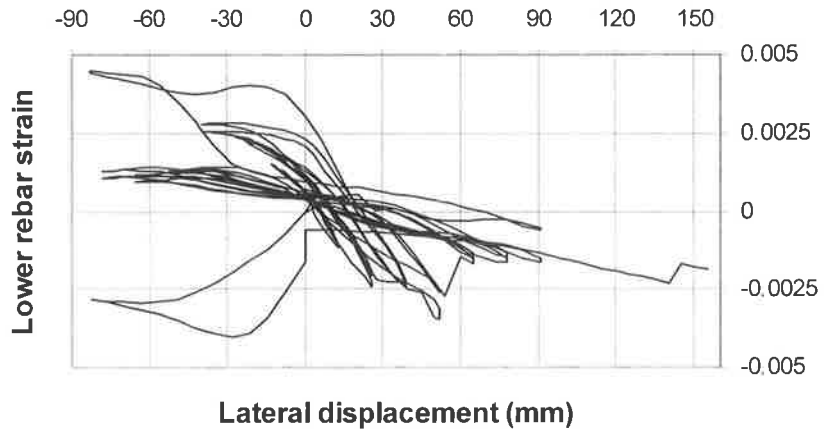

Fig. 11.29 Measured strains in lower reinforcing bar for specimen 4ACP6

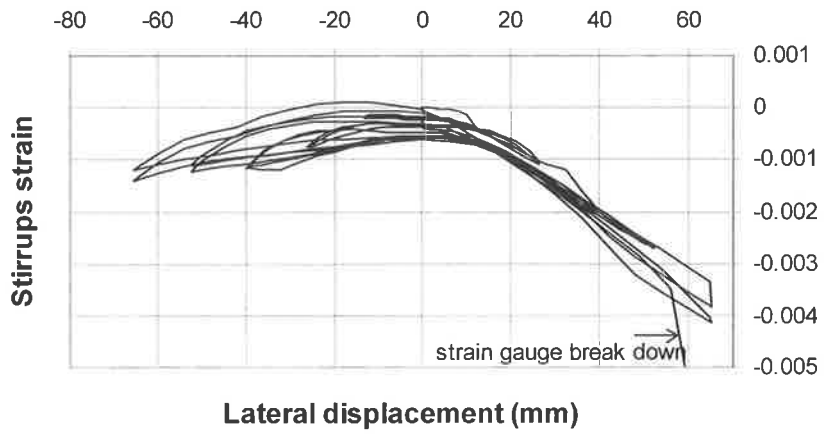

Fig. 11.30 Measured strains in stirrups for specimen 4ACP6

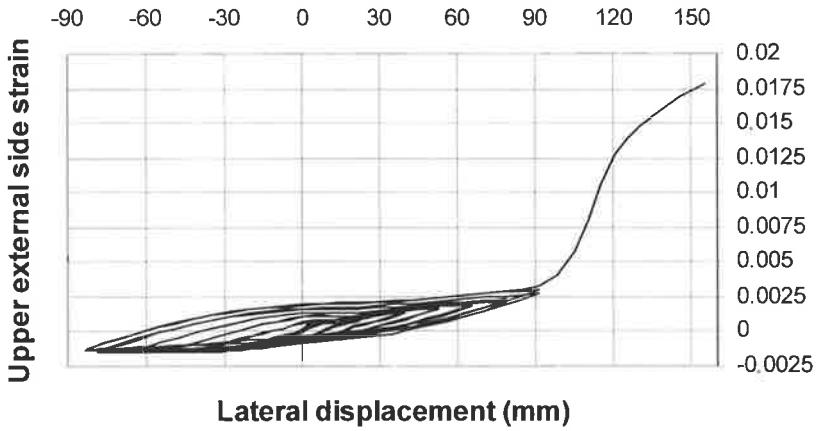

Fig. 11.31 Measured strain in steel plate on upper external side for specimen 4ACP6

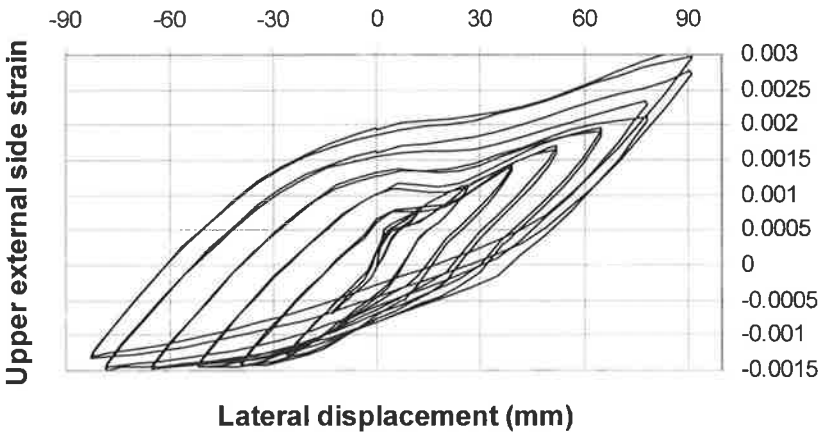

Fig. 11.32 Enlarged part of Fig.11.31

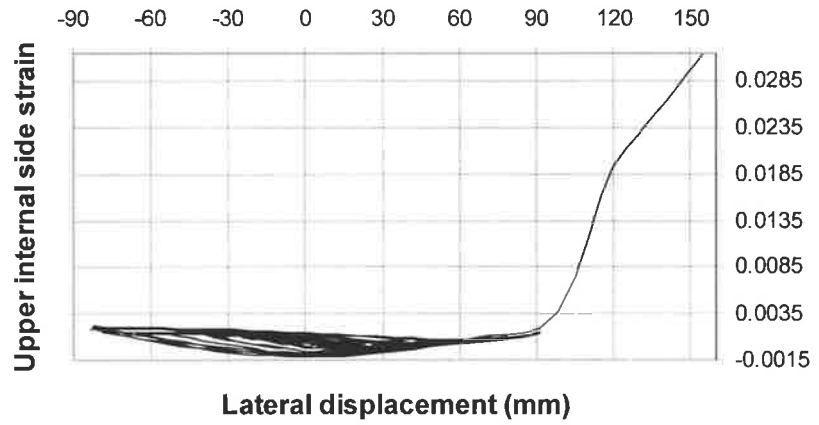

Fig. 11.33 Measured strain in steel plate on upper internal side for specimen 4ACP6

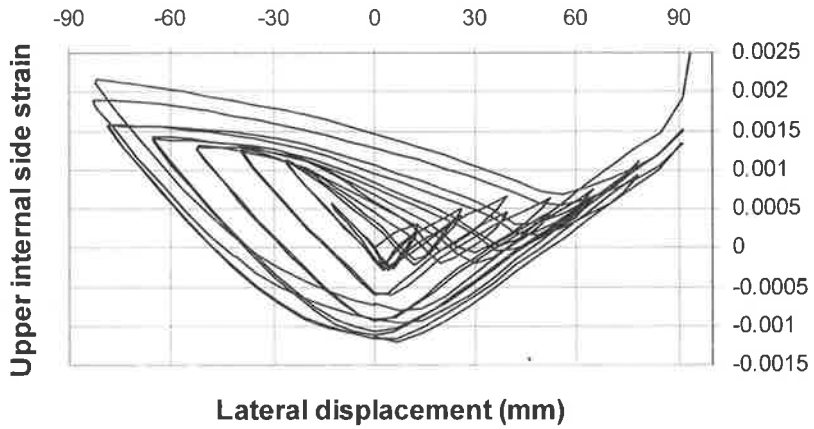

Fig. 11.34 Enlarged part of Fig.11.33

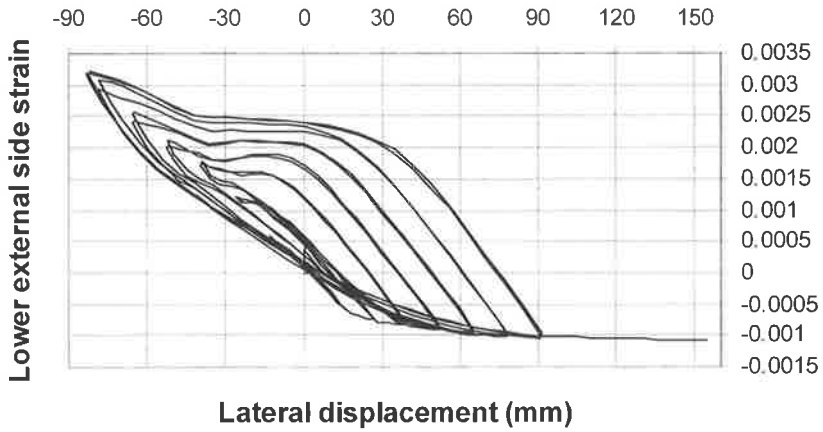

Fig. 11.35 Measured strain in steel plate on lower external side for specimen 4ACP6

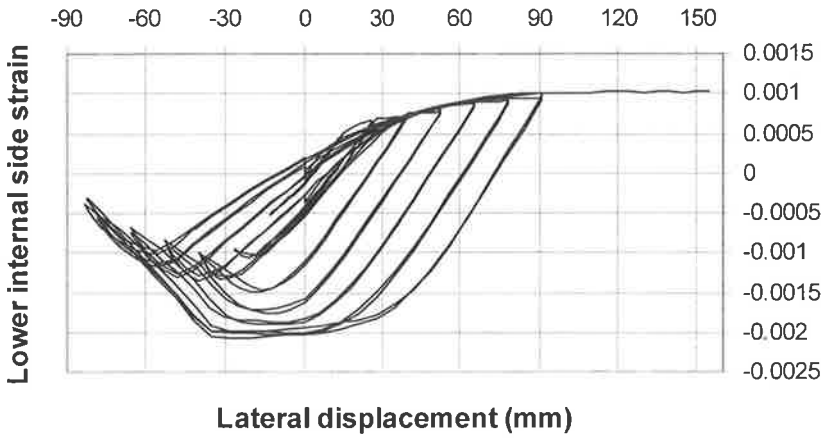

Fig. 11.36 Measured strain in steel plate on lower internal side for specimen 4ACP6

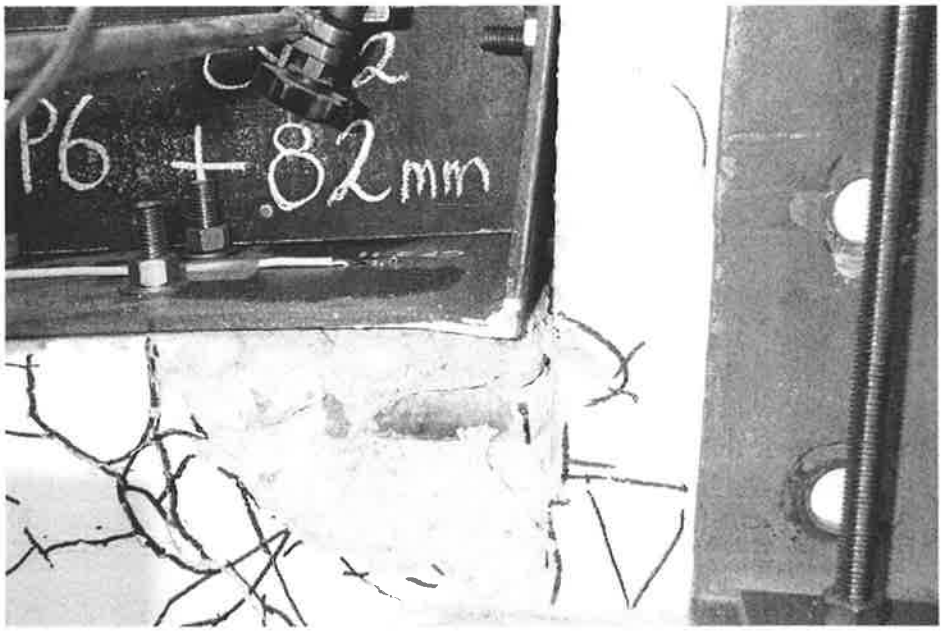

Fig. 11.37 Open up of steel plate at -82mm of 2nd cycle for specimen 4ACP6

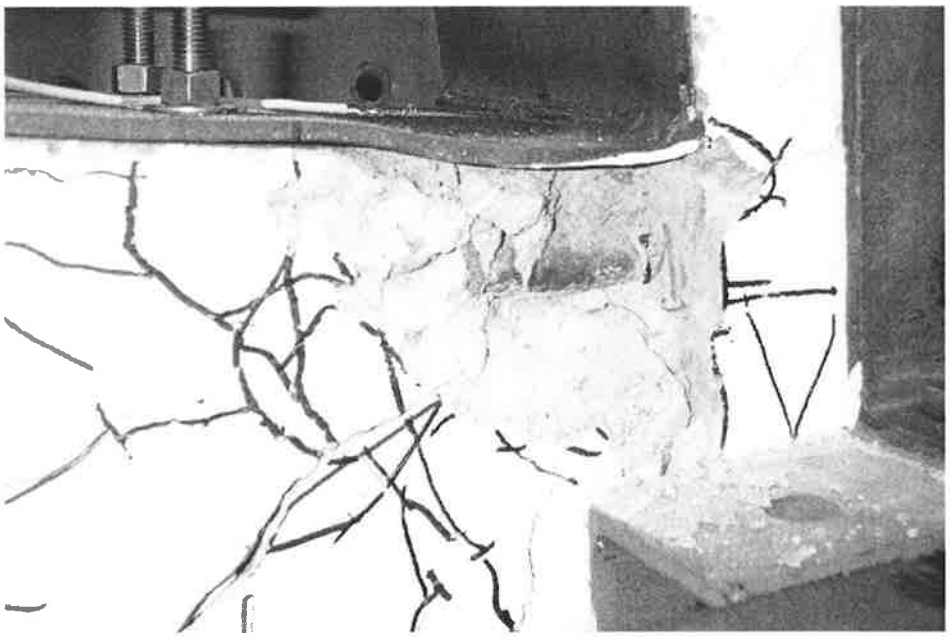

Fig. 11.38 Rear view at +150mm displacement for specimen 4ACP6

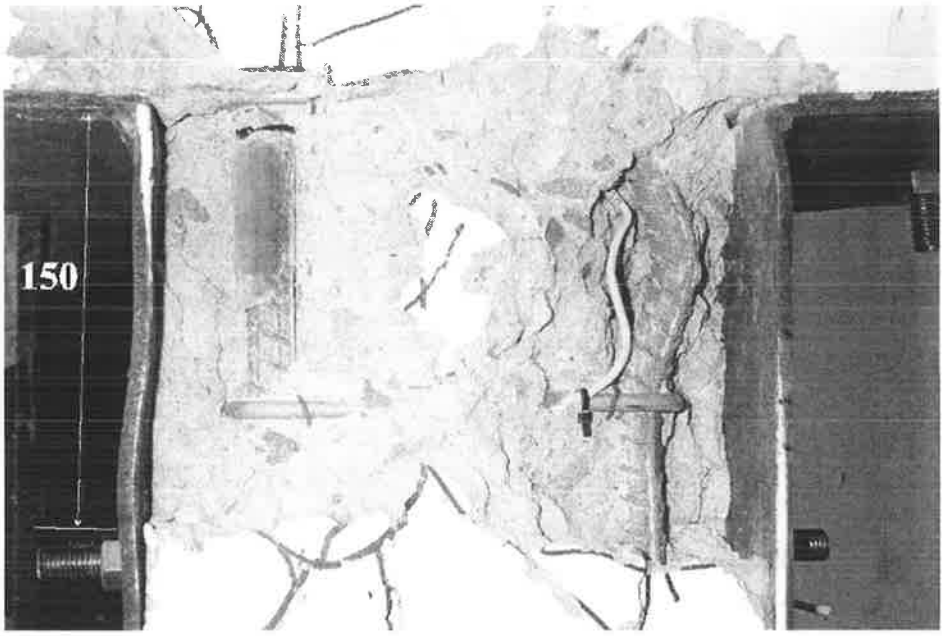

Fig. 11.39 Rear view of plastic hinge zone after testing for specimen 4ACP6

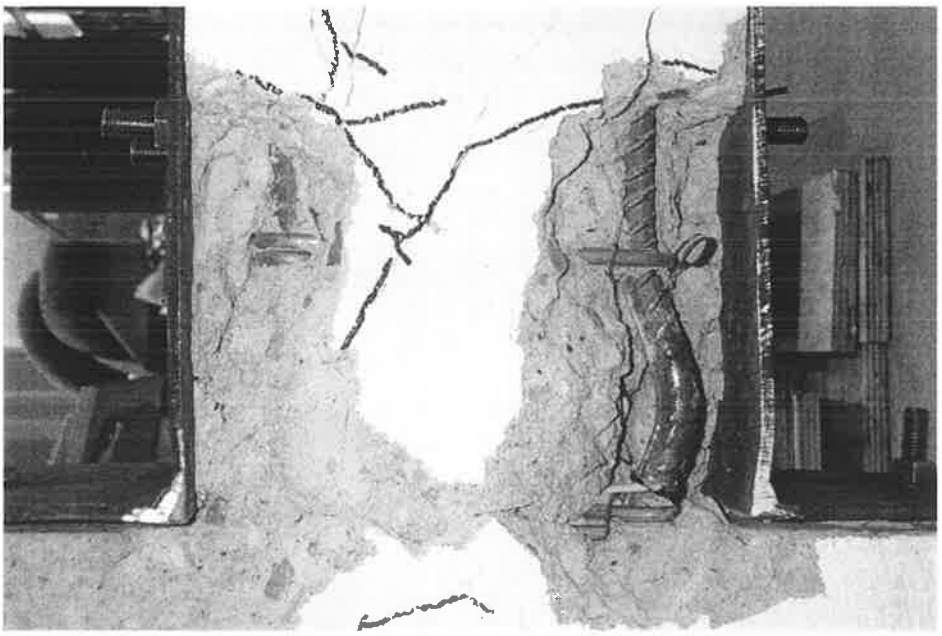

Fig. 11.40 Front view of plastic hinge zone after testing for specimen 4ACP6

11.6 TEST RESULTS OF SPECIMEN 2BCP6G

This test consisted of applying quasi-static cyclic loading to the column with 6mm thick high tensile strength steel plates bolted on both the tension and compression sides (partial interaction plating). Bottom gaps between the steel plate and the beam stub were also set in this test on both plates as per Fig.9.17. The design gap width was 1.2mm on both sides. However, the maximum gap width measured immediately before the test when the test specimen was placed in its test position was about 2mm for both plates, and was apparently not equal for the two sides. The reason was discussed in Section 9.2.3. It also seemed that part of the base plate touched the concrete face of the stub.

This test was conducted from 27th to 29th of June 2001 at a concrete age of 353 days. The load versus deflection response for the column is given in Fig.11.41. The lateral load varied from a range of –51.4kN to 32.8kN.

The measured strains in the reinforcing bars and steel plates are shown in Figs.11.42-11.47. Figure 11.42 shows that the upper reinforcing bars reached a tensile strain of 0.003 at the negative peak point (-51.4kN, -32.3mm) of Fig.11.41. At the positive peak point (32.8kN, 26.1mm) of Fig.11.41, the tensile strain of the lower reinforcing bars was 0.0009 as shown in Fig.11.43. The range of the strain variations in Fig.11.42 and Fig.11.43 suggests that both the upper and lower reinforcement experienced alternative tension and compression yielding. The stirrup strain was very small and did not yield throughout the test (ε_{sy}=0.00345) which varied in a range of −0.0006 to +0.0006. The stirrup strain was much smaller and very different from the other five specimens that experienced only tensile strain, as seen from Fig.11.44. The compression strain in the stirrups started to occur in cycles with amplitudes greater than

52mm and when the displacement decreased from these peak values. The reason for a smaller stirrup strain may be due to the much higher yield strain of the plate that prevented the concrete from excessive crushing and dilation. However, the reason for the compression strain to occur was not clear. A possible explanation is that the stirrup experienced flexural bending under expansion of concrete and the strain gauge was on the compression face of the stirrup bar. Under an amplitude (peak) displacement, the concrete dilation was maximum and the stirrups experienced a large axial elongation which gave a tensile strain. When the column moved back from its amplitude (peak) position, the concrete dilation was relieved but the bending in the stirrups remained which gave a compressive strain in the strain gauge. The variation range of plate strains in Figs 11.45 to 11.47 apparently suggests that the steel plates did not yield on both faces at any displacement (the monotonic yield strain was about 0.004). The strain gauge for the internal side of the lower plate was not working in the test.

A problem occurred in this test when the steel plate on the tension side lifted up, as shown in Fig.11.48. This lifting up of the steel plate invalidated the displacement measurement at point C, as it could no longer reflect the true rotation of the beam stub. This problem was not discovered until the very late stages of the test. It had never been a problem in other tests where two bolts on the side of the stub were used to anchor the plate, as shown in Figs.9.15 and 9.16, and the LVDT point C (or D) never moved closer to the column face than the lower bolt. However, only one bolt on the far side of the stub was installed in this test, as shown in Fig.9.17 and Fig.11.48. The inside bolt was removed because of concerns that the tension resistance from the tension steel plate may be too high for this type of high strength steel plate if the inside bolt was used. As

mentioned in Chapter 5, this increased tension resistance was not desirable from a ductility point of view.

To calculate the lateral force for the response curve of Fig.11.41, it is necessary to know the rotation of the stub (as discussed in Section 9.6.1). To solve this problem, the formula discussed in Section 9.6.2, where measurement points B, C and D were used to calculate the measurement at point E, as shown in Fig.9.25, were used to calculate the stub rotation. In this case, measurement points E, B and D were used to calculate the measurement at point C, when it was pulled up. When it was pushed down, points E, B and C were used to calculate the displacement of point D. When both displacements at points C and D are known, the stub rotation can then be calculated. The whole response curve of Fig.11.41 was produced using this calculated stub rotation.

On the third day (for the last cycle) of the test, measurement points C and D were moved to the opposite face of the stub to avoid the problem of plate lifting. The specimen was pushed and then pulled to the maximum allowable displacement of the test setup in this last cycle. The result is shown in Fig.11.49 with the solid lines. The previous cycles obtained from the calculated stub rotation are shown in the figure by dotted lines. It can be seen that the transmission from the previous cycles to the last cycle, which was produced with direct measurement at points C and D, is considered to be acceptable. This confirmed, indirectly, that the calculation of the stub rotation mentioned in the previous paragraph was acceptable.

The progressive damage to the specimen is shown in Figures B.49 to B.72 in Appendix B. The "+" and "-" signs of displacement on the small black board were

opposite to the sign convention of Fig.11.41. The correct sign is given in the respective titles of the figures.

During the test, the gaps for the upper and lower plates seemed to close at a lateral displacement of about ±10mm. Signs of concrete crushing were first noticed at about ±39mm of lateral displacement. The crushing of the concrete continued to develop with further increase in displacement. However, the steel plates were able to provide adequate compressive resistance to replace the strength lost from the crushed concrete. In the maximum pull position (-100mm displacement) of the last cycle, the positions of the horizontal actuator and the vertical jack were held for about 10 minutes. No significant drop of loading was observed in this period, which was taken to reflect the stability of the specimen at the final position. The integrity of the specimen was also evident from the response curve (Fig.11.41) where no excessive degradation was indicated up to the end of the test.

Figures11.50 and 11.51 show the damage in the specimen at the conclusion of testing when loosened concrete was removed. It is clearly seen that significant concrete crushing occurred in the plastic hinge zone. However, the degree of concrete crushing was lower compared to the other two cyclic tests. The steel plates were still flat and showed no sign of yielding or buckling in Figs.11.50 and 11.51. Buckling of the reinforcing bars is clearly evident in these figures. The condition of the bolts is shown by Figs.11.52 and 11.53 after removal of the steel plate. It can be seen that no excessive slip had occurred in the bolts, as no sign of concrete crushing around the bolts is visible.

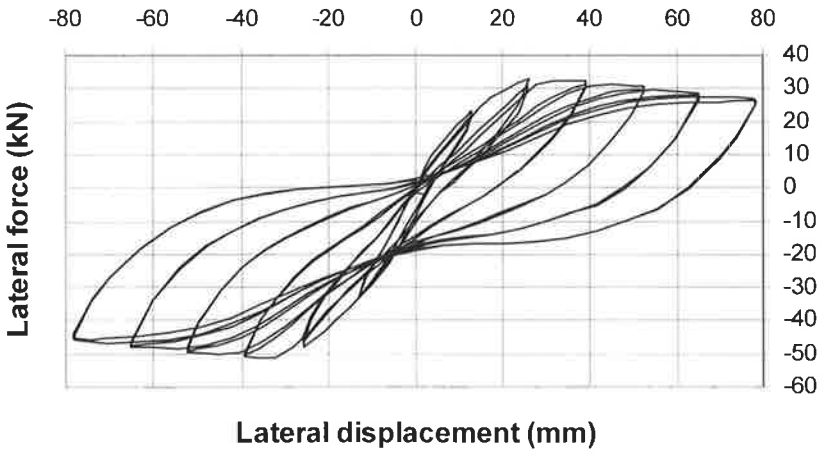

Fig. 11.41 Response of column specimen 2BCP6G

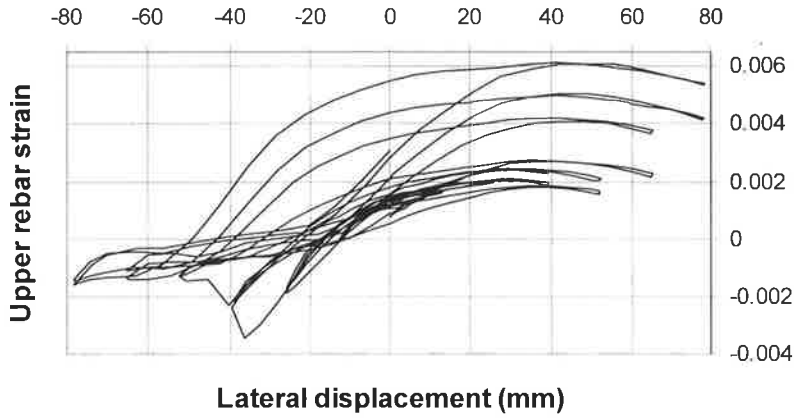

Fig. 11.42 Measured strain in upper reinforcing bar for specimen 2BCP6G

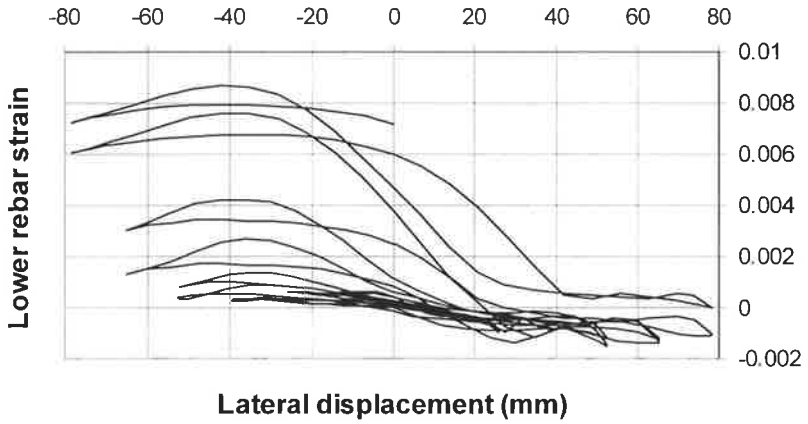

Fig. 11.43 Measured strain in lower reinforcing bar for specimen 2BCP6G

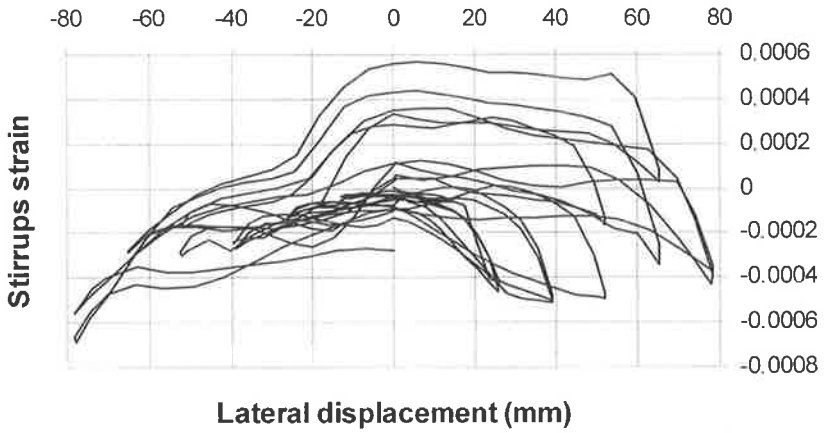

Fig. 11.44 Measured strain in stirrups for specimen 2BCP6G

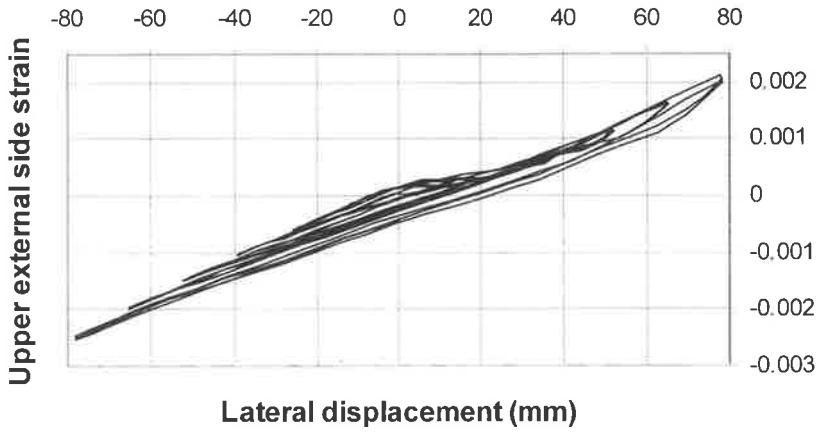

Fig. 11.45 Measured strain of steel plate on upper external side for specimen 2BCP6G

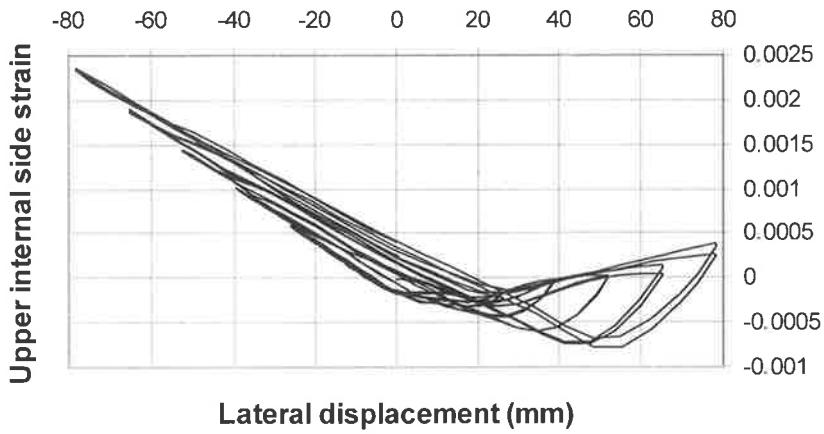

Fig. 11.46 Measured strain of steel plate on upper internal side for specimen 2BCP6G

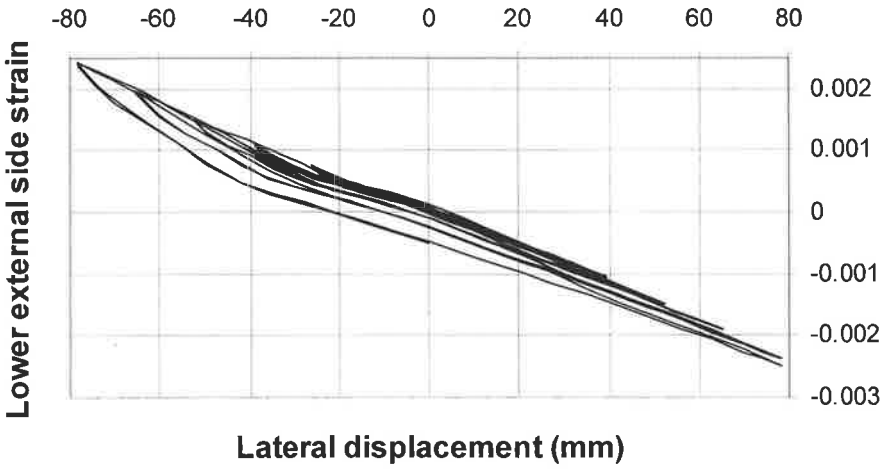

Fig. 11.47 Measured strain of steel plate on lower external side for specimen 2BCP6G

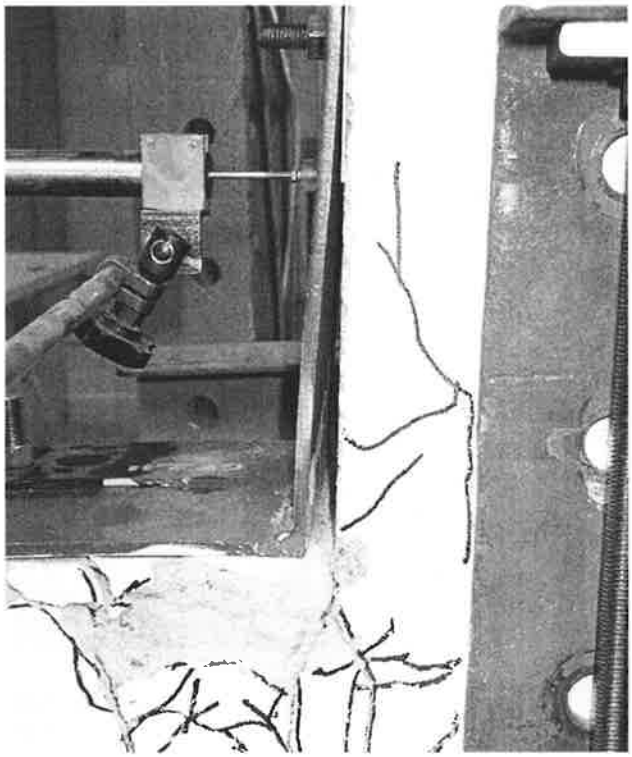

Fig. 11.48 Error in measure point C due to plate lifting up

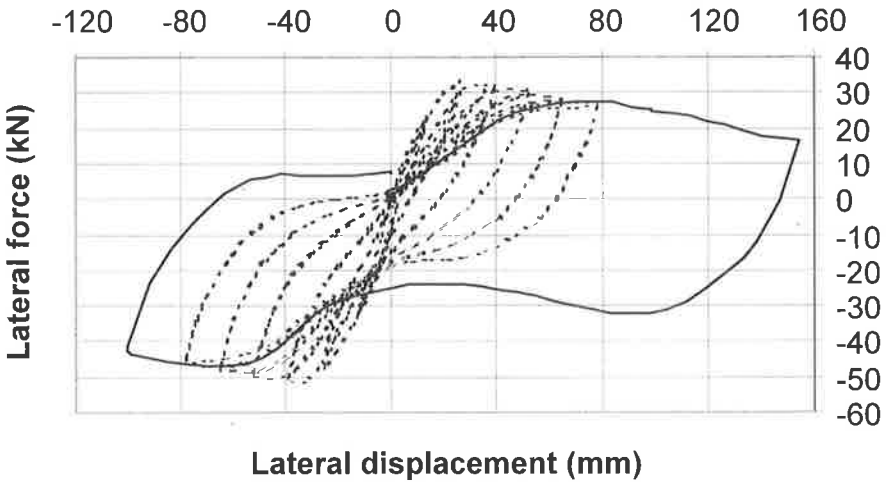

Fig. 11.49 Last cycle of test for specimen 2BCP6G after changing instrumentation

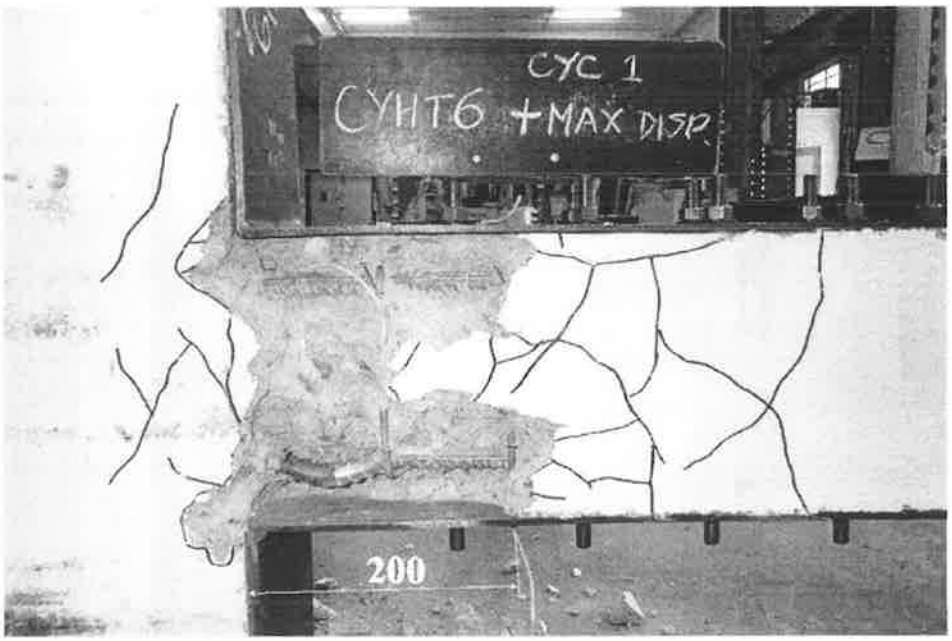

Fig. 11.50 Front view after testing for specimen 2BCP6G

Fig. 11.51 Rear view after testing for specimen 2BCP6G

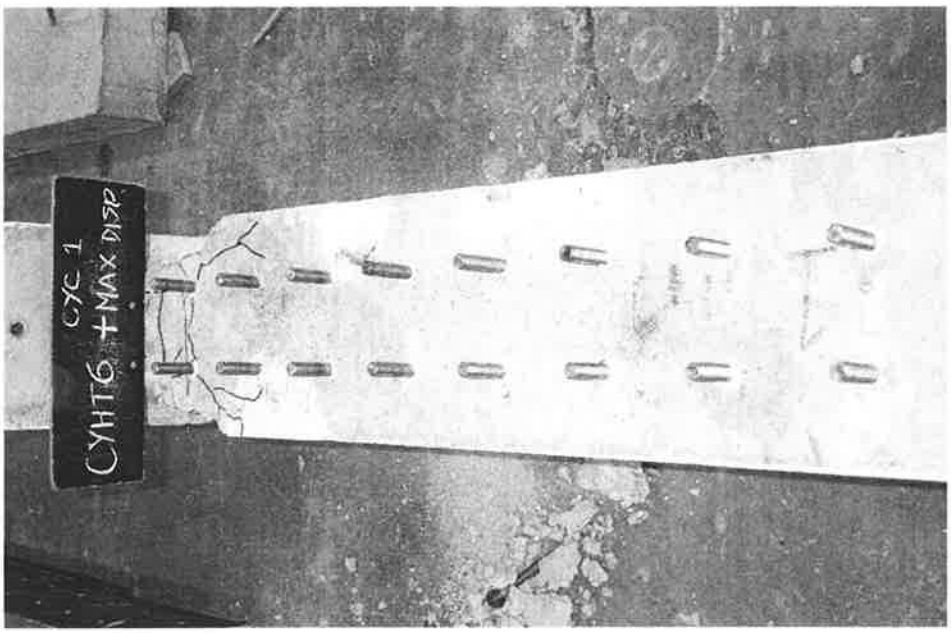

Fig. 11.52 Bolts after testing for specimen 2BCP6G

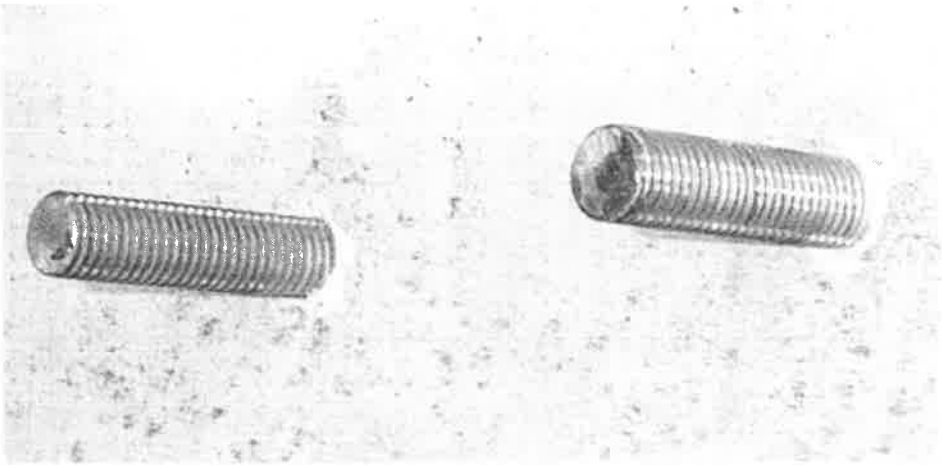

Fig. 11.53 Enlarged view of Fig.11.52

In summary, three monotonically and three cyclically loaded columns were tested to investigate the plating effect. The test setup and procedures were considered to be simple but successful and the target of the tests was achieved. Another feature of the experimental work was that the cost was relatively low. The total cost for the materials and labor (for lab technicians) was about AUD$15,000.

CHAPTER 12 COMPARSIONS AND DISCUSSIONS OF TEST RESULTS

The test results are analyzed and discussed in this chapter. In Section 12.1, comparisons are made between columns with different plating details to see the effects of plating. The test results are compared to the numerical results in Section 12.2 to verify and evaluate the accuracy of the numerical program.

12.1 COMPARSION BETWEEN TEST RESULTS

The test results discussed in this section are the original test results without modification to account for the self-weight of the test specimen and strengthening frames. It is intended to keep the test results as original as possible in this part of discussion. However, the self-weight, that affects the peak force by about 5-7%, will be included in Section 12.2 where the test results are compared to the numerical results.

12.1.1 Monotonic Tests

To compare the test results, the three monotonic response curves are plotted together in Fig.12.1. The peak points and post-peak softening slopes of the response curves are summarized in Table 12.1. From numerical simulations in Chapter 5, it was found that the first yielding of the tension reinforcing bars usually occurs at the peak point of a response curve (see Figs.5.6 and 5.7). This is the case for columns 1AMR and 1BMP6, where it can be seen from column 4 of Table 12.1 that the strains of the tensile bars at the peak points were very close to the yield strain of the reinforcing bar, i.e. 0.0025-0.0026 as

obtained from the reinforcing bar tests in Chapter 10. However, the peak point strain for 2AMF12 is smaller than the yield strain. This measured strain may not be accurate for the reason given in Section 9.4, because the strain difference between the strain on the top face and bottom face of a bar due to the curvature is estimated to be as big as 0.0003 at that peak point.

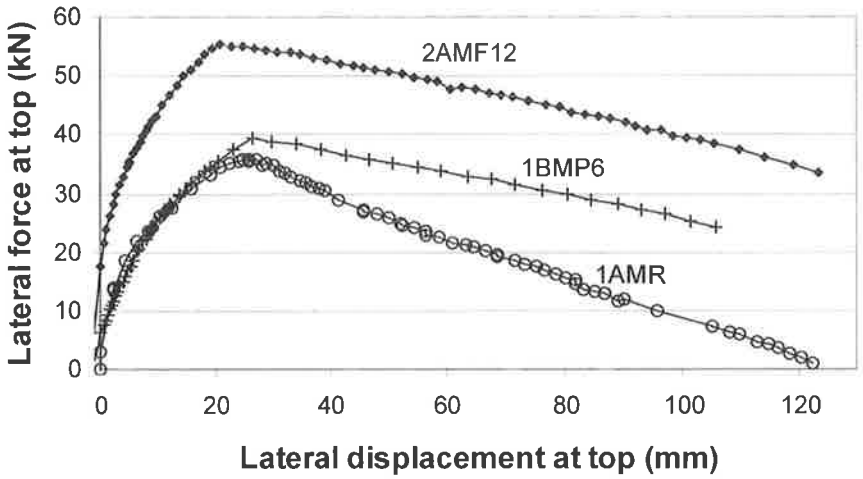

Fig. 12.1 Comparison of monotonic test results

Table 12.1 Summary of test results

	Peak point			Post-peak Softening slope (kN/mm)	Ductility factor	Ultimate displace-ment (mm)	Failure mode
	Displace -ment (mm)	Lateral force (kN)	Tensile bar strain				
1AMR	25.7	35.9	0.0027	0.36	1.6	41	Concrete crushing
1BMP6	26.3	39.3	0.0025	0.19	2.7	71	Plate buckling
2AMF12	20.7	55.3	0.0021	0.21	3.8	79	Not applicable

The ductility factors in Table 12.1 is defined by Eq.5.1 in Section 5.2 as $\mu = \Delta_u / \Delta_y$, where Δ_y is the yield displacement (same as the displacement at the peak point) of a response curve, and Δ_u is the ultimate lateral displacement at a point on the softening branch where the lateral resistance force equals 80% of the corresponding peak force, as given in the seventh column of Table 12.1. The tested specimens are depicted in Fig.12.2, where Δ is the final displacement at which the test stopped. It is clearly seen in Fig.12.2 that the damage to the test specimens reduced with the increase in strength of the plating system.

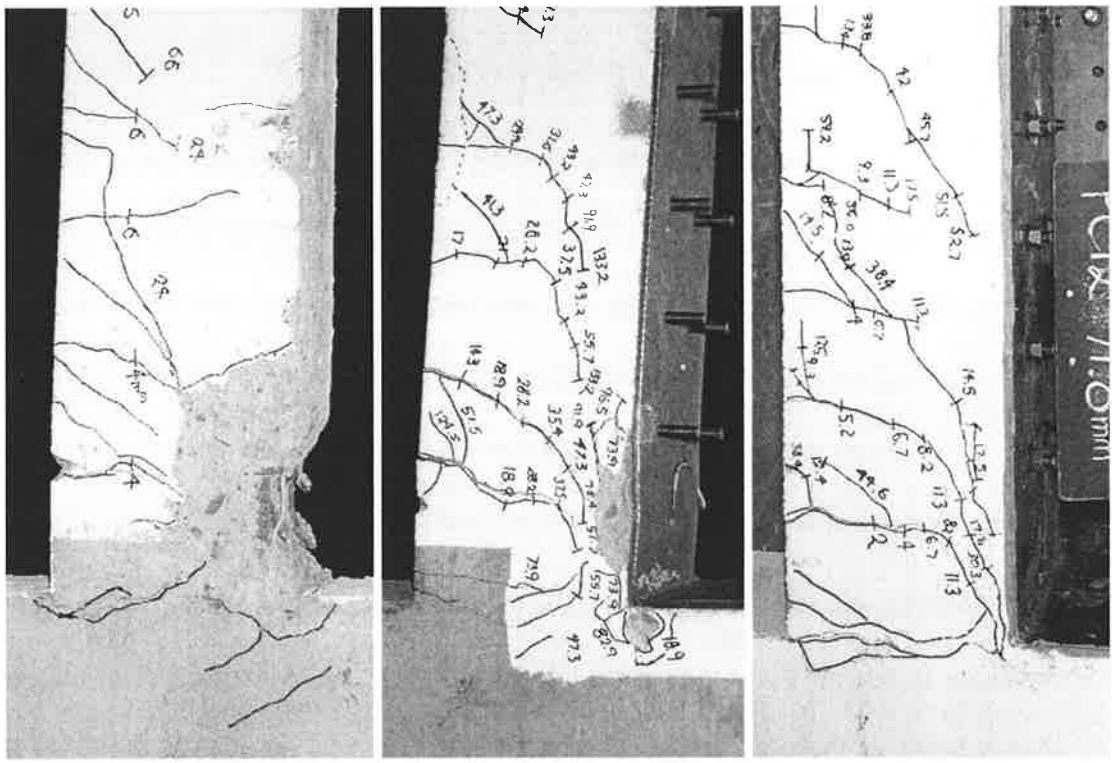

(a) 1AMR (Δ=120mm) Lost of axial capacity

(b) 1BMP6 (Δ=106mm) steel plate buckled

(c) 2AMF12 (Δ=125mm) No failure

Fig. 12.2 Conditions of monotonically tested specimens

From the test results, the following observations can be made:

1. Plating increases column strength. This strength enhancement is clearly seen in the third column of Table 12.1. It was also evident from the cyclic tests. The strength enhancement was largely caused by the transferring of compression force from the RC section to the steel plate, which increased the lever arm of the compression resultant and hence the resistant moment of the column cross-sections.

2. Plating reduces the post-peak softening slope. The post-peak slopes for the plated columns 1BMP6 and 2AMF12 are less steep than that for the un-plated column 1AMR, as shown in the fifth column of Table 12.1. This reduction of slope is also caused by the transmission of the axial force from the RC column to the steel plate, which is referred to as "strength stiffening" in Chapter 5.

3. The displacement ductility factor is increased by plating, as shown in Table 12.1. The reason for this increase in ductility is that the plating reduces the axial load on the RC column. The fact that increasing the axial load on the RC column reduces the ductility of the RC columns is well documented in the literature (Watson. 1994; Watson and Park 1994). From this point of view, tension plating is not beneficial as it increases the total compression force on the RC column and hence reduces the ductility.

4. Plating can increase the deformation capacity. The displacement capacity of structural members is critical for structures to survive a severe seismic attack. The ultimate displacement of the test columns was clearly increased by plating, as shown in the seventh column of Table 12.1.

5. The amount of strength increase due to plating can be managed and, where necessary, minimised. The strength increment of 1BMP6 is much smaller than that of 2AMF12. As discussed in Chapter 5, it is possible to design the plating so as to not increase the peak strength of the column but only reduce the degradation slope in the softening branch and thereby improve ductility of the column.

12.1.2 Cyclic Tests

For comparison, the cyclic test results are superimposed in Fig.12.3.The purpose of the cyclic tests was to identify the toughness and suitability of the proposed plating system under cyclic or dynamic loading. However, the same observations as previously made for the monotonic tests can also be made from the cyclic test results. In addition, the following cyclic behavior can be observed from the test results:

1. Cyclic degradation between cycles reduces by plating. It can be seen by comparing Fig.11.20, Fig.11.27 and Fig.11.41 that the strength reduction between cycles at the same amplitude of displacement was reduced by plating. This is another indication of improvement on structural robustness and integrity.
2. Plating increases the energy absorption capacity of the members. This is evident by comparing the enclosed area of the response curves.

The conditions of the tested specimens are depicted in Fig.12.4, in which "failure" means the final loss of axial load carrying capacity where the test could not continue any further. The damage to column 4ACP6 which was plated by 6mm thick mild steel plates was less severe as compared to column 3ACR which lost the axial load carrying capacity under a much smaller displacement excursion than that for column 4ACP6. The damage to column 2BCP6G which was plated by 6mm thick high yield steel plates was further

reduced as compared to 4ACP6 under a similar displacement excursion, as shown in Fig.12.4.

It is noted in Fig.12.3 that column 2BCP6G that was plated with high strength steel plates has a smaller positive peak strength than the normal steel plated column 4ACP6. Furthermore, the negative peak strength is much greater than the positive peak strength for 2BCP6G itself. The reason for this will be further discussed in Section 12.2.7.

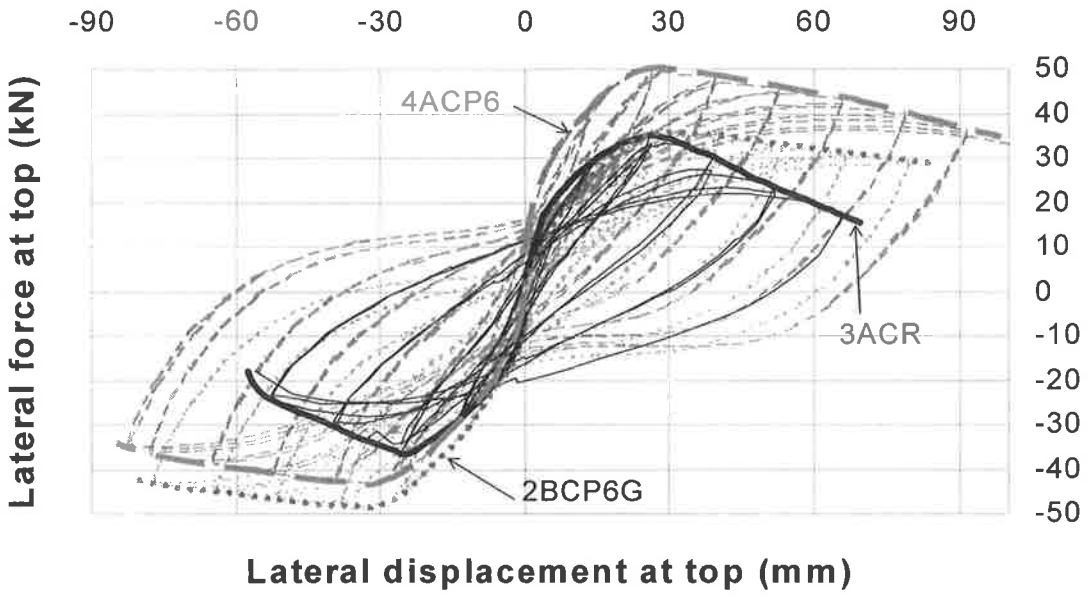

Fig. 12.3 Comparison of cyclic test results

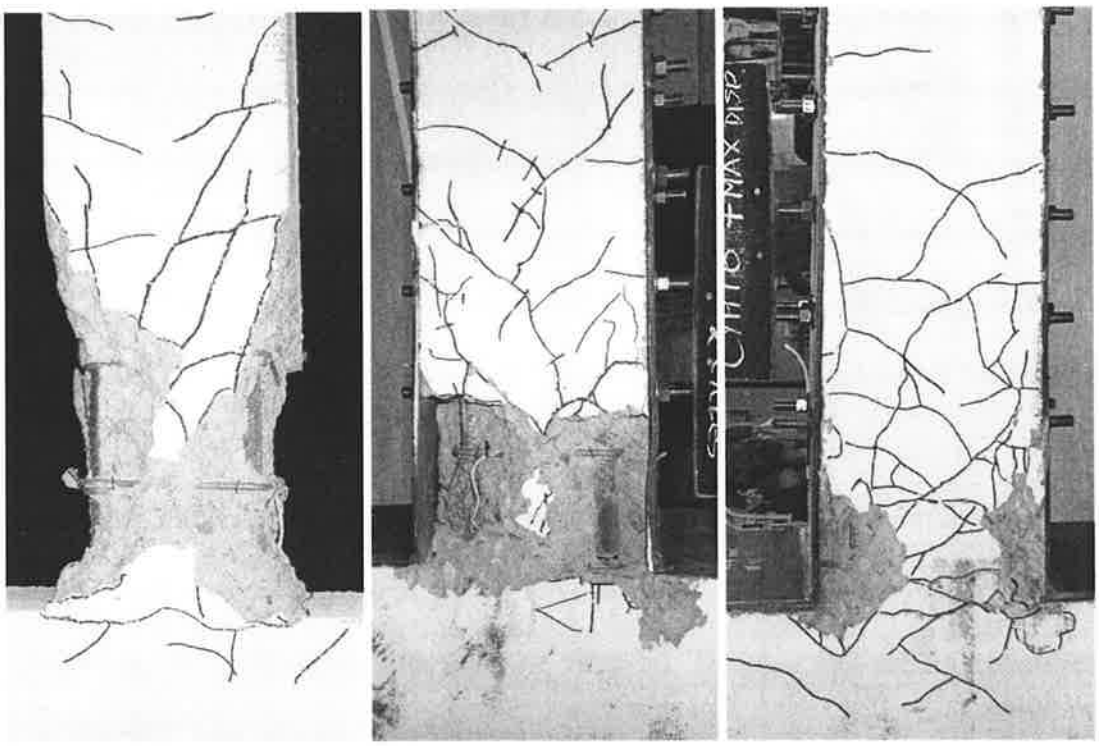

(a) 3ACR (Δ=-56~65mm) Loss of axial capacity (b) 4ACP6 (Δ=-82~150mm) Plate buckled, no failure (c) 2BCP6G (Δ=-100~150mm) No plate buckle, no failure

Fig. 12.4 Conditions of the cyclically tested specimens

12.2 COMPARISON OF TEST RESULTS WITH NUMERICAL RESULTS

The numerical response of the test columns was determined using the numerical program "PLTCOL" described in Chapter 4 and compared to the test results. This comparison can verify the accuracy of the numerical analysis. It can also give a deeper insight into the various factors that affect the response.

In the numerical simulations, the input data are based on average geometrical dimensions measured from the test specimens and average material properties obtained from Chapter 10. The compressive strength and Young's modulus of the concrete are

based on cylinder CLY10 as summarized in Table 10.1 (Chapter 10). The reason for not using other cylinders is that some of the cylinder test results were considered as unreasonable because of their lower strength compared with other cylinders tested earlier. It was also found after these cylinder tests that there was excessive honeycombing inside that downgraded the strength. After comparing all the test results in Table 10.1, CLY10 is considered to be the most representative of all the concrete at an age of 200 days and above.

As mentioned before, the test results excluded the self-weight of the test specimen and the attached strengthening frames. This gravity load was about 5-7% of the peak resistance of the test columns. In order to make the comparisons as reasonable as possible, the test results are adjusted to include this gravity load. Details of the adjustment are discussed in the following section.

12.2.1 Adjustment of Test Results to Include Self-Weight

As indicated in Section 9.5.4, the readings of the initial test point were set to zeros for all instrumentation when no vertical and horizontal loads were applied. However, the self-weight of the specimen and the attached strengthening frames had already applied an initial lateral force and, hence, an initial lateral displacement to the test column. This self-weight for an unplated column with the strengthening frames attached was measured to be 6kN, which was estimated to give a 2.5kN additional lateral force to the test column. For plated columns, this additional lateral force was estimated to be approximately 2.7kN.

Consequently, an initial lateral displacement due to the gravity load was also applied to the test column before the start of loading. The displacement of an elastic cantilever column can be calculated by

$$\Delta = \frac{F \cdot L^3}{3EI} \tag{12.1}$$

However, the initial displacement cannot be estimated using Eq.12.1, although the system is linear elastic at that stage. The reason is that Eq.12.1 is only applicable to a fixed end column, while the test column is not fixed at its base but is more like spring connected at the end. The rotational stiffness of the bottom cross-section relative to the imaginary rigid beam stub, which is considered as the fixed ground of the cantilever column, cannot be estimated by a given formula. This rotational stiffness at the base cannot be ignored either, as will be seen in the next section from the test and numerical results.

Nevertheless, this initial displacement can be easily estimated using the initial stiffness of the response curve. For example, the initial lateral response stiffness is found to be 4.8kN/mm for column 1AMR, which is the slope of the straight line connecting the first two test points. It is significantly different from the elastic stiffness of $K = \frac{3EI}{L^3}$=7.1 kN/mm given by Eq.12.1. Using the stiffness of 4.8kN/mm, the initial displacement by the gravity load is simply given by 2.5/4.8=0.52mm. In this way, all the initial displacements can be calculated using the initial force and initial stiffness of the corresponding response curves.

The adjustment to the test results is made, therefore, by shifting the original response curve horizontally to an initial displacement and vertically to an initial force. The adjusted response curves for the monotonic tests are shown by solid lines in Fig.12.5

in comparison with the original results shown with dotted lines. The cyclic test results are similarly adjusted. All the comparisons between the test results and numerical results in the next 6 sections are made to the adjusted test results.

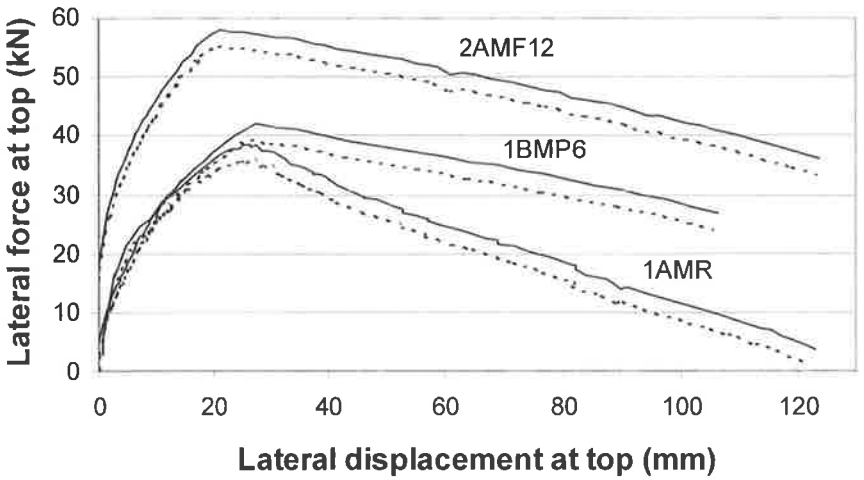

Fig. 12.5 Adjusted test results to include self-weight of specimens

12.2.2 Column 1AMR

The input data for the specimen used in the numerical simulation are summarized below. The definitions of the parameters are given in previous chapters and are summarized in the Notation.

- Geometry

  L=1218mm, $B\times D$=200mm×200mm, a=35.7mm.

- Material

  f_{co}=40.2MPa, ε_{co}=0.002(assumed), E_c=27941MPa, f_{cl}=3.95MPa.
  f_{sy}=548.8MPa, E_s=197424MPa, E_h=827.5MPa,
  R_o=20, α_1=19, α_2=0.3 (assumed based on Gomes and Appleton 1997)
  f_{hy}=690.5MPa.

The applied axial load is N = 360kN. The confined concrete strength inside the centerline of the stirrups is 45.5MPa, which is calculated from the confinement by stirrups of ϕ6@100mm (refer to Section 4.4.3 for calculation). In the numerical simulation, the RC cross-section is discretised into 24 horizontal layers by 24 vertical slices. Longitudinally, it is discretised into 9 segments with lengths of 318mm, 100mm, 100mm, 100mm, 100mm, 100mm, 100mm, and 200mm from the top to the bottom of the column. Mander's model and Menegotto-Pinto's model are used for the stress-strain relations of the concrete and longitudinal reinforcing bars, respectively.

Curve A in Fig.12.6 is produced assuming a fixed base and a plastic hinge length of 200mm which is calculated from Eq.4.56a, i.e. $L_p = 0.08 \cdot L + 6 \cdot d_b$=193.4≈200mm. Curve B is calculated using Eq.4.56b, i.e. $L_p = 0.08 \cdot L + 0.022 \cdot f_{sy} \cdot d_b$=291≈300mm. It is obvious from curves A and B that increasing the plastic hinge length decreases the descending slope of the column in the post peak softening part. However, it has little effect before the column yields.

Curve C is produced considering the base rotation, as described in Section 4.2.4, which is caused by the yield penetration of reinforcing bars into the beam stub and the subsequent pull out of the bars from the face of the stub. The plastic hinge lengths above the base L_{pa} and below the base L_{pb} are calculated using Eq.4.56c and Eq.4.56d, respectively:

$L_{pa} = 0.08 \cdot L$ =0.08*1218=97.4mm≈100mm

$L_{pb} = 0.022 \cdot f_{sy} \cdot d_b$=0.022*548.8*16=193.2≈200mm

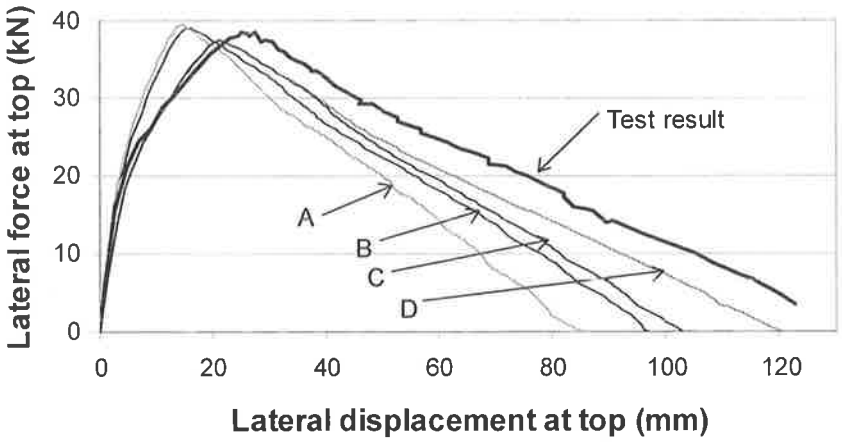

Fig. 12.6 Numerical results for specimen 1AMR

Curve D is calculated with the same plastic hinge arrangement as curve C. However, a stronger confinement is considered in this case. In previous calculations, the first stirrup at the base of the column was ignored. However, this first stirrup also takes part in confining the concrete in practice. From the damage extent of the tested specimen in Fig.11.3, it can be seen that the concrete crushing zone is about 150mm long. There were 2 stirrups in this crushed zone including the first stirrup. If these two stirrups were considered to be fully effective in confining the concrete during the test, then the effective spacing of the stirrups should be adjusted to 75mm. Using a stirrup spacing of 75mm, the confined concrete strength inside the centerline of stirrups is 48.8*MPa*.

From Fig12.6, curve D gives the best fit to the test results. This part of the numerical exercise supports the discussion in Section 4.2.4 that the base rotation should be considered properly in order to get a more accurate displacement. In fact, without modeling the base rotation properly, the numerical model cannot represent the initial elastic stiffness correctly. Theoretically, the displacement of an elastic cantilever column

is given by Eq.12.1, which leads to the elastic column stiffness of $K = \frac{3EI}{L^3}$ =7.1 kN/mm. Using the first two points of the numerical and test results, the initial elastic stiffnesses are calculated from the slope of the line connecting the two points to be 6.7, 6.4, 4.6, 4.6 and 4.8 (kN/mm) respectively for curves A, B, C, D and the test curve. Obviously, the initial stiffness of curves A and B, which assumes a fixed base without rotation, is close to the theoretical value of 7.1kN/mm. The initial stiffness for curves C and D, which consider a base rotation by allowing the bottom curvature to be extended into the base an additional length of L_{pb}, is much closer to the experimental initial stiffness of 4.8kN/mm. This analysis further justifies the base rotation model in Section 4.2.4.

For simplicity, only the numerical results of curve D are compared to the test results in Fig.12.7. It should also be noted that the shear deformation is not considered in the numerical models. The shear deformation due to shear cracking (not the elastic shear deformation) was measured for specimen 2AMF12 in Fig.11.8 and found to be almost in direct proportion to lateral displacement. This shear deformation was about 7mm at a displacement of 100mm for specimen 2AMF12. If a similar shear deformation is assumed for specimen 1AMR, it will bring the numerical result closer to the test result.

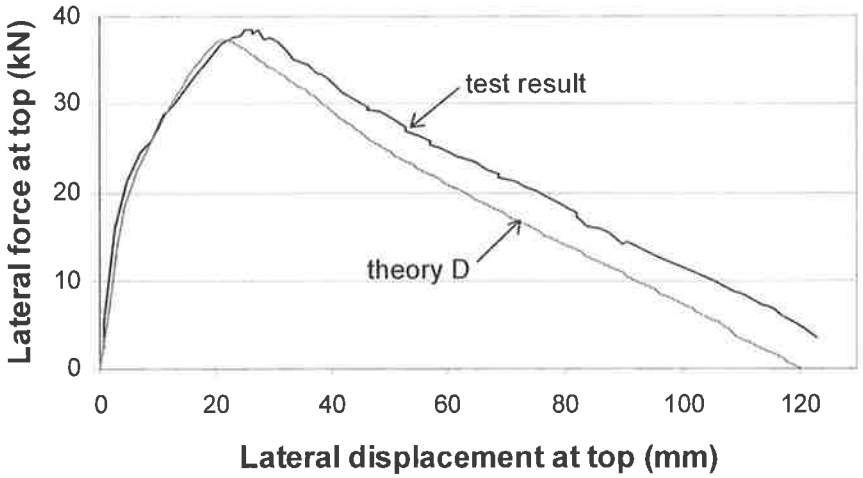

Fig. 12.7 Comparison of test result with theory for specimen 1AMR

12.2.3 Column 2AMF12

All the input data of this specimen are the same as for specimen 1AMR with the following additional data for the steel plate:

f_{py}=306.9MPa, E_p=198679MPa, and E_{ph}=600MPa.

The cross-section of the steel plate is discretised into 15 layers in the numerical model. The confined concrete strength inside the centerline of stirrups is 48.8*MPa*, the same as that for curve D of Fig.12.6. The plastic hinge arrangement is also the same as for curve D of Fig.12.6, i.e. L_{pa}=100mm and L_{pb}=200mm.

The numerical result is given in Fig.12.8 and compared with the test result. The initial stiffnesses for the numerical result and for the test result are 9.0kN/mm and 9.4kN/mm, respectively. The numerical column seems stiffer than the test column near the top of the ascending branch in Fig.12.8. The difference may be caused by the full-

interaction assumption in the numerical model. In the test column, some minor cracks were noticed on the interface at the bottom of the steel plate that signified some slip in that small region. When slip occurs in a column, the plating system and hence the plated column is less stiff as compared to the full-interaction column.

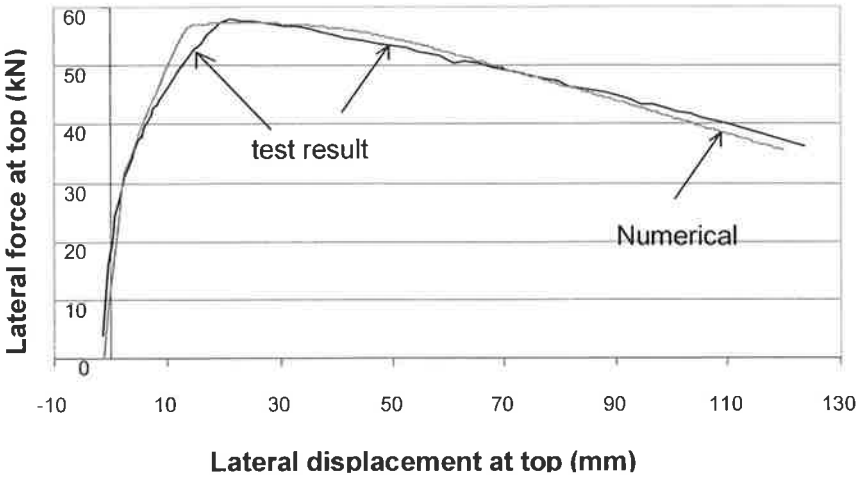

Fig. 12.8 Comparison of test result with theory for specimen 2AMF12

12.2.4 Column 1BMP6

The input data for this column are the same as that given in Section 12.2.3 but with the steel plate properties changed to

f_{py}=307.3MPa, E_p=200031MPa, E_{ph}=600MPa

The bolt properties are

F_{by}=30kN, K_b=23kN/mm, K_{bh}=0.7kN/mm.

The numerical result is shown in Fig.12.9 (marked with "numerical 1") together with the test result. Obviously a large difference exists between the numerical and test result even in the elastic deformation stage.

The reason can be found by comparing the three monotonic test results shown in Fig.12.1. It can be seen that this plated test column 1BMP6 is even "softer" than the un-plated benchmark specimen 1AMR in the initial stage of loading. In fact, the initial lateral deformation stiffness of column 1BMP6 is about 3.3kN/mm, which is lower than that of the un-plated column 1AMR of 4.8kN/mm. Apparently, the test result of 1BMP6 is "unreasonable" as the plated column should be stiffer than the un-plated one.

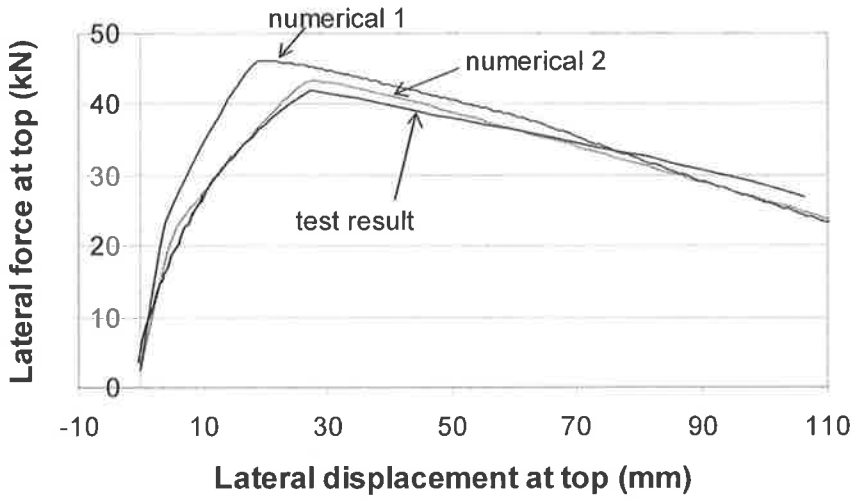

Fig. 12.9 Comparison of test result with theory for specimen 1BMP6

Actually, the problem comes from the letter "B" in the name of the specimen "1BMP6", as "1B" denotes that this was the second test on specimen "1" and it was tested on the previously strengthened side of column 1AMR. In the first test of a virgin specimen, the un-tested column on the other side experiences some sort of unavoidable damage under deformation, although the deformation is largely reduced by the very strong strengthening frames. More importantly, the anchorage of the longitudinal reinforcing bars is undermined due to slippage of the bars, as shown in Fig.12.10.

Therefore, in the second test of the same specimen, the bond condition of the reinforcing bars inside the beam stub has been deteriorated. In other word, more slippage inside the stub will be incurred for a same force in a reinforcing bar. This is the reason why the plated specimen 1BMP6 behaved "softer" than the unplated specimen 1AMR.

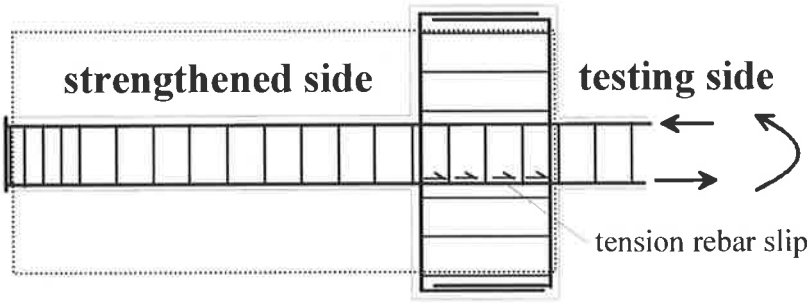

Fig. 12.10 Slippage of reinforcing bars

Based on the above analysis, specimen 1BMP6 would have a larger base rotation than the virgin column for the same applied base moment due to the poorer base anchorage condition of the longitudinal reinforcing bars, as discussed in Section 4.2.4. In this case, the deteriorated base anchorage of the bars can be simulated in the numerical analysis by using a larger plastic hinge length below the base, which means a deeper strain penetration into the column base. Another numerical analysis is conducted using L_{pb}=450mm instead of the original 200mm (the length of L_{pb} is not the yield penetration length, it is a scale used to quantify the base rotation). The result is shown in Fig.12.9 and is marked with "numerical 2". As expected, it gives a much closer agreement to the test result.

Specimen 2BCP6G had the same problem that will be discussed in Section 12.2.7, which further supports the above analysis.

12.2.5 Column 3ACR

All the input data for this column is the same as for column 1AMR. The confined concrete strength inside the centerline of the stirrups is the same as that for curve D of Fig.12.6, i.e. 48.8*MPa*. The plastic hinge arrangement is also the same, i.e. L_{pa}=100mm and L_{pb}=200mm. The numerical result is given in Fig.12.11 and compared with the test result. This numerical result is considered as very close to the test result, which further verifies the accuracy of the computer program "PLTCOL".

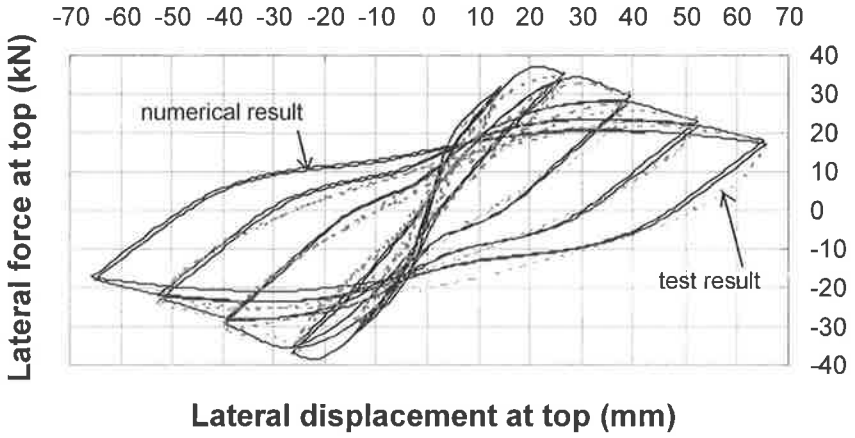

Fig. 12.11 Comparison of test result with theory for specimen 3ACR

12.2.6 Column 4ACP6

The input data for this column is the same as that used to get the result of "numerical 1" for column 1BMP6. The numerical result is given in Fig.12.12 and is compared with the test result.

The agreement between the test and the numerical results is not as good as in the previous 4 columns, especially near the end of the unloading branch where all the

unloading branches of the numerical results seem to be pinched toward the origin of the chart.

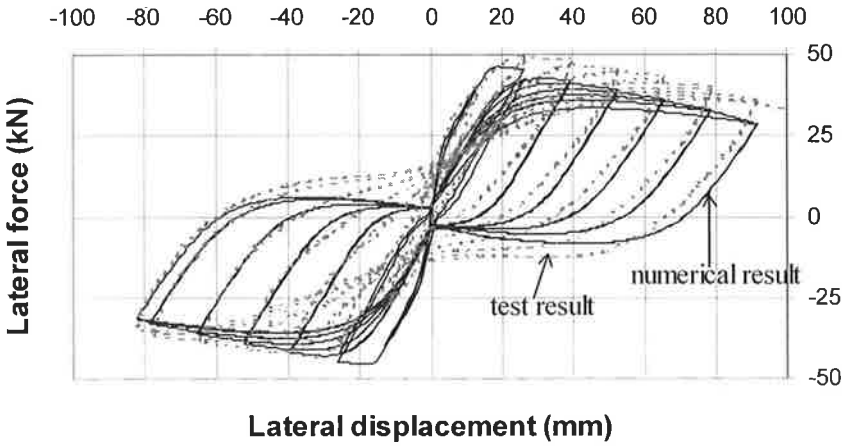

Fig. 12.12 Comparison of test result with theory for specimen 4ACP6

12.2.7 Column 2BCP6G

Column 2BCP6G also presented some complications for the numerical modeling as it was the second test on specimen 2 and base gaps were provided. For a second test on a specimen, the bond condition of the longitudinal bars in the beam stub region has deteriorated from the first test (as discussed in Section 12.2.4) so that the specimen behaves softer than that of a first test. The test result reproduced in Fig.12.13 shows that column 2BCP6G exhibited a very un-symmetrical response with a positive peak resistance of 35.5kN and a negative peak resistance of 48.7kN. Compared with the result of the plated column 4ACP6 in Fig.12.12, the positive peak of this column is significantly smaller.

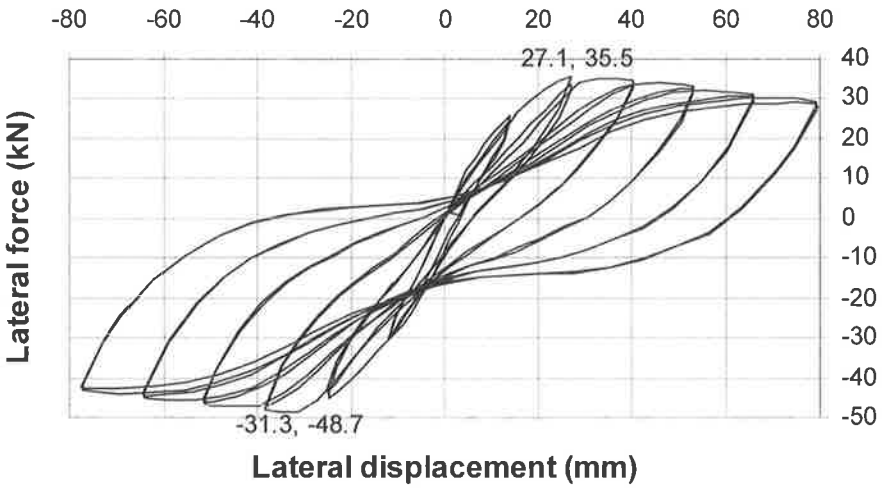

Fig. 12.13 Test result of column 2BCP6G

There could be two reasons for this peak reduction. One is due to the gap effect as discussed in Chapter 5. A numerical simulation is given in Fig.12.14 in comparison with the test result, where a 1.2mm base gap for the upper plate (compression plate at positive response) and no gap for the lower plate are assumed. The input data for this numerical analysis is the same as that used to get the result of "numerical 1" for specimen 1BMP6 (no bond deterioration assumed at base), except that the steel plate properties are changed to f_{py}=734.4MPa, E_p=196798MPa. The un-symmetrical gap widths on the two sides are assumed without experimental justification. As discussed in Section 11.6, the design gap width was 1.2mm on both sides. However, the actual gap width was difficult to measure as it varied from 0~2mm.

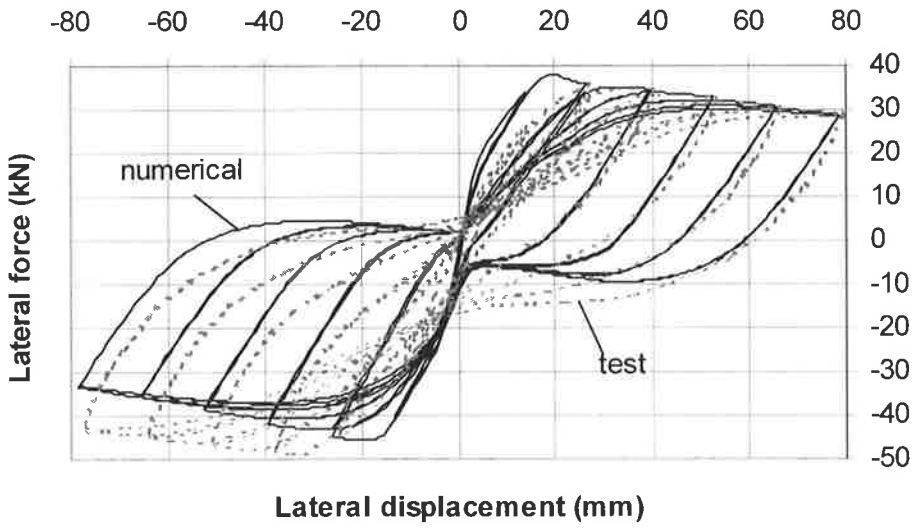

Fig. 12.14 Numerical simulation with un-symmetrical base gaps on two sides

While the respective positive and negative peak strengths of the numerical results are closer to the test results by including the un-symmetrical base gap, the slope of the test curves in the elastic response part on the positive side is still much smaller than that of the numerical ones in Fig.12.14. This suggests a second possible reason for the reduction of the positive peak. As discussed in Section 12.2.4, the deterioration of bond for the tension bars caused by the previous test of column 2AMF12 on specimen 2 caused the softening of the support condition. Careful inspection of specimen 2 revealed that the tension side of column 2AMF12 was also the tension side of the positive response in Fig.12.13. This is the most likely explanation for the un-symmetrical response: the deterioration of bond in the tension bars from the previous test was more severe than that in the compression bars. The tension bars of the monotonically loaded column 2AMF12 slipped significantly under a maximum strain excursion up to 0.9% (see Fig.11.6), while the deformation in the compression bars was much smaller (0.3% of strain in Fig.11.6).

Strengthened by the steel plate on the compression face, it can be imagined and can be seen in Fig.11.10 that the slip of the compression bars inside the stub would be much smaller than that of the tension bars. Because the bond deterioration to the tension bars of the negative response in Fig.12.13 is much smaller, the negative peak is therefore much bigger than the positive peak. However, this un-symmetrical support condition cannot be modeled by the present computer program. Therefore, no further numerical simulations can be carried out to verify this result.

12.3 CONCLUDING REMARKS OF THE COMPARISON

In summary, comparisons between the test results confirmed the theoretical predictions that the proposed new plating system can be used to increase both the strength and ductility, or ductility without significant strength enhancement of RC columns. The comparisons between the tests and the numerical simulations showed that the computer program "PLTCOL" is reasonably accurate. It also showed that the base rotation at the support due to yield penetration and bond breakdown of reinforcement must be modeled adequately to get a reasonable response.

CHAPTER 13 CONCLUSIONS AND RECOMMENDATIONS

13.1 SUMMARY

This work investigated the seismic retrofitting of square/rectangular shaped RC columns. Due to the deficiency of the rectangular shape in providing confinement, existing retrofit techniques of jacketing/wrapping rectangular columns with steel or FRP materials do not provide a good solution to the problem. A new concept of retrofitting rectangular columns that have a potential concrete crushing failure mode in the plastic hinge zone, by composite partial interaction plating, was proposed and studied in this work. Numerical, mathematical and experimental research was conducted to study the effectiveness of this new technique. The results from these studies show that it is possible to use this technique to achieve the following purposes of:

1. increasing both the strength and ductility of RC columns; or
2. increasing ductility without significant increase in strength.

A practical design methodology that is suitable for engineer to use with a hand calculator was developed to design the plating system to achieve the design requirement of a target displacement or inter-story drift ratio.

Several theoretical breakthroughs, discoveries or improvements were made in the course of this PhD work that include:

- The discovery of key composite parameters that govern the degree of interaction between the two elements connected by shear connectors. This result was obtained through mathematical transformation. It gives engineers clear indications as to what to do if they want to increase or reduce the composite interaction in the member. It also provides a theoretical background for related design guidelines. This part of the work was regarded by both reviewers of an international journal as an important paper.
- The derivation of a general (universal) relation between the overall deformations of a composite member and the slip on its interface.
- Development of a simple method to calculate the P-Δ effect. With this method, the column response curve is first calculated without considering the P-Δ effect and then converted to a new response curve by a very simply formula. The converted response curve was proved theoretically to be very close to the actual response curve with the P-Δ effect strictly considered.
- Discovery of typical forms (shapes) of slip distributions in a full non-linear member, which can be very different from the classic slip distribution that has been previously used as design guides. The typical forms were mathematically derived, numerically verified and physically explained.
- Formation of an elastic-plastic model and introduction of a non-zero boundary condition in the linear elastic analysis that effectively extended the linear theory to non-linear analysis and ultimate limit state design.

- Introduction and substantiation of a new but very simple method of identifying the ultimate displacement of an old (pre-1971) RC member using the ultimate strain of the concrete.
- Proof and explanation of the existence of the "focal point" which was discovered by Seracino et al. (2001) and regarded as a new concept in composite structure design.
- Development of a numerical procedure to calculate the response of a partial interaction composite member.

There were several other interesting but minor findings, such as minor modification to the Priestley and Park (1987) model of the plastic hinge which substantially improved the accuracy of numerical simulation results; and the identification and correction of a minor problem in the famous Mander, Priestley and Park concrete stress-strain model.

13.2 CONCLUDING REMARKS

13.2.1 Numerical Models

The numerical models to calculate the response of a reinforced concrete cantilever column with steel or FRP plates attached by gluing or bolting to the faces of the column were developed. The model is based on the moment-curvature analysis of cross-sections using a segmental layered method. The deflection of the column is obtained by integration of curvatures of cross-sections along the length. A deformation control procedure is used in the analysis that can follow the ascending and descending (softening) parts of the response curve as well as cyclic loading without difficulty. Non-linearity in materials is catered for through proper stress-strain models, as is the

geometric non-linearity. The P-Δ effect can be considered either through a rigorous method, which is based on iteration procedures, or a simplified method developed in this work which gives no additional computation load other than that for the response without considering the P-Δ effect. An iterative procedure is developed to account for partial interaction, i.e. slip, at the interface between the plates and the RC column. The computer program can also model general variations in lateral confinement to the concrete as well as the formation of plastic hinges at the large deformation stage.

13.2.2 Numerical Simulations

From the study of Chapter 5, the following conclusions on the ductility of plated columns can be drawn:

1. The ductility factor of the column is largely affected by the axial load and the length of the column. Columns with larger axial loads and/or smaller lengths will have smaller ductility factors.
2. Partial interaction plating increases the ductility factor due to the "strength stiffening" effect caused by transferring the compressive axial load from the RC column to the plate on the compression face of the column.
3. A good plating system is less stiff, or with minimal stiffness, before yielding of the column, but the stiffness of the system (plate and bolts) shall be sufficient to get adequate strength stiffening after yielding of the column in order to minimise the steepness of (i.e. flatten) the post-peak softening slope of load-displacement curve.

4. Yielding of the plating system (plate and bolt) stops further strength stiffening and causes the load-displacement curve to descend faster. To extend the strength stiffening part, the yielding of the plating system should be deferred as late as possible by using a stronger plating system. However, the maximum extent of strength stiffening is achieved when the reinforcement at the compression face yields in tension, after which no further strength stiffening is possible.

Another important conclusion is that the classic slip distribution is applicable only at the serviceability limit state. The slip distribution may be very different from the classic one at the ultimate limit state where the maximum slip may occur in the plastic hinge rather than at the point of zero-moment.

13.2.3 Linear Elastic Analysis

The analytical work of Chapter 6 extended the classical linear theory of composite beams. The unique features of this work were that it included an axial load to extend the original theory from beams to columns and prestressed beams. By introducing the non-zero boundary conditions associated with the plastic hinge and an elastic zone plus a plastic hinge model, the theory was further extended from linear elastic (serviceability limit state) analysis to encompass analyses at the non-linear deformation stage (ultimate limit state). It was found that the response of composite members is governed by only a few key composite parameters derived and introduced in this study, regardless of the large number of variables involved. This finding revealed the fundamentals of composite interaction and improved composite theory that can be used for the eventual formation of design guidelines and procedures. This work also revealed a clearer insight into the

distributions of slip along the member and theoretically explained that the classic slip distribution is only one of the general forms of slip distributions. The conditions at which the largest slip occurs at the maximum moment position instead of at the zero moment position as suggested by the classic linear theory were specified.

13.2.4 Ultimate Displacement of Old RC Columns

It was concluded from the study in Chapter 7 that the onset of the ultimate concrete strain on the extreme compressive fibre can be used to identify the ultimate curvature of an RC section with little confinement, such as in old RC columns with inadequately designed and detailed stirrups. Other conclusions include:

1) Complete failure of a plain concrete section occurs when the ultimate curvature is exceeded in a cross-section. The ultimate curvature of a plain concrete section depends on the concrete material property ε_{cu}, axial load level as well as cross-section depth.

2) The longitudinal reinforcement reduces the deformation capacity of an RC section when the axial load level is lower than the critical load. However, it is vice versa for an RC section with axial load levels higher than the critical load. The critical axial load is typically 30% of the crush load.

13.2.5 Design of Plating System

A displacement based design procedure was developed in Chapter 8 to design the details of the plating system. This design procedure makes sure that full yielding of the plating system including the steel plates and the bolts does not occur at the design target

displacement (ultimate displacement). In the mean time, the concrete strain in the extreme compressive fibre of the plastic hinge just reaches its ultimate strain (spalling strain) at this target displacement. This design philosophy guarantees the plated RC column to work in the "strength stiffening" range of its response curve, that was shown to be a stable deformation stage in Section 5.2.2. The integrity of the concrete is also guaranteed by equating the ultimate displacement of the RC column to the design target displacement so that significant deterioration in the concrete will not occur.

This design procedure is simple and suitable for engineers to use with the help of a hand calculator.

13.2.6 Experimental Works

Six half-scale columns were designed, manufactured and tested. The results of these tests confirmed the theoretical conclusions on the effectiveness of the new retrofitting system, and verified the accuracy of the numerical simulations by the computer program "PLTCOL".

The overall test design including the test set up, which is different from the test rigs reported in the literature, was very successful in term of simplicity, low cost, stability and safety.

13.3 RECOMMENDATIONS AND FUTHER WORK

From the study of this work, the effectiveness of the new retrofit system is beyond doubt, at least for those circumstances considered in this research. However, the completed study was only an initial step towards the new concept of using composite plating to

retrofit RC columns. Many issues and practical problems are yet to be addressed and solved. For example, more experimental tests are needed on larger scale columns to obtain sufficient experimental evidence before it can be finally accepted in engineering. As this work concentrates on the concrete failure mode in a plastic hinge zone, other failure modes, i.e. shear failure and lap slice failure, are yet to be studied. On the other hand, only compression and tension face plating shown in Fig.13.1(a) was considered in this study. Therefore, this technique in its current form would be applicable primarily for columns subject to one-way bending. It is applicable mainly for RC buildings that are stiffened in one direction by strong shear walls or bridge columns that are restricted to move in one direction.

Further research is needed to investigate a plating scheme that can take load from any direction or under two way bending. To do so, the other two cases shown in Figs.13.1(b) and (c) must be studied.

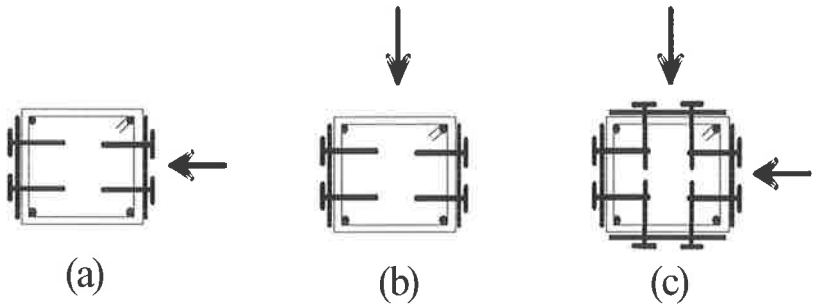

Fig. 13.1 Plating schemes

Actually the retrofit scheme studied in this work as shown in Fig.3.1 is only one way to make use of composite action to retrofit RC columns. Other schemes of composite plating may also be investigated in the future. For example, the plating system shown in

Fig.13.2 is also a partial interaction plating system. This system is almost exactly the same as the traditional steel jacketing, except that the plate bears on the cap beam/footing (or with a much smaller gap than that provided for jacketing). However, it is theoretically a composite plating system instead of a jacketing system. The reason is that the longitudinal force in the plate reduces the compression force in the concrete of the RC column that inhibits the concrete from excessive crushing and dilating in the transverse direction. Without significant dilation of concrete, no significant passive confinement in the hoop direction will be mobilised. Therefore, it does not rely on confinement to stop concrete crushing, instead it relies on the composite action to increase the compressive resistance of the column to stop the concrete from crushing.

With the scheme of Fig.13.2, the plate is in full interaction (no slip) with the column in the bonded region as indicated, but it has no interaction with the column in the un-bonded region. Therefore, overall it is a partial interaction system. Bonding of the plate can be achieved by injection of cement grout or glue into the gap between the plate and the column. As there is a large bonding area, the bond strength is expected to be sufficient. If not, measures, such as stud shear connectors, can be used to provide a sufficient interaction between the plate and the column. In the un-bonded region, the face of the column could be painted with a coat of de-bonding agent before grouting. The system shown in Fig.13.2 works with the same mechanism as that in Fig.3.1. However, it has the following additional advantages as compared to Fig.3.1:

- It is applicable to columns under two way bending. The lateral load can be applied in any direction.

- It is effective for shear defective columns as the enclosed steel plate can be considered as additional stirrups.
- No bolt is used, hence it avoids drilling of holes in existing working columns.
- Because the retrofit system is almost exactly the same as the traditional jacketing system which has been widely used in engineering, it can be readily accepted by engineers and contractors.

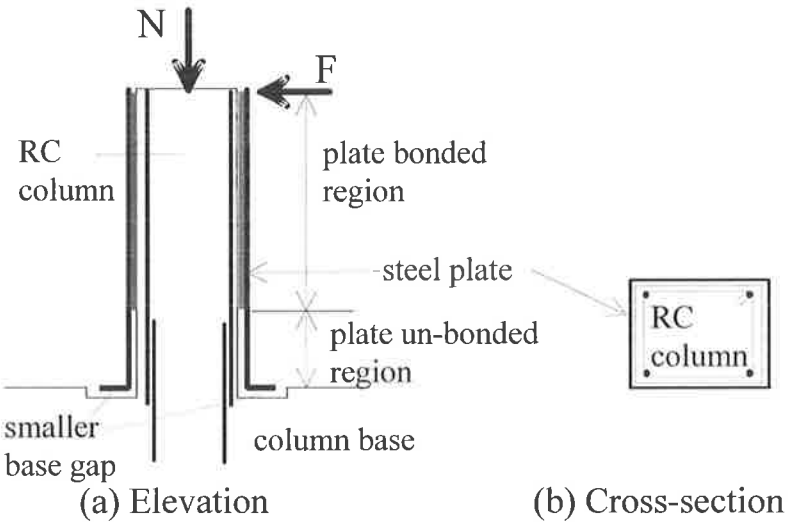

Fig. 13.2 An improved plating system

REFERENCES

1. Aboutaha, R.S. (2000). "Cyclic response of a new steel-concrete composite frame system". *Proc. 12th World Conf. on Earthquake Engineering*, paper no. 0324, New Zealand.
2. Aboutaha, R. S., Engelhardt, M.D., Jirsa, J. O., and Kreger, M. E. (1999). "Rehabilitation of shear critical concrete columns by use of rectangular steel jackets". *ACI Structural Journal*, **96**(1), 68-78.
3. Aboutaha, R. S., Engelhardt, M.D., Jirsa, J. O., and Kreger, M. E. (1996). "Retrofit of concrete columns with inadequate lap splices by the use of rectangular steel jackets." *Earthquake Spectra*, **12**(4), 693-714.
4. Aboutaha, R.S. and Machado, R.I. (1999). "Seismic resistance of steel-tubed high-strength reinforced-concrete columns". *Journal of Structural Engineering*, ASCE, **125**(5), 485-494.
5. Aboutaha, R.S. and Machado, R.I. (1998). "Seismic resistance of steel confined reinforced concrete (SCRC) columns". *Structural Design of Tall Buildings*, **7**(3), 251-260.
6. Abrams, D. (1996). "Effects of scale and loading rate with tests of concrete and masonry structures". *Earthquake Spectra*, **12**(1), 13-28.
7. Ahmad, S.H. and Shah, S.P. (1982). "Stress-strain curves of concrete confined by spiral reinforcement". *J. Am. Concrete Inst.*, **79**(6), 484-490.

8. Alcocer, Sergio M. (1993). "RC frame connections rehabilitated by jacketing." *Journal of Structural Engineering*, ASCE, **119**(5), 1413-1431.

9. Alcocer, Sergio M.; Jirsa, James O. (1993). "Strength of reinforced concrete frame connections rehabilitated by jacketing." *ACI Structural Journal*, **90**(3), 249-261.

10. Almusallam, T.H. and Alsayed, S.H. (1995). "Stress-strain relationship of normal, high-strength and lightweight concrete". *Magazine of Concrete Research*, **47**(170), 39-44.

11. Arockiasamy, M. (2000). "Recent developments in retrofitting and strengthening of structures using continuous fibers – a review". *Proc. of the ACUN-2 International Composites Conference on Composites in the Transportation Industry*, 14-18 Feb. 2000, University of New South Wales, Sydney, Australia, 39-43.

12. Assa, B. and Nishiyama, M. (1998). "Prediction of load-displacement curve of high-strength concrete under simulated seismic loading". *ACI Structural Journal*, **95**(5), 547-557.

13. Attard, M.M. and Setunge, S. (1996). "Stress-strain relationship of confined and unconfined concrete". *ACI Materials Journal*, **93**(5), 432-442.

14. Bahn, B.Y. and Hsu, C.T.T. (1998). "Stress-strain of concrete under cyclic loading". *ACI Material Journal*, **95**(2), 178-193.

15. Balan, T.A.;Filippou, F.C. and Popov, E.P. (1998). "Hysteretic model of ordinary and high-strength reinforcing steel". *Journal of Structural Engineering,* ASCE, **124**(3), 288-297.

16. Banthia, N. (2000). "Sprayed fiber reinforced plastics for repairs and strengthening". *Proc. of the ACUN-2 International Composites Conference on Composites in the*

Transportation Industry, 14-18 Feb. 2000, University of New South Wales, Sydney, Australia, 61-67.

17. Bayrak, O. and Sheikh, S.A. (1998). "Confinement reinforcement design considerations for ductile HSC columns". *Journal of Structural Engineering*, ASCE, **124**(9), 999-1010.
18. Bayrak, O. and Sheikh, S.A. (1997). "Earthquake resistance of 100MPa concrete columns". *Proc. 1st International conference High Strength Concrete*, July 13-18, 1997, Kona, Hawaii, 122-135.
19. Berwanger, C. (1975). "Effect of axial load on the moment-curvature relationship of reinforced concrete members". *ACI SP 50-11*, pp.263-288, American Concrete Institute, Detroit.
20. Biddah, A; Ghobarah, A. and Aziz, T.S. (1997). "Upgrading of nonductile reinforced concrete frame connections". *Journal of Structural Engineering,* ASCE, **123**(8), 1001-1010.
21. Blong, R.W. (1993). "Hazard Microzonation of Melbourne". *Proceedings of Earthquake Engineering and Disaster Reduction Seminar*, Australian Earthquake Engineering Society, Melbourne, pp107-117.
22. Bonacci, J.F. (2000). "Service-life extension of RC infrastructure with externally-bonded FRP composites". *Proc. of the ACUN-2 International Composites Conference on Composites in the Transportation Industry*, 14-18 Feb. 2000, University of New South Wales, Sydney, Australia. pp.102-109.

23. Boyd, P.F.; Cofer, W.F. and McLean, D.I. (1995). "Seismic performance of steel-encased concrete columns under flexural loading". *ACI Structural Journal*, **92**(3), 355-364.

24. Bracci, Joseph M.; Reinhorn, Andrei M.; and Mander, John B. (1995a). "Seismic resistance of reinforced concrete frame structures designed for gravity loads: Performance of structural system." *ACI Structural Journal*, **92**(5), 597-609.

25. Bracci, Joseph M.; Reinhorn, Andrei M.; and Mander, John B. (1995b). "Seismic retrofit of reinforced concrete buildings designed for gravity loads: Performance of structural model." *ACI Structural Journal*, **92**(6), 711-723.

26. Bradford, M.A.; Gilbert, R.I.; and Sun, S.C.-H. (1999). "Time-dependent analysis of reinforced concrete structures using the layered finite element method". *Structural Engineering and Mechanics,* **8**(6), Techno- Press Taejon South Korea, *561-578.*

27. Bradford, M.A. and Nguyen, S.H. (1994) "Computer-derived behaviour of slender concrete-filled steel tubes". *Proceedings of EURO-C 1994 International Conference on Computer Modeling of Concrete Structures*, Mar 22-25, 1994, Innsbruck, Austria, Pineridge Press Ltd, p853.

28. Bradford, M.A. and Gilbert, R.I. (1992). "Non-linear time-dependent behavior of slender concrete-filled rectangular steel columns". *Proceedings of the Institution of Civil Engineers Structures and Buildings*, vol.94, 179-186

29. Bradford, M.A. (1991). "Design of short concrete filled RHS sections". *Civil Engineering Transactions*, Institution of Engineers, Australia, vol.CE33, no.3, pp.189-194.

30. Bradford, M.A. and Gilbert, R.I. (1990). "Time dependent analysis and design of composite columns". *Journal of Structural Engineering*, ASCE, **116**(2), 3338-3357.

31. Bridge R.Q. (1976). "Concrete filled steel tubular columns". *Civil Engineering Transactions*, Institution of Engineers, Australia, vol.CE18, no.2, pp.127-133.

32. Bridge, R.Q., O'Shea M.D. and Zhang, J.Q. (1997). "Load moment interaction curves for concrete filled tubes". *Proceedings of the Fifteenth Australian Conference on the Mechanics of Structures and Materials,* Melbourne, Australia, 8-10 Dec. 1997, pp.141-146.

33. Bridge, R.Q. and Roderick, J.W. (1978). "Behavior of built-up composite columns". *Journal of Structural Engineering*, ASCE, Vol.104(ST7), pp.1141-1155.

34. Bridge, R. and Webb, J. (1992). "Thin walled circular concrete filled steel tubular columns". ASCE, *Composite construction in Steel and Concrete II*, June 14-19, 1992, pp.634-649.

35. Burnet, M.J. and Oehlers, D.J. (2001) "Fracture of mechanical shear connectors in composite beams". *Mechanics of Structures and Machines*, **29**(1).

36. Cai, S.H. and Jiao, C. (1984). "Ultimate strength of concrete-filled tube columns". *Proceedings of Engineering Foundation Conference on Composite Construction in Steel and Concrete,* ASCE, pp.702-710.

37. Calvi, G.M. and Kingsley, G.R. (1995) "Displacement-based seismic design of multi-degree-of-freedom bridge structures." *Earthquake Engineering & Structural Dynamic*, **24**(9), 1247-1266.

38. Carol, I., Prat, P.C. and Bazant, Z.P. (1992). "New explicit microplane model for concrete: theoretical aspects and numerical implementation". *Int. J. Solids and Struct.*, **29**(9), 1173-1191.

39. CEB 1996. *RC ELEMENTS UNDER CYCLIC LOADING*. CEB State of the Art Report. Thomas Telford.

40. CEB 1997. *FASTENNINGS FOR SEISMIC RETROFITTING*. CEB State of the Art Report. Thomas Telford.

41. Chaallal, O. and Shahawy, M. (2000). "Performance of fiber-reinforced polymer-wrapped reinforced concrete column under combined axial-flexural loading". *ACI Structural Journal*, **97**(4), 659-668.

42. Chai, Y.H. (1996). "Analysis of the seismic characteristics of steel-jacketed circular bridge columns." *Earthquake Engineering & Structural Dynamics*, **25**(2), 149-161.

43. Chai, Y. H., Priestley, M. J. N., and Seible, F. (1994). "Analytical model for steel-jacketed RC circular bridge columns." *Journal of Structural Engineering*, ASCE, **120**(8), 2358-2376.

44. Chai, Yuk Hon; Priestley, M.J. Nigel; Seible, Frieder. (1991). "Seismic retrofit of circular bridge columns for enhanced flexural performance." *ACI Structural Journal*, **88**(5), 572-584.

45. Chai, Y.H.; Priestley, M.J.N. and Seible, F. (1990). "Retrofit of bridge columns for enhanced seismic performance". *Proceedings of the U.S.-Japan Workshop on Seismic Retrofit of Bridge*, Tsukuba, Japan, December 1990.

46. Cirtek, L. (2001). "RC columns strengthened with bandage – experimental program and design recommendations". *Construction and Building Materials*, v.15, pp.341-349.

47. Crawford, John E.; Malvar, L. Javier; Wesevich, James W.; Valancius, Joseph; Reynolds, Aaron D. (1997). "Retrofit of reinforced concrete structures to resist blast effects." *ACI Structural Journal*, **94**(4), 371-377.

48. Desayi, P.; Iyengar, K.T. and Reddy, T.S. (1979). "Stress-strain characteristics of concrete confined in steel spirals under repeated loading". *Materials and Structures*, v.12, pp.375-383.

49. Demers, M. and Neale, K.W. (1999). "Confinement of reinforced concrete columns with fiber-reinforced composite sheets – an experimental study". *Can. J. Civ. Eng.*, v.26, pp.226-241.

50. Dodd, L.L. and Restrepo-Posada J.I. (1995). "Model for predicting cyclic behavior of reinforcing steel". *Journal of Structural Engineering,* ASCE, **121**(3), 433-445.

51. Dritsos, Stephanos E. (1997). "Jacket retrofitting of reinforced concrete columns". Construction Repair, **11**(4), 35-40.

52. El-Dash, K.M. and Ahmad, S.H. (1995). "A model for the stress-strain relationship of spirally confined normal and high-strength concrete columns". *Magazine of Concrete Research*, **47**(171), 177-184.

53. El-Dash, K.M. and Ahmad, S.H. (1994). "A model for the stress-strain relationship of rectangular confined normal and high strength concrete columns". *Materials and Structures*, v.27, pp.572-579.

54. Elhassan, Rami M.; Hart, Gary C. (1995). "Analysis and seismic strengthening of concrete structures." *Structural Design of Tall Buildings*, **4**(1), 71-90.

55. Elnashai, A.S. and Elghazouli, A.Y. (1993). "Performance of composite steel/concrete members under earthquake loading. Part I: analytical model". *Earthquake Engineering and Structural Dynamics*, Vol.22, pp.315-345.

56. Ersoy, U.; Tankut, A.T. and Suleiman, R. (1993). "Behavior of jacketed columns". *ACI Structural Journal*, **90**(3), 288-293.

57. Fam, A. and Rizkalla, S. (2000). "Hybrid FRP/concrete structural members". *Proc. of the ACUN-2 International Composites Conference on Composites in the Transportation Industry*, 14-18 Feb. 2000, University of New South Wales, Sydney, Australia. pp.191-197.

58. Fardis, M.N. and Khalili, H. (1981). "Concrete encased in fiberglass-reinforced plastic". *ACI Journal*, v.78, pp.440-445.

59. Foster, S.J. and Attard, M.M. (1997). "Ductility and strength in HSC columns". *Proc. 1st International conference High Strength Concrete*, July 13-18, 1997, Kona, Hawaii, pp.201-214.

60. Frangou, M.; Pilakoutas, K. and Dritsos, S. (1995). "Structural repair/strengthening of RC columns". *Construction and Building Materials*, **9**(5), 259-266.

61. Fujii, M.; Kobayashi, K.; Miyagawa, T.; Inoue, S. and Matsumoto, T. (1988). "A study on the application of a stress-strain relation of confined concrete". *Proc. JCA Cement and Concrete*, v.42, Japan Cement Assn., Tokyo, Japan, pp.311-314.

62. Furlong, R.W. (1967). "Strength of steel-encased concrete beam columns". *Journal of Structural Engineering*, ASCE, **93**(5), 113-124.

63. Furlong, R.W. (1968). "Design of steel-encased concrete beam-columns". *Journal of Structural Engineering*, ASCE, Vol. 94, No.ST1, pp. 267-281.

64. Gardner, N.J. and Jacobson, E.R. (1968). "Structural behavior of concrete filled steel tubes". Proceeding, American Concrete Institute, Vol.65, No.1, pp.66-69.

65. Gardner, J. and Jacobson, R. (1967). "Structural behavior of concrete filled steel tubes". ACI, Journal, No.64-38, July 1967, pp.404-413.

66. Ge, H. and Usami, T. (1992). "Strength of concrete-filled thin-walled steel box column: experiment". *Journal of Structural Engineering*, ASCE, **118**(11), 3036-3054.

67. Gergely, Ioan; Pantelides, Chris P.; Nuismer, Ralph J.; and Reaveley, Lawrence D. (1998). "Bridge pier retrofit using fiber-reinforced plastic composites." *Journal of Composites for Construction*, **2**(4), 165-174.

68. Ghobarah, A.; Aziz, Tarek S. and Biddah, Ashraf. (1997). "Rehabilitation of reinforced concrete frame connections using corrugated steel jacketing." *ACI Structural Journal*, **94**(3), 283-294.

69. Ghobarah, A.; Aziz, Tarek S. and Biddah, Ashraf. (1996). "Seismic rehabilitation of reinforced concrete beam-column connections". *Earthquake Spectra*, **12**(4), 761-780.

70. Gomes, A. and Appleton, J. (1997). "Nonlinear cyclic stress-strain relationship of reinforcing bars including buckling". *Engineering Structures*, **19**(10), 822-826.

71. Green, M.F. (2000). "Canadian perspective on rehabilitation of structures with FRP materials". *Proc. of the ACUN-2 International Composites Conference on Composites in the Transportation Industry*, 14-18 Feb. 2000, University of New South Wales, Sydney, Australia. pp.127-135.

72. Green, N.B. (1987). *Earthquake Resistant Building Design and Construction.* Elsevier Science Publishing Co. Inc., New York.

73. Hajjar, J.F. and Gourley, B.C. (1996). "Representation of concrete filled steel tube cross-section strength". *Journal of Structural Engineering*, ASCE, **122**(11), 1327-1336.

74. Hakuto, S. Park, R. and Tanaka, H. (1995). "Retrofitting of reinforced concrete moment resisting frames". *Research Report 95-4*, Dept. of Civil Engineering, University of Canterbury, August 1995.

75. Hanna, S. and Jones, R. (1997). "Composite wraps for aging infrastructures: concrete columns". *Composite Structures*, **38**(1-4), 57-64.

76. Hoshikuma, J.; Kawashima, K; Nagaya, K. and Taylor, A.W. (1997). "Stress-strain model for confined reinforced concrete in bridge piers". *Journal of Structural Engineering*, ASCE, **123**(5), 624-633.

77. Hwang, Thomas T.; and Wehnes, William C. (1997). "California refinery meets seismic codes using new wrapping technique." *Oil and Gas Journal*, **95**(13), 70-72.

78. Jasim, N.A. (1999). "Deflections of partially composite beams with linear connector density". *Journal of Construction Steel Research*, v.49, pp.241-254.

79. Johnson, R.P. and Molenstra, N. (1991). "Partial shear connection in composite beams in buildings." *Proc. Instit. of Civil Engineers*, London, Part 2, Vol. 91, 679-704.

80. Karbhari, V.M. (2001). "Material considerations in FRP rehabilitation of concrete structures". *Journal of Materials in Civil Engineering*, ASCE, **13**(2), 90-97.

81. Karbhari, V.M. (2000). "FRP composites for infrastructure renewal – status and challenges for the 21st century". *Proc. of the ACUN-2 International Composites Conference on Composites in the Transportation Industry*, 14-18 Feb. 2000, University of New South Wales, Sydney, Australia. pp.51-60

82. Karbhari, V.M.; Eckel II, D.A. (1994). "Effect of cold regions climate on composite jacketed concrete columns." *Journal of Cold Regions Engineering*, **8**(3), 73-86.

83. Karbhari, V.M. and Gao, Y. (1997). "Composite jacketed concrete under uniaxial compression-verification of simple design equations". *J. Mat. In Civ. Engrg.*, ASCE, **9**(4), 185-193.

84. Karsan, I.D. and Jirsa, J.O. (1969). "Behavior of concrete under compressive loadings". *J. Struct. Div.*, **95**(12), 2543-2563.

85. Katsumata, H.; Kobatake, Y.; and Takeda, T. (1988). "Study with carbon fiber for earthquake-resistance capacity of existing reinforced concrete columns". *Proceedings of the Ninth World Conference on Earthquake Engineering,* Aug.2-9, 1988, Tokyo, v.7, pp. 517-522.

86. Kendall, E. Atkinson. (1978). *An Introduction to Numerical Analysis.* John Wiley & Sons, New York.

87. Kent, D.C. and Park, R. (1971). "Flexural members with confined concrete". *J. Struct. Div.*, ASCE, **97**(7), 1969-1990.

88. Kilpatrick, A.E. and Rangan, B.V. (1999). "Tests on high-strength concrete-filled steel tubular columns". *ACI Structural Journal,* **96**(2), 268-274.

89. Kilpatrick, A.E. and Rangan, B.V. (1997). *Deformation-control analysis of composite concrete columns*. Civil Engineering Research Report, No.3/97, Curtin University of Technology, Perth, Australia, July 1997, 116pp.

90. Kloppel, V.K. and Goder, W. (1957a). "An investigation of the load carrying capacity of concrete-filled steel tubes and development of design formula". *Der Stahlbau*, Vol.26, No.1, pp.1-10.

91. Kloppel, V.K. and Goder, W. (1957b). "An investigation of the load carrying capacity of concrete-filled steel tubes and development of design formula". *Der Stahlbau*, Vol.26, No.2, pp.44-50.

92. Knowels, R. and Park, R. (1969). "Strength of concrete filled steel tubular columns". *Journal of Structural Division*, ASCE, Vol. 95, No. ST.12, pp.2565-2587.

93. Knowels, R. and Park, R. (1970). "Axial load design for concrete filled steel tubes". *Journal of Structural Division*, ASCE, Vol. 96, No. ST.10, pp.2125-2153.

94. Kwon, Y.B.; Song, J.Y. and Kon, K.S. (2000). "The structural behavior of concrete-filled steel piers". *Proceedings of the 16th Congress of IABSE, Lucerne*, Switzerland, Sept.18-21.

95. Lau, K.T. and Zhou, L.M. (2001). "The mechanical behavior of composite-wrapped concrete cylinders subjected to uniaxial compression load". *Composite Structures*, v.52, pp.189-198.

96. Liddell, D.P., Ingham, J.M. and Davidson B.J. (2001). "Influence of loading history on the ultimate displacement of ductility 6-current design concrete structure". *Proceedings of Australian Structural Engineering Conference*. 29 April-2 May 2001. Gold Coast, Australia. Pp. 231-238.

97. Liddell, D.P. (2000). *Influence of Loading History on Ultimate Displacement of Concrete Structures.* M.Eng. thesis, University of Auckland, New Zealand.

98. Liu, A. and Park, R. (2001). "Seismic behavior and retrofit of pre-1970's as-built exterior beam-column joints reinforced by plain round bars". *Bulletin of the New Zealand Society for Earthquake Engineering*, **34**(1), 68-81.

99. Liu, H.K.; Tai, N.H. and Chen C.C. (2000). "Compression strength of concrete columns reinforced by non-adhesive filament wound hybrid composites". *Composites: Part A*, v.31, pp.221-233.

100. Liu, J. and Foster, S.J. (1998). "Finite-element model for confined concrete columns". *Journal of Structural Engineering*, ASCE, **124**(9), 1011-1017.

101. Lohr, W.S. (1934). "Concrete encased in steel shells proposed". *Engineering News Record*, Vol.113, pp.760-762.

102. Lynn, A., Moehle, J.P., Mahin, S.A. and Holmes, W.T. (1996). "Seismic evaluation of existing reinforced concrete building columns". *Earthquake Spectra*, **12**(4), 715-739.

103. Machida, A.; Mutsuyoshi, H. and Adhikary, B.B. (2000). "Recent developments in repair and strengthening of concrete structures". *Proceedings of the 16th Congress of IABSE, Lucerne*, Switzerland, Sept.18-21.

104. Madas, P. and Elnashai, A.S. (1992). "A new passive confinement model for the analysis of concrete structures subjected to cyclic and transient dynamic loading". *Earthquake Engineering and Structural Dynamics*, vol.21, pp.409-431.

105. Maher, A. and Darwin, D. (1982). "Mortar constituent of concrete in compression". *ACI Journal*, v.79, pp.100-109.

106. Mander, J. B., Priestley, M. J. N., and Park, R. (1988a). "Theoretical stress-strain model for confined concrete." *Journal of Structural Engineering*, ASCE, **114**(8), 1804-1826.

107. Mander, J. B., Priestley, M. J. N., and Park, R. (1988b). "Observed stress-strain behavior of confined concrete." *Journal of Structural Engineering*, ASCE, **114**(8), 1827-1849.

108. Marino, S.; Kedgwick, J.; Yasuzaki, C. and Kanazawa, S. (1992). "Behavior of concrete-filled steel tubular three-dimensional subassembleages". ASCE, *Composite construction in Steel and Concrete II*, June 14-19, 1992, pp.726-741.

109. Marsh, Lee. (1992) "Seismic retrofits for R/C column bar splices". *Proceedings of the 1992 Structures Congress*, ASCE, San Antonio, Texas, April13-15, 1992.

110. Martinez-Rueda, J.E. and Elnashai, A.S. (1997). "Confined concrete model under cyclic load". *Materials and Structures*, Vol.30, pp139-147.

111. Melchers, R.E. (Ed.) (1990). *Newcastle Earthquake Study*. The Institution of Engineers, Australia.

112. Mirmiran, A.; Zagers, K. and Yuan, W. (2000). "Nonlinear finite element modeling of concrete confined by fiber composites". *Finite Elements in Analysis and Design*, v.35, pp79-96.

113. Mirmiran, A. and Shahawy, M. (1997). "Behavior of concrete columns confined by fiber composites". *Journal of Structural Engineering*, ASCE, **123**(5), 583-590.

114. Mirmiran, A., Shahawy, M., Samaan, M., El Echary, H., Mastrapa, J.C. and Pico, O. (1998). "Effect of column parameters on FRP-confined concrete." *Journal of Composites for Construction*, **2**(4), 175-185.

115. Moehle, J.P. (1996) "Displacement based seismic design criteria". *Proceedings of the Eleventh World Conference on Earthquake Engineering*, Pergamon, Elsevier Science Ltd, Disc 4, Paper No.2125.

116. Moehle, J.P. and Mahin, S.A. (1991) "Observations on the behavior of reinforced concrete buildings during earthquakes". *ACI SP-127, Earthquake-Resistant Concrete Structures: Inelastic Response and Design*, ed. S.K. Ghosh, American Concrete Institute, Farmington Hills, Michigan, pp.67-89.

117. Monti, G.; Nistico, N. and Santini, S. (1998). "Design equations for FRP wrapping and steel jacketing of bridge piers". *Proc. 11th ECEE*, Balkema, Rotterdam, the Netherlands.

118. Muguruma, H.; Watanabe, S.; Katsuta, S. and Tanaka, S. (1980). "A stress-strain model of confined concrete". *Proc. JCA Cement and Concrete*, v.34, Japan Cement Assn., Tokyo, Japan, pp.429-432.

119. Nakanishi, K.; Kitada, T. and Nakai, H. (1999). "Experimental study on ultimate strength and ductility of concrete filled steel columns under strong earthquake". *Journal of Constructional Steel Research*, v.51, pp.297-319.

120. Nanni, A. and Bradford, N.M. (1995). "FRP-jacketed concrete under uniaxial compression". *Construction and Building Materials*, **9**(2), 115-124.

121. Neville, A.M. (1981). *Properties of Concrete.* Third Edition, Longman Scientific & Technical, Singapore.

122. Newmark, N.M.; Siess, C.P. and Viest, I.M. (1951). "Test and analysis of composite beams with incomplete interaction". *Proceeding Society for Experimental Stress Analysis*, 9, No.1, 75-92.

123. Newmark, N.M.; Siess, C.P. and Viest, I.M. (1952). "Studies of slab and beam highway bridges, Part III – Small scale tests of shear connectors and composite T-beams". *Bulletin 396*, University of Illinios, Urbana, Illinios.

124. Oehlers, D. J. and Bradford, M.A. (1995). *Composite Steel and Concrete Structural Members-Fundamental Behaviour.* Elsevier Science Ltd, Oxford, OX1GB, U.K.

125. Okamato, T. and Maeno, T. (1988). "Experimental study on rectangular steel tube columns infilled with ultra high strength concrete hardened by centrifugal force." *Annual Meeting of AIJ, Proceedings*, Chiba, Oct. 1988, pp.1359.

126. Orito, Y.; Sato, T.; Tanaka, N.; and Watanabe, Y. (1989). "Study on the unbonded steel tube concrete structure". *U.S.-Japan seminar Composite Construction*, pp.786-804.

127. O'Shea M.D. and Bridge, R.Q (2000). "Design of circular thin-walled concrete filled steel tubes". *Journal of Structural Engineering, ASCE*, **126**(11), 1295-1303.

128. O'Shea M.D. and Bridge, R.Q (1999). "The effects of local buckling and confinement in concrete filled circular steel tubes". *Proceedings of the 16th Australian Conference on the Mechanics of Structures and Materials, Sydney*, Australia, 8-10 Dec. 1999, pp.321-326.

129. Pantelides, C.P.; Marriott, N.; Gergely, J. and Reaveley, L.D. (2000). "Seismic rehabilitation of damaged bridge piers with FRP composites". *Proceedings of the 16th Congress of IABSE, Lucerne*, Switzerland, Sept.18-21.

130. Park, R. (2001). "Improving the resistance of structures to earthquakes". *Bulletin of the New Zealand Society for Earthquake Engineering*, **34**(1), 1-39.

131. Park, R.; Kent, D.C. and Sampson, R.A. (1972). "Reinforced concrete members with cyclic loading". *Journal of Structural Engineering*, ASCE, v.98, pp.1341-1359.

132. Park, R., Priestley, M.J.N. and Gill, W.D. (1982). "Ductility of square confined concrete columns", *J. Struct. Div.* ASCE, v.108, pp.929-950.

133. Parvin, A. and Wang, W. (2001). "Behavior of FRP jacketed concrete columns under eccentric loading". *Journal of Composites for Construction*, ASCE, **5**(3), 146-152.

134. Paulay, T. and Priestley, M.J.N. (1992). *Seismic Design of Reinforced Concrete and Masonry Buildings.* John Wiley and Sons, Inc. New York.

135. Pekau, O.A.; Zhang, Z.X. and Liu, G.T. (1992). "Constitutive model for concrete in strain space". *Journal of Engineering Mechanics*, ASCE, **118**(9), 1907-1927.

136. Pessiki, S.; Harries, K.A.; Kestner, J.T.; Sause, R. and Ricles, J.M. (2001). "Axial behavior of reinforced concrete columns confined with FRP jackets". *Journal of Composites for Construction*, ASCE, **5**(4), 237-245.

137. Pham, L. and Griffith, M. (1995). *Report on the January 17, 1995 Great Hyogo-Ken Nanbu (Kobe) Earthquake*. Joint report from CSIRO Division of Building, Construction and Engineering and Department of Civil and Environmental Engineering at The University of Adelaide, Report No.DBCE Doc 95/175(M), 55p.

138. Picher, F., Rochette, P. and Labossiere, P. (1996). "Confinement of concrete cylinders with CFRP". *Proc. 1st Int. Conf. on Composites in Infrastructure*, ICCI'96, H. Saadatmanesh and M.R. Ehsani, eds., 829-841.

139. Popovics, S. (1973). "A numerical approach to the complete stress-strain curve of concrete". *Cement and Concrete Research*, v.3, pp.583-599.

140. Popovics, S. (1970). "A review of stress-strain relationships for concrete". *ACI Journal*, v.67, pp.243-248.

141. Priestley, M.J.N. (1997) "Displacement-based seismic assessment of reinforced concrete buildings". *Journal of Earthquake Engineering*, **1**(1), 157-192.

142. Priestley, M.J.N. (1998) "Displacement based approaches to rational limit states design of new structrues." *Proceedings of the Eleventh European Conference on Earthquake Engineering*, 6-11 Sept. 1998, Paris, France, pp 317-335.

143. Priestley, M. J. N.and Park, R. (1987). "Strength and ductility of concrete bridge columns under seismic loading". *ACI Structural Journal,* **84**(1), 61-76.

144. Priestley, M.J.N.; Seible, F. (1995). "Design of seismic retrofit measures for concrete and masonry structures." *Construction and Building Materials*, **9**(6), 365-377.

145. Priestley, M. J. N., Verma, R., and Xiao, Y. (1994a). "Seismic shear strength of reinforced concrete columns." *Journal of Structural Engineering*, ASCE, **120**(8), 2310-2329.

146. Priestley, M. J. N., Seible, F., Xiao, Y., and Verma, R. (1994b). "Steel jacket retrofitting of reinforced concrete bridge columns for enhanced shear strength-part1: theoretical consideration and test design." *ACI Structural Journal,* **91**(4), 394-405.

147. Priestley, M. J. N., Seible, F., Xiao, Y., and Verma, R. (1994c). "Steel jacket retrofitting of reinforced concrete bridge columns for enhanced shear strength-part2: test results and comparison with theory." *ACI Structural Journal,* **91**(5), 537-551.

148. Rangan, B.V. (1991). "Design of slender hollow steel columns filled with concrete". *Proceeding, International conference on steel and aluminum structures*, 22-24 May 1991, Singapore, pp.104-112.

149. Rangan, B.V. and Joyce, M. (1992). "Strength of eccentricity loaded slender steel tubular columns filled with high-strength concrete". *ACI Structural Journal*, **89**(6), 676-681.

150. Ramirez, J.L.; Barcena, J.M.; Urreta, J.I.; Sanchez, J.A. (1997). "Efficiency of short steel jackets for strengthening square section concrete columns". *Construction and Building Materials*, **11**(5-6). 345-352.

151. Ramirez, Jose L. (1996). "Ten concrete column repair methods." *Construction and Building Materials*, **10**(3), 195-202.

152. Razvi, S.R. and Saatcioglu, M. (1989). "Confinement of reinforced concrete columns with welded wire fabric". *ACI Structural Journal*, **86**(6), 615-623.

153. Restrepo-Posada, J.I; Dodd, L.L.; Park, R. and Cooke, N. (1994). "Variables affecting cyclic behavior of reinforcing steel". *Journal of Structural Engineering, ASCE*, **120**(11), 3178-3195.

154. Richart, F.E., Brandtzaeg, A. and Brown, R.L. (1928). "A study of the failure of concrete under combined compressive stresses". *Bulletin No. 185,* University of Illinois Engineering Experimental Station, Urbana, Ill.

155. Richart, F.E., Brandtzaeg, A. and Brown, R.L. (1929). "The failure of plain and spirally reinforced concrete in compression". *Bulletin No. 190,* University of Illinois Engineering Experimental Station, Urbana, Ill.

156. Rochette, P. and Labossière, P. (1996). "A plasticity approach for concrete columns confined with composite materials". *Adv. Composite Mat. in Bridges and Struct.*, M. M. El-Badry, ed., Canadian Soc. for Civ. Engrg., Montreal, Canada, 359-366.

157. Rochette, P. and Labossière, P. (2000). "Axial testing of rectangular column models confined with composites". *Journal of Composites for Construction*, ASCE, **4**(3), 129-136.

158. Rodriguez, Mario E. and Santiago, Sergio A. (1998). "Simulated seismic load tests on two-story waffle-flat-plate structure rehabilitated by jacketing." *ACI Structural Journal*, **95**(2), 129-141.

159. Rodriguez, M.; and Park, R. (1994). "Seismic load tests on reinforced concrete columns strengthened by jacketing." *ACI Structural Journal*, **91**(2), 150-159.

160. Russell, W.A. (1953). "Structural properties of light-gage tubular columns". Housing Research paper, No.12, Housing and Home Finance Agency, Oct. 1953.

161. Saadatmanesh, H., Ehsani, M. R., and Jin, L. (1996). "Seismic strengthening of circular bridge pier models with fiber composites". *ACI Structural Journal,* **93**(6), 639-647.

162. Saadatmanesh, H., Ehsani, M. R., and Li, M. W. (1994). "Strength and ductility of concrete columns externally reinforced with fibre composite straps." *ACI Structural Journal,* **91**(4), 434-447.

163. Saafi, M., Toutanji, H.A. and Li, Z. (1999). "Behavior of concrete columns confined with fiber reinforced polymer tubes". *ACI Material Journal*, **96**(4), 500-509.

164. Saatcioglu, M. and Razvi, S.R. (1992). "Strength and ductility of confined concrete". *Journal of Structural Engineering*, ASCE, **118**(6), 1590-1607.

165. Saatcioglu, M. and Razvi, S.R. (1998). "High-strength concrete columns with square sections under concentric compression". *Journal of Structural Engineering*, ASCE, **124**(12), 1438-1447.

166. Sakai, J. and Kawashima, K. (2000). "An unloading and reloading stress-strain model for concrete confined by tie reinforcements". ". *Proc. 12th World Conf. on Earthquake Engineering*, paper no. 1431, New Zealand.

167. Sakino, K.; and Sun, Y.P. (2000). "Steel jacketing for improvement of column strength and ductility". *Proc. 12th World Conf. on Earthquake Engineering*, paper no. 2525, New Zealand.

168. Sakino, K.; Sun, Y.P. and Aklan, A. (1996). "Effects of wall thickness of steel tube on the behavior of square tubed R/C columns". *11th World Conf. On Earthquake Engrg.*

169. Sakino, K. and Ishibashi, H. (1985). "Experimental studies on concrete filled square steel tubular short columns subjected to cyclic shearing force and constant axial force'. *Transactions of the Architectural Institute of Japan,* No.353, July, pp.81-89.

170. Samaan, M., Mirmiran, A. and Shahawy, M. (1998). "Model of concrete confined by fiber composites". *Journal of Structural Engineering*, ASCE, **124**(9), 1025-1031.

171. Seible, Frieder; Priestley, M.J. Nigel; Hegemier, Gilbert A.; Innamorato, Donato. (1997). "Seismic retrofit of RC columns with continuous carbon fiber jackets." *Journal of Composites for Construction*, **1**(2), 52-62.

172. Seracino, R., Oehlers, D.J. and Yeo, M.F. (2001) "Partial-interaction flexural stresses in composite steel and concrete bridge beams", *Engineering Structures*, **23**(9), 1186-1193.

173. Shah, S.P. and Ahmad S.H. (1994). *High Performance Concrete: Properties and Applications.* McGraw-Hill, Inc., New York.

174. Shah, S.P.; Fafitis, A. and Arnold, R. (1983). "Cyclic loading of spirally reinforced concrete". *Journal of Structural Engineering*, ASCE, v.109, pp.1695-1710.

175. Shahawy, M.; Mirmiran, A. and Beitelman, T. (2000). "Tests and modeling of carbon-wrapped concrete columns". *Composites Part B – Engineering*, **31**(6-7), 471-480.

176. Shams, Mohammad; Saadeghvaziri, M. Ala. (1997). "State of the art of concrete-filled steel tubular columns." *ACI Structural Journal*, **94**(5), 558-571.

177. Sheikh, S.A. and Khoury, S.S. (1997). "A performance-based approach for the design of confining steel in tied columns". *ACI Structural Journal*, **94**(4), 421-431.

178. Sheikh, S.A. and Khoury, S.S. (1993). "Confined concrete columns with stubs". *ACI Structural Journal*, **90**(4), 414-431.

179. Sheikh, S.A. and Uzumeri, S.M. (1982). "Analytical model for concrete confinement in tied columns". *J. Struct. Div.,* ASCE, **108**(12), 2703-2722.

180. Sheikh, S.A. and Uzumeri, S.M. (1980). "Strength and ductility of tied concrete columns". *J. Struct. Div.,* ASCE, **106**(5), 1079-1102.

181. Sinha, B.P.; Gerstle, K.H. and Tulin, L.G. (1964). "Stress-strain relations for concrete under cyclic loading". *ACI Journal*, v.61, pp.195-210.

182. Spoelstra, M.R. and Monti, G. (1999). "FRP-confined concrete model". *Journal of Composites for Construction*, **3**(3), 143-150.

183. Sugano, S. and Nagashima, T. (1992). "Seismic behavior of concrete filled tubular steel columns". ASCE, *10th Structural Congress '92, Proceedings*, Apr. 13-15, 1992, pp. 914-917.

184. Tamai, S.; Sato, T. and Okamoto, M. (2000). "Hysteresis model of steel jacketed RC columns for railway viaducts". *Proceedings of the 16th Congress of IABSE,* Lucerne, Switzerland, Sept.18-21.

185. Tan, T.H. and Yip, W.K. (1999). "Behavior of axially loaded concrete columns confined by elliptical hoops"" *ACI Structural Journal*, **96**(6), 967-971.

186. Taylor, A.W.; Stone, W.C. (1994). "Jacket thickness requirements for seismic retrofitting of circular bridge columns". *Symp Pract Solutions Bridge Strengthening Rehabil* Apr 5-6 1993 1994 Sponsored by: Iowa State University. Iowa State Univ Press p 249-258.

187. Teh, K.F.; Tan, J.; Lin, S.H. and Yaw, S.Y. (1999) "Retrofitting existing reinforced concrete columns by bolting steel plates to their sides". *4th year undergraduate project report*, Dept. Civil & Environmental Engng, The University of Adelaide.

188. Teng, J.G.; Chen, J.F.; Smith, S.T. and Lam, L. (2000). *RC Structures Strengthened with FRP Composites*, Hong Kong Polytechnic University.

189. Thériault, M. and Neale, K.W. (2000). "Design equations for axially loaded reinforced concrete columns strengthened with fibre reinforced polymer wraps". *Can. J. Civ. Eng.*, v.27, pp.1011-1020.

190. Timoshenko, S., *Strength of Materials - Part I &II*, 3rd edn, D. VAN NOSTRAND COMPANY, INC., New York, 1955.

191. Tomii, M. (1993). "Non-hooped reinforced concrete columns and beam-column connections laterally confined in bellows square steel tube". *Proceedings of Tom Paulay Symposium,* La Jolla, California, September, pp.383-402.

192. Tomii, M. (1991). "Ductile and strong columns composed of steel tube, infilled concrete and longitudinal steel bars". *Special Volume, Proceedings, Third International Conference on Steel-Concrete Composite Structures, ASCCS*, Fukuoka, Japan, Sept., pp.39-66.

193. Tomii, M.; Sakino, K. and Xiao, Y. (1987). "Ultimate moment of reinforced concrete short columns confined in steel tube'. *Proceedings of the Pacific Conference on Earthquake Engineering,* New Zealand, V.2, 5-8 Aug. 1987, pp 11-22.

194. Tomii, M and Sakino, K. (1979). "Elasto-plastic behavior of concrete filled square steel tubular beam-columns". *Trans. Arch. Inst. Japan*, Vol.280, pp111-120.

195. Tomii, M. and Yoshimaro, K. (1977). "Experimental studies on concrete filled steel tubular columns under concentric loading". *International Colloquium on Stability of Structures Under Static and Dynamic Loads*, Washington DC. May17-19, 1977, pp.718-741.

196. Tomii, M., Matsui, C. and Sakino, K. (1973). "Concrete filled steel tube structures". *Tokyo Regional Conference, IABSE-ASCE Tall Building Conference*, Tokyo, Japan.

197. Toutanji, H.A. (1999). "Stress-strain characteristics of concrete columns externally confined with advanced fiber composite sheets". *ACI Material Journal*, **96**(3), 397-404.

198. Uehan, Fumiaki and Meguro, Kimiro (2000). "Vulnerability evaluation of jacketed viaduct using microtremor measurement & numerical simulation". *Proc. 12th World Conf. on Earthquake Engineering*, paper no. 1458, New Zealand.

199. Uy, B. (2001). "Strength of short concrete filled high strength steel box columns". *Journal of Construction Steel Research*, v.57, pp.113-134.

200. Uy, B. (2000). "Strength of concrete filled steel box columns incorporating local buckling". *Journal of Structural Engineering*, ASCE, **126**(3), 341-352.

201. Valluvan, Raj; Kreger, Michael E.; Jirsa, James O. (1993). "Strengthening of column splices for seismic retrofit on nonductile reinforced concrete frames." *ACI Structural Journal*, **90**(4), 432-433.

202. Wang, Y.C. and Restrepo, J.I. (2001). "Investigation of concentrically loaded reinforced concrete columns confined with glass fiber-reinforced polymer jackets". *ACI Structural Journal*, **98**(3), 377-385.

203. Warner, R.F.; Rangan, B.V.; Hall, A.S.; and Faulkes, K.A. (1998). *Concrete Structures.* Longman Group Limited, Australia.

204. Watson, S. and Park, R. (1994). "Simulated seismic load tests on reinforced concrete columns". *Journal of Structural Engineering*, ASCE, **120**(6), 1825-1849.

205. Watson, S., Zahn, F.A. and Park, R. (1994). "Confining reinforcement for concrete columns". *Journal of Structural Engineering*, ASCE, **120**(6), 1798-1824.

206. Xiao, Y., Wu, H., and Martin, G. R. (1999). "Prefabricated composite jacketing of RC columns for enhanced shear strength." *Journal of Structural Engineering*, ASCE, **125**(3), 255-264.

207. Xiao, Y., Ma, R. (1997). "Seismic retrofit of RC circular columns using prefabricated composite jacketing." *Journal of Structural Engineering*, ASCE, **123**(10), 1357-1364.

208. Xiao, Y., Ma, R. (1995). *Full scale testing of a typical parking structure column retrofitted with carbon fiber composite wrapping*. Research Report No. USC-SERR-95/03, Department of Civil Engineering, University of Southern California, Oct. 1995.

209. Yankelevsky, D.Z. and Reinhardt, H.W. (1987). "Model for cyclic compressive behavior of concrete". *Journal of Structural Engineering*, ASCE, v.113, pp.225-240.

210. Yao, J.; Li X. and Li, Z. (2001). "Experimental study of a circular concrete column reinforced with a composite tube". *Composites Science and Technology*, v.61, pp. 1881-1887.

APPENDIX A YOUNG'S MODULUS TEST CHARTS

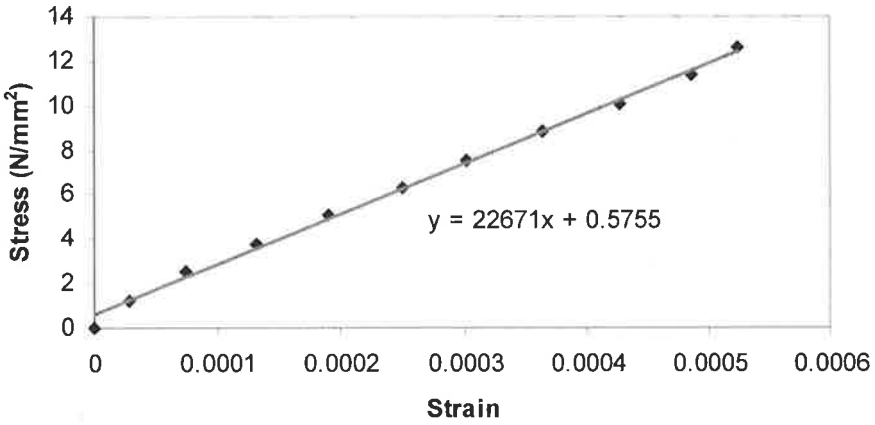

Fig. A.1 Young's Modulus test of CYL01

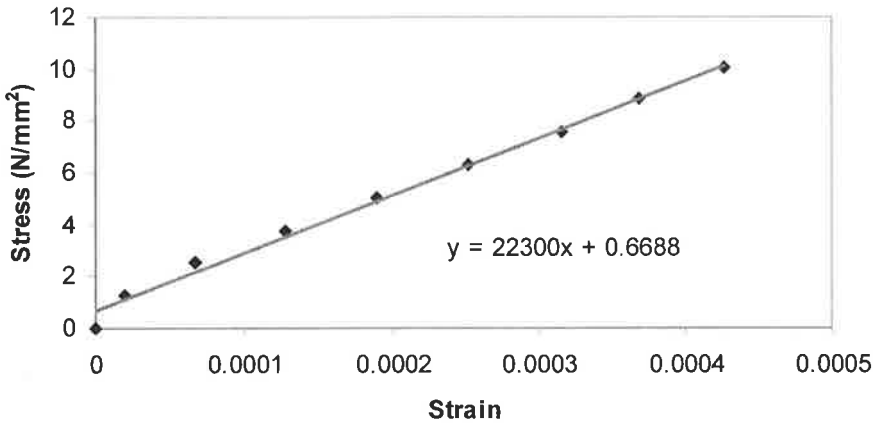

Fig. A.2 Young's Modulus test of CYL02

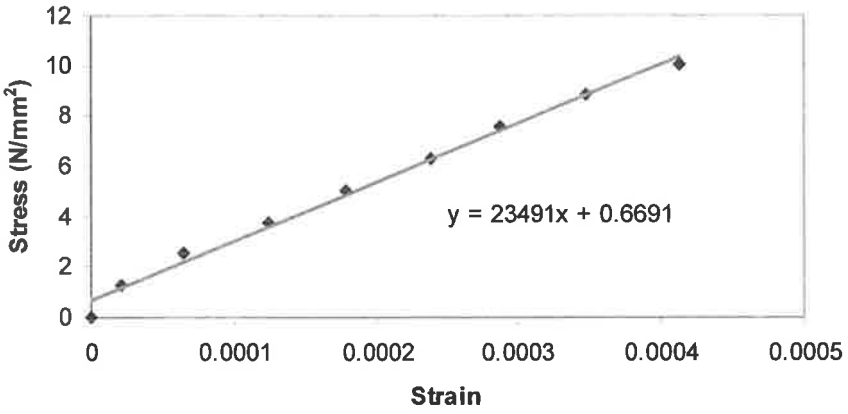

Fig. A.3 Young's Modulus test of CYL03

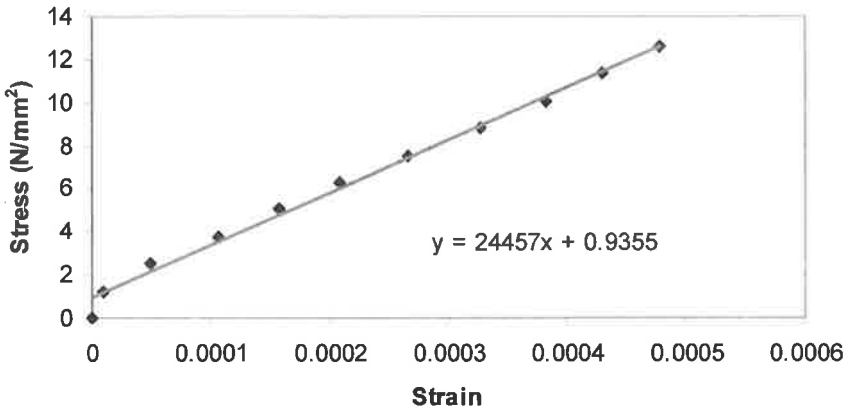

Fig. A.4 Young's Modulus test of CYL04

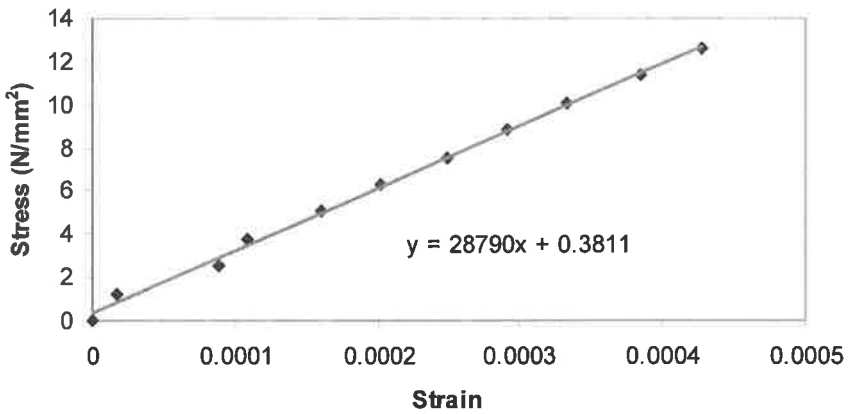

Fig. A.5 Young's Modulus test of CYL05

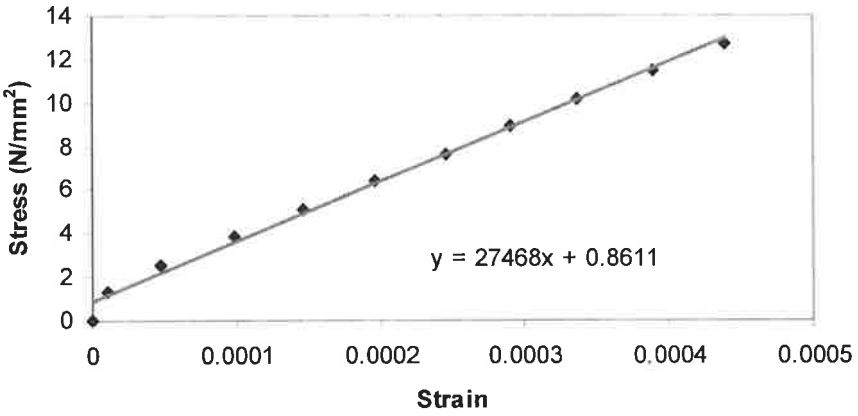

Fig. A.6 Young's Modulus test of CYL06

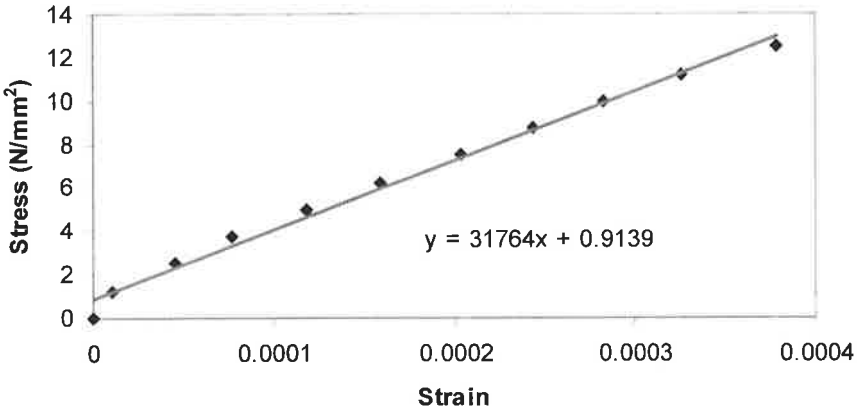

Fig. A.7 Young's Modulus test of CYL07

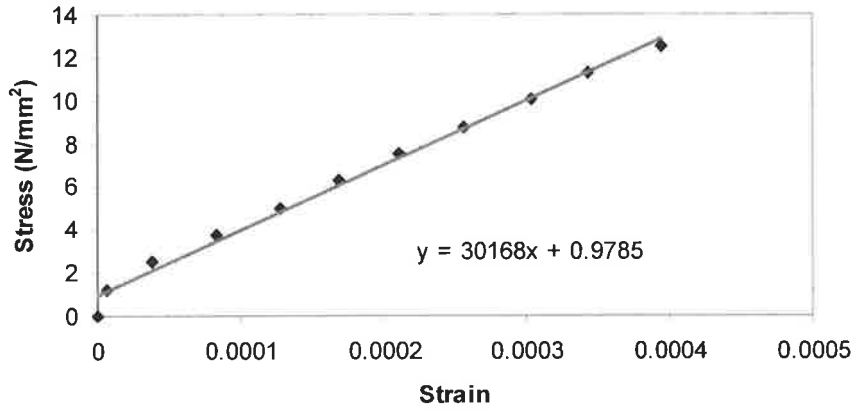

Fig. A.8 Young's Modulus test of CYL08

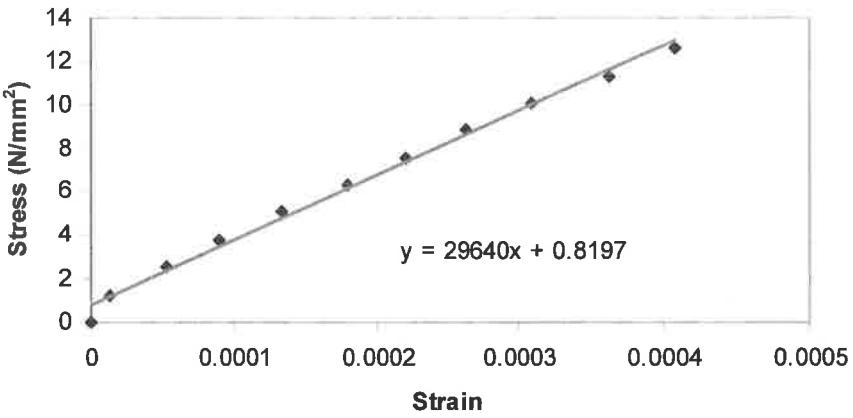

Fig. A.9 Young's Modulus test of CYL09

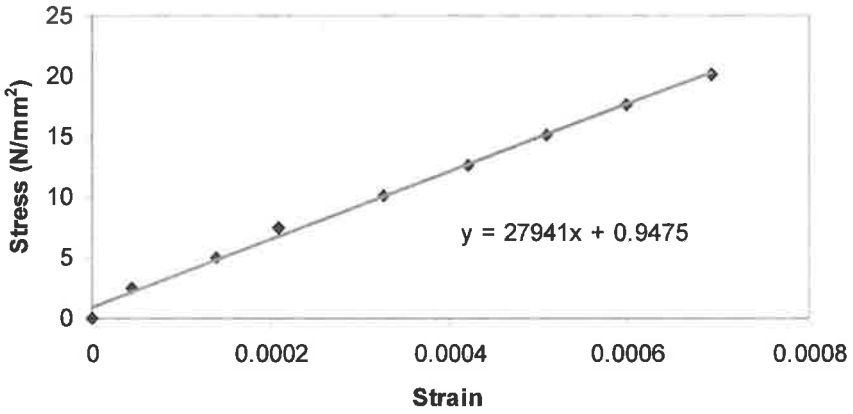

Fig. A.10 Young's Modulus test of CYL10

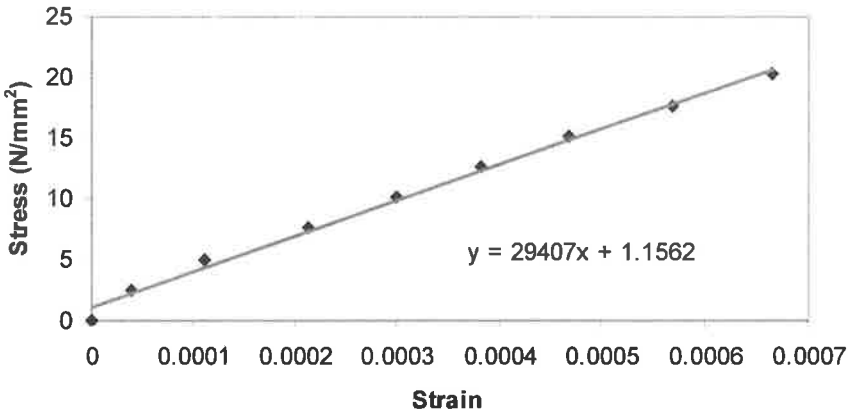

Fig. A.11 Young's Modulus test of CYL11

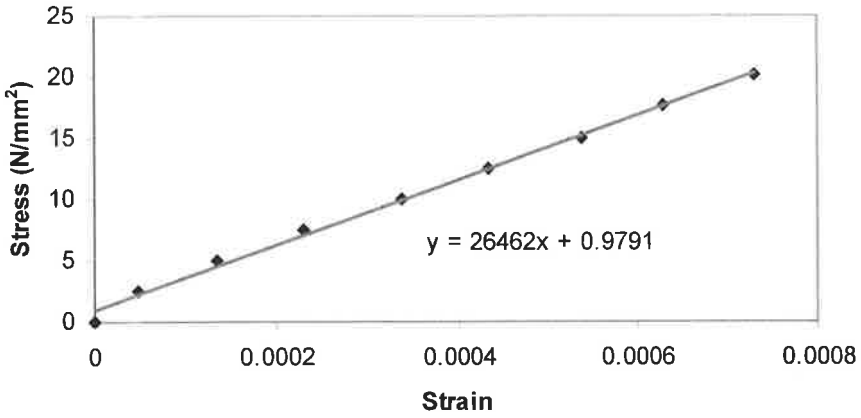

Fig. A.12 Young's Modulus test of CYL12

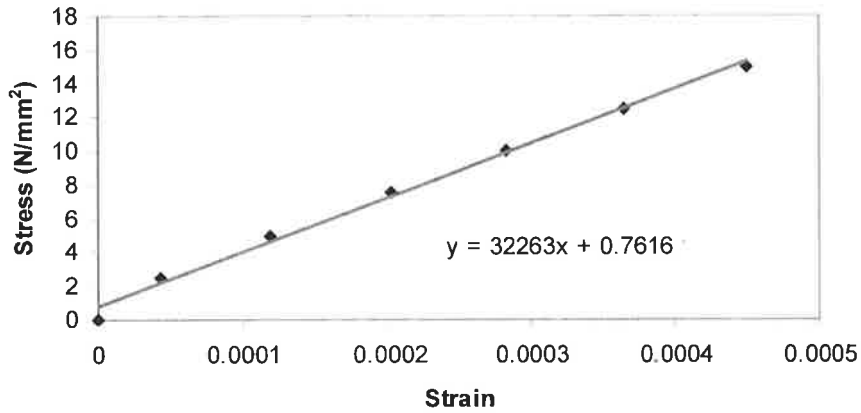

Fig. A.13 Young's Modulus test of CYL15

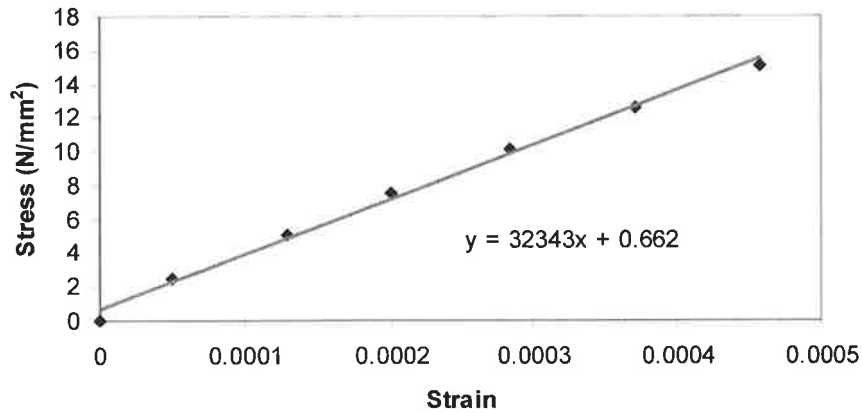

Fig. A.14 Young's Modulus test of CYL16

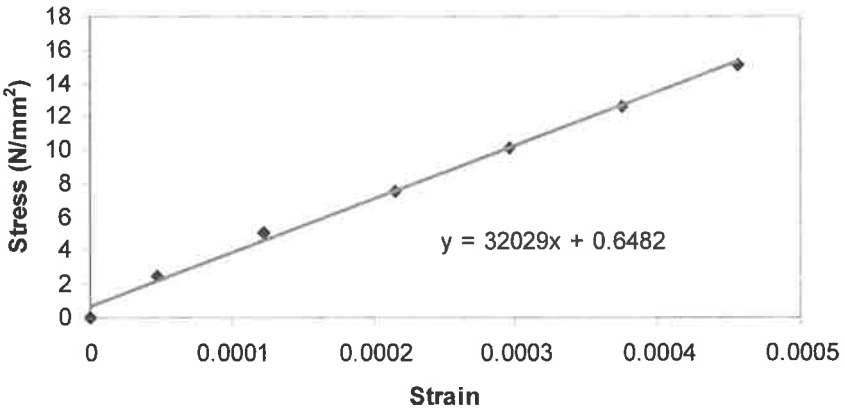

Fig. A.15 Young's Modulus test of CYL18

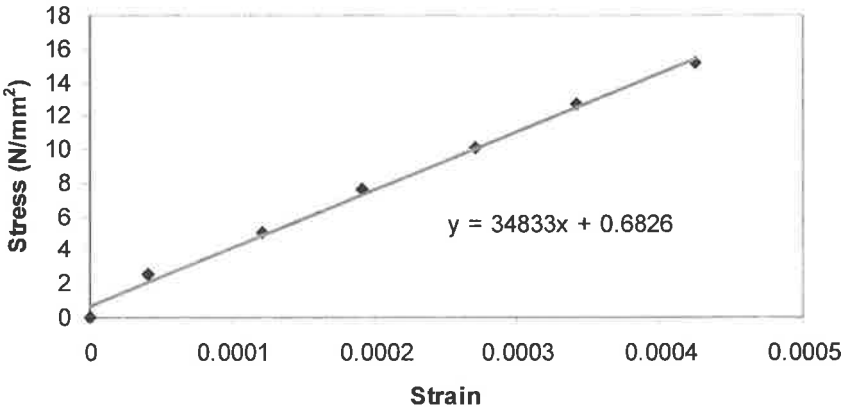

Fig. A.16 Young's Modulus test of CYL19

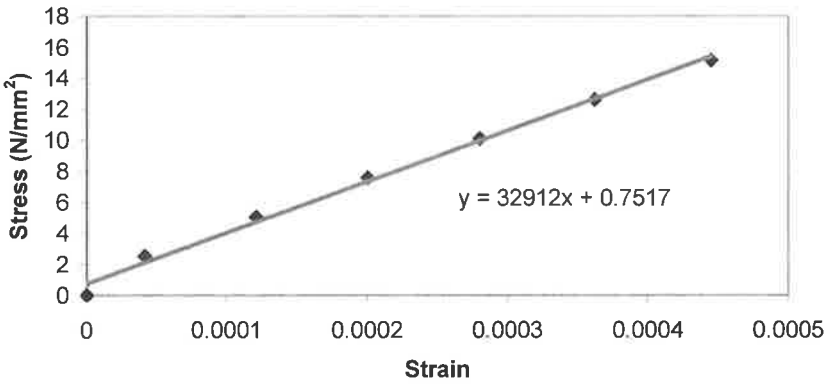

Fig. A.17 Young's Modulus test of CYL20

APPENDIX B TEST PHOTOGRAPHS

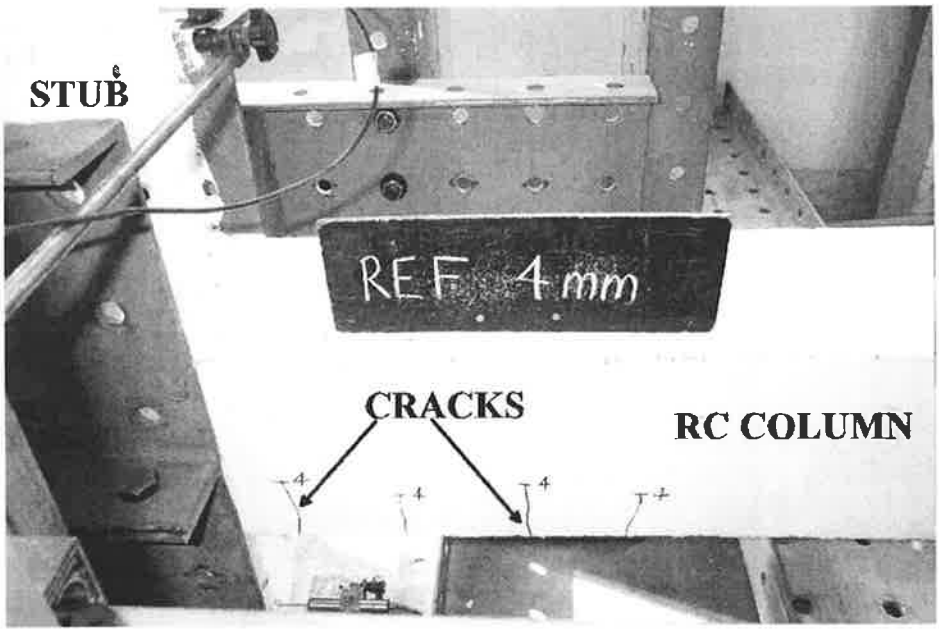

Fig. B.1 Front view at displacement of 7mm for specimen 1AMR

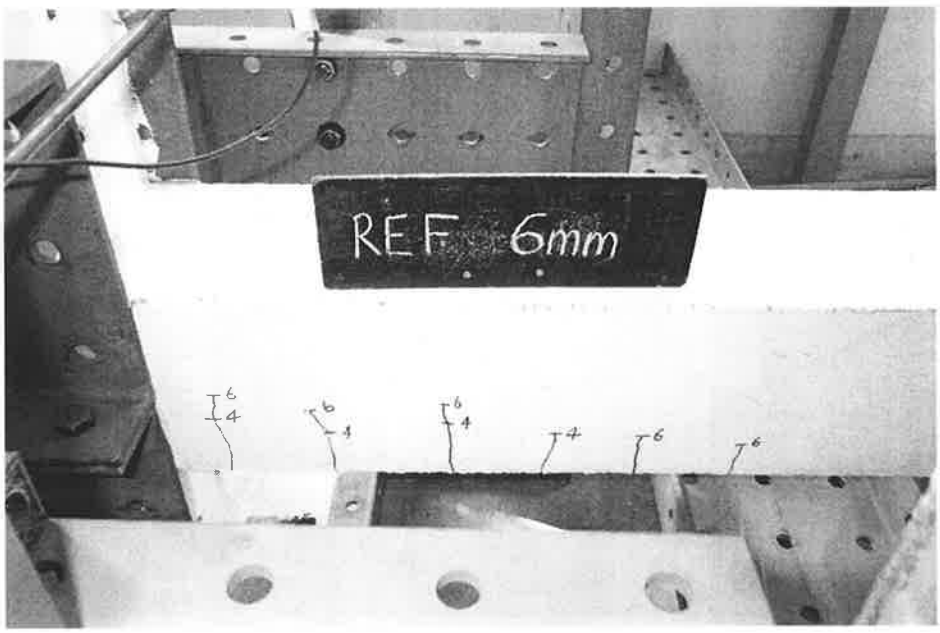

Fig. B.2 Front view at displacement of 12mm for specimen 1AMR

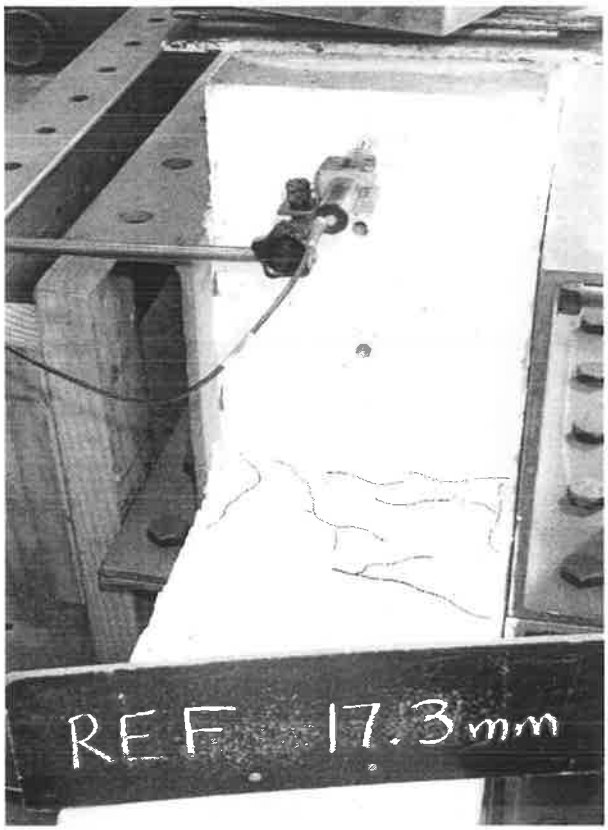

Fig. B.3 Top view at displacement of 28mm for specimen 1AMR

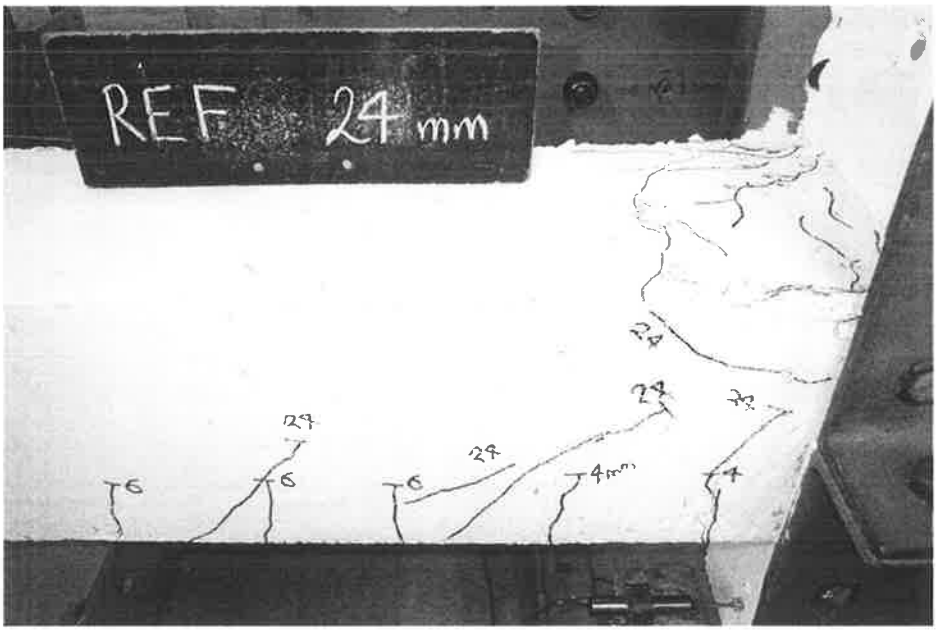

Fig. B.4 Rear view at displacement of 41mm for specimen 1AMR

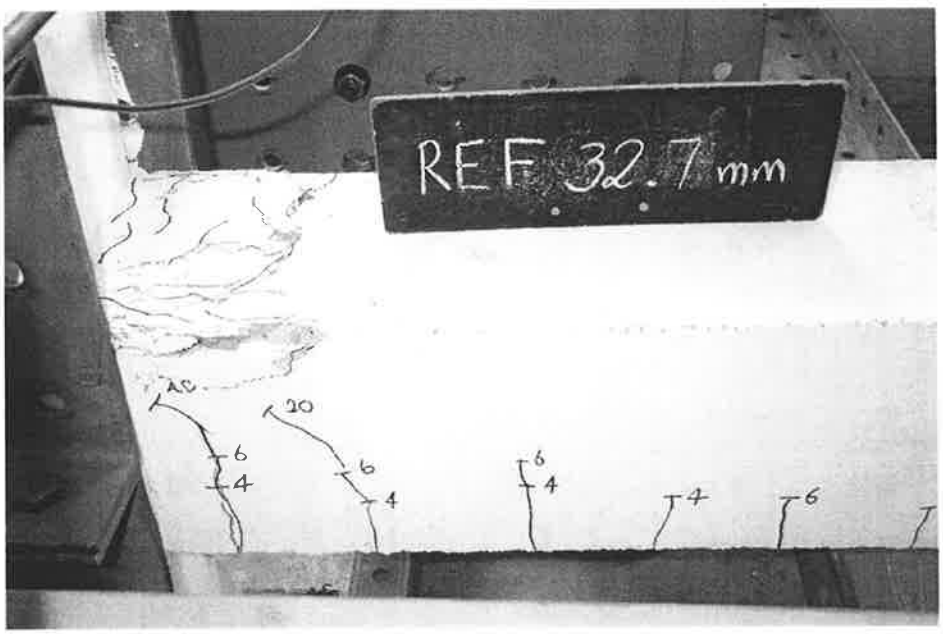

Fig. B.5 Front view at displacement of 57mm for specimen 1AMR

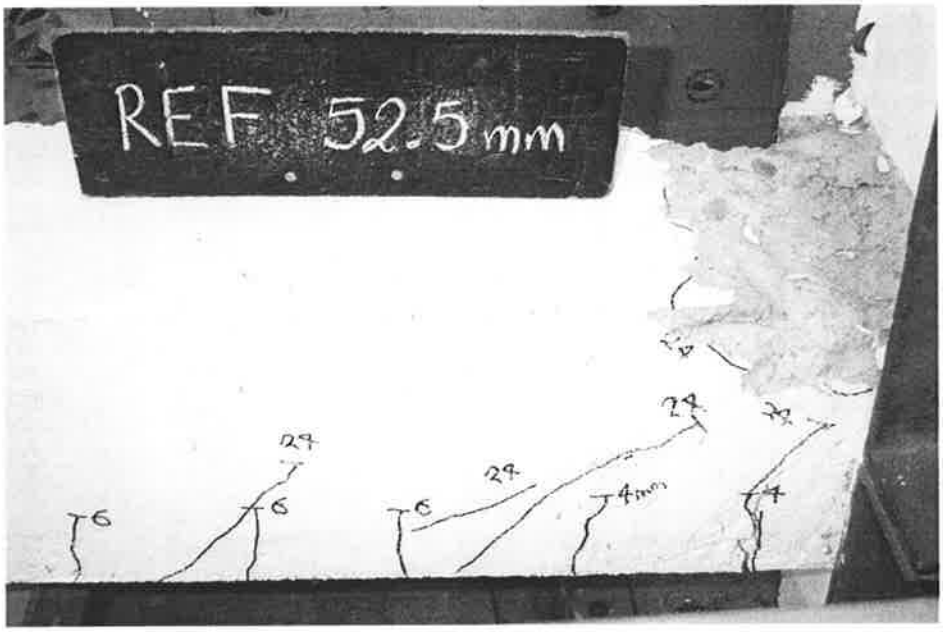

Fig. B.6 Rear view at displacement of 89mm for specimen 1AMR

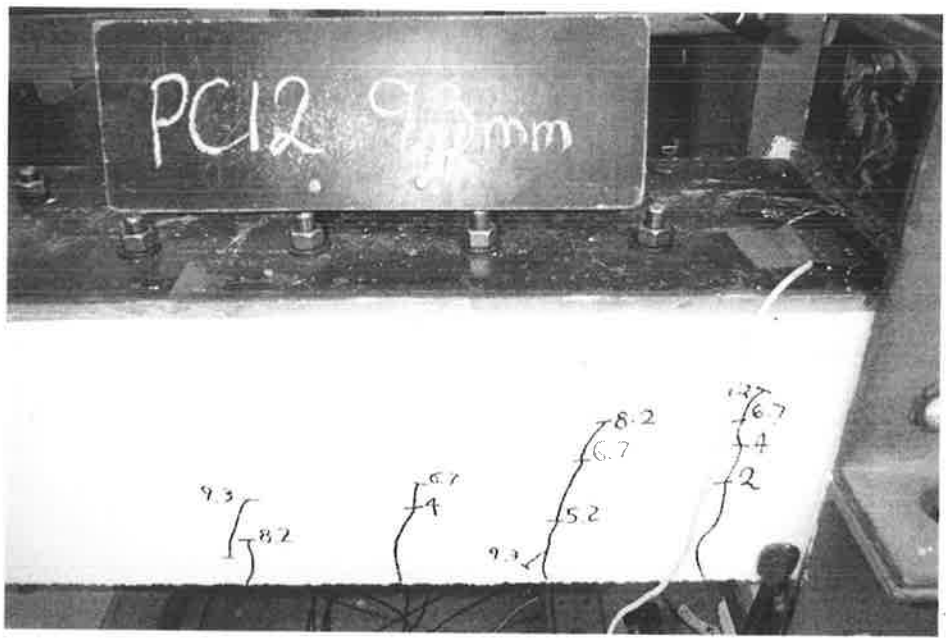

Fig. B.7 Rear view at displacement of 10mm for specimen 2AMF12

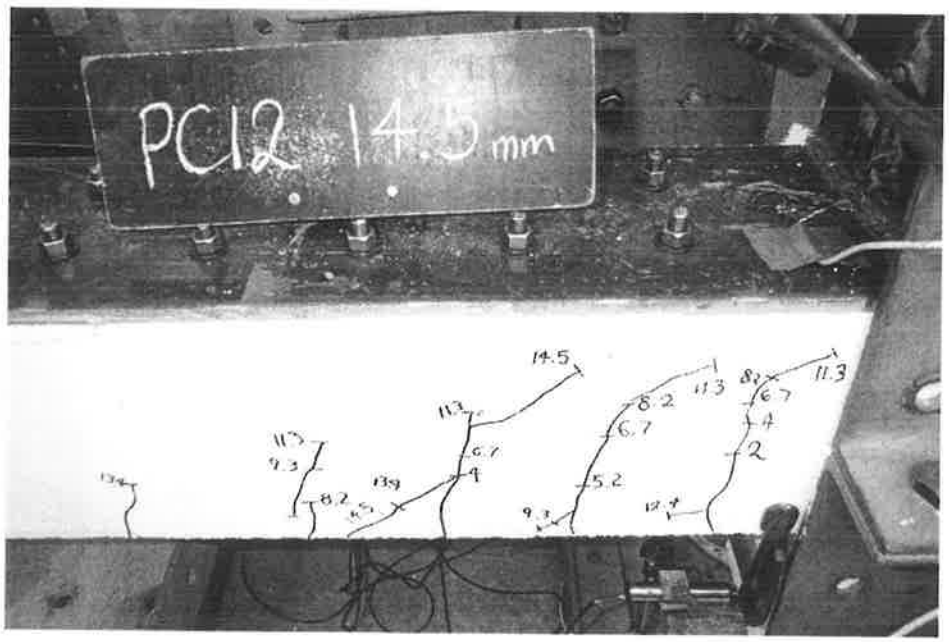

Fig. B.8 Rear view at displacement of 16mm for specimen 2AMF12

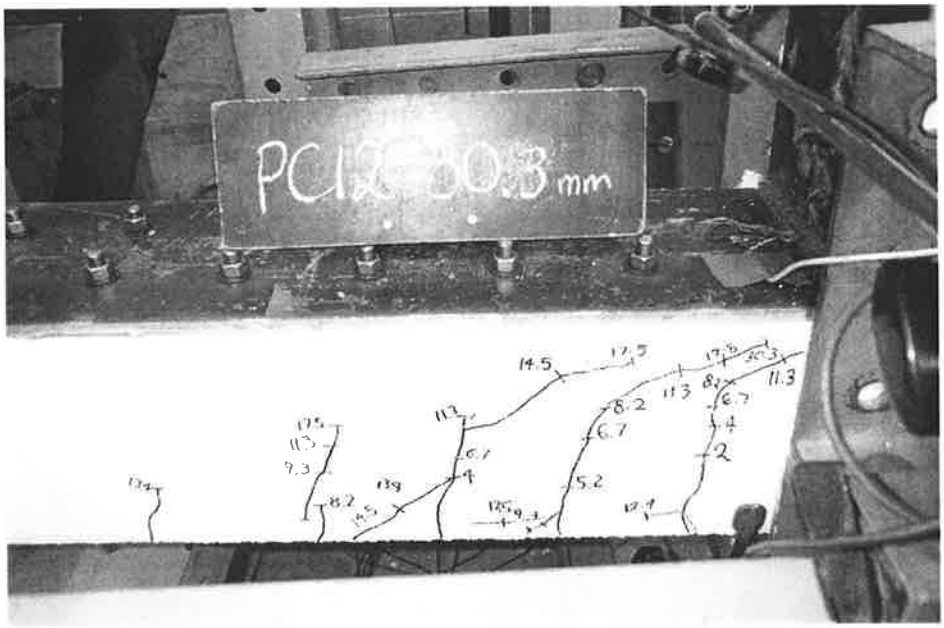

Fig. B.9 Rear view at displacement of 42mm for specimen 2AMF12

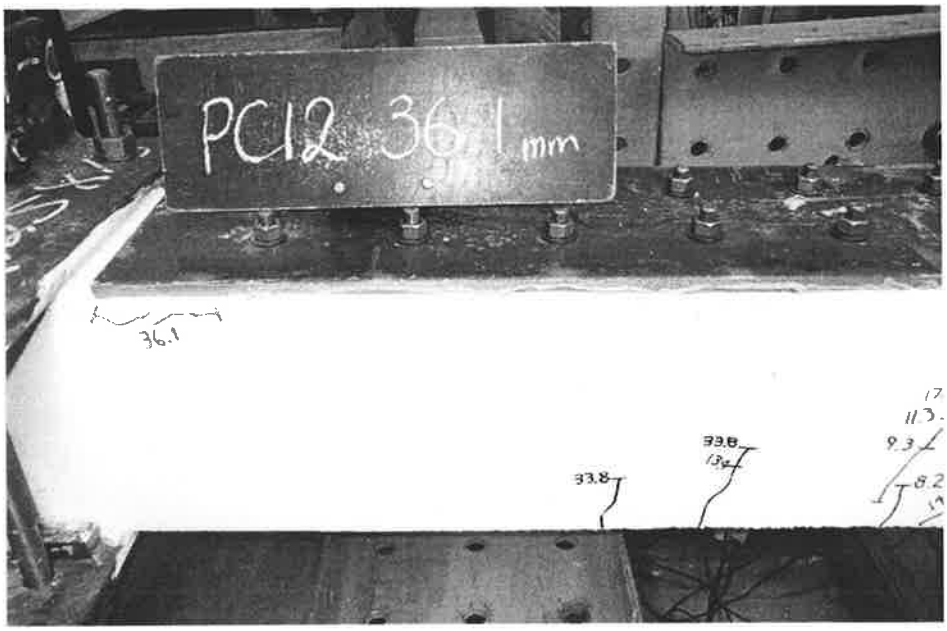

Fig. B.10 Rear view at displacement of 52mm for specimen 2AMF12

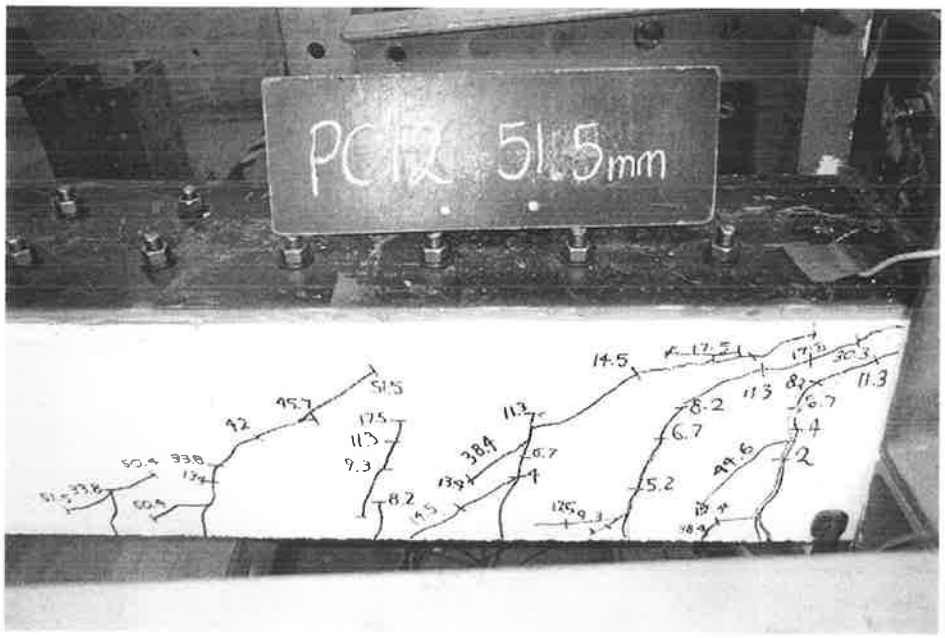

Fig. B.11 Rear view at displacement of 82mm for specimen 2AMF12

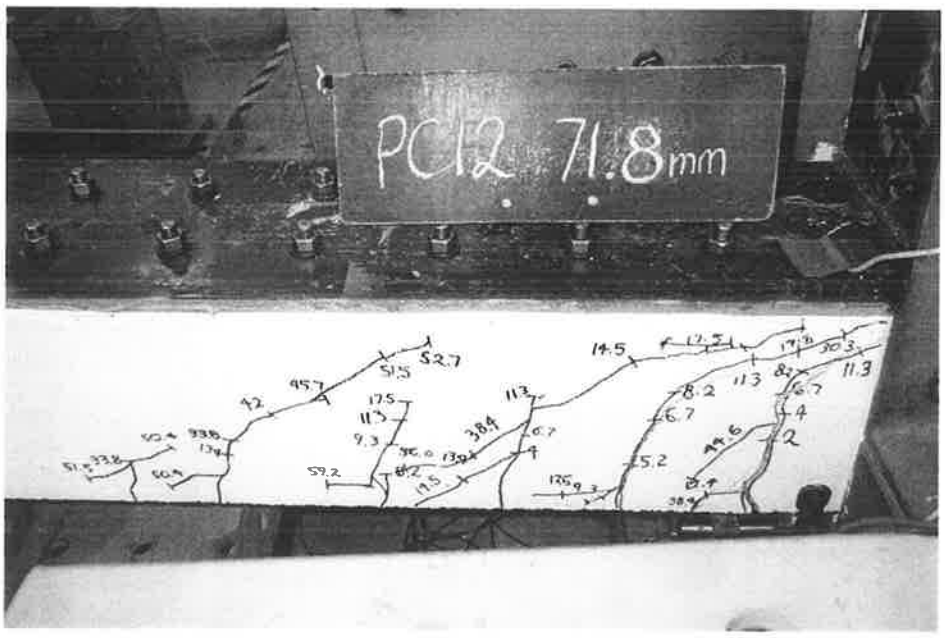

Fig. B.12 Rear view at displacement of 124mm for specimen 2AMF12

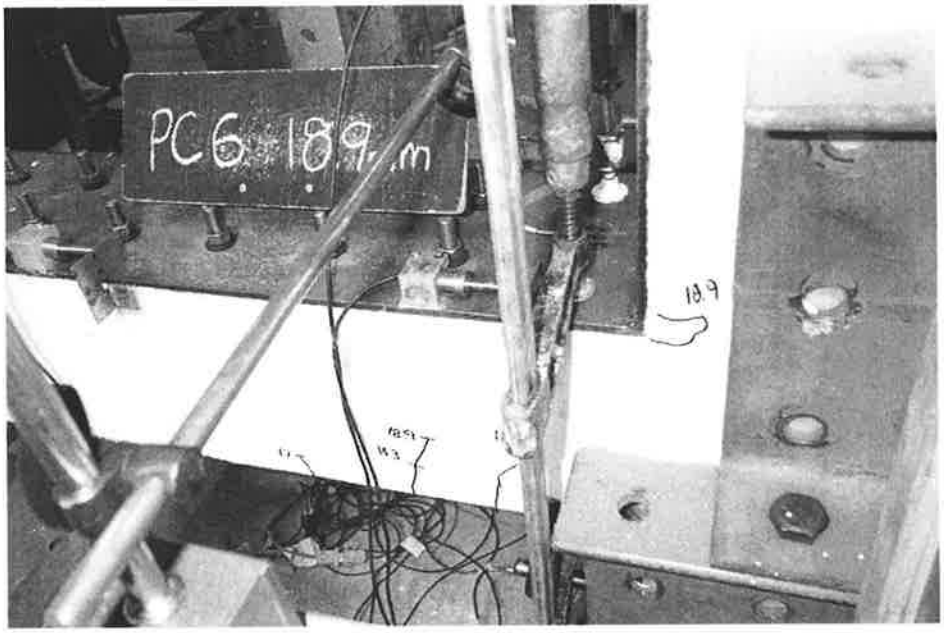

Fig. B.13 Rear view at displacement of 6.5mm for specimen 1BMP6

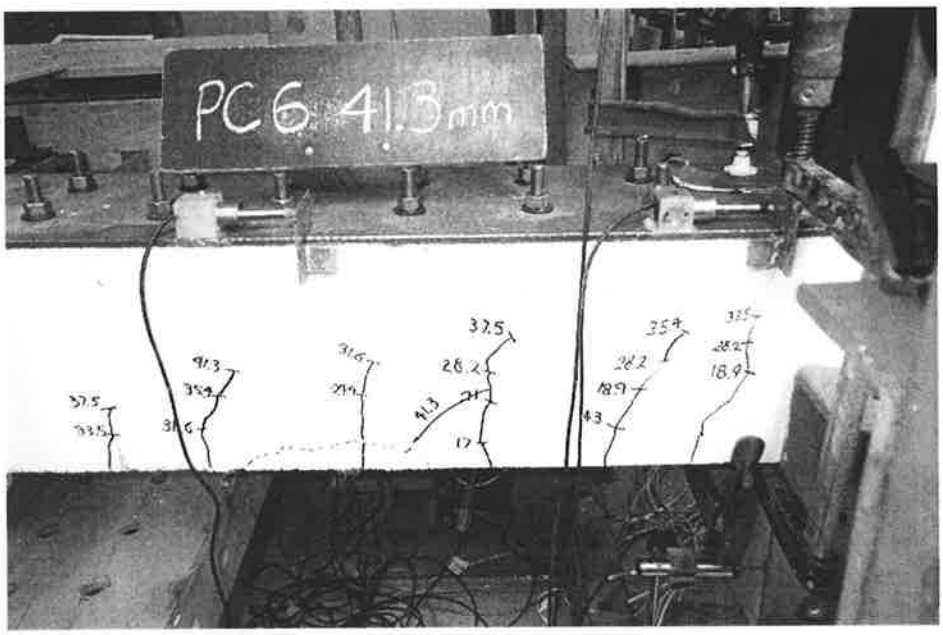

Fig. B.14 Rear view at displacement of 19mm for specimen 1BMP6

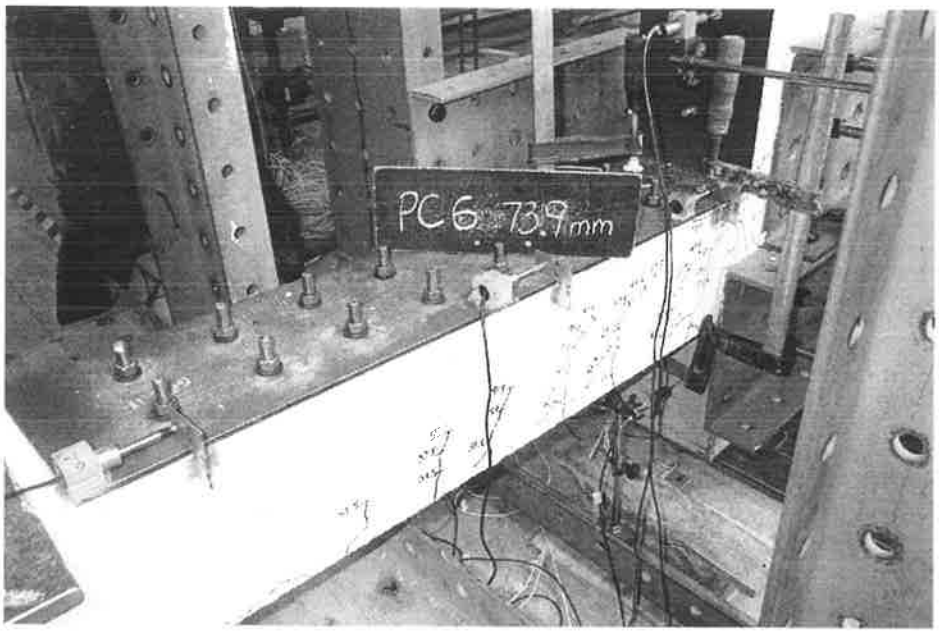

Fig. B.15 Rear view at displacement of 46mm for specimen 1BMP6

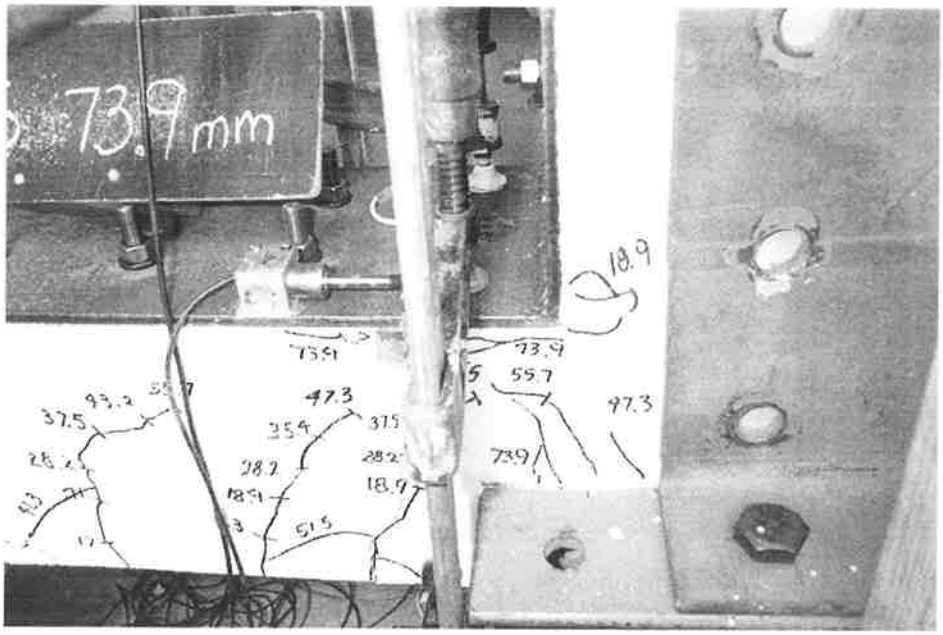

Fig. B.16 Enlarged view of Fig.B.15

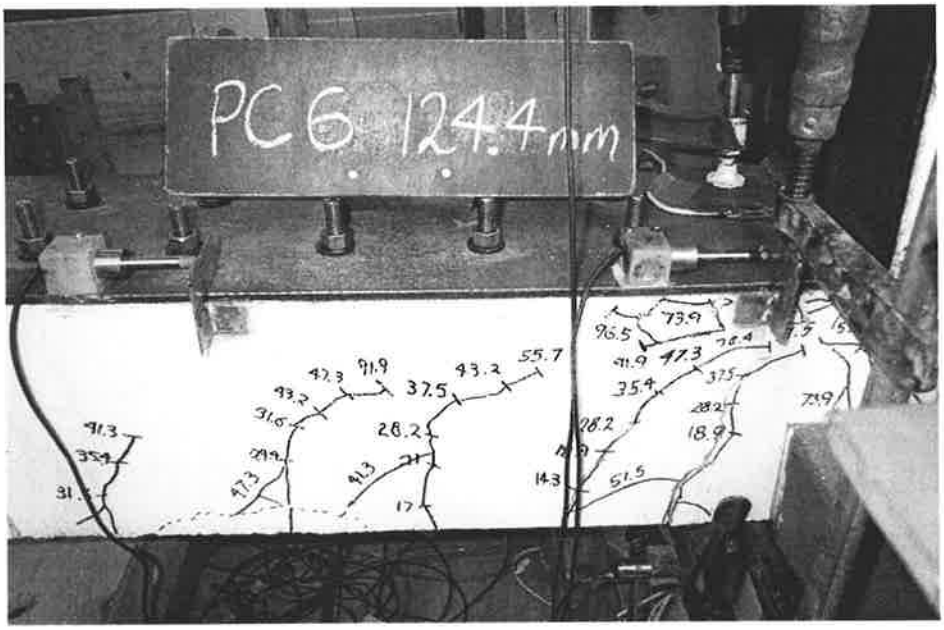

Fig. B.17 Rear view at displacement of 93mm for specimen 1BMP6

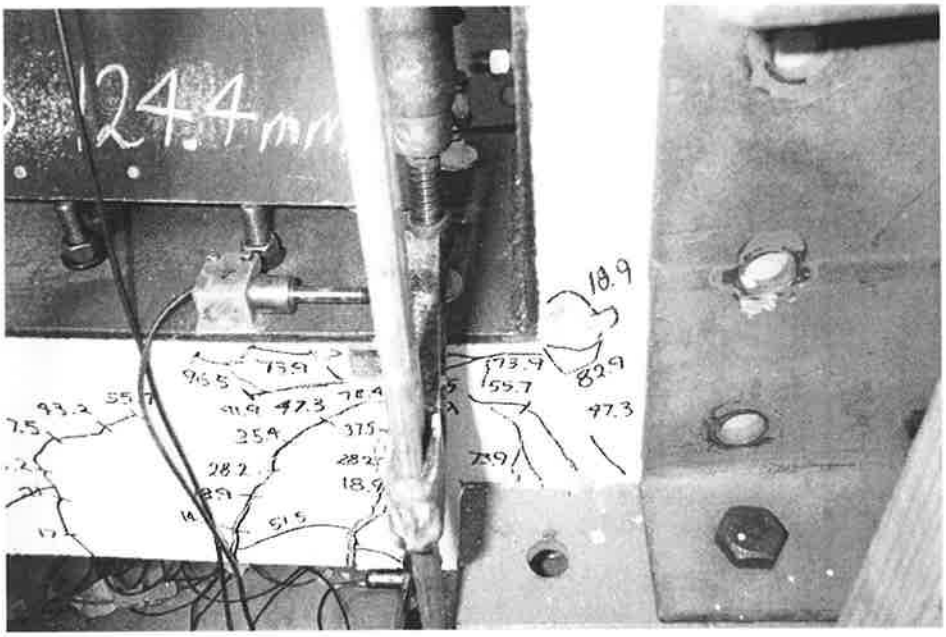

Fig. B.18 Enlarged view of Fig.B.17

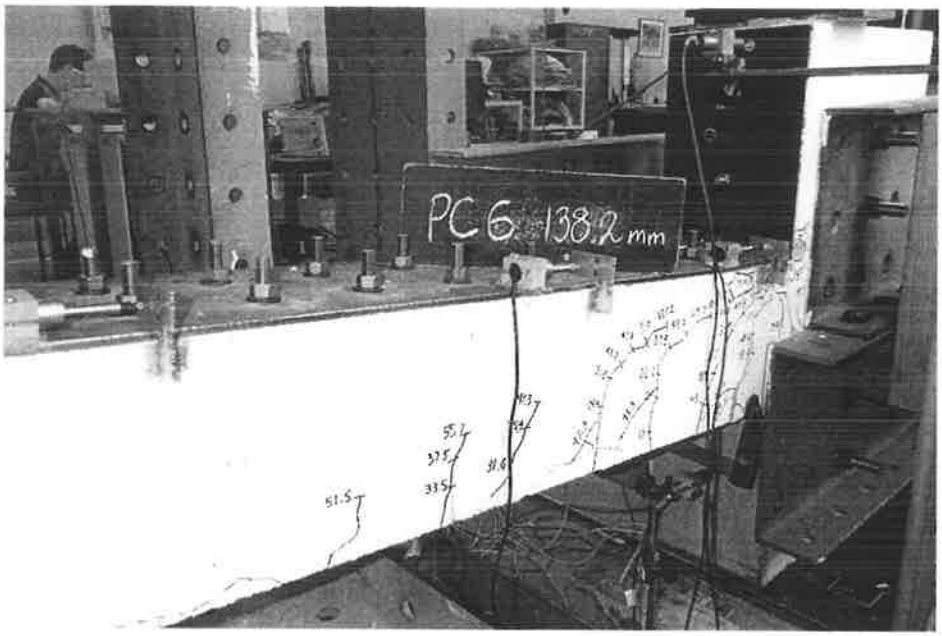

Fig. B.19 Rear view at displacement of 106mm for specimen 1BMP6

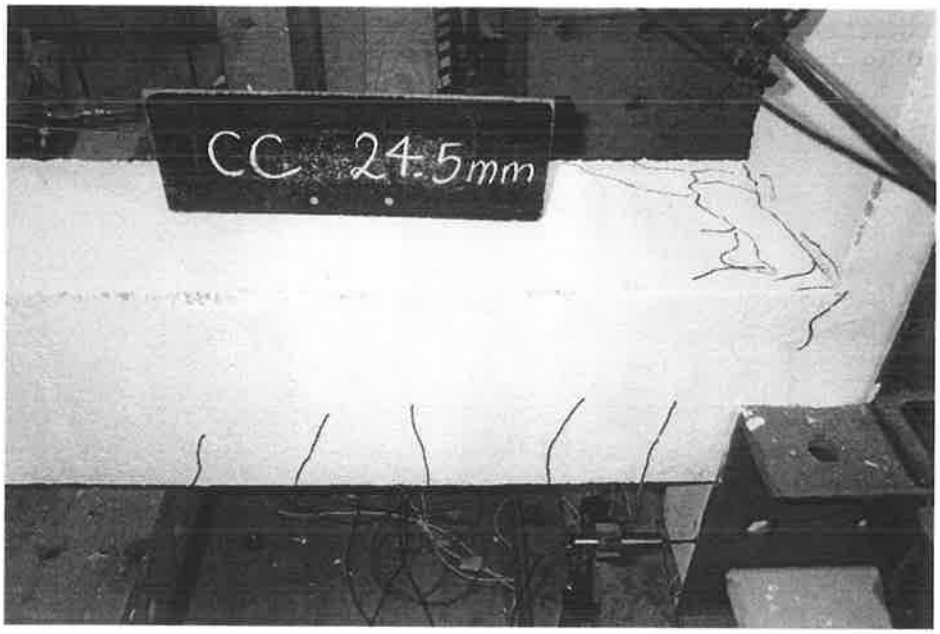

Fig. B.20 Rear view at +24.5mm displacement of 2nd cycle for specimen 3ACR

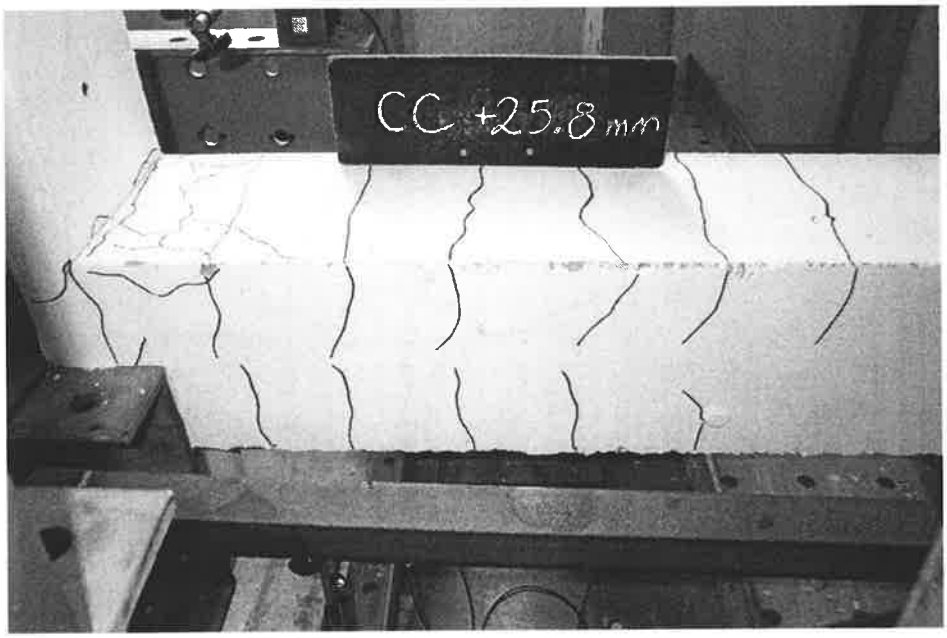

Fig. B.21 Front view at –25.8mm displacement of 2nd cycle for specimen 3ACR

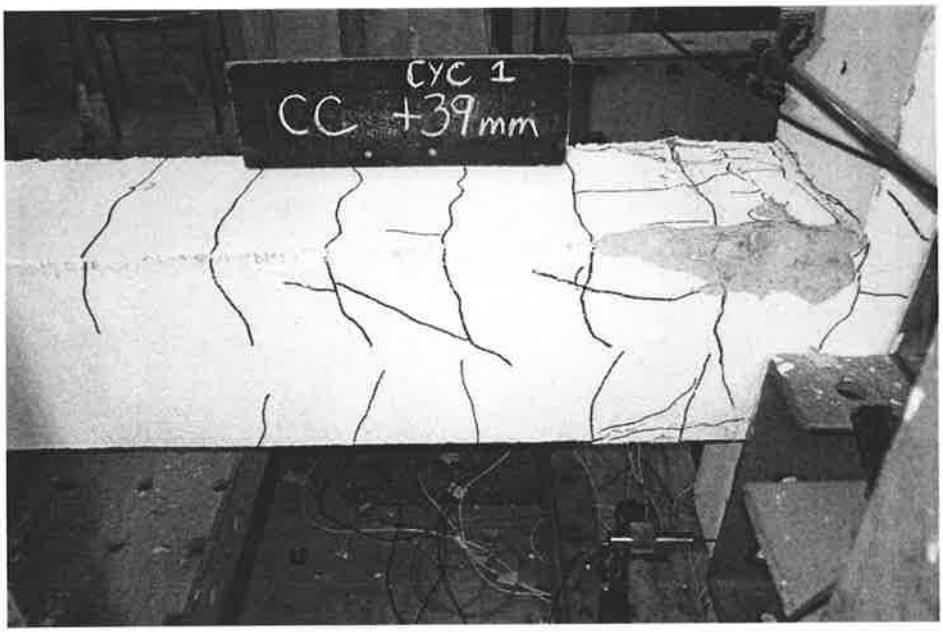

Fig. B.22 Rear view at –39mm displacement of 1st cycle for specimen 3ACR

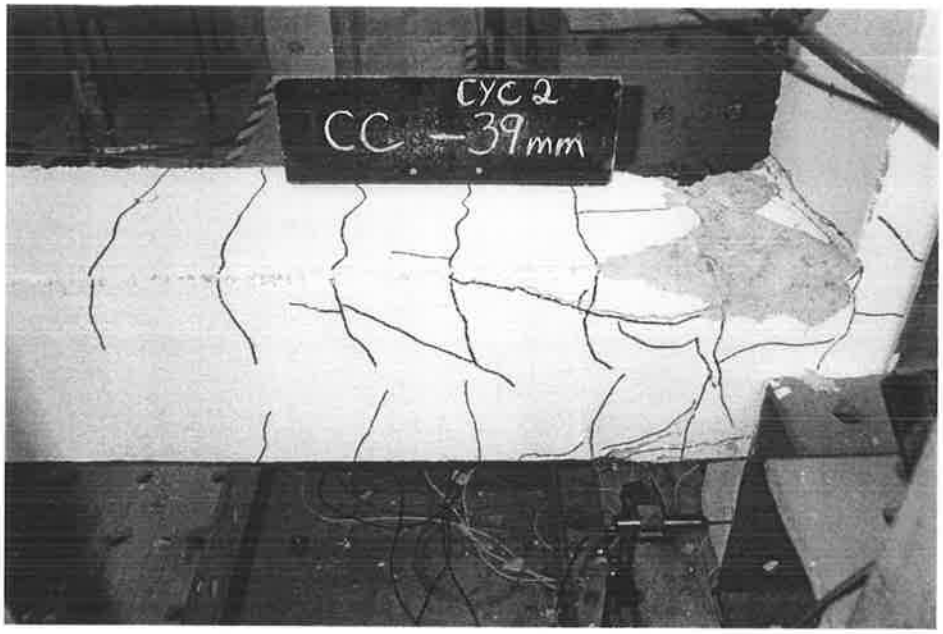

Fig. B.23 Rear view at +39mm displacement of 2nd cycle for specimen 3ACR

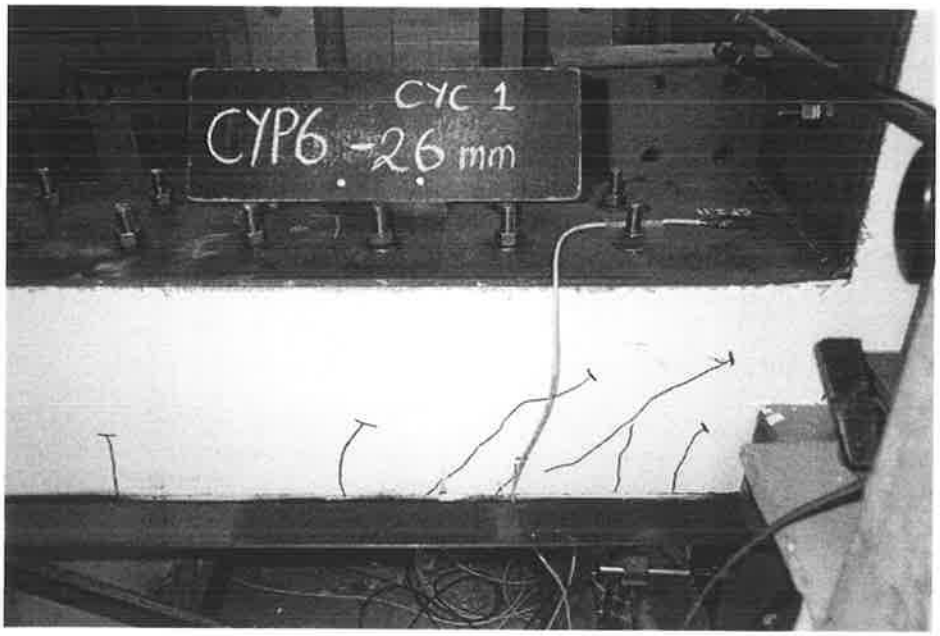

Fig. B.24 Rear view at +26mm displacement of 1st cycle for specimen 4ACP6

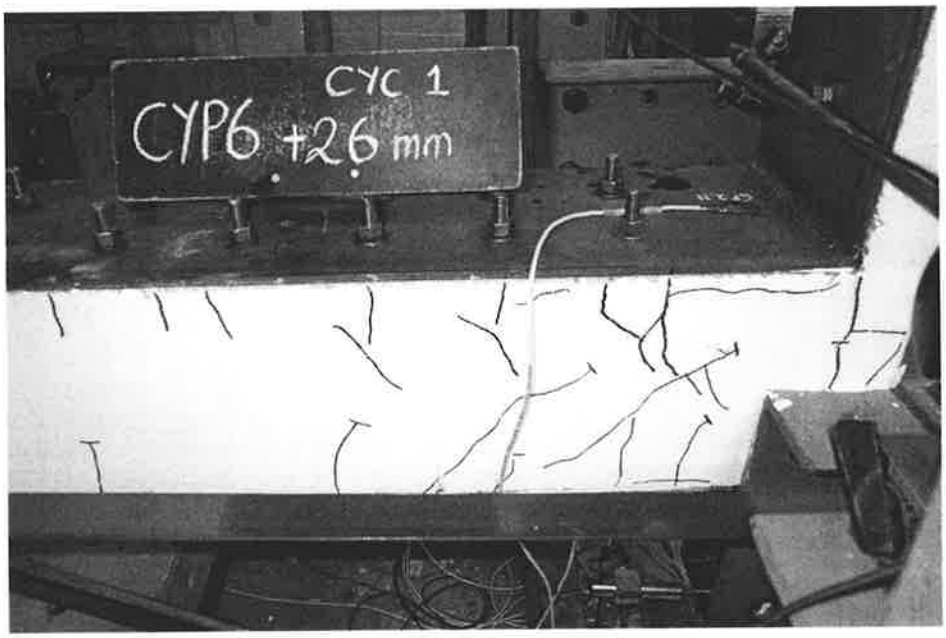

Fig. B.25 Rear view at –26mm displacement of 1st cycle for specimen 4ACP6

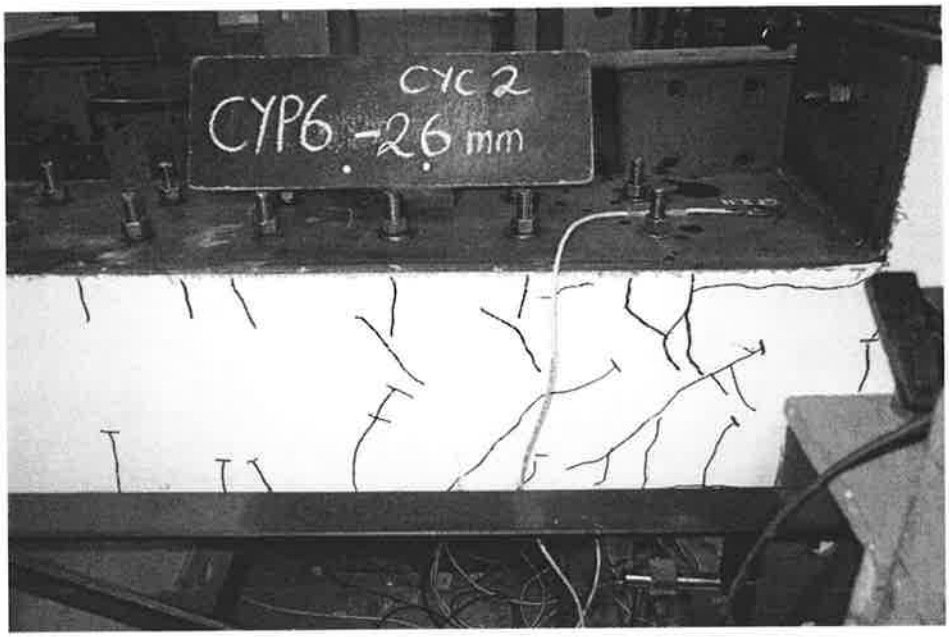

Fig. B.26 Rear view at +26mm displacement of 2nd cycle for specimen 4ACP6

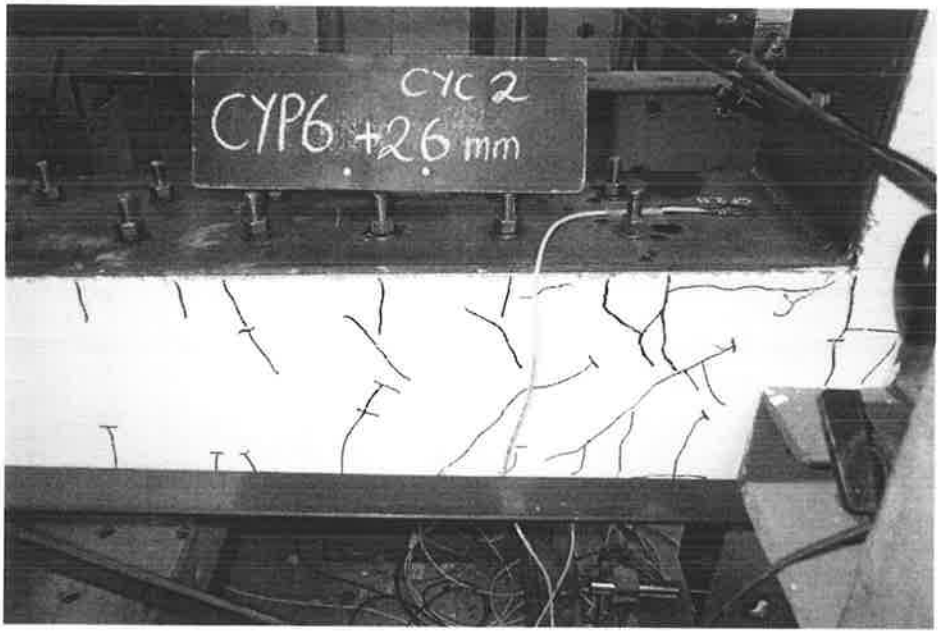

Fig. B.27 Rear view at -26mm displacement of 2nd cycle for specimen 4ACP6

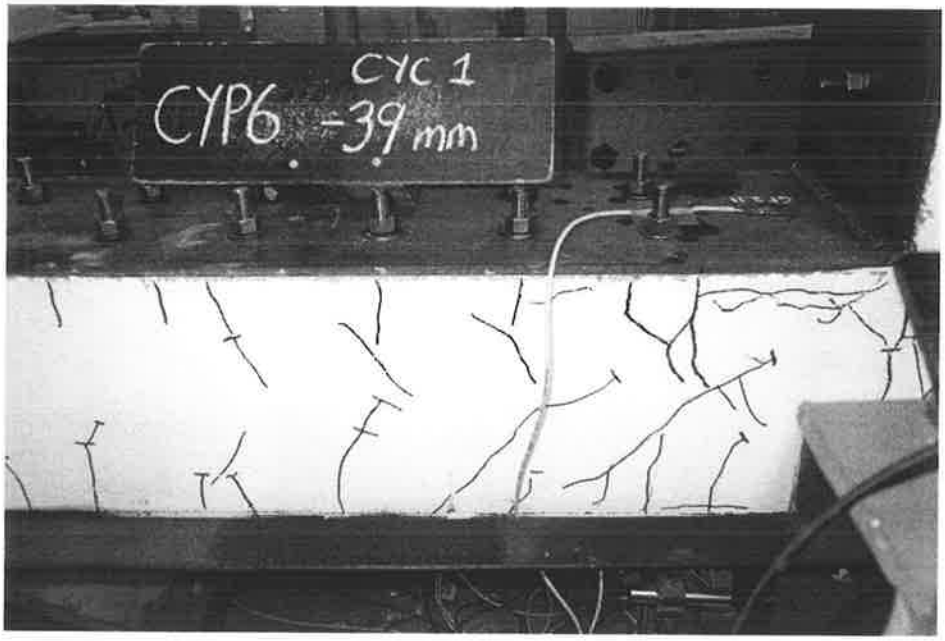

Fig. B.28 Rear view at +39mm displacement of 1st cycle for specimen 4ACP6

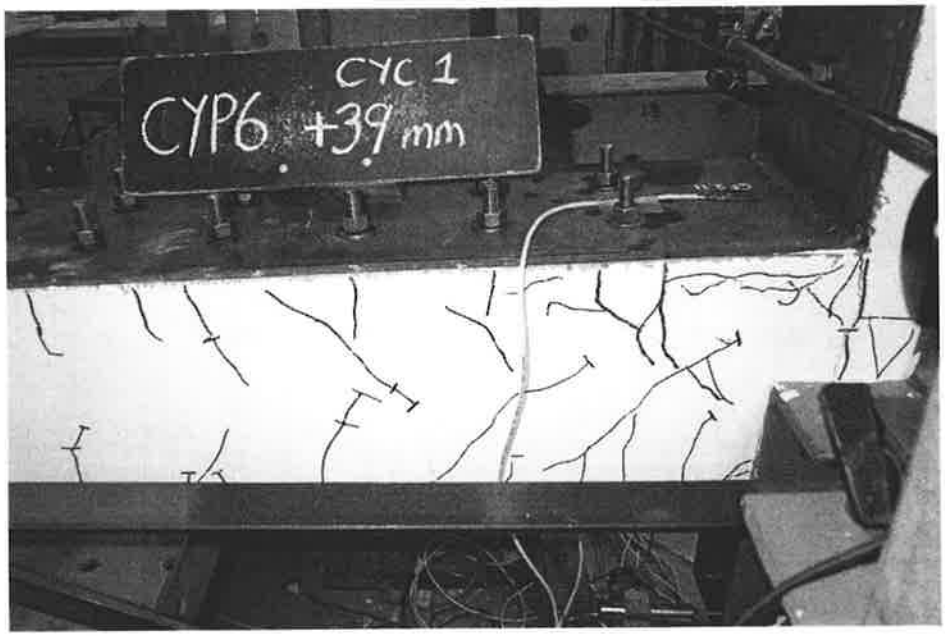

Fig. B.29 Rear view at -39mm displacement of 1st cycle for specimen 4ACP6

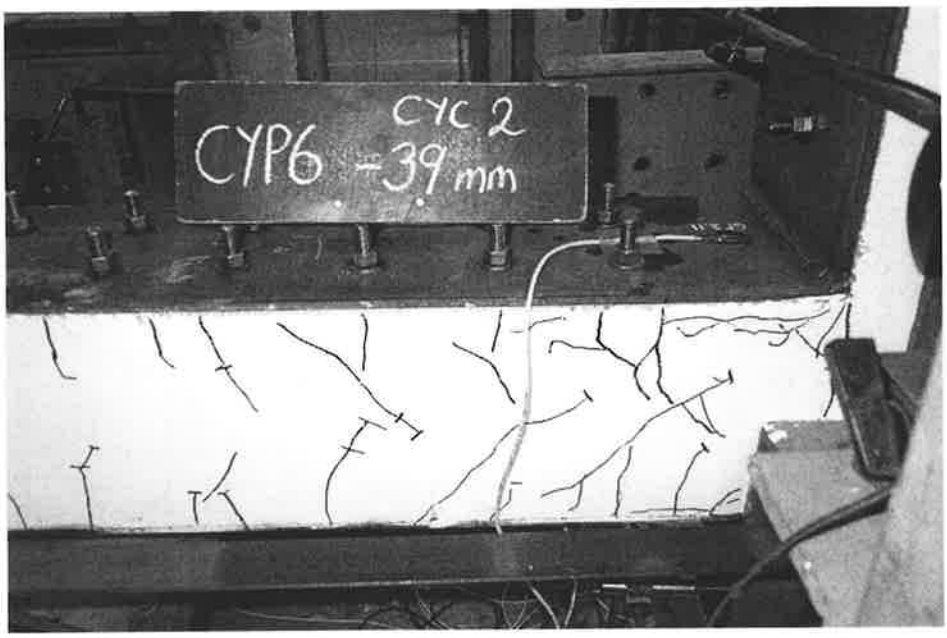

Fig. B.30 Rear view at +39mm displacement of 2nd cycle for specimen 4ACP6

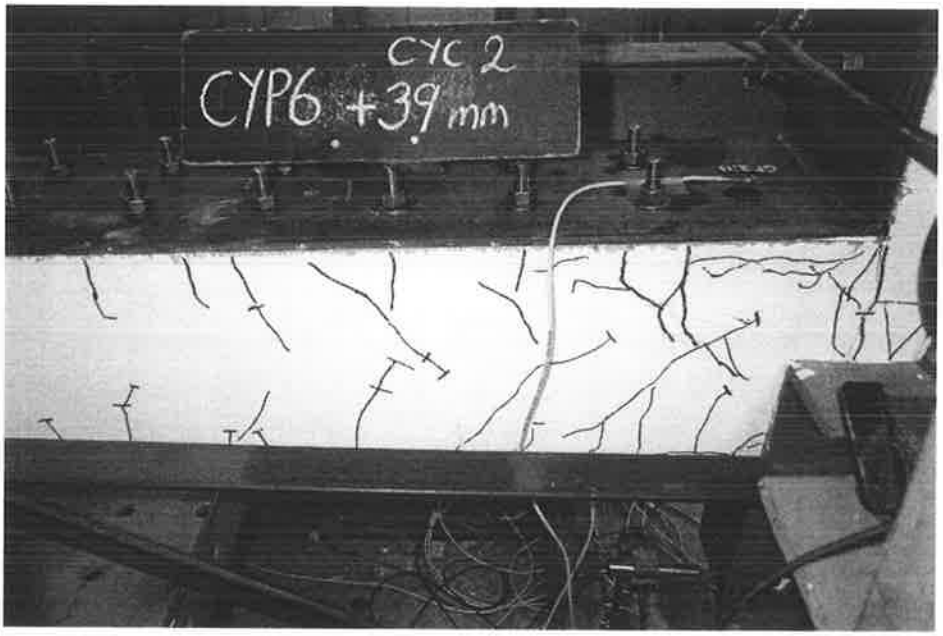

Fig. B.31 Rear view at -39mm displacement of 2nd cycle for specimen 4ACP6

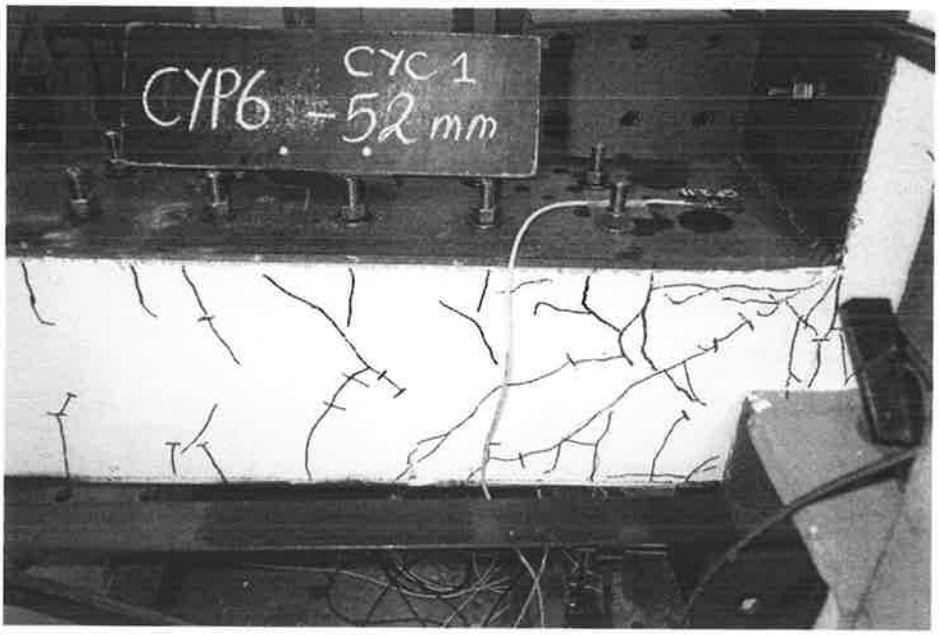

Fig. B.32 Rear view at +52mm displacement of 1st cycle for specimen 4ACP6

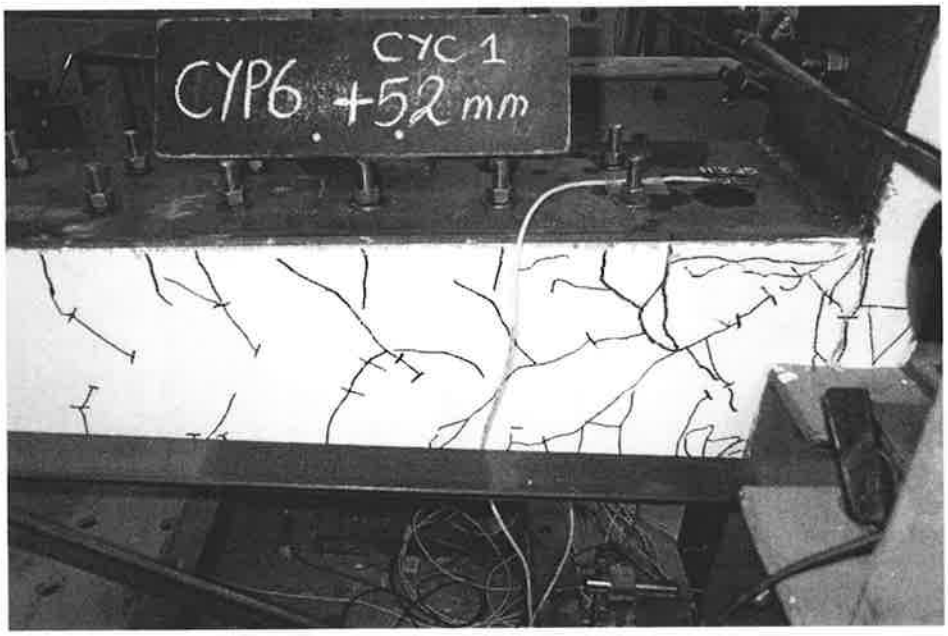

Fig. B.33 Rear view at -52mm displacement of 1st cycle for specimen 4ACP6

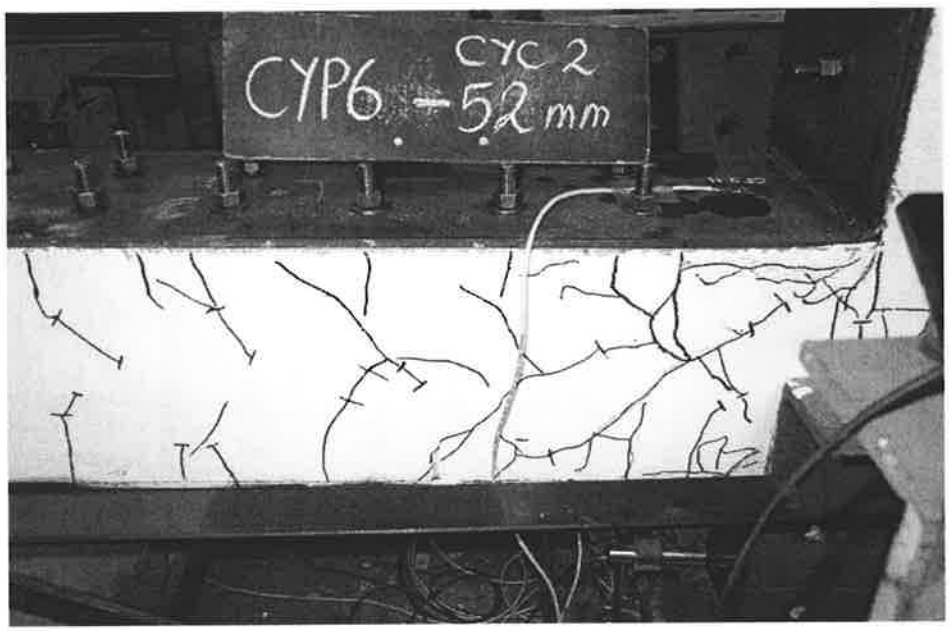

Fig. B.34 Rear view at +52mm displacement of 2nd cycle for specimen 4ACP6

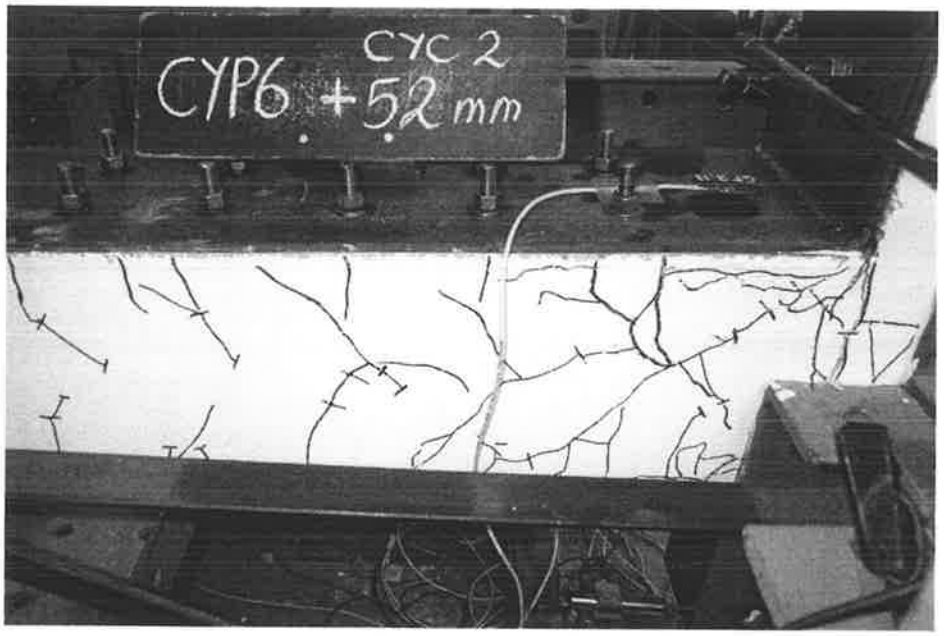

Fig. B.35 Rear view at -52mm displacement of 2nd cycle for specimen 4ACP6

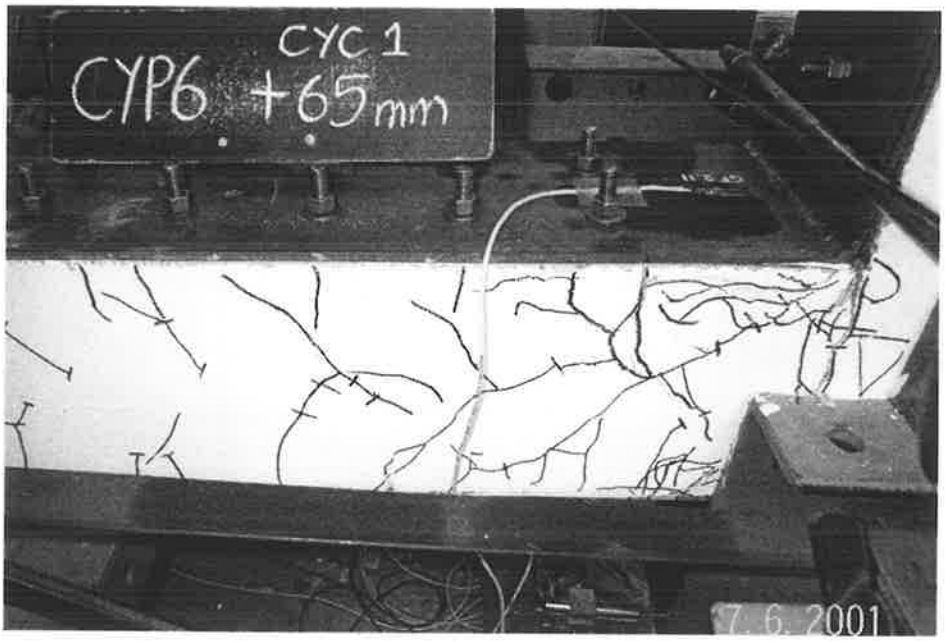

Fig. B.36 Rear view at -65mm displacement of 1st cycle for specimen 4ACP6

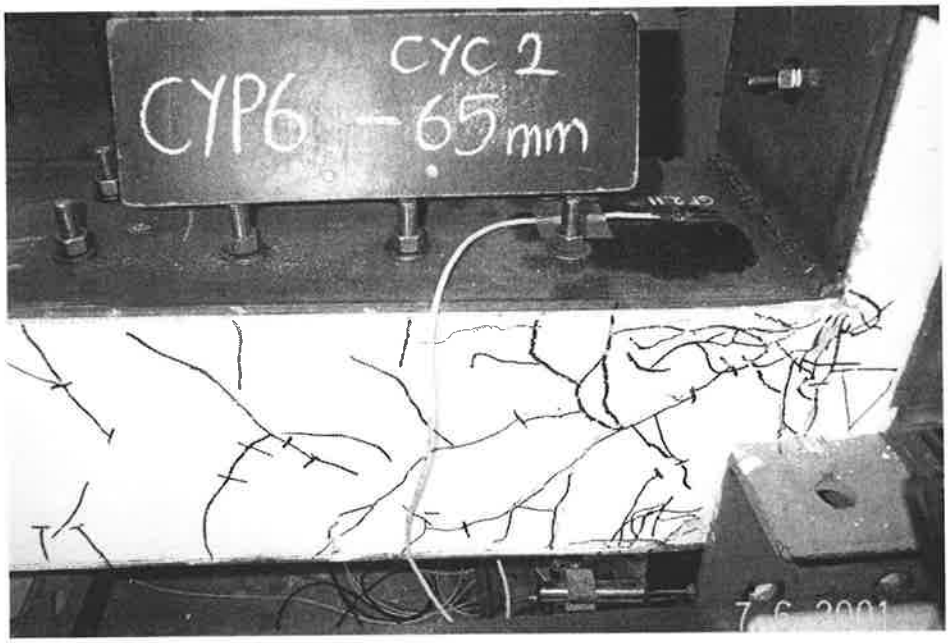

Fig. B.37 Rear view at +65mm displacement of 2nd cycle for specimen 4ACP6

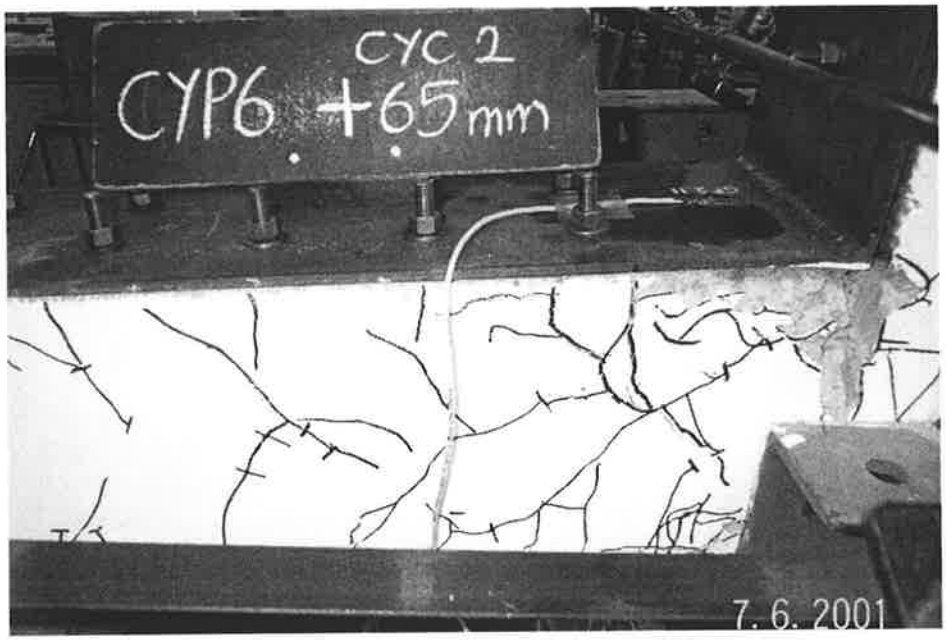

Fig. B.38 Rear view at -65mm displacement of 2nd cycle for specimen 4ACP6

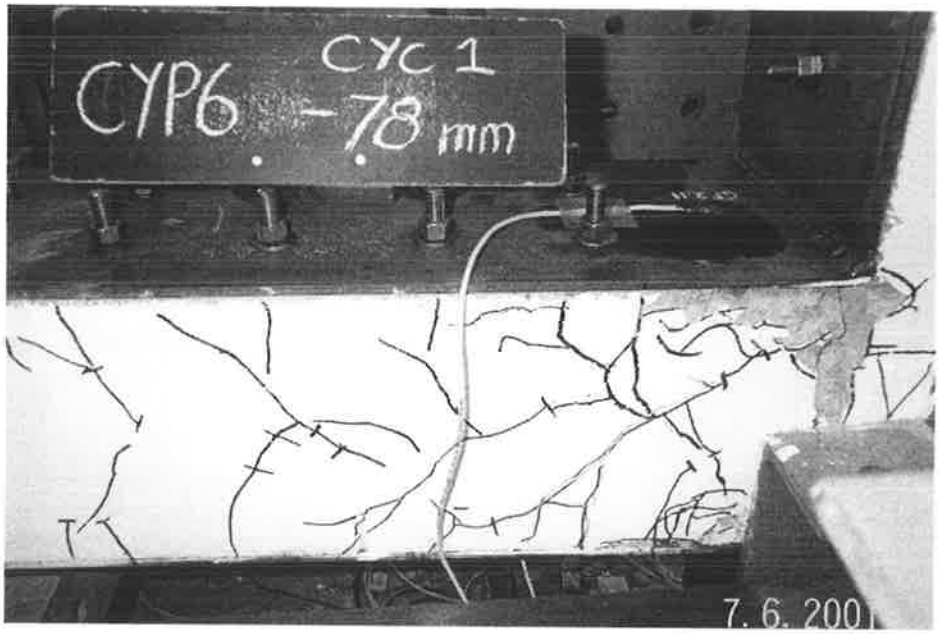

Fig. B.39 Rear view at +78mm displacement of 1st cycle for specimen 4ACP6

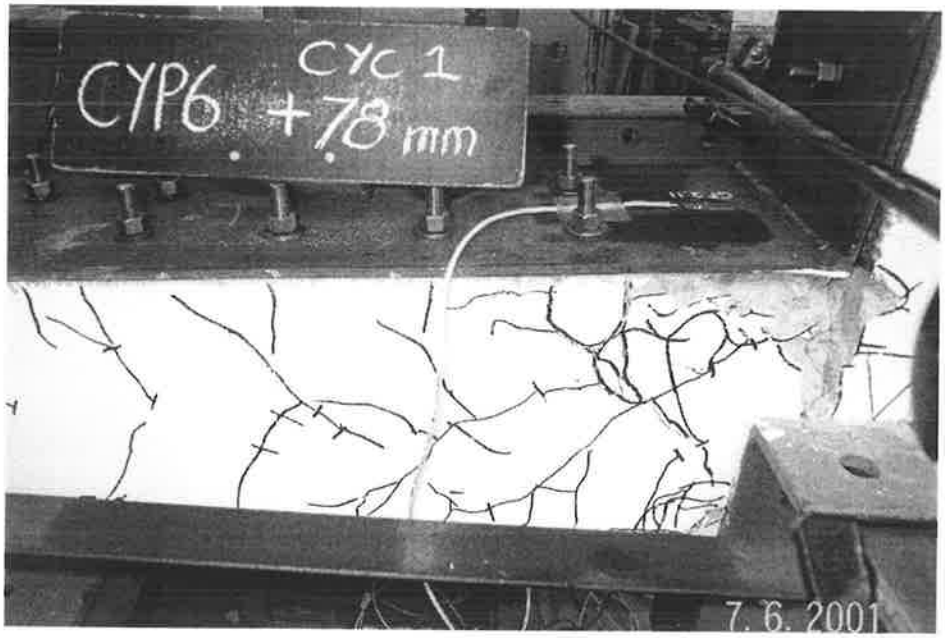

Fig. B.40 Rear view at -78mm displacement of 1st cycle for specimen 4ACP6

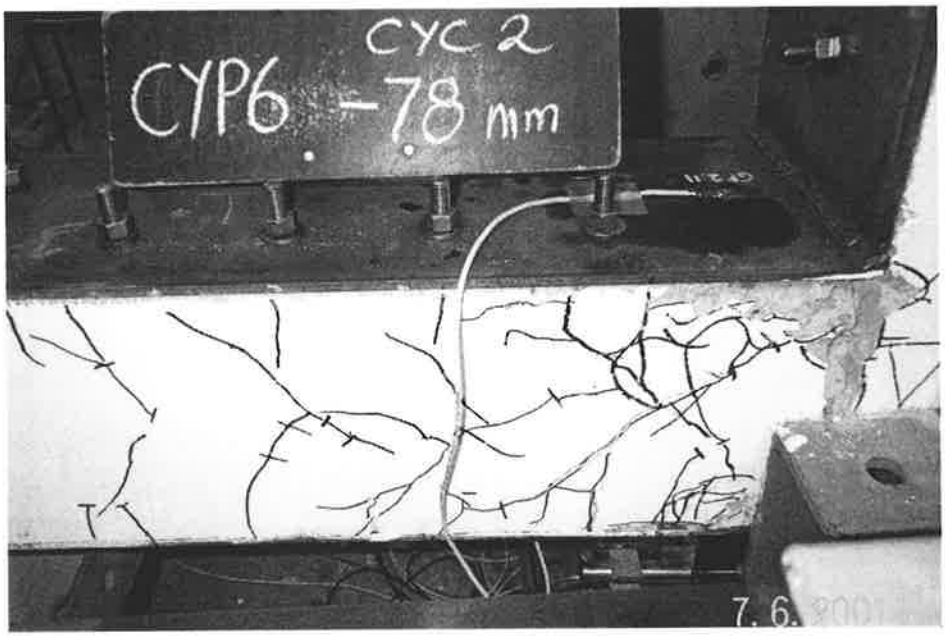

Fig. B.41 Rear view at +78mm displacement of 2nd cycle for specimen 4ACP6

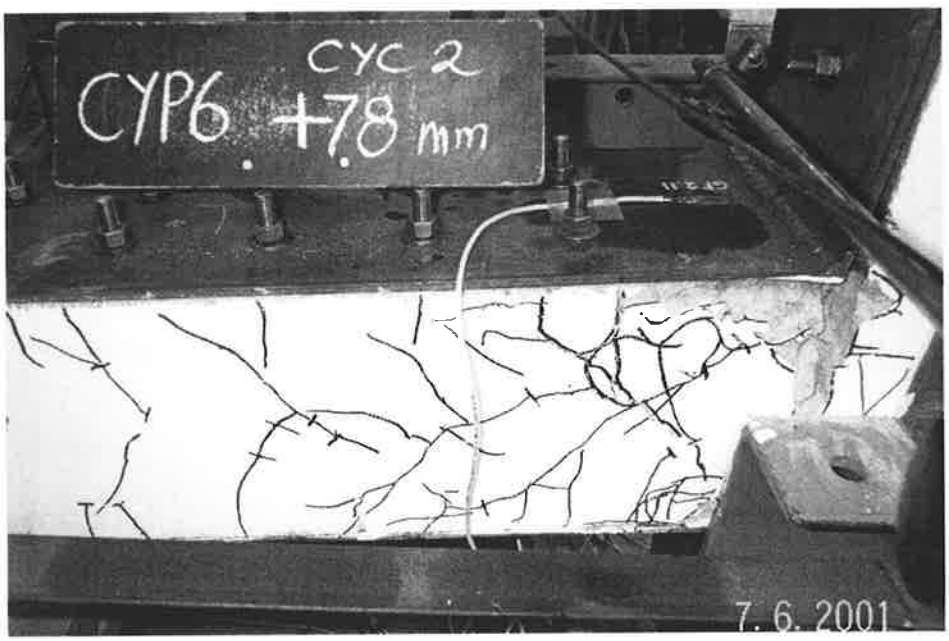

Fig. B.42 Rear view at -78mm displacement of 2nd cycle for specimen 4ACP6

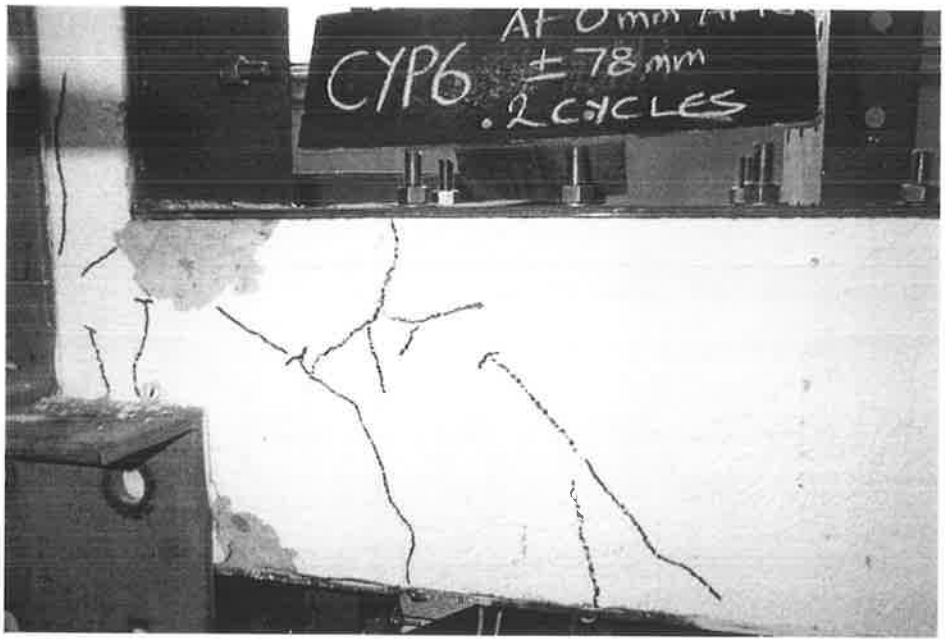

Fig. B.43 Front view after 2 cycles of ±78mm displacement for specimen 4ACP6

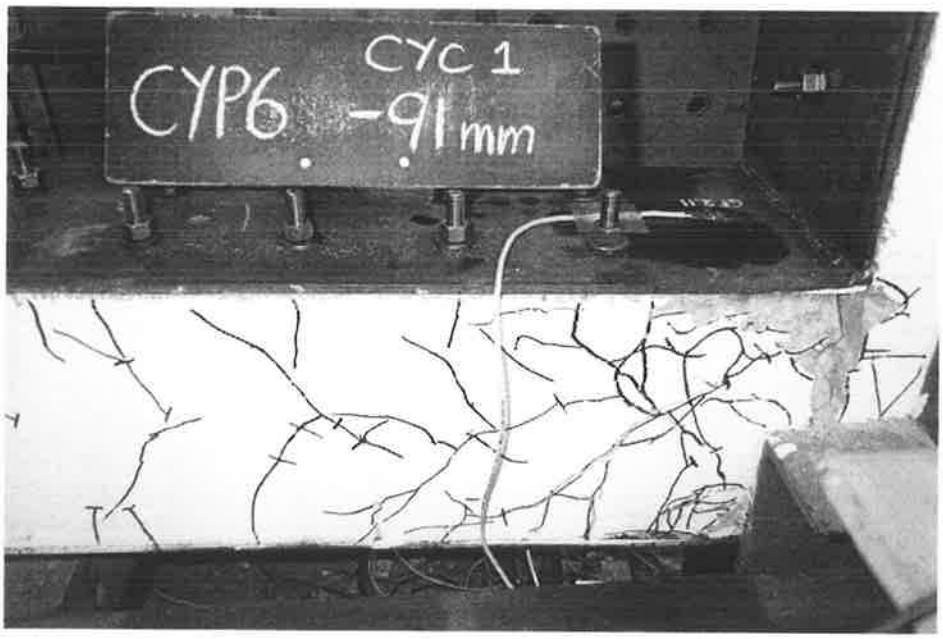

Fig. B.44 Rear view at +91mm displacement of 1st cycle for specimen 4ACP6

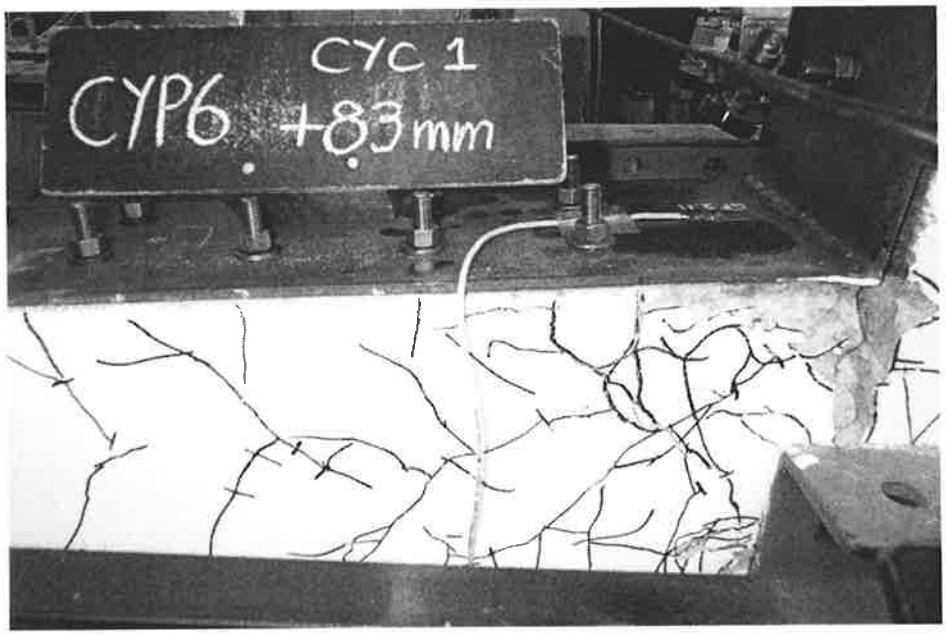

Fig. B.45 Rear view at -83mm displacement of 1st cycle for specimen 4ACP6

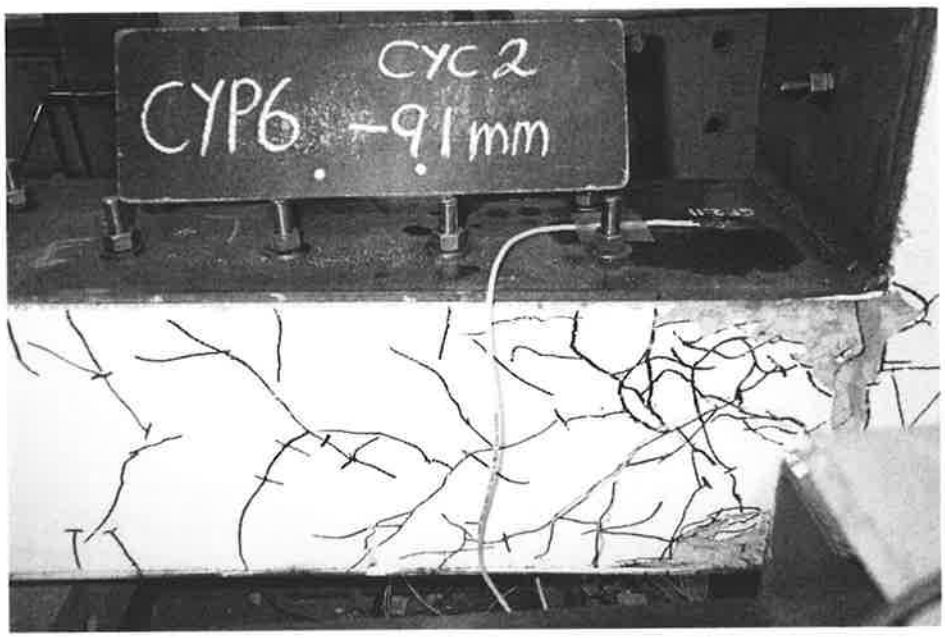

Fig. B.46 Rear view at +91mm displacement of 2nd cycle for specimen 4ACP6

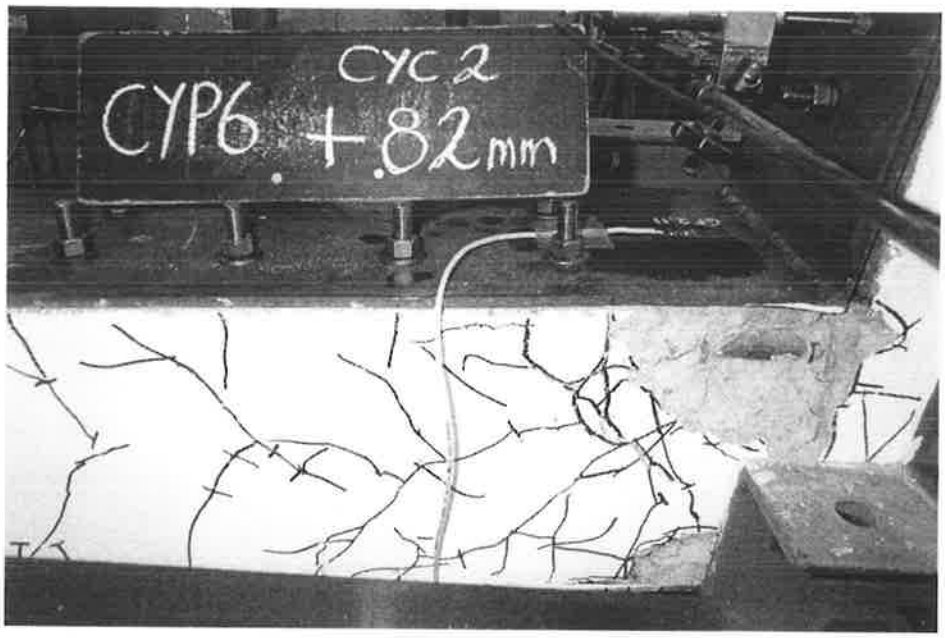

Fig. B.47 Rear view at -82mm displacement of 2nd cycle for specimen 4ACP6

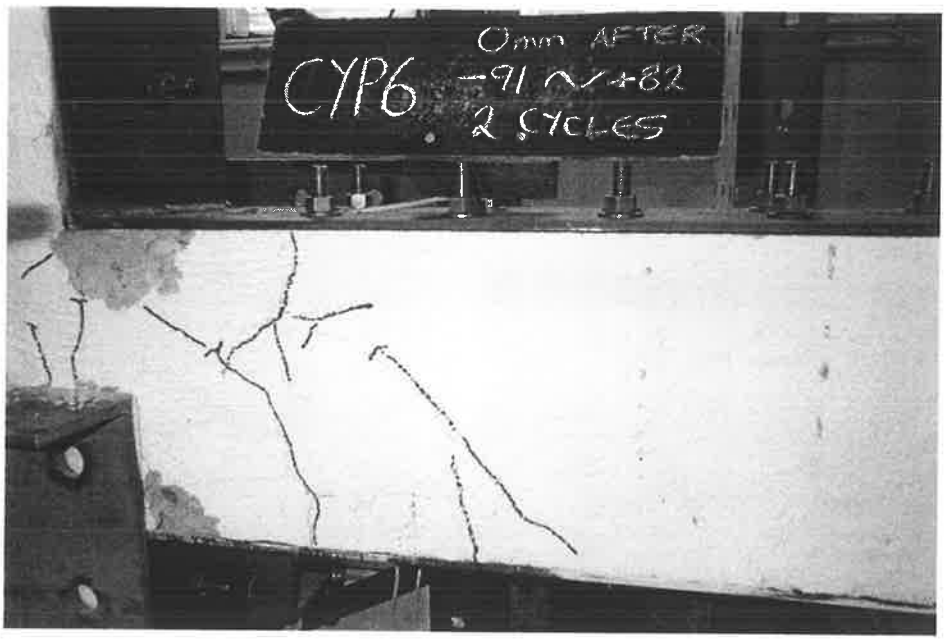

Fig. B.48 Front view after 2 cycles of –82mm to +91mm for specimen 4ACP6

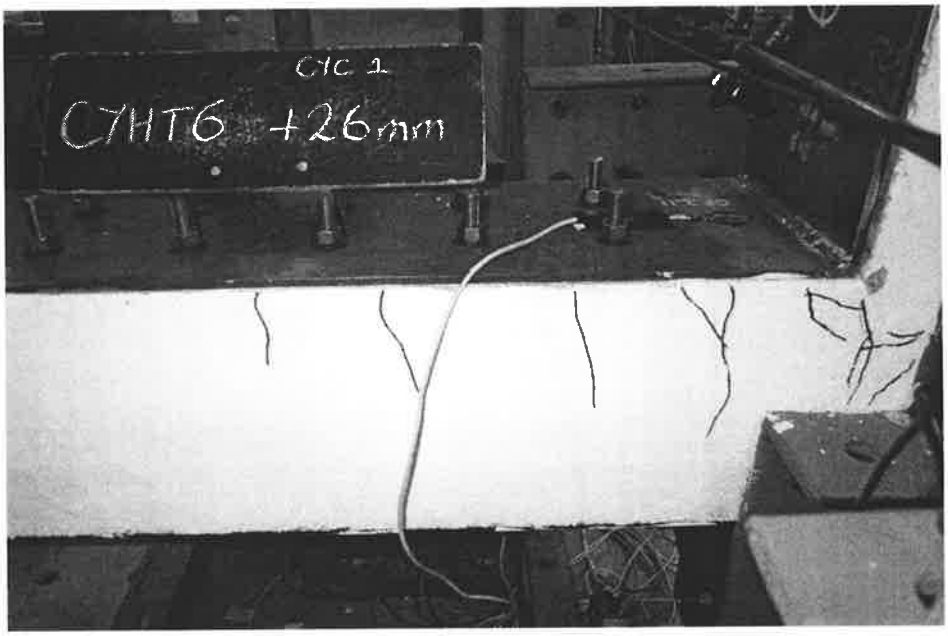

Fig. B.49 Rear view at -26mm displacement of 1st cycle for specimen 2BCP6G

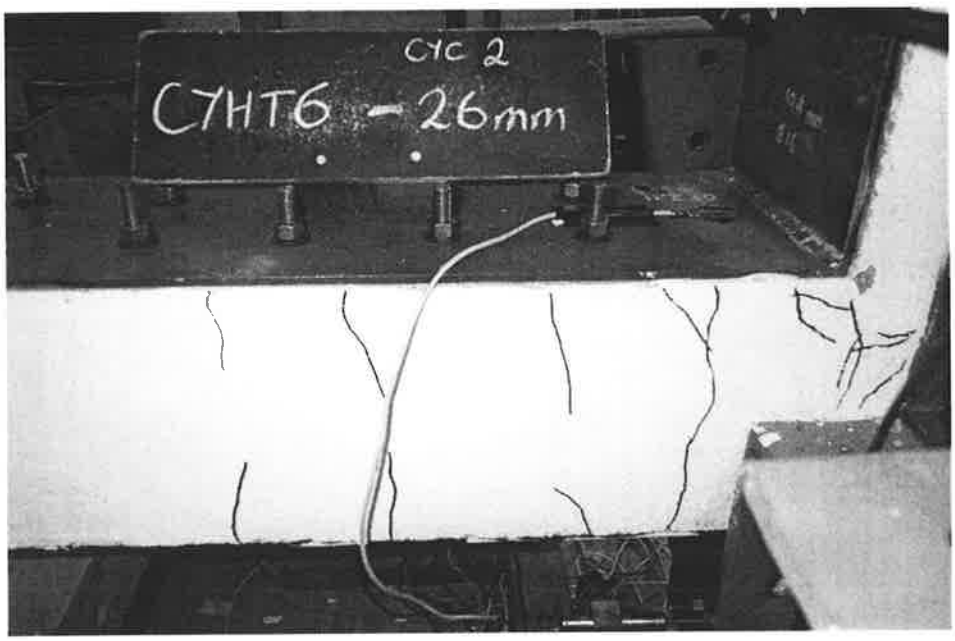

Fig. B.50 Rear view at +26mm displacement of 2nd cycle for specimen 2BCP6G

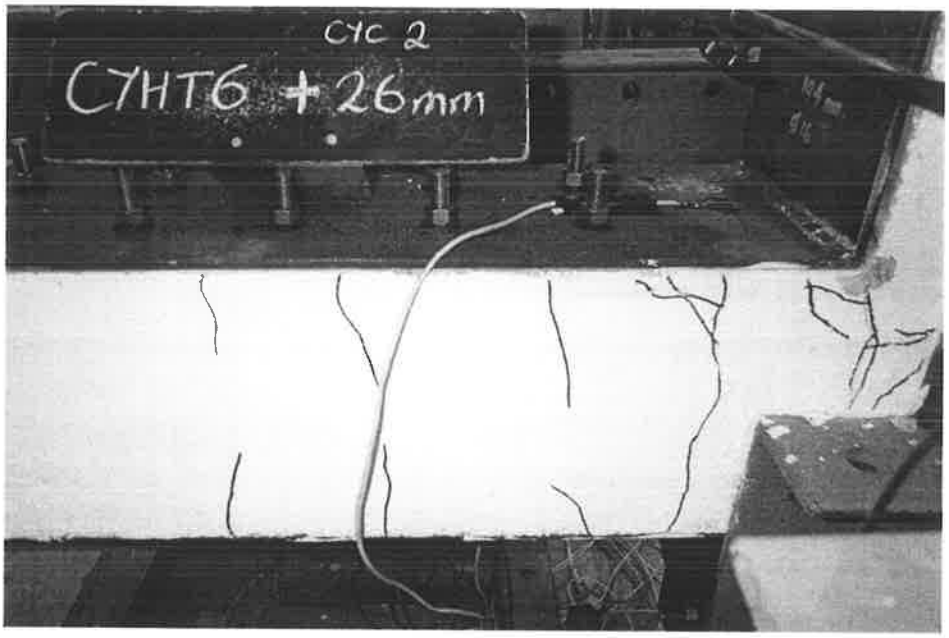

Fig. B.51 Rear view at -26mm displacement of 2nd cycle for specimen 2BCP6G

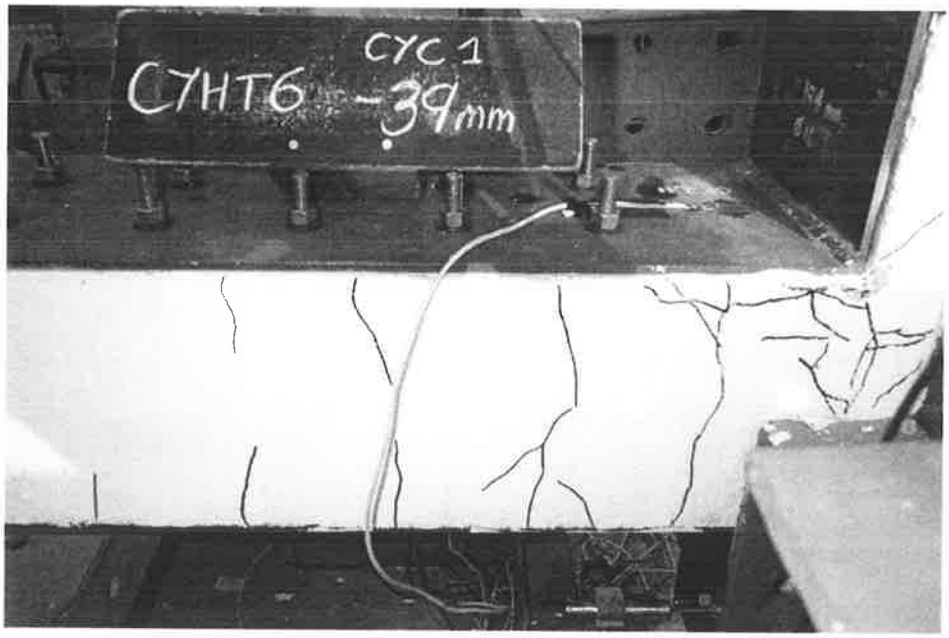

Fig. B.52 Rear view at +39mm displacement of 1st cycle for specimen 2BCP6G

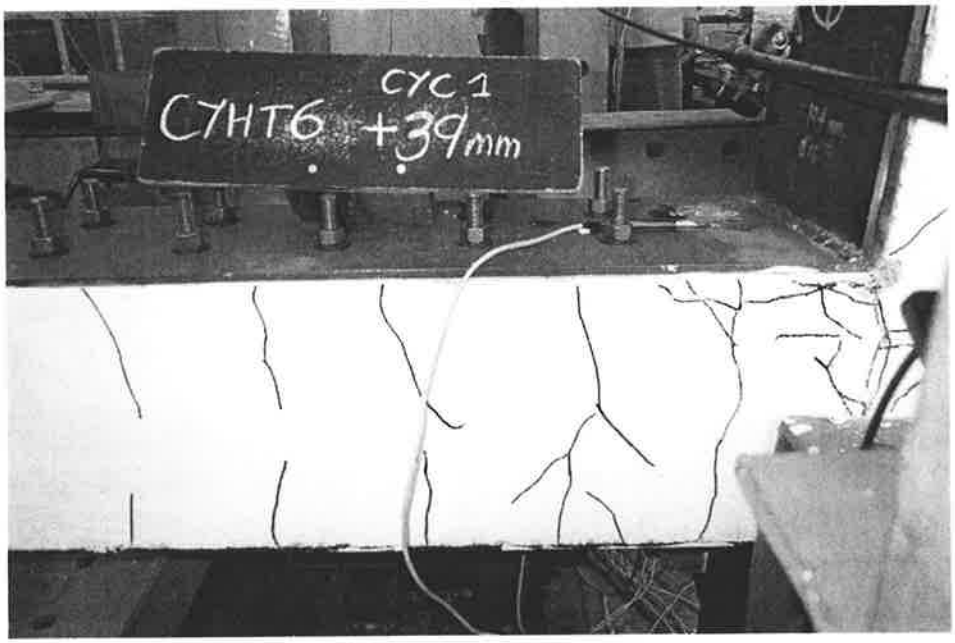

Fig. B.53 Rear view at -39mm displacement of 1st cycle for specimen 2BCP6G

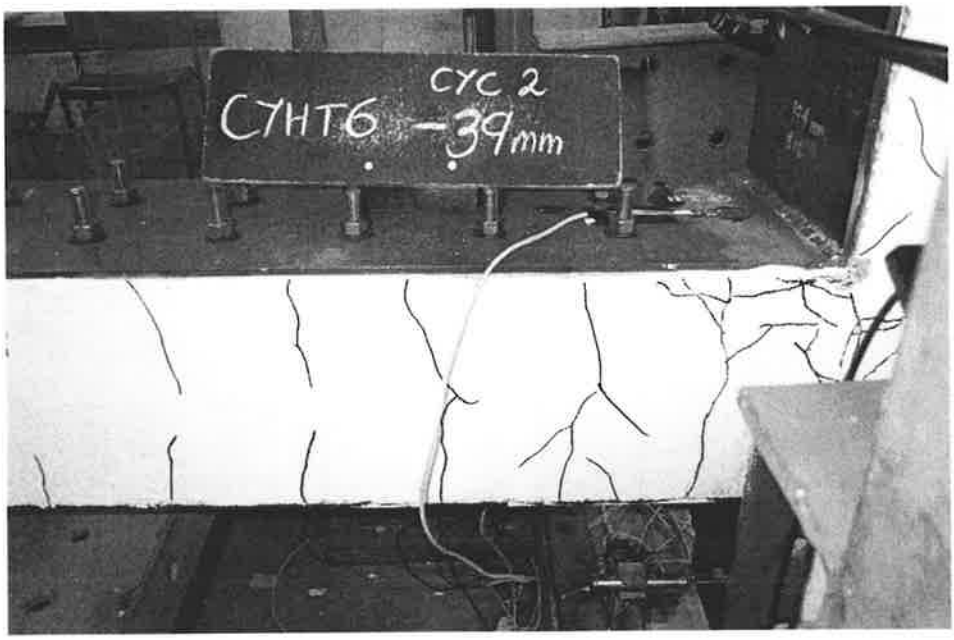

Fig. B.54 Rear view at +39mm displacement of 2nd cycle for specimen 2BCP6G

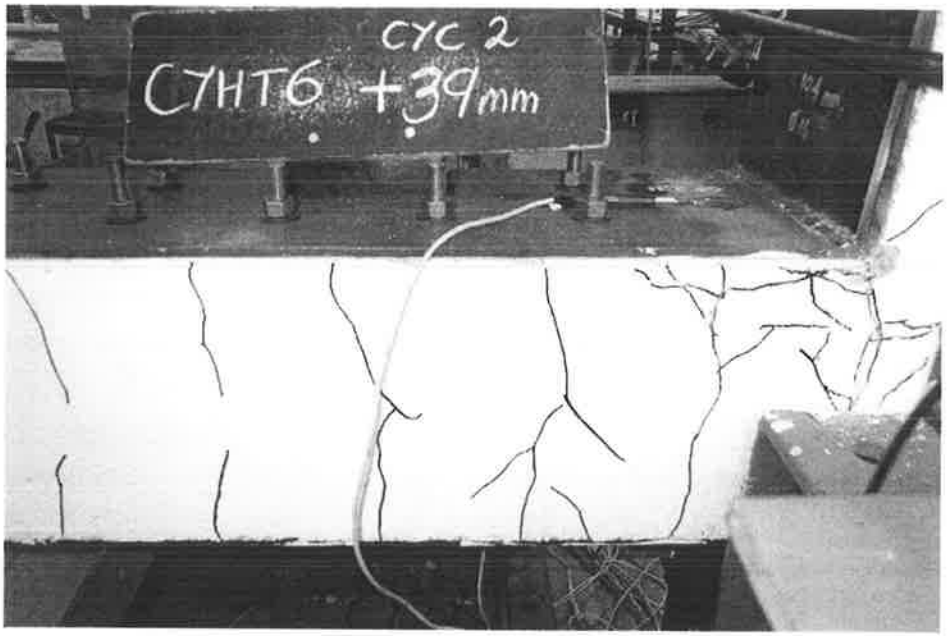

Fig. B.55 Rear view at -39mm displacement of 2nd cycle for specimen 2BCP6G

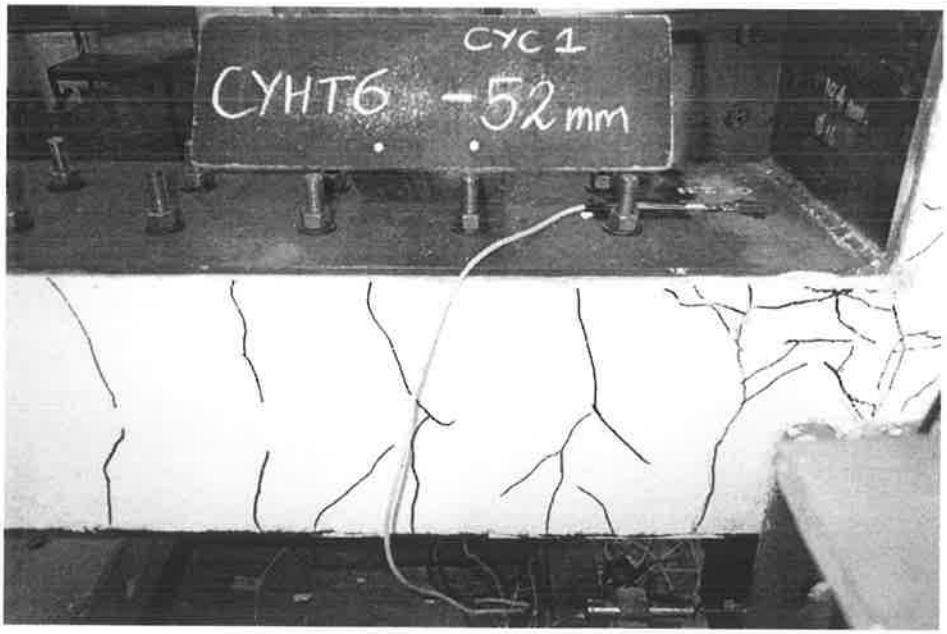

Fig. B.56 Rear view at +52mm displacement of 1st cycle for specimen 2BCP6G

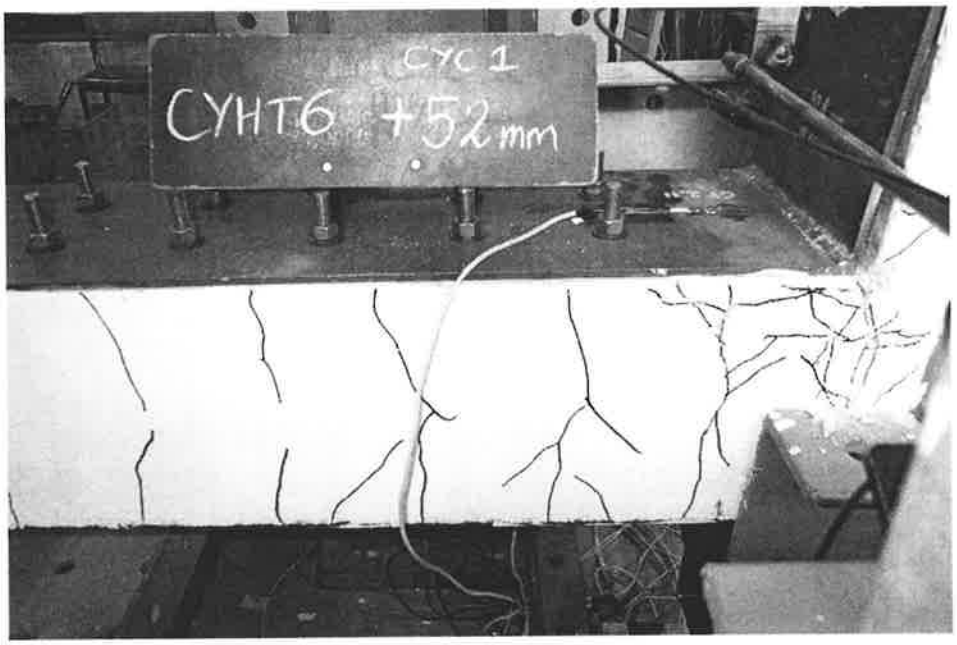

Fig. B.57 Rear view at -52mm displacement of 1st cycle for specimen 2BCP6G

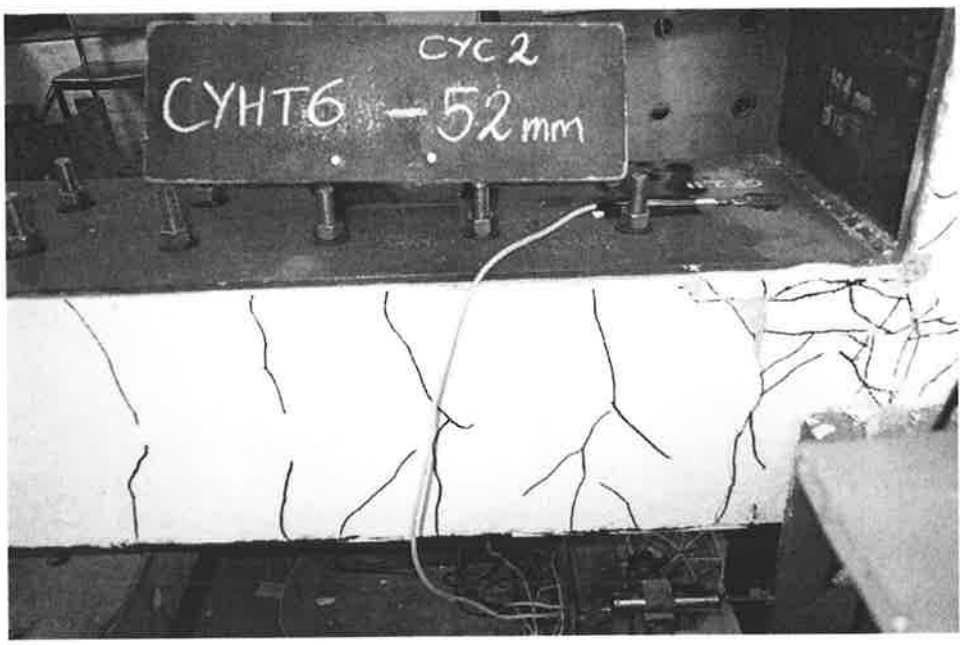

Fig. B.58 Rear view at +52mm displacement of 2nd cycle for specimen 2BCP6G

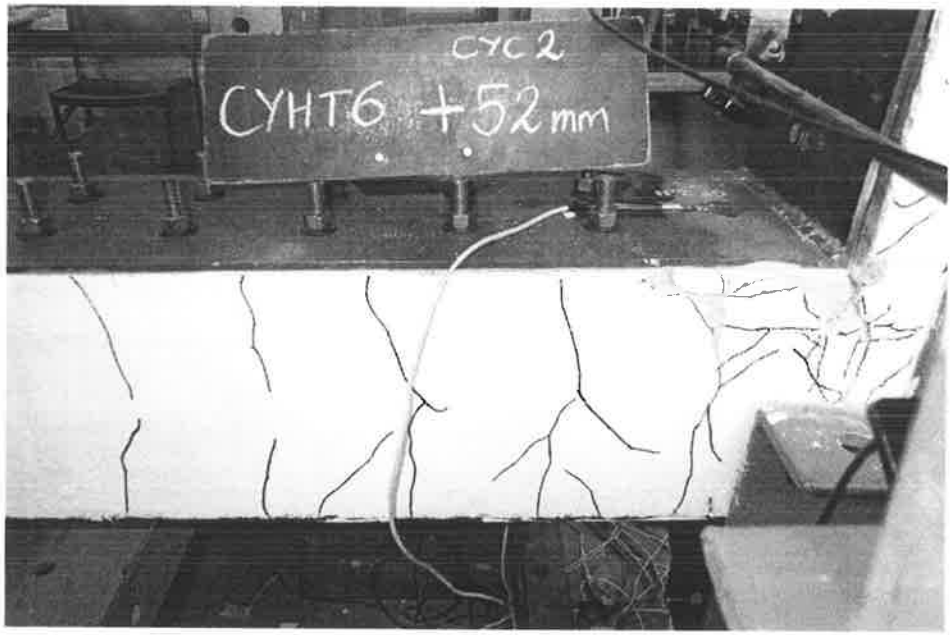

Fig. B.59 Rear view at -52mm displacement of 2nd cycle for specimen 2BCP6G

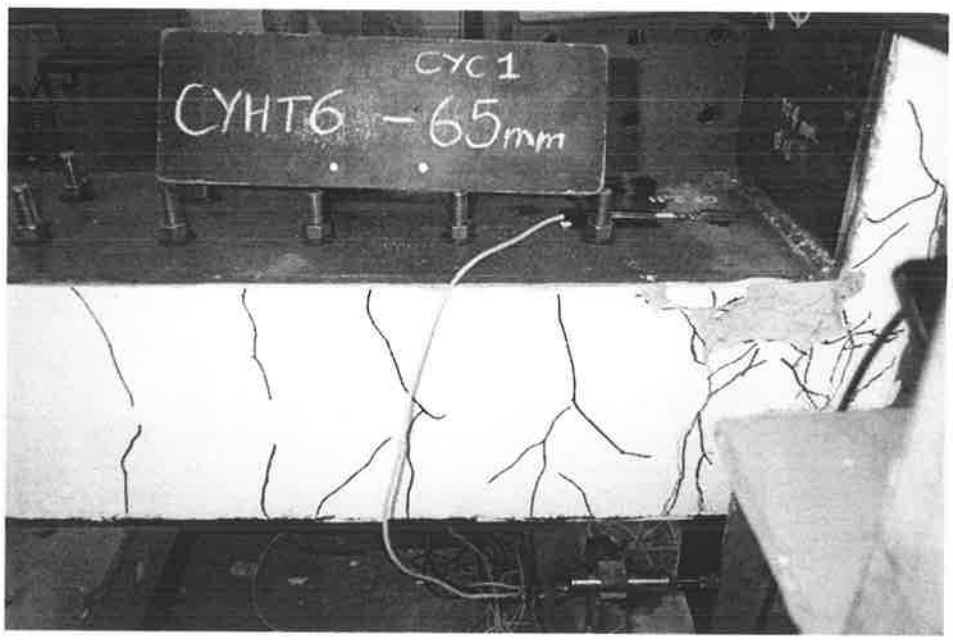

Fig. B.60 Rear view at +65mm displacement of 1st cycle for specimen 2BCP6G

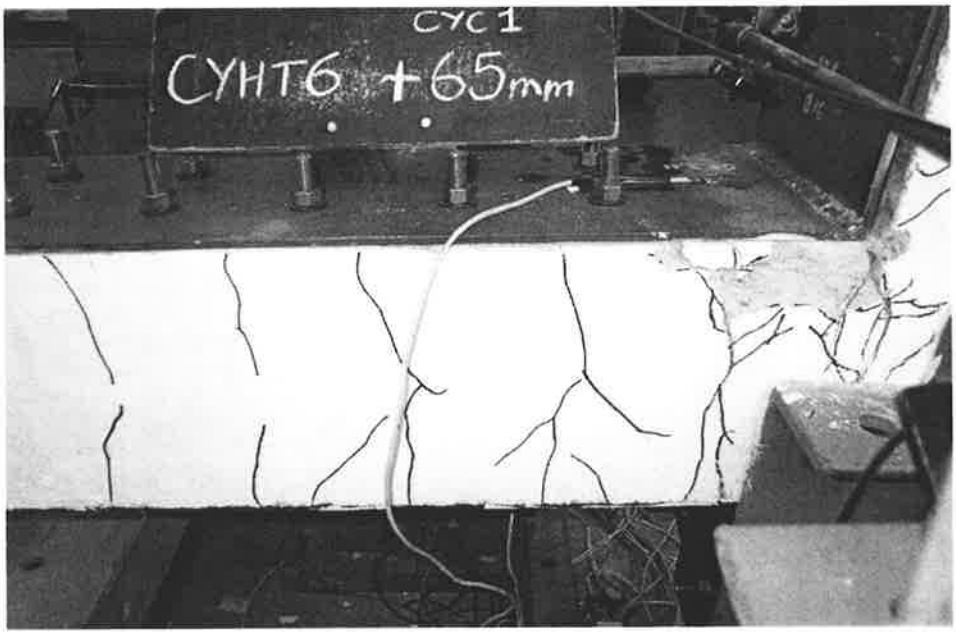

Fig. B.61 Rear view at -65mm displacement of 1st cycle for specimen 2BCP6G

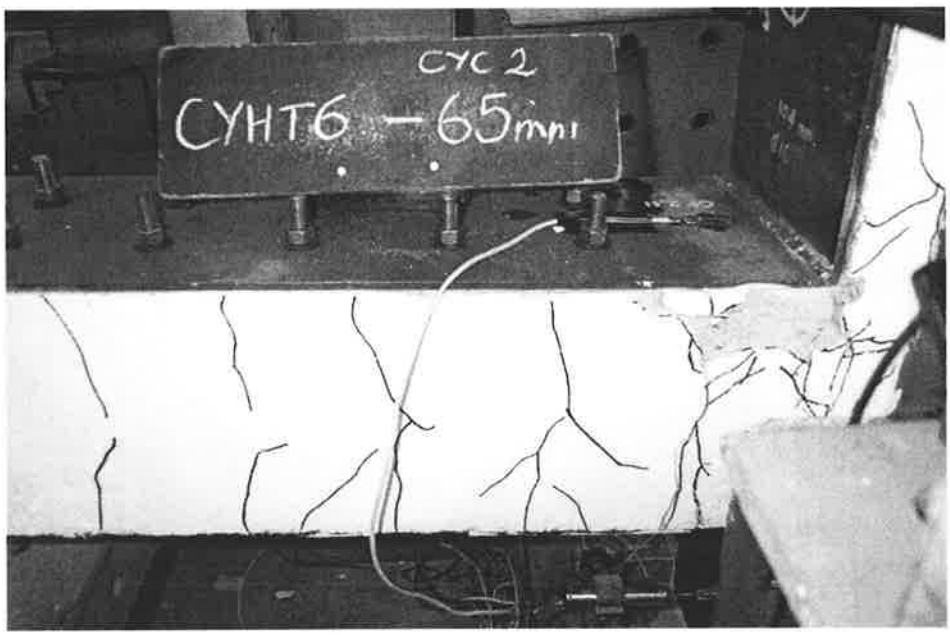

Fig. B.62 Rear view at +65mm displacement of 2nd cycle for specimen 2BCP6G

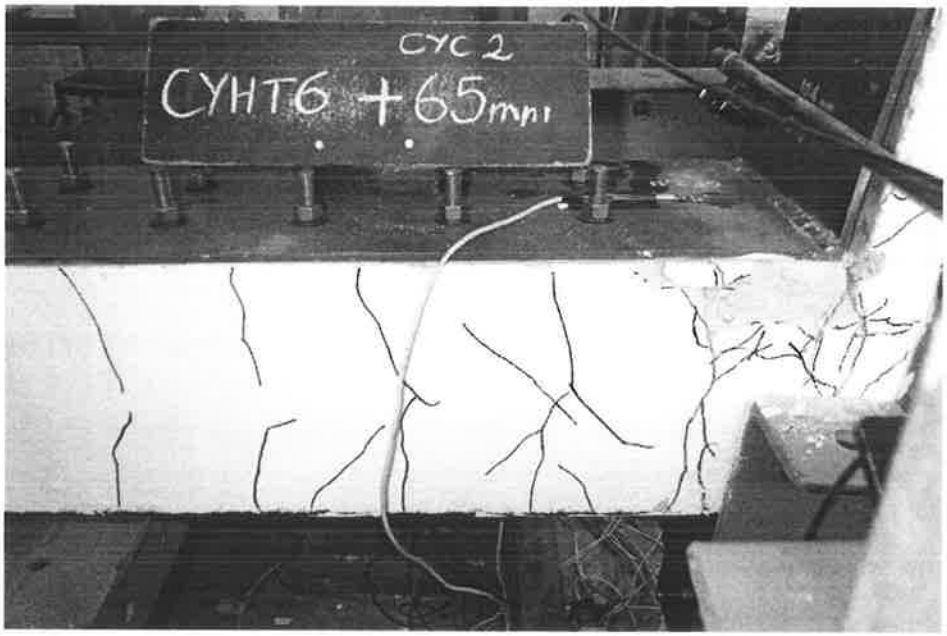

Fig. B.63 Rear view at -65mm displacement of 2nd cycle for specimen 2BCP6G

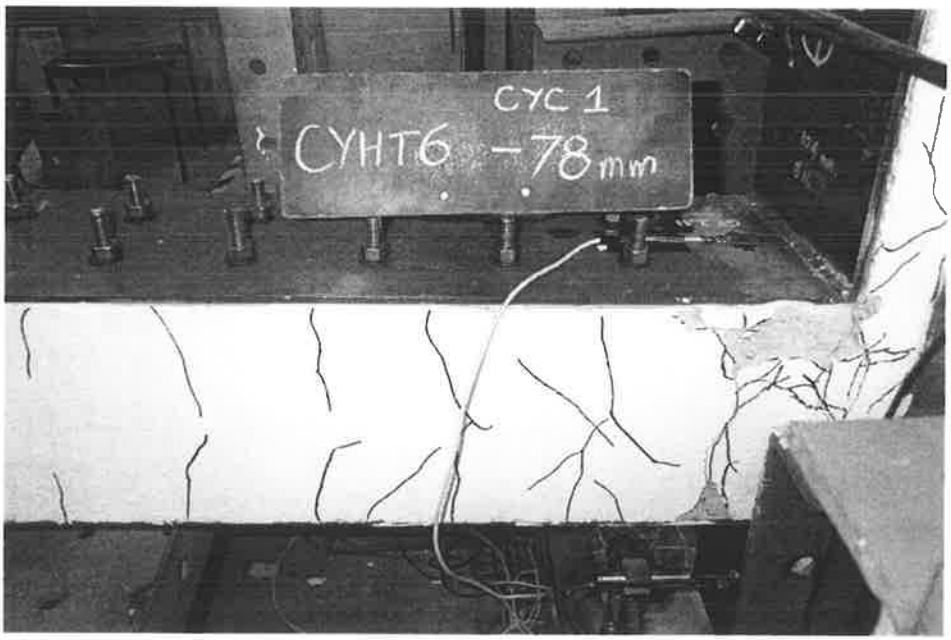

Fig. B.64 Rear view at +78mm displacement of 1st cycle for specimen 2BCP6G

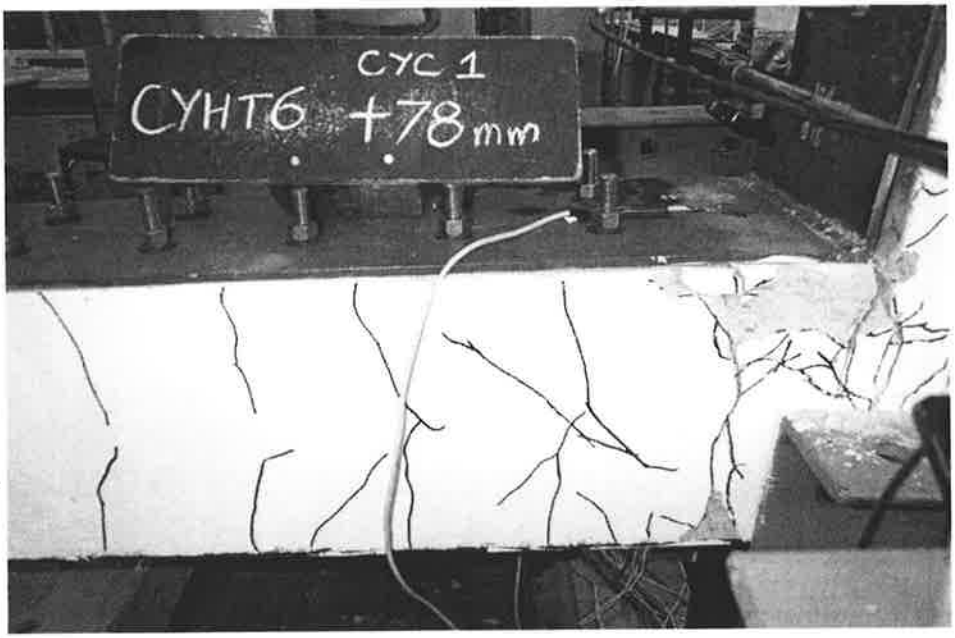

Fig. B.65 Rear view at -78mm displacement of 1st cycle for specimen 2BCP6G

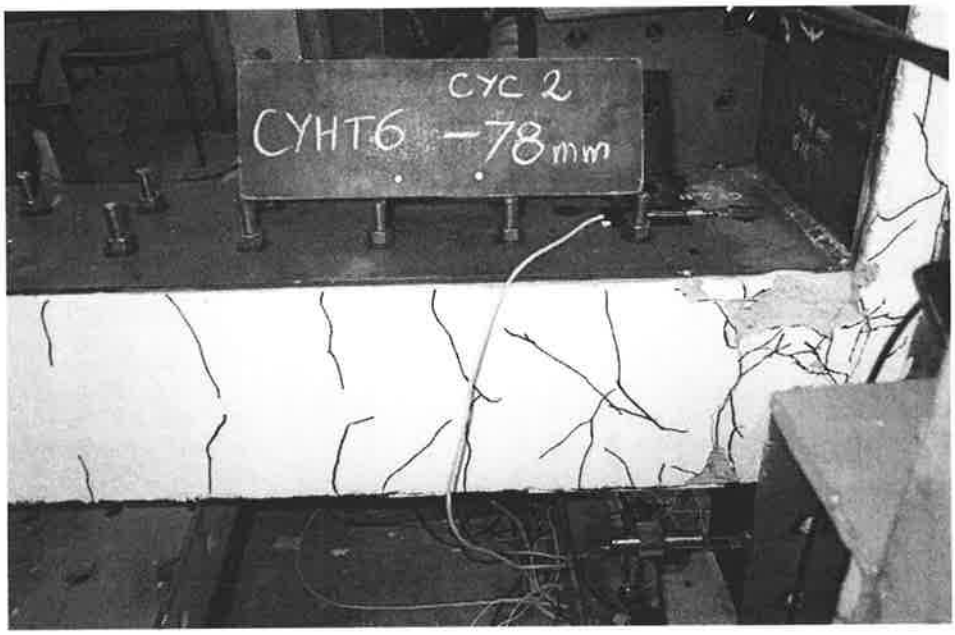

Fig. B.66 Rear view at +78mm displacement of 2nd cycle for specimen 2BCP6G

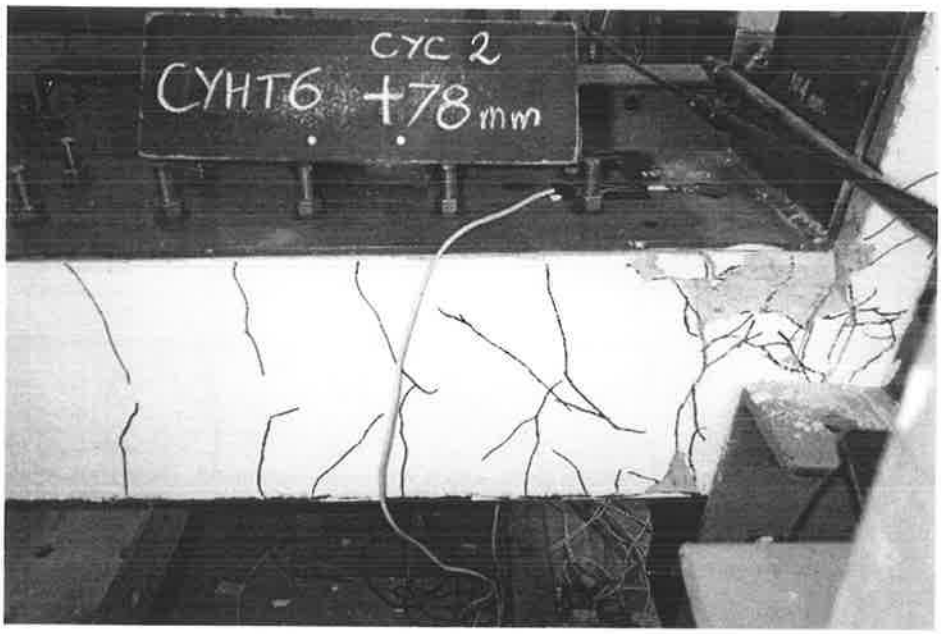

Fig. B.67 Rear view at -78mm displacement of 2nd cycle for specimen 2BCP6G

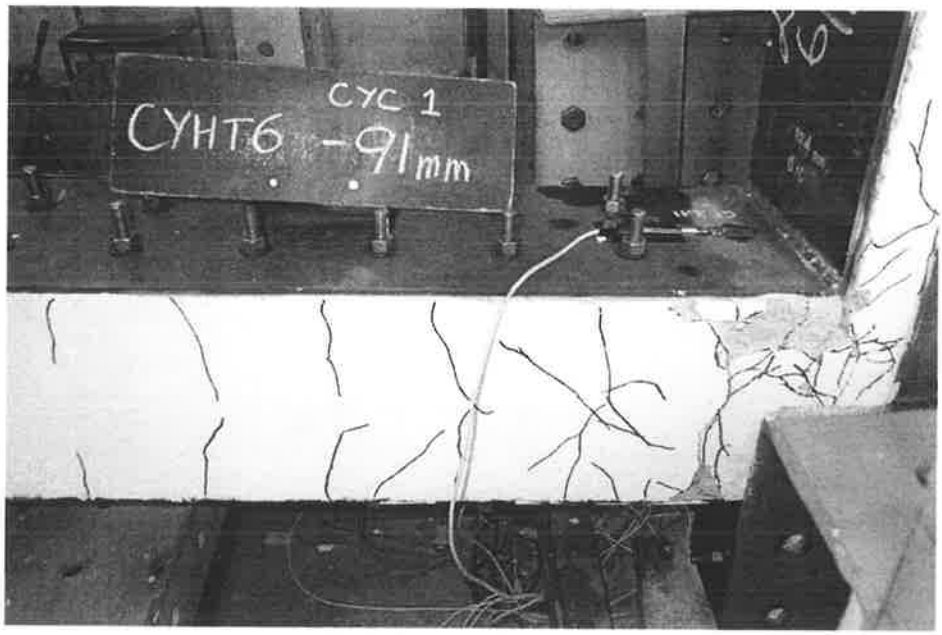

Fig. B.68 Rear view at +91mm displacement for specimen 2BCP6G

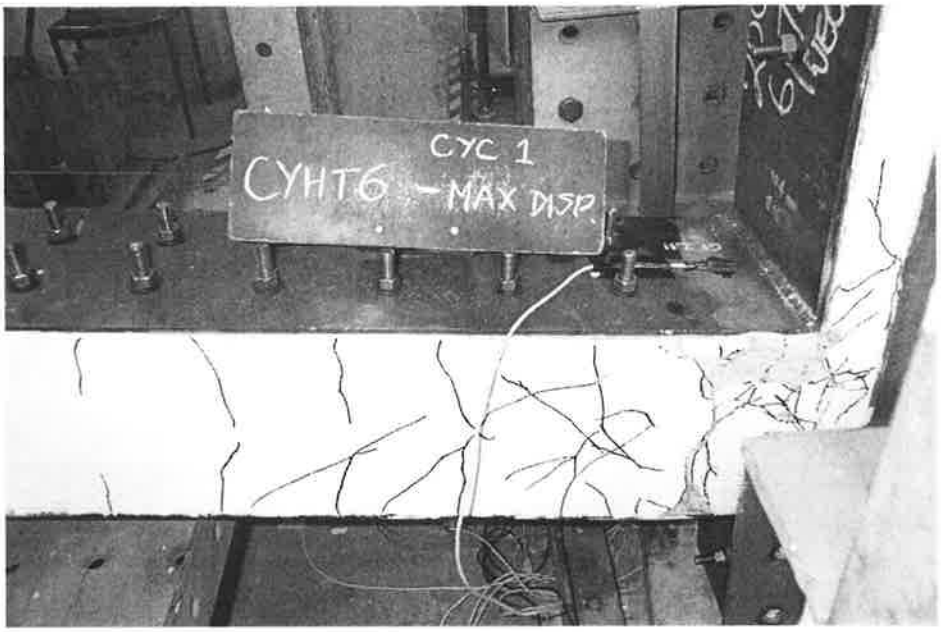

Fig. B.69 Rear view at +154mm displacement for specimen 2BCP6G

Fig. B.70 Front view at +154mm displacement for specimen 2BCP6G

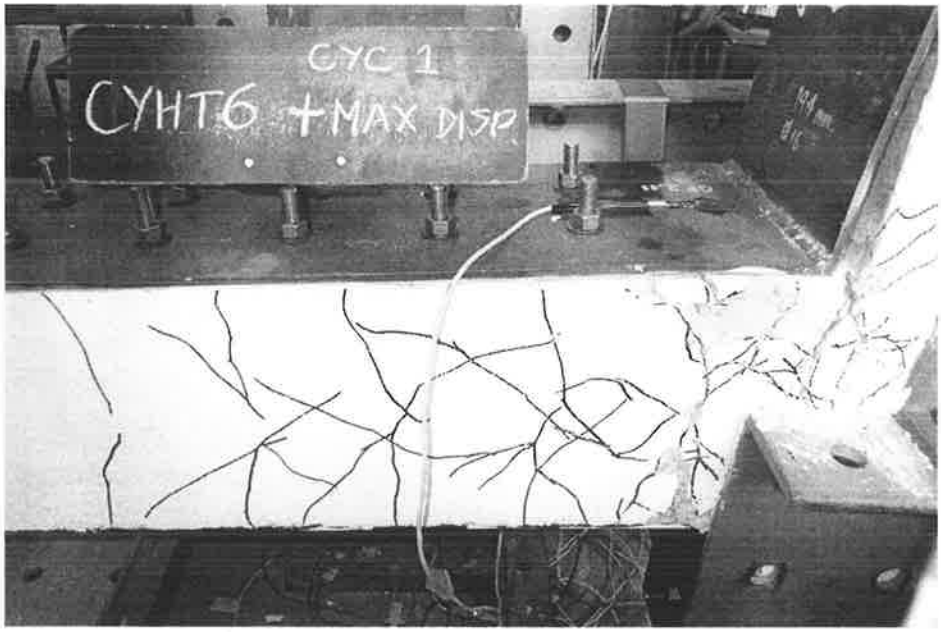

Fig. B.71 Rear view at -100mm displacement for specimen 2BCP6G

Fig. B.72 Front view at -100mm displacement for specimen 2BCP6G